TRANSACTIONS
OF THE ASME
Series E

Journal of APPLIED MECHANICS

June 1961

DYNAMICS • VIBRATIONS • ELASTICITY • LUBRICATION AND WEAR
RHEOLOGY • FRACTURES • STRUCTURES • HYDRAULICS • AERODYNAMICS
INTERNAL FLOW • MECHANICAL PROPERTIES OF METALS • THERMODYNAMICS
TURBULENCE • HEAT TRANSFER • COMPUTING DEVICES AND METHODS
BOUNDARY LAYERS • AEROELASTICITY • EXPERIMENTAL STRESS ANALYSIS

Published Quarterly by
THE AMERICAN SOCIETY OF MECHANICAL ENGINEERS

TRANSACTIONS OF THE ASME
Series E

EDITORIAL DEPARTMENT
Editor, J. J. JAKLITSCH, JR.
Consulting Editor, LEO BLOOGETT
Art Editor, HENRY BALFOUR
Production, HILDA K. WILGUS

APPLIED MECHANICS DIVISION
Chairman, A. M. WAHL
Secretary, E. REISSNER
Technical Editor, D. C. DRUCKER
Technical Editor, J. KESTIN
Honorary Editor, JOHN M. LESSELLS

OFFICERS OF THE ASME
President, W. H. BYRNE
Secretary, O. B. SCHIER, II
Treasurer, E. J. KATES
Assistant Treasurer, H. J. BAUER

PUBLICATIONS COMMITTEE
Chairman, HEMPLEY H. BLACKBURN
R. D. MINDLIN
MARTIN GOLAND
VITO L. SALERNO
F. J. HEINZE
Junior Representatives
J. W. FOLLANSBEE
STEWART H. ROSS

REGIONAL ADVISORY BOARD
Region I, H. M. ROGERS, JR.
Region II, ROBERT E. ABBOTT
Region III, A. F. BOCHENEK
Region IV, FRANCIS C. SMITH
Region V, WM. J. TITZEL
Region VI, C. R. EARLE
Region VII, RALPH L. SCORAH
Region VIII, G. CORRY McDONALD
Region IX, M. S. UMBENHAUER
Region X, CARL J. ECKHARDT

Published quarterly by The American Society of Mechanical Engineers. Publication office at 20th and Northampton Streets, Easton, Pa. The editorial department is located at the headquarters of the Society, 29 West Thirty-Ninth Street, New York 18, N. Y. Cable address, "Mechaneer," New York. Price $3.00 a copy, $10.00 annually; to members, $1.50 a copy, $5.00 annually. Add 50 cents for postage to all countries outside the United States and Canada. Changes of address must be received at Society headquarters seven weeks before they are to be effective on the mailing list. Please send old as well as new address. . . . By-Law: The Society shall not be responsible for statements or opinions advanced in papers or . . . printed in its publications (B13, Par. 4). . . . Second-class mail privileges authorized at Easton, Penna. . . . This publication is authorized to be mailed at the special rates of postage prescribed by Section 132.122 . . . © Copyrighted, 1961, by The American Society of Mechanical Engineers. Reprints from this publication may be made on condition that full credit be given the TRANSACTIONS OF THE ASME, Series E—Journal of Applied Mechanics, and the author, and that date of publication be stated.

TRANSACTIONS OF THE ASME
is indexed by the Engineering Index, Inc.

Journal of APPLIED MECHANICS

VOLUME 28 • SERIES E • NUMBER 2
June 1961

CONTENTS

TECHNICAL PAPERS

161 **On the Probability Densities of the Output of Some Random Systems** (60—WA-18)
Frank Kozin

165 **Transient Capillary Rise in Reduced and Zero-Gravity Fields** (60—WA-201)
Robert Siegel

171 **Minimum Transfer Time for a Power-Limited Rocket** (61—APM-6)
George Leitmann

179 **Adiabatic Analysis of Elastic, Centrally Pivoted, Sector, Thrust-Bearing Pads** (60—WA-104)
B. Sternlicht, G. K. Carter, and E. B. Arwas

188 **The Effect of a Longitudinal Gravitational Field on the Supercavitating Flow Over a Wedge** (61—APM-2)
A. J. Acosta

193 **On Transient Thermal Stresses in Viscoelastic Materials With Temperature-Dependent Properties** (60—WA-124)
Rokuro Muki and Eli Sternberg

208 **Thermodynamic Analysis of the Darcy Law** (61—APM-5)
R. G. Mokadam

213 **A Bifurcation Phenomenon of Static Friction** (61—APM-7)
F. F. Ling and R. S. Weiner

218 **Propagations of Elastic Waves Generated by Dynamical Loads on a Circular Cavity** (61—APM-12)
A. C. Eringen

223 **On Classical Plate Theory and Wave Propagation** (61—APM-3)
M. A. Medick

229 **Extensional Vibrations of Elastic Orthotropic Spherical Shells** (61—APM-14)
W. H. Hoppmann II and W. E. Baker

238 **Experiments on the Postbuckling Behavior of Square Plates Loaded in Edge Compression** (60—WA-103)
Noboru Yamaki

245 **Stress Distribution on the Boundary of a Circular Hole in a Large Plate During Passage of a Stress Pulse of Long Duration** (61—APM-4)
A. J. Durelli and W. F. Riley

252 **On the Aeroelastic Instability of Bluff Cylinders** (61—APM-8)
G. V. Parkinson and N. P. H. Brooks

259 **A Modification of the Coulomb-Mohr Theory of Fracture** (60—WA-31)
Burton Paul

269 **The Effect of Shear and Normal Forces on the Fully Plastic Moment of a Beam of Rectangular Cross Section** (60—WA-102)
B. G. Neal

275 **On Normal Vibrations of a General Class of Nonlinear Dual-Mode Systems**
R. M. Rosenberg

284 **Uniqueness in the Optimum Design of Structures** (61—APM-1)
T. C. Hu and R. T. Shield

288 **The Bending, Buckling, and Flexural Vibration of Simply Supported Polygonal Plates by Point-Matching** (60—WA-38)
H. D. Conway

(Continued on inside back cover)

On the Probability Densities of the Output of Some Random Systems

FRANK KOZIN
Professor,
Division of Engineering Sciences,
Purdue University,
Lafayette, Ind

The probability density, mean, and variance of the displacement of simple linear one-degree-of-freedom systems are investigated when the spring constants and the initial conditions are random variables. The ensemble mean motion is found to be considerably different from the "mean" motion obtained by first averaging over the spring constants. Furthermore, it is found that only the first and second moments of the initial conditions affect the first and second moments of the displacement.

THE SUBJECT of disordered systems, which has been of interest in the past in physics and physical chemistry, is gaining renewed interest in the fields of mechanical and electrical engineering [1].[1]

This is perhaps owing to the fact that we are becoming fully aware that we cannot measure exactly [2, 3], nor can we manufacture exactly. Therefore we can only know the parametric values governing a system, at best, within some predetermined range.

It would appear that the natural tools available to study systems, under this philosophy, can be found within the theory of probability.

In this paper we will treat the simple oscillating system without damping (damping presents no new problem and can be treated within the same framework). The spring constants are assumed to be randomly distributed among a discrete number of possible choices. Two sets of initial conditions will be studied, one random in nature, the other deterministic.

We will obtain the joint probability density of the displacement and velocity of the system by solving a partial differential equation known to physicists, but not too widely used in engineering literature. The derivation of the differential equation will be given in the Appendix.

We will derive and study graphically the mean and variance of the response of the system, and point out some interesting facts pertinent to each of these quantities.

Derivation of Joint Probability Density Function

Consider the system

$$\ddot{x}(t) + \omega^2 x(t) = 0$$
$$x(t_0) = x_0, \quad \dot{x}(t_0) = u_0 \tag{1}$$

where any of x_0, u_0, ω^2 may only be known probabilistically; that is, the joint probability density function $p_0(x, u, \omega^2)$ of the three parameters is given.

Our method is to reduce the system (1) to one of first-order differential equations

$$\dot{x}(t) = u(t)$$
$$\dot{u}(t) = -\omega^2 x(t) \tag{2}$$
$$x(t_0) = x_0, \quad u(t_0) = u_0$$

and study the system (2) in the phase space; that is, in the (x, u) space.

To determine the joint probability density function $p(x, u, \omega; t)$ we must solve (see Appendix) the initial value problem

$$\frac{\partial p}{\partial t} = -u \frac{\partial p}{\partial x} + \omega^2 x \frac{\partial p}{\partial u}$$
$$p(x, u, \omega;\ t_0) = p_0(x, u, \omega^2) \tag{3}$$

In order to solve (3), we study the first integrals of the associated La Grange system [4],

$$\frac{dt}{1} = \frac{dx}{u} = -\frac{du}{\omega^2 x} = \frac{dp}{0} \tag{4}$$

From (4), we have

$$p(x, u, \omega;\ t) = F[\varphi_x(x, u, t, t_0, \omega), \varphi_u(x, u, t, t_0, \omega), \omega^2] \tag{5}$$

where

$$x = \varphi_x(x_0, u_0, t, t_0, \omega) = x_0 \cos \omega(t - t_0) + \frac{u_0}{\omega} \sin \omega(t - t_0)$$
$$u = \varphi_u(x_0, u_0, t, t_0, \omega) \tag{6}$$
$$= -\omega x_0 \sin \omega(t - t_0) + u_0 \cos \omega(t - t_0)$$

are first integrals of the Lagrange system. The arbitrary function F must be determined by the initial condition.

Using the fact that

$$x_0 = \varphi_x(x, u, t_0, t, \omega) = x \cos \omega(t_0 - t) + \frac{u}{\omega} \sin \omega(t_0 - t)$$
$$u_0 = \varphi_u(x, u, t_0, t, \omega) \tag{7}$$
$$= -\omega x \sin \omega(t_0 - t) + u \cos \omega(t_0 - t)$$

for any t, we have

$$x = \varphi_x(x, u, t_0, t_0, \omega)$$
$$u = \varphi_u(x, u, t_0, t_0, \omega) \tag{8}$$

Making use of (8), our initial condition may be satisfied as follows:

$$p_0(x, u, \omega^2) = p(x, u, \omega;\ t_0)$$
$$= F[\varphi_x(x, u, t_0, t_0, \omega), \varphi_u(x, u, t_0, t_0, \omega), \omega^2] \tag{9}$$
$$= F(x, u, \omega^2)$$

[1] Numbers in brackets designate References at end of paper.

Contributed by the Applied Mechanics Division and presented at the Winter Annual Meeting, New York, N. Y., November 27–December 2, 1960, of THE AMERICAN SOCIETY OF MECHANICAL ENGINEERS.
Discussion of this paper should be addressed to the Editorial Department, ASME, 29 West 39th Street, New York, N. Y., and will be accepted until July 10, 1961. Discussion received after the closing date will be returned. Manuscript received by ASME Applied Mechanics Division, March 28, 1960. Paper No. 60—WA-18.

Thus F is determined and we have our final result

$$p(x, u, \omega;\ t) = p_0(\varphi_x, \varphi_\omega, \omega^2)$$
$$= p_0\left(x\cos\omega(t_0 - t) + \frac{u}{\omega}\sin\omega(t_0 - t),\right.$$
$$\left. -\omega x\sin\omega(t_0 - t) + u\cos\omega(t_0 - t), \omega^2\right) \quad (10)$$

Examples

In what follows we will consider two distinct cases, one with deterministic, the other with random initial conditions. In each case ω^2 is random, and in both cases all three quantities are assumed to be independent.

Case(a). For this case we assume that x_0 and u_0 are deterministic with values 0 and 1 for $t_0 = 0$. Also, ω^2 can take the value ω_i^2 with probability p_i, $i = 1, \ldots, n$. Therefore,

$$p_0(x, u, \omega^2) = \delta(x)\delta(u - 1)\sum_{i=1}^{n} p_i\delta(\omega^2 - \omega_i^2) \quad (11)$$

where $1 = \sum_{i=1}^{n} p_i$, and δ is the impulse function. For this case (10) yields

$$p(x, u, \omega;\ t) = \delta\left(x\cos\omega t - \frac{u}{\omega}\sin\omega t\right)\delta(\omega x\sin\omega t$$
$$+ u\cos\omega t - 1)\sum_{i=1}^{n} p_i\delta(\omega^2 - \omega_i^2) \quad (12)$$

We shall determine the mean and the variance of the displacement; that is

$$\overline{x(t)} = E[x(t)], \quad \sigma^2(t) = E[x^2(t)] - \overline{x(t)}^2 \quad (13)$$

For the mean

$$\overline{x(t)} = \int dx \int du \int d\omega^2 x\left\{\delta\left(x\cos\omega t - \frac{u}{\omega}\sin\omega t\right)\right.$$
$$\left.\delta(\omega x\sin\omega t + u\cos\omega t - 1)\sum_{i=1}^{n} p_i\delta(\omega^2 - \omega_i^2)\right\} \quad (14)$$

We integrate out the u variable first. We can only have a contribution within this integration if

$$u = \omega x\frac{\cos\omega t}{\sin\omega t} = \frac{1 - \omega x\sin\omega t}{\cos\omega t} \quad (15)$$

and thus for

$$x = \frac{\sin\omega t}{\omega}$$

The integral (14) becomes

$$\bar{x} = \int dx \int d\omega^2 x\left\{\delta\left(x - \frac{\sin\omega t}{\omega}\right)\sum_{i=1}^{n} p_i\delta(\omega^2 - \omega_i^2)\right\}$$
$$= \int d\omega^2\left\{\frac{\sin\omega t}{\omega}\sum_{i=1}^{n} p_i\delta(\omega^2 - \omega_i^2)\right\} \quad (16)$$
$$= \sum_{i=1}^{n} p_i\frac{\sin\omega_i t}{\omega_i}$$

In exactly the same fashion one finds that

$$E[x^2(t)] = \int dx \int du \int d\omega^2 x^2\left\{\delta\left(x\cos\omega t - \frac{u}{\omega}\sin\omega t\right)\right.$$
$$\left.\cdot\delta(\omega x\sin\omega t + u\cos\omega t - 1)\sum_{i=1}^{n} p_i\delta(\omega^2 - \omega_i^2)\right\} \quad (17)$$
$$= \sum_{i=1}^{n} p_i\left(\frac{\sin\omega_i t}{\omega_i}\right)^2$$

Hence the variance is given as

$$\sigma^2(t) = \sum_{i=1}^{n} p_i\left(\frac{\sin\omega_i t}{\omega_i}\right)^2 - \left(\sum_{i=1}^{n} p_i\frac{\sin\omega_i t}{\omega_i}\right)^2 \quad (18)$$

Case (b). For this case x_0 is Gaussian with mean zero and variance one, and u_0 is Gaussian with mean and variance both one. All other hypotheses are identical to Case (*a*).

Therefore for this case we have

$$p_0(x, u, \omega^2) = \frac{1}{2\pi}e^{-\frac{x^2 + (u-1)^2}{2}}\sum_{i=1}^{n} p_i\delta(\omega^2 - \omega_i^2) \quad (19)$$

As in Case (*a*) we will determine the mean and the variance of the displacement.

By straightforward calculations, we find

$$\overline{x(t)} = \frac{1}{2\pi}\int dx \int du \int d\omega^2 x$$
$$\left\{\exp - {}^1/_2\left[\left(x\cos\omega t - \frac{u}{\omega}\sin\omega t\right)^2\right.\right.$$
$$\left.\left. + (\omega x\sin\omega t + u\cos\omega t - 1)^2\right]\sum_{i=1}^{n} p_i\delta(\omega^2 - \omega_i^2)\right\} \quad (20)$$
$$= \int d\omega^2\left\{\frac{\sin\omega t}{\omega}\sum_{i=1}^{n} p_i\delta(\omega^2 - \omega_i^2)\right\}$$
$$= \sum_{i=1}^{n} p_i\frac{\sin\omega_i t}{\omega_i}$$

And similarly,

$$E[x^2(t)] = \frac{1}{2\pi}\int dx \int du \int d\omega^2 x^2$$
$$\left\{\exp - {}^1/_2\left[\left(x\cos\omega t - \frac{u}{\omega}\sin\omega t\right)^2\right.\right.$$
$$\left.\left. + (\omega x\sin\omega t + u\cos\omega t - 1)^2\right]\cdot\sum_{i=1}^{n} p_i\delta(\omega^2 - \omega_i^2)\right\} \quad (21)$$
$$= \sum_{i=1}^{n} p_i\left[\cos^2\omega_i t + \frac{\sin^2\omega_i t}{\omega_i^2}\right]$$

The results (20) and (21), together, yield the variance

$$\sigma^2(t) = \sum_{i=1}^{n} p_i\left[\cos^2\omega_i t + \frac{\sin^2\omega_i t}{\omega_i^2}\right]$$
$$- \left(\sum_{i=1}^{n} p_i\frac{\sin\omega_i t}{\omega_i}\right)^2 \quad (22)$$

Results and Discussion

Before entering into a general discussion of the results of the preceding section, we wish to comment upon the fact that the

means in each case are the same. This is by no means a coincidence, as the following lemma shows.

Lemma. Let (x, u) be the solution of the system (2), with arbitrary initial probability density function $p_0(x, u)p_\omega(\omega^2)$ with means $\bar{x}_0$, $\bar{u}_0$, then $E[x(t)]$, $E[u(t)]$ are independent of $p_0(x, u)$.

Proof. We show the proof for $E[x(t)]$, since $E[u(t)]$ would follow in the same fashion. Now

$$E[x(t)] = \int dx \int du \int d\omega^2 x \left\{ p_0 \left(x \cos \omega t - \frac{u}{\omega} \sin \omega t, \omega x \sin \omega t + u \cos \omega t \right) p_\omega(\omega^2) \right\} \quad (23)$$

We make the transformation,

$$\xi = x \cos \omega t - \frac{u}{\omega} \sin \omega t \quad (24)$$

$$\eta = \omega x \sin \omega t + u \cos \omega t$$

$$\omega = \omega$$

Therefore the Jacobian is

$$J = \begin{vmatrix} \cos \omega t & \frac{\sin \omega t}{\omega} & \frac{\partial x}{\partial \omega} \\ -\omega \sin \omega t & \cos \omega t & \frac{\partial u}{\partial \omega} \\ 0 & 0 & 1 \end{vmatrix} = 1 \quad (25)$$

Hence,

$$E[x(t)] = \int d\xi \int d\eta \int d\omega^2 \left\{ \left(\xi \cos \omega t + \eta \frac{\sin \omega t}{\omega} \right) p_0(\xi, \eta) p_\omega(\omega^2) \right\}$$

$$= \bar{x}_0 \int d\omega^2 \{ \cos \omega t \, p_\omega(\omega^2) \} + \bar{u}_0 \int d\omega^2 \left\{ \frac{\sin \omega t}{\omega} p_\omega(\omega^2) \right\} \quad (26)$$

Q.E.D.

We notice also using the foregoing method that if x_0 and u_0 are independent of one another

$$E[x^2(t)] = \bar{x}_0^2 \int d\omega^2 \{ \cos^2 \omega t p_\omega(\omega^2) \} + 2\bar{x}_0 \bar{u}_0 \int d\omega^2 \left\{ \frac{\sin \omega t \cos \omega t}{\omega} p_\omega(\omega^2) \right\} + \bar{u}_0^2 \int d\omega^2 \left\{ \frac{\sin^2 \omega t}{\omega^2} p_\omega(\omega^2) \right\} \quad (27)$$

Hence the variance is also independent of the initial distribution of displacement and velocity. It is a function only of the first and second moments.

These results concerning the single linear oscillator show that the response depends mainly upon the distributions of the parameter values and not upon the distributions of the initial conditions. After a little reflection, it can be seen readily that the foregoing is true owing to the fact that the initial conditions enter into the solution only as a linear coefficients. Therefore we can conclude that the same is true of the arbitrary linear system with random constant coefficients due to the fact that the initial conditions enter into the solution linearly. Therefore the average displacement or velocity of the linear system depends only upon the average values of the initial conditions and not upon how they are distributed.

Along with the mean and variance, another function is basic when studying second-order random properties. This is the covariance function $\Gamma(t_1, t_2)$, defined as,

$$\Gamma(t_1, t_2) = E[x(t_1)x(t_2)] - E[x(t_1)]E[x(t_2)] \quad (28)$$

For our cases,

$$\Gamma(t_1, t_2) = \bar{x}_0^2 \int d\omega^2 \left\{ \cos \omega(t_1 - t_0) \cos \omega(t_2 - t_0) \sum_{i=1}^{n} p_i \delta(\omega^2 - \omega_i^2) \right\} + \frac{\bar{x}_0 \bar{u}_0}{\omega} \int d\omega^2 \left\{ \sin \omega(t_1 + t_2 - 2t_0) \sum_{i=1}^{n} p_i \delta(\omega^2 - \omega_i^2) \right\} + \frac{\bar{u}_0^2}{\omega^2} \int d\omega^2 \left\{ \sin \omega(t_1 - t_0) \cos \omega(t_2 - t_0) \sum_{i=1}^{n} p_i \delta(\omega^2 - \omega_i^2) \right\} - E[x(t_1)]E[x(t_2)] \quad (29)$$

We notice that spectral density techniques are useless here since the covariance function is not a function of $t_2 - t_1$, but depends upon each value. Hence the power spectral density function does not exist.

Now let us consider numerically the results of the section, "Derivation of Joint Probability Function." For the graphs, Fig. 1, the mean (16) and variances (18) and (22) are plotted in the dimensionless forms

$$F_1(\tau) = \sum_{i=1}^{n} p_i \left(\frac{\sin \frac{\omega_i}{\omega_0} \tau}{\frac{\omega_i}{\omega_0}} \right)$$

$$F_2(\tau) = \sum_{i=1}^{n} p_i \left(\frac{\sin \frac{\omega_i}{\omega_0} \tau}{\frac{\omega_i}{\omega_0}} \right)^2 - \left(\sum_{i=1}^{n} p_i \frac{\sin \frac{\omega_i}{\omega_0} \tau}{\frac{\omega_i}{\omega_0}} \right)^2 \quad (30)$$

$$F_3(\tau) = \sum_{i=1}^{n} p_i \left[\cos^2 \frac{\omega_i}{\omega_0} \tau + \frac{\sin \frac{\omega_i}{\omega_0} \tau}{\left(\frac{\omega_i}{\omega_0} \right)^2} \right] - \left(\sum_{i=1}^{n} p_i \frac{\sin \frac{\omega_i}{\omega_0} \tau}{\frac{\omega_i}{\omega_0}} \right)^2$$

The discrete distribution of the ω_i^2 was taken to approximate the one-dimensional Gaussian distribution. The probabilities of the $(\omega_i/\omega_0)^2$ taking the values $1 - 3\Delta_0$, $1 - 2\Delta_0$, $1 - \Delta_0$, 1, $1 + \Delta_0$, $1 + 2\Delta_0$, $1 + 3\Delta_0$ are, respectively, 0.0060, 0.0606, 0.2417, 0.3834, 0.2417, 0.0606, and 0.0060. The mean is 1 and the standard deviation is 0.052 with $\Delta_0 = 0.05$.

The general properties of the graphs in Fig. 1 are that of high-frequency oscillations superimposed upon that of a low-frequency oscillation. For $\tau \approx 125$ the graphs repeat as mirror images. Thus the total period of the low-frequency oscillation is $\tau \approx 250$. Notice that the high-frequency oscillations of the variances are approximately two times that of the high-frequency oscillations of the mean. Furthermore, zero mean corresponds to the maxima of the variances and the stationary points of the mean correspond to the minima of the variances. Hence when the mean is zero the range of values the displacement can take is largest and when the mean is stationary the range of values the displacement can take is smallest. The foregoing comments are rather obvious results that can be inferred directly from the

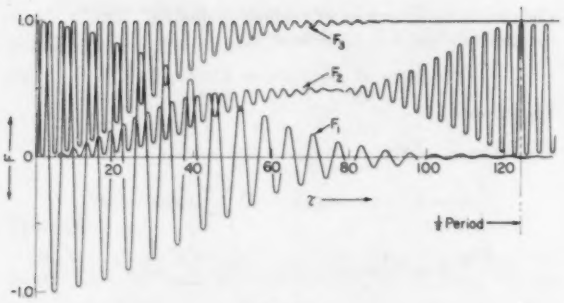

Fig. 1

graphs in Fig. 1. However, there is one important feature that stands out above the rest, concerning the mean motion itself. The mean motion is *not* the simple oscillatory motion that one would obtain by averaging on the ω first and then obtaining the solution of the "averaged" equation. Therefore, upon consideration of this type of motion obtained by first averaging on the ω-values, one finds a rather distinct error between it and the actual ensemble average motion of the system. This certainly is an illustration of the fact that care must be taken in applying average methods to large batches of oscillators.

Conclusion

We have presented a methodological approach to the study of a simple random system. This approach yields the first probability density function in the phase space of the system. Hence any statistical property that can be derived from this probability function can be studied explicitly. The method presented is by no means limited to the case treated. In subsequent studies the method will be applied to various types of linear, nonlinear, free, forced, and coupled random systems. It is our feeling that this type of analysis will be of value in modern engineering design procedure.

Acknowledgment

The author wishes to express his gratitude to Prof. J. L. Bogdanoff for his very helpful discussions and advice concerning this study.

References

1 P. F. Chenea and J. L. Bogdanoff, "Impedance of Some Disordered Systems," Colloquium on Mechanical Impedance Methods for Mechanical Vibrations, ASME Annual Meeting, 1958.

2 M. Born, "Continuity, Determinism, and Reality," *Kgl. Danske Videnskabernes Selskabs Matematisk-Fysiske Meddelelser*, vol. 30, 1955, pp. 1–26.

3 L. Brillouin, "Inevitable Experimental Errors, Determinism, and Information Theory," *Information and Control*, vol. 2, 1959, pp. 45–63.

4 E. Goursat, "Differential Equations," Dover Publications, Inc., New York, N. Y., 1959, translated by E. Hedrick and O. Dunbell.

5 B. G. Dostupov and V. S. Pugachev, "The Equation for the Integral of a System of Ordinary Differential Equations Containing Random Parameters," *Automatika i Telemekhanika*, vol. 18, 1957, p. 620.

6 M. S. Bartlett, "Stochastic Processes," Cambridge University Press, Cambridge, England, 1955.

APPENDIX

This Appendix is devoted to the derivation of the partial differential equation satisfied by the density function.

In a recent paper Dostupov and Pugachev [5] studied the system

$$\begin{aligned} \dot{x}_1 &= f_1(x_1, \ldots, x_n;\ V_1, \ldots, V_m;\ t) \\ &\vdots \\ \dot{x}_n &= f_n(x_1, \ldots, x_n;\ V_1, \ldots, V_m;\ t) \end{aligned} \tag{31}$$

where the V_i, $i = 1 \ldots, m$, are random parameters with a known joint probability density function. Using the theory of transformations of function of real variables, they derive what is essentially the Liouville equation, having as a solution the joint density function $p(x_1, \ldots, x_n;\ V_1, \ldots, V_m;\ t)$ in the phase space of solution of the system (31).

We shall develop the same equation starting with the probability concept of the characteristic function.

We define the characteristic function Φ as,

$$\Phi(\theta_1, \ldots, \theta_n;\ \varphi_1, \ldots, \varphi_m;\ t) = E\left[\exp i\left(\sum_{j=1}^{n} \theta_j x_j(t) + \sum_{k=1}^{m} \phi_k V_k\right)\right], \qquad i = \sqrt{-1} \tag{32}$$

This is essentially the Fourier transform of the probability density function $p(x, \ldots, x_n;\ V_1, \ldots, V_m;\ t)$. Equation (32) can be differentiated with respect to t to yield

$$\frac{\partial \Phi}{\partial t} = E\left[i \sum_{j=1}^{n} \theta_j \dot{x}_j(t) \exp i\left(\sum_{j=1}^{n} \theta_j x_j(t) + \sum_{k=1}^{m} \varphi_k V_k\right)\right] \tag{33}$$

Using (31), one obtains

$$\begin{aligned} \frac{\partial \Phi}{\partial t} &= E\left[i \sum_{j=1}^{n} \theta_j f_j \exp i\left(\sum_{j=1}^{n} \theta_j x_j(t) + \sum_{k=1}^{m} \varphi_k V_k\right)\right] \\ &= i \sum_{i=1}^{n} \theta_i E\left[f_j \exp i\left(\sum_{j=1}^{n} \theta_j x_j(t) + \sum_{k=1}^{m} \varphi_k V_k\right)\right] \end{aligned} \tag{34}$$

Upon taking the inverse Fourier transform of equation (34), we have

$$\frac{\partial p(x_1), \ldots, x_n;\ V_1, \ldots, V_m;\ t)}{\partial t} = -\sum_{j=1}^{n} \frac{\partial [f_j(x_1, \ldots, x_n;\ V_1, \ldots, V_m;\ t) \cdot p(x_1, \ldots, x_n;\ V_1, \ldots, V_m;\ t)]}{\partial x_j} \tag{35}$$

Having given the initial probability density function $p_0(x_1, \ldots, x_n;\ V_1, \ldots, V_m;\ t_0)$, the problem of determining $p(x_1, \ldots, x_n;\ V_1, \ldots, V_m;\ t)$, from equation (35) becomes the initial value problem for first-order partial differential equations.

We mention here that a generalization of the foregoing procedure due to Bartlett [6] has many far-reaching applications to systems in which the coefficients are random functions rather than random parameters.

Transient Capillary Rise in Reduced and Zero-Gravity Fields

ROBERT SIEGEL
Lewis Research Center,
NASA, Cleveland, Ohio.
Mem. ASME

Experimental information is given on the transient "capillary" rise of water into vertical tubes subjected to reduced and zero-gravity fields. The tubes ranged in internal diameter from 0.075 to 1.295 in. The response in a low-gravity environment is of interest in studying the behavior of liquid systems for space vehicles. An approximate analysis is presented to aid in the interpretation of the data and predict the transient rise. Photographs are given which illustrate the behavior in short tubes where the water is able to move beyond the top of the tube during part of the zero-gravity period.

When the end of a tube or piece of porous material is immersed in liquid which wets the surface, capillary action will cause the liquid to penetrate into the tube or material. An understanding of the dynamics of this penetration process arising from the surface-tension force is of importance, for example, in soil mechanics, the wetting of textiles, and in lubrication. Consequently, there is a fairly extensive literature on this subject. A few of the references pertinent to the present study are [1] to [3],[1] and these in turn provide additional bibliography of general interest.

The present interest in capillary motion arose in connection with liquid systems for use in space-flight applications. In a satellite or space vehicle an environment may be encountered with a very low or zero-gravity field. In this instance the weight of the liquid becomes very small, and if the fluid has a free surface, the surface tension may have a significant effect in moving the liquid about. An experiment by Reynolds [4] has demonstrated how important the surface tension can be under reduced gravity conditions. A container with a small pool of mercury in it was allowed to fall freely a distance of several feet. Photographs of the behavior in the resulting zero-gravity field showed that the surface tension caused the mercury to lift itself from the bottom of the container and form a mass suspended away from the surface. If a container is partially filled with liquid that wets the walls, then in zero gravity, surface tension will cause the fluid to creep over the internal surfaces of the container. For this type of behavior Benedikt [5] has briefly discussed the interaction of surface tension with the inertia and viscous forces. The purpose of this paper is to obtain additional information on this type of interaction. The situation which was selected for experimental study was the rise of a liquid from a reservoir into vertical tubes.

The equilibrium height to which liquid will rise in a vertical tube is given by the relation

$$L = \frac{2\sigma \cos \theta}{a\rho g} \tag{1}$$

This is found by simply equating the upward surface-tension force with the downward gravity force acting on the liquid column. It is obvious that the rise of the liquid will become very great as g approaches zero. One way of studying the influence of reduced gravity is simply to incline the tube [1]. For a horizontal capillary, the surface-tension force is no longer opposed by the gravity field and the liquid can theoretically creep for an infinite distance along the tube. Experimentally it is found that at large penetrations there may be a very slow irregular motion or the flow may cease because of a "sticking" friction. It would not be possible to conduct this type of experiment with large-diameter tubes. The present work utilizes a falling-platform type of experimental equipment in which large-diameter tubes can be studied. The experimental equipment will first be described. Experimental results for long tubes will then be given, and an approximate analysis will be presented to help interpret the behavior. Then tubes will be considered which are sufficiently short so that, during the period of zero gravity, liquid fills the tube and begins to move out of the top end. Photographs are given to illustrate this process.

Experimental Apparatus

The experimental equipment used here has been described in detail in two previous papers [6] and [7] which are concerned with boiling heat transfer in reduced and zero-gravity fields. Hence only a brief description need be given here. A sketch of

[1] Numbers in brackets designate References at end of paper.

Contributed by the Applied Mechanics Division and presented at the Winter Annual Meeting, New York, N. Y., November 27–December 2, 1960, of The American Society of Mechanical Engineers.

Discussion of this paper should be addressed to the Editorial Department, ASME, 29 West 39th Street, New York, N. Y., and will be accepted until July 10, 1961. Discussion received after the closing date will be returned. Manuscript received by ASME Applied Mechanics Division, July 8, 1960. Paper No. 60—WA-201.

Nomenclature

a = tube radius
g = gravity field, ng_0
g_0 = earth gravity, 32.16 ft/sec²
h = depth of tube entrance below fluid level in reservoir
K = loss coefficient for developing laminar profile in entrance region
L = equilibrium height of liquid in tube above level in reservoir
m = coefficient in expression for decreased surface tension
n = fraction of earth gravity, g/g_0
p = static pressure; p_1, atmospheric pressure
t = time
Z = dependent variable defined as z^2
z = fluid height above tube entrance; z_0, initial height
β = coefficient of $(dz/dt)^2$ term in equation of motion
γ = coefficient of term representi. g inertia of fluid in reservoir
θ = contact angle
ν = kinematic viscosity
ρ = mass density
σ = surface tension

the equipment is shown in Fig. 1. It consists of a cross-shaped platform which can be raised and then dropped a distance of 9 ft. At the end of the fall, metal spikes attached to the bottom of the platform penetrate into a sand bed and stop the equipment. During free fall all gravity forces vanish in the frame of reference of the apparatus. For fractional gravity fields the platform is partially counterweighted. A high-speed motion-picture camera is mounted on the platform so that the action of the fluid system under study can be observed.

The experiments were all conducted using distilled water at room temperature (75 F). A small amount of powdered red dye was dissolved in the water to aid in photographing the fluid. The surface tensions of the water with and without dye were compared with a tensiometer and the dye was found to have no effect. The colored water was placed in a rectangular tank about 6 in. long and 4 in. wide which had lucite windows in the front and back faces. The back window was frosted so that a light could be placed behind it to provide back illumination for the motion pictures.

The tests conducted with long tubes will be discussed now, and information on the behavior in short tubes will be presented later. Glass tubes with seven different internal diameters were used during the experiment; 0.075, 0.129, 0.196, 0.269, 0.317, 0.750, and 1.295 in. The tubes were mounted on two lucite sheets, the five smaller tubes being in one group and the two large ones in a second group. One group of tubes was tested at a time. The tubes were about 8 in. long and the lucite sheet which held them was clamped to the reservoir so that the tubes extended $^1/_2$ in. below the water surface for the five small tubes, and $^3/_4$ in. for the two large tubes. The tube entrances were flared to form a bell-mouth entry so that the flow would enter smoothly.

The experimental procedure was as follows: The tank was cleaned thoroughly and then partially filled with dyed distilled water. The glass tubes were cleaned with chromic-acid solution, rinsed with distilled water, and dried with clean warm air. The platform was then raised into position 9 ft above the sand bed. The lucite sheet holding the tubes was carefully lowered into the reservoir. The high-speed motion-picture camera was started and $^1/_2$ sec later the platform was released. Each test was repeated two or three times.

Experimental Results for Long Tubes

The rise of the water into the tubes was measured from the motion-picture films. A measuring scale had been mounted next to the tubes as a scale of reference. The film viewer used to make the measurements was equipped with movable micrometer hairlines so that the liquid levels could be found very accurately. Measurements were made of the change of each liquid level from its initial height as a function of time. To fix the time scale during the transient period, a timing light within the camera had placed a mark on the film every $^1/_{120}$ sec. A vertical measuring scale which was fixed in space was also in the viewing field of the camera. The zero time for the beginning of the transient process could be detected when this fixed scale started to move in the motion picture. As far as could be determined, the initial liquid heights in the tubes were in agreement with those predicted by equation (1). For the tubes with large diameters, the initial rise was so small that it could not be measured with reasonable accuracy.

Gravity Field of 12.6 Per Cent. In Fig. 2, results are given for the fluid rise which occurred after the gravity field was suddenly reduced to 12.6 per cent of normal gravity. This gravity field was obtained by partially counterweighting the platform. The data represent an average of two runs. The scatter between the runs ranged from 5 to 15 per cent for the various tubes, except for the first few tenths of a second where the percentage differences were

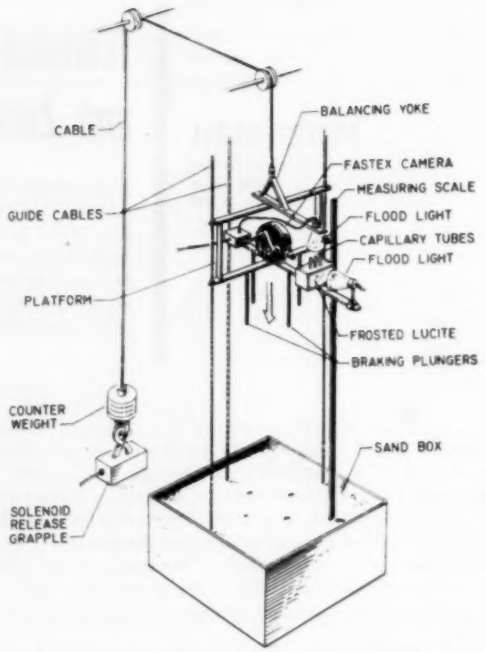

Fig. 1 Schematic diagram of counterweighted platform

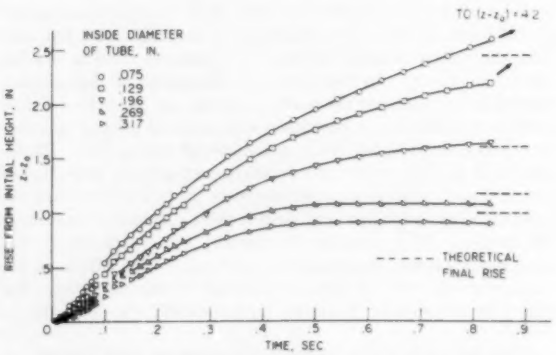

Fig. 2 Experimental capillary rise following a sudden change from normal gravity to 12.6 per cent gravity

sometimes much larger because of the small heights involved. When comparing different runs, sometimes the liquid would start moving a little more slowly one time than another. However, after an initial period of 0.2 sec or so, the data became reasonably reproducible. As discussed in [1], the action of the surface-tension force is generally somewhat irregular so that better reproducibility might not be expected. The horizontal lines at the ends of the curves give the theoretical final rise which was computed from equation (1) by determining the final height and subtracting the original height. Within the short duration of the drop, three of the tubes were able to attain their final equilibrium heights.

Zero Gravity. Fig. 3 shows the response in a zero-gravity field. This figure provides information for the two large-diameter tubes as well as for the five smaller ones given in Fig. 2. The two largest tubes were not tested in 12.6 per cent gravity because the equilibrium heights were so small that good accuracy could not

be obtained. It is noted that, for the small-diameter tubes, there is some crossing of the curves for zero gravity. This crossing was noted in each individual run so that the averaging of the data did not distort this behavior. The data for the five small tubes are an average of two runs while those for the two large tubes represent an average of three runs. For the largest tube, which was more than 1 in. diam, the transient response was sufficiently rapid so that a substantial rise could be observed during the short duration of the experiment. The reason why the rise in the largest tube is somewhat irregular for small times is not known.

Analysis for Long Tubes

As mentioned in [1] a number of analyses have been made to try to predict the transient movement of liquids into vertical, inclined, and horizontal capillaries. These analyses have not been very successful and generally predict penetration velocities much larger than those which actually occur. In [2] it is proposed that there are turbulent losses in the fluid which would yield lower penetration rates when taken into account. In [3], the author feels that turbulence would not be present due to the low Reynolds numbers involved, and says that if all the drag and inertia forces are taken into account good results are obtained. We shall then start with the equation proposed in [3] as it is simple enough to yield a closed solution for the zero-gravity case.

The co-ordinate system used in the analysis is shown in Fig. 4. According to [3] we equate the following terms:

Surface-tension force $= 2\pi a\sigma \cos\theta$

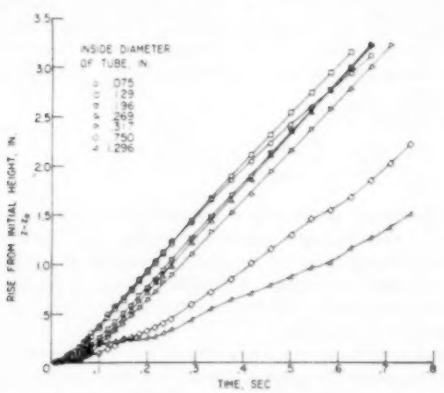

Fig. 3 Experimental capillary rise following a sudden change from normal gravity to zero gravity

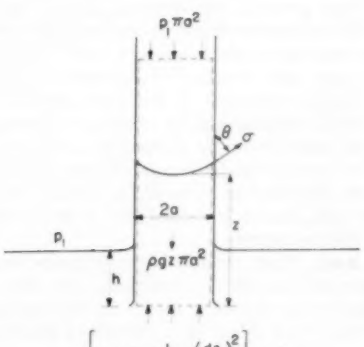

Fig. 4 Configuration of flow system

Weight of fluid $= \pi a^2 \rho n g_0 (z - h)$

Rate of change of momentum $= \dfrac{d}{dt}\left(\pi a^2 z\rho \dfrac{dz}{dt}\right)$

Laminar friction drag $= 8\pi\rho\nu z \dfrac{dz}{dt}$

This results in the following equation of motion for the fluid in the tube:

$$\frac{2\sigma \cos\theta}{a} - \frac{8\rho\nu}{a^2} z \frac{dz}{dt} - \rho n g_o (z - h) = \rho \frac{d}{dt}\left(z \frac{dz}{dt}\right) \quad (2)$$

If the system is in a zero-gravity field then $n = 0$ and one term drops out of the equation. The remaining two terms which contain z can be expressed as a new variable $Z = z^2$ so that

$$z \frac{dz}{dt} = \frac{1}{2} \frac{dZ}{dt}$$

The resulting equation can then be solved subject to the boundary conditions:

At

$$t = 0;\ z = h + \frac{2\sigma \cos\theta}{a\rho g_o} = z_0, \quad \text{and} \quad \frac{dz}{dt} = 0$$

The solution was given in 1923 by Bosanquet [8] as

$$z^2 = \frac{1}{16} \frac{\sigma a^3}{\rho\nu^2} \cos\theta \,(e^{-8\nu t/a^2} - 1) + \left(\frac{1}{2} \frac{\sigma a}{\rho\nu} \cos\theta\right) t + z_o^2 \quad (3)$$

Using the properties of water at room temperature and $\cos\theta = 1$, this relation has been evaluated for three of the tubes used in the present experiment. A comparison with the data is shown in Fig. 5(*a*). The predicted values are much larger than those obtained experimentally. However, the analysis does indicate a few interesting features. One is the crossing of the curves in zero gravity which was also observed experimentally. For the small-diameter tubes, during about the first second, the theory indicates a rise which is fairly linear with time (approximately constant velocity) and this is the trend of the data. The data do not extend to large enough times to exhibit the final trend of the analytical curves. According to equation (3), for large times the height should vary as the square root of time. This is the behavior for fluid motion in a long horizontal capillary [1] and occurs when the inertia of the fluid is negligible compared with the viscous drag. Thus the data only indicate an initial part of the transient. In the large tubes the fluid inertia has a greater influence so the drag does not become predominant until a longer period of time has elapsed. Hence the analytical curve for the large-diameter tube will cross the curves for the smaller tubes only after a longer time than is shown. From equation (3) we have for large times,

$$z = \left[\left(\frac{1}{2} \frac{\sigma a}{\rho\nu} \cos\theta\right) t\right]^{1/2} \quad (3a)$$

This will satisfy equation (2) for $n = 0$ when the inertia on the right side is set equal to zero. Equation (3*a*) shows that the tube with the largest diameter will have the highest fluid level after sufficient time has elapsed. Unfortunately, the present experiments were of insufficient time duration to demonstrate clearly whether or not this behavior does exist, but some crossing of the curves was noted.

Losses in Entrance Region. Since equation (3) yields values which are too high, an improvement might be made by adding addi-

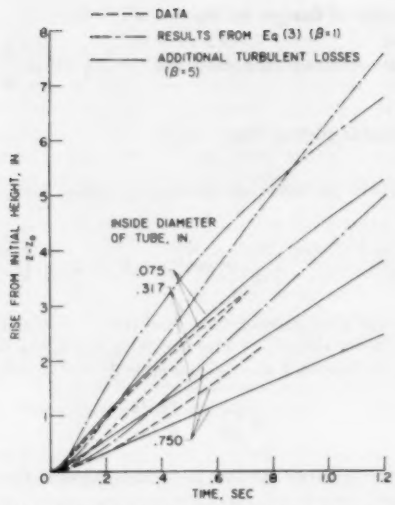

Fig. 5(a) Effect of turbulent losses on rise in zero gravity

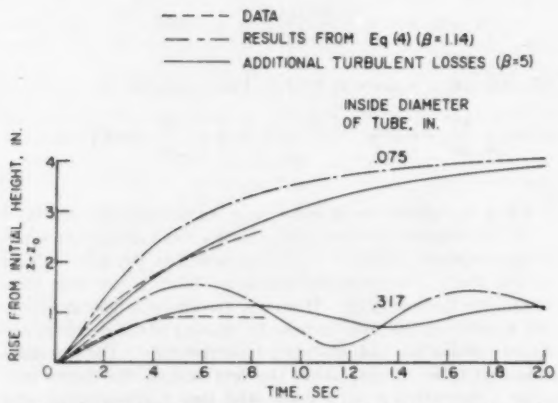

Fig. 5(b) Effect of turbulent losses on rise in 12.6 per cent gravity

tional drag or loss terms. In the hydrodynamic entrance region of a tube there are additional pressure losses resulting from the momentum changes necessary to develop the velocity profile. This is discussed, for example, in [9] and [10]. To include this loss we shall derive the equation of motion in more detail by considering the control volume shown dotted in Fig. 4. The net force in the upward z-direction will be equated to the sum of the net momentum outflow in that direction and the momentum change with time. The downward forces are the weight of the fluid in the control volume, $\rho n g_c \pi a^2 z$; laminar friction drag, $8\pi\rho\nu z(dz/dt)$; the pressure force, $p_i \pi a^2$; and an additional drag term, due to the development of the boundary layer in the entrance region, which can be expressed as

$$\frac{1}{2}\,\rho\left(\frac{dz}{dt}\right)^2 \pi a^2 K$$

According to the analysis of Langhaar [11], a reasonable value for K is 1.28. If we assume a frictionless acceleration of the fluid from reservoir to the tube entrance, than from Bernoulli's equation the upward pressure force at the bottom of the control volume is

$$\left[p_i + \rho n g_c h - \frac{1}{2}\,\rho\left(\frac{dz}{dt}\right)^2\right]\pi a^2$$

The upward force arising from the surface tension is $2\pi a\sigma\cos\theta$. The net outflow of momentum in the z-direction is $-\pi a^2\rho(dz/dt)^2$, and the change of momentum in the control volume with time is

$$\frac{d}{dt}\left(\rho\pi a^2 z\,\frac{dz}{dt}\right)$$

During the transient some of the fluid in the reservoir outside of the tube entrance must also be put into motion. This provides an additional inertia term since this fluid has not been included in the control volume. This term has been discussed in [12] for flow through an orifice, and although the geometry used here is somewhat different, the results in [12] should indicate the form of the term. For the present this inertia term will be omitted but its effect will be discussed later.

The foregoing terms are equated according to the momentum law, and the resulting equation of motion can be put into the form

$$\frac{d^2z}{dt^2} = -\frac{1.14}{z}\left(\frac{dz}{dt}\right)^2 - \frac{8\nu}{a^2}\,\frac{dz}{dt} + \frac{g_c}{z}\left(\frac{2\sigma}{a\rho g_c}\cos\theta + h n\right) - n g_c \quad (4)$$

The only difference between this result and equation (2) is a slight change in the coefficient of the $(dz/dt)^2$ term, and hence no improvement in the theory has resulted. Since the analytical solution given previously for equation (2) was only for zero gravity, equation (4) was solved for a gravity field equal to 12.6 per cent of normal gravity so that a comparison could be made with the rest of the experimental data. The solution was carried out numerically on a digital computer (IBM 704) using the Runge-Kutta method of forward integration. The initial conditions were:

At $t = 0$

$$z_o = \frac{2\sigma\cos\theta}{a\rho g_c} + h, \quad \text{and} \quad \frac{dz}{dt} = 0$$

The properties of water at 75 F were used and $\cos\theta$ was set equal to unity. For the larger tube shown in Fig. 5(b), the theoretical curve overshoots the final equilibrium position and then undergoes a damped oscillation. This shows that the equation of motion is underdamped and additional terms are needed to provide agreement with the data.

In past experience [1] it has been found that equations of the type in equation (4) generally give poor results when trying to predict transient capillary rise. A few possibilities exist which may account for this. In [1], a resistance at the meniscus is postulated, while in [2] it is thought that turbulence may be present. There probably would be an eddying motion in the vicinity of the meniscus owing to the adjustment of the velocity distribution to a more uniform shape in that region. Also, for the rise in large tubes the Reynolds number could exceed the value for transition because of the large diameter. Another possibility is that the shape of the meniscus and hence the angle of contact are different during the motion, and that the upward component of the surface-tension force during the transient is then different from that under steady conditions. Some of these possibilities will now be examined and a predictive equation eventually will be derived.

Turbulent Drag. Since turbulent drag depends approximately on the square of the velocity, additional turbulent dissipation can be introduced by increasing the $(dz/dt)^2$-term in equation (4). For convenience we shall call the coefficient of this term β so that from the derivation $\beta = 1.14$. Equation (4) was numerically integrated for a few larger β-values and the results for $\beta = 5$ are given in Figs. 5(a) and (b). For zero gravity, the results for the

smallest tube have been improved, but those for the large tubes are too low. Hence the additional loss does not help predict the data in a consistent way, but does provide better results in some instances. For 12.6 per cent gravity the additional loss helps damp the oscillations given by the equation and provides better agreement with the data. The addition of turbulent losses alone to the equation does not seem to account sufficiently for the inadequacy of equation (4).

Decreased Surface Tension. Now we start again with equation (4) and change another term. Perhaps during the upward transient motion the vertical component of the surface-tension force is decreased owing to a reduction in contact angle. The inertia of the flow in the central region of the tube cross section may tend to make the meniscus less curved for a rising column, while for a falling column the meniscus may become more curved. If we assume that the change in the vertical force component is proportional to the velocity, we can determine the effect this will have by letting the surface tension force be multiplied by the factor,

$$1 - m\frac{dz}{dt} \tag{5}$$

where m is a numerical constant to be chosen. Since dz/dt ranges up to about 4 ips, if we let m be about 0.1 sec/in. this will cause a reasonable reduction in the vertical surface-tension force during an upward transient flow. Equation (4) was numerically integrated with σ multiplied by equation (5). The results are given in Figs. 6(*a*) and (*b*).

For zero gravity the analysis is in good agreement for the smaller tubes, but yields values which are too high as the tube diameter is increased. The poorer results for large tubes may result from the inertia of the fluid in the reservoir which will be discussed in the next paragraph. For 12.6 per cent gravity the agreement in the range of the data is satisfactory, but the solution still oscillates somewhat for the larger of the two tubes.

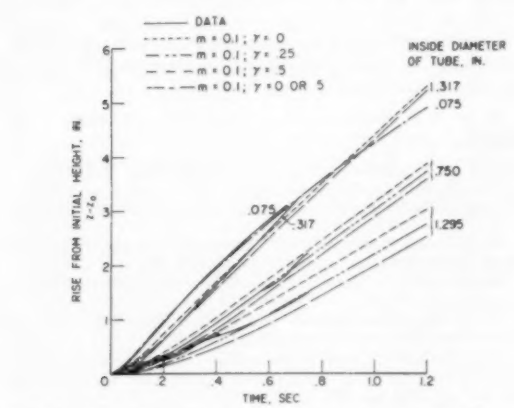

Fig. 6(a) Effect of reduced surface tension and inertia of fluid in reservoir on rise in zero gravity

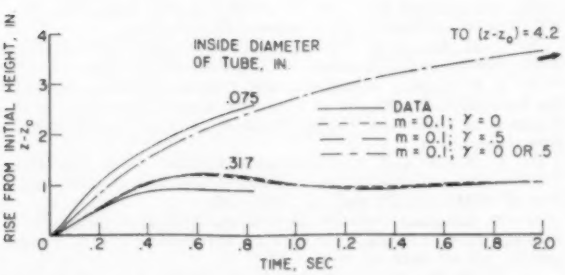

Fig. 6(b) Effect of reduced surface tension and inertia of fluid in reservoir on rise in 12.6 per cent gravity

Inertia of Fluid in Reservoir. To account for the inertia of the fluid in the reservoir we can use the results in [12],[2] where flow through an orifice is analyzed. When this term is included, the d^2z/dt^2 in equation (4) is multiplied by

$$1 + \gamma\frac{\pi a}{z} \tag{6}$$

where γ has a value of 0.5 for the orifice geometry considered in [12]. This was substituted into the equation of motion which already included the reduced surface-tension factor given in equation (5) with $m = 0.1$. The results of the numerical solution are given in Fig. 6. For small-diameter tubes the inertia of the fluid in the reservoir has a negligible effect, while for the largest tube at zero gravity the effect is excessive and the analytical curve is too low. Since a γ of 0.5 does not actually apply for the geometry in the experiment, a γ of 0.25 was tried which brought the analysis into good agreement with the data. Hence, by making an allowance for the inertia in the reservoir and by adding a reduced surface-tension factor, we have found an equation of motion which gives good predictions for capillary rise in zero gravity. For 12.6 per cent gravity the solution is still slightly oscillatory but gives an indication of the time for the transient process to occur. The oscillations are increased for larger tubes but the rise for large tubes is so small that the problem becomes unimportant. The final equation is

$$\left(1 + 0.25\frac{\pi a}{z}\right)\frac{d^2z}{dt^2} = -\frac{1.14}{z}\left(\frac{dz}{dt}\right)^2 - \frac{8\nu}{a^2}\frac{dz}{dt} + \frac{1}{z}\frac{2\sigma}{a\rho}\cos\theta\left(1 - 0.1\frac{dz}{dt}\right) + \frac{g_o h n}{z} - ng_o \tag{7}$$

where $\cos\theta$ has been set equal to unity in the present calculations.

Rise in Short Tubes

A photographic study was made of the rise in zero gravity of water into tubes which were sufficiently short so that during the drop test the fluid could reach the top of the tube. The three tubes used for this study had the following inside diameters: 0.196, 0.317, and 0.750 in. The tubes were placed in the reservoir so that the tops of the two smaller tubes were $1^1/_4$ in. above the water surface while the top of the largest tube was $^3/_4$ in. above the surface. The top end of each tube was cut off square and then fire-polished in a flame to make the edge smooth. The bottom end was flared into a bellmouth so that the water could enter smoothly. The tubes were cleaned with chromic-acid solution on both the outside and inside surfaces. In the previous tests the outsides of the tubes had not been given any special attention. In the test with short tubes we would want to see if the fluid could in any way move beyond the tops of the tubes and down the outside, so it was necessary to have the outside and top edge as clean as the inside.

Fig. 7 illustrates the process after the system is suddenly placed in zero gravity. The smallest tube reveals the most information so we shall discuss it in detail. After 0.3 sec the fluid has almost reached the top of the tube. After the top is reached the inertia carries the fluid beyond the top, and at 0.5 sec a spherical mass of fluid protrudes from the end. The surface of this spherical mass then begins to contract, evidently moving toward a minimum surface-energy condition. After about 0.65 sec the water has all been pushed back into the tube. The fluid inertia then carries it down below the top of the tube as shown on the last picture which gives the configuration at the end of the

[2] Reference [12], p. 1295.

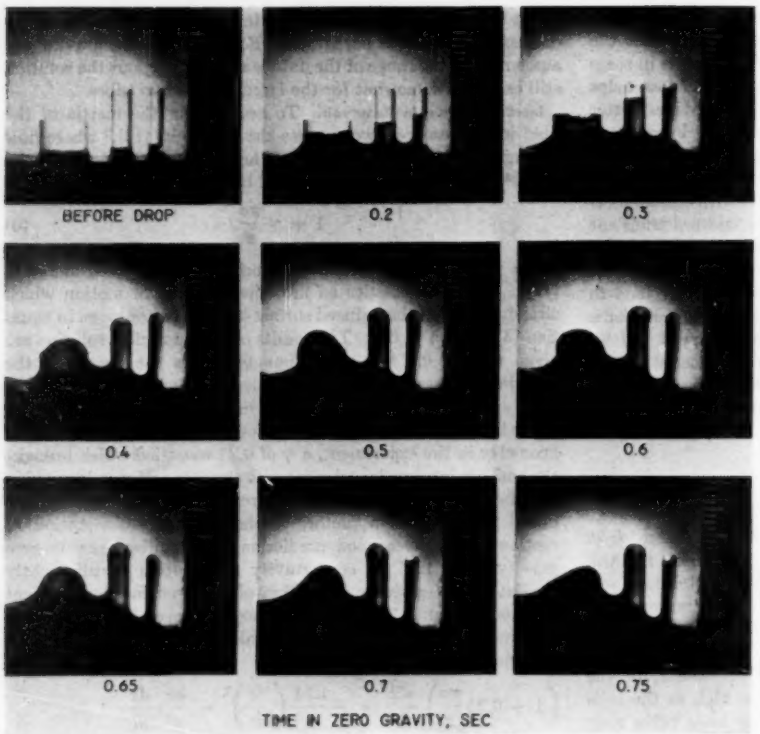

Fig. 7 Rise in short tubes after a change from normal gravity to zero gravity. Tube diameters: 0.196, 0.317, and 0.750 in.

run. For longer times in zero gravity the fluid level would be expected to repeat this oscillatory process with greatly diminished amplitude and eventually came to rest at the top of the tube. Since the outside of each tube was very clean, the surface tension pulls the liquid from the reservoir up the outside of the tubes to some extent. For the largest tube the rise on the outside was almost as large as on the inside. It appears that the fluid in the reservoir was also sloshed slightly to the left during the test. This was probably caused by a slight disturbance when the platform was released.

Conclusions

1 The transient response of water rising into tubes as a result of the surface-tension force is quite rapid in low-gravity fields. For tubes with internal diameters of about 1 in., a rise of about 2 in. can occur in less than a second for a zero-gravity field.

2 An approximate analysis was formulated which can be used to compute the fluid rise in zero gravity. To obtain good analytical predictions it was found necessary to reduce the vertical component of the surface-tension force during the upward motion. For large tubes with diameters greater than $^3/_4$ in. the inertia of the fluid in the reservoir must be included in the equation of motion.

3 In zero gravity, at large times the liquid in the tube with the largest diameter will have the highest rise.

4 For short tubes in zero gravity the inertia of the fluid carries it above the top of the tube and the surface tension then pulls it back into the tube. It is expected that the fluid would eventually come to rest at the top of the tube.

Acknowledgment

The author appreciates some interesting discussions on this subject with C. M. Usiskin and J. M. Savino. Royal Boyd constructed and helped operate the experimental equipment. Eileen M. Norris read the motion-picture films, programmed the numerical computations, and plotted the curves.

References

1 G. F. N. Calderwood and E. W. J. Mardles, "The Rate of Flow of Liquids Into Capillaries Under the Action of Surface Forces," *The Journal of the Textile Institute, Transactions*, vol. 46, 1955, pp. T 161–170.

2 W. A. Rense, "Rate of Rise of Water in Capillary Tubes," *Journal of Applied Physics*, vol. 15, 1944, pp. 436–437.

3 Gerald Pickett, "Rate of Rise of Water in Capillary Tubes," *Journal of Applied Physics*, vol. 15, 1944, p. 623.

4 W. C. Reynolds, "Behavior of Liquids in Free Fall," *Journal of the Aero/Space Sciences*, vol. 26, 1959, p. 847.

5 E. T. Benedikt, "Scale of Separation Phenomena in Liquids Under Conditions of Nearly Free Fall," *American Rocket Society Journal*, vol. 29, 1959, pp. 150–151.

6 R. Siegel and C. M. Usiskin, "A Photographic Study of Boiling in the Absence of Gravity," TRANS. ASME, Series C, *Journal of Heat Transfer*, vol. 81, 1959, pp. 230–236.

7 C. M. Usiskin and R. Siegel, "An Experimental Study of Boiling in Reduced and Zero Gravity Fields," ASME Paper No. 60—HT-10 to be published in the *Journal of Heat Transfer*.

8 C. H. Bosanquet, "On the Flow of Liquids Into Capillary Tubes," *Philosophical Magazine*, vol. 45, 1923, pp. 525–531.

9 A. H. Shapiro, R. Siegel, and S. J. Kline, "Friction Factor in the Laminar Entry Region of a Smooth Tube," *Proceedings of the Second U. S. Congress of Applied Mechanics*, University of Michigan, June, 1954.

10 F. Kreith and R. Eisenstadt, "Pressure Drop and Flow Characteristics of Short Capillary Tubes at Low Reynolds Numbers," TRANS. ASME, vol. 79, 1957, pp. 1070–1079.

11 H. Langhaar, "Steady Flow in the Transition Length of a Straight Tube," JOURNAL OF APPLIED MECHANICS, vol. 9, TRANS. ASME, vol. 64, 1942, pp. A-55–A-58.

12 P. M. Morse and H. Feshbach, "Methods of Theoretical Physics," McGraw-Hill Book Company, Inc., New York, N. Y., 1953, p. 1295.

Minimum Transfer Time for a Power-Limited Rocket

GEORGE LEITMANN[1]

Associate Professor
of Engineering Science,
University of California,
Berkeley, Calif.

The problem considered is that of determining the acceleration program leading to minimum transfer time for a power-limited rocket moving between prescribed positions and velocities in a constant gravitational field. It is found that flight must take place at maximum power and that the thrust-acceleration components are linear functions of time. The case of rectilinear transfer between positions of rest is treated in detail, and the results are compared with those previously obtained for a constant-acceleration transfer.

Foreword

DURING recent years, many investigations of optimum rocket trajectories have been undertaken. Most of these have dealt with problems of conventional thrust-limited rockets. Within the framework of the general research task, this paper is the first attempt at treating optimization questions involving energy-separate, power-limited rockets.

Introduction

During recent years, prospects for travel in interplanetary space have brightened considerably. Consequently, interest has arisen in problems of propulsion and flight mechanics peculiar to flight outside the atmosphere. Whereas flight in the atmosphere often demands thrust application in the direction of the earth's gravitational field and hence relatively high thrust, flight in space, e.g., escape from or transfer between planets, can be accomplished by directing thrust essentially normal to the field—hence requiring little thrust. Such problems of escape from orbits, transfer between orbits, and interplanetary transfer have received considerable attention [1–13].[2] The referenced studies deal with transfer trajectories attained by more or less reasonable acceleration programs, although not necessarily optimum in any sense.

Other investigators have discussed physical means for achieving low-thrust flights of long duration [14–26]. Proposals for so-called exotic propulsion systems have been based on these studies. Proposed thrust-producing devices range from rockets utilizing jets of ions to those employing jets of photons. Energy sources considered are either internal, based on conversion of mass into kinetic energy, or external; e.g., deriving energy from the sun. One salient feature of these propulsion systems is the independence of energy source and working fluid, i.e., matter (or, more generally, momentum carrier) expelled from the rocket. In this respect, such advanced engines differ from those used in conventional, chemically powered rockets in which energy source and working fluid are one and the same. This independence of energy source and working fluid is of importance in considering optimum acceleration programs, since it permits the programming of thrust by separate variations of exhaust speed and mass-flow rate. Another important aspect of low-thrust rockets is the strong dependence of power-plant mass on power delivered. Hence exotic propulsion devices are power limited. For conventional rockets of constant exhaust speed, this power limitation becomes simply thrust limitation.

Recently, R. E. Roberson [27] pointed out the need for studies of optimum trajectories of low-thrust rockets. Such investigations have fallen into three categories [28–38]: Trajectories of maximum "efficiency," i.e., obtaining maximum velocity for given energy expenditure; trajectories of minimum working-fluid consumption; and trajectories of minimum flight time. Since the energy supply of rockets utilizing internal sources is limited, although no doubt very large, attaining maximum

[1] Also, Research Scientist, Lockheed Missiles and Space Division, Lockheed Aircraft Corporation, Sunnyvale, Calif.

[2] Numbers in brackets designate References at end of paper.

Presented at the Summer Conference of the Applied Mechanics Division, Chicago, Ill., June 14–16, 1961, of THE AMERICAN SOCIETY OF MECHANICAL ENGINEERS.

Discussion of this paper should be addressed to the Editorial Department, ASME, 29 West 39th Street, New York, N. Y., and will be accepted until July 10, 1961. Discussion received after the closing date will be returned. Manuscript received by ASME Applied Mechanics Division, April 13, 1960. Paper No. 61—APM-6.

Nomenclature

c = exhaust speed
d = mass of structure and payload per unit initial mass
f = mass of working fluid per unit initial mass
g = acceleration of gravity (not necessarily earth's), constant
m = mass of rocket
p = mass of power plant per unit initial mass
t = time
t_b = operating time
t_f = transfer time
u, v = Cartesian components of velocity in inertial space
x, y = Cartesian components of position in inertial space
E = energy converted into kinetic energy of rocket and jet
K = first integral, constant
K_1 = $p(P/m_0)^{-1}$
K_2 = mass of tanks per unit mass of working fluid
P = power
V_e = characteristic speed
α = $2P/m_0$
β = $-\dot{\mu}$
γ = real variable
λ = undetermined multiplier
μ = m/m_0
φ = thrust direction angle relative to x-axis, positive counterclockwise

Subscripts

f = final
0 = initial
min = minimum
max = maximum
$\cdot$ = differentiation with respect to time t

"efficiency" is of some importance as is minimizing of weight. However, use of low-thrust devices generally results in long flight times which may be undesirable, indeed even untenable in the case of manned flight. Hence attempts at reducing flight times are not to be overlooked. The pioneering papers of Preston-Thomas [29, 31, 32] deal with minimum transfer-time trajectories employing various nonoptimum acceleration programs, optimization being carried out with respect to the distribution of powered and coasting portions of the flight, and with respect to internal mass distribution of rocket components.

The study presented here deals with the determination of optimum acceleration programs leading to minimum transfer times for power-limited rockets transferring between prescribed positions and velocities in a constant gravitational field. A detailed analysis is made of rectilinear transfer, and the results are compared with those obtained previously for nonoptimum programs.

Equations of Motion and First Variation

The equations of motion of a rocket flying in a plane[3] and subject to a constant gravitational field are

$$\begin{aligned} \dot{u} &= \frac{c\beta}{\mu}\cos\varphi \\ \dot{v} &= \frac{c\beta}{\mu}\sin\varphi - g \\ \dot{x} &= u \\ \dot{y} &= v \\ \dot{\mu} &= -\beta \end{aligned} \tag{1}$$

The power is expressed by

$$2\frac{P}{m_0} = \beta c^2 = \alpha \tag{2}$$

The power-limited nature of the rockets under consideration requires that

$$\alpha_{\min} \leq \alpha \leq \alpha_{\max} \tag{3}$$

where $\alpha_{\min}$ and $\alpha_{\max}$ are specified.[4] Since the thrust direction angle φ is not defined for unpowered flight, we shall take

$$\alpha_{\min} > 0 \tag{4}$$

but allow for coasting flight by letting $\alpha_{\min} \to 0$ as closely as desired. Furthermore, it will be assumed that the exhaust speed c and the mass flow rate β possess at most a finite number of infinite values on $0 \leq t \leq t_f$, so that

$$\beta > 0, \quad c \neq 0 \tag{5}$$

except possibly at isolated points of the interval. It will be seen from the solution that these assumptions are indeed valid.

In addition to the equations of motion and constraint, the following initial and final conditions apply:

$$t = 0 \begin{cases} x = 0 \\ y = 0 \\ u = u_{0i} \\ v = v_0 \\ \mu = 1 \end{cases} \qquad t = t_f \begin{cases} x = x_f \\ y = y_f \\ u = u_f \\ v = v_f \\ \mu = \mu_f \end{cases} \tag{6}$$

[3] Planar motion is assumed for the sake of simplicity. All results hold for three-dimensional motion.

[4] At a later stage of the discussion, optimization with respect to internal mass distribution will yield an optimum value for $\alpha_{\max}$.

It is desired to minimize a function G of the boundary conditions where

$$G = t_f \tag{7}$$

subject to the following side conditions:

$$\begin{aligned} \varphi_1 &= \dot{u} - \frac{c\beta}{\mu}\cos\varphi = 0 \\ \varphi_2 &= \dot{v} - \frac{c\beta}{\mu}\sin\varphi + g = 0 \\ \varphi_3 &= \dot{x} - u = 0 \\ \varphi_4 &= \dot{y} - v = 0 \\ \varphi_5 &= \dot{\mu} + \beta = 0 \\ \varphi_6 &= \beta c^2 - \alpha = 0 \\ \varphi_7 &= (\alpha - \alpha_{\min})(\alpha_{\max} - \alpha) - \gamma^2 = 0 \end{aligned} \tag{8}$$

where γ is a real variable [39] and subject to boundary conditions (6). The problem is that of Bolza [40], so that the functional to be minimized is

$$J = G + \int_0^{t_f} F\,dt \tag{9}$$

where

$$F = \sum_{j=1}^{7} \lambda_j \varphi_j$$

and the $\lambda_j(t)$ are undetermined multipliers, not all zero, which are continuous everywhere on $0 \leq t \leq t_f$ with the possible exception of corners of the extremal arc.

The Euler-Lagrange equations resulting from the vanishing of the first variation of J are

$$\begin{aligned} &\dot{\lambda}_1 + \lambda_3 = 0 \\ &\dot{\lambda}_2 + \lambda_4 = 0 \\ &\dot{\lambda}_3 = 0 \\ &\dot{\lambda}_4 = 0 \\ &\dot{\lambda}_5 - \frac{c\beta}{\mu^2}(\lambda_1\cos\varphi + \lambda_2\sin\varphi) = 0 \\ &\frac{c}{\mu}(\lambda_1\cos\varphi + \lambda_2\sin\varphi) - \lambda_5 - \lambda_6 c^2 = 0 \\ &\beta\left[\frac{1}{\mu}(\lambda_1\cos\varphi + \lambda_2\sin\varphi) - 2\lambda_6 c\right] = 0 \\ &\frac{c\beta}{\mu}(\lambda_1\sin\varphi - \lambda_2\cos\varphi) = 0 \\ &\lambda_6 + \lambda_7(2\alpha - \alpha_{\max} - \alpha_{\min}) = 0 \\ &\lambda_7\gamma = 0 \end{aligned} \tag{10}$$

Since the fundamental function F does not contain time t explicitly, there exists a first integral of equations (10):

$$K = \lambda_1\dot{u} + \lambda_2\dot{v} + \lambda_3\dot{x} + \lambda_4\dot{y} + \lambda_5\dot{\mu} = \text{const} \tag{11}$$

The corresponding transversality condition is

$$dt_f + [\lambda_1 du + \lambda_2 dv + \lambda_3 dx + \lambda_4 dy + \lambda_5 d\mu - K dt]_0^{t_f} = 0 \tag{12}$$

However, in view of boundary conditions (6),

$$du,\ dv,\ dx,\ dy,\ d\mu]_0^{t_f} = 0$$

and

$$dt]_0 = 0 \tag{13}$$

so that

$$K = 1 \tag{14}$$

Some of the Euler-Lagrange equations are easily integrated. Thus,

$$\begin{aligned} \lambda_3 &= \text{const} \\ \lambda_4 &= \text{const} \\ \lambda_1 &= \lambda_{10} - \lambda_3 t \\ \lambda_2 &= \lambda_{20} - \lambda_4 t \end{aligned} \tag{15}$$

In view of the assumptions embodied in inequalities (5), the thrust

$$c\beta \neq 0 \tag{16}$$

except possibly at isolated points of the interval, so that from equation $(10)_3$

$$\tan \varphi = \frac{\lambda_2}{\lambda_1} \tag{17}$$

From equations (17) and (15) it follows that $\tan \varphi$ is continuous on $0 \leq t \leq t_f$ except at most once when $\lambda_1 = 0$ but $\lambda_2 \neq 0$. However, equation (17) yields two principal values of φ, namely,

$$\varphi = \varphi_1$$

and (18)

$$\varphi = \varphi_1 + \pi$$

Thus φ may experience discontinuous jumps of magnitude π. Furthermore, there exists an ambiguity regarding the choice of the principal value of φ. These questions will be answered in the ensuing discussion.

Weierstrass-Erdmann Corner Conditions

Since c, β, and φ do not occur in differentiated form, all of them and hence $\dot{u}$ and $\dot{v}$ could be discontinuous, resulting in corners of the extremal arc. For the problem at hand the corner conditions [40] are simply

$$\begin{aligned} \lambda_{j-} &= \lambda_{j+}, \quad j = 1, 2, \ldots 5 \\ \text{and} \qquad K_- &= K_+ \end{aligned} \tag{19}$$

Thus the λ_j, $j = 1, 2, \ldots 5$, and K have equal values on both sides of a corner.

Composition of Extremal Arc

From equations $(8)_7$ and $(10)_{10}$ it follows that when

$$\begin{aligned} &\lambda_7 = 0, \quad \gamma \neq 0, \quad \text{then} \quad \alpha_{\min} < \alpha < \alpha_{\max} \\ &\lambda_7 \neq 0, \quad \gamma = 0, \quad \text{then} \quad \alpha = \alpha_{\min} \quad \text{or} \quad \alpha = \alpha_{\max} \\ &\lambda_7 = 0, \quad \gamma = 0, \quad \text{then} \quad \alpha = \alpha_{\min} \quad \text{or} \quad \alpha = \alpha_{\max} \end{aligned} \tag{20}$$

We arrive at the rather obvious and not very useful conclusion that flight must take place at one of the permitted power levels. The question concerning the choice of optimum power level is thus far unanswered. The necessary condition that the first variation vanish does not seem to provide the answer. However, other conditions are necessary for the existence of a minimum value, and we shall turn to them now.

The Weierstrass E-Function

Two questions concerning the optimum trajectories were left unanswered, namely, the choice of the principal value of φ and the selection of optimum power level.

A necessary condition for the existence of a minimum value of transfer time t_f is

$$E \geq 0 \tag{21}$$

where

$$E = F(\dot{z}_i^*, z_i^*) - F(\dot{z}_i, z_i) - \sum_{i=1}^{10} (\dot{z}_i^* - \dot{z}_i) \frac{\partial F}{\partial \dot{z}_i} \tag{22}$$

and

$$\begin{aligned} z_i &= u, v, x, y, \mu, \alpha, \beta, \gamma, c, \varphi, \\ u^* &= u, \quad v^* = v, \quad x^* = x, \quad y^* = y, \quad \mu^* = \mu \end{aligned}$$

For the problem considered, inequality (21) is

$$\beta\kappa - \beta^*\kappa^* \geq 0 \tag{23}$$

where

$$\kappa = \frac{c}{\mu} (\lambda_1 \cos \varphi + \lambda_2 \sin \varphi) - \lambda_3 \tag{24}$$

Inequality (23) must hold for all values of c^*, β^*, and φ^*, which satisfy side conditions (8), but not all equal to their optimum values. Thus if

$$\beta^* = \beta, \quad c^* = c, \quad \varphi^* \neq \varphi \tag{25}$$

inequality (23) becomes

$$\lambda_1 \cos \varphi + \lambda_2 \sin \varphi \geq \lambda_1 \cos \varphi^* + \lambda_2 \sin \varphi^* \tag{26}$$

Thus φ must assume values which maximize the expression $\lambda_1 \cos \varphi + \lambda_2 \sin \varphi$. Hence φ must satisfy equation (17) and

$$\lambda_1 \cos \varphi + \lambda_2 \sin \varphi \geq 0 \tag{27}$$

This condition removes the ambiguity concerning the choice of the principal value of φ. Furthermore, then φ is continuous with the possible exception of the instant when λ_1 and λ_2 pass through zero simultaneously. This can happen but once. At such an instant, φ experiences a discontinuous jump of π.

If

$$\beta^* = \beta, \quad c^* \neq c, \quad \varphi^* = \varphi \tag{28}$$

Inequality (23) yields

$$\beta(c - c^*) \geq 0 \tag{29}$$

whence

$$\alpha \geq \alpha^* \tag{30}$$

In order to satisfy inequality (30) for all admissible values of α^*,

$$\alpha = \alpha_{\max} \tag{31}$$

That is, flight must take place at maximum power throughout the interval $0 \leq t \leq t_f$.

The Clebsch Condition

In order that t_f take on a minimum value, it is also necessary [40] that

$$\sum_{i=1}^{10}\sum_{j=1}^{10}\frac{\partial^2 F}{\partial z_i \partial z_j}\pi_i\pi_j \geq 0 \tag{32}$$

where the $z_i = u, v, x, y, \mu, c, \varphi, \alpha, \beta, \gamma$, and the π_{si}, not all zero, satisfy the constraints

$$\sum_{i=1}^{10}\frac{\partial \varphi_k}{\partial z_i}\pi_{si} = 0, \quad k = 1, 2, \ldots 7 \tag{33}$$

Then, in view of equations (10), inequality (32) becomes

$$\frac{c\beta}{\mu}(\lambda_1 \cos\varphi + \lambda_2 \sin\varphi)(\pi_\varphi)^2 + 2\lambda_6\beta(\pi_c)^2 - 2\lambda_7[(\pi_\alpha)^2 + (\pi_\gamma)^2] \geq 0 \tag{34}$$

For

$$\pi_c = \pi_\alpha = \pi_\gamma = 0, \quad \pi_\varphi \neq 0 \tag{35}$$

inequality (34) requires that

$$\lambda_1 \cos\varphi + \lambda_2 \sin\varphi \geq 0 \tag{36}$$

which is the same as inequality (27).

For

$$\pi_\varphi = \pi_c = 0, \quad \pi_\alpha \neq 0 \quad \text{or} \quad \pi_\gamma \neq 0 \tag{37}$$

inequality (34) yields

$$\lambda_7 \leq 0 \tag{38}$$

However, from equation (17) it follows that

$$\sin\varphi = \frac{\pm\lambda_2}{(\lambda_1^2 + \lambda_2^2)^{1/2}}, \qquad \cos\varphi = \frac{\pm\lambda_1}{(\lambda_1^2 + \lambda_2^2)^{1/2}} \tag{39}$$

so that inequality (36) leads to

$$\lambda_1 \cos\varphi + \lambda_2 \sin\varphi = (\lambda_1^2 + \lambda_2^2)^{1/2} \tag{40}$$

i.e., the choice of the + sign in equations (39).

Combining equations $(10)_6$ and $(10)_7$ then gives

$$(\lambda_1^2 + \lambda_2^2)^{1/2} = 2\lambda_6\mu c \tag{41}$$

If

$$\lambda_6 = 0 \tag{42}$$

on a nonzero interval, equation (42) requires that

$$\lambda_1 = \lambda_2 = 0 \tag{43}$$

so that from equations $(10)_1$ and $(10)_2$

$$\lambda_3 = \lambda_4 = 0 \tag{44}$$

and from equation $(10)_6$, then,

$$\lambda_5 = 0 \tag{45}$$

However, equations (43)–(45) violate[5] equation (14) so that

$$\lambda_6 \neq 0 \tag{46}$$

on a finite interval. Consequently, only the inequality applies in equations (27) and (36). Furthermore, from equation $(10)_9$ it is seen that for

$$\alpha = \alpha_{\min} \tag{47}$$

[5] Note that the requirement that not all λ_j vanish is also violated here.

λ_6 and λ_7 have the same sign. Thus by inequalities (38) and (46)

$$\lambda_6 < 0, \qquad \lambda_7 < 0 \tag{48}$$

However, then for

$$c > 0 \tag{49}$$

inequality (48) violates equation (41). Hence,

$$\alpha \neq \alpha_{\min} \tag{50}$$

But by inequality (46) and conditions (20)

$$\alpha = \alpha_{\min} \quad \text{or} \quad \alpha = \alpha_{\max} \tag{51}$$

so that

$$\alpha = \alpha_{\max} \tag{52}$$

only. This is the same as equation (31) of the preceding section.

Solution

Since operation at constant, maximum power is optimum, the remaining Euler-Lagrange equation, equation $(10)_5$, may be integrated. Equation $(10)_5$ may now be written

$$\mu^2 c\dot{\lambda}_5 = \alpha_{\max}(\lambda_1^2 + \lambda_2^2)^{1/2} \tag{53}$$

Elimination of λ_6 from equations $(10)_6$ and $(10)_7$ yields

$$2\mu c\beta\lambda_5 = \alpha_{\max}(\lambda_1^2 + \lambda_2^2)^{1/2} \tag{54}$$

Combination of equations (53) and (54) and integration lead to

$$\lambda_5 = \frac{\lambda_{50}}{\mu^2} \tag{55}$$

so that equation (54) becomes

$$\mu c = \frac{2\lambda_{50}}{(\lambda_1^2 + \lambda_2^2)^{1/2}} \tag{56}$$

where

$$c^2\beta = \alpha_{\max} \tag{57}$$

Equations $(8)_{1-3}$, (17), (56), and (57), together with boundary conditions (6), can be solved for $u, v, x, y, \mu, c, \beta$, and φ. Furthermore, in view of the first integral, equation (14), multipliers λ_j, $j = 1, 2, \ldots 5$, are related. Equation (14) may be written

$$1 = \beta\lambda_5 - \lambda_2 g + \lambda_3 u + \lambda_4 v \tag{58}$$

However, from equations (54) and (56)

$$\beta\lambda_5 = \frac{\lambda_1^2 + \lambda_2^2}{4\lambda_{50}}\alpha_{\max} \tag{59}$$

Thus at $t = 0$, equation (58) is

$$1 = \frac{\lambda_{10}^2 + \lambda_{20}^2}{4\lambda_{50}}\alpha_{\max} - \lambda_{20} g + \lambda_3 u_0 + \lambda_4 v_0 \tag{60}$$

relating the initial values of the multipliers.

Formally, the process of integration involves a four-parameter match by iteration. The initial values of four of the λ_j, $j = 1, 2, \ldots 5$, are assumed and the fifth one follows from equation (60). Integration then proceeds until, say $\mu = \mu_f$, at which time the prescribed values of u, v, x, and y must be met. However, the situation is not as grim as it might appear. For, by equations (39) and (56), equations $(8)_{1-4}$ become

$$\dot{u} = \frac{\alpha_{max}}{2\lambda_{50}} (\lambda_{10} - \lambda_3 t)$$

$$\dot{v} = \frac{\alpha_{max}}{2\lambda_{50}} (\lambda_{20} - \lambda_4 t) - g \tag{61}$$

$$\dot{x} = u$$

$$\dot{y} = v$$

Also, from equations (56) and (57)

$$\frac{\dot{\mu}}{\mu^2} = -\frac{\alpha_{max}}{4\lambda_{50}^2} [(\lambda_{10} - \lambda_3 t)^2 + (\lambda_{20} - \lambda_4 t)^2] \tag{62}$$

and from equation (58) at $t = t_f$

$$1 = \frac{\alpha_{max}}{4\lambda_{50}} [(\lambda_{10} - \lambda_3 t)^2 + (\lambda_{20} - \lambda_4 t)^2] - (\lambda_{20} - \lambda_4 t) g + \lambda_3 u_f + \lambda_4 v_f \tag{63}$$

Equations (61) and (62) are easily integrated so that, together with equations (60) and (63), the multipliers λ_{10}, λ_{20}, λ_3, λ_4, λ_{50}, and the transfer time t_f can be expressed in terms of the boundary conditions. This clearly obviates the need for iteration.

It may be noted that by equation (62) β passes through zero when $\lambda_1 = \lambda_2 = 0$ simultaneously, at which instant c passes through infinity; the thrust $c\beta$ remains finite, however, and passes through zero when β does. This can occur at most once, bearing out earlier assumptions concerning the number of infinities of c and β. Since no upper bound was placed on c (or β), infinitely large values of c (or β) were not ruled out. Of course, real propulsion systems are not capable of providing infinitely high exhaust speeds.[6] One could introduce upper limits on c and β, constraining the motion more and leading to a "poorer" optimum, i.e., a longer transfer time. In other words, the transfer time achieved by following the ideal program deduced here is the smallest local minimum.

Rectilinear Transfer

The problem of rectilinear transfer in field-free space between prescribed positions and zero velocities has been discussed by Preston-Thomas [29, 31, 32]. In his investigations he assumed either the exhaust speed c or the acceleration $\dot{u}$ to be constant. The problem of transfer of a power-limited rocket with constant exhaust speed is equivalent to that of transfer of a thrust-limited rocket and falls in the class of problems discussed in [41].

Here it has been shown that neither constant exhaust speed nor constant acceleration is optimum, but rather acceleration which varies linearly with time. The equations of motion for rectilinear transfer are

$$\dot{u} = \frac{\alpha_{max}}{2\lambda_{50}} (\lambda_{10} - \lambda_3 t)$$

$$\dot{x} = u \tag{64}$$

$$\frac{\dot{\mu}}{\mu^2} = -\frac{\alpha_{max}}{4\lambda_{50}^2} (\lambda_{10} - \lambda_3 t)^2$$

and the first integral at $t = 0$ and $t = t_f$, respectively, is

$$1 = \frac{\alpha_{max}}{4\lambda_{50}} \lambda_{10}^2 + \lambda_3 u_0$$

$$1 = \frac{\alpha_{max}}{4\lambda_{50}} (\lambda_{10} - \lambda_3 t_f)^2 + \lambda_3 u_f \tag{65}$$

[6] Note that no relativistic considerations have been taken into account in this treatment.

The boundary conditions are

$$t = 0 \begin{cases} x = 0 \\ u = 0, \\ \mu = 1 \end{cases} \qquad t = t_f \begin{cases} x = x_f \\ u = 0 \\ \mu = \mu_f \end{cases} \tag{66}$$

Then from equations (65)

$$t_f = 2 \frac{\lambda_{10}}{\lambda_3} \tag{67}$$

Thrust direction reversal occurs when

$$\lambda_1 = 0 \tag{68}$$

i.e., at

$$t = \frac{\lambda_{10}}{\lambda_3} = \tfrac{1}{2} t_f \tag{69}$$

as might be expected from the symmetry of the situation.

Upon double integration of equation $(64)_1$ and use of equation (67) it follows that

$$\lambda_{10} = \frac{t_f^2}{3x_f} \tag{70}$$

so that equation (67) gives

$$\lambda_3 = \frac{2}{3} \frac{t_f}{x_f} \tag{71}$$

Substitution of equation (70) in equation $(65)_1$ yields

$$\lambda_{50} = \frac{\alpha_{max}}{36} \frac{t_f^4}{x_f^2} \tag{72}$$

Thus all multipliers have been expressed in terms of the boundary conditions and the transfer time.

Integration of equation $(64)_3$ results in

$$\frac{1 - \mu_f}{\mu_f} = \frac{\alpha_{max}}{12\lambda_{50}^2} \lambda_{10}^2 t_f \tag{73}$$

which, together with equations (70) and (72), gives the expression for the minimum transfer time

$$t_f = \left[\frac{12 x_f^2}{\alpha_{max}} \frac{\mu_f}{1 - \mu_f} \right]^{1/3} \tag{74}$$

One can now compare this result with those found by Preston-Thomas under the assumption of constant exhaust speed or constant acceleration [32]. To do so, one must use the same assumptions concerning the structure of the rocket as were utilized by Preston-Thomas. These are:

The power-plant mass is proportional to the maximum power output; i.e.,

$$p = K_1 \frac{P}{m_0} = K_1 (\tfrac{1}{2} \alpha_{max}) \tag{75}$$

The mass of tanks is proportional to the working fluid mass. That is, the mass of working fluid and associated containers is given by

$$(1 + K_2) f \tag{76}$$

Also, if one neglects the mass converted into energy compared with the other masses involved,

$$\mu_f = 1 - f \tag{77}$$

Under these conditions, equation (74) becomes

$$t_f = \left[\frac{6x_f^2K_1(1-f)}{pf}\right]^{1/3} \tag{78}$$

Preston-Thomas [32] has found that minimum transfer time for constant exhaust speed is given by

$$t_f = \left[\frac{27x_f^2\phi K_1 f}{4p\ln^2(1-f)}\right]^{1/3} \tag{79}$$

where

$$\phi = 2 + \frac{4[2 + f - 2(1-f)^{1/3}]}{f\ln(1-f)}$$

and for constant acceleration by

$$t_f = \left[\frac{27x_f^2K_1(1-f)}{4pf}\right]^{1/3} \tag{80}$$

Of these last two programs, the latter (i.e., constant acceleration) results in shorter transfer time as can be seen from a comparison of equations (79) and (80). However, employment of acceleration varying linearly with time leads to a further saving of about 4 per cent in the transfer time t_f, equations (78) and (80).

Since t_f is expressed as an explicit function of p and f, it is possible to determine the relation between p and f which minimizes transfer time with respect to internal mass distribution. In other words, it is possible to find the optimum power level. The relation among the various component masses of the rocket is given by

$$1 = p + (1 + K_2)f + d \tag{81}$$

If the mass of structure and payload (i.e., the dead mass d) is specified, t_f must be minimized with respect to p and f subject to the constraint expressed by equation (81). This results in the relationship

$$p = f(1-f)(1+K_2) \tag{82}$$

so that t_f minimum with respect to acceleration program *and* internal mass distribution is

$$t_f = \left[\frac{6x_f^2K_1}{(1+K_2)f^2}\right]^{1/3} \tag{83}$$

where

$$f = 1 - \left(1 - \frac{1-d}{1+K_2}\right)^{1/2} \tag{84}$$

Since the expressions for t_f resulting from constant and linear acceleration, respectively, differ only by a numerical factor, the result of optimization with respect to internal mass distribution is the same in both cases.

The optimum acceleration program yielding minimum transfer time is obtained by programming exhaust speed c, mass flow rate β, and thrust direction angle φ in the following manner: From equations $(64)_2$ and (69)–(72)

$$\mu = \frac{\alpha_{\max}t_f^3}{\alpha_{\max}t_f^3 + 6x_f^2[1 - (1 - 2t/t_f)^2]} \tag{85}$$

so that, using equations (56) and (69)–(72),

$$c = \frac{\alpha_{\max}t_f^3 + 6x_f^2[1 - (1 - 2t/t_f)^2]}{6x_f t_f|1 - 2t/t_f|} \tag{86}$$

Then it follows from equation $(64)_2$ that

$$\beta = \frac{36x_f^2\mu^2}{t_f^4\alpha_{\max}}(1 - 2t/t_f)^2 \tag{87}$$

Also,

$$\begin{aligned} \varphi &= 0 \quad \text{for} \quad t < \tfrac{1}{2}t_f \\ \varphi &= \pi \quad \text{for} \quad t > \tfrac{1}{2}t_f \end{aligned} \tag{88}$$

Equations (86) and (87) again show the behavior of c, β, and thrust $c\beta$ at the singular point $t = \frac{1}{2}t_f$. That is, β and $c\beta$ pass through zero as c passes through infinity.

From equations $(64)_1$ and (69)–(72),

$$u = \frac{6x_f}{t_f}[t/t_f - (t/t_f)^2] \tag{89}$$

and, in particular, at $t = \frac{1}{2}t_f$

$$u = u_{\max} = \frac{3}{2}\frac{x_f}{t_f} \tag{90}$$

The same expression for maximum speed holds in the case of constant acceleration [32]. However, the value of $u_{\max}$ is slightly higher here since t_f is somewhat smaller.

A few words concerning energy expenditure are now in order. When a constant-acceleration program is used, energy expenditure is minimum for a given characteristic speed

$$V_e = 2u_{\max} \tag{91}$$

(For example, see [38].) Thus, in the case of linear acceleration, energy expenditure is higher for two reasons:

1 Linear acceleration is not optimum with respect to conversion of internal to kinetic energy of the rocket.

2 The characteristic speed is somewhat higher in the case of linear acceleration than for constant acceleration.

The total energy converted (into kinetic energy of rocket and jet) is given by

$$\frac{E}{m_0} = \frac{pt_b}{K_1} \tag{92}$$

For constant acceleration [32],

$$t_b = \tfrac{8}{3}t_f \tag{93}$$

whereas for linear acceleration

$$t_b = t_f \tag{94}$$

However, the difference in t_f amounts to only 4 per cent, so that the energy required for achieving minimum transfer time using the optimum, linear acceleration program is nearly $^3/_8$ of that required for transfer with constant acceleration.

One notes that the optimum acceleration program suffers from two disadvantages as compared with the constant acceleration program:

1 Very high (ideally, infinite) exhaust speed is demanded at one instant of the flight. If this requirement is ruled out by placing an upper bound on the exhaust speed, a longer transfer time will result.

2 Almost a half more energy is used in the transfer.

Whether or not the relatively small gain in diminished transfer time outweighs these drawbacks is, of course, a decision which must rest on the requirements of a particular mission. In any event, it is important to note that the constant-acceleration program is very nearly optimum—at least for rectilinear transfer.

The behavior of the variables of interest, namely, u, c, β, and $c\beta$, is shown as a function of time in Figs. 1–4 for the numerical

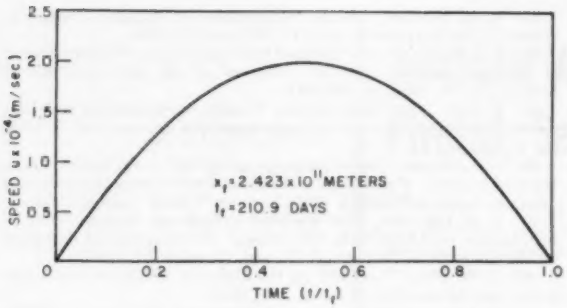

Fig. 1

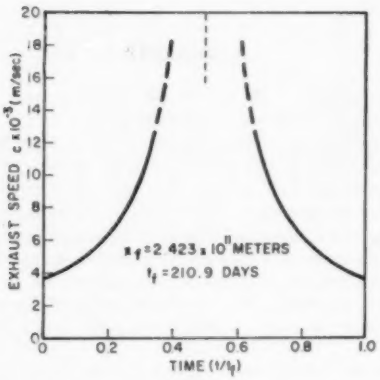

Fig. 2

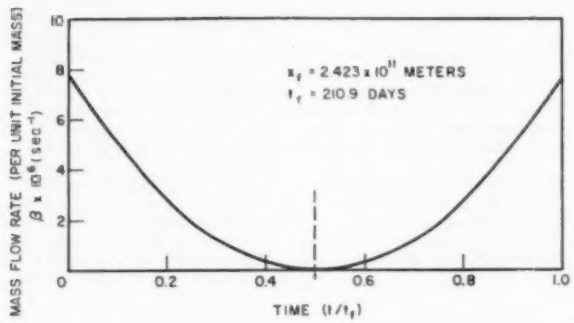

Fig. 3

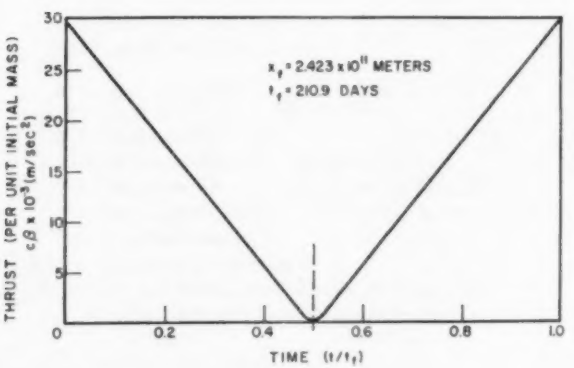

Fig. 4

example used by Preston-Thomas [31]. The parameters for this example are

$$x_f = 2.423 \times 10^{11} \text{ m}$$

$$1 - d = 0.83$$

$$K_1 = 4.8 \times 10^{-3} \text{ kg/watt}$$

$$K_2 = 0.1$$

$$p = 0.275$$

$$f = 0.504$$

References

1 G. F. Forbes, "The Trajectory of a Powered Rocket in Space," *Journal of the British Interplanetary Society*, vol. 9, 1950, pp. 75–79.

2 H. Preston-Thomas, "Generalized Interplanetary Orbits," *Journal of the British Interplanetary Society*, vol. 11, 1952, pp. 76–85.

3 H. Preston-Thomas, "Interorbital Transport Techniques," *Journal of the British Interplanetary Society*, vol. 11, 1952, pp. 173–193.

4 H. S. Tsien, "Take-off From Satellite Orbit," *Journal of the American Rocket Society*, vol. 23, 1953, pp. 233–236.

5 E. Sänger, "Flight Mechanics of Photon Rockets," *Aero Digest*, vol. 73, 1956, pp. 68–70, 72–73.

6 E. Stuhlinger, "The Flight Path of an Electrically Propelled Space Ship," *Jet Propulsion*, vol. 27, 1957, pp. 410–414, 397.

7 H. F. Michielsen, "The Case for the Low Acceleration Space Ship," *Astronautica Acta*, vol. 3, 1957, pp. 130–152.

8 J. B. Peterson, "Note on 'Take-off From Satellite Orbit,'" *Jet Propulsion*, vol. 27, 1957, pp. 1263–1264.

9 A. Dobrowolski, "Satellite Orbit Perturbations Under a Continuous Radial Thrust of Small Magnitude," *Jet Propulsion*, vol. 28, 1958, pp. 687–689.

10 J. Copeland, "Interplanetary Trajectories Under Low-Thrust Radial Acceleration," *ARS Journal*, vol. 29, 1959, pp. 267–271.

11 E. Rodriguez, "Method for Determining Steering Programs for Low-Thrust Interplanetary Vehicles," *ARS Journal*, vol. 29, 1959, pp. 783–788.

12 F. M. Perkins, "Flight Mechanics of Low-Thrust Space Craft," *Journal of the Aero/Space Sciences*, vol. 26, 1959, pp. 291–297.

13 E. Levin, "Low-Thrust Transfer Between Circular Orbits," ASME Paper No. 59—Av-2, 1959.

14 L. R. Shepherd and A. V. Cleaver, "The Atomic Rocket-4," *Journal of the British Interplanetary Society*, vol. 8, 1949, pp. 59–70.

15 A. C. Clarke, "Electromagnetic Launching as a Major Contribution to Space-Flight," *Journal of the British Interplanetary Society*, vol. 9, 1950, pp. 261–267.

16 L. Spitzer, Jr., "Interplanetary Travel Between Satellite Orbits," *Journal of the American Rocket Society*, vol. 22, 1952, pp. 92–96.

17 G. F. Forbes, "The Thrust Available From Electronic Acceleration," *Journal of Space Flight*, vol. 4, 1952.

18 E. Stuhlinger, "Possibilities of Electrical Space Ship Propulsion," *Bericht über den V. Internationalen Astronautischen Kongress*, 1954, Vienna, Austria, 1955, pp. 100–119.

19 E. Sänger, "Zur Mechanik der Photonen-Strahlantriebe," *Mitteilungen aus dem Forschungsinstitut für Physik der Strahlantriebe*, Stuttgart, No. 5, 1956.

20 R. W. Bussard, "A Nuclear-Electric Propulsion System," *Journal of the British Interplanetary Society*, vol. 15, 1956, pp. 297–304.

21 L. R. Shepherd, "Interstellar Flight," Realities of Space Travel, McGraw-Hill Book Company, Inc., New York, N. Y., 1957, p. 395.

22 H. Preston-Thomas, "Interorbital Transport Techniques," Realities of Space Travel, McGraw-Hill Book Company, Inc., New York, N. Y., 1957, p. 174.

23 K. A. Ehricke, "On the Application of Solar Power in Space Flight," *Seventh International Astronautical Congress Proceedings*, 1956, p. 451–506.

24 R. W. Bussard and R. D. DeLauer, "Nuclear Rocket Propulsion," McGraw-Hill Book Company, Inc., New York, N. Y., 1958.

25 R. H. Boden, "Ion Rocket Engine Systems—A Summary," *Aero/Space Engineering*, vol. 18, 1959 p. 67–71, 75.

26 R. N. Edwards and H. Brown, "Ion Rockets for Small Satellites," ARS Preprint No. 789–59, 1959 (unpublished paper).

27 R. E. Roberson, "Space Guidance and Control," *Astronautical Sciences Review*, vol. 1, 1959, p. 18.

28 P. Blanc, "Note on Rocket Propulsion With Separate Energy Source," *Mémorial de l'Artillerie Francaise*, vol. 25, 1951, p. 103–116.

29 H. Preston-Thomas, "Two Aspects of the Time Element in Interplanetary Flight," *Bericht über den V. Internationalen Astronautischen Kongress*, Vienna, Austria, 1955, pp. 150–156.

30 D. M. Cole, "Minimum Time Interplanetary Orbits," *Proceedings of the American Astronautical Society*, vol. 4, 1958, Paper No. 39.

31 H. Preston-Thomas, "A Note on 'A Nuclear Electric Propulsion System,'" *Journal of the British Interplanetary Society*, vol. 16, 1958, pp. 508–517.

32 H. Preston-Thomas, "Some Design Parameters of a Simplified Ion Rocket," *Journal of the British Interplanetary Society*, vol. 16, 1958, pp. 575–583.

33 H. F. Michielsen, "Minimum Weight and Optimum Flight Path of Low-Acceleration Space Vehicles," *Proceedings of the American Astronautical Society*, Western Regional Meeting, August, 1958, Paper No. 29.

34 R. H. Olds, "Optimum Variation of Exhaust Velocity During Burning," *Jet Propulsion*, vol. 28, 1958, pp. 405–406.

35 R. R. Newton, "On the Optimization of Physical Propulsion Systems," *Jet Propulsion*, vol. 28, 1958, pp. 752–753.

36 C. J. Wang, et al., "Thrust Optimization of a Nuclear Rocket of Variable Specific Impulse," *Journal of the American Rocket Society*, vol. 29, 1958, pp. 341–344.

37 R. Fox, "Optimum Exhaust Velocity Programming and Propulsion Efficiency," *Journal of the Astronautical Sciences*, vol. 6, 1959, pp. 13–16.

38 G. Leitmann, "Some Remarks on the Optimum Operation of a Nuclear Rocket," *Proceedings of the Tenth International Astronautical Congress*, London, England, 1959, Springer Verlag, Vienna, 1960.

39 F. A. Valentine, "The Problem of Lagrange With Differential Inequalities as Added Side Conditions," Dissertation, Department of Mathematics, University of Chicago, Chicago, Ill., 1937.

40 G. A. Bliss, "Lectures on the Calculus of Variations," University of Chicago Press, Chicago, Ill., 1946.

41 G. Leitmann, "On a Class of Variational Problems in Rocket Flight," *Journal of the Aero/Space Sciences*, vol. 26, 1959, pp. 586–591.

Adiabatic Analysis of Elastic, Centrally Pivoted, Sector, Thrust-Bearing Pads[1]

B. STERNLICHT[2]
G. K. CARTER[3]
E. B. ARWAS[4]

This paper emphasizes the importance of temperature in thrust-bearing analysis. The analysis presented consists of simultaneous solution of the momentum, energy, and elasticity equations for centrally pivoted, sector-shaped, thrust-bearing pads. Elastic deformations due to the pressure distribution and thermal gradients are considered. Laminar and adiabatic conditions are assumed in the fluid film, and the lubricant is incompressible.

Introduction

PIVOTED-PAD thrust bearings present a special problem in thrust-bearing analysis. This is due to the fact that the pads of such bearings are generally supported on a finite number of "point" or "line" contacts. Thus, under heavy load, the pads deform both directly due to the load and because of the thermal gradients that are generated by the shear losses. Furthermore, the magnitudes of these deformations are often several times the minimum thickness of the fluid film on which the bearing operates. At various times in the past, attempts were made to show the major influence of pad deformations on bearing performance [1, 2, 3].[5] This previous work, however, was limited to infinitely wide bearings and much simplified estimates of the elastic deflections. In a recent paper [4] the authors derived an approximate equation which related pad deflection to thrust load and used it to show how pad dimensions can be optimized (from the standpoints of minimum film thickness and maximum temperature), taking account of the elastic properties of the pads. In none of this previously published work, however, were the elastic deflections calculated from solutions of the governing equations for sector-shaped pads, nor were thermal distortions included.

This paper extends previous work by incorporating in the analysis a numerical solution of the elasticity equation, including both the pressure and the temperature-gradient terms. The elastic deflections, calculated from the elasticity equation, are superposed on the radial and circumferential pad inclination to yield the film shape. This is introduced into the Reynolds and energy equations, which are then solved in their finite-difference form to yield the pressure and temperature profiles over the pads. An iterative procedure is followed until the solution which satisfies all three equations, their boundary conditions, and moment equilibrium is obtained. This final solution yields the true film shape and the corresponding pressure and temperature profiles and, hence, the total load, oil flow, and horsepower loss, as functions of pad geometry, minimum film thickness, speed and oil viscosity.

Here, the method of solution is outlined and its application is illustrated by means of a calculation performed for a typical configuration. In particular, the importance of thermal distortions and oil inlet temperature are described, as well as an indirect

[1] The work described here was performed under contract to the Bureau of Ships, Navy Department, Washington, D. C.

[2] Consulting Engineer—Hydrodynamics, General Electric Company, Schenectady, N. Y. Assoc. Mem. ASME.

[3] Senior Application Engineer, General Electric Company, Schenectady, N. Y.

[4] Engineer—Fluid Film Bearings, General Electric Company, Schenectady, N.Y. Assoc. Mem. ASME.

[5] Numbers in brackets designate References at end of paper.

Contributed by the Applied Mechanics Division and presented at the Winter Annual Meeting, New York, N. Y., November 27–December 2, 1960, of THE AMERICAN SOCIETY OF MECHANICAL ENGINEERS.

Written discussion on this paper should be addressed to the Editoral Department, ASME, 29 West 39th Street, New York, N. Y., and will be accepted until July 10, 1961. Discussion received after the closing date will be returned. First draft of manuscript received by ASME Applied Mechanics Division, August 18, 1959; final draft received July 6, 1960. Paper No. 60—WA-104.

Nomenclature

$A_{i,j}, A_{ij}$ = deflection coefficients, equations (4) and (21), in.
C_p = specific heat, Btu/lb deg F
D = flexural rigidity $= \dfrac{Et^3}{12(1-\nu^2)}$, lb-in.
E = elastic modulus, psi
e = deflection derivative, equation (14), in.
f = deflection functions, equations (4), (21), (34)
g = deflection derivative, equation (13), in.$^{-1}$
h = film thickness, in.
h_{min} = minimum film thickness, in.
$I_{i,j}, I_{ij}$ = set of deflection coefficients comprising matrices
J = mechanical equivalent of thermal energy (=9339 in-lb/Btu)
$J_{i,j}$ = inverse of $I_{i,j}$ matrix
$K_{ij}, \bar{K}_{ij}$ = set of deflection coefficients comprising matrices
k = deflection derivative, equation (15), in.$^{-1}$
L = radial length of pad, in.
M_x, M_y = edge bending moments per unit length, in-lb/in.
m = deflection modes; e.g., equation (7)
m_x, m_y = internal bending moments per unit length, in-lb/in.
N = speed of rotation, rps
n = deflection modes; e.g., equation (7)
P = pressure differential across pad, psi
p = unit loading, psi
p_{avg} = average unit loading, psi
q_r = surface temperature gradient, radially, deg F/in.
q_θ = surface temperature gradient, circumferentially, deg F/radian
R = outside radius of pad, in.
r = radial co-ordinate, in.
r_c = radial co-ordinate, Fig. 11, in.

(Continued on next page)

method of determining minimum film thickness, based on temperature measurements.

Governing Equations and Method of Analysis

The following assumptions are made in the analysis described in this paper:

1 Steady-state conditions prevail in the film.
2 Lubricant is Newtonian and incompressible.
3 Flow in clearance spaces is laminar and adiabatic.
4 Lubricant inertia forces are neglected.
5 Pressure and shear effects on viscosity are neglected.
6 Variations of the specific heat of the lubricant with pressure and temperature are neglected.

When the first four of these assumptions are valid, the hydrodynamic pressures (which are generated in the fluid film that separates the bearing pads from the runner) may be calculated by integrating Reynolds' equation:

$$\frac{\partial}{\partial r}\left(\frac{rh^3}{\mu}\frac{\partial p}{\partial r}\right)+\frac{\partial}{\partial \theta}\left(\frac{h^3}{\mu r}\frac{\partial p}{\partial \theta}\right)=6\omega r\frac{\partial h}{\partial \theta} \tag{1}$$

In order to integrate equation (1) for any given geometry and speed, the viscosity and film thickness need to be known as functions of position. For petroleum oil, in the range of present-day thrust-bearing practice, shear and pressure effects on viscosity are very small [5]. The local viscosity values are then functions only of the local film temperatures and the viscosity-temperature characteristics of the oil. In the present analysis, adiabatic conditions are assumed and the temperature distribution is obtained by integrating the following equation (energy equation, reference [6]) simultaneously with equation (1):

$$\frac{\mu}{h}(\omega r)^2+\frac{h^3}{12\mu}\left[\left(\frac{\partial p}{r\partial\theta}\right)^2+\left(\frac{\partial p}{\partial r}\right)^2\right]$$

$$-C_p\rho gJ\left[\left(\frac{r\omega h}{2}-\frac{h^3}{12\mu}\frac{\partial p}{r\partial\theta}\right)\frac{\partial T}{r\partial\theta}-\frac{h^3}{12\mu}\frac{\partial p}{\partial r}\frac{\partial T}{\partial r}\right]=0 \tag{2}$$

The film shape, for pivoted pads, is determined by the tilt of the pads, radially and circumferentially, and by the deflections which result from the hydrodynamic pressures over the pads and the temperature gradients across the pads. In the present analysis, the pad deflections are calculated from the integration of the following equation (elasticity equation, references [7] and [8]):

$$\nabla^2(\nabla^2 w)=\frac{12(1-\nu^2)p}{Et^3}+\frac{(1+\nu)}{t}\nabla^2(\alpha\Delta T)$$

where

$$\nabla^2=\left(\frac{\partial^2}{\partial r^2}+\frac{1}{r}\frac{\partial}{\partial r}+\frac{1}{r^2}\frac{\partial^2}{\partial\theta^2}\right) \tag{3}$$

Equation (3) is integrated for both the pad and support plate. Local values of pad thickness are used so that the effects of changes in geometry are considered.

The boundary conditions used with the foregoing equations are:

(*a*) Pressures fall to zero around the pad perimeter.
(*b*) Pad inlet oil is at groove-mixing temperature.
(*c*) Radial temperature gradients are zero along the inner and outer circumferences of the pads, because of the cooling effect of the surrounding oil.
(*d*) Shear and bending moments are zero around the pad perimeter.

Since pad deformations under high loads may produce diverging film thicknesses (and hence breakdown of the film) near the trailing edges of the pads, an additional condition is imposed. This states that the hydrodynamic pressures over the pads are nowhere smaller than atmospheric.

Equations (1–3) are integrated simultaneously, using numerical methods and an iterative procedure. Finite differences are used for the integration of the Reynolds and energy equations, as described in [9] and [10]. The elasticity equation is integrated using the minimum energy principle, as described in Appendix 1.

The iterative procedure used for the simultaneous solution of the equations is described briefly as follows:

1 For a given geometry, speed, and minimum film thickness, integrate the Reynolds and energy equations, using a preliminary estimate of the deflections. This integration is carried out (as described in [9] and [10]) and the pad inclinations are obtained as those values which yield a pressure profile whose center of pressure passes through the axis of the pivot.

2 The elasticity equation is then integrated for the pressure and temperature profiles obtained in step 1.

3 The Reynolds and energy equations are integrated once again, but this time for a pad which has the elastic deflections calculated in step 2.

The foregoing procedure is repeated until the differences between two successive iterations fall within a specified small limit.

From the final values of the film thickness, pressure, and temperature profiles obtained as just described, the remaining items of interest such as total load carried on the pads, oil flow, and horsepower loss are calculated in the same manner as in reference [4]. The estimated accuracy of the calculations is discussed in Appendix 2.

Nomenclature

r_0 = radius of support pad, Fig. 11, in.
r_p = radial co-ordinate of pivot, in.
$r_p\%$ = radial co-ordinate of pivot = $100[r_p-(R-L)]/L$, in.
s = deflection modes; e.g., equation (6)
T = temperature, deg F
T_{avg} = average film temperature, deg F
T_{GR} = groove mixing temperature, deg F
T_{max} = maximum film temperature, deg F
t = pad thickness, in.
V = energy of bending, lb-in.
V_{sp} = energy of bending of support plate, lb-in.
V_p = energy of bending of pad, lb-in.
W = potential energy associated with load, lb-in.
W_p = potential energy associated with pressure loading, lb-in.
W_T = potential energy associated with equivalent temperature loading, lb-in.
w = elastic deflection, in.
w_0 = deflection of rim of support plate, in.
α = linear coefficient of thermal expansion, 1/deg F
δ = increment
ΔT = temperature difference across pad, deg F
θ = angular co-ordinate, radians
θ_p = angular co-ordinate of pivot, radians
$\theta_p\%$ = angular co-ordinate of pivot = $100\ (\theta_p/\theta_T)$, radians
θ_{TOT} = pad subtended angle, radians
μ = absolute viscosity, lb sec/sq in.
ν = Poisson's ratio
ϕ_e = angular co-ordinate, Fig. 1(*a*)
ω = angular velocity, radians/sec

Discussion

Performance of Elastic Pads. The two limiting criteria of thrust-bearing performance are maximum film temperature and minimum film thickness. Generally, however, the main emphasis in the literature, as well as in design practice, has been on film thickness, with little attention devoted to maximum temperature. This is because isothermal bearing analysis was used almost exclusively in the past. The results of the more complete study described in this paper in which both temperature variations and elasticity are included have convinced the authors that, if anything, this emphasis should be reversed. In the following discussion, we will attempt to show that the film temperature is the major limitation of thrust-bearing performance because of its effect on the viscosity of the lubricant and the deflected shape of the pad. It will also be shown that when the bearing temperature is obtained, either analytically or experimentally, the minimum film thickness is also automatically defined.

To illustrate the results obtainable from the analysis, consider a 31-in-OD, eight pad bearing that has the dimensions outlined in Fig. 1(*a*). In the calculations, the pad is divided into a 13 × 13 field and the thickness profile is represented by the set of thicknesses in each mesh as shown in Fig. 1(*b*). The temperature gradients across the pad are determined from the difference between the film temperatures and the temperature distribution along the bottom face of the pad [see equation (27), Appendix 1]. The film temperatures are obtained from the solution of the energy equation, while the bottom face temperatures are assumed to be at groove temperature along the inlet edge and to rise at the rate of 40 deg F per radian, proceeding toward the trailing edge. This gradient was obtained from as yet unpublished data gathered during operation of a bearing of this size where the back face temperatures of the pads were measured at several points between the leading and trailing edges.

The following lubricant properties were assumed in the calculations:

Oil—Navy Designation 2190T
μ at 100 F = 12.5×10^{-6} lb sec/in.^{2}

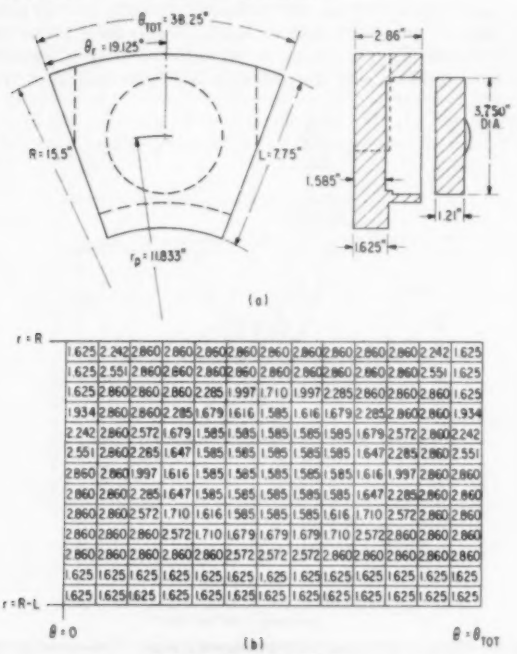

Fig. 1 Pad dimensions

μ at 210 F = 1.15×10^{-6} lb sec/in.^{2}
c_p (average) = 0.5 Btu/lb × deg F
ρ (average) = 0.84×10^{-4} lb sec^2/in.^{4}

The calculated charts of temperature versus unit loading and minimum film thickness versus unit loading for this bearing are shown in Figs. 2 and 3, respectively. Note that, whereas the minimum film thickness is a function of both load and speed, the film temperatures were found to be very nearly independent of speed. The reason for this is that, for a given unit loading, both the shear losses and the lubricant flow increase with speed. The film temperatures, which increase with shear loss but decrease with flow are then found to remain essentially constant over a wide range of speeds.

As shown in Fig. 2, a housing inlet temperature of 115 F was used. However, the temperature at which the oil enters each pad is much higher, owing to mixing in the grooves of cold inlet oil with hot oil discharged from the preceding pad. The groove-mixing-temperature curve shown in Fig. 2 was, therefore, used in the calculations. This curve was plotted from experimental data obtained by the authors and other investigators. The curves of "average film temperature," "average pad-outlet temperature,"

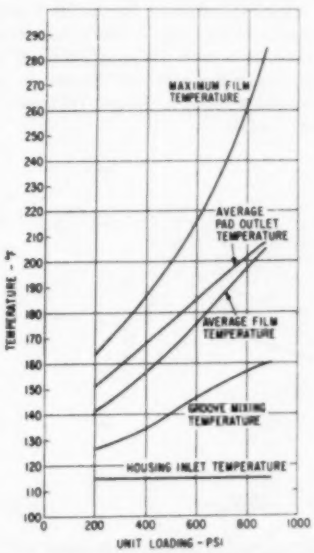

Fig. 2 Oil temperatures versus unit loading (pad geometry per Fig. 1; oil 2190T)

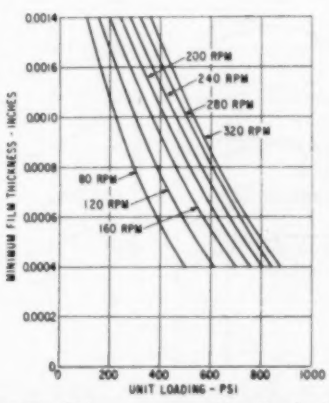

Fig. 3 Minimum film thickness versus unit loading (pad geometry per Fig. 1; oil 2190T)

and "maximum film temperature," also shown in Fig. 2, were calculated from the integrations of equations (1), (2), and (3).

Fig. 2 shows that the average film temperature and the average pad-outlet temperature are comparable. They are, however, very much smaller than the maximum film temperature, particularly at high loads. In addition, the slope of the maximum film-temperature curve is seen to increase quite rapidly with load. It is clear from this that:

(*a*) The bearing-oil drain temperature, which is often used to monitor the condition of a bearing, is in fact a very poor indicator of impending bearing failure.

(*b*) With a heavily loaded bearing, even a moderate increase in load may raise the maximum temperature to a dangerous level.

Influence of Geometric Parameters. Figs. 4 and 5 show, respectively, the effects of variations in pad thickness and L/R ratio on bearing performance. In Fig. 4 the designation "standard pad" refers to the pad shown in Fig. 1. Note that at high load, a 30 per cent increase in pad thickness (over that of Fig. 1) would achieve a substantial increase in minimum film thickness and an even more important reduction in the maximum temperature. The reason for such improvement lies in the smaller elastic deflections of the thicker pads. Fig. 5 shows that there is a definite optimum L/R ratio from both the standpoints of minimum film thickness and maximum temperature. While the optimum L/R ratio varies with the load, it is in the general region of 0.5, within the range of loads studied.

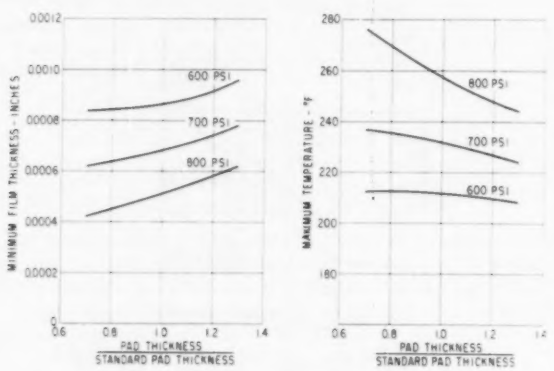

Fig. 4 Influence of pad thickness (oil 2190T; N = 5.33 rps)

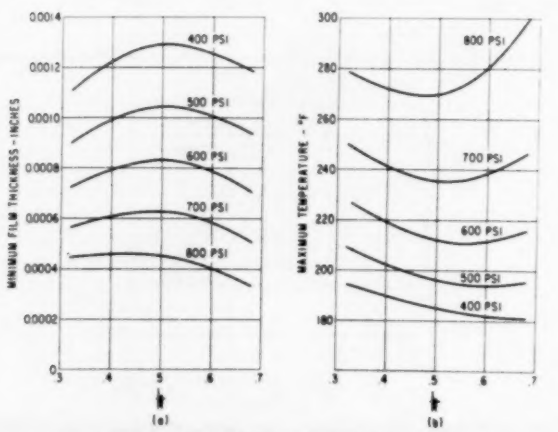

Fig. 5 Influence of L/R ratio (oil 2190T; N = 5.33 rps)

Influence of Groove Temperature. Fig. 6, which shows the relation between the minimum film thickness and the maximum temperature for a range of groove temperatures and unit loads, brings out a key point of this paper. This figure shows that for the given bearing geometry and speed, the maximum temperature can be used to predict the minimum film thickness with an accuracy of better than ±0.0001 in. If, in addition, the groove temperature is also known, then the minimum film thickness can be predicted even more closely. Thus maximum temperature can be employed to measure minimum film thickness. This is most significant, for such temperature measurements are, in general, much easier to make than direct measurements of film thickness with presently available indicators. Also, based on the foregoing, their potential accuracy in determining minimum film thickness appear to be superior to that of the presently available, direct indicators of film thickness. In practice also, such measurements may be used to provide a rapid response method for monitoring impending bearing failure.

Fig. 6 also shows the very important influence of groove temperature on bearing performance. To illustrate this point, note the very important gain that can be achieved by a 30-deg F reduction in groove temperature when the bearing is operating under 700 psi load (data from Fig. 6), Table 1.

Table 1

P_{avg}, psi	T_{GR}, deg F	h_{min}, in.	T_{max}, deg F
700	160	0.00063	240
700	130	0.00093	197

Comparison With Rigid Pad. Thus far the discussion has been limited to centrally pivoted pads which deform elastically under load, and because of the thermal gradients generated by the shear losses. The negative effects of large deformations which occur under high loads was pointed out. However, it must be remembered that, particularly for the case of centrally pivoted pads, some deformation is desirable for adequate load capacity. The reason for this is that, in order to satisfy equilibrium of moments, the resultant of the hydrodynamic pressures must pass through the pivot. Thus, for the case of centrally pivoted pads, the pressure profiles should be nearly symmetrical about the radial center line. As shown in [4], this condition is achieved when the active faces of the pads exhibit a slight convexity. Be-

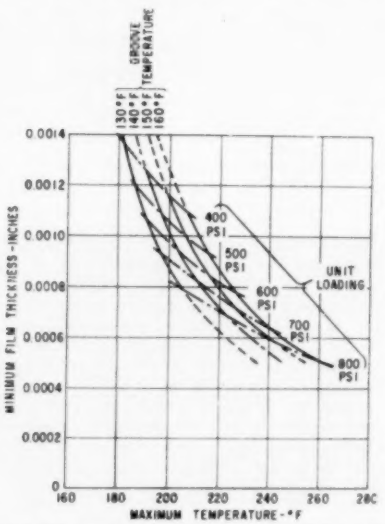

Fig. 6 Influence of groove mixing temperature (pad dimensions per Fig. 1; oil 2190T; N = 5.33 rps)

cause of the deflections, elastic pivoted pads will achieve this convexity automatically when run under load.

In the case of flat rigid pads, it is generally desirable to have an off-center pivot, so that the nonsymmetrical pressure profiles, associated with flat inclined sliders can be achieved. A centrally pivoted, rigid, flat pad, on the other hand, must rely on the viscosity variations over its length, to allow generation of hydrodynamic pressure which satisfy moment equilibrium.

Table 2 compares, at one operating point, the unit loads and maximum temperatures for an elastic, centrally pivoted pad with those for a rigid pad with optimum pivot and with a central pivot. Note that the unit loads carried by the elastic pad and by the flat, rigid pad with optimum pivot are comparable, whereas that carried by the flat, rigid, centrally pivoted pad is much smaller.

Table 2

R = 15.5 in. T_{GR} = 130 F
L = 7.75 in. h_{min} = 0.001 in.
θ_T = 38.25 deg Oil = 2190 T
N = 5.33 rps

Type of pad	Unit loading, psi	Max. film temp, deg F
Rigid flat pad with optimum pivot ($r_p\%$ = 51; $\theta_p\%$ = 61)	660	179
Rigid flat pad, centrally pivoted ($r_p\%$ = 51; $\theta_p\%$ = 50)	370	204
Elastic, initially flat pad, centrally pivoted (thickness and pivot location per Fig. 1)	642	194

Influence of Thermal Distortion. The influence of thermal distortion of the pads on bearing performance is shown in Figs. 7 and 8. In these figures, the minimum film thickness and maximum temperature are plotted versus unit load from the results obtained using three methods of analysis:

(*a*) Present analysis—complete solution, including thermal distortion.

(*b*) Present analysis, but neglecting thermal distortion.

(*c*) Simplified analysis of reference [4]. (In this method thermal deflections were neglected and it was assumed that the pads deform to a spherical shape under load. Using a simplified representation of the pads, the radius of curvature of the deformed pad, R_c, was related to the load, W, the average pad thickness, t, and the modulus, E, by the expression $R_c = 2.23Et^3/W$.)

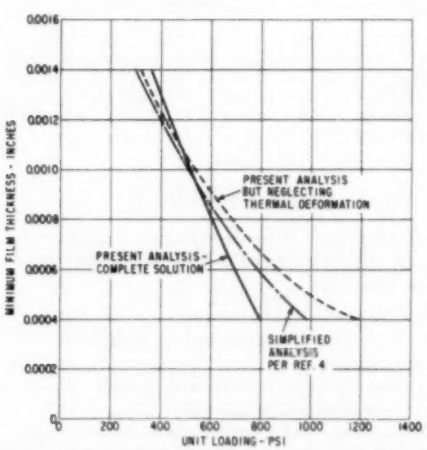

Fig. 7 Comparison of analytical results—minimum film thickness versus unit loading

The calculations were made in all three cases for the following pad geometry and operating conditions:

R = 15.5 in.
L = 6.75 in.
t = 2.2 in. (uniform thickness)
N = 5.33 rps
Oil = 2190 T
T_{GR} = per plot of groove mixing temperature in Fig. 2

Note in Figs. 7 and 8 that, at least at loads up to 600 psi, the results obtained using the simplified analysis of [4], were reasonably close to those obtained using the present analysis, but neglecting thermal distortion. When, however, thermal distortion is introduced in the analysis, as seen in Figs. 7 and 8, the situation is drastically different at high loads.

At unit loads greater than about 600 psi the complete analysis, including thermal deformations, predicts much smaller minimum film thickness and higher maximum temperatures. Thermal distortions are thus seen to have a major effect on bearing performance and must be included when designing bearings to operate under high unit loads.

Fig. 9 shows the film-thickness contour lines, at a minimum

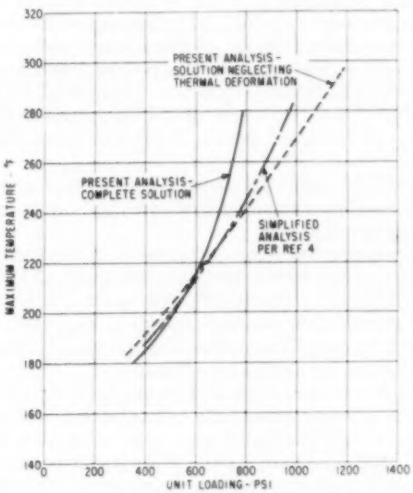

Fig. 8 Comparison of analytical results—maximum temperature versus unit loading

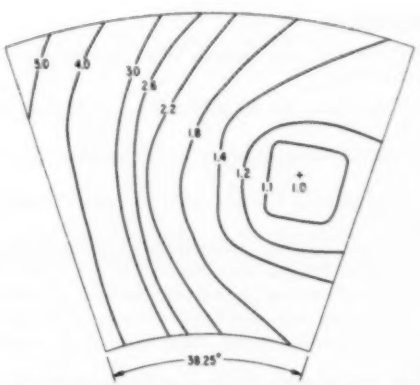

Fig. 9 Contour lines of h/h_{min} for h_{min} = 0.0004 in. Thermal deflections neglected (R = 15.5 in.; L = 7.25 in.; t = 2.2 in.; N = 5.33 rps; oil 2190-T).

film thickness of 0.0004 in. where thermal distortions are neglected. Fig. 10 shows the contour lines for the same minimum film thickness, but with the thermal distortions included. Note from these figures that:

(*a*) The pad deformations are several times the minimum film thickness.

(*b*) The thermal deflections are of the same order as those directly due to the hydrodynamic pressures.

These figures underline again the importance of elasticity in pivoted-pad thrust-bearing analysis and the need to include the effects of thermal distortions in such analysis.

Summary of Conclusions

The afore-mentioned method of analysis was used for steady-state bearing performance calculations for a wide range of bearing sizes and geometries. In this paper, typical results were presented for one of these sizes in order to illustrate the results that are obtained with this method of analysis. While a number of conclusions may be drawn from the results, the authors feel the following are the most important ones:

1 Elastic deflections of the pads are several times the minimum film thickness. Thermal distortions are of the same order as those due directly to the hydrodynamic pressure loading. These deflections drastically affect the performance of the bearing and must be included in the analysis. Analysis which neglects pad elasticity and the effects of thermal gradients gives an erroneous and optimistic picture of thrust-bearing operation at high loads.

For operation under high loads, improvement of performanc can be gained by minimizing deflections and by lowering the groove-mixing temperature.

2 The maximum temperature reached in the film is drastically different from both the average film temperature and the average drain temperature. The slope of the maximum temperature versus unit-load curve rises very sharply at high loads. Highly loaded bearings of conventional design have, therefore, little margin of safety for overload conditions.

3 Accurate determination of the minimum film thickness in a bearing can be made theoretically by temperature measurements alone. It is desirable for this purpose to measure both the maximum film temperature and the groove temperature. This method offers greater accuracy than present direct film-thickness indicators.

Recommendations

The authors feel that future thrust-bearing investigations should be aimed at:

1 Modification of the energy equation, to include heat conduction.

2 Analysis of thrust bearings under transient conditions in the fluid film.

3 Analysis of thrust bearings under turbulent conditions in the fluid film.

4 Meticulous and well-instrumented experimental study of tilting-pad thrust-bearing performance. It is realized that such experimental work would undoubtedly be both difficult and expensive. It is, however, essential in order to test the validity of analytical work and present understanding of bearing performance.

5 Utilize the analytical and experimental results to optimize the dimensions of bearing designs in present use and to generate new designs capable of much improved load-carrying capacity.

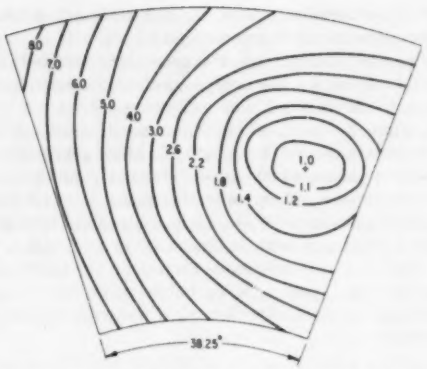

Fig. 10 Contour lines of h/h_{min} for h_{min} = 0.0004 in. Thermal deflections included (R = 15.5 in.; L = 7.25 in.; t = 2.2 in.; N = 5.33 rps; oil 2190 T).

Acknowledgments

The authors wish to thank Mr. J. C. Reid, Jr., Bureau of Ships, for constructive suggestions and assistance in performing the work described in this paper; and Miss M. A. Havill, General Electric Company, who programmed the equations and carried out the calculations.

References

1 A. A. Raimondi and J. Boyd, "The Influence of Surface Profile on the Load Capacity of Thrust Bearings With Centrally Pivoted Pads," TRANS. ASME, vol. 77, 1955, pp. 321–330.

2 S. Abramovitz, "Theory for a Slider Bearing With a Convex Pad Surface: Side Flow Neglected," *Franklin Institute Journal*, vol. 259, 1955, pp. 221–233.

3 F. Osterle and E. Saibel, "The Effect of Bearing Deformation in Slider Bearing Lubrication," ASLE Preprint No. 57AM2B-2.

4 B. Sternlicht, J. C. Reid, Jr., and E. B. Arwas, "Performance of Elastic, Centrally Pivoted, Sector Thrust Bearing Pads—Part 1," ASME Paper No. 60—Lub-10.

5 B. Sternlicht, "Influence of Pressure and Temperature on Oil Viscosity in Thrust Bearings," TRANS. ASME, vol. 80, 1958, pp. 1108–1112.

6 W. F. Cope, "The Hydrodynamical Theory of Film Lubication," *Proceedings of the Royal Society of London*, England, vol. 197, 1949, p. 201.

7 S. Timoshenko, "Theory of Plates and Shells," McGraw-Hill Book Company, Inc., New York, N. Y., 1940, chapter 3.

8 J. N. Goodier, "Thermal Stresses and Deformation," JOURNAL OF APPLIED MECHANICS, vol. 24, TRANS. ASME, vol. 79, 1957, pp. 467–474.

9 B. Sternlicht and F. J. Maginniss, "Application of Digital Computers to Bearing Design," TRANS. ASME, vol. 79, 1957, pp. 1483–1493.

10 B. Sternlicht, "Energy and Reynolds Considerations in Thrust Bearing Analysis," IME Conference on Lubrication and Wear, London, England, October, 1957.

APPENDIX 1

Assumed Conditions. Aside from the usual assumptions of elasticity theory, the following have been used in the numerical solution of equation (3):

(*a*) Only deflection due to bending is considered; the contributions due to shear deformation and to membrane and crushing stresses are omitted.

(*b*) The support plate, or button, is circular, of uniform thickness, and at uniform temperature.

(*c*) The support point is at the center of the support plate.

(*d*) Load is transmitted between the support plate and the sector pad through line contact around the outer edge of the

plate; the two parts are in contact around the entire circumference.

(*e*) No moment is transmitted through the plate-to-pad joint.

(*f*) Sharp discontinuities in the pad thickness are averaged out over finite area subdivisions; and local stress concentrations are ignored.

(*g*) Temperature of the bottom of the pad is assumed to vary linearly with radial and circumferential locations.

(*h*) Temperature of the top of the pad is assumed the same as the lubricant film temperature.

(*i*) No attempt is made to consider actual heat-flow distribution; the temperature, in effect, is assumed to act as if it varies linearly through the pad thickness at every point.

Co-ordinate Systems. The three sets of co-ordinates used are shown in Fig. 11. Axis-of-rotation co-ordinates (r, θ_c) are used for subdividing the pad and for calculations based on these subdivisions, including all integrations over the pad surface and boundary. Point-of-support co-ordinates (r_c, ϕ_c) are used for description of the deformation modes of both the pad and the support plate. Rectangular co-ordinates (X, Y) are used for load moment and center-of-pressure eccentricity calculations. The location of the support point (r_p, θ_p), the circle of contact between pad and support plate ($r_c = r_0$), and the boundary co-ordinates of the pad are also shown.

Energy of Bending. The selection of deformation-mode functions is critical; it was made in this case with consideration of the symmetry of the support pad and of the unimportance of the absolute level of the system. Consequently, the reference for deflection calculation is taken as the average location of the edge of the support plate; and the shape of the pad is written

$$w = \sum_i A_i f_i(r_c, \phi_c) \tag{4}$$

where A_i is a coefficient of length dimension, and f_i is a dimensionless-mode shape.

The actual deflection-mode shapes for the pad were chosen from among the axially symmetric and wave-deflection modes arising in the solution in polar co-ordinates of the plate-bending equation

$$\nabla^4 w = \frac{p}{D} \tag{5}$$

for uniform plate thickness, and axially symmetric or wave distributions of load q. These modes were classified as follows:

Symmetric

$$\left(\frac{r_c}{r_0}\right)^{2+s} - 1 \qquad s = 0, 2, 3, 4, \ldots \tag{6}$$

Nonsymmetric type I

$$\left(\frac{r_c}{r_0}\right)^m \begin{cases} \sin n\phi_c \\ \cos n\phi_c \end{cases} \quad \begin{matrix} n = \underbrace{2, 3, 4}_{n}; \ \underbrace{5, 6, \ldots}_{5} \\ m = \end{matrix} \tag{7}$$

Nonsymmetric type II

$$\left(\frac{r_c}{r_0}\right)^{m+s}\left[\left(\frac{r_c}{r_0}\right)^2 - 1\right] \begin{cases} \sin n\phi_c \\ \cos n\phi_c \end{cases} \quad \begin{cases} m = 2, 3: \ s = 0, 2, 3, 4, \ldots \\ m = 4, 5: \ s = 0, 1, 2, 3, \ldots \end{cases} \tag{8}$$

Solutions involving $\ln r$ are not included in this list, although they too could be used if desired. The type I nonsymmetric terms are

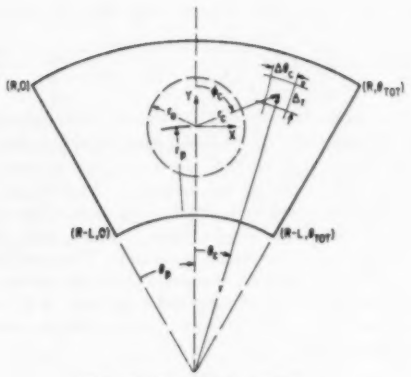

Fig. 11 Co-ordinate system

written to be the only ones involving nonzero deflection at the support-plate edge, and hence to give the only coupling with that plate.

The boundary condition on the support plate is, therefore, of the form

$$w_0 = \sum_i A_i \begin{cases} \sin n\phi_c \\ \cos n\phi_c \end{cases} \tag{9}$$

corresponding to any type I terms. For a uniform circular plate under edge load giving such an edge deflection, the bending equation can be solved with the following result:

$$w = \sum_i \frac{A_i n(n-1)(1-\nu)}{2(2n+1+\nu)} \left(\frac{r_c}{r_0}\right)^n \left\{(n+1)\frac{(n+2)-\nu(n-2)}{n(n-1)(1-\nu)} - \left(\frac{r_c}{r_0}\right)^2\right\} \begin{cases} \sin n\phi_c \\ \cos n\phi_c \end{cases} \tag{10}$$

where ν is Poisson's ratio.

In polar co-ordinates, the bending energy of a plate with surface S can be written as the following surface integral:

$$V = \int_S \frac{D}{2}\left[(g+e)^2 - 2(1-\nu)ge + 2(1-\nu)k^2\right] dS \tag{11}$$

where

$$D = \frac{Et^3}{12(1-\nu)^2} \tag{12}$$

is the stiffness in terms of Young's modulus E and plate thickness t; and

$$e = \frac{1}{r}\frac{\partial w}{\partial r} + \frac{1}{r^2}\frac{\partial^2 w}{\partial \theta^2} \tag{13}$$

$$g = \frac{\partial^2 w}{\partial r^2} \tag{14}$$

$$k = \frac{\partial}{\partial r}\left(\frac{1}{r}\frac{\partial w}{\partial \theta}\right) \tag{15}$$

are the deflection derivatives. In the case of the support plate, the deflection (10) can be substituted and gives the bending energy

$$V_{SP} = \sum_i A_i^2 \frac{\pi D}{2r_0^2} \frac{n^2(n^2-1)(1-\nu)(3+\nu)}{(2n+1+\nu)} \tag{16}$$

The variation, which is of interest in the Ritz method, is

$$\delta V_{SP} = \sum_i A_i \delta A_i \frac{\pi D}{r_0^2} \frac{n^2(n^2-1)(1-\nu)(3+\nu)}{(2n+1+\nu)} \quad (17)$$

In the case of the bearing pad, the nature of the cutouts and the shape of the pad make direct integration for the energy impractical. The result is, therefore, approximated by computing an average or mean value of the integrand for each of the subdivisions of surface used in the lubrication calculation; and these are summed using the weight factors which were developed for the integration of pressure to give load. These weight factors are not quite appropriate for the bending energy, but seem within the accuracy of other approximations. Actually, it is convenient to program the calculation of the variation of the bending energy directly; symbolically,

$$\delta V_P = \sum_{i,j} \bar{I}_{ij} A_i \delta A_j \quad (18)$$

The coefficients $\bar{I}_{ij}$ correspond to integrals of the form

$$\bar{I}_{ij} = \int_S D \{(g_i + e_i)(g_j + e_j) - (1-\nu)(g_i e_j + g_j e_i) + 2(1-\nu) k_i k_j\} dS \quad (19)$$

In this case, both subscript i and subscript j refer to the individual deflection modes and can range over all the modes which are under consideration for the pad. In general, the cross-coupling terms will not cancel, as they do in the case of the support plate; so that the terms of I_{ij} can form a complete matrix of order equal to the number of assumed modes. The $\bar{I}_{ij}$ matrix is obviously symmetric, however, limiting the number of combinations that have to be calculated to that extent.

The variation of the total bending energy is the sum of the pad and support plate values:

$$\delta V = \delta V_P + \delta V_{SP} \quad (20)$$

The result of this summation is a matrix I_{ij} of coefficients for the parameters $A_i \delta A_j$, which differs from the pad matrix $\bar{I}_{ij}$ only in those main diagonal terms corresponding to type I wave moves coupling with the support plate. The resulting matrix I_{ij} is, therefore, also symmetric. In the present case, this represents the total elastic-energy variation; and since it depends only upon the assumed deflection modes and the pad and plate geometry, it can be computed initially before starting any of the iterative stages of the bearing program. Moreover, for the point-supported bearing it turns out that I_{ij} is the complete matrix of coefficients of the linear equations which have to be solved for the deformation parameters A_i, consequently, the initial calculations can also include the inversion of I_{ij} to the solution matrix J_{ij}, giving a further reduction in the amount of calculation required in the iteration loops.

Load Energy Variation. The energy variation corresponding to the lubricant pressure loading is given by the variation of

$$W_P = -\int_S P \sum_j A_j f_j(r_c, \phi_c) dS \quad (21)$$

where P is the pressure differential across the pad, and is equal to the pressure computed from the solution of the lubrication equations. The support plate is assumed free from pressure differentials. Since the pressure is known only at discrete points, the centers of the mesh areas, numerical integration is again indicated. This is carried out for each deflection mode in the same way as the integration of pressure to obtain total load. The result gives the constants $\bar{K}_j$ of the expression

$$\delta W_p = \sum_j \bar{K}_j \delta A_j \quad (22)$$

This is the only mechanical loading that needs to be considered.

There is, however, a contribution to the deflection due to the temperature variation through the pad thickness; any possible similar effect in the support plate has been neglected. Rather than attempt a rigorous analysis of this effect, the assumptions were made with the objective of conceptually replacing the temperature effect by an equivalent mechanical loading, the energy variation then being relatively simple to write. Thus the listed assumptions effectively describe the temperature field as varying linearly through the pad thickness at every point. Deformation in the plane of the pad could be prevented under these circumstances by developing an internal bending moment, expressed in rectangular co-ordinates, of

$$M_x = M_y = D(1+\nu)\alpha \frac{\Delta T}{t} \quad (23)$$

where α is the thermal-expansion coefficient. These moments are per unit length in the appropriate directions.

The development of such internal moments requires, in effect, a distributed moment loading of

$$m_x = -(1+\nu)\alpha \frac{\partial}{\partial x}\left(D \frac{\Delta T}{t}\right) \quad (24)$$

$$m_y = -(1+\nu)\alpha \frac{\partial}{\partial y}\left(D \frac{\Delta T}{t}\right) \quad (25)$$

each of these being expressed per unit surface area; and, in addition, concentrated edge moments around the free boundary given by expression (23). The total effect of the temperature distribution, and of the foregoing distributed and concentrated moment loads, is to maintain the pad flat and at the same time in moment equilibrium.

Therefore the deflection due to temperature can be represented by the effect of applying moment loading equal and opposite to that just described. The potential energy associated with such a load can be written as

$$W_T = \int_S \left(-m_x \frac{\partial w}{\partial x} - m_y \frac{\partial w}{\partial y}\right) dS - \int_l M_l \frac{\partial w}{\partial n} dl \quad (26)$$

the line integral being taken around the boundary of the pad. Again, as a practical matter, the integrals are approximated by appropriate summations, and the energy variation is calculated directly. Allowance for the description of temperature variation on the bottom of the pad is made by writing the temperature differential as

$$\Delta T = T - \left\{T_{GR} + q_\theta \cdot \theta + q_r \cdot \frac{\theta}{\theta_{TOT}} \cdot [r - (R - L)]\right\} \quad (27)$$

where T_{GR} is the oil-inlet edge temperature; and q_r, q_θ allow for the first-power variation along the radial and circumferential directions.

The (x, y) co-ordinates indicated in (23) through (26) need not be identified rigorously with a fixed co-ordinate system, as their function is ultimately only to give means of computing energy density, which is then integrated by the summation method. In the program, they are interpreted as being the local radial and tangential directions at each mesh center or boundary point, since these were the best directions for carrying out the necessary numerical differentiations.

The result of the foregoing temperature calculations is another set of load potential-energy terms corresponding to δW_T; the total

$$\delta W = \delta W_p + \delta W_T \quad (28)$$

comprises a set of coefficients K_j for the parameters δA_j.

Deflection Equations. By the minimum or stationary-energy principle, the equilibrium state is approximated when

$$\delta(V + W) = 0 \tag{29}$$

or

$$\sum_{i,j} I_{ij} A_i \delta A_j + \sum_j K_j \delta A_j = 0 \tag{30}$$

Since the variation of the A's are arbitrary, this is equivalent to the set of linear equations represented by the matrix equation

$$[I_{ij}][A_i] + [K_j] = 0 \tag{31}$$

The solution is

$$[A_i] + [I_{ij}]^{-1}[K_j] = 0 \tag{32}$$

or

$$[A_i] = -[J_{ij}][K_j] \tag{33}$$

The load-energy vector K_j is calculated at each appropriate point in the program, and multiplied by the initially calculated inverse matrix J_{ij} to get the new set of deflection coefficients A_i.

Functions Used. In the program development, and in the calculations made so far, six deflection modes have been used. They are as follows:

Symmetric

$$f_1 = \left(\frac{r_c}{r_0}\right)^2 - 1$$

$$f_2 = \left(\frac{r_c}{r_0}\right)^4 - 1 \tag{34}$$

Nonsymmetric type I

$$f_3 = \left(\frac{r_c}{r_0}\right)^2 \sin 2\phi_c$$

$$f_4 = \left(\frac{r_c}{r_0}\right)^2 \cos 2\phi_c$$

Nonsymmetric type II

$$f_5 = \left(\frac{r_c}{r_0}\right)^2 \left[\left(\frac{r_c}{r_0}\right)^2 - 1\right] \sin 2\phi_c$$

$$f_6 = \left(\frac{r_c}{r_0}\right)^2 \left[\left(\frac{r_c}{r_0}\right)^2 - 1\right] \cos 2\phi_c$$

The choice was made somewhat arbitrarily, to include all the types of functions, and to match to as good an approximation as possible what is known and suspected about the pad deformation. The validity of the choice has not been tested, but operation of the method appears to be successful.

APPENDIX 2

A 13 × 13 mesh was used in the numerical integration of equations (1), (2), and (3). This was the finest grid that could be used in the program. It was also finer than any previously used by the authors or reported in the literature on bearing analysis. Comparison was made at one point, with a calculation made using an 11 × 11 mesh. The resulting pressure and temperature fields agreed within 1 per cent.

Since an iterative method was used in the calculations, limits were set to determine when the final solution was achieved. There were as follows:

(*a*) Successive iterations of the pressure field had to repeat within 0.1 per cent.

(*b*) Successive iterations of elastic deflections had to repeat within 3×10^{-6} in.

(*c*) The resultant of the pressure field had to coincide with the pivot point within 0.2×10^{-3} in.

The authors feel that these limits were sufficient to insure that:

(*a*) Errors in calculated maximum temperature <5 deg F.

(*b*) Errors in calculated minimum film thickness $\ll 0.0001$ in.

With regard to the calculated oil flow and horsepower loss, however, much larger errors are introduced in the necessary numerical calculation of the pressure gradients at the edges [4]. Based on observation of the point scatter obtained from a large number of calculations, it is felt that, in extreme cases, the calculated oil flow and friction losses may be in error by as much as 10 per cent.

The Effect of a Longitudinal Gravitational Field on the Supercavitating Flow Over a Wedge

A. J. ACOSTA
Associate Professor,
Division of Engineering,
California Institute of Technology,
Pasadena, Calif. Assoc. Mem. ASME

The free-streamline flow past a symmetrical wedge in the presence of a longitudinal gravitational field is determined with a linearized theory. The proportions of the cavity depend upon the cavitation number and Froude number. The drag coefficient is likewise affected by gravity, though to a smaller extent.

In recent years a number of papers treating linearized free-streamline problems have appeared subsequent to Tulin's introductory paper on this subject [1].[1] Among these may be mentioned Wu's extension of Tulin's method for supercavitating hydrofoils with arbitrary shape and cavitation number [2], hydrofoils with cavitation only near the leading edge [3], supercavitating hydrofoils in cascade [4], and Cohen's work on wall-interference effects [5]. In all of these works the hydrofoil is assumed to be in a force-free field. However, Parkin recently has estimated the effect of a gravity field normal to the direction of the flow by means of a simplified representation of the gravity effect on the cavity boundary condition [6]. As yet the problem of the longitudinal gravity field does not seem to have been discussed.

Fully cavitated flows are known to occur in axial gravitational fields. The cavity associated with vertical water entry or exit is one example. An effect similar to that of axial gravity occurs when fully cavitating flow takes place in a large water tunnel with slightly diverging walls. The longitudinal pressure gradient that results from the variable cross section plays a role much like that of a force field. It appears then, that to have an understanding of free-streamline problems in all cases of possible technical interest, the effect of an axial or longitudinal gravitational field must be examined.

Formulation of Problem

A sketch of the cavitating wedge is shown in Fig. 1 where for convenience all lengths are made dimensionless by dividing by the length of the wedge L. The central idea of thin-airfoil theory is the linearization of the surface boundary conditions. The analysis is further simplified by fulfilling these conditions on the axis rather than on an approximate neighboring shape. In linearized free-streamline theory both of these simplifications are made. In the spirit of these approximations we will require that the velocity never differ too much from the free-stream velocity and, further, that the slope of the body must be small.

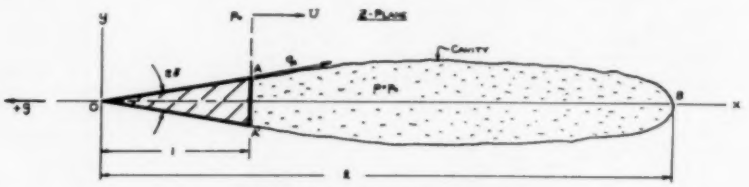

Fig. 1 Sketch of cavity configuration

Nomenclature

a,b,A,B = constants
C_D = drag coefficient $\left(D \Big/ \frac{\rho}{2} U^2 L\right)$
C_p = pressure coefficient $= (p - p_\infty)/\rho U^2/2$
D = drag force
F^2 = Froude number squared (U^2/gL)
g = gravitational acceleration
$i = \sqrt{-1}$
K = cavitation number $[(p_0 - p_c)/\rho U^2/2]$
L = length of wedge
l = cavity length divided by L
p = pressure
q_c = characteristic velocity on the cavity $[U\,(1 + K)^{1/2}]$
S = dimensionless cavity cross-sectional area
U = velocity at infinity
u = perturbation velocity in direction of U
v = perturbation velocity normal to U
$w = u - iv$
x, y = Cartesian co-ordinates in physical plane
$z = x + iy$
γ = wedge, semi-apex angle
ρ = fluid density
ζ = transformed plane
$(\ )_c$ = quantity on cavity
$(\ )_0$ = quantities far from the body but in plane of base of weged
$\overline{(\ )}$ = the complex conjugate

[1] Numbers in brackets designate References at the end of the paper.

Presented at the Summer Conference of the Applied Mechanics Division, Chicago, Ill., June 14–16, 1961, of THE AMERICAN SOCIETY OF MECHANICAL ENGINEERS.

Discussion of this paper should be addressed to the Editorial Department, ASME, 29 West 39th Street, New York, N. Y., and will be accepted until July 10, 1961. Discussion received after the closing date will be returned. Manuscript received by ASME Applied Mechanics Division, July 7, 1960. Paper No. 61—APM-2.

In the thin-airfoil theory, the characteristic velocity is the velocity at infinity. However, it was shown by Wu [2] that a better approximation to the nonlinear theory was obtained if the velocity on the cavity was used as the characteristic velocity. In the case presently to be considered, the fluid velocity along the cavity is not constant owing to the effect of gravity. For the purpose of definiteness, the fluid velocity at the base of the wedge is used as the characteristic velocity. The connection between the characteristic velocity and the free-stream velocity is provided by the Bernoulli equation

$$p_0 + \frac{\rho U^2}{2} + \rho g = p_c + \frac{\rho}{2} q_c^2 + \rho g = p + \frac{\rho}{2} q^2 + \rho g x \quad (1)$$

The reference datum for the longitudinal gravity field is taken at $x = 0$. Thus if $K = (p_0 - p_c)/\rho U^2/2$, $q_c = U\ (1 + K)^{1/2}$. The velocity vector q is

$$q = q_c + u + iv \quad (2)$$

where u, v are perturbation velocity components assumed to be much smaller than q_c. We now define a pressure coefficient based upon the free-stream dynamic pressure and the cavity pressure:

$$C_p = \frac{p - p_c}{\rho U^2/2} = \frac{2g(1 - x)}{U^2} - \frac{2uq_c}{U^2} \quad (3)$$

where u^2, v^2 have been neglected compared to q_c^2. It should be noted from equation (1) that the gravity force points upstream, Fig. 1.

As in other thin-airfoil theories, the boundary conditions are applied on the chord line of the profile which in the present case is the slit of length l on the real z-axis. The formulation of the problem can now be completed by stating the boundary conditions. They are:

(a) $v = \pm q_c\gamma$ on the wedge $(0 \leq x \leq 1)$,
(b) $C_p = 0$ on the cavity or from equation (3)

$$\frac{u}{q_c} = \frac{g(1 - x)}{q_c^2} \quad \text{for} \quad 1 \leq x \leq l$$

(c) As $z \to \infty$, $q_c + u \to U$, $v \to 0$. Thus

$$\frac{u}{q_c} = \frac{1}{(1 + K)^{1/2}} - 1 \quad \text{far from the body}$$

(d) The combination of body and cavity must be closed. The equivalent statement is that the net source strength must be zero.
(e) Lastly, the flow cannot contain nonintegrable singularities on the slit or have multiple values off the slit. (4)

Conditions $(a) - (e)$ are sufficient to determine the flow field although it has not been proved that the solution is unique.[2]

[2] Other linearized models of the flow are possible. For example, see Cohen's linearized model of the notched hodograph [5]. However, for the present purpose Tulin's original model seems simplest.

Solution

The complex velocity $w = u - iv$ is an analytic function of $z = x + iy$. It can therefore be transformed to other more convenient planes in such a way that w is the same at corresponding points. The plane chosen for analysis is the semicircular plane shown in Fig. 2. It is the same as that used by Wu [7] except that the physical plane is transformed onto the upper-half ζ-plane. The appropriate boundary conditions are also shown in Fig. 2.

It can be verified that the mapping function that transforms the z-plane onto the upper half ζ-plane is

$$z = l\left[1 - \frac{4(l - 1)\zeta^2}{(\zeta^2 - \zeta_1^2)(\zeta^2 - \zeta_2^2)}\right] \quad (5)$$

where ζ_1, ζ_2 are the roots of

$$0 = \zeta^4 + 2\zeta^2(2l - 1) + 1 = (\zeta^2 - \zeta_1^2)(\zeta^2 - \zeta_2^2) \quad (6)$$

For reference, these roots are

$$\zeta_1 = i\,[l^{1/2} + (l - 1)^{1/2}]$$
$$\zeta_2 = i\,[l^{1/2} - (l - 1)^{1/2}] \quad (7)$$

Note that ζ_1 is exterior to the unit circle and represents the point $z = \infty$.

The solution proceeds as follows: Separate w into two terms that satisfy the following conditions:

For w_1

$$v_1 = \pm q_c\gamma \quad \text{on the wedge},$$
$$u_1 = g/q_c \quad \text{on the cavity} \quad (4a)$$

For w_2

$$v_2 = 0 \text{ on the wedge}$$
$$u_2 = -\frac{gx}{q_c} \quad \text{on the cavity} \quad (4b)$$

The sum of $w_1 + w_2$ must satisfy the remainder of conditions (4). The solution of w_1 subject to the foregoing restrictions is

$$w_1 = -\frac{2\gamma}{\pi} q_c \ln\frac{\zeta + i}{\zeta - i} + iA\left(\zeta - \frac{1}{\zeta}\right) + B \quad (8)$$

where A, B are real constants. From $(4a)$, $B = g/q_c$ but A cannot yet be determined.

Term w_2 poses somewhat more of a problem. It can be seen from equation (5) that $x(\zeta)$ is a complicated function. However, a simple closed-form solution for w_2 can be obtained by use of the transformation function, equation (5), and suitable images. Such a possibility is immediately suggested since on the real ζ-axis (i.e., on the cavity) equation (5) is equal to x. Hence we might suspect that $w_2(\zeta) \sim z$. However, $z(\zeta)$ cannot be directly used as the velocity function since it has a pole at ζ_1 (or $z = \infty$). (ζ_2 is interior to the unit circle and therefore does not represent a point in

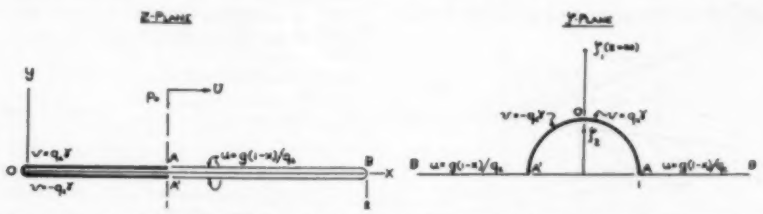

Fig. 2 Sketch showing physical plane (z-plane) and transformed plane. Appropriate boundary conditions are marked on diagram.

the physical plane.) What must be done, therefore, is to remove the singularity at ζ_1 and add suitable images to make v_2 zero on the unit circle. At the same time the contribution of the images on the real (ζ) axis must be purely imaginary to maintain the property $u_2 \sim x$ there. With these preliminaries it can be seen that

$$w_2 = -\frac{gl}{q_c}\left[1 - \frac{4(l-1)\zeta^2}{(\zeta^2-\zeta_1^2)(\zeta^2-\zeta_2^2)} + \frac{2(l-1)\zeta_1}{(\zeta-\zeta_1)(\zeta_1^2-\zeta_2^2)} + \frac{2(l-1)\bar{\zeta}_1}{\left(\frac{1}{\zeta}-\bar{\zeta}_1\right)(\bar{\zeta}_1^2-\bar{\zeta}_2^2)} - \frac{2(l-1)\bar{\zeta}_1}{(\zeta-\bar{\zeta}_1)(\bar{\zeta}_1^2-\bar{\zeta}_2^2)} - \frac{2(l-1)\zeta_1}{\left(\frac{1}{\zeta}-\zeta_1\right)(\zeta_1^2-\zeta_2^2)}\right]$$

obeys the requirements of equation (4*b*). With the aid of equation (7) this expression is capable of considerable simplification and becomes, after some manipulation,

$$w_2 = -\frac{gl}{q_c}\left\{1 - \left(\frac{l-1}{l}\right)^{1/2}\left[\frac{\zeta_1}{\zeta+\zeta_1} - \frac{\zeta_2}{\zeta+\zeta_2}\right]\right\} \quad (9)$$

The complete velocity function is $w_1 + w_2$ or

$$\frac{w}{q_c} = \frac{w_1+w_2}{q_c} = -\frac{2\gamma}{\pi}\ln\frac{\zeta+i}{\zeta-i} + i\frac{A}{q_c}\left(\zeta - \frac{1}{\zeta}\right) - \frac{g}{q_c^2}(l-1) + \frac{gl}{q_c^2}\left(\frac{l-1}{l}\right)^{1/2}\left[\frac{\zeta_1}{\zeta+\zeta_1} - \frac{\zeta_2}{\zeta+\zeta_2}\right] \quad (10)$$

We have yet to determine A and to find the relation between γ, K, and g. However, conditions (*c*) and (*d*) of (4) remain to be fulfilled. These operations can be carried out in the ζ-plane, but as pointed out in [7], it is easier to work in the z-plane for this purpose. We require according to this method the expansion of $w(z)$ for large z in the form

$$w(z) = a_0 + \frac{a_1 + ib_1}{z} + \frac{a_2 + ib_2}{z^2} + \dots \quad (11)$$

Then from (*c*) of equation (4)

$$a_0 = \frac{1}{(1+K)^{1/2}} - 1 \quad (12)$$

and from (*d*)

$$a_1 = 0 \quad (13)$$

As $z \to \infty$, $\zeta \to \infty$ also. ζ can be found in terms of $1/z$ from equation (5) with the result

$$\zeta = \zeta_1\left[1 + \frac{[l(l-1)]^{1/2}}{2z} + \frac{[l(l-l)]^{1/2}}{8z^2}\{2l + 1 + [l(l-1)]^{1/2}\} + 0\left(\frac{1}{z^3}\right)\right] \quad (14)$$

Substitution of (14) into (10) and simplification gives the desired form

$$\frac{w}{q_c} = -\frac{\gamma}{\pi}\ln\frac{l^{1/2}+1}{l^{1/2}-1} - \frac{A}{q_c}2l^{1/2} - \frac{g}{2q_c^2}(l-1) + \frac{1}{z}\left[\frac{\gamma}{\pi}l^{1/2} - \frac{A}{q_c}(l-1)l^{1/2} - \frac{g}{8q_c^2}(l-1)^2\right] + \frac{1}{z^2}\left[\frac{\gamma}{4\pi}(l+1)l^{1/2} - \frac{A}{4q_c}(l-1)(3l+1)l^{1/2} - \frac{gl}{16q_c^3}(l-1)(l^2-1)\right] + \dots \quad (15)$$

The constant A can now be found as indicated by equation (13) and is

$$A = \frac{\gamma q_c}{\pi(l-1)}\left[1 - \frac{\pi g(l-1)^2}{8\gamma q_c^2 l^{1/2}}\right] \quad (16)$$

Equations (15) and (16) constitute the solution. In the next section the principal results are summarized.

Results

We obtain first the relation between the cavity length l, the cavitation number K, and the gravity effect. Let $F^2 = U^2/g$ be the square of the Froude number (recall that the length of the wedge is unity—in the general case $F^2 = U^2/gL$). With equations (16) and (13) we get

$$1 - \frac{1}{(1+K)^{1/2}} - \frac{l-1}{4F^2(1+K)} = \frac{\gamma}{\pi}\left[\ln\frac{l^{1/2}+1}{l^{1/2}-1} + \frac{2l^{1/2}}{l-1}\right] \quad (17)$$

The cavity area (for unit wedge length) is shown in [7] to be $S = -2\pi a_2$. It then follows from equations (15) and (16) that the cavity area is

$$S = \gamma l^{3/2} - \frac{\pi}{16F^2}\frac{(l-1)^3}{1+K} \quad (18)$$

The drag coefficient of the body can be expressed as

$$C_D = D\Big/\frac{\rho}{2}U^2L = -\oint_{\text{body}} C_p\,dy = -\oint_{\text{body}}\left[\frac{2g(1-x)}{U^2} - \frac{2uq_c}{U^2}\right]dy \quad (19)$$

in which the expression for the pressure coefficient equation (3) has been used. Now $dy = dx\,v/q_c$ and furthermore $2uv = -\mathrm{Im}(w^2)$ so that equation (19) can be written

$$C_D = -\oint_{\text{body}}\frac{2g(1-x)}{U^2}\,dy - \frac{1}{U^2}\,\mathrm{Im}\oint_{\text{body}} w^2 dz \quad (20)$$

since on the wetted portion of the body $dz = dx$ (Im denotes the imaginary part). The contour around the body can be considered a part of a contour H that encloses the body, cavity, and the cavity closure denoted by ϵ, Fig. 3. The second term of equation

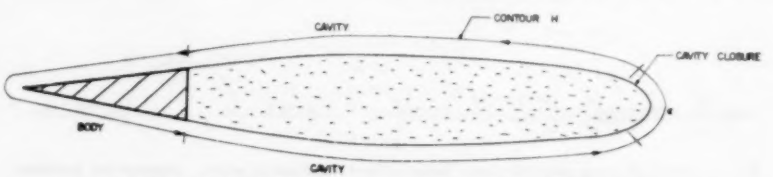

Fig. 3 Definition sketch of contour used in evaluation of drag integral

(20) can now be transformed further by deforming contour H until it consists of a circle of large radius. It is seen immediately from equations (11), (13) that w^2 has no simple pole within H, hence

$$0 = \oint_H w^2 dz = \oint_{\text{body}} w^2 dz + \oint_{\text{cavity}} w^2 dz + \oint_c w^2 dz$$

or

$$-\operatorname{Im} \oint_{\text{body}} w^2 dz = \operatorname{Im} \oint_c w^2 dz + \operatorname{Im} \oint_{\text{cavity}} w^2 dz$$

$$= \operatorname{Im} \oint_c w^2 dz - \oint_{\text{cavity}} 2g(1 - x) \frac{v}{q_c} dx$$

where boundary condition (4*b*) has been used in the second of these integrals. The expression for the drag coefficient now becomes

$$C_D = - \oint_{\text{body + cavity}} \frac{2g(1 - x)}{U^2} dy + \frac{1}{U^2} \operatorname{Im} \oint_c w^2 dz$$

We only need to observe that

$$\oint dy = 0$$

is precisely the closure condition and that

$$\oint x \, dy = S,$$

thus

$$C_D = \frac{2S}{F^2} + \frac{1}{U^2} \operatorname{Im} \oint_c w^2 dz \tag{21}$$

Apart from its effect on w, the gravity field gives rise to a buoyant force equal to the product of the area S and the specific weight of the fluid. Indeed, this contribution to the drag coefficient could have been written down without calculation. The usefulness of equation (21) is in the fact that the velocity function w has a particularly simple expansion about the point $z = l$. In fact as

$$z \to l, \zeta \to 2i(l - 1)^{1/2} \Big/ \left(\frac{z}{l} - 1\right)^{1/2} \tag{22}$$

the velocity function, equation (10), becomes

$$w(z) \to -2A(l - 1)^{1/2} \Big/ \left(\frac{z}{l} - 1\right)^{1/2} \tag{23}$$

Straightforward application of equation (21) gives the final result

$$C_D = \frac{8\gamma^2(1 + K)}{\pi} \left(\frac{l}{l - 1}\right) + \frac{2\gamma l^{1/2}}{F^2} \tag{24}$$

Discussion

The expressions for cavity length, area, and drag coefficient were calculated as a function of cavitation number and Froude number for a wedge with a 15-deg semiapex angle. These results are shown in the graphs of Figs. 4, 5, 6. The cavity length is strikingly affected by gravity, Fig. 4. (Recall that positive F^2 or gravity effect means that the gravity force points upstream and negative F^2 downstream.) As one would anticipate, the effect of a positive Froude number is to increase the cavity length, since in this case the flow proceeds into a region of decreasing pressure. Conversely, the effect of negative Froude numbers is to shorten the cavity. Indeed, for a given (negative) Froude number, the cavity length is finite for $K = 0$. In the absence of gravity ($F^2 = \infty$), the cavity length is infinite for $K = 0$. On

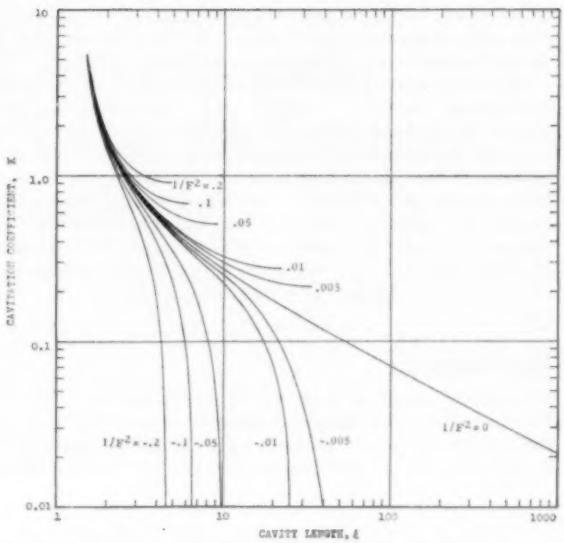

Fig. 4 Cavity length versus cavitation number for various values of Froude number. The semiwedge angle is 15 deg ($\gamma = 15$ deg).

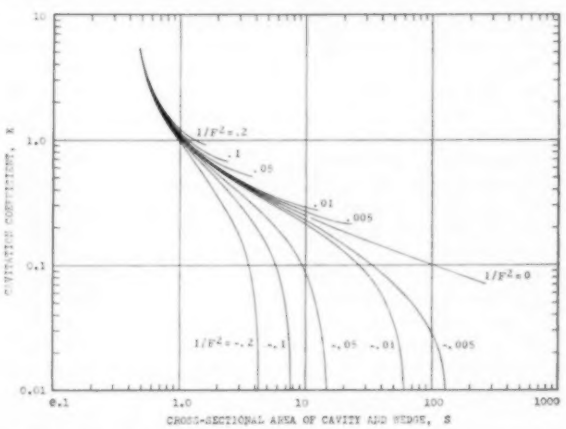

Fig. 5 Dimensionless cavity area versus cavitation number as a function of Froude number for $\gamma = 15$ deg

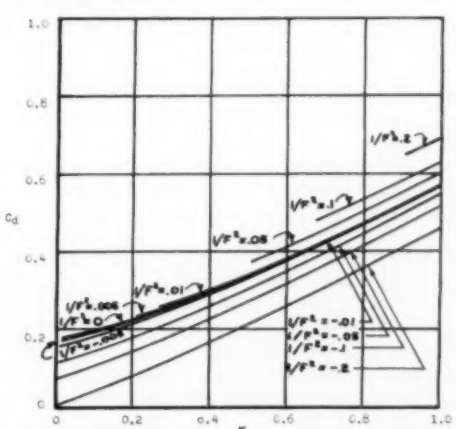

Fig. 6 Drag coefficient versus cavitation number as a function of Froude number for various cavitation numbers

the other hand, for a given positive Froude number, there is a minimum value of the cavitation number. In Fig. 4 the curves of l versus K are not extended beyond this minimum.

The effect of gravity on the drag coefficient, Fig. 6, is somewhat less important than on the length or area. The trend is again as one would expect from physical grounds; namely, that when the force field points upstream, the drag force is increased. Negative values of F^2 decrease the drag force for the same reason. These effects may be partly likened to a horizontal buoyant force as inspection of equation (21) shows. From an inspection of Fig. 5 it appears that the buoyant terms could actually give rise to a negative drag coefficient for a sufficiently strong downstream gravity vector. Such a condition is not likely to occur, however, in practice.

Acknowledgments

The author would like to express his appreciation to Prof. T. Y. Wu for many stimulating discussions on this subject, and to acknowledge the work of calculation and illustration done by Mr. R. Johnstone. This work was supported by the Office of Naval Research, Contract Nonr—220(24). Reproduction in whole or part is permitted for any purpose of the United States Government.

References

1 M. P. Tulin, "Steady Two-Dimensional Cavity Flows About Slender Bodies," Taylor Model Basin Report No. 834, 1953.

2 T. Y. Wu, "A Note on the Linear and Nonlinear Theories for Fully Cavitated Hydrofoils," California Institute of Technology, Hydrodynamics Laboratory Report No. 21-22, 1956.

3 A. J. Acosta, "A Note on Partial Cavitation of Flat Plate Hydrofoils," California Institute of Technology, Report E-19.9, 1955.

4 H. Cohen and C. D. Sutherland, "Finite Cavity Cascade Flow," Rensselaer Polytechnic Institute, RPI Mathematics Report No. 14.

5 H. Cohen, C. D. Sutherland, and Y. Tu, "Wall Effects in Cavitating Hydrofoil Flow," *Journal of Ship Research*, vol. 1, November 1957, pp. 31–39.

6 B. R. Parkin, "A Note on the Cavity Flow Past a Hydrofoil in a Liquid With Gravity," California Institute of Technology, Engineering Division Report No. 47-9, 1957.

7 T. Y. Wu, "A Simple Method for Calculating the Drag in the Linear Theories of Cavity Flows," California Institute of Technology, Engineering Division, Report 85-5, 1957.

On Transient Thermal Stresses in Viscoelastic Materials With Temperature-Dependent Properties[1]

ROKURO MUKI
Research Associate,
Division of Applied Mathematics,
Brown University,
Providence, R. I.

ELI STERNBERG
Professor,
Division of Applied Mathematics,
Brown University,
Providence, R. I.
Assoc. Mem. ASME

This paper deals with the quasi-static analysis of transient thermal stresses in the linear theory of viscoelastic solids with temperature-dependent properties. The underlying constitutive law rests on the temperature-time equivalence hypothesis. Following an exposition of the theoretical framework exact solutions to two specific problems are deduced: The first concerns the thermal stresses in a slab of infinite extent, generated by a temperature field that depends arbitrarily on the thickness co-ordinate and time; the second application concerns the stresses produced in a sphere by an arbitrary time-dependent radially symmetric temperature distribution. The numerical illustrations of the results obtained include a quantitative study based on actual test data for a polymethyl methacrylate.

1 Introduction

THE analysis of thermal stresses in viscoelastic materials has been the object of increasing concern during recent years. A quasi-static treatment of such problems, within the linear theory of homogeneous, isotropic viscoelastic solids and in the absence of thermomechanical coupling, presents no major difficulties even for transient temperature fields, provided the physical properties of the material are assumed to be independent of the temperature. In this event, as shown in [1],[2] an elementary extension of the correspondence principle[3] which links the linear theories of elasticity and viscoelasticity ordinarily permits a systematic reduction of the problem to an associated (uncoupled) thermoelastic problem.

The foregoing type of analysis was applied in [1], as well as in several subsequent studies, to the solution of various specific boundary-value problems. Unfortunately, however, such a treatment, which disregards the influence of temperature upon the basic response characteristics of the material, is remote from physical reality; for it is well known that the rate processes of viscoelasticity are highly sensitive to temperature changes.

The importance, in thermal-stress problems, of effects which stem from the temperature dependence of the viscoelastic properties was emphasized by Freudenthal [3, 4]. Hilton [5] considered such effects in connection with the plane problem of a hollow incompressible Kelvin cylinder, which is exposed to a radially symmetric temperature field.[4] Rongved [6], in an interesting investigation, arrived at an explicit solution for the transient thermal stresses in a compressible Maxwell sphere, on the assumption that the viscosity is an arbitrary function of the temperature, and supposing the latter to possess polar symmetry about the center of the sphere.

More recently, Morland and Lee [7] returned to linear thermoviscoelastic stress analysis of materials with temperature-dependent characteristics on the basis of the temperature-time equivalence hypothesis originally proposed by Leaderman [8]. According to this hypothesis all basic response functions (e.g., the relaxation moduli and creep compliances in shear and dilatation) are affected by a constant temperature change only within a corresponding uniform shift of the logarithmic time scale. The same postulate was introduced in a slightly different form by Ferry [9], and materials exhibiting such behavior have been termed "thermorheologically simple" by Schwarzl and Staverman [10]. The postulate has been confirmed experimentally[5] for a variety of viscoelastic materials.

The constitutive law adopted by Morland and Lee [7] is obtained through a natural extension of the shift hypothesis to variable (time-dependent) temperature fields. In case the temperature varies with time, the extended law implies a (nonlinear) dependence of the instantaneous stress state at each material point of the body upon the entire local temperature history. The application contained in [7], however, is confined to a *steady-state* temperature field; it consists of a plane-strain analysis of the stresses arising in a hollow circular cylinder which is maintained at a steady radial distribution of temperature and is subjected to a suddenly applied uniform internal pressure. Moreover, in this example, the assumption that the material is *incompressible* is made consistently.[6]

The theoretical developments presented in [7] provide for the possibility that the temperature dependence of the responses in shear and in dilatation are governed by two distinct shift functions. Yet, such an eventuality is precluded by the underlying assumption of a thermorheologically simple solid since the relaxation modulus in tension displays the shift property if, and only if, the two shift functions just mentioned are identical. For

---

[1] The results communicated in this paper were obtained in the course of an investigation conducted under Contracts Nonr-562(25) of Brown University, Providence, R. I., with the Office of Naval Research, Washington, D. C.

[2] Numbers in brackets designate References at end of paper.

[3] See, for example, Lee [2].

[4] The inclusion of thermal expansion in [5] is not altogether consistent with the accompanying assumption of mechanical incompressibility.

Contributed by the Applied Mechanics Division and presented at the Winter Annual Meeting, New York, N. Y., November 27–December 2, 1960, of THE AMERICAN SOCIETY OF MECHANICAL ENGINEERS.

Discussion of this paper should be addressed to the Editorial Department, ASME, 29 West 39th Street, New York, N. Y., and will be accepted until July 10, 1961. Discussion received after the closing date will be returned. Manuscript received by ASME Applied Mechanics Division, July 6, 1960. Paper No. 60—WA-124.

[5] Experimental evidence, as well as additional references to related theoretical considerations, are cited in an expository article by Schwarzl and Staverman [11], and by Payne [12].

[6] Thus thermal expansion is also neglected; cf. footnote 4.

this reason, and to avoid superfluous complications, we shall (without loss of physically meaningful generality) stipulate from the start that the entire response of the material is characterized by a single shift function, in so far as its temperature dependence is concerned.

It is the purpose of the present investigation, which was suggested by, and is complementary to, the work of Morland and Lee [7], to explore the consequences of the temperature-time equivalence hypothesis in circumstances involving time-dependent temperature fields. Following an exposition of the theoretical framework, which is intended to be clarifying, we deduce exact solutions to two specific problems. The first of these concerns thermal stresses and deformations in an infinite slab that is free from loading and is constrained to a purely transverse motion. The stress-inducing temperature distribution is permitted to vary arbitrarily across the finite slab thickness, is otherwise independent of position, and may have an arbitrary dependence on time. The second application concerns the thermal stresses and displacements in a sphere which, in the absence of loads, is under the influence of an arbitrary radially symmetric transient temperature field.

The treatment of the slab problem introduces no restrictions (beyond the hypothesis of linearity, homogeneity, and isotropy) of the viscoelastic response in shear and dilatation. In contrast, the problem of the sphere is dealt with on the assumption that the behavior in dilatation is purely elastic, but compressibility is taken into account. In either problem the results obtained alternatively accommodate stress-strain relations which are specified in terms of a relaxation law, a creep law, or through given differential operators. Further, the temperature dependence of the shift function and of the coefficient of thermal expansion remain unrestricted.

Both solutions just described are particularized for viscoelastic solids of the Maxwell or Kelvin type and are contrasted with the corresponding behavior of an ideally elastic medium. It is found that the surface displacements in the problem of the sphere are entirely independent of the deviatoric response and thus coincide for an elastic material and for *any* material whose dilatational response is linearly elastic. This conclusion may be of interest from an experimental point of view.

The paper concludes with illustrative numerical results appropriate to the case in which the respective temperature field is a solution of the (uncoupled) heat-conduction equation and is induced by a suddenly applied uniform change in the surface temperature of the body under consideration. Especially instructive are the numerical values reached for a polymethyl methacrylate, which are based on available relaxation-test data. These results indicate the radical qualitative and quantitative changes arising in the thermal stresses computed for an actual viscoelastic material once the fiction of a temperature-independent response is abandoned.

2 Fundamental Field Equations for Isothermal Conditions

In preparation for the developments to follow we recall first the relevant quasi-static system of field equations in the *isothermal* linear theory of viscoelasticity.[7] With reference to rectangular Cartesian co-ordinates x_i, the linearized displacement-strain relations in the usual indicial notation[8] appear as

$$\epsilon_{ij}(x, t) = \frac{1}{2}\left[\frac{\partial}{\partial x_j} u_i(x, t) + \frac{\partial}{\partial x_i} u_j(x, t)\right] \tag{1}$$

Here, as in the sequel, the single argument x stands for the triplet of co-ordinates (x_1, x_2, x_3), while t denotes the time; u_i and ϵ_{ij} designate the Cartesian components of the displacement vector and of the infinitesimal strain tensor. In the absence of body forces, and under neglect of the inertia forces, the equations of motion reduce to the equilibrium equations

$$\frac{\partial}{\partial x_j}\sigma_{ij}(x, t) = 0, \quad \sigma_{ji} = \sigma_{ij}, \tag{2}$$

where σ_{ij} are the components of the stress tensor.

With a view toward stating certain alternative forms of the linear stress-strain relations for a homogeneous and isotropic viscoelastic solid we introduce the deviatoric components of stress and strain through

$$s_{ij} = \sigma_{ij} - \frac{1}{3}\delta_{ij}\sigma, \quad e_{ij} = \epsilon_{ij} - \frac{1}{3}\delta_{ij}\epsilon,$$
$$\sigma = \sigma_{kk}, \quad \epsilon = \epsilon_{kk}, \tag{3}$$

in which δ_{ij} is the Kronecker delta. Turning first to constitutive laws in integral form, we cite the *relaxation integral law*

$$s_{ij}(x, t) = \int_{-\infty}^{t} G_1(t - t')\frac{\partial}{\partial t'} e_{ij}(x, t')dt',$$
$$\sigma(x, t) = \int_{-\infty}^{t} G_2(t - t')\frac{\partial}{\partial t'}\epsilon(x, t')dt', \tag{4}$$

and the *creep integral law*

$$e_{ij}(x, t) = \int_{-\infty}^{t} J_1(t - t')\frac{\partial}{\partial t'} s_{ij}(x, t')dt',$$
$$\epsilon(x, t) = \int_{-\infty}^{t} J_2(t - t')\frac{\partial}{\partial t'}\sigma(x, t')dt'. \tag{5}$$

Here $G_1(t)$, $G_2(t)$ and $J_1(t)$, $J_2(t)$ are the relaxation moduli and creep compliances (in shear and isotropic compression) at the uniform temperature under consideration. In this connection we stipulate that

$$G_\beta(t) = 0, \quad J_\beta(t) = 0 \quad (\beta = 1, 2) \text{ for } -\infty < t < 0. \tag{6}$$

Alternatively, for a medium with a finite and discrete spectrum of relaxation and retardation times, the linear constitutive law admits the *differential-operator representation*

$$P_1(D)s_{ij}(x, t) = Q_1(D)e_{ij}(x, t),$$
$$P_2(D)\sigma(x, t) = Q_2(D)\epsilon(x, t), \tag{7}$$

provided

$$D = \frac{\partial}{\partial t}, \quad P_\beta(D) = \sum_{n=0}^{N_\beta} p_\beta^{(n)} D^n, \quad Q_\beta(D) = \sum_{n=0}^{M_\beta} q_\beta^{(n)} D^n,$$
$$p_\beta^{(N_\beta)} \neq 0, \quad q_\beta^{(M_\beta)} \neq 0 \quad (\beta = 1, 2). \tag{8}$$

Thus P_β and Q_β $(\beta = 1, 2)$ are polynomial operators of degree N_β and M_β, respectively, whereas the coefficients $p_\beta^{(n)}$, $q_\beta^{(n)}$ are material constants.

The familiar connection between the foregoing three variants of the stress-strain law is obtained with the aid of the Laplace transform. Suppose $F(x, t)$ is a function of position and time, and adopt the notation

$$F^*(x, \eta) = \mathfrak{L}\{F(x, t);\ \eta\} = \int_{-\infty}^{\infty} F(x, t)\exp(-\eta t)dt, \tag{9}$$

whence $F^*(x, \eta)$ is the two-sided Laplace transform (with respect to t) of $F(x, t)$, η being the transform parameter. Applying the transform to (4), (5), and making use of the convolution theorem

[7] See, for example, the expository article by Lee [13].

[8] All Latin subscripts, unless otherwise specified, range over the integers (1, 2, 3) and summation over repeated subscripts is implied.

we conclude, under suitable regularity assumptions,[9] that (4) and (5) are equivalent if

$$G_\beta^*(\eta) = \frac{1}{\eta^2 J_\beta^*(\eta)} \quad (\beta = 1, 2). \tag{10}$$

Similarly, the equivalence of (4) and (7) is assured by

$$G_\beta^*(\eta) = \frac{Q_\beta(\eta)}{\eta P_\beta(\eta)} \quad (\beta = 1, 2), \tag{11}$$

while (5) and (7) are equivalent provided

$$J_\beta^*(\eta) = \frac{P_\beta(\eta)}{\eta Q_\beta(\eta)} \quad (\beta = 1, 2). \tag{12}$$

Equations (11), (12) permit the passage from a given differential-operator law to an equivalent stress-strain law of the hereditary integral type. On the other hand, a given law of the type (4) or (5) admits a (strictly) equivalent representation of the form (8) only if the Laplace transforms of the corresponding memory functions are rational.

In addition to the relaxation moduli in shear and isotropic compression (dilatation), we shall have occasion to make use of the "relaxation modulus in extension" and of "Poisson's ratio" for a viscoelastic material. The definition of these concepts[10] may be based on a uniaxial tensile relaxation test at constant strain, which is characterized by

$$\begin{aligned} &\epsilon_{11} = \epsilon_0 H(t), \quad \sigma_{11} = \sigma_{11}(t), \\ &\sigma_{22} = \sigma_{33} = 0, \quad \sigma_{ij} = 0 \ (i \neq j), \end{aligned} \tag{13}$$

where $H(t)$ is the Heaviside unit step-function given by

$$H(t) = \begin{cases} 1 & \text{for } 0 < t < \infty \\ 0 & \text{for } -\infty < t < 0 \end{cases} \tag{14}$$

The defining equations for the tensile modulus $\bar{E}(t)$ and for Poisson's ratio $\bar{\nu}(t)$, both of which are time-dependent, now appear as

$$\bar{E}(t) = \frac{\sigma_{11}(t)}{\epsilon_0}, \quad \bar{\nu}(t) = \frac{-\epsilon_{22}(t)}{\epsilon_0} \tag{15}$$

In order to reach the relations connecting $\bar{E}(t)$, $\bar{\nu}(t)$ and $G_1(t)$, $G_2(t)$, we first eliminate from (4), with the aid of (13), (3), all components of stress and strain except $\sigma_{11}(t)$ and $\epsilon_{22}(t)$. On applying the Laplace transform to the resulting pair of equations we arrive at

$$\begin{aligned} \sigma_{11}^*(\eta) &= G_1^*(\eta)[\epsilon_0 - \eta\epsilon_{22}^*(\eta)], \\ \sigma_{11}^*(\eta) &= G_2^*(\eta)[\epsilon_0 + 2\eta\epsilon_{22}^*(\eta)], \end{aligned} \tag{16}$$

from which, in view of (15),

$$\begin{aligned} \bar{E}(t) &= \mathfrak{L}^{-1}\left\{\frac{3G_1^*(\eta)G_2^*(\eta)}{G_1^*(\eta) + 2G_2^*(\eta)};\ t\right\}, \\ \bar{\nu}(t) &= \mathfrak{L}^{-1}\left\{\frac{G_2^*(\eta) - G_1^*(\eta)}{\eta[G_1^*(\eta) + 2G_2^*(\eta)]};\ t\right\}, \end{aligned} \tag{17}$$

if we employ the usual notation for the inverse transform.

It will be helpful for our future purposes to particularize the preceding discussion for certain important special viscoelastic media. In the case of the *elastic solid* the constants entering (8) have the values

$$\begin{aligned} &N_1 = M_1 = 0, \quad p_1^{(0)} = 1, \quad q_1^{(0)} = 2\mu, \\ &N_2 = M_2 = 0, \quad p_2^{(0)} = 1, \quad q_2^{(0)} = 3k, \end{aligned} \tag{18}$$

whence (7) become

$$s_{ij}(x, t) = 2\mu e_{ij}(x, t), \quad \sigma(x, t) = 3k\epsilon(x, t), \tag{19}$$

in which μ is the shear modulus and k the bulk modulus. It will also be convenient to recall the relations

$$\begin{aligned} k &= \frac{E}{3(1 - 2\nu)}, \quad \mu = \frac{E}{2(1 + \nu)}, \\ E &= \frac{9k\mu}{3k + \mu}, \qquad \nu = \frac{3k - 2\mu}{2(3k + \mu)}, \end{aligned} \tag{20}$$

where E and ν are the (constant) Young's modulus and Poisson's ratio of the elastic material. In accordance with (11), (12), (8), and (18), the corresponding relaxation and creep moduli, in shear and dilatation, reduce to

$$\begin{aligned} G_1(t) &= 2\mu H(t), \quad J_1(t) = \frac{1}{2\mu} H(t), \\ G_2(t) &= 3kH(t), \quad J_2(t) = \frac{1}{3k} H(t), \end{aligned} \tag{21}$$

while from (17), (20), and (21),

$$\bar{E}(t) = EH(t), \quad \bar{\nu}(t) = \nu H(t) \tag{22}$$

For the *Maxwell solid*[11] the dilatational response is elastic, whereas the behavior in shear, with reference to (8), is characterized by

$$N_1 = M_1 = 1, \quad p_1^{(0)} = \frac{1}{\tau_0}, \quad p_1^{(1)} = 1, \quad q_1^{(0)} = 0, \quad q_1^{(1)} = 2\mu, \tag{23}$$

so that the first of (7) becomes

$$\frac{\partial}{\partial t} s_{ij}(x, t) + \frac{1}{\tau_0} s_{ij}(x, t) = 2\mu \frac{\partial}{\partial t} e_{ij}(x, t), \tag{24}$$

where μ and τ_0 designate the shear modulus and the relaxation time of the solid. The corresponding memory functions for shear in this instance are found to be

$$G_1(t) = H(t)2\mu \exp\left(-\frac{t}{\tau_0}\right), \quad J_1(t) = \frac{H(t)}{2\mu}\left(1 + \frac{t}{\tau_0}\right), \tag{25}$$

whereas $\bar{E}(t)$ and $\bar{\nu}(t)$ here take the form

$$\begin{aligned} \bar{E}(t) &= H(t)E \exp\left[-\frac{2}{3}(1 + \nu)\frac{t}{\tau_0}\right], \\ \bar{\nu}(t) &= \frac{H(t)}{2}\left\{1 - (1 - 2\nu)\exp\left[-\frac{2}{3}(1 + \nu)\frac{t}{\tau_0}\right]\right\}, \end{aligned} \tag{26}$$

if the *constants* E and ν appearing in (26) are defined formally through the last two of (20) in terms of the shear and bulk modulus of the Maxwell solid. The physical significance of E and ν in the present context is apparent from

$$\bar{E}(0+) = E, \quad \bar{\nu}(0+) = \nu, \tag{27}$$

as is immediate from (26).

[9] In order not to detract from the main purpose of this investigation we shall, throughout the analysis, refrain from stating explicitly the regularity assumptions needed to justify the formal Laplace-transform manipulations used. For a rigorous treatment of this transform, reference may be made to Van der Pol and Bremmer [14].

[10] For other definitions of Poisson's ratio in the context of viscoelasticity theory, see [11], p. 73.

[11] The following definition, strictly speaking, refers to a solid which exhibits Maxwell behavior in shear but is elastically compressible. For the sake of brevity we shall, however, consistently use the term "Maxwell solid" in this restricted sense.

Finally, we cite the corresponding results for the *Kelvin solid* (cf. footnote 11), which are obtained in a strictly analogous manner. Now

$$N_1 = 0, \quad M_1 = 1, \quad p_1^{(0)} = 1, \quad q_1^{(0)} = 2\mu, \quad q_1^{(1)} = 2\mu\,\tau_0 \tag{28}$$

in (8) and the first of (7) assume the form

$$s_{ij}(x, t) = 2\mu\left[\tau_0 \frac{\partial}{\partial t}\, e_{ij}(x, t) + e_{ij}(x, t)\right], \tag{29}$$

where μ retains its previous significance, but τ_0 at present stands for the retardation time. The dilatational response is again elastic. The associated shear moduli of relaxation and creep are

$$G_1(t) = 2\mu[H(t) + \tau_0\delta(t)], \qquad J_1(t) = \frac{H(t)}{2\mu}\left[1 - \exp\left(-\frac{t}{\tau_0}\right)\right], \tag{30}$$

provided $\delta(t)$ stands for Dirac's delta function. Further,

$$\begin{aligned} \bar{E}(t) &= H(t)E\left\{1 + \frac{2(1+\nu)}{1-2\nu}\exp\left[-\frac{3}{1-2\nu}\frac{t}{\tau_0}\right]\right\}, \\ \bar{\nu}(t) &= H(t)\left\{\nu - (1+\nu)\exp\left[-\frac{3}{1-2\nu}\frac{t}{\tau_0}\right]\right\}, \end{aligned} \tag{31}$$

in which E and ν are once more defined formally through the last two of (20). Evidently

$$\bar{E}(t) \to E, \quad \bar{\nu}(t) \to \nu \quad \text{as} \quad t \to \infty, \tag{32}$$

which accounts for the physical significance of the constants E and ν in the case of the Kelvin solid.

3 Modification of the Constitutive Law: Influence of Temperature. Temperature-Time Equivalence.

The constitutive laws discussed in the preceding section rest on the assumption that the entire body is permanently maintained at a uniform temperature. Accordingly, the response functions $G_\beta(t)$ and $J_\beta(t)$ entering (4) and (5), as well as the material parameters $p_\beta^{(n)}$, $q_\beta^{(n)}$ appearing in (8), are to be regarded as having been determined at the relevant fixed "base temperature," which is henceforth designated by T_0.

We now turn to the modifications arising in the stress-strain law if the temperature field is variable with position and time. With a view toward the analytical formulation of the temperature-time equivalence hypothesis we confine our attention at first to the effect of a uniform temperature change, i.e., a change in the base temperature, and temporarily consider merely the temperature dependence of the relaxation moduli. To this end, let $\mathcal{G}_\beta(t, T)$, $(\beta = 1, 2)$ be the relaxation moduli (in shear and dilatation) at the *constant temperature* T so that, in accordance with previous agreements,

$$\mathcal{G}_\beta(t, T_0) = G_\beta(t) \equiv L_\beta(\log t) \qquad (\beta = 1, 2) \tag{33}$$

The postulate of thermorheologically simple behavior then takes the form

$$\mathcal{G}_\beta(t, T) = L_\beta[\log t + \psi(T)] \qquad (\beta = 1, 2), \tag{34}$$

where the "shift function" $\psi(T)$ obeys

$$\psi(T_0) = 0, \quad \frac{d\psi}{dT} > 0. \tag{35}$$

Setting

$$\psi(T) = \log \varphi(T), \tag{36}$$

one gathers from (35) that the shift factor $\varphi(T)$ conforms to

$$\varphi(T_0) = 1, \quad \varphi(T) > 0, \quad \frac{d\varphi}{dT} > 0 \tag{37}$$

and is thus a positive, monotone-increasing function of T throughout the range of validity of (34). Also, (34), by virtue of (33) and (36), yield

$$\mathcal{G}_\beta(t, T) = G_\beta(\xi) \qquad (\beta = 1, 2), \tag{38}$$

provided the "reduced time" ξ is defined by

$$\xi = t\varphi(T). \tag{39}$$

Consequently, the entire one-parameter family of response-function pairs $\mathcal{G}_\beta(t, T)$ is completely determined by its single member $G_\beta(t) = \mathcal{G}_\beta(t, T_0)$ once $\psi(T)$ is known for the temperature range in question. The shift-function $\psi(T)$, and hence the shift-factor $\varphi(T)$, in turn, represent an intrinsic property of the material under consideration.

Equations (38), (39) enable us to pass from (4), which holds at the base temperature T_0, to the corresponding relaxation integral law applicable at any constant temperature T. This transition is evidently effected by replacing $G_\beta(t - t')$ $(\beta = 1, 2)$ in (4) with $G_\beta(\xi - \xi')$, where ξ is given by (39) and $\xi' = t'\varphi(T)$, provided the body (in the absence of loads) is considered to be in the unstrained state at the uniform temperature T.

Next, suppose the medium is under the influence of a *variable temperature field* $T(x, t)$. In this event the foregoing modification of the constitutive law (4) requires a twofold amendment. First, to allow for the temperature dependence of the response functions in the presence of a time-dependent temperature distribution, the definition (39) of the reduced time ξ must be generalized consistent with the postulated temperature-time equivalence. Second, thermal expansion must be taken into account in the equation governing the dilatational response of the material. In this manner Morland and Lee [7] arrive at the generalized relaxation integral law

$$\begin{aligned} s_{ij}(x, t) &= \int_{-\infty}^{t} G_1(\xi - \xi')\frac{\partial}{\partial t'}\, e_{ij}(x, t')dt', \\ \sigma(x, t) &= \int_{-\infty}^{t} G_2(\xi - \xi')\frac{\partial}{\partial t'}\,[\epsilon(x, t') - 3\alpha_0\Theta(x, t')]dt', \end{aligned} \tag{40}$$

where

$$\xi = f(x, t) = \int_0^t \varphi[T(x, \lambda)]d\lambda, \quad \xi' = f(x, t'), \tag{41}$$

while the "pseudo-temperature" $\Theta(x, t)$ is defined by

$$\Theta(x, t) = \frac{1}{\alpha_0}\int_{T_0}^{T(x,t)} \alpha(T')dT', \quad \alpha_0 = \alpha(T_0) \tag{42}$$

Here $\alpha(T)$ is the temperature-dependent coefficient of thermal expansion and α_0 its value at the base-temperature T_0; $G_1(t)$ and $G_2(t)$, as before, are the relaxation moduli measured at T_0. Equations (41), in contrast to (39), imply a dependence of the reduced time ξ upon both position and the physical time.

If, in particular, $\alpha(T)$ is constant, (42) become

$$\alpha(T) = \alpha_0, \quad \Theta(x, t) = T(x, t) - T_0. \tag{43}$$

Further, in case $T(x, t)$ is constant, the reduced time ξ given in (41) coincides with that defined in (39). Finally, (40) degenerate into (4) when $T(x, t) = T_0$. Examining the structure of (40), and bearing in mind (41), (42), one notes that the temperature enters (40) both through the reduced time ξ and through the pseudo-temperature Θ. The instantaneous stresses at each

material point of the body are, in general, functionals of the entire preceding local strain and temperature history; these functionals are linear in the strains but nonlinear in the temperature.

Analogous considerations apply to the generalization of the creep law (5), which—under nonisothermal conditions—assumes the modified form

$$e_{ij}(x, t) = \int_{-\infty}^{t} J_1(\xi - \xi') \frac{\partial}{\partial t'} s_{ij}(x, t')dt',$$
$$\epsilon(x, t) = \int_{-\infty}^{t} J_2(\xi - \xi') \frac{\partial}{\partial t'} \sigma(x, t')dt' + 3\alpha_0\Theta(x, t) \tag{44}$$

Here $J_\beta(t)$ ($\beta = 1, 2$) are the creep compliances at the base temperature T_0, whereas ξ, Θ, and α_0 retain the meaning attached to them in (41), (42).

The integral laws (40), (44) involve the physical time t through $\xi = f(x, t)$, as well as explicitly. It is expedient to eliminate any explicit reference to t from these equations in favor of the reduced time ξ. For this purpose we note from (41), with the aid of (37), that $\xi = f(x, t)$, for fixed (x_1, x_2, x_3), is a monotone increasing function of t. Hence $f(x, t)$ in (41) may be inverted with respect to t, so that

$$t = g(x, \xi), \quad t' = g(x, \xi') \tag{45}$$

Also, by (41) and (45),

$$\frac{\partial \xi}{\partial t} = \varphi[T(x, t)], \quad \frac{\partial t}{\partial \xi} = \left(\frac{\partial \xi}{\partial t}\right)^{-1}. \tag{46}$$

Suppose $F(x, t)$ is any function of position and time. Then, to avoid ambiguity, we shall consistently adopt the notation

$$F(x, t) = \hat{F}(x, \xi) = F[x, g(x, \xi)]. \tag{47}$$

It should be emphasized that F and $\hat{F}$ are distinct functions unless $\xi = t$, i.e., unless $\varphi(T) \equiv 1$. Moreover, $\hat{F}(x, \xi)$ needs to be distinguished from $F(x, \xi)$, the values of which are obtained by replacing the argument t in $F(x, t)$ with ξ, rather than by subjecting t to the first of the transformations (45).

We now use (45) to change the variable of integration in (40), (44) from t' to ξ'. Employing the notation (47) and taking account of (46), we are thus led to the *relaxation integral law*

$$s_{ij}(x, \xi) = \int_{-\infty}^{\xi} G_1(\xi - \xi') \frac{\partial}{\partial \xi'} \hat{e}_{ij}(x, \xi')d\xi',$$
$$\hat{\sigma}(x, \xi) = \int_{-\infty}^{\xi} G_2(\xi - \xi') \frac{\partial}{\partial \xi'} [\hat{\epsilon}(x, \xi') - 3\alpha_0\hat{\Theta}(x, \xi')]d\xi', \tag{48}$$

and to the *creep integral law*

$$\hat{e}_{ij}(x, \xi) = \int_{-\infty}^{\xi} J_1(\xi - \xi') \frac{\partial}{\partial \xi'} \hat{s}_{ij}(x, \xi')d\xi',$$
$$\hat{\epsilon}(x, \xi) = \int_{-\infty}^{\xi} J_2(\xi - \xi') \frac{\partial}{\partial \xi'} \hat{\sigma}(x, \xi')d\xi' + 3\alpha_0\hat{\Theta}(x, \xi). \tag{49}$$

We have yet to discuss the extension of the constitutive law (7) to nonisothermal conditions (for a thermorheologically simple material). This generalization may be reached most economically by taking the Laplace transform of (48) with respect to ξ and by subsequent use of (11). On applying the corresponding inverse transforms, one thus obtains the modified *differential operator law*

$$P_1(\hat{D})\hat{s}_{ij}(x, \xi) = Q_1(\hat{D})\hat{e}_{ij}(x, \xi),$$
$$P_2(\hat{D})\hat{\sigma}(x, \xi) = Q_2(\hat{D})[\hat{\epsilon}(x, \xi) - 3\alpha_0\hat{\Theta}(x, \xi)], \tag{50}$$

in which

$$\hat{D} = \frac{\partial}{\partial \xi} \tag{51}$$

and the polynomial operators P_β, Q_β ($\beta = 1, 2$), as before, are given by (8). When $T(x, t) = T_0$, (50) reduces to (7).

If the medium is elastic, the differential operators in (50) according to (8), (18), and (51), fail to involve the reduced time, whence the response is independent of the temperature in this special instance.[12] Elastic materials with temperature-dependent characteristics thus do not belong to the class of thermorheologically simple viscoelastic solids, i.e., the assumption that the "elastic constants" vary with temperature is inconsistent with the temperature-time equivalence hypothesis.

We now pursue further the limitations imposed by the shift postulate. Suppose the material parameters $p_\beta^{(n)}$ ($n = 0, 1, 2, \ldots N_\beta$; $\beta = 1, 2$) and $q_\beta^{(n)}$ ($n = 0, 1, 2, \ldots M_\beta$; $\beta = 1, 2$) in the isothermal differential operator law (7), (8) are replaced by functions of the temperature, while at the same time the thermal-expansion term is inserted in the second of (7). Such a formal modification of (7), (8) evidently results in a stress-strain law appropriate to a linear (homogeneous and isotropic) viscoelastic solid with temperature-dependent properties. It is clear, however, that an arbitrary independent assignment of the functions $p_\beta^{(n)}(T)$ and $q_\beta^{(n)}(T)$ is incompatible with the temperature-time equivalence hypothesis; for this hypothesis implies that the temperature dependence of the response of the material is governed by a single function of the temperature,[13] namely, by the shift-factor $\varphi(T)$.

In connection with the foregoing remarks, consider the particular cases of the Maxwell and Kelvin solids. In either instance the dilatational response is elastic and hence temperature independent. On the other hand, specializing the first of (50) in accordance with (23) and (28), and using (45), (46), (47), one obtains for a thermorheologically simple Maxwell solid

$$\frac{\partial}{\partial t} s_{ij}(x, t) + \frac{1}{\tau(T)} s_{ij}(x, t) = 2\mu \frac{\partial}{\partial t} e_{ij}(x, t), \tag{52}$$

while for a Kelvin solid of the same type

$$s_{ij}(x, t) = 2\mu\left[\tau(T) \frac{\partial}{\partial t} e_{ij}(x, t) + e_{ij}(x, t)\right], \tag{53}$$

where

$$\tau(T) = \frac{\tau_0}{\varphi(T)}. \tag{54}$$

Further, from (54) and (37) follows

$$\tau(T_0) = \tau_0, \quad \tau(T) > 0, \quad \frac{d\tau}{dT} < 0 \tag{55}$$

Comparing (52), (53) with (24), (29), we identify the function $\tau(T)$ in (52) and (53) as a temperature-dependent relaxation time and retardation time, respectively. This function may be specified at will, subject to (55), without contradicting the shift hypothesis. In contrast, μ must remain constant if the materials under consideration are to exhibit thermorheologically simple behavior.

At this stage we may proceed to the formulation of boundary-value problems in the quasi-static linear theory of thermorheo-

[12] The same conclusion may alternatively be based on (40) or (44) in conjunction with (21) and (41).

[13] It is worth noting that if the stresses and strains in (50) are referred to the physical time t by recourse to (41) and (47), there results a constitutive law of the form (7), (8); the coefficients $p_\beta^{(n)}$, $q_\beta^{(n)}$, however, then depend not only on $T(x, t)$ but also on the successive time derivatives of the temperature, unless $N_\beta \leq 1$, $M_\beta \leq 1$ for (50).

logically simple (homogeneous and isotropic) viscoelastic solids. The corresponding complete system of field equations consists of the displacement-strain relations (1), the stress equations of equilibrium (2), together with the constitutive law (48), (49), or (50).

To these field equations, which must hold throughout the region $\mathfrak{D}$ occupied by the medium, we must adjoin suitable initial and boundary conditions. In the applications to follow we shall suppose the body to be initially undisturbed, so that

$$u_i(x, t) = \sigma_{ij}(x, t) = \Theta(x, t) = 0 \text{ in } \mathfrak{D}\ (-\infty < t < 0) \quad (56)$$

Also, we shall assume that the boundary $\mathfrak{B}$ of $\mathfrak{D}$ is permanently free from surface tractions; i.e.,

$$\sigma_{ij}(x, t)n_j(x) = 0 \text{ on } \mathfrak{B} \quad (0 < t < \infty). \quad (57)$$

The mechanical properties of the material—represented by the relaxation moduli $G_\beta(t)$, the equivalent creep compliances $J_\beta(t)$, or the material parameters $p_\beta^{(\alpha)}$ and $q_\beta^{(\alpha)}$—are to be regarded as given quantities, as are the shift factor $\varphi(T)$ and the coefficients of thermal expansion $\alpha(T)$. The foregoing formulation of the problem presupposes further that the temperature $T(x, t)$, and hence the pseudo-temperature $\Theta(x, t)$, is a known function. In the absence of thermomechanical coupling, the temperature field may, in particular, be the solution of an independent heat-conduction problem. In this event $T(x, t)$ is governed by the (uncorrected) equation of heat conduction

$$\kappa\nabla^2 T(x, t) = \frac{\partial}{\partial t}\, T(x, t), \quad (58)$$

in conjunction with the appropriate initial and boundary conditions. Here ∇^2 is the Laplacian operator and κ the thermal diffusivity of the material.

We now consider two specific examples which belong to the class of thermoviscoelastic boundary-value problems just described.

4 Transient Thermal Stresses in a Viscoelastic Slab

For our present purposes it is convenient to depart from indicial notation. Thus let the Cartesian co-ordinates, previously designated by (x_1, x_2, x_3), now be denoted by (x, y, z). Consider a slab of infinite extent and finite thickness $2a$, bounded by the planes $z = \pm a$. Let the slab be under the influence of a temperature field of the form

$$T = T(z, t), \quad (59)$$

and be constrained to the purely transverse motion characterized by the displacement field

$$u_x = u_y = 0, \quad u_z = u_z(z, t). \quad (60)$$

It is required to determine $u_z(z, t)$, as well as the associated thermal stresses, in accordance with the field equations, initial, and boundary conditions outlined at the end of Section 3. The following analysis is based on the relaxation integral law (48) but the results will be adapted also to the case in which the response of the material is prescribed in terms of the creep compliances or is specified in differential-operator form.

By (60), (1) the components of strain here become

$$\epsilon_{xx} = \epsilon_{yy} = \epsilon_{xy} = \epsilon_{yz} = \epsilon_{zx} = 0, \quad \epsilon_{zz} = \frac{\partial u_z}{\partial z}, \quad (61)$$

while (61) and (3) yield for the dilatation and the deviatoric strains

$$\epsilon = \epsilon_{zz}, \quad e_{xx} = e_{yy} = -\frac{1}{2}e_{zz} = -\frac{1}{3}\epsilon, \quad e_{xy} = e_{yz} = e_{zx} = 0. \quad (62)$$

From (62), (3), and (48) follow

$$\sigma_{xx} = \sigma_{yy}, \quad \sigma_{xy} = \sigma_{yz} = \sigma_{zx} = 0, \quad (63)$$

$$\sigma = 2\sigma_{xx} + \sigma_{zz}, \quad s_{xx} = s_{yy} = -\frac{1}{2}s_{zz} = -\frac{1}{3}(\sigma_{zz} - \sigma_{xx}),$$
$$s_{xy} = s_{yz} = s_{zx} = 0. \quad (64)$$

Clearly, the functions appearing in (61) to (64) depend on z and t alone. The constitutive law (48), by virtue of (62) and (64), now yields the pair of integral equations

$$\hat{\sigma}_{zz}(z, \xi) - \hat{\sigma}_{xx}(z, \xi) = \int_{-\infty}^{\xi} G_1(\xi - \xi')\frac{\partial}{\partial\xi'}\,\hat{\epsilon}(z, \xi')d\xi',$$
$$\hat{\sigma}_{zz}(z, \xi) + 2\hat{\sigma}_{xx}(z, \xi) = \int_{-\infty}^{\xi} G_2(\xi - \xi')\frac{\partial}{\partial\xi'}\,[\hat{\epsilon}(z, \xi') - 3\alpha_0\hat{\Theta}(z, \xi')]d\xi', \quad (65)$$

while the equilibrium equations (2), because of (63), (60), reduce to the single nontrivial equation

$$\frac{\partial}{\partial z}\,\sigma_{zz}(z, t) = 0. \quad (66)$$

The boundary conditions (57) at present demand that

$$\sigma_{zz}(z, t) = 0 \quad \text{for} \quad z = \pm a, \quad (67)$$

and from (66), (67)

$$\sigma_{zz}(z, t) = \hat{\sigma}_{zz}(z, \xi) \equiv 0. \quad (68)$$

We now apply the Laplace transform (with respect to ξ) to (65), make use of the convolution theorem and, bearing in mind (6), (68), arrive at

$$\hat{\sigma}_{zz}^*(z, \eta) = -\eta G_1^*(\eta)\hat{\epsilon}^*(z, \eta),$$
$$2\hat{\sigma}_{zz}^*(z, \eta) = \eta G_2^*(\eta)[\hat{\epsilon}^*(z, \eta) - 3\alpha_0\hat{\Theta}^*(z, \eta)], \quad (69)$$

the notation being accounted for by (47) and (9), provided in the latter (x, t) is replaced by (z, ξ). Eliminating $\hat{\epsilon}^*(z, \eta)$ between (69) one has

$$\hat{\sigma}_{zz}^*(z, \eta) = -\frac{3\alpha_0 G_1^*(\eta)G_2^*(\eta)}{2G_1^*(\eta) + G_2^*(\eta)}\,\eta\hat{\Theta}^*(z, \eta). \quad (70)$$

Let an auxiliary function $R(\xi)$ be defined by

$$R(\xi) = \mathfrak{L}^{-1}\left\{\frac{G_1^*(\eta)G_2^*(\eta)}{2G_1^*(\eta) + G_2^*(\eta)};\ \xi\right\}. \quad (71)$$

Then (69), in view of the initial conditions (56), implies

$$\hat{\sigma}_{zz}(z, \xi) = -3\alpha_0\int_0^{\xi} R(\xi - \xi')\frac{\partial}{\partial\xi'}\,\hat{\Theta}(z, \xi')d\xi' \quad (0 < \xi < \infty), \quad (72)$$

or, upon changing variables from the reduced to the physical time by means of (45), (46), (47),

$$\sigma_{zz}(z, t) = -3\alpha_0\int_0^{t} R[\xi(z, t) - \xi(z, t')]\frac{\partial}{\partial t'}\,\Theta(z, t')dt' \quad (0 < t < \infty), \quad (73)$$

where $\xi(z, t) \equiv f(z, t)$ is given by (41). The remaining components of stress vanish identically, except for σ_{yy}, which coincides with σ_{zz}.

According to (61), (62) the only nonvanishing displacement component is given by

$$u_z(z, t) = \int_0^z \epsilon(\zeta, t)d\zeta, \quad (74)$$

if the median plane $z = 0$ is assumed to remain fixed. Also, from (10) and the first of (69)

$$\hat{\epsilon}^*(z, \eta) = -J_1^*(\eta)\eta\hat{\sigma}_{zz}^*(z, \eta), \tag{75}$$

where $J_1(t)$ is the creep compliance in shear. Inverting (75) and referring the resulting equation to the physical time, we reach upon substitution into (74),

$$u_z(z, t) = -\int_0^z \int_0^t J_1[\xi(\zeta, t) - \xi(\zeta, t')] \frac{\partial}{\partial t'} \sigma_{zz}(\zeta, t')dt'd\zeta \qquad (0 < t < \infty). \tag{76}$$

This completes the solution of the problem at hand. The function $R(\xi)$, entering the stress formula (73), is defined in (71) in terms of the relaxation moduli $G_\beta(t)$ $(\beta = 1, 2)$. If the response of the material is given instead through the creep compliances $J_\beta(t)$ or through the polynomial operators P_β, Q_β of (8), equation (71), because of (10), (11), is to be replaced with

$$R(\xi) = \mathfrak{L}^{-1}\left\{\frac{1}{\eta^2[J_1^*(\eta) + 2J_2^*(\eta)]}; \xi\right\} \tag{77}$$

or with

$$R(\xi) = \mathfrak{L}^{-1}\left\{\frac{Q_1(\eta)Q_2(\eta)}{\eta[P_1(\eta)Q_2(\eta) + 2P_2(\eta)Q_1(\eta)]}; \xi\right\}, \tag{78}$$

accordingly. Similarly, the creep compliance J_1 appearing in the displacement formula (76) may alternatively be replaced with the inverse Laplace transform of $1/\eta^2G_1^*(\eta)$ or of $P_1(\eta)/\eta Q_1(\eta)$.

For future convenience we cite also the form taken on by $R(\xi)$ if the dilatational response of the material is purely elastic. In this event, as is apparent from (8), (18), (21),

$$G_2^*(\eta) = \frac{3k}{\eta}, \quad J_2^*(\eta) = \frac{1}{3k\eta}, \quad P_2(\eta) = 1, \quad Q_2(\eta) = 3k. \tag{79}$$

Further, we may, without ambiguity, presently set

$$G_1(t) = G(t), \quad J_1(t) = J(t), \quad P_1 = P, \quad Q_1 = Q. \tag{80}$$

By virtue of (79), (80), equations (71), (77), (78) then reduce to

$$R(\xi) = \mathfrak{L}^{-1}\left\{\frac{3kG^*(\eta)}{3k + 2\eta G^*(\eta)}; \xi\right\}, \tag{81}$$

$$R(\xi) = \mathfrak{L}^{-1}\left\{\frac{3k}{2\eta + 3k\eta^2 J^*(\eta)}; \xi\right\}, \tag{82}$$

$$R(\xi) = \mathfrak{L}^{-1}\left\{\frac{3kQ(\eta)}{\eta[3kP(\eta) + 2Q(\eta)]}; \xi\right\}. \tag{83}$$

We now particularize $R(\xi)$ further by considering the special cases of the elastic solid, the Maxwell solid, and the Kelvin solid. Inserting in (82) the values of $J^*(\eta) = J_1^*(\eta)$ implied by (21), (25), (30), performing the corresponding inversions, and using (20) in all three instances to express k, μ in terms of E, ν, we are thus led to the following results:

For the *elastic solid*

$$R(\xi) = \frac{H(\xi)E}{3(1 - \nu)}, \tag{84}$$

for the *Maxwell solid*

$$R(\xi) = \frac{H(\xi)E}{3(1 - \nu)} \exp\left(-\frac{\beta\xi}{\tau_0}\right), \tag{85}$$

and for the *Kelvin solid*

$$R(\xi) = \frac{H(\xi)E}{3(1 - \nu)}\left[1 + \beta\gamma \exp\left(-\frac{\gamma\xi}{\tau_0}\right)\right], \tag{86}$$

where

$$\beta = \frac{1 + \nu}{3(1 - \nu)}, \quad \gamma = \frac{3(1 - \nu)}{2(1 - 2\nu)}. \tag{87}$$

Substitution of (84), (85), (86) into (73), after obvious simplifications, yields the subsequent formulas for σ_{zz} corresponding to the three particular types of solids under consideration. For the *elastic solid*

$$\sigma_{zz}(z, t) = -\frac{\alpha_0 E}{1 - \nu}\Theta(z, t), \tag{88}$$

for the *Maxwell solid*

$$\sigma_{zz}(z, t) = -\frac{\alpha_0 E}{1 - \nu} \exp\left[-\frac{\beta}{\tau_0}\xi(z, t)\right] \cdot \int_0^t \exp\left[\frac{\beta}{\tau_0}\xi(z, t')\right] \frac{\partial}{\partial t'}\Theta(z, t')dt', \tag{89}$$

and for the *Kelvin solid*

$$\sigma_{zz}(z, t) = -\frac{\alpha_0 E}{1 - \nu}\left\{\Theta(z, t) + \beta\gamma \exp\left[-\frac{\gamma}{\tau_0}\xi(z, t)\right] \cdot \int_0^t \exp\left[\frac{\gamma}{\tau_0}\xi(z, t')\right] \frac{\partial}{\partial t'}\Theta(z, t')dt'\right\}. \tag{90}$$

The foregoing three specialized results for σ_{zz} are valid for $0 < t < \infty$; the corresponding formulas for u_z are immediate from (76), (21), (25), (30).

The solution for the Maxwell solid clearly tends to that characteristic of the elastic medium as the relaxation time τ_0 approaches infinity. These two solutions also coalesce in the limit as $t \to 0$, the initial response of the Maxwell solid being elastic. If

$$\frac{\partial}{\partial t}\Theta(z, t) \to 0 \quad \text{as} \quad t \to \infty, \tag{91}$$

then $\sigma_{zz}(z, t) \to 0$ in (89) as $t \to \infty$, so that the Maxwell plate relaxes into a stressless steady state.

The solution appropriate to the Kelvin solid, in turn, evidently tends to the elasticity solution as the retardation time τ_0 approaches zero; the same is true in the limit as $t \to \infty$, provided (91) holds.

Finally, we mention a recent investigation by Landau, Weiner, and Zwicky [15] which deals with certain aspects of the foregoing problem for a viscoelastic, perfectly plastic material. In [15], however, the viscoelastic behavior is restricted to be of the Maxwell type.

5 Transient Thermal Stresses in a Viscoelastic Sphere

As a second application of the theory summarized in Section 3, we consider the thermal deformations and stresses in a sphere, induced by an arbitrary radially symmetric temperature distribution. For this purpose we introduce spherical co-ordinates (r, θ, ϕ) by means of the mapping

$$x_1 = r\sin\theta\cos\phi, \quad x_2 = r\sin\theta\sin\phi, \quad x_3 = r\cos\theta, \qquad 0 \le r < \infty, \quad 0 \le \theta \le \pi, \quad 0 \le \phi < 2\pi. \tag{92}$$

Let the sphere have the radius a and be centered at the origin. The temperature field then has the form

$$T = T(r, t). \tag{93}$$

Because of the polar symmetry of the problem, the spherical components of displacement conform to

$$u_r = u_r(r, t), \quad u_\theta = u_\phi = 0, \tag{94}$$

whence (1), referred to spherical co-ordinates, yield the strains

$$\epsilon_{rr} = \frac{\partial u_r}{\partial r}, \quad \epsilon_{\theta\theta} = \epsilon_{\phi\phi} = \frac{u_r}{r}, \quad \epsilon_{r\theta} = \epsilon_{\theta\phi} = \epsilon_{\phi r} = 0. \tag{95}$$

From (95), (3) follow

$$\epsilon = \epsilon_{rr} + 2\epsilon_{\theta\theta} = \frac{1}{r^2}\frac{\partial}{\partial r}(r^2 u_r),$$

$$e_{rr} = -2e_{\theta\theta} = -2e_{\phi\phi} = \epsilon_{rr} - \frac{\epsilon}{3} = \frac{2r}{3}\frac{\partial}{\partial r}\left(\frac{u_r}{r}\right), \tag{96}$$

$$e_{r\theta} = e_{\theta\phi} = e_{\phi r} = 0.$$

Appealing once more to the polar symmetry of the present problem we have

$$\sigma_{\theta\theta} = \sigma_{\phi\phi}, \qquad \sigma_{r\theta} = \sigma_{\theta\phi} = \sigma_{\phi r} = 0, \tag{97}$$

and (97), (3) imply

$$\sigma = \sigma_{rr} + 2\sigma_{\theta\theta}, \quad s_{rr} = -2s_{\theta\theta} = -2s_{\phi\phi} = \frac{2}{3}(\sigma_{rr} - \sigma_{\theta\theta}),$$

$$s_{r\theta} = s_{\theta\phi} = s_{\phi r} = 0. \tag{98}$$

Furthermore, all of the functions appearing in (95) to (98) evidently depend on r and t, exclusively. For later convenience we note here also the identity

$$r^2\frac{\partial}{\partial r}\epsilon(r, t) = \frac{3}{2}\frac{\partial}{\partial r}[r^2 e_{rr}(r, t)], \tag{99}$$

which is an immediate consequence of (96).

In view of the restricted form (93) of the temperature field, the reduced time ξ in the current circumstances becomes a function of r and t alone. Replacing (41) with

$$\xi = f(r, t) = \int_0^t \varphi[T(r, \lambda)]d\lambda, \quad \xi' = f(r, t'), \tag{100}$$

and in analogy to (45), (47), we now adopt the notation

$$t = g(r, \xi), \quad F(r, t) = \hat{F}(r, \xi) = F[r, g(r, \xi)]. \tag{101}$$

The analysis of the problem under consideration will be based on the generalized relaxation integral law (48), but the dilatational response of the solid will, from the start, be assumed purely elastic. On setting $G_1(t) = G(t)$, as in (80), and with reference to spherical co-ordinates, the first of (48) at present reduces to the single equation

$$\hat{s}_{rr}(r, \xi) = \int_{-\infty}^{\xi} G(\xi - \xi')\frac{\partial}{\partial \xi'}\hat{e}_{rr}(r, \xi')d\xi', \tag{102}$$

the remaining deviatoric stress-strain relations being met identically by virtue of (96) and (98). On the other hand, using in the second of (48) the special form of $G_2(t)$ appearing in (21), and referring the resulting equation to spherical co-ordinates, we gather that

$$\sigma(r, t) = 3k[\epsilon(r, t) - 3\alpha_0\Theta(r, t)], \tag{103}$$

where the pseudo-temperature $\Theta(r, t)$, in accordance with (42) and (93), is given by

$$\Theta(r, t) = \frac{1}{\alpha_0}\int_{T_0}^{T(r,t)} \alpha(T')dT'. \tag{104}$$

The equilibrium equations (2), in turn, because of (97) and since all spherical stress components are independent of θ and ϕ, now yield the single equation

$$\frac{\partial}{\partial r}\sigma_{rr}(r, t) + \frac{2}{r}[\sigma_{rr}(r, t) - \sigma_{\theta\theta}(r, t)] = 0. \tag{105}$$

In view of (98), we may rewrite (105) as

$$\frac{\partial}{\partial r}[r^2 s_{rr}(r, t)] + \frac{r^2}{3}\frac{\partial}{\partial r}\sigma(r, t) = 0. \tag{106}$$

Substitution into (106) for $\sigma(r, t)$ from (103), and use of (99), lead to

$$\frac{\partial}{\partial r}[r^2 s_{rr}(r, t)] = -\frac{3k}{2}\left\{\frac{\partial}{\partial r}[r^2 e_{rr}(r, t)] - 2\alpha_0 r^2\frac{\partial}{\partial r}\Theta(r, t)\right\}, \tag{107}$$

from which, upon integration with respect to r,

$$s_{rr}(r, t) = -\frac{3k}{2}[e_{rr}(r, t) - h(r, t)], \tag{108}$$

provided

$$h(r, t) = \frac{2\alpha_0}{r^3}\int_0^r \rho^3\frac{\partial}{\partial \rho}\Theta(\rho, t)d\rho. \tag{109}$$

Next, we apply to (108) the change of the time variable indicated in (100), (101), and use the resulting equation to eliminate $\hat{e}_{rr}(r, \xi)$ from (102). This procedure leads to the following integral equation for $\hat{s}_{rr}(r, \xi)$:

$$\hat{s}_{rr}(r, \xi) = \int_{-\infty}^{\xi} G(\xi - \xi')\frac{\partial}{\partial \xi'}\left[\hat{h}(r, \xi') - \frac{2}{3k}\hat{s}_{rr}(r, \xi')\right]d\xi' \tag{110}$$

Taking the Laplace transform of (110) with respect to ξ, invoking the convolution theorem, and keeping (6) in mind, we arrive at

$$\hat{s}_{rr}^*(r, \eta) = \frac{3kG^*(\eta)}{3k + 2\eta G^*(\eta)}\eta\hat{h}^*(r, \eta). \tag{111}$$

Inverting (111), we find with the aid of (56) that

$$\hat{s}_{rr}(r, \xi) = \int_0^{\xi} R(\xi - \xi')\frac{\partial}{\partial \xi'}\hat{h}(r, \xi')d\xi' \quad (0 < \xi < \infty), \tag{112}$$

if $R(\xi)$ is *defined* by (81) in terms of the relaxation modulus in shear. As shown earlier, $R(\xi)$ admits the alternative representations (82) and (83), in terms of the creep compliance $J(t) = J_1(t)$ and the operators $P = P_1$, $Q = Q_1$, respectively. Referring (112) to the physical time t by means of the transformations (101), and substituting for $h(r, t')$ from (109), there results

$$s_{rr}(r, t) = \frac{2\alpha_0}{r^3}\int_0^t R[\xi(r, t) - \xi(r, t')]\int_0^r \rho^3\frac{\partial^2\Theta(\rho, t')}{\partial\rho\,\partial t'}d\rho\,dt' \quad (0 < t < \infty). \tag{113}$$

With a view toward the explicit determination of the normal stress $\sigma_{rr}(r, t)$ we observe, on the basis of (98), that (105) may also be written as

$$\frac{\partial}{\partial r}\sigma_{rr}(r, t) = -\frac{3}{r}s_{rr}(r, t), \tag{114}$$

and note that the boundary conditions (57) at present require

$$\sigma_{rr}(a, t) = 0. \tag{115}$$

From (114), (115) follows

$$\sigma_{rr}(r, t) = 3 \int_r^a \frac{s_{rr}(\rho, t)}{\rho} \, d\rho, \tag{116}$$

and (113), (116) finally yield

$$\sigma_{rr}(r, t) = -6\alpha_0 \int_a^r \int_0^t \frac{1}{\lambda^4} R[\xi(\lambda, t) - \xi(\lambda, t')] \cdot \int_0^\lambda \rho^3 \frac{\partial^2 \Theta(\rho, t')}{\partial \rho \, \partial t'} \, d\rho \, dt' d\lambda \tag{117}$$

for $0 < t < \infty$. Further, by (97), (98)

$$\sigma_{\theta\theta}(r, t) = \sigma_{\phi\phi}(r, t) = \sigma_{rr}(r, t) - \frac{3}{2} s_{rr}(r, t). \tag{118}$$

Since the spherical components of shear stress vanish identically the desired thermal stresses are completely determined by (117), (118), (113), in conjunction with (81), (82), or (83), and (100), (104). In particular, one is led to

$$\sigma_{\theta\theta}(a, t) = -\frac{3\alpha_0}{a^3} \int_0^t R[\xi(a, t) - \xi(a, t')] \cdot \int_0^a \rho^3 \frac{\partial^2 \Theta(\rho, t')}{\partial \rho \, \partial t'} \, d\rho \, dt' \quad (0 < t < \infty). \tag{119}$$

Our next objective is to find the nonvanishing radial displacement $u_r(r, t)$. To this end we note that the equilibrium equation (105) is equivalent to

$$\frac{1}{r^2} \frac{\partial}{\partial r} [r^2 \sigma_{rr}(r, t)] = \frac{1}{r} [\sigma_{rr}(r, t) + 2\sigma_{\theta\theta}(r, t)], \tag{120}$$

whereas (103), which asserts that the dilatational response is elastic, by virtue of (96) and (98), implies

$$3k \left\{ \frac{1}{r^2} \frac{\partial}{\partial r} [r^2 u_r(r, t)] - 3\alpha_0 \Theta(r, t) \right\} = \sigma_{rr}(r, t) + 2\sigma_{\theta\theta}(r, t). \tag{121}$$

From (120), (121) we draw

$$\frac{\partial}{\partial r} [r^2 u_r(r, t)] = \frac{1}{3k} \frac{\partial}{\partial r} [r^2 \sigma_{rr}(r, t)] + 3\alpha_0 r^2 \Theta(r, t). \tag{122}$$

Integrating (122) with respect to r, we obtain the desired result

$$u_r(r, t) = \frac{r}{3k} \sigma_{rr}(r, t) + \frac{3\alpha_0}{r^2} \int_0^r \rho^2 \Theta(\rho, t) d\rho \quad (0 < t < \infty). \tag{123}$$

It is important to observe that (123) was deduced without recourse to the deviatoric stress-strain law (102), and hence holds for *any* isotropic and homogeneous material whose dilatational response—in the presence of infinitesimal deformations—is linearly elastic. In particular, for any such material

$$u_r(a, t) = \frac{3\alpha_0}{a^2} \int_0^a \rho^2 \Theta(\rho, t) d\rho,$$

$$\epsilon_{\theta\theta}(a, t) = \frac{3\alpha_0}{a^3} \int_0^a \rho^2 \Theta(\rho, t) d\rho, \tag{124}$$

as may be inferred from (123) by means of (115) and (95). The strikingly simple formulas (124) for the surface values of the radial displacement and of the circumferential strain are apt to be of interest in connection with the experimental verification of the assumption that the material behaves elastically in isotropic compression.

The solution just established may be simplified if the temperature field (93) satisfies the heat-conduction equation (58), and provided the coefficient of thermal expansion is constant. In these circumstances (104) becomes

$$\Theta(r, t) = T(r, t) - T_0, \tag{125}$$

while by (58), (125),

$$\frac{1}{r^2} \frac{\partial}{\partial r} \left[r^2 \frac{\partial}{\partial r} \Theta(r, t) \right] = \frac{1}{\kappa} \frac{\partial}{\partial t} \Theta(r, t), \tag{126}$$

whence, using integration by parts,

$$\int_0^r \rho^3 \frac{\partial^2 \Theta(\rho, t)}{\partial \rho \, \partial t} \, d\rho = \kappa r^4 \frac{\partial}{\partial r} \left[\frac{1}{r} \frac{\partial}{\partial r} \Theta(r, t) \right]. \tag{127}$$

By virtue of (127), equations (113), (117) are now reducible to

$$s_{rr}(r, t) = 2\alpha_0 \kappa r \int_0^t R[\xi(r, t) - \xi(r, t')] \frac{\partial}{\partial r} \left[\frac{1}{r} \frac{\partial}{\partial r} \Theta(r, t') \right] dt', \tag{128}$$

$$\sigma_{rr}(r, t) = -6\alpha_0 \kappa \int_a^r \int_0^t R[\xi(\rho, t) - \xi(\rho, t')] \cdot \frac{\partial}{\partial \rho} \left[\frac{1}{\rho} \frac{\partial}{\partial \rho} \Theta(\rho, t') \right] dt' d\rho, \tag{129}$$

whereas (119) becomes

$$\sigma_{\theta\theta}(a, t) = -3\alpha_0 \kappa a \int_0^t R[\xi(a, t) - \xi(a, t')] \cdot \left\{ \frac{\partial}{\partial r} \left[\frac{1}{r} \frac{\partial}{\partial r} \Theta(r, t') \right] \right\}_{(r=a)} dt'. \tag{130}$$

Finally, we list the special forms assumed by the stress field for the particular cases of the elastic solid, the Maxwell solid, and the Kelvin solid. The following results, which are valid for $0 < t < \infty$, are obtained from (113), (117), (118) with the aid of (84), (85), (86), after some elementary manipulations:

For the *elastic solid*

$$\sigma_{rr}(r, t) = \frac{2\alpha_0 E}{1 - \nu} \left[\frac{1}{a^3} \int_0^a \rho^2 \Theta(\rho, t) d\rho - \frac{1}{r^3} \int_0^r \rho^2 \Theta(\rho, t) d\rho \right]. \tag{131}$$

$$\sigma_{\theta\theta}(r, t) = \frac{\alpha_0 E}{1 - \nu} \left[\frac{2}{a^3} \int_0^a \rho^2 \Theta(\rho, t) d\rho + \frac{1}{r^3} \int_0^r \rho^2 \Theta(\rho, t) d\rho - \Theta(r, t) \right]. \tag{132}$$

These formulas agree with the well-known solution of the present problem in classical elasticity theory.[14]

For the *Maxwell solid*

$$\sigma_{rr}(r, t) = \frac{-2\alpha_0 E}{1 - \nu} \int_a^r \frac{1}{\lambda^4} \exp\left[-\frac{\beta}{\tau_0} \xi(\lambda, t) \right] \cdot \int_0^t \exp\left[\frac{\beta}{\tau_0} \xi(\lambda, t') \right] \int_0^\lambda \rho^3 \frac{\partial^2 \Theta(\rho, t')}{\partial \rho \, \partial t'} \, d\rho \, dt' d\lambda, \tag{133}$$

[14] See, for example, Timoshenko-Goodier [16], p. 147, et seq.

$$\sigma_{\theta\theta}(r, t) = \sigma_{rr}(r, t) - \frac{\alpha_0 E}{(1-\nu)r^3} \exp\left[-\frac{\beta}{\tau_0}\,\xi(r, t)\right] \cdot \int_0^t \exp\left[\frac{\beta}{\tau_0}\,\xi(r, t')\right] \int_0^r \rho^3 \frac{\partial^2\Theta(\rho, t')}{\partial\rho\,\partial t'}\,d\rho\,dt' \quad (134)$$

Formulas (133), (134) are in agreement with Rongved's [6] solution, which is confined to the Maxwell solid.

For the *Kelvin solid*

$$\sigma_{rr}(r, t) = \frac{2\alpha_0 E}{1-\nu}\left\{\frac{1}{a^3}\int_0^a \rho^2\Theta(\rho, t)d\rho - \frac{1}{r^3}\int_0^r \rho^2\Theta(\rho, t)d\rho - \beta\gamma\int_a^r \frac{1}{\lambda^4}\exp\left[-\frac{\gamma}{\tau_0}\,\xi(\lambda, t)\right]\int_0^t \exp\left[\frac{\gamma}{\tau_0}\,\xi(\lambda, t')\right] \cdot \int_0^\lambda \rho^3 \frac{\partial^2\Theta(\rho, t')}{\partial\rho\,\partial t'}\,d\rho\,dt'd\lambda\right\}, \quad (135)$$

$$\sigma_{\theta\theta}(r, t) = \sigma_{rr}(r, t) - \frac{\alpha_0 E}{1-\nu}\left\{\Theta(r, t) - \frac{3}{r^3}\int_0^r \rho^2\Theta(\rho, t)d\rho + \frac{\beta\gamma}{r^3}\exp\left[-\frac{\gamma}{\tau_0}\,\xi(r, t)\right]\int_0^t \exp\left[\frac{\gamma}{\tau_0}\,\xi(r, t')\right] \cdot \int_0^r \rho^3 \frac{\partial^2\Theta(\rho, t')}{\partial\rho\,\partial t'}\,d\rho\,dt'\right\}. \quad (136)$$

The foregoing special results exhibit the limit behavior described at the end of Section 4, in the discussion of the solution to the problem of the slab. Thus the solutions appropriate to the Maxwell and the Kelvin solid tend to the solution for the elastic solid in the respective limit as the relaxation time approaches infinity and as the retardation time approaches zero. The initial response of the Maxwell solid is again confirmed to be elastic. Further, if

$$\frac{\partial}{\partial t}\,\Theta(r, t) \to 0 \quad \text{as} \quad t \to \infty, \quad (137)$$

the stresses in the Maxwell sphere tend to zero as $t \to \infty$, while those in the Kelvin sphere, in this limit, coincide with the steady-state stresses of the elastic sphere.

In the present context reference ought to be made to a recent paper by Nowinski [17], in which the problem treated in this section is solved for an elastic sphere whose Young's modulus and Poisson's ratio are assumed to be prescribed functions of the temperature. As emphasized in Section 3, such an assumption is inadmissible within the temperature-time equivalence hypothesis underlying our investigation.

Before turning to a discussion of numerical results, we mention that the foregoing analysis of transient thermal deformations and stresses in a viscoelastic sphere is readily generalized to the corresponding problem for a viscoelastic spherical shell.

6 Specialization of the Temperature Field. Numerical Results. Discussion.

We now illustrate the solutions established in the preceding two sections with numerical examples. In this connection we consider first results appropriate to the problem of the slab, treated in Section 4.

Suppose the temperature field $T(z, t)$ introduced in (59), satisfies the heat-conduction equation (58) (for a constant thermal diffusivity κ) and obeys the initial and boundary conditions

$$T(z, t) = T_0 \quad (-a \le z \le a, \quad -\infty < t < 0), \qquad T(z, t) = T_1 \quad (z = \pm a, \quad 0 < t < \infty), \quad (138)$$

which correspond to a sudden uniform heating (or cooling) of the two plane faces of the slab. Let us assume, further, that the coefficient of thermal expansion is constant so that[15]

$$\Theta(z, t) = T(z, t) - T_0, \quad (139)$$

and let

$$\Theta_1 = T_1 - T_0. \quad (140)$$

The solution to the heat-conduction problem governed by (58), (138) is well known and admits the alternative representations[16]

$$\Theta(z, t) = \Theta_1\left\{1 - \frac{4}{\pi}\sum_{n=0}^{\infty}\frac{(-1)^n}{2n+1}\exp\left[-\frac{(2n+1)^2\pi^2\kappa t}{4a^2}\right] \cdot \cos\frac{(2n+1)\pi z}{2a}\right\}, \quad (141)$$

$$\Theta(z, t) = \Theta_1\sum_{n=0}^{\infty}(-1)^n\left\{\operatorname{erfc}\left[\frac{2n+1-z/a}{2(\kappa t/a^2)^{1/2}}\right] + \operatorname{erfc}\left[\frac{2n+1+z/a}{2(\kappa t/a^2)^{1/2}}\right]\right\}, \quad (142)$$

where erfc designates the complementary error function defined by

$$\operatorname{erfc}(\omega) = \frac{2}{\sqrt{\pi}}\int_\omega^\infty \exp(-\lambda^2)d\lambda. \quad (143)$$

While (141) is advantageous to use for large values of t, the error-function representation (142) is better suited for the numerical evaluation of the temperature distribution at small time values. For future convenience we cite here also the power-series development

$$\operatorname{erfc}(\omega) = 1 - \frac{2}{\sqrt{\pi}}\sum_{n=0}^{\infty}\frac{(-1)^n\omega^{2n+1}}{(2n+1)\,\underline{|n}}, \quad (144)$$

as well as the semiconvergent expansion, valid as $\omega \to \infty$,

$$\operatorname{erfc}(\omega) = \frac{\exp(-\omega^2)}{\sqrt{\pi}\,\omega}\left[\sum_{n=0}^{m}\frac{(-1)^n\,\underline{|2n}}{(2\omega)^{2n}\,\underline{|n}} + O(\omega^{-2m-2})\right]. \quad (145)$$

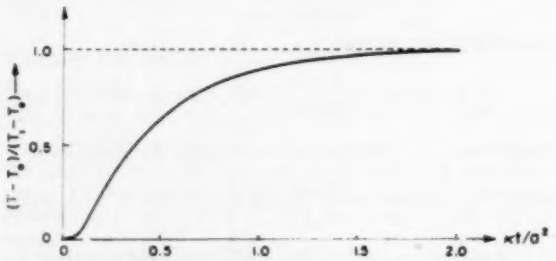

Fig. 1 Slab. Time dependence of temperature at $z = 0$

Fig. 1 displays the time variation of the temperature in the middle plane of the slab and is based on (141), (142).

In order to find the normal stress σ_{zz} at the faces of the slab, induced by the temperature distribution under consideration, we note on the basis of (9), (47) and (138), (139), (140) that

$$\hat{\Theta}^*(a, \eta) = \mathfrak{L}\{\hat{\Theta}(a, \xi);\ \eta\} = \frac{\Theta_1}{\eta}. \quad (146)$$

Consequently, from (70)

[15] See Equation (43).

[16] See Carslaw and Jaeger [18], p. 83, and [19], p. 275.

$$\dot{\sigma}_{xx}(a, \xi) = \dot{\sigma}_{xx}(-a, \xi) = -3\alpha_0\Theta_1 R[\xi(a, t)], \qquad (147)$$

where $R(\xi)$ is the auxiliary response function given by (71), and the reduced time $\xi(a, t)$, because of (41), (138), has the form

$$\xi(a, t) = \varphi(T_1)t \quad (0 < t < \infty). \qquad (148)$$

For a Maxwell or a Kelvin solid (148), by virtue of (54), becomes

$$\xi(a, t) = \frac{\tau_0 t}{\tau(T_1)} \quad (0 < t < \infty), \qquad (149)$$

where $\tau(T)$ is the relaxation or the retardation time of the material at the temperature T, and $R(\xi)$ here is given by (85) or (86), respectively. For the elastic solid $R(\xi)$ has the degenerate form (84).

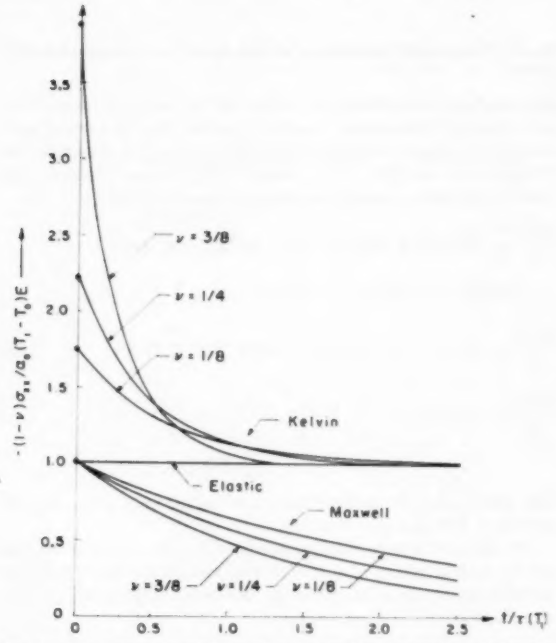

Fig. 2 Slab. Time dependence of σ_{xx} at surface for various Poisson's ratios

Fig. 2 shows the time dependence of the normal stress σ_{xx} at the faces $z = \pm a$ for an elastic solid, for a Maxwell solid, and for a Kelvin solid, corresponding to the values $\nu = 1/8, 1/4, 3/8$ of Poisson's ratio.[17] These graphs were obtained with the aid of (147), (148), (149), (84), (85), and (86). Since the surface temperature of the slab is constant for $t > 0$, the temperature dependence of the relaxation (or retardation) time affects merely the time scale in Fig. 2.

A more revealing discussion of the influence of temperature-dependent viscoelastic properties upon the thermal stresses arising in the slab problem necessitates an examination of these stresses in the interior of the body, where the temperature field (141), (142) varies with time. We therefore turn our attention next to the normal stress σ_{xx} in the middle plane $z = 0$. Further, aiming at a quantitative appraisal of the effects under investigation, we depart from the oversimplified models of the Maxwell and Kelvin solids and base the subsequent computations on available experimental data for an actual material, i.e., for polymethyl methacrylate.

[17] Recall (27) and (32), which account for the meaning of E and ν in Fig. 2.

In dealing with this particular high polymer we shall adhere to the assumption that κ and α are constants. The discrepancies introduced by this approximation[18] are likely to be insignificant compared to the influence of the temperature upon the mechanical response, especially if the temperature changes are confined to a sufficiently narrow range (in the example to follow we choose $T_0 = 80$ C, $T_1 = 110$ C). In addition, we shall presume the response of the material in dilatation (isotropic compression) to be purely elastic. Such a hypothesis appears to be reasonably adequate for high polymers, at least in the transition range between the glassy and the rubbery state,[19] which is of primary importance for the purpose at hand.

The thermorheologically simple character of polymethyl methacrylate was established by Bischoff, Catsiff, and Tobolsky [20], through tensile relaxation tests which indicate that this high polymer obeys the shift law with considerable accuracy for temperatures from 40 to 125 C. The results reported in [20] supply the values of the time-dependent Young's modulus $\bar{E}(t)$ and of the shift factor $\varphi(T)$ for this temperature range. On the other hand, Hoff [21], in tests conducted at -25 to 50 C, observed the constant initial value $\bar{\nu}(0) \doteq 0.35$ of Poisson's ratio.

The experimental information just cited is sufficient to determine the relaxation modulus in shear $G_1(t) \equiv G(t)$ and the (constant) bulk modulus k, once the dilatational response of the material is regarded to be elastic. It is more expedient, however, to express the required response function $R(\xi)$, given in (81) in terms of $G(t)$ and k, from the start in terms of $\bar{E}(t)$ and $\bar{\nu}(0)$. To this end we gather from (17), (79), (80) that

$$G(\xi) = \mathfrak{L}^{-1}\left\{\frac{6k\bar{E}^*(\eta)}{9k - \eta\bar{E}^*(\eta)};\ \xi\right\}. \qquad (150)$$

By (150) (81), and the first of (20),

$$R(\xi) = \frac{2E}{3(1-2\nu)}\,\mathfrak{L}^{-1}\left\{\frac{1}{\eta} - \frac{1}{\eta[1 + (1-2\nu)\eta\bar{E}^*(\eta)/E]};\ \xi\right\}. \qquad (151)$$

Here

$$E = \bar{E}(0), \quad \nu = \bar{\nu}(0) \qquad (152)$$

and thus characterize the initial elastic response of the material.

We proceed to the explicit determination of $R(\xi)$ for polymethyl methacrylate. According to [20], the experimental measurements of $\bar{E}(t)$ may be adequately described by the empirical formula

$$\log_{10}\bar{E}(t) = 8.85 - 1.5\ \mathrm{erf}[0.31(\log_{10}t - 3.6)] \text{ at } 80\text{ C}, \quad (153)[20]$$

in which the units of $\bar{E}$ and t are dynes/cm^2 and hr, respectively. Since it is highly inconvenient to obtain the Laplace transform of $\bar{E}(t)$ in the representation (153), we introduce instead the analytically more advantageous approximate representation

$$\bar{E}(t) = 10^{8.85}\{63.0(t + 3.98)^{-1/2} + 0.0316 - 15.5[7.94(t + 3.98)^{-3/2} - \exp(-1.89t)]\} \text{ at } 80\text{ C}. \quad (154)$$

Fig. 3 shows that the values of $\bar{E}(t)$ based on (154) agree closely with those resulting from (153) for the entire time range. The shift factor $\varphi(T)$, in turn, for T between 80 and 110 C, admits the approximation

[18] Reliable information concerning the actual temperature dependence of κ and α for polymethyl methacrylate seems to be lacking in the experimental literature.

[19] See [11], p. 77, et seq. There is an obvious need for further experimental corroboration of this common theoretical assumption.

[20] Actually, the formula given in [20] applies to the base temperature 110 C and has been modified accordingly.

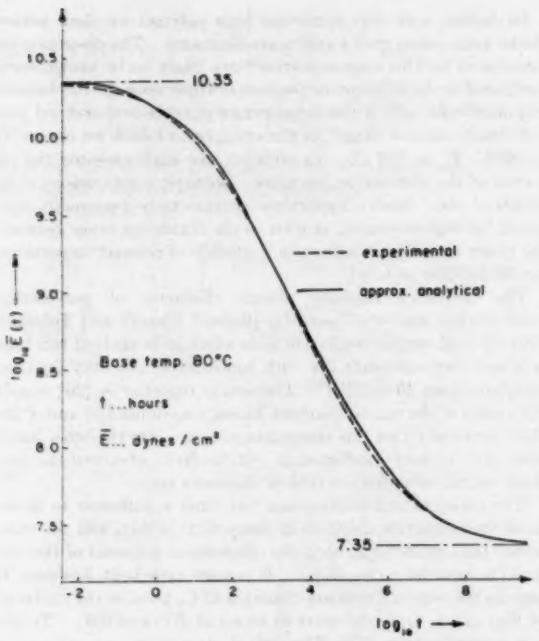

Fig. 3 Time dependence of Young's modulus for polymethyl methacrylate

$$\varphi(T) = 10^{3.8} \exp\left\{-\frac{6.908}{10^3}(110 - T) \cdot [T - 40 + 0.0365(T - 80)^2]\right\}, \quad (155)$$

which refers to the base temperature $T_0 = 80$ C, the units of T being degrees centigrade. From (155) the reduced time ξ may be computed by numerical evaluation of the definite integral in (41) for any given $T(z, t)$.

Applying the Laplace transform to (154) and using the first of (152), we reach[21]

$$\frac{\bar{E}^*(\eta)}{E} = \sqrt{\pi}\, A\eta^{-1/2} \exp(b\eta)\, \operatorname{erfc}(b\eta)^{1/2} - \frac{2B}{\sqrt{b}}\left[1 - (\pi b\eta)^{1/2} \exp(b\eta)\, \operatorname{erfc}(b\eta)^{1/2}\right] + \frac{C}{\eta} + \frac{D}{\eta + c}, \quad (156)$$

with

$$E = 10^{10.3}, \quad b = 3.98, \quad c = 1.89, \quad A = 1.99, \quad B = 3.89, \quad C = 10^{-2}, \quad D = 0.490. \quad (157)$$

It is clear from (151) that the transform of the desired auxiliary response function $R(\xi)$ is fully specified by (156), (157) together with the experimental value $\nu = \bar{\nu}(0) = 0.35$. The complete determination of the corresponding inverse Laplace transform, i.e., of $R(\xi)$ for the entire range $0 < \xi < \infty$, in a form convenient for further numerical work, presents great analytical difficulties. For this reason we adopt the usual asymptotic method[22] for finding the required inverse transform and, with the aid of (144), (145), (151), (156), (157), deduce separate approximate representations of $R(\xi)$, valid for sufficiently small and sufficiently large values of ξ, respectively. The results of these highly cumbersome computations—the details of which will be omitted here—indicate that the intermediate range of ξ-values may be covered adequately by a linear interpolation for $R(\xi)$ if $\log \xi$ is chosen as the independent variable. The values of $R(\xi)$ thus obtained, and used in the subsequent stress computation, are given by

$$\left.\begin{aligned} \frac{R(\xi)}{E} &= 0.513 - 0.193\,[1 - \exp(-1.89\xi)] + 0.0234\xi - 0.0476\xi^2 + 0.0465\xi^3 - 0.0301\xi^4 \quad (0 \le \xi \le 0.398), \\ \frac{R(\xi)}{E} &= 0.366 - 0.121 \log_{10}\xi \quad (0.398 \le \xi \le 70.8), \\ \frac{R(\xi)}{E} &= 0.000666 + \frac{1}{\sqrt{\xi}}\left(1.33 - \frac{10.6}{\xi} + \frac{114}{\xi^2} - \frac{951}{\xi^3}\right) \quad (70.8 \le \xi < \infty). \end{aligned}\right\} \quad (158)$$

The graph of $R(\xi)$, plotted on a semilogarithmic scale, is presented in Fig. 5.

We are now in a position to compute σ_{zz} as a function of time in the middle plane $z = 0$ of a polymethyl methacrylate slab which is under the influence of the temperature field (141), (142). For illustrative purposes we choose

$$T_0 = 80 \text{ C}, \quad T_1 = 110 \text{ C}, \quad a^2/\kappa = 1 \text{ hr}. \quad (159)$$

Since

$$\alpha \doteq 8 \times 10^{-5}/\text{C}, \quad \kappa \doteq 8 \text{ cm}^2/\text{hr} \quad (160)$$

for this material,[23] the last of (159) corresponds to a slab thickness of approximately 5.7 cm. Inserting (159) into (141), (142), setting $z = 0$, and bearing (139), (140) in mind, we reach the appropriate values of $T(0, t)$. Substituting the latter into (155), and thereafter evaluating the integral in (41) by the usual numerical procedure, we arrive at the relevant values of the reduced time $\xi(0, t)$. Once $\xi(0, t)$ is known, $\sigma_{zz}(0, t)$ follows from (73), with the aid of (141), (142), and (158), through the numerical evaluation of the definite integral in (73).

The results of the calculations just outlined, which were carried out in part on an IBM 650 computer, are displayed as Curve 1 in Fig. 6. Curve 2, in the same diagram, shows the behavior of $\sigma_{zz}(0, t)$ predicted on the assumption that the response of the material is temperature-independent; this curve is based on the values of the tensile modulus of relaxation appropriate to the aver-

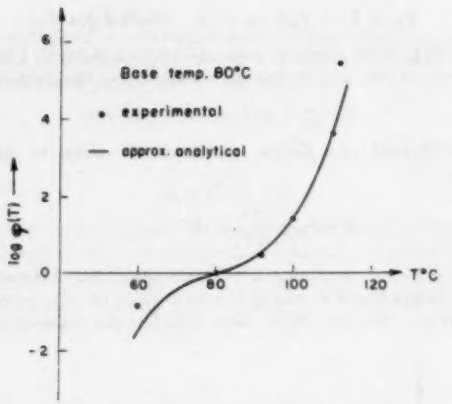

Fig. 4 Temperature dependence of shift factor for polymethyl methacrylate

[21] See [22], p. 267.

[22] See, for example, [19], p. 271, et seq.

[23] These approximate values are based on experimental information cited by Simonds and Ellis [23], p. 44. The temperatures at which the underlying measurements were carried out are not given in [23].

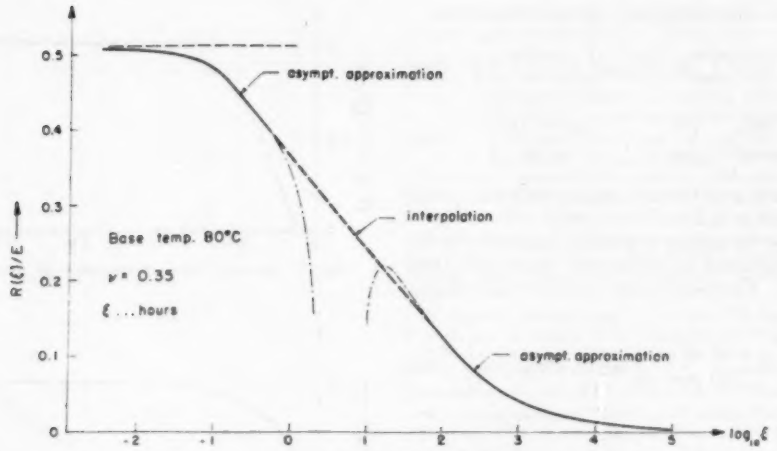

Fig. 5 Values of $R(\xi)$ for polymethyl methacrylate

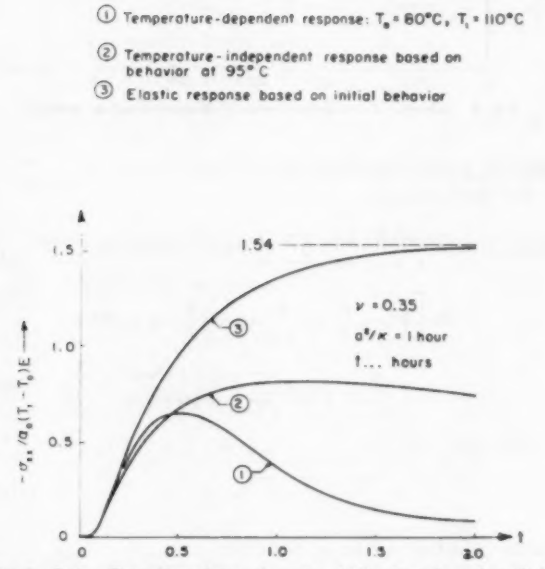
① Temperature-dependent response: T0 = 80°C, T1 = 110°C
② Temperature-independent response based on behavior at 95° C
③ Elastic response based on initial behavior
1.54
ν = 0.35
a²/κ = 1 hour
t ... hours
-σzz/σ0(T1 - T0)E
t

Fig. 6 Slab. Time dependence of σ_{zz} in middle plane for polymethyl methacrylate

age surface temperature of 95 C. Curve 3, finally, illustrates the time variation of $\sigma_{zz}(0, t)$ in an elastic slab whose elastic constants coincide with the corresponding initial values $E = E(0)$ and $\nu = \nu(0)$ for polymethyl methacrylate. We observe that for an initial period of about 10 min the three curves almost coalesce, the response of the material being nearly elastic (and hence temperature independent) during this early stage. For approximately the first 25 min, Curve 2 slightly underestimates the "actual" stress values, as was to be anticipated; throughout this period, as is evident from Fig. 1, the temperature at $z = 0$ is less than the average temperature of 95 C on which the modulus $E(t)$ underlying Curve 2 is based. Later on, however, Curve 2 progressively overestimates the stress values predicted by Curve 1, reaching a maximum value at $t \doteq 1$ hr which exceeds the "true" maximum (occurring at $t \doteq 1/2$ hr) by over 25 per cent. The stress relaxation according to Curve 1 is seen to be far more rapid than that implied by Curve 2; after a 2-hr period the actual stress is less than 15 per cent of the corresponding value indicated in curve 2. These conclusions clearly confirm the totally unrealistic character of any viscoelastic thermal-stress analysis which neglects the temperature dependence of the viscoelastic properties.

The remaining numerical results relate to the problem of the sphere, solved in Section 5. Once again we assume α and κ to be constant and consider the special case in which the temperature field is induced by a sudden uniform change of the surface temperature. Thus $T(r, t)$, introduced in (93), is assumed to be the solution in (58) which satisfies the initial and boundary conditions

$$\begin{aligned} T(r, t) &= T_0 \quad (0 \leq r \leq a, \quad -\infty < t < 0), \\ T(r, t) &= T_1 \quad (r = a, \quad 0 < t < \infty). \end{aligned} \tag{161}$$

In accordance with (104) we now have

$$\Theta(r, t) = T(r, t) - T_0 \tag{162}$$

and on setting

$$\Theta_1 = T_1 - T_0 \tag{163}$$

the known solution[24] to the present heat-conduction problem appears as

$$\Theta(r, t) = \Theta_1 \left[1 + \frac{2a}{\pi r} \sum_{n=1}^{\infty} \frac{(-1)^n}{n} \exp\left(-\frac{n^2 \pi^2 \kappa t}{a^2} \right) \sin \frac{n\pi r}{a} \right]. \tag{164}$$

This representation of the solution is well adapted to computations involving large values of t. An alternative representation, suitable for small time values, is given by

$$\Theta(r, t) = \frac{\Theta_1 a}{r} \sum_{n=0}^{\infty} \left\{ \operatorname{erfc} \left[\frac{2n + 1 - r/a}{2(\kappa t/a^2)^{1/2}} \right] - \operatorname{erfc} \left[\frac{2n + 1 + r/a}{2(\kappa t/a^2)^{1/2}} \right] \right\}. \tag{165}$$

Formula (165) is analogous to (142) and may be deduced by strictly analogous means.[25] The values of $\Theta(0, t)$ follow from

[24] Reference [18], p. 200.
[25] Reference [19], p. 275.

(164), (165) through an elementary limit process which yields

$$\Theta(0, t) = \Theta_1\left[1 + 2\sum_{n=1}^{\infty}(-1)^n \exp\left(-\frac{n^2\pi^2\kappa t}{a^2}\right)\right], \quad (166)$$

$$\Theta(0, t) = \frac{2\Theta_1}{(\pi\kappa t/a^2)^{1/2}}\sum_{n=0}^{\infty}\exp\left[-\frac{(2n+1)^2}{4\kappa t/a^2}\right]. \quad (167)$$

Fig. 7 shows the variation of the temperature with time at the center of the sphere and is based on (166), (167).

Explicit formulas for the surface displacement generated in the present instance are obtained by substitution from (164), (165) into the first of (124). Carrying out the required integration we find that

$$u_r(a, t) = a\alpha_0\Theta_1\left[1 - \frac{6}{\pi^2}\sum_{n=1}^{\infty}\frac{1}{n^2}\exp\left(-n^2\pi^2\kappa t/a^2\right)\right] \quad (168)$$

and, alternatively,

$$u_r(a, t) = 3a\alpha_0\Theta_1\left[-\frac{\kappa t}{a^2} + \frac{2}{\sqrt{\pi}}\left(\frac{\kappa t}{a^2}\right)^{1/2} + \frac{4}{\sqrt{\pi}}\left(\frac{\kappa t}{a^2}\right)^{1/2}\sum_{n=1}^{\infty}\exp\left(-\frac{n^2a^2}{\kappa t}\right) - 4\sum_{n=1}^{\infty} n\,\mathrm{erfc}\left(\frac{n}{(\kappa t/a^2)^{1/2}}\right)\right]. \quad (169)$$

As is clear from the discussion in Section 5, these results, which are plotted in Fig. 8, are valid for any material with a purely elastic dilatational response.

Finally, we examine the surface values of $\sigma_{\theta\theta}$ for the temperature field at hand. In view of (161) the reduced time ξ at $r = a$ is once again given by (148). Bearing this in mind and taking the Laplace transform[25] with respect to t in (130), we arrive at

$$\sigma_{\theta\theta}^*(a, \eta) = -\frac{3\alpha_0\kappa a}{\varphi(T_1)}R^*\left[\frac{\eta}{\varphi(T_1)}\right]\left\{\frac{d}{dr}\left[\frac{1}{r}\frac{d}{dr}\Theta^*(r, \eta)\right]\right\}_{r=a} \quad (170)$$

Furthermore, (161) and (58) readily yield

$$\Theta^*(r, \eta) = \frac{a\Theta_1\sinh(r^2\eta/\kappa)^{1/2}}{r\eta\sinh(a^2\eta/\kappa)^{1/2}}. \quad (171)$$

Confining our attention henceforth to the special cases of the elastic, the Maxwell, and the Kelvin solid, we now use (84), (85), (86), as well as (54), and invert (170). In this manner we are led to the following results:

For the *elastic solid*

$$\sigma_{\theta\theta}(a, t) = -\frac{6\alpha_0\Theta_1 E}{(1-\nu)\pi^2}\sum_{n=1}^{\infty}\frac{1}{n^2}\exp\left(-n^2\pi^2\kappa t/a^2\right). \quad (172)$$

For the *Maxwell solid*

$$\sigma_{\theta\theta}(a, t) = -\frac{\alpha_0\Theta_1 E}{1-\nu}\left\{\left[1 - \frac{3}{\delta} + \frac{3}{\sqrt{\delta}}\cot\sqrt{\delta}\right]\exp\left(-\delta\kappa t/a^2\right) + 6\sum_{n=1}^{\infty}\frac{\exp\left(-n^2\pi^2\kappa t/a^2\right)}{n^2\pi^2 - \delta}\right\}, \quad (173)$$

where

$$\delta = \frac{a^2\beta}{\kappa\tau(T_1)} \neq n^2\pi^2 \quad (n = 1, 2, \ldots), \quad (174)$$

[25] Note that it is not permissible to substitute (164) into (130) if $r = a$ because of the discontinuity of $\Theta(a, t)$ at $t = 0$.

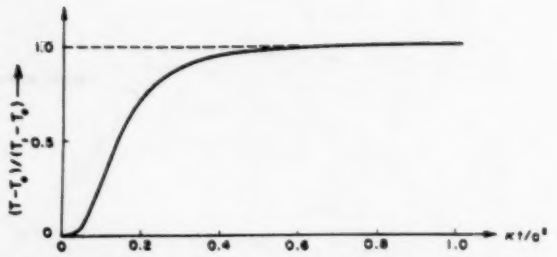

Fig. 7 Sphere. Time dependence of temperature at center.

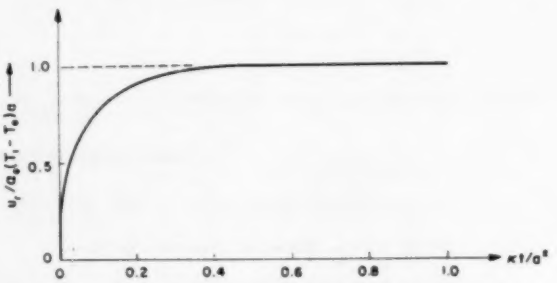

Fig. 8 Sphere. Time dependence of displacement at surface.

and β is given by the first in (87).

For the *Kelvin solid*

$$\sigma_{\theta\theta}(a, t) = -\frac{\alpha_0\Theta_1 E}{1-\nu}\left\{\frac{6}{\pi^2}\sum_{n=1}^{\infty}\frac{1}{n^2}\exp\left(-n^2\pi^2\kappa t/a^2\right) + \beta\gamma\left[\left(1 - \frac{3}{\delta} + \frac{3}{\sqrt{\delta}}\cot\sqrt{\delta}\right)\exp\left(-\delta\kappa t/a^2\right) + 6\sum_{n=1}^{\infty}\frac{\exp\left(-n^2\pi^2\kappa t/a^2\right)}{n^2\pi^2 - \delta}\right]\right\}, \quad (175)$$

where now

$$\delta = \frac{a^2\gamma}{\kappa\tau(T_1)} \neq n^2\pi^2 \quad (n = 1, 2, \ldots), \quad (176)$$

while γ is defined by the second of (87).

The infinite series appearing in (172), (173), (175) are rapidly convergent except in the vicinity of $t = 0$. For small time values, useful representations of $\sigma_{\theta\theta}(a, t)$ may be deduced by an appropriate asymptotic inversion of (170).

Thus, for the *elastic solid*, as $t \to 0$,

$$\sigma_{\theta\theta}(a, t) = -\frac{\alpha_0\Theta_1 E}{1-\nu}\left\{1 + \frac{3\kappa t}{a^2} - \frac{6}{\sqrt{\pi}}\left(\frac{\kappa t}{a^2}\right)^{1/2} + O\left[\left(\frac{\kappa t}{a^2}\right)^{1/2}\exp\left(-\frac{a^2}{\kappa t}\right)\right]\right\}. \quad (177)$$

For the *Maxwell solid*, as $t \to 0$,

$$\sigma_{\theta\theta}(a, t) = -\frac{\alpha_0\Theta_1 E}{1-\nu}\left\{\left(1 - \frac{3}{\delta}\right)\exp\left(-\frac{\delta\kappa t}{a^2}\right) + \frac{3}{\delta} - 3\left(\frac{\kappa t}{a^2}\right)^{1/2}\sum_{n=0}^{\infty}\frac{(-1)^n}{\Gamma(3/2+n)}\left(\frac{\delta\kappa t}{a^2}\right)^n + O\left[\left(\frac{\kappa t}{a^2}\right)^{1/2}\exp\left(-\frac{a^2}{\kappa t}\right)\right]\right\}, \quad (178)$$

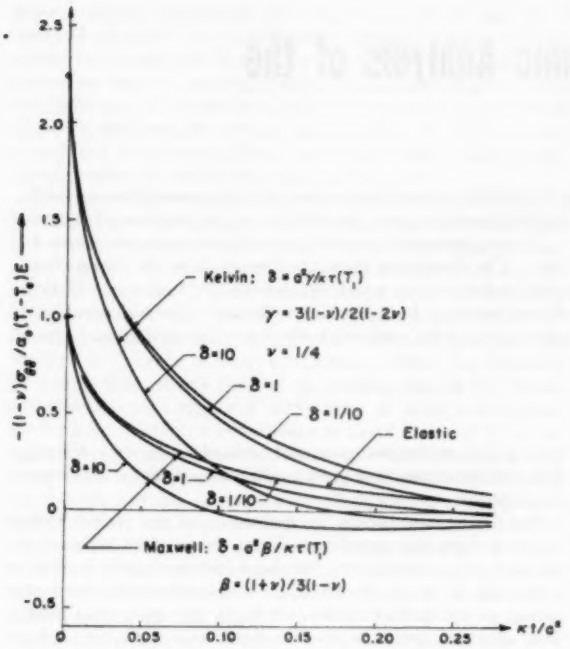

Fig. 9 Sphere. Time dependence of $\sigma_{\theta\theta}$ at surface for various values of parameter δ.

in which Γ denotes the Gamma function and δ is defined through (174).

For the *Kelvin solid*, as $t \to 0$,

$$\sigma_{\theta\theta}(a,t) = -\frac{\alpha_0\Theta_1 E}{1-\nu}\left\{1 + \frac{3\kappa t}{a^2} - \frac{6}{\sqrt{\pi}}\left(\frac{\kappa t}{a^2}\right)^{1/2} + \beta\gamma\left[\left(1-\frac{3}{\delta}\right)\exp\left(-\frac{\delta\kappa t}{a^2}\right) + \frac{3}{\delta} - 3\left(\frac{\kappa t}{a^2}\right)^{1/2}\sum_{n=0}^{\infty}\frac{(-1)^n}{\Gamma(3/2+n)}\left(\frac{\delta\kappa t}{a^2}\right)^n\right] + O\left[\left(\frac{\kappa t}{a^2}\right)^{1/2}\exp\left(-\frac{a^2}{\kappa t}\right)\right]\right\}, \quad (179)$$

where δ is again given by (176).

Equations (172), (173), (175) and (177), (178), (179) were used to compute $\sigma_{\theta\theta}$ at $r = a$ as a function of time, for several values of the parameter δ. The corresponding numerical results are presented in Fig. 9. It should be noted that the curve belonging to a Maxwell solid with $\delta = 1/10$ is practically coincident with the curve representing the elastic solid.

References

1 E. Sternberg, "On Transient Thermal Stresses in Linear Viscoelasticity," Proceedings, Third U. S. National Congress of Applied Mechanics, ASME, New York, N. Y., 1958, p. 673.

2 E. H. Lee, "Stress Analysis in Viscoelastic Bodies," *Quarterly of Applied Mathematics*, vol. 8, 1955, p. 183.

3 A. M. Freudenthal, "Effect of Rheological Behavior on Thermal Stresses," *Journal of Applied Physics*, vol. 25, 1954, p. 1110.

4 A. M. Freudenthal, "On Inelastic Thermal Stresses in Flight Structures," *Journal of the Aeronautical Sciences*, vol. 21, 1954, p. 772.

5 H. H. Hilton, "Thermal Stresses in Thick-Walled Cylinders Exhibiting Temperature-Dependent Viscoelastic Properties of the Kelvin Type," *Proceedings*, Second U. S. National Congress of Applied Mechanics, ASME, New York, N. Y., 1954, p. 547.

6 L. Rongved, "Residual Stress in Glass Spheres," Technical Report No. 16, Contract Nonr 266(09), Department of Civil Engineering and Engineering Mechanics, Columbia University, July, 1954.

7 L. W. Morland and E. H. Lee, "Stress Analysis for Linear Viscoelastic Materials With Temperature Variation," Technical Report No. 1, Contract NOrd 18594, Division of Applied Mathematics, Brown University, Providence, R. I., September, 1959, to appear in *Transactions*, Society of Rheology, vol. 4, 1960.

8 H. Leaderman, "Elastic and Creep Properties of Filamentous Materials," Textile Foundation, Washington, D. C., 1943, p. 175.

9 J. D. Ferry, "Mechanical Properties of Substances of High Molecular Weight. VI Dispersion in Concentrated Polymer Solutions and its Dependence on Temperature and Concentration," *Journal of the American Chemical Society*, vol. 72, 1950, p. 3746.

10 F. Schwarzl and A. J. Staverman, "Time-Temperature Dependence of Linear Viscoelastic Behavior," *Journal of Applied Physics*, vol. 23, 1952, p. 838.

11 A. J. Staverman and F. Schwarzl, "Linear Deformation Behavior of High Polymers," Chapter 1 in *Die Physik der Hochpolymeren*, edited by H. A. Stuart, vol. 4, Springer, Berlin, Germany, 1956.

12 A. R. Payne, "Temperature-Frequency Relationships of Dielectric and Mechanical Properties of Polymers, The Rheology of Elastomers," edited by P. Mason and N. Wookey, Pergamon Press, New York, N. Y., 1958, p. 86.

13 E. H. Lee, "Viscoelastic Stress Analysis," Proceedings, First Symposium on Naval Structural Mechanics, Pergamon Press, New York, N. Y., 1960, p. 456.

14 B. Van der Pol and H. Bremmer, "Operational Calculus," Second Edition, Cambridge University Press, Cambridge, England, 1955.

15 H. G. Landau, J. H. Weiner and E. E. Zwicky, Jr., "Thermal Stress in a Viscoelastic-Plastic Plate With Temperature-Dependent Yield Stress," JOURNAL OF APPLIED MECHANICS, vol. 27, TRANS. ASME, vol. 82, Series E, June, 1960, pp. 297–302.

16 S. Timoshenko and J. N. Goodier, "Theory of Elasticity," McGraw-Hill Book Company, Inc., New York, N. Y., 1951.

17 J. Nowinski, "Thermoelastic Problem for an Isotropic Sphere With Temperature Dependent Properties," *Zeitschrift für angewandte Mathematik und Physik*, vol. 10, 1959, p. 565.

18 H. S. Carslaw and J. C. Jaeger, "Conduction of Heat in Solids," Second Edition, Oxford University Press, Oxford, England, 1947.

19 H. S. Carslaw and J. C. Jaeger, "Operational Methods in Applied Mathematics," Second Edition, Oxford University Press, Oxford, England, 1947.

20 J. Bischoff, E. Catsiff and A. V. Tobolsky, "Elastoviscous Properties of Amorphous Polymers in the Transition Region —I," *Journal of the American Chemical Society*, vol. 74, 1952, p. 3378.

21 E. A. W. Hoff, "Some Mechanical Properties of a Commercial Polymethyl Methacrylate," *Journal of Applied Chemistry*, vol. 2, 1952, p. 441.

22 Staff of the Bateman Manuscript Project, "Table of Integral Transforms," vol. 1, McGraw-Hill Book Company, Inc., New York, N. Y., 1954.

23 H. R. Simonds and C. Ellis, "Handbook of Plastics," D. Van Nostrand Company, Inc., New York, N. Y., 1943.

Thermodynamic Analysis of the Darcy Law

R. G. MOKADAM
Department of Mechanical Engineering, Indian Institute of Technology, Kharagpur, S. E. Ry., India

The Darcy law is used extensively to describe the flow of fluids through porous media. According to this law the fluid flow is linearly dependent upon the pressure gradient and the gravitational force. The proportionality factor is generally known as the permeability of the porous medium. The Darcy law cannot be derived from the Navier-Stokes equation since this equation includes terms which characterize the fluid only. With the help of nonreversible thermodynamics it is possible to develop a general equation of motion of a fluid through a porous body, and obtain the Darcy law as a special case of such an equation.

EXTENSIVE use of the Darcy law has been made to describe the flow of fluids through porous media. According to this law the flow is linearly dependent upon the pressure gradient and the gravitational force. The proportionality factor is generally known as the permeability of the porous medium. It is supposed to be equal to a constant divided by the viscosity of the fluid, and, according to Muskat [1],[1] the constant depends only upon the porous medium. Thus the permeability of a porous medium for nonviscous fluids will become infinity. Muskat [1] states that the Darcy law may be taken as the dynamical basis for all problems of viscous fluid flow through porous media. Carman [2] gives a detailed account of how the Darcy law has been applied to the viscous, molecular, or partly viscous flow of fluids through porous media. For viscous flow the permeability is defined as before. For partly viscous or slip flow the permeability is supposed to be equal to a sum of two terms one of which includes the viscosity of the fluid. For the molecular flow the permeability is independent of the viscosity of the fluid.

Darcy [3] originally formulated the law to obtain the average or apparent flow rates of fluids through porous media in one-dimensional flow. However, it is now used to describe the flow field in two or three-dimensional problems. In such cases the fluid velocity is assumed to be a continuous function of the space co-ordinates.

The Darcy law cannot be derived from the Navier-Stokes equation since this equation includes terms which characterize the fluid only. By suitably defining a thermodynamic system, it is possible to apply the technique of nonreversible thermodynamics to the problem of flow of fluids through porous media. This approach yields a general equation of motion of a fluid through a porous medium. The Darcy law can then be obtained as a special case of such an equation.

Thermodynamic System

In an actual system consisting of a porous medium and a fluid it is possible, in principle, to consider an infinitesimal volume which will contain the fluid only, and describe the fluid flow through a porous medium by the application of the laws of thermodynamics and hydrodynamics. In practice, however, it has not been possible to analyze the problem of fluid flow through porous media with the help of the foregoing procedure owing to the complex boundary conditions as a result of intricate structure of the porous media.

In order to simplify the boundary conditions and make the problem amenable to theoretical analysis, we shall consider a model of a porous medium which was developed by the author in his PhD thesis.[2] In this model, it is assumed that the porous medium is isotropic and that it consists of fine solid particles uniformly scattered and fixed in space. Shrinking or swelling of the

[1] Numbers in brackets designate References at end of paper.

Presented at the Summer Conference of the Applied Mechanics Division, Chicago, Ill., June 14–16, 1961, of THE AMERICAN SOCIETY OF MECHANICAL ENGINEERS.

Discussion of this paper should be addressed to the Editorial Department, ASME, 29 West 39th Street, New York, N. Y., and will be accepted until July 10, 1961. Discussion received after the closing date will be returned. Manuscript received by ASME Applied Mechanics Division, March 29, 1960. Paper No. 61—APM-5.

[2] "Irreversible Thermodynamics of Vapor Transmission Through Porous Media," PhD thesis, University of Minnesota, 1953.

Nomenclature

e = total internal energy per unit mass of fluid phase
F = gravitational force per unit mass
F_f = frictional force per unit volume of system
F_{ij} = bulk stress components
F_{ij}' = intrinsic stress components
L_{ww}, L_{ss}, etc. = Onsager or phenomenological coefficients
l = kinetic energy per unit mass of fluid phase
l_0 = reference length of porous medium
o = potential energy per unit mass of fluid phase
p = bulk pressure of fluid phase
p' = intrinsic pressure of fluid phase
p'' = dimensionless intrinsic pressure of fluid phase
Δp = reference pressure differential across porous medium
$\bar{q}$ = total heat flow per unit area of system
$\bar{q}_w$ = heat flow through fluid phase per unit area of system
$\bar{q}_s$ = heat flow through solid phase per unit area of system
r = density concentration of fluid phase, or porosity of system
r_s = density concentration of solid phase
s = entropy per unit mass of fluid phase
s_s = entropy per unit mass of solid phase
T = temperature of system
t = time

(*Continued on next page*)

porous medium is neglected, and the density of the particles is assumed constant. Any infinitesimal volume of the system is assumed to contain both the solid and the fluid phases. In other words, the matter in any infinitesimal volume of the system under consideration will always be a solid-fluid mixture. For the fluid phase we shall consider a single liquid or gas. It will also be assumed that the porous medium is a nonadsorbent. This assumption precludes the existence of an adsorbed phase.

It will thus be noted that at any point in the system we have a mixture of the solid and the fluid phases. Thus an infinitesimal volume of the system will be equal to the sum of the infinitesimal volumes of the phases, and its state will be defined by the properties of the phases. These properties will be called intrinsic or actual properties. However, for the purpose of analysis we do not admit of an infinitesimal volume which will be occupied only by the fluid or the solid phase of the system. Hence it is necessary to assume that, at any point in the system, each of the phases occupies the entire volume of the system. In order to accommodate this assumption, it is necessary to modify some of the properties of the phases. These modified properties will be called bulk properties. It will be shown that there is a definite relationship between the intrinsic or actual and bulk properties of the phases. From the foregoing discussion it is obvious that in the application of equations of thermodynamics and hydrodynamics to an infinitesimal volume of the system, it will be necessary to use the bulk properties of the phases. Thus our thermodynamic system consists of a solid-fluid mixture in which each of the phases is assumed to occupy the entire volume of the system. In this manner an essentially heterogeneous system can be treated as if it were continuous. Henceforth all properties, which are not specifically described as bulk properties, will be considered as intrinsic or actual properties.

At any point in the system let the volume of the system be V. In this volume, V, the actual volume, pressure, density, and temperature of the fluid phase are denoted by V', p', ρ', and T, respectively. These are called the intrinsic properties of the fluid phase. As indicated earlier, the same mass of the fluid (occupying V') will be assumed to occupy the entire volume, V, of the system, and its bulk properties will be denoted by V, p, ρ, and T. There is no difference between the intrinsic and the bulk temperature of the fluid phase. A similar classification of properties will also be made for the solid phase. At any point in the system,

$$\frac{V'}{V} = \frac{\rho}{\rho'} = r \tag{1}$$

where r is defined as the density or volume concentration of the fluid phase. It will be noted that r is in fact the porosity of the system. Considering both the phases we have

$$r + r_s = 1, \quad \text{and} \quad dr = 0 \tag{2}$$

where r_s is the volume concentration of the solid phase, and it is constant.

Guggenheim [4] defines the pressure of a fluid phase as a thermodynamic property which when multiplied by a differential change in the volume of the fluid phase gives a reversible work done by that phase. This definition will be used to correlate the intrinsic and the bulk pressure of the fluid phase. Thus if $d\omega'$ is the reversible work done by the fluid phase for a differential change dV' in its intrinsic volume,

$$d\omega' = p'dV' \tag{3}$$

If the foregoing work is based upon a differential change, dV, of the volume of the system, the coefficient of dV can be considered as the bulk pressure of the fluid phase. From equations (1), (2), and (3) we have

$$d\omega' = p'r\,dV = p\,dV \tag{4}$$

It will be noted that $p\,dV$ is also the total reversible work done by the system since the solid phase is fixed in space, and dV causes only inclusion (or exclusion) of more solid particles. Equation (4) defines the bulk pressure of the fluid phase, and it satisfies the assumption that the fluid phase occupies the entire volume, V, of the system. The bulk pressure can be considered as a normal force, due to the fluid, per unit area of the system at a given point. Since the intrinsic pressure of the fluid phase is a component of its total intrinsic stress tensor, $\bar{\phi}'$, we shall define the bulk stress tensor, $\bar{\phi}$, by

$$\bar{\phi} = r\bar{\phi}' \tag{5}$$

The stress tensor is included in the analysis to obtain generality in the treatment of the problem. The bulk stress tensor can be considered as the total force, due to the fluid, per unit area of the system at a given point.

For reasons stated earlier, it is necessary to use the bulk properties, as defined, in the development of the continuity, momentum, energy, and entropy equations. For continuous systems they are generally written with reference to an infinitesimal volume of the system on "per unit volume" basis. To begin with, these equations will be written independently for the two phases. From these we shall obtain an equation giving the local time rate of change of entropy of a unit volume of the system for the analysis of various nonreversible phenomena. It will be noted that the assumption, that each of the phases occupies the entire volume of the system, has no effect on the specific properties (based on a unit mass) of the phases with the exception, of course, of the specific volume.

Continuity Equation

According to the model of the system, an infinitesimal volume of the system at any point is assumed to contain both the phases

Nomenclature

t' = dimensionless time
u = molecular internal energy of fluid phase per unit mass
u_s = molecular internal energy of solid phase per unit mass
V = volume of system
V' = intrinsic volume of fluid phase
$\bar{V}$ = velocity of fluid phase
$\bar{V}'$ = dimensionless velocity of fluid phase
V_0 = reference velocity of fluid phase
$d\omega'$ = infinitesimal reversible work done by fluid phase
x, y, z = space co-ordinates
x', y', z' = dimensionless space co-ordinates
ρ = bulk density of fluid phase
ρ_s = bulk density of solid phase
ρ' = intrinsic density of fluid phase
$\bar{\phi}$ = bulk stress tensor of fluid phase
$\bar{\phi}'$ = intrinsic stress tensor of fluid phase
σ = total entropy production per unit volume of system
σ' = entropy production due to viscous flow per unit volume of system
δ_{ij} = Kronecker delta
μ_v μ_s = shear and volume viscosities, respectively, of fluid phase

and each is assumed to occupy the entire volume. The velocity $\bar{V}$ of the fluid phase is therefore defined as the fluid mass-flow rate per unit area of the system, at a given point, divided by the bulk density of the fluid phase at that point. Like other properties $\bar{V}$ is considered to be a continuous function of the space and time co-ordinates. Hence for the conservation of mass of the fluid phase we have

$$\frac{\partial \rho}{\partial t} = -\text{div } \rho \bar{V} \tag{6}$$

Equation (6) also represents the conservation of mass of the system since the solid phase is stationary. For any extensive property of the fluid phase like entropy or molecular internal energy, we have

$$\frac{\partial \rho s}{\partial t} = \rho \frac{ds}{dt} - \text{div } (\rho s \bar{V}) \tag{7}$$

where s is the specific entropy of the fluid phase.

The relation between the local and the substantial time derivatives is given by

$$\frac{d}{dt} = \frac{\partial}{\partial t} + \bar{V} \cdot \text{grad} \tag{8}$$

Equations (7) and (8) could be written along the motion of the center of mass of the system. This alternative procedure is, however, unsatisfactory in the present case. Consequently, the substantial time derivatives of the properties of the phases will be counted along their respective velocities. Since the solid phase is stationary, the local and the substantial time derivatives, in this case, will be the same.

Momentum Equation

The system is a solid-fluid mixture, and the solid phase is stationary. The fluid phase will be accelerated as a result of the bulk stress tensor, gravitational force, and a "frictional" force. The bulk stress tensor represents transfer of momentum between the fluid contained in an infinitesimal volume of the system and the fluid immediately adjacent to this volume, whereas the frictional force represents transfer of momentum between the stationary solid and the moving fluid in the infinitesimal volume. The action of the stress tensor is an external effect while the action of the frictional force is an internal effect. Let $\bar{F}$ be the gravitational force per unit mass, and $\bar{F}_f$ be the frictional force per unit volume of the system. Then

$$\rho \frac{d\bar{V}}{dt} = \text{div } \bar{\bar{\phi}} + \rho \bar{F} + \bar{F}_f \tag{9}$$

Energy Equation

If e, u, l, and o are the specific values of the total, molecular internal, kinetic and potential energies, respectively, of the fluid phase,

$$\rho e = \rho(u + l + o) \tag{10}$$

For the conservation of energy of the fluid phase we have

$$\frac{\partial \rho e}{\partial t} = -\text{div } \{\rho(u + l + o)\bar{V} + \bar{q}_g - \bar{\bar{\phi}} \cdot \bar{V}\} + \bar{F}_f \cdot \bar{V} \tag{11}$$

where $\bar{q}_g$ is the heat flow through the fluid phase per unit area of the system. The last term represents transfer of work between the phases resulting from the frictional force. Assuming that the gravitational field is time independent we have

$$\frac{\partial \rho o}{\partial t} = -\text{div } (po\bar{V}) - \rho \bar{F} \cdot \bar{V} \tag{12}$$

From equations (7) to (12) we get

$$\frac{\partial \rho u}{\partial t} = \bar{\bar{\phi}} : \text{grad } \bar{V} - \text{div } (\rho u \bar{V} + \bar{q}_g) \tag{13}$$

where $\bar{\bar{\phi}} : \text{grad } \bar{V}$ is the first scalar invariant of the tensor $\bar{\bar{\phi}} \cdot \text{grad } \bar{V}$.

Corresponding to equation (13), the law of conservation of energy of the solid phase of the system will be given by

$$\frac{\partial \rho_s u_s}{\partial t} = -\text{div } \bar{q}_s - \bar{F}_f \cdot \bar{V} \tag{14}$$

where ρ_s and u_s are the bulk density and specific molecular internal energy, respectively, of the solid phase, and $\bar{q}_s$ is the heat flow through the solid phase per unit area of the system.

Entropy Equation

Following Gibbs, the rate of change of entropy of the fluid phase is given by

$$T\rho \frac{ds}{dt} = \rho \frac{du}{dt} - \frac{p}{\rho} \frac{d\rho}{dt} \tag{15}$$

where s is the specific entropy of the fluid phase.

From equations (6), (8), and (15) we get

$$T\rho \frac{ds}{dt} = \rho \frac{du}{dt} + p \text{ div } \bar{V} \tag{16}$$

From equations (7), (8), (13), and (16) we have

$$\frac{\partial \rho s}{\partial t} = \frac{1}{T} \{\bar{\bar{\phi}} : \text{grad } \bar{V} + p \text{ div } \bar{V} - \text{div } \bar{q}_g\} - \text{div } \rho s \bar{V} \tag{17}$$

Considering no temperature difference between the solid and the fluid phases, for the solid phase, corresponding to equation (17), we have

$$\frac{\partial \rho_s s_s}{\partial t} = -\frac{1}{T} (\text{div } \bar{q}_s + \bar{F}_f \cdot \bar{V}) \tag{18}$$

where s_s is the specific entropy of the solid phase.

The local time rate of change of entropy of the system will be given by

$$\frac{\partial}{\partial t} (\rho s + \rho_s s_s) = \frac{1}{T} \{\bar{\bar{\phi}} : \text{grad } \bar{V} + p \text{ div } \bar{V} - \text{div } \bar{q} - \bar{F}_f \cdot \bar{V}\} - \text{div } \rho s \bar{V} \tag{19}$$

where $\bar{q}$ is the sum of $\bar{q}_g$ and $\bar{q}_s$. It is the total heat flow per unit area of the system.

Now

$$\bar{\bar{\phi}} : \text{grad } \bar{V} + p \text{ div } \bar{V} \equiv \Sigma_i \Sigma_j (p\delta_{ij} - F_{ij}) \frac{\partial V_j}{\partial x_i} \tag{20}$$

where i and j are x, y, z, and $x_x \equiv x$, $x_y \equiv y$, $x_z \equiv z$, and δ_{ij} is the Kronecker delta. F_{ij} represents the bulk stress components of the bulk stress tensor.

From equations (19) and (20), we have

$$\frac{\partial}{\partial t} (\rho s + \rho_s s_s) = \frac{1}{T} \left\{ \Sigma_i \Sigma_j (p\delta_{ij} - F_{ij}) \frac{\partial V_j}{\partial x_i} \right\} - \bar{F}_f \cdot \frac{\bar{V}}{T} - \bar{q} \cdot \frac{\text{grad } T}{T^2} - \text{div } (\bar{q}/T + \rho s \bar{V}) \tag{21}$$

From equation (21) the rate of generation of entropy, σ, per unit volume of the system is

$$\sigma = \frac{1}{T}\left\{\Sigma_i\Sigma_j(p\delta_{ij} - F_{ij})\frac{\partial V_j}{\partial x_i}\right\} - \bar{F}_f\cdot\frac{\bar{V}}{T} - \bar{q}\cdot\frac{\text{grad } T}{T^2} \quad (22)$$

The nonreversible changes in the system are therefore due to viscous flow, heat conduction, and fluid motion in the presence of frictional force. The first term is a scalar product of the quantities which are second-order tensors, whereas the last two terms are scalar products of the quantities which are first-order tensors. Owing to difference in their tensorial character, no coupling between the first and the other two terms exists. A coupling between the last two terms is assumed.

Phenomenological Equations

Considering fluid motion and heat flow as fluxes dependent upon both temperature gradient and frictional force, we can write the following phenomenological equations

$$\bar{q} = -L_{uu}\frac{\text{grad } T}{T^2} - L_{u\omega}\bar{F}_f \quad (23)$$

$$\frac{\bar{V}}{T} = -L_{\omega u}\frac{\text{grad } T}{T^2} - L_{\omega\omega}\bar{F}_f \quad (24)$$

where L_{uu}, $L_{u\omega}$, $L_{\omega u}$, and $L_{\omega\omega}$ are called Onsager or phenomenological coefficients. In the foregoing equations frictional force and temperature gradient are considered as forces. The equations are called phenomenological since they require experimental verification. A linear relation between the forces and the fluxes is assumed here. If the foregoing equations are valid,

$$L_{u\omega} = L_{\omega u} \quad (25)$$

Equation (25) represents the Onsager reciprocal relations, and indicates how the cross phenomena, heat transfer due to frictional force, and the fluid motion due to temperature gradient, are connected. L_{uu} and $L_{\omega\omega}$ are indicative of the thermal conductivity and the permeability, respectively, of the system. Assuming the existence of the cross phenomena, the author [5] has shown that the sign and magnitude of $L_{u\omega}$ or $L_{\omega u}$ are dependent upon the Joule-Thomson coefficient of the fluid phase.

For the first term in equation (22), we can consider the stress tensor as a flux and the velocity gradient as a force, and assume a linear relation between the two. Since they are tensors of the second order, a separate phenomenological equation is necessary to connect these two terms. The bulk stress tensor in equation (22) is related to the intrinsic stress tensor through equation (5). Thus

$$\Sigma_i\Sigma_j(p\delta_{ij} - F_{ij}) = r\Sigma_i\Sigma_j(p'\delta_{ij} - F_{ij}') \quad (26)$$

If σ' is the entropy generation per unit volume of the system as a result of viscous flow, equations (22) and (26) give

$$\sigma' = \frac{r}{T}\left\{\Sigma_i\Sigma_j(p'\delta_{ij} - F_{ij}')\frac{\partial V_j}{\partial x_i}\right\} \quad (27)$$

Connecting the intrinsic stress tensor with the velocity gradient, we obtain the following phenomenological equation:

$$p'\delta_{ij} - F_{ij}' = \mu_s\left\{\left(\frac{\partial V_j}{\partial x_i} + \frac{\partial V_i}{\partial x_j}\right) - \tfrac{2}{3}\delta_{ij}\,\text{div}\,\bar{V}\right\} + \mu_v\delta_{ij}\,\text{div}\,\bar{V} \quad (28)$$

where the phenomenological coefficients μ_s and μ_v are the intrinsic or actual shear and volume viscosities, respectively, of the fluid phase. Since the system is isotropic, the stress tensor in this case is symmetric. If the hydrostatic pressure, p', is considered as equal to the mean value of the normal components of the intrinsic stress tensor, the volume viscosity is zero. Normally this is the case. Equation (28) is the well-known law of viscosity. From equations developed in the foregoing, general equation of motion and the Darcy law will now be derived.

Equation of Motion

From equations (9), (26), and (28) we have

$$\rho\frac{d\bar{V}}{dt} = -r\,\text{grad}\,p' + r\mu_s\left(\tfrac{1}{3}\,\text{grad div}\,\bar{V} + \text{div grad}\,\bar{V}\right) + \rho\bar{F} + \bar{F}_f \quad (29)$$

To describe the fluid motion, equations (24) and (29) are necessary. From these we get

$$\rho\frac{d\bar{V}}{dt} = -r\,\text{grad}\,p' + r\mu_s\left(\tfrac{1}{3}\,\text{grad div}\,\bar{V} + \text{div grad}\,\bar{V}\right) + \rho\bar{F} - \frac{\bar{V}}{TL_{\omega\omega}} - \frac{1}{T^2}\left(\frac{L_{\omega u}}{L_{\omega\omega}}\right)\text{grad}\,T \quad (30)$$

Except for the last two terms, equation (30) is similar to the Navier-Stokes equation. In fact, if the thermodynamic system consists of the fluid alone, equation (30) reduces to the exact form of the Navier-Stokes equation. In equation (29) the viscous term represents exchange of momentum between the fluid in an infinitesimal volume of the system and the fluid in the immediate neighborhood of this volume when these fluid elements are moving at different velocities. The frictional force represents the exchange of momentum between the fluid and the solid phases in the same infinitesimal volume of the system. This force is defined by the equation (24). As the porosity, r, of the system is decreased the exchange of momentum resulting from frictional force will become more significant than the exchange of momentum resulting from viscous effect.

Equation (30) can be applied to describe fluid flow through an actual porous medium if we can define the various properties and consider them as continuous functions of time and space co-ordinates throughout the extent of the porous medium. According to Muskat [1] this can be done in terms of what he describes as "macroscopic" properties. It therefore follows that we can use equation (30) in terms of these properties. It will then be seen that the velocity used by Muskat [1] is equal to $r\bar{V}$, and that the viscous effect in equation (30) is macroscopic in character. As indicated earlier, the viscous term becomes less significant than the frictional force as the porosity, r, is decreased. This view is also supported by the observations of Iberall [6]. Generally, the inertial effect is neglected because of the low velocity of the fluid. Therefore assuming isothermal conditions and neglecting the inertial and viscous effects, equations (1) and (30) give

$$\bar{V} = -rTL_{\omega\omega}(\text{grad}\,p' - \rho'\bar{F}) \quad (31)$$

Equation (31) represents the Darcy law. If the gravitational effect is also neglected we have

$$\bar{V} = -rTL_{\omega\omega}(\text{grad}\,p') \quad (32)$$

The coefficient in equations (31) and (32) is $rTL_{\omega\omega}$. This can be defined as the permeability of the system and it will be a property of the system which consists of the solid and the fluid phases. The Darcy law can thus be considered as a special case of equation (30). The permeability can be obtained from experimental data. However, since it is indicative of the mechanism of the frictional force we can deduce its dependence upon the viscosity of the fluid. Using Muskat's terminology, if the fluid flow is viscous on the "microscopic" level, the frictional force will

depend upon the viscosity of the fluid. Therefore the permeability will be a function of the viscosity. For the slip flow, the frictional force will depend partially upon the viscosity of the fluid and so the permeability will depend only in part upon the viscosity. If the flow is molecular, the frictional force and therefore the permeability will be independent of the viscosity of the fluid. In the second case, the viscous term in equation (30) will be much less significant than in the first case, whereas this term will drop out entirely in the case of a molecular flow.

Except in the case of rarefied fluids (particularly gases), a slip or molecular flow is obtained only in very low-porosity media. In such cases the viscous term in equation (30) will be quite negligible, and the coefficient L_{vm} in equations (24) and (30) will not be zero. As the author [5] has shown, this coefficient will then depend upon the Joule-Thomson coefficient of the fluid phase. On the basis of this it has been possible to explain the findings of Denbigh [7] on the spontaneous flow of carbon dioxide and hydrogen through rubber membranes as a result of a temperature gradient. If the flow is viscous on the microscopic level, L_{vm} is zero, and the term containing temperature gradient in equation (30) will drop out. It will be observed that whereas the Navier-Stokes equation may be considered as a microscopic counterpart of equation (30) for a viscous flow, the same will not be true for a slip or molecular flow. This is due to the fact that the Navier-Stokes equation is based upon a continuous system which contains the fluid only. On the other hand, in a slip or molecular flow even a system containing only the fluid is essentially discontinuous. The system (solid-fluid mixture) that has been used in the present analysis is also basically heterogeneous but continuous in a macroscopic sense. Hence equation (30) is much more representative of the fluid flow through porous media than the Navier-Stokes equation.

To obtain an idea of the relative importance of the various terms in equation (30) for viscous flow, we can rewrite it in dimensionless form. Using double-primed symbols to represent dimensionless quantities, and taking V_0 as reference velocity, l_0 as the reference length of the porous medium, and Δp as the reference pressure differential across the porous medium, we have

$$\bar{V} = V_0 \bar{V}'', \; x = l_0 x'', \; y = l_0 y'', \; z = l_0 z'',$$

$$p' = (\Delta p) p'', \quad \text{and} \quad t = \frac{l_0}{V_0} t'' \qquad (33)$$

In equation (30) we can drop the term containing temperature gradient, and also omit the gravity term since its order of magnitude is not in question. In order to simplify notation the terms in vector parlance in the dimensionless equation will be with reference to dimensionless co-ordinates. From equations (1), (30), and (33) we have

$$\left(\frac{\rho' V_0 l_0}{\mu_s}\right)\left(\frac{V_0 \mu_s}{l_0 \Delta p}\right)\frac{d\bar{V}''}{dt''} = -\operatorname{grad} p'' + \left(\frac{\mu_s V_0}{l_0 \Delta p}\right)\left(\tfrac{1}{3}\operatorname{grad}\operatorname{div}\bar{V}'' + \operatorname{div}\operatorname{grad}\bar{V}''\right) - \bar{V}''\left(\frac{v_0 l_0}{rTL_{vm}\Delta p}\right) \qquad (34)$$

We take the order of magnitude of the coefficient of dimensionless velocity as equal to that of the dimensionless pressure gradient, namely, unity. From Fig. 8 in Muskat's book [1] an idea of the order of magnitude of the coefficients of remaining terms in equation (34) can be obtained. In this figure the "friction factor" is plotted against Reynolds numbers. Both of these quantities include the "average grain diameter" as one of the parameters. Taking an example of unconsolidated sand, it can be shown that

$$\left(\frac{\mu_s V_0}{l_0 \Delta p}\right) \ll (10)^{-3} \quad \text{(any value of Reynolds number)}$$

$$\left(\frac{\rho' V_0 l_0}{\mu_s}\right)\left(\frac{V_0 \mu_s}{l_0 \Delta p}\right) \ll (10)^{-1} \quad \text{(Reynolds number = 1000)} \qquad (35)$$

$$\ll (10)^{-2} \quad \text{(Reynolds number = 10)}$$

$$\ll (10)^{-3} \quad \text{(Reynolds number = 1)}$$

We arrive at similar conclusions for other porous media. Therefore the viscous term in equation (30) appears to be quite insignificant. The acceleration term can also be neglected for low values of Reynolds numbers.

Conclusion

Equation (30) can be treated as a general equation of fluid flow through porous media. The Darcy law is valid only for isothermal flow in which the inertial and viscous effects are negligible. Inertial effects can be neglected for low values of Reynolds number. The viscous effect appears to be quite insignificant in the cases cited in the foregoing. For very highly porous media it may not be so. The relationship between the permeability and viscosity will depend upon the nature of the flow as indicated earlier and as stated by Carman [2]. Slip or molecular flow can be described accurately with the help of equation (30) by omitting the inertial and the viscous terms. Such types of flow cannot be described by the Navier-Stokes equation. Although it is not possible to deduce the exact magnitude of the permeability from equation (30), this equation together with equations (23) and (24) includes a number of thermodynamic phenomena which are beyond the scope of the Darcy law or the Navier-Stokes equation.

In the foregoing analysis the phases were considered as in thermal equilibrium. However, such a condition does not obtain in regenerative heat exchangers. The author is presently engaged in the analysis of fluid flow and heat transfer in porous media where the solid-phase temperature differs from the fluid-phase temperature.

References

1 M. Muskat, "The Flow of Homogeneous Fluids Through Porous Media," McGraw-Hill Book Company, Inc., New York, N. Y., 1937.

2 P. C. Carman, "The Flow of Gases Through Porous Media," Butterworths Scientific Publications, London, England, 1956.

3 H. Darcy, "Les fontaines publiques de la ville de Dijon," Victor Dalmont, Paris, France, 1856.

4 E. A. Guggenheim, "Thermodynamics: An Advanced Treatment for Chemists and Physicists," Interscience Publishers, Inc., New York, N. Y., 1949, chapter 1.

5 R. G. Mokadam, "Joule-Thomson Effect in Discontinuous System," *Proceedings of The Third Congress on Theoretical and Applied Mechanics*, Bangalore, India, 1957.

6 A. S. Iberall, "Permeability of Glass Wool and Other Highly Porous Media," *Journal of The National Bureau of Standards*, vol. 45, 1950, pp. 398–406.

7 K. G. Denbigh, "The Thermodynamics of the Steady State," John Wiley & Sons, Inc., New York, N. Y., 1951.

F. F. LING
Associate Professor,
Department of Mechanics,
Rensselaer Polytechnic Institute,
Troy, N. Y.
Mem. ASME

R. S. WEINER
Northwestern University,
Evanston, Ill.

A Bifurcation Phenomenon of Static Friction[1]

Measurements are reported of electric contact resistance, actual area of contact, static friction, adhesion and pure shear for lead on lead. The data exhibit a statistical bifurcation of friction. In other words, below extreme pressures, statistically there are two branches of the coefficient of friction versus normal load relationship. The nature of one of the branches is explicable exclusively in terms of the weld-junction or adhesion theory of friction. The nature of the other, however, is not so explicable. This points to the existence of what Holm [1][2] called the Y-term of friction, the nature of which has yet to be satisfactorily explained.

Introduction

To the student of mechanics, solid friction is, more often than not, that necessary evil which enters a problem in the boundary condition(s). The mechanism of friction is usually of no direct concern to him so long as there is a law of friction at his disposal. From Amontons' second law (1699) emerged the much used Coulomb friction (1785). However, with the increasing use of extreme pressures (normal load per unit area comparable to yield point), that is, conditions under which Amontons' second law is not generally valid, clearly, a more adequate law must be found.

To this end, several theories on the mechanism of friction have been advanced since the turn of the century; by far the most popular one is the weld-junction or adhesion theory. To further test the validity of the adhesion theory, the following quantities have been measured over a wide range of loads: Electric contact resistance, actual area of contact, static friction, adhesion, and pure shear. So far as the authors are aware, these quantities as a group have never been measured in a single experiment.

The data exhibit a statistical bifurcation of friction. In other words, below extreme pressures, statistically there are two branches of the coefficient of friction versus normal load relationship. The bifurcation feature extends to the adhesion, versus normal load and the pure shear versus normal load relationships.

It is shown that one of the branches of the friction curve is explicable exclusively in terms of the weld-junction or adhesion theory. The nature of the other, however, is not so explicable.

Measurements of Electric Contact Resistance, Actual Area of Contact, Friction, Adhesion, and Pure Shear

The main features of the apparatus consist of the following: Two interchangeable specimens are made in the form of cylinders, S in Fig. 1. The details of the specimen are shown in Fig. 2. The apparent area of contact is an annular region 0.50 in. ID and 0.55 in. OD. These dimensions were selected on the basis that the thickness of the region be small compared to the radius of the region, and that the area be sufficiently small so that the whole of the apparent area of contact can deform plastically within the range of the normal load that can be applied. The latter condition was applied with lead specimens in mind. A solid right circular cylindrical block, A in Fig. 1, is used as the main body of the apparatus. A circular opening transverse to the cylinder makes it possible to see and to reach the test section. The test section is where the two specimens meet. The specimen below the opening can be inserted through it and can be secured from motion. The upper specimen is secured snugly in a plunger, B, which is in turn free to rotate and to move axially in A. The essence of the construction is in the precision of the dimensions and the preparation of the plunger and its mating part. There are sixteen holes in A, J in Fig. 1, which constitute air inlets for the air bearing formed by the plunger and the vertical hole in A. The diametral clearance is 0.003 in. Compressed air is fed to the inlets through a filter, a pressure regulator, and a header. For stability, the air pressure has to be maintained below certain limits. A satisfactory pressure of 70 psi was used throughout the experiments.

Torque is measured by applying forces to a pair of strings, attached to a spool which is an integral part of the plunger. These forces form a couple so that no net lateral force is applied. Normal load is applied by a lever arrangement with suitable places to apply dead weights. A bracket, D in Fig. 1, is attached to the lever. When the lever is loaded so as to make D act downward, the hardened steel ball which is shown, attached to D, transmits load to the plunger. When the lever is loaded so as to make D act upward, the ball transmits the load to the plunger through the hardened steel disk, C, with a slightly concave surface. When the load is on, it is possible to rotate the plunger for measuring static friction by applying a torque to initiate rotation. The initiation of rotation is detected by the breaking of an electric circuit when rotation begins.

Electric contact resistance is measured by standard technique. The actual area of contact is measured by scanning the specimen used for adhesion measurement under a microscope in a systematic manner. The tests are conducted in a dust-free, temperature and moisture-controlled room with temperature arbitrarily set at 68 F and relative humidity at 50 per cent. The data reported here are for lead specimens. Specimens are machined, and the burrs are removed by passing a special facing tool over the end face three times, each time reducing the amount of cut by 50 per cent of the previous cut.

Cleaning consists of dipping specimens in carbon tetrachloride for 5 min and boiling in alcohol for 15 min, followed by one hr of drying and cooling in the test room described. Of concern here is a standard preparation of clean specimens and not the particu-

[1] This work was supported, in part, by the Air Force Office of Scientific Research, ARDC, under Contract No. AF 49(638)-67.

[2] Numbers in brackets designate References at end of paper.

Presented at the Summer Conference of the Applied Mechanics Division, Chicago, Ill., June 14–16, 1961, of The American Society of Mechanical Engineers.

Discussion of this paper should be addressed to the Editorial Department, ASME, 29 West 39th Street, New York, N. Y., and will be accepted until July 10, 1961. Discussion received after the closing date will be returned. Manuscript received by ASME Applied Mechanics Division, June 15, 1960. Paper No. 61—APM-7.

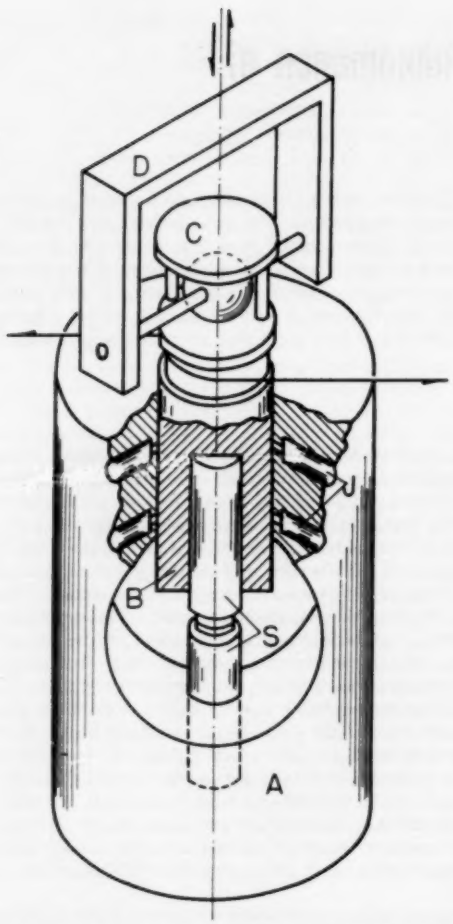

Fig. 1 Schematic diagram of test apparatus: *A*—test block; *B*—plunger; *C*—disk for lifting; *D*—lifting bracket; *S*—specimens; *J*—air nozzles

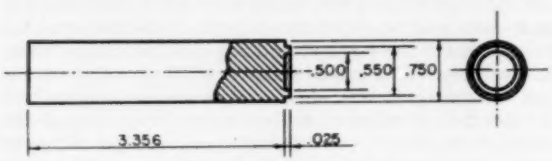

Fig. 2 Details of specimens

lar kind or thickness of film. The specimens are inserted in the block and the plunger which is then inserted in the block before compressed air is turned on. The specimens are separated by an air gap until testing time. All forces are measured by dead weights. For large forces, a spring scale can be used to measure the torque. The resisting torque inherent in the air bearing, by calibration, corresponds to a coefficient of friction of less than 0.003. The resistance to longitudinal motion, by calibration, is negligible.

Results

Fig. 3 shows contact resistance versus normal load. There are five runs, each consisting of loading and unloading. For instance, the triangular points with vertexes pointing upward represent the case where the maximum load is 37 kg. Since here only the

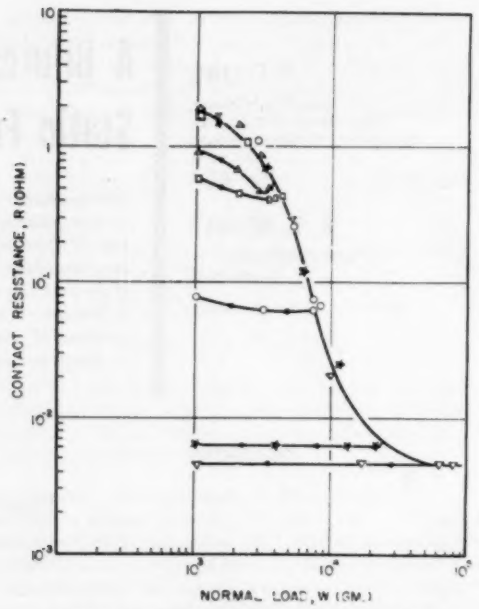

Fig. 3 Contact resistance versus normal load

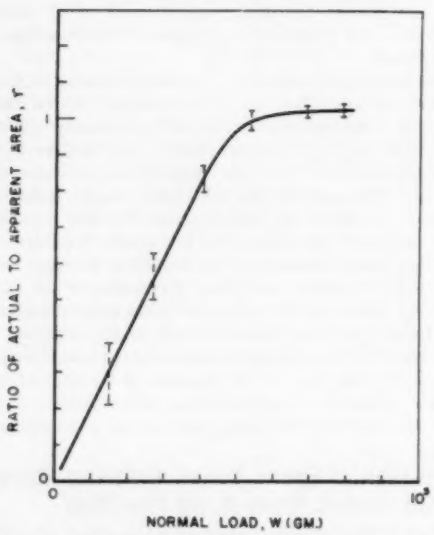

Fig. 4 Ratio of actual to apparent area versus normal load

qualitative nature of the resistance-load relationship is of interest, no attempt is made to relate actual area of contact to load from these data because of the uncertainty of the relationship between actual area of contact and resistance and because of the uncertainty of whether both constriction and film resistance are involved. However, the data have the following to offer: (*a*) Between 3 kg and 10 kg, the film must have broken to a large extent as there is a sharp decrease in resistance; (*b*) between 7 kg and 20 kg, elastic recovery ceases to be pronounced; and (*c*) around 50 kg, the actual area of contact approaches the apparent area of contact. The *R-W* curves shown are similar to those reported by Campbell [2].

Fig. 4 shows the result of scanning the specimen after the adhesion measurement under the microscope, ratio of the actual to

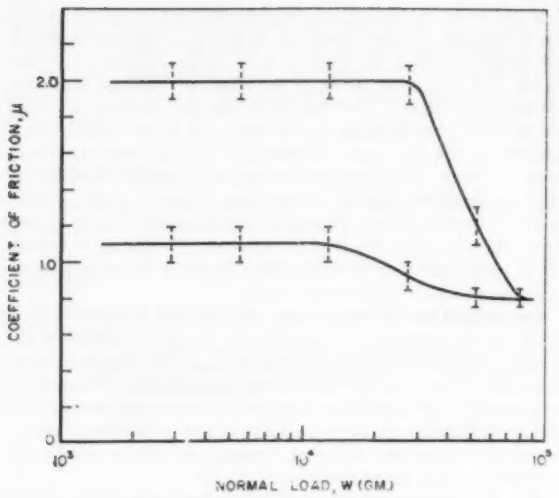

Fig. 5 Coefficient of friction versus normal load

apparent area of contact, r, versus load. The statistical spread at lower loads is larger than that at higher loads. Note that the value of r exceeds unity at $W = 60$ kg because the whole area has yielded plastically and the apparent area used in this computation was the undeformed area. Again, it would appear that r approaches unity at about $W = 50$ kg.

Next is a plot of coefficient of friction versus normal load, shown in Fig. 5. For a given value of W, the values of μ from a large number of tests clustered around two distinct values. A typical plot of the frequency of occurrence versus μ diagram would be roughly a double Gaussian curve in series. For $W < 10$ kg, the peaks of the Gaussian curves would occur at $\mu = 1.1$ and $\mu = 2$, respectively. The branches coalesce at $W = 80$ kg, Fig. 5.

We refer to this statistical phenomenon as bifurcation of the coefficient of friction versus normal load relationship. In so far as the authors know, this fact has never been observed and reported in the literature. In a way this is understandable, because no report has been found in which more than a few points are taken for this type of relationship. The bifurcation appears quite distinctly when one acquires a large number of data. Now the data fall between, very roughly, $\mu \cong 1$ and $\mu \cong 2$ which is what Bowden and Tabor [3] have reported for lead on lead although they did not observe the bifurcation feature.

The other feature to be noted is the rapid convergence of the upper branch to the lower branch as the normal load approaches that which makes the actual area of contact approach the apparent area of contact. This loading condition is sometimes referred to as extreme pressure. The lower branch is definitely lowered as a result of extreme pressure but not significantly. The important thing is that it stays within the order of unity. The duration of loading before measurement is one hour.

Fig. 6 shows the relationship between the coefficient of adhesion, the ratio of lifting force to normal load, and normal load. These data are for a duration of loading before measurement of one hr. Two features are worth noting: The coefficient of adhesion is zero until approximately $W = 14$ kg; there is a bifurcation of the coefficient of adhesion versus normal load relationship also. The lower branch has a maximum at approximately $W = 30$ kg.

In a similar fashion, Fig. 7 shows the relationship between coefficient of shear and normal load. The coefficient of shear is defined as the ratio of the equivalent shearing force after the normal load has been carefully removed, ($\hat{F}$) (torque divided by the average radius of the annular area of contact) to the normal load.

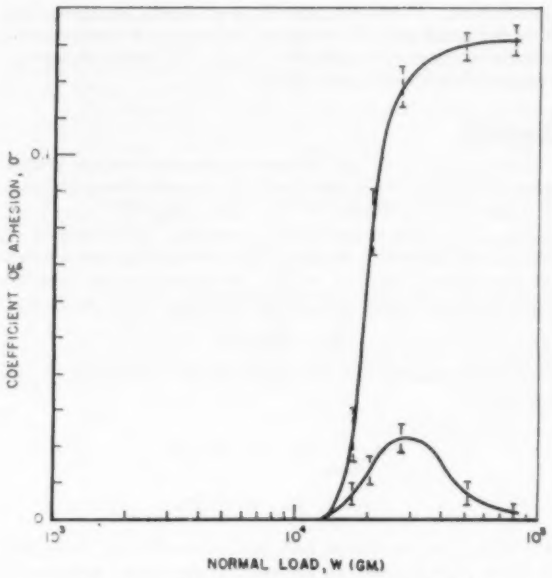

Fig. 6 Coefficient of adhesion versus normal load

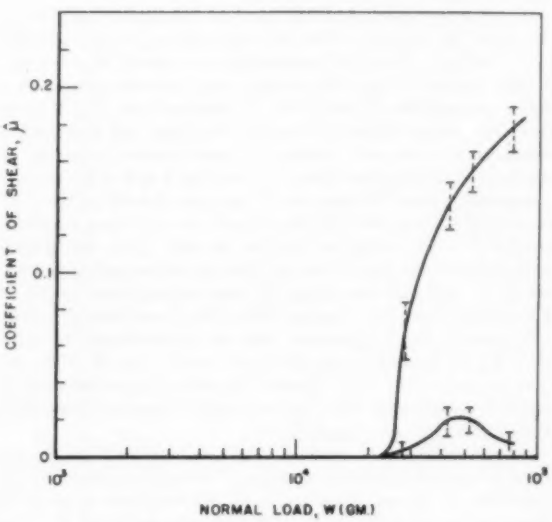

Fig. 7 Coefficient of shear versus normal load

It is really a measure of the shear stress in the absence of normal stress at the interface, macroscopically speaking, for $r < 1$; r is the ratio of the actual area of contact, A, to the apparent area of contact, A_a. This is so because

$$\hat{\mu} = \frac{\hat{F}}{W} = \frac{1}{p_m} \frac{\hat{F}}{(W/p_m)}$$

where p_m is the so-called yield pressure. For $r < 1$, $A = W/p_m$; therefore

$$\hat{\mu} \sim \hat{F}/A \sim \text{shear stress}$$

For $r \geq 1$,

$$\hat{\mu} W \sim \hat{F}/A_a \sim \text{shear stress}$$

These data are also for a duration of loading of one hour before

measurement. Coefficient of shear is zero until approximately $W = 25$ kg and there is a statistical bifurcation of the coefficient of shear versus normal load relationship. The lower branch has a maximum at approximately 50 kg.

Discussion

Yield Pressure. Although the scanning method is not so precise as one would like, it has been possible to measure the actual area of contact A from which $r = A/A_a$ was computed; r is shown in Fig. 4. A_a is the apparent area of contact. The constancy of the slope of the lower part of the r-W curve in Fig. 4 shows that the approximate formula $A = W/p_m$ is rather good, and from the slope, p_m can be computed. A simple computation shows that

$$p_m = 2530 \text{ psi}$$

Very approximately, the r-W curve may be represented by the formulas

$$r = \frac{1}{A_a p_m} W \quad \text{for} \quad W < W_t$$

$$r = 1 \quad \text{for} \quad W \geqslant W_t$$

where W_t is the transitional load, in this case 47.5 kg. According to Fig. 3, W_t is indicated by the fact that the contact resistance R ceases to be dependent upon W. We see a value about the same as the foregoing one.

If one uses properties of lead from an independent source [4] one gets yield stress $s_y = 800$ psi; and using $p_m \simeq 3s_y$, one gets $p_m \simeq 2400$ psi. From this one calculates a value of $W_t = 43$ kg.

Unfortunately it would be impossible to extract more quantitative information on the A-W relationship from Fig. 3 since there are the uncertainties of whether both film and constriction resistance are operative. Without a more definite knowledge of this fact, the formulas of Holm [1] relating R and A are useless.

Amontons' Laws. In the case of the upper branch of the μ-W curve in Fig. 5, for $W < W_b$ Amontons' laws of friction are valid, and for $W > W_b$ neither of the laws is valid. This checks with earlier theoretical work of one of the authors regarding the adhesion or weld-junction theory [5] and experimental results of Finnie and Shaw [6]. In the case of the lower branch of the μ-W curve in Fig. 5, Amontons' laws are approximately valid for $W < W_b$, the deviation occurring for $W \sim W_t$. For $W > W_b$ the laws are not valid. This checks with earlier theoretical work of one of the authors [5] regarding the classical interlock theory and Feng's plastic roughening theory [7].

The Role of Adhesion or Welding. Fig. 6 shows the adhesion coefficient for one hour duration of loading. Although no data of other durations are shown, there are some less abundant data which show that adhesion does grow with time as it should [8, 9]. The fact that there is no adhesion, in the absence of tangential forces, for $W < 14$ kg is due to the release of elastic energy which helps to break whatever joints there were [10]. It does not mean that there is no adhesion for all loads before the measurement took place. The fact that there is release of elastic energy is implied by the rise in electric contact resistance upon unloading as shown in Fig. 3 for loads less than 10 kg. The statistical bifurcation of the σ-W curve, Fig. 6, shows that there are strong joints and weak joints for the same duration of loading. It would appear that this is a function of the nature of surface films. For weak joints, the lower branch, it is not possible to give any explanation of the maximum of σ. The decrease of σ for $W > W_b$, or the state of extreme pressure, may account for the tapering of μ in Fig. 5 (lower branch).

Fig. 7 shows the same phenomena of strong adhesion and weak adhesion statistically with regard to the resulting shear stresses. As pointed out before, μW measures the shear stress for $W \geqslant W_t$; it would be interesting to calculate the order of magnitude of the shear stresses. For the upper branch in Fig. 7, calculation shows, for instance, a stress of 750 psi at $W = 78$ kg. This is to be compared with the shear stress of pure lead of 1065 psi given by Bowden and Tabor. The fact that these stresses are lower than those found from shearing macroscopic solid cylinders may be explained by the fact that full strength had not been developed after one hour. It is also possible that there is still some elastic recovery operative so that the actual area of contact at $W = 78$ kg is not as large as the apparent area of contact used in the caculation; that is, when the load is removed. Of course, the shear stress under load may be much higher owing to the state of combined stress which exists at the joints.

Bifurcation of Static Friction of Lead. By far, the most astonishing result is the statistical bifurcation of the data. What is the nature of the upper and lower branches? In the foregoing we referred to the strong and weak joints, respectively. We now examine these more carefully. Since we must have adhesion for all values of W although the tests did not show it because of elastic recovery, we see the following anomaly as to the mechanism which may apply in the two cases:

Fig. 8 shows the experimental points from Fig. 5, the circled points. Now suppose the so-called adhesion or weld-junction theory is operative exclusively, then

$$\mu = \frac{s}{p_m} \quad \text{for} \quad W < W_t \tag{1}$$

and $\mu = A_a s/W$ for $W \geqslant W_t$. Let μ_t denote μ for $W = W_t$, then

$$\mu = \mu_t W_t/W \quad \text{for} \quad W \geqslant W_t \tag{2}$$

Here we have assumed that both s and p_m are independent of W. Equations (1) and (2) are also shown in Fig. 8 by the dashed curves. Note that we fill in these curves without using any specific values of s and p_m. We merely assume that the mechanism is adhesion or welding exclusively.

We see that the upper branch of the experimental curve is well expressed by the theoretical curves, as crude as they may be. On the other hand, apparently the lower branch cannot be expressed adequately by the theoretical curves representing the adhesion theory, certainly not for $W \sim W_t$. From the discussion of

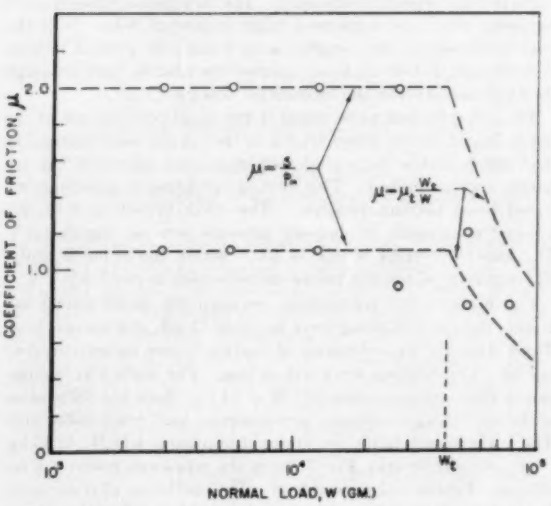

Fig. 8 Comparison of coefficients of friction versus normal load. o o o o o, experimental points from Fig. 7; – – – –, theoretical curves computed by formulas in text.

Amontons' laws, the lower branch looks more like the result of one of the interlock mechanisms or what Holm [1] called the Y-term of friction, which has yet to be explained satisfactorily.

This result agrees with earlier experimental work of one of the authors [11] which showed that the adhesion theory does not always apply.

Acknowledgment

The authors are indebted to Dr. Wm. R. Osgood for his valuable criticisms.

References

1 R. Holm, "Electric Contacts," Hugo Gebers Förlag, Stockholm, Sweden, 1946.

2 W. E. Campbell, "Use of Statistical Control in Corrosion and Contact Resistance Studies," *Transactions of The Electrochemical Society*, Inc., vol. 81, 1942, p. 377.

3 F. P. Bowden and D. Tabor, "Friction and Lubrication of Solids," Clarendon Press, Oxford, England, 1950.

4 "Metals Handbook," American Society of Metals, 1948.

5 F. F. Ling, "Some Factors Influencing the Area-Load Characteristics of Semismooth Contiguous Surfaces Under 'Static' Loading," TRANS. ASME, vol. 80, 1958, p. 1113.

6 I. Finnie and M. C. Shaw, "The Friction Process in Meta Cutting," TRANS. ASME, vol. 78, 1956, p. 1649.

7 I. M. Feng, "Metal Transfer and Wear," *Journal of Applied Physics*, vol. 23, 1952, p. 1011.

8 F. P. Bowden and G. W. Rowe, "The Adhesion of Clean Metals," *Proceedings of The Royal Society*, London, England, series A, vol. 233, 1956, p. 429.

9 F. F. Ling, "Adhesion, Pure Shear and Friction Measurements and Welding Aspect of Friction," AFOSR-TN-58-281, AD 154 183, 1958.

10 W. P. Mason, "Adhesion Between Metals and Its Effect on Fixed and Sliding Contacts," *Transactions of The American Society of Lubrication Engineers*, vol. 2, 1959, p. 39.

11 F. F. Ling and R. C. Lucek, "On Model Studies of Metallic Surface Asperities," *Journal of Applied Physics*, vol. 30, 1959, p. 1559.

A. C. ERINGEN
Professor,
Division of Engineering Sciences,
Purdue University,
Lafayette, Ind.

Propagations of Elastic Waves Generated by Dynamical Loads on a Circular Cavity[1]

The Fourier-transform technique has been employed to solve the exterior elasto-dynamic problem concerning the region outside a circular cavity in a plane elastic body. The normal and tangential tractions acting at the surface of the circular cavity are prescribed as arbitrary functions of the polar angle θ, and the time t. The case of impact, blast, and moving loads are studied in detail.

THE studies of vibrations of spherical and cylindrical cavities go back to Jaerisch [1, 2],[2] Lamb [3], Chree [4, 5], Love [6], and Basset [7]. Later Sezawa [8], Kromm [9], and Selberg [10] published papers which were concerned with the more restricted problem of a circular cavity subject to uniform blast loading. More recently Miklowitz [11] has found another application of the foregoing problem in a suddenly punched, stretched, elastic plate.

The present study on the hole was completed about five years ago. Because of the difficulties involved in carrying out a numerical example, namely, that of a cavity loaded with a suddenly applied and suddenly released pressure (Dirac delta function), the publication was postponed. When our attention was drawn to the Kromm and Selberg papers by Miklowitz's paper, we decided that this problem can be looked upon as completely settled. However, the general exterior problem concerning the circular cavity for an arbitrarily prescribed fixed and moving load is far from being complete.[3]

Recently the moving-load portion of the present paper was added which we believe has important applications in the design of beds for cylindrical bearings.

Formulation of Problem

The equations of motion of plane, homogeneous, isotropic media in terms of plane polar co-ordinates r and θ and the time t are [13] (see Fig. 1):

$$\begin{aligned} \gamma u_{,tt} &= (\lambda + 2\mu)\Delta_{,r} - 2\mu r^{-1}\omega_{,\theta}, \\ \gamma v_{,tt} &= (\lambda + 2\mu)r^{-1}\Delta_{,\theta} + 2\mu\omega_{,r} \end{aligned} \tag{1}$$

where $u(r, \theta, t)$ and $v(r, \theta, t)$ are the components of the displacement vector, λ and μ are the Lamé constants, and γ is the mass density per unit volume. The dilatation Δ and rotation ω are related to u, v by

$$r\Delta = (ru)_{,r} + v_{,\theta}, \quad 2r\omega = (rv)_{,r} - u_{,\theta} \tag{2}$$

Subscripts after a comma represent differentiation; i.e.,

$$u_{,\theta} \equiv \partial u/\partial\theta, \quad \text{etc. . .}$$

Elimination of u and v among (1) and (2) leads to

$$\begin{aligned} &\alpha_1^2 r^2 \Delta_{,tt} = r(r\Delta_{,r})_{,r} + \Delta_{,\theta\theta}, \quad \alpha_1^2 = \gamma/(\lambda + 2\mu), \\ &\alpha_2^2 r^2 \omega_{,tt} = r(r\omega_{,r})_{,r} + \omega_{,\theta\theta}, \quad \alpha_2^2 = \gamma/\mu \end{aligned} \tag{3}$$

These are the equations of dilatational and rotational waves.

The components σ_{rr}, $\sigma_{r\theta}$, $\sigma_{\theta\theta}$ of the stress tensor are given by

$$\begin{aligned} &\sigma_{rr} = \lambda\Delta + 2\mu u_{,r}, \quad \sigma_{r\theta} = \mu r^{-1}u_{,\theta} + \mu r(v/r)_{,r} \\ &\sigma_{\theta\theta} = \lambda\Delta + 2\mu r^{-1}(v_{,\theta} + u) \end{aligned} \tag{4}$$

The problem is to solve (1), (2) under a given σ_{rr} and $\sigma_{r\theta}$ at the surface $r = a$ of a circular cavity in an infinite plate:

$$\sigma_{rr}(a, \theta, t) = \sigma_0(\theta, t), \quad \sigma_{r\theta}(a, \theta, t) = \tau_0(\theta, t); \tag{5}$$

subject to further conditions the stress waves generated at the cavity are advancing into the medium $r > a$ (i.e., diverging waves) and vanish at $r = \infty$.

The General Solution

The solutions of (3) that are periodic in θ are the real parts of

$$\bar{\Delta} = \sum_{-\infty}^{\infty} A_n H_n^{(1)}(\rho_1)e^{in\theta}, \quad \bar{\omega} = \sum_{-\infty}^{\infty} B_n H_n^{(1)}(\rho_2)e^{in\theta}, \tag{6}$$

$$\rho_i = \alpha_i \tau r, \quad i = \sqrt{-1}, \quad (n = 0, \pm 1, \pm 2, \ldots),$$

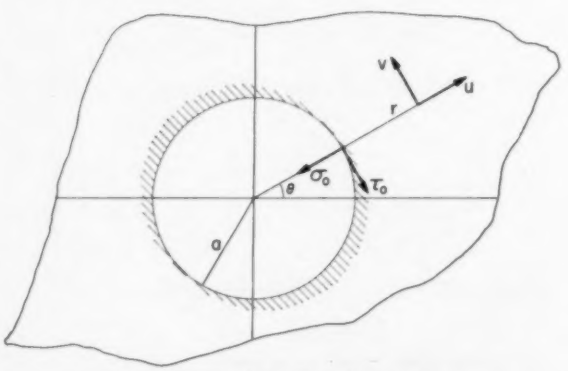

Fig. 1 Circular hole with surface tractions

---

[1] Sponsored by the Office of Naval Research.

[2] Numbers in brackets designate References at end of paper.

[3] The interior problem, namely, the circular disk subject to arbitrary surface loading, was given in a previous paper [12].

Presented at the Summer Conference of the Applied Mechanics Division, Chicago, Ill., June 14–16, 1961, of THE AMERICAN SOCIETY OF MECHANICAL ENGINEERS.

Discussion of this paper should be addressed to the Editorial Department, 29 West 39th Street, New York, N. Y., and will be accepted until July 10, 1961. Discussion received after the closing date will be returned. Manuscript received by ASME Applied Mechanics Division, May 10, 1960. Paper No. 61—APM-12.

where $H_n^{(1)}(\rho_j)$ are Hankel functions of the first kind and A_n and B_n are complex constants of integration. The barred quantities represent the Fourier transforms; i.e.,

$$\bar{F}(\tau) = \int_{-\infty}^{\infty} e^{it\tau} F(t)dt, \tag{7}$$

$$F(t) = \frac{1}{2\pi}\int_{-\infty}^{\infty} e^{-it\tau}\bar{F}(\tau)d\tau \tag{8}$$

We note that $H_n^{(2)}(\rho_j)$ has been discarded from the solution (6) of (3) since it does not satisfy the Sommerfeld radiation condition; namely,

$$\lim_{r\to\infty} r^{1/2}\left(\frac{\partial\bar{\Delta}}{\partial r} - i\alpha_1\tau\bar{\Delta}\right) = 0$$

A similar condition holds for $\bar{\omega}$. This condition assures that the waves are outgoing from the source.

Upon substituting (6) into (2) after taking the Fourier transform of (2) we obtain:

$$\bar{u} = \sum_{-\infty}^{\infty} U_n(r\tau)e^{in\theta}, \quad \bar{v} = \sum_{-\infty}^{\infty} V_n(r\tau)e^{in\theta}, \tag{9}$$

where

$$\begin{aligned} r^{-1}U_n(r\tau) &= -A_n\rho_1^{-1}H_n'^{(1)}(\rho_1) + iB_n\,2n\rho_2^{-2}H_n^{(1)}(\rho_2), \\ r^{-1}V_n(r\tau) &= -iA_n n\rho_1^{-2}H_n^{(1)}(\rho_1) - B_n 2\rho_2^{-1}H_n'^{(1)}(\rho_2) \end{aligned} \tag{10}$$

Here the primes represent differentiation; i.e.,

$$H_n'^{(1)}(\rho_1) \equiv dH_n^{(1)}(\rho_1)/d\rho_1$$

We now combine (4), (6) and (9) to obtain the stress components:

$$\begin{aligned} \bar{\sigma}_{rr}/2\mu &= \sum_{-\infty}^{\infty}[A_n N_{1n}(r\tau) + B_n N_{2n}(r\tau)]e^{in\theta}, \\ \bar{\sigma}_{r\theta}/2\mu &= \sum_{-\infty}^{\infty}[A_n S_{1n}(r\tau) + B_n S_{2n}(r\tau)]e^{in\theta}, \\ \bar{\sigma}_{\theta\theta}/2\mu &= \sum_{-\infty}^{\infty}[A_n T_{1n}(r\tau) + B_n T_{2n}(r\tau)]e^{in\theta}, \end{aligned} \tag{11}$$

where

$$\begin{aligned} N_{1n}(r\tau) &= (\lambda/2\mu)H_n^{(1)}(\rho_1) + (1 - n^2\rho_1^{-2})H_n^{(1)}(\rho_1) \\ &\quad + \rho_1^{-1}H_n'^{(1)}(\rho_1), \\ N_{2n}(r\tau) &= -2in\rho_2^{-2}H_n^{(1)}(\rho_2) + 2in\rho_2^{-1}H_n'^{(1)}(\rho_2), \\ S_{1n}(r\tau) &= in\rho_1^{-2}H_n^{(1)}(\rho_1) - in\rho_1^{-1}H_n'^{(1)}(\rho_1), \\ S_{2n}(r\tau) &= (1 - 2n^2\rho_2^{-2})H_n^{(1)}(\rho_2) + 2\rho_2^{-1}H_n'^{(1)}(\rho_2), \\ T_{1n}(r\tau) &= (\lambda/2\mu)H_n^{(1)}(\rho_1) + n^2\rho_1^{-2}H_n^{(1)}(\rho_1) \\ &\quad - \rho_1^{-1}H_n'^{(1)}(\rho_1), \\ T_{2n}(r\tau) &= -N_{2n}(r\tau) \end{aligned} \tag{12}$$

Dynamic Tractions Applied to Cavity

We now consider the problem of the propagation of waves generated under the dynamic surface tractions applied to the surface $r = a$ of the cavity. Expanding the tractions $\bar{\sigma}_\theta(\theta, \tau)$ and $\bar{\tau}_\theta(\theta, \tau)$ into Fourier series and equating them to $\bar{\sigma}_{rr}$ and $\bar{\sigma}_{r\theta}$ at $r = a$ we obtain

$$\begin{aligned} A_n &= (2\mu D_n)^{-1}[S_{2n}(a\tau)\bar{\sigma}_n - N_{2n}(a\tau)\bar{\tau}_n], \\ B_n &= (2\mu D_n)^{-1}[-S_{1n}(a\tau)\bar{\sigma}_n + N_{1n}(a\tau)\bar{\tau}_n], \end{aligned} \tag{13}$$

$$D_n(a\tau) = N_{1n}(a\tau)S_{2n}(a\tau) - N_{2n}(a\tau)S_{1n}(a\tau),$$

where $\bar{\sigma}_n$ and $\bar{\tau}_n$ are finite Fourier transforms of the cavity tractions.

$$\left.\begin{matrix}\bar{\sigma}_n \\ \bar{\tau}_n\end{matrix}\right\} = \frac{1}{2\pi}\int_0^{2\pi}\left\{\begin{matrix}\bar{\sigma}_\theta(\theta,\tau) \\ \bar{\tau}_\theta(\theta,\tau)\end{matrix}\right\} e^{-in\theta}d\theta \quad (n = 0, \pm1, \pm2, \ldots) \tag{14}$$

Substituting (13) into (9) and (11) we find

$$\begin{aligned} 2\mu r^{-1}\bar{u} &= \sum_{-\infty}^{\infty}[\bar{\sigma}_n u_n^{(1)}(r\tau) + \bar{\tau}_n u_n^{(2)}(r\tau)]e^{in\theta}, \\ 2\mu r^{-1}\bar{v} &= \sum_{-\infty}^{\infty}[\bar{\sigma}_n v_n^{(1)}(r\tau) + \bar{\tau}_n v_n^{(2)}(r\tau)]e^{in\theta}, \\ \bar{\sigma}_{rr} &= \sum_{-\infty}^{\infty}[\bar{\sigma}_n \sigma_{1n}^{(1)}(r\tau) + \bar{\tau}_n \sigma_{1n}^{(2)}(r\tau)]e^{in\theta}, \\ \bar{\sigma}_{r\theta} &= \sum_{-\infty}^{\infty}[\bar{\sigma}_n \tau_n^{(1)}(r\tau) + \bar{\tau}_n \tau_n^{(2)}(r\tau)]e^{in\theta}, \\ \bar{\sigma}_{\theta\theta} &= \sum_{-\infty}^{\infty}[\bar{\sigma}_n \sigma_{2n}^{(1)}(r\tau) + \bar{\tau}_n \sigma_{2n}^{(2)}(r\tau)]e^{in\theta}, \end{aligned} \tag{15}$$

where

$$\begin{aligned} u_n^{(1)}(r\tau) &= -[D_n(a\tau)]^{-1}[(\alpha_1 r\tau)^{-1}H_n'^{(1)}(\alpha_1 r\tau)S_{2n}(a\tau) \\ &\quad + 2in(\alpha_2 a\tau)^{-2}H_n^{(1)}(\alpha_2 a\tau)S_{1n}(a\tau)], \\ v_n^{(1)}(r\tau) &= -[D_n(a\tau)]^{-1}[in(\alpha_1 r\tau)^{-2}H_n^{(1)}(\alpha_1 r\tau)S_{2n}(a\tau) \\ &\quad - 2(\alpha_2 r\tau)^{-1}H_n'^{(1)}(\alpha_2 r\tau)S_{1n}(a\tau)], \\ \sigma_{1n}^{(1)}(r\tau) &= [D_n(a\tau)]^{-1}[S_{2n}(a\tau)N_{1n}(r\tau) - S_{1n}(a\tau)N_{2n}(r\tau)], \\ \tau_n^{(1)}(r\tau) &= [D_n(a\tau)]^{-1}[S_{2n}(a\tau)S_{1n}(r\tau) - S_{1n}(a\tau)S_{2n}(r\tau)], \\ \sigma_{2n}^{(1)}(r\tau) &= [D_n(a\tau)]^{-1}[S_{2n}(a\tau)T_{1n}(r\tau) - S_{1n}(a\tau)T_{2n}(r\tau)], \end{aligned} \tag{16}$$

The functions $u_n^{(2)}$, $v_n^{(2)}$, $\sigma_{1n}^{(2)}$, $\tau_n^{(2)}$, and $\sigma_{2n}^{(2)}$ are obtained from the corresponding ones with superscript (1) above by replacing $S_{1n}(a\tau)$ and $S_{2n}(a\tau)$ by $-N_{1n}(a\tau)$ and $-N_{2n}(a\tau)$, respectively.

This formally completes the problem. We now give some special cases which are of practical interest.

Special Cases

(i) *Zero surface shear:* $\bar{\tau}_n = 0$.

(ii) *Normal tractions with central symmetry and* (*i*): $\bar{\sigma}_n = \bar{\sigma}_{-n}$.

(iii) *Normal tractions with constant amplitude over* $0 \le \theta \le \alpha$ and (*i*):

$$\bar{\sigma}_0(\theta, \tau) = \begin{cases} \bar{\sigma}_0(\tau) & 0 \le \theta \le \alpha \\ 0 & \alpha \le \theta \le 2\pi \end{cases} \tag{17}$$

Hence

$$\bar{\sigma}_n = -(2\pi\, in)^{-1}(e^{-in\alpha} - 1)\bar{\sigma}_0(\tau), \tag{18}$$

(iv) *Concentrated load and* (*i*): In this case we have (18) with

$$\lim_{\substack{\alpha\to 0 \\ \bar{\sigma}_0\to\infty}} \bar{\sigma}_0(\tau)a\alpha = \bar{P}_0(\tau), \tag{19}$$

where $\bar{P}_0(\tau)$ is the Fourier transform of the concentrated time-dependent load $P_0(t)$ acting at $r = a$, $\theta = 0$. Using (19) in (18), we get

$$\bar{\sigma}_n = \bar{P}_0(\tau)/2\pi a \tag{20}$$

(v) *Impulsive concentrated load and* (*i*): In this case the con-

centrated load $P_0(t) = P_0\delta(t)$, where P_0 is constant and $\delta(t)$ is the Dirac delta function defined by

$$\delta(t) = \begin{cases} \infty & t = 0 \\ 0 & t \neq 0 \end{cases} \qquad \int_{-\infty}^{\infty} \delta(t)dt = 1$$

Thus
$$\bar{P}_0(\tau) = P_0, \qquad \bar{\sigma}_n = P_0/2\pi a \tag{21}$$

(vi) *Uniform pulsating load and* (*i*): This type of normal traction may be expressed by

$$\sigma_0(\theta, t) = p_0 e^{-i\omega t}, \quad \tau_0(\theta, t) = 0 \tag{22}$$

Consequently

$$\bar{\sigma}_0(\theta, \tau) = 2\pi p_0\delta(\omega - t), \quad \bar{\tau}_0(\theta, \tau) = 0$$

$$\bar{\sigma}_n = \begin{cases} 2\pi p_0\delta(\omega - \tau), & n = 0, \\ 0, & n \neq 0 \end{cases} \tag{23}$$

Therefore all terms in the series vanish except the term for which $n = 0$. In obtaining (23) we use the formal relation

$$2\pi\delta(u) = \int_{-\infty}^{\infty} e^{-iut}\,dt$$

Combining (23) with the first two equations of (15) and taking the inverse transform we obtain

$$u = [(\lambda + 2\mu)\alpha_1\omega a H_0^{(1)}(\alpha_1\omega a) - 2\mu H_1^{(1)}(\alpha\,\omega a)]^{-1} a p_0 H_1^{(1)}(\alpha_1\omega r)e^{-i\omega t}, \tag{24}$$

$$v = 0$$

This result is in complete agreement with that of [14].

(vii) *Blast loading and* (*i*):

$$\sigma_0 = p_0\delta(t), \quad \tau_0 = 0, \quad \bar{\sigma}_0 = \bar{\sigma}_0 = p_0, \qquad \bar{\sigma}_n = 0, \quad n > 0 \tag{25}$$

Hence, combining (25) with (15) and inverting, we find

$$u = \frac{p_0}{4\pi\mu\alpha_1}\int_{-\infty}^{\infty} \frac{H_1^{(1)}(\xi x)e^{-iy\xi}}{\beta\xi H_1^{(1)}(\xi) - H_1^{(1)}(\xi)}\,d\xi, \quad v = 0, \qquad x = r/a, \quad y = t/\alpha_1 a, \quad \beta = (\lambda + 2\mu)/2\mu \tag{26}$$

This result is in agreement with those of [9]-[11]. Careful examination shows that (26) is a convergent integral. However, the stress components obtained by using (26) and differentiating under the integral sign diverge. The severity of the loading is responsible for the nonuniform convergence of (26). Thus the stresses must be obtained after (26) is evaluated. This, of course, makes the computations very difficult, contrary to the three-dimensional counterpart of this problem; namely, for a spherical cavity.[4]

Moving Loads

(i) *Moving normal and tangential tractions:* Moving tractions at the surface of the cavity $r = a$ may be represented by

$$\sigma_0(\theta, t) = \sigma_1(\theta - \Omega t), \quad \tau_0(\theta, t) = \tau_0(\theta - \Omega_1 t) \tag{27}$$

The Fourier transforms of these are

$$\bar{\sigma}_0(\theta, \tau) = 2e^{i\tau\theta/\Omega}s_0(\tau/\Omega), \quad \bar{\tau}_0(\theta_1\tau) = 2e^{i\tau\theta/\Omega_1}s_1(\tau/\Omega_1), \qquad s_0(\tau/\Omega) = \frac{1}{2\Omega}\int_{-\infty}^{\infty} \sigma_0(\varphi)e^{-i\tau\varphi/\Omega}d\varphi, \tag{28}$$

and

$$\bar{\sigma}_n = \begin{cases} 2s_0(\tau/\Omega) & \text{when } \tau/\Omega = n, \\ s_0(\tau/\Omega)\,\dfrac{1}{i\pi}\,\dfrac{1}{(\tau/\Omega) - n}\left[e^{2i\pi\left(\frac{\tau}{\Omega} - n\right)} - 1\right] & \text{when } \tau/\Omega \neq n \end{cases} \tag{29}$$

A similar expression for $s_1(\tau/\Omega)$ may be obtained from $s_0(\tau/\Omega)$ by replacing Ω and $\sigma_0(\varphi)$ by Ω_1 and $\tau_0(\varphi)$, respectively.

(ii) *Moving periodic tractions:* Let us assume that the moving tractions (27) can be expanded into Fourier series

$$\sigma_0(\theta - \Omega t) = (Q_0/\pi a)\sum_{-\infty}^{\infty} p_n e^{in(\theta - \Omega t)}, \qquad \tau_0(\theta - \Omega_1 t) = (Q_0/\pi a)\sum_{-\infty}^{\infty} q_n e^{in(\theta - \Omega_1 t)} \tag{30}$$

where p_n and q_n are complex. Substituting the Fourier transforms of these into (14) we obtain

$$\bar{\sigma}_n = (2Q_0/a)p_n\delta(n\Omega - \tau), \qquad \bar{\tau}_n = (2Q_0/a)q_n\delta(n\Omega_1 - \tau) \tag{31}$$

Components of the displacement vector and the stress tensor can now be obtained by combining (31) with (15) and taking the inverse transform. Hence

$$\begin{aligned}
(2\pi a\mu/Q_0 r)u &= \sum_{-\infty}^{\infty} p_n u_n^{(1)}(r\,\Omega\,n)e^{in(\theta - \Omega t)} + q_n u_n^{(2)}(r\Omega_1 n)e^{in(\theta - \Omega_1 t)}, \\
(2\pi a\mu/Q_0 r)v &= \sum_{-\infty}^{\infty} p_n v_n^{(1)}(r\,\Omega\,n)e^{in(\theta - \Omega t)} + q_n v_n^{(2)}(r\,\Omega_1\,n)e^{in(\theta - \Omega_1 t)}, \\
(\pi a/Q_0)\sigma_{rr} &= \sum_{-\infty}^{\infty} p_n \sigma_{1n}^{(1)}(r\,\Omega\,n)e^{in(\theta - \Omega t)} + q_n\sigma_{1n}^{(2)}(r\,\Omega_1\,n)e^{in(\theta - \Omega_1 t)}, \\
(\pi a/Q_0)\sigma_{r\theta} &= \sum_{-\infty}^{\infty} p_n \tau_n^{(1)}(r\,\Omega\,n)e^{in(\theta - \Omega t)} + q_n\tau_n^{(2)}(r\,\Omega_1\,n)e^{in(\theta - \Omega_1 t)}, \\
(\pi a/Q_0)\sigma_{\theta\theta} &= \sum_{-\infty}^{\infty} p_n \sigma_{2n}^{(1)}(r\,\Omega\,n)e^{in(\theta - \Omega t)} + q_n\sigma_{2n}^{(2)}(r\,\Omega_1\,n)e^{in(\theta - \Omega_1 t)},
\end{aligned} \tag{32}$$

where the functions with superscript (1) such as $u_n^{(1)}(r\,\Omega\,n)$ are obtained from (16) by taking $\tau = \Omega n$ and those with superscript (2) are obtained from the corresponding ones by taking $\tau = \Omega_1 n$.

(iii) *Single moving concentrated load* (*Fig. 2*): This technically

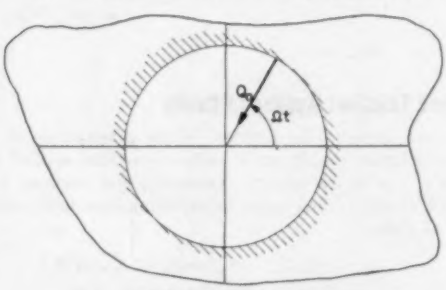

Fig. 2 Moving load

[4] See, for instance, Eringen [15].

important case is obtained from case (ii) by taking formally:

$$\sigma_0(\theta - \Omega t) = (Q_0/a)\delta(\theta - \Omega t) \tag{33}$$

Consequently, the Fourier coefficients p_n and q_n of (30) are

$$p_n = 1/2, \quad q_n = 0 \tag{34}$$

The stress displacement components now follow from using (34) in (32).

Here we study the structure of the displacement u in further detail. Substituting (34) into u of (32) we will have

$$u = (Q_0 r/4\pi a\mu) \sum_{-\infty}^{\infty} u_n^{(1)}(r\,\Omega\,n) \exp\,[in(\theta - \Omega t)] \tag{35}$$

This expression can be put into the form

$$u = (Q_0 r/4\pi a\mu)\left[-\frac{a^2}{r^2} + 2\sum_{n=1}^{\infty} Re\{u_n^{(1)}(r\,\Omega\,n) \exp\,[in(\theta - \Omega t)]\}\right] \tag{36}$$

where for $u_n^{(1)}(r\Omega n)$ we have

$$u_n^{(1)} = K(r\Omega n)/D(\alpha\Omega n)$$

$$\begin{aligned} K(r\Omega n) = {} & -\frac{1}{(\alpha_1\Omega)^2}\frac{1}{r^2 n} H_n^{(1)}(\alpha_1\Omega rn)H_n^{(1)}(\alpha_2\Omega rn) \\ & + \frac{2}{(\alpha_1\Omega)^2(\alpha_2\Omega)}\frac{1}{r^3n^2} H_n^{(1)}(\alpha_1\Omega rn)H_{n+1}^{(1)}(\alpha_2\Omega rn) \\ & + \left\{\frac{1}{\alpha_1\Omega}\frac{1}{rn} + \frac{2}{(\alpha_1\Omega)(\alpha_2\Omega)^2}\frac{1}{r^2n^2}\right\} \\ & \cdot H_{n+1}^{(1)}(\alpha_1\Omega rn)H_n^{(1)}(\alpha_2\Omega rn) - \frac{2}{(\alpha_1\Omega)(\alpha_2\Omega)}\frac{1}{r^2n^2} \\ & \cdot H_{n+1}^{(1)}(\alpha_1\Omega rn)H_{n+1}^{(1)}(\alpha_2\Omega rn), \end{aligned}$$

$$\begin{aligned} D(\alpha\Omega n) = {} & \left[\frac{\lambda+2\mu}{2\mu} - \frac{\lambda+2\mu}{\mu(\alpha_2\Omega)^2}\left(1-\frac{1}{n}\right)\frac{1}{a^2} \right. \\ & \left. - \frac{1}{(\alpha_1\Omega)^2}\left(1-\frac{1}{n}\right)\frac{1}{a^2}\right] H_n^{(1)}(\alpha_1 a\Omega n)H_n^{(1)}(\alpha_2 a\Omega n) \\ & - \left[\frac{1}{\alpha_1\Omega}\frac{1}{an} + \frac{2}{(\alpha_1\Omega)(\alpha_2\Omega)^2}\frac{1-n^2}{a^3n^2}\right] \\ & \cdot H_{n+1}^{(1)}(\alpha_1\Omega an)H_n^{(1)}(\alpha_2\Omega an) - \left[\frac{\lambda+2\mu}{\mu}\frac{1}{\alpha_2\Omega}\frac{1}{an}\right. \\ & \left. + \frac{2}{(\alpha_1\Omega)^2(\alpha_2\Omega)}\frac{1-n^2}{a^3n^2}\right] H_n^{(1)}(\alpha_1\Omega an)H_{n+1}^{(1)}(\alpha_2\Omega an) \\ & + \left[\frac{2}{(\alpha_1\Omega)(\alpha_2\Omega)}\frac{1-n^2}{a^3n^2}\right] H_{n+1}^{(1)}(\alpha_1\Omega an)H_{n+1}^{(1)}(\alpha_2\Omega an), \\ & H_n^{(1)}(z) = J_n(z) + iY_n(z) \end{aligned} \tag{37}$$

Note that the combination of (36) and (37) does not yield a result from which a physical picture can be extracted. The only way that we can obtain a meaningful result is to examine (36) in the light of various types of approximations.

(a) *Rapidly Moving Load.* If the tangential velocity $a\Omega$ is much greater than the speed of dilatational waves in the medium we can make an approximation to (36) as follows: In this case we have

$$\Omega a \gg 1/\alpha \quad \text{or} \quad n\alpha\Omega a \gg n$$

In this case we have the asymptotic expression

$$H_n^{(1)}(\alpha\Omega an) \to (2/\pi\alpha\Omega an)^{1/2} \exp\,[i\alpha\Omega an - \tfrac{1}{2}\pi i(n + \tfrac{1}{2})]$$

Since $r \geq a$ this expression will be valid also for $H_n(\alpha\Omega rn)$. Using the asymptotic values of H_n and discarding terms $(\alpha\Omega n)^{-n}$ for $n \geq 3$, after rather lengthy manipulations, we find

$$\begin{aligned} 4\pi\mu\, u/Q_0 = {} & -\frac{1}{\rho} + \left(\frac{\lambda+2\mu}{2\mu}\right)^{-1}\sum_{n=1}^{\infty}\left\{-\frac{2}{\rho n}\left[\frac{1}{(\alpha_1\Omega a)^2 n}\right.\right. \\ & + \frac{\lambda+2\mu}{\mu(\alpha_1\Omega a)(\alpha_2\Omega a)n} + \frac{\lambda+2\mu}{\mu(\alpha_1\Omega a)(\alpha_2\Omega a)\rho n} \\ & \left. - \frac{\lambda+2\mu}{2\mu(\alpha_1\Omega a)^2\rho}\right]\cos n[\theta + \Omega(r-a)(\alpha_1+\alpha_2) - \Omega t] \\ & \left. + \frac{2}{\rho n}\left(\frac{\lambda+2\mu}{\mu}\frac{1}{\alpha_1\Omega a}\right)\sin n[\theta + \Omega(r-a)(\alpha_1+\alpha_2) - \Omega t]\right\} \end{aligned} \tag{38}$$

where $\rho = r/a$.

The series contain all modes of oscillations. For a given mode (given n) along a circle r = const, after the arrival of waves, the disturbance rotates with the same angular velocity as the load; however, it remains behind the load at a phase angle of $\Omega(r-a)(\alpha_1+\alpha_2)$. The occurrence of the sum of speeds of shear and dilatational waves in this phase angle is significant. Here $1/\rho$ represents the static solution for a pressure $Q_0/2\pi a$.

(b) *Slowly Moving Load.* (Near field.) When the speed of moving load is much less than the speed of sound in the medium we have a quasi-steady motion. In this case $\alpha\Omega r \ll 1$ and in the neighborhood of the hole we have

$$H_n^{(1)}(\alpha\Omega rn) \to -i(n-1)!2^n/\pi(\alpha_1\Omega rn)^n, \quad n > 0$$

In this case (36) simplifies into

$$\begin{aligned} 4\pi\mu\, u/Q_0 = {} & -\frac{1}{\rho} - \frac{3}{\rho^3(\alpha_2\Omega a)}\cos(\theta - \Omega t) \\ & + \sum_{2}^{\infty}\left\{2\rho^{-n-2}n^{-4}(n^2-1)^{-1}\left[\frac{1}{\left(1+\frac{1}{n}\right)^{n+1}} - \frac{1}{n^4}\right]^{-1}\right. \\ & \left.\left[\frac{1}{\left(1+\frac{1}{n}\right)^{n+1}} - 1\right]\cos n(\theta - \Omega t)\right\} \end{aligned} \tag{39}$$

Here we again find the static solution $1/\rho$. In the neighborhood of the cavity (small ρ) we find that the displacement follows the load with the same angular velocity; however, the amplitude of the displacement diminishes as ρ^{-2}.

(c) *Slowly Moving Load.* (Far field.) If the speed of the load is much less than speed of sound, i.e., $\alpha\Omega a \ll 1$

$$H_n^{(1)}(\alpha\Omega an) \to -i(n-1)!2^n/\pi(\alpha\Omega an), \quad n > 0$$

and r is very large $\alpha\Omega_1 r \gg 1$, hence

$$H_n^{(1)}(\alpha\Omega rn) \to (2/\pi a\Omega rn)^{1/2} \exp\,[i\alpha\Omega rn - \tfrac{1}{2}\pi i(n + \tfrac{1}{2})]$$

then (36) is simplified a great deal by omitting terms of order $1/(\alpha\Omega r)^2$ as compared to $1/(\alpha\Omega r)$. The result is

$$\begin{aligned} 4\pi\mu u/Q_0 = {} & -\frac{1}{\rho} \\ & + \left(\frac{\alpha_2}{\alpha_1}\right)^{1/2}\frac{\pi}{2\rho}(\alpha_1\Omega a)^2\cos\,[\theta + \Omega r(\alpha_1+\alpha_2) - \Omega t] \\ & + \sum_{n=2}^{\infty}\left(\frac{\alpha_2}{\alpha_1}\right)^{1/2}\frac{2\pi}{\rho}(-1)^{n+1}(\alpha_1\Omega a)^{n+1}(\alpha_2\Omega a)^{n+1} \\ & \left(1+\frac{1}{n}\right)^{n+1}\left(\frac{n}{2}\right)^{2n}\left[\frac{n^4(n^2-1)}{\left(1+\frac{1}{n}\right)^{n+1}} - (n^2-1)\right]^{-1} \\ & \cdot\cos n[\theta + \Omega r(\alpha_1+\alpha_2) - \Omega t] \end{aligned} \tag{40}$$

Here again the static displacement field is present. The waves at large distances have the same angular velocity. The phase angle again, as in the case (a), is behind the load, is proportionate to the distance from the cavity, and depends on the sum of the velocity of equivoluminal and irrotational waves.

There is no particular difficulty in computing displacements from (38), (39) and (40) for these special cases.

(iv) *Two concentrated diametrically opposite moving loads:* In this case we write

$$\sigma_\delta(\theta - \Omega t) = (Q_0/a)[\delta(\theta - \Omega t) + \delta(\theta + \pi - \Omega t)], \quad \tau_\theta = 0 \quad (41)$$

Hence

$$p_n = \begin{cases} 1 & \pm n = 0, 2, 4, 6, \ldots, \\ 0 & \pm n = 1, 3, 5, \ldots \end{cases}$$

With the use of the principle of superposition, formulas for any number of moving concentrated loads can be written down immediately. The simplifications of the previous cases studied for a single moving load can be achieved in a similar fashion.

Acknowledgment

The author wishes to thank Mr. J. P. Jones for his care in checking the analysis, and Mr. N. Jordan for carrying out the approximations concerning the moving load.

References

1 P. Jaerisch, "Über die Elastischen Schwingungen einer Isotropen Kugel," *Journal für die reine und angewandte Mathematik*, vol. 88, 1880, pp. 131–145.

2 P. Jaerisch, "Allgemeine Integration der Elasticitätsgleichungen für die Schwingungen und das Gleichgewicht Isotroper Rotationskörper," *Journal für die reine und angewandte Mathematik*, vol. 104, 1889, pp. 177–210.

3 H. Lamb, "On the Vibrations of an Elastic Sphere," *Proceedings of the London Mathematical Society*, vol. 13, 1881–1882, pp. 189–212.

4 C. Chree, "The Equations of an Isotropic Elastic Solid in Polar and Cylindrical Coordinates, Their Solution and Application," *Transactions of the Cambridge Philosophical Soicety*, vol. 14, 1889, pp. 250–369.

5 C. Chree, "Forced Vibrations in Isotropic Elastic Solid Spheres and Spherical Shells," *Transactions of the Cambridge Philosophical Society*, vol. 16, 1897, pp. 14–57.

6 A. E. H. Love, "The Free and Forced Vibrations of an Elastic Spherical Shell Containing a Given Mass of Liquid," *Proceedings of the London Mathematical Society*, vol. 19, 1888, pp. 170–207.

7 A. B. Basset, "On the Radial Vibrations of a Cylindrical Elastic Shell," *Proceedings of the London Mathematical Society*, vol. 21, 1889, pp. 53–58.

8 K. Sezawa, "Dilatational and Distortional Waves Generated From a Cylindrical or a Spherical Origin," *Bulletin of the Earthquake Research Institute*, Tokyo University, vol. II, March 1927, p. 13.

9 A. Kromm, "Zur Ausbreitung von Stosswellen in Kreislochscheiben," *Zeitschrift für angewandte Mathematik und Mechanik*, vol. 28, 1948, pp. 104–114, 297–303.

10 H. L. Selberg, "Transient Compression Waves From Spherical and Cylindrical Cavities," *Arkiv för Fysik*, vol. 5, 1952, pp. 97–108.

11 J. Miklowitz, "Plane-Stress Unloading Waves Emanating From a Suddenly Punched Hole in a Stretched Elastic Plate," JOURNAL OF APPLIED MECHANICS, vol. 27, Trans. ASME, vol. 82, Series E, March, 1960, pp. 165–171.

12 A. C. Eringen, "Response of an Elastic Disk of Impact and Moving Loads," *Quarterly Journal of Mechanics and Applied Mathematics*, vol. 8, 1955, pp. 385–393.

13 A. E. H. Love, "A Treatise on the Mathematical Theory of Elasticity," fourth edition, Dover Publications, New York, N. Y., 1944, p. 288.

14 R. D. Mindlin and T. R. Kane, "Response of an Elastic Solid to an Oscillating Pressure Within a Cavity," Technical Report No. 7, CU-8-53-ONR-266(09)-CE, April, 1953.

15 A. C. Eringen, "Elasto-Dynamic Problem Concerning the Spherical Cavity," *Quarterly Journal of Mechanics and Applied Mathematics*, vol. 10, 1957, pp. 257–270.

M. A. MEDICK
Senior Staff Scientist,
Research and Advanced
Development Division,
Avco Corporation,
Wilmington, Mass.

On Classical Plate Theory and Wave Propagation

The purpose of this investigation is to assess the applicability of classical plate theory in describing the response of a flat plate of large radius to a sharp, transient loading applied over a small surface area by evaluating its predictions and comparing them with some preliminary experiments

This paper is concerned with response of a flat plate of large radius to a sharp, transient loading applied over a small surface area; that is, for a given loading time history, the time dependence of the transverse displacement is sought at various points in the plate. The major purpose of the present investigation is to assess the applicability of classical plate theory to this problem by evaluating its predictions and comparing them with some preliminary experiments.

Some analytical studies on the dynamic response of a plate to concentrated and distributed transient loads within the classical theory have already been performed by several investigators [1, 2, 3];[1] however, for the most part, the results have been left in general terms, and little attempt has been made so far to answer the questions of applicability raised in the foregoing.

The use of the classical (or elementary) theory is somewhat anomalous in a wave-propagation problem since it does not yield the expected wave front separating disturbed and undisturbed regions; that is, even in an infinite plate, the classical theory predicts a (spurious) response at all points of the plate immediately after application of a localized loading. Loosely speaking, this is related to the fact that any disturbance may be considered to consist of a superposition of disturbances of various wave lengths, and the classical theory asserts that the velocity of propagation of a component of the disturbance becomes infinite as its wave length approaches zero. On the other hand, the classical theory would be expected to provide reliable results for long wave-length disturbances; i.e., long relative to the plate thickness.[2] It seems plausible that, in actuality, most of the energy transferred to a plate (even by a very sharp impact) would be associated with these longer wave lengths; it will be seen that, consistent with this conjecture, the early, short wave-length high-frequency response given by the classical theory is of very low amplitude. Consequently, hope exists that at any point of the plate not too close to the loading area reliable results might be furnished by the classical theory for times greater than those associated with the passage of the spurious (but insignificant) high-frequency motion.

An improved plate theory that takes into account transverse-shear deformations and rotatory inertia would predict finite propagation velocities of disturbances [5]. However, analytical solutions are not easily obtained on the basis of the improved theory and hence it is not felt worth while to press efforts for extracting such solutions before the predictions of the classical theory are fully assessed and exploited.

The preliminary experimental results [6] used in this paper to compare with theory were obtained from plates subjected to penetration by high-speed projectiles.

Conclusions

According to classical plate theory, a localized transient loading produces an aperiodic, oscillatory transverse displacement at all points of the plate. Experiments indicate that, except for an initial time interval, during which the displacement amplitudes are very small fractions of the maximum response, the quantitative predictions of the classical theory are accurate at points in the plate at least several thicknesses removed from the area of loading. On the basis of both theory and experiment, this critical initial time interval is roughly $2\,(r/c)$, where r is the distance from the center of loading, and c is the characteristic velocity $(E/\rho)^{1/2}$.

Except for times comparable to the duration of loading, the plate response is primarily dependent upon the total impulse transmitted to the plate, and is dependent to only a much lesser degree on the details of the load-time history; this appears to be borne out not only by theoretical studies, but also by the successful correlation of analytical results with those obtained from penetration tests on plates.

Theoretical Plate Response

According to classical plate theory, the small transverse deflection of a thin, homogeneous, isotropic, elastic plate subjected to a concentrated, normal, time-dependent force, $Pf(t)$, at the origin is governed by the equation

$$D\nabla^4 w(r, t) + \rho h\ddot{w}(r, t) = \frac{Pf(t)\delta(r)}{2\pi r}, \qquad (1)$$

where

$$\nabla^4 = \left(\frac{\partial^2}{\partial r^2} + \frac{1}{r}\frac{\partial}{\partial r}\right)^2$$

and $\delta(r)$ is a Dirac delta function. $w(r, t)$ is the transverse displacement of the mid-plane of the plate; ρ is the mass density; and D is the plate bending stiffness; i.e.,

$$D = \frac{Eh^3}{12(1 - \nu^2)},$$

where E is Young's modulus, h is the plate thickness, and ν is

[1] Numbers in brackets designate References at end of paper.

[2] For a more complete discussion of the relationship between the approximate classical theory and three-dimensional elasticity theory, the reader may consult [4].

Presented at the Summer Conference of the Applied Mechanics Division, Chicago, Ill., June 14–16, 1961, of THE AMERICAN SOCIETY OF MECHANICAL ENGINEERS.

Discussion of this paper should be addressed to the Editorial Department, ASME, 29 West 39th Street, New York, N. Y., and will be accepted until July 10, 1961. Discussion received after the closing date will be returned. Manuscript received by ASME Applied Mechanics Division, February 24, 1960. Paper No. 61—APM-3.

Poisson's ratio. The usual dot notation is employed to denote differentiation with respect to time.

Since the response of a plate of arbitrarily large radius is sought, the transverse displacement w must satisfy appropriate finiteness conditions as r approaches infinity as well as at the origin, $r = 0$.

Assuming that the plate is initially undeformed and at rest, the solution of equation (1) under these conditions is easily obtained by means of integral transforms (e.g., see [1], article 20.3). Thus it can be shown that, for $r > 0$, $t > 0$,

$$w(r, t) = \frac{P}{4\pi(\rho h D)^{1/2}} \int_0^t \int_0^\lambda f(\xi) \sin\left(\frac{ar^2}{t-\lambda}\right) \frac{d\lambda}{(t-\lambda)}\, d\xi, \tag{2}$$

where

$$a = \frac{1}{4}\left(\frac{\rho h}{D}\right)^{1/2}$$

The transverse velocities and accelerations can be obtained by formal differentiation.

The classical plate response directly under the applied force is useful in constructing simulations of plates subjected experimentally to localized impulsive loadings. Thus it is easily seen that, for $t > 0$, at the origin:

The *acceleration* is

$$\ddot{w}(0, t) = \frac{P}{8(\rho h D)^{1/2}} \dot{f}(t), \tag{3}$$

the *velocity* is

$$\dot{w}(0, t) = \frac{P}{8(\rho h D)^{1/2}} f(t), \tag{4}$$

and the *displacement* is

$$w(0, t) = \frac{P}{8(\rho h D)^{1/2}} \int_0^t f(\xi)\, d\xi \tag{5}$$

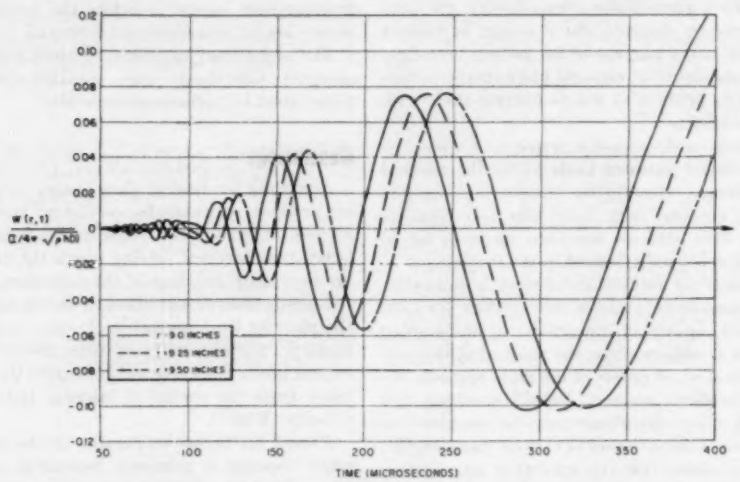

Fig. 1 Spatial variation of nondimensionalized ratio of displacement to applied impulse for a duration of loading of 18 microsec

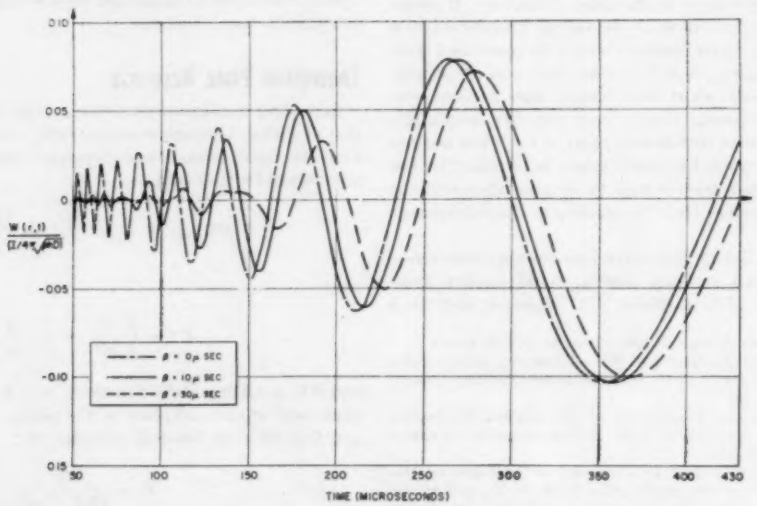

Fig. 2 Time variation of nondimensionalized ratio of displacement to applied impulse for various durations of loading

It should be observed that the displacement, $w(0, t)$, is proportional to the impulse transmitted to the plate.

Furthermore, if the driving-point impedance is defined as

$$I_{dp} = \lim_{r \to 0} 2\pi r \left(\frac{\text{shear force/unit circumferential length}}{\text{transverse velocity of sector of plate}} \right) \quad (6)$$

then

$$I_{dp} = 8(\rho h D)^{1/2} = 4h^2 \left[\frac{\rho E}{3(1 - \nu^2)} \right]^{1/2} \quad (7)$$

Thus the driving-point impedance is a real quantity independent of the time dependence of the applied force [2, 3].

Discussion and Comparison of Theory With Appropriate Experiment

According to the classical plate theory, a localized transient load produces an aperiodic, oscillatory transverse displacement at all points of the plate immediately upon application of the load (for example, see equation (2) for the response due to a concentrated load).

Some curves showing typical theoretical displacement-response patterns are given in Fig. 1. These curves give the displacement of a ¼-in-thick aluminum plate at points 9.0, 9.25, and 9.50 in. from the point of application of a concentrated force of square-wave time dependency, equation (12), with an impulse duration, β, of 18 microsec. The quantity I in the denominator of the expression plotted as ordinate in the figure is equal to the total impulse, $P\beta$, transmitted to the plate. The smooth spatial variation of the response is evident from an inspection of Fig. 1; in particular, the translation in time of the extrema should be noted.

Fig. 2 shows for the same plate and type of loading the effect of varying the duration of loading. The nondimensional displacement-time history at $r = 10$ in. is shown for loading durations, β, of zero, 10, and 30 microsec. The most important implication of this comparison is the relative insensitivity of the large amplitude portion of the response to small variations in the duration of loading for the same impulse.

A curious characteristic of the response at any point in the plate is an anomalous, low-amplitude, precursor pattern (e.g., in Fig. 1 between 95 and 110 microsec at $r = 9.5$ in.) which immediately precedes the establishment of a smooth aperiodic, oscillatory pattern of much larger amplitudes. The location in time of this precursor pattern is quite sensitive to the duration of loading (e.g., in Fig. 2 the pattern appears between 70 and 85 microsec for $\beta = 10$ microsec and between 130 and 150 microsec for $\beta = 30$ microsec) and vanishes as the duration of loading approaches zero.

In order to delineate the limits of usefulness and applicability of the classical theory for the types of loading considered in this paper a preliminary correlation with the experimental results [6], [7] was established. In the particular experiment used in this correlation, flat plates (¼-in-thick 6061-T6 aluminum) were penetrated by high-speed projectiles (55 grain 220-Swift; impact velocity of 4000 fps) and the ensuing time history of the transverse deflection at various points was recorded by means of condenser microphone pickups, Fig. 3. Representative photographs of the oscillograph recording of the output of the condenser microphone pickups showing the characteristic, aperiodic, oscillatory displacement response are given in Fig. 4. Plate dimensions and pickup locations were such that rather long time histories could be obtained without being influenced by the boundaries.

The theoretical simulation of the projectile (¼ in. diam) penetration of the plate with its finite contact time between plate and projectile was taken to be a concentrated normal force with a square-wave time dependency. Effectively, this simulation postulates that, except for times comparable to the duration of loading, the plate response is primarily dependent upon the total impulse, i.e., the area under the force-time curve of the applied force, transmitted to the plate, and is dependent to only a much lesser degree on the details of the force-time history. This conjecture arises in part from the foregoing theoretical discussion in connection with Fig. 2 and is corroborated, as will be seen, by the successful correlation with the experimental response. The total impulse transmitted to the plate was estimated as follows. The loss of momentum suffered by the projectile on the basis of the measurement of its impact and exit velocities was made (see [6] for details of measurement). However, the plate was observed to suffer a loss of mass upon penetration in the form of fragments, and so the momentum imparted to these fragments was estimated by assuming they left the plate with the exit velocity of the projectile. Hence the actual impulse imparted to the plate was estimated by subtracting the fragment momentum from the momentum loss of the projectile. If the impulse-time duration β is arbitrarily set equal to the time necessary for the projectile traveling with its average velocity during penetration to traverse a distance equal to the plate thickness plus projectile length, the magnitude of the impulsive force is then determined since the total impulse is known.

The successful correlation of theory and experiment at various points in the plate is graphically given in Figs. 5 through 7. It can be seen in all cases that, after a small initial time interval during which both theory and experiment show low-amplitude,

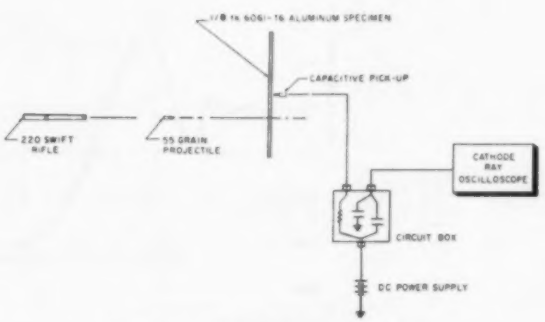

Fig. 3 Experimental layout—top view

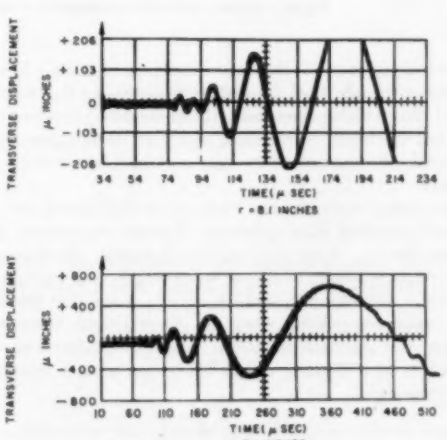

Fig. 4 Experimental displacement time history

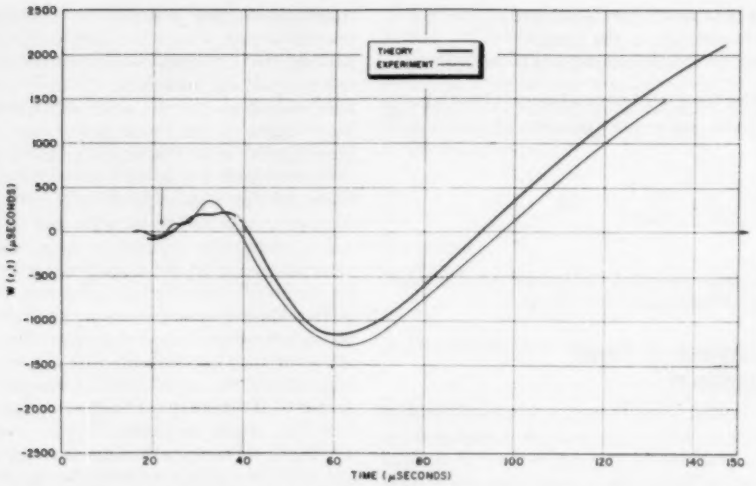

Fig. 5 Displacement time histories; $r = 2.2$ in. NOTE: At left, "μ seconds" should read "μ inches."

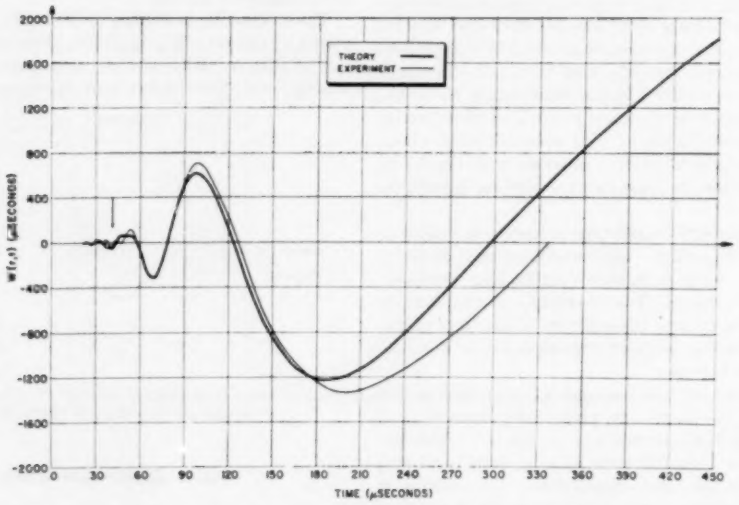

Fig. 6 Displacement time histories; $r = 4.1$ in. NOTE: At left, "μ seconds" should read "μ inches."

high-frequency motion, the agreement is very good. It is quite interesting to note that, immediately preceding this time range of good quantitative agreement, the anomalous precursor pattern predicted by theory corresponds to a very similar precursor pattern obtained esperimentally; e.g., see Fig. 7 between 95 and 120 microsec.

A theoretical estimate can be made of the critical initial time interval preceding good agreement between experiment and the classical theory. Note that, as time increases, the displacement at any point increases in spatial wave length; for example, equation (16). A working hypothesis may be made that the classical theory becomes reliable when the wave length becomes some multiple N of the plate thickness. A rough calculation shows that this occurs at a distance r from the origin after a time interval approximately

$$\bar{\tau} = \frac{N}{8}\left(\frac{r}{c}\right),$$

where c is the characteristic velocity $(E/\rho)^{1/2}$.

The values of $\bar{\tau}$ found on the basis of $N = 16$, shown by the vertical arrows in Figs. 5 through 7, are seen to agree well with the times at which good agreement of theory and experiment begins. The rule

$$\bar{\tau} = 2\left(\frac{r}{c}\right)$$

may therefore be accepted, tentatively, as a good estimate of the critical time.

The quantitative predictions of the classical theory retain their accuracy even for points only several thicknesses removed from the loading area as illustrated in the comparison given in Fig. 5 for the response of the plate at a distance 2.2 in. from the center of loading. It is interesting to note from Figs. 5 through 7 that the experimental displacement *extrema* tend to exceed their theoretical counterparts at points close to the impact area, i.e., at 2.2 and 4.1 in., while they are in turn exceeded by their theoretical counterparts at points further removed; e.g., at 10.1

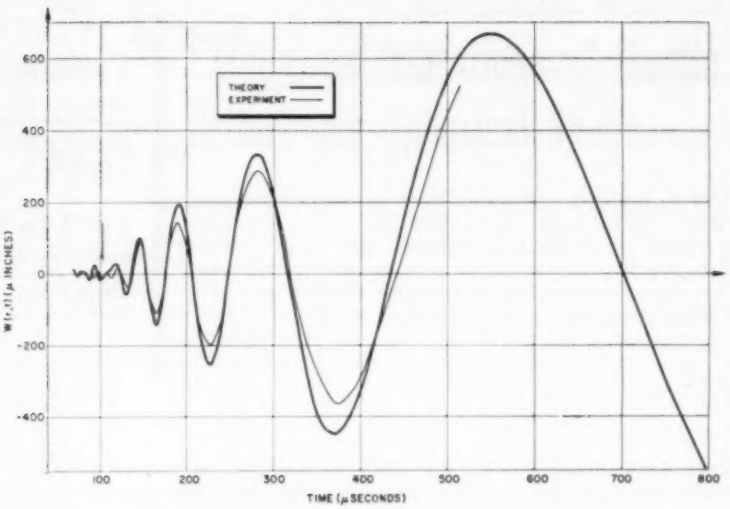

Fig. 7 Displacement time histories; $r = 10.1$ in.

in. Although a direct experimental measurement of the transverse velocity was not made, it appears evident that the transverse velocity-time history predictions of the classical theory will be accurate within limitations similar to those inferred from the displacement correlation.

Acknowledgment

The author wishes to thank Prof. Bernard Budiansky of Harvard University for his advice and suggestions during the course of this investigation.

References

1 I. N. Sneddon, "Fourier Transforms," McGraw-Hill Book Company, Inc., New York, N. Y., 1951.

2 D. A. Thomas, "Characteristic Impedances for Flexure Waves in Thin Plates," *Journal of the Acoustical Society of America*, vol. 30, 1958, p. 220.

3 C. Zener, "Intrinsic Inelasticity of Large Plates," *Physical Review*, vol. 59, 1941, p. 669.

4 R. D. Mindlin, "An Introduction to the Mathematical Theory of Vibrations of Elastic Plates," U. S. Army Signal Corps, Engineering Laboratories Monograph, Fort Monmouth, N. J., 1956.

5 W. E. Jahsman, "Propagation of Abrupt Circular Wave Fronts in Elastic Sheets and Plates," *Proceedings of the 3rd U. S. National Congress of Applied Mechanics*, ASME, June, 1958, pp. 195–202.

6 J. R. Steele and M. A. Medick, "Experimental Investigation of Wave Propagation in Isotropic Elastic Plates," to be published.

7 M. A. Medick, "Wave Propagation in Isotropic Elastic Plates," RAD-TR-9-60-4, Avco Corporation, Wilmington, Mass., January, 1960.

8 C. O. Dohrenwend, D. C. Drucker and P. Moore, "Transverse Transient Impacts," *Proceedings of the Society for Experimental Stress Analysis*, vol. 1, 1944, pp. 1–10.

9 P. E. Duwez, D. S. Clark, D. S. Wood, and D. H. Hyers, "The Behavior of Large Plates Under Impact Loading," National Defense Research Committee, Report No. A-254, OSRD No. 3292, DV.2, 1944.

APPENDIX

Variation of the Response of a Plate to a Concentrated Normal Force With Various Time Dependencies

In the cases that follow, the plate response to a concentrated force of arbitrary time dependence, $f(t)$, will be evaluated for certain explicit forms of $f(t)$. A subscript on w, $\dot{w}$, or $\ddot{w}$ refers to the case designation.

Case 1. Suppose $f(t)$ is a step function in time, i.e.,

$$f(t) = \begin{cases} 1, & t > 0, \\ 0, & t < 0, \end{cases} \tag{8}$$

then for $r > 0$, $t > 0$,
the *acceleration* is

$$\ddot{w}_1(r, t) = \frac{P}{4\pi(\rho h D)^{1/2}} \frac{\sin(ar^2/t)}{t}, \tag{9}$$

the *velocity* is

$$\dot{w}_1(r, t) = \frac{P}{4\pi(\rho h D)^{1/2}} \left[\frac{\pi}{2} - Si\left(\frac{ar^2}{t}\right)\right], \tag{10}$$

and the *displacement* is

$$w_1(r, t) = \frac{P}{4\pi(\rho h D)^{1/2}} tH(ar^2/t), \tag{11}$$

where

$$H(x) = \pi/2 - Si(x) + xCi(x) - \sin(x)^*$$

with

$$Si(x) = \int_0^x \frac{\sin t}{t}\, dt, \quad \text{and} \quad Ci(x) = \int_\infty^x \frac{\cos t}{t}\, dt$$

Case 2. Suppose $f(t)$ has the form

$$f(t) = \begin{cases} 1, & \ldots \quad 0 < t \leq \beta, \\ 0 & \ldots \qquad t > \beta \end{cases} \tag{12}$$

It is clear that the form of the present solution may be immediately deduced from that of case (1). For example,

$$U_2(r, t) = U_1(r, t) - \begin{cases} 0, \ldots & \ldots\ldots\ldots t < \beta, \\ U_1(r, t - \beta) & \ldots\ldots\ldots t > \beta, \end{cases} \tag{13}$$

* In Sneddon's results for similar problems he introduces a function $F(x)$ which corresponds to $H(x)$; however, the definition of $F(x)$ given in reference [1], page 139, equation (120), apparently omits a sine term.

where $U(r, t)$ may represent transverse acceleration, velocity, or displacement.

Case 3. A limiting case of interest is obtained by setting $f(t)$ equal to the unit impulse function $I(t)$. Thus, if the impulsive force is denoted by

$$J \cdot I(t),$$

the total impulse is

$$\int_0^\infty J \cdot I(t)dt = J$$

Hence the *acceleration* is

$$\ddot{w}_3(r, t) = \frac{-J}{4\pi(\rho hD)^{1/2}t^2}\left[\sin\left(\frac{ar^2}{t}\right) + \left(\frac{ar^2}{t}\right)\cos\left(\frac{ar^2}{t}\right)\right], \tag{14}$$

the *velocity* is

$$\dot{w}_3(r, t) = \frac{J}{4\pi(\rho hD)^{1/2}}\frac{\sin\left(\frac{ar^2}{t}\right)}{t}, \tag{15}$$

and the *displacement* is

$$w_3(r, t) = \frac{J}{4\pi(\rho hD)^{1/2}}\left[\frac{\pi}{2} - Si\left(\frac{ar^2}{t}\right)\right]. \tag{16}$$

W. H. HOPPMANN II
Professor,
Department of Mechanics,
Rensselaer Polytechnic Institute,
Troy, N. Y.
Mem. ASME

W. E. BAKER
Ballistic Research Laboratories,
Aberdeen Proving Ground,
Aberdeen, Md.
Mem. ASME

Extensional Vibrations of Elastic Orthotropic Spherical Shells

The extensional vibrations (momentless) of spherical shells of elastic orthotropic material have been studied theoretically. Equations of motion have been derived and solved. The principal directions of the elastic compliances are assumed to be along parallels of latitude and along meridians. In addition to the case of orthotropic shells of uniform thickness, the analysis may be applied in the case of shells with stiffeners attached. Special consideration is given to the isotropic shell as a limiting case of the orthotropic shell.

In the literature there is a paper on the free vibrations of isotropic elastic shells by Love [2].[1] In particular, for the spherical shell, he deduces that the characteristic shapes are associated Legendre polynominals and discusses the frequency equation.

In some modern applications of the theory of shells it is desirable to know the response to dynamic loading. In the present paper a study is made of the vibrations of spherical shells for this purpose. Furthermore, the equations of the isotropic shell are generalized in order to apply them to a shell composed of orthotropic material. This development anticipates the use of the analogy of such shells to those containing orthogonal systems of stiffeners. The problem of the flexure of orthogonally stiffened cylindrical shells has been treated elsewhere [3]. In that paper may be seen the treatment of the analog between uniformly thick shells of orthotropic materials and isotropic shells with uniformly spaced stiffeners. In the present paper the study will be made of shells of uniformly thick orthotropic materials. Of course the solutions for the vibration of orthotropic shells can be specialized readily to the case of isotropic shells which are of considerable value in proposed technological applications. It may be noted that, although stiffeners are primarily used to resist flexure, in the theory of vibration of complete spherical shells it is shown by a theorem of Jellett that the deformation is essentially extensional [1]. The stiffener system, however, is anticipated in the present study because in actual applications it must be assumed that the uniformly thick portion of the shell may at times yield and then it will be necessary to resist flexural loading by means of the stiffener system. Also, statical point loadings on the shell may cause local damage which will be prevented or limited in extent by the stiffeners. Such being the case, there is need to know what the purely extensional reaction to the loading will be when stiffeners are used.

Type of Stiffened Spherical Shell

An easy way to conceive of the shell treated here is to consider a globe with the two usual poles, north and south. One group of stiffeners will correspond to the meridians and the other group will correspond to parallels of latitude. Furthermore it should be assumed that the stiffness is homogeneous over the whole sphere; that is, the stiffness of each stiffener is less near the poles than near the equator. The obvious reason for this requirement is the fact that the stiffeners of the longitudinal system converge at the poles and those of the latitudinal system shrink to a point. In fact, the poles are necessarily small regions of isotropy. This fact was pointed out for anisotropic plates by Carrier [4].

The stiffness is assumed constant through the thickness of the shell but to vary with direction in the tangent plane at any point of the shell surface. The principal directions for stiffness or for the elastic compliances will be along the longitude and along the latitude at any point. The resulting stiffness tensor is homogeneous; i.e., it does not vary from point to point on the spherical surface.

Stiffness is in a sense symmetrical with respect to the diameter through the two poles of the sphere. Furthermore, in the present study it will be assumed that the load will be explosive, isotropic, and initiated at a point along the diameter through the poles. Hence the loading of the shell will be symmetrical with respect to this diameter and we need consider only vibrations symmetrical with respect to it. Accordingly, the equations of motion will be developed for these conditions. While some like Horace Lamb [1] consider that flexure effects in a vibrating complete spherical shell will be negligible, others may entertain some doubt on this point. It is therefore the hope of the authors that investigations may be conducted in the future for the purpose of determining how closely the results of this paper agree with the results from actual vibration experiments. The authors plan in the future to perform some experiments along the lines described in a paper by one of them [3].

Equations of Motion

For the uniformly thick shell of orthotropic material the stress-strain relations are [3]

$$\begin{aligned} \epsilon_\phi &= c_{11}\sigma_\phi + c_{12}\sigma_\theta \\ \epsilon_\theta &= c_{21}\sigma_\phi + c_{22}\sigma_\theta \\ \gamma &= c_{33}\tau \end{aligned} \tag{1}$$

or

$$\sigma_\phi = \frac{c_{22}\epsilon_\phi - c_{12}\epsilon_\theta}{c^*} \tag{2}$$

and

$$\sigma_\theta = \frac{c_{11}\epsilon_\theta - c_{21}\epsilon_\phi}{c^*}$$

[1] Numbers in brackets designate References at end of paper.

Presented at the Summer Conference of the Applied Mechanics Division, Chicago, Ill., June 14–16, 1961, of The American Society of Mechanical Engineers.

Discussion of this paper should be addressed to the Editorial Department, ASME, 29 West 39th Street, New York, N. Y., and will be accepted until July 10, 1961. Discussion received after the closing date will be returned. Manuscript received by ASME Applied Mechanics Division, June 17, 1960. Paper No. 61—APM-14.

where

$$c_{12} = c_{21}$$

and

$$c^* = \begin{vmatrix} c_{11} & c_{12} \\ c_{21} & c_{22} \end{vmatrix} \tag{3}$$

c_{11} corresponds to direction of ϕ-changing, c_{22} corresponds to direction of θ-changing.

If the effective thickness of shell is h_s and N_ϕ, N_θ are the forces per unit length of section corresponding to σ_ϕ, σ_θ then

$$N_\phi = \frac{h_s}{c^*}(c_{22}\epsilon_\phi - c_{12}\epsilon_\theta)$$

and (4)

$$N_\theta = \frac{h_s}{c^*}(c_{11}\epsilon_\theta - c_{21}\epsilon_\phi)$$

Assume that the deformation is momentless; that is, the membrane-type stresses are of major concern. Then if we introduce inertia forces and external loading normal to the surface the equations of motion may be written [5]:

$$\frac{\partial}{\partial\phi}(N_\phi \sin\phi) - N_\theta \cos\phi = \rho a \sin\phi\, h_m \frac{\partial^2 v}{\partial t^2}$$

and

$$N_\phi + N_\theta - ap(\phi, t) = \rho h_m a \frac{\partial^2 w}{\partial t^2} \tag{5}$$

w = radial displacement, positive toward center
v = tangential displacement (tangent to meridian), positive toward north pole
ρh_m = mass per unit area of shell
a = mean radius of the thin shell
$p(\phi, t)$ = load function (symmetric with respect to diameter through north and south poles)

The strains in terms of the displacements may be written [5]:

$$\epsilon_\phi = \frac{1}{a}\frac{dv}{d\phi} - \frac{w}{a}, \quad \epsilon_\theta = \frac{v}{a}\cot\phi - \frac{w}{a} \tag{6}$$

Substituting equation (6) into equation (4) for N_ϕ, N_θ and then substituting the values of N_ϕ, N_θ into equations (5), we obtain the equations of motion in terms of displacements as follows:

$$\frac{\partial^2 v}{\partial\phi^2} + \cot\phi\frac{\partial v}{\partial\phi} + (\alpha - \beta\cot^2\phi) + \gamma\frac{\partial w}{\partial\phi} + \delta\cot\phi w = A\frac{\partial^2 v}{\partial t^2} \tag{7}$$

and

$$\frac{\partial v}{\partial\phi} + \epsilon\cot\phi v + kw = B\frac{\partial^2 w}{\partial t^2} + Cp(\phi, t)$$

where

$$A = \rho\frac{h_m}{h_s}\frac{a^2c^*}{c_{22}}, \quad B = \rho\frac{h_m}{h_s}\frac{a^2c^*}{(c_{22} - c_{21})}, \quad C = \frac{a^2c^*}{h_s(c_{22} - c_{21})}$$

$$\alpha = \frac{c_{12}}{c_{22}}, \quad \beta = \frac{c_{11}}{c_{22}}, \quad \gamma = \frac{c_{12}}{c_{22}} - 1, \quad \delta = \frac{c_{11}}{c_{22}} - 1,$$

$$\epsilon = \frac{c_{11} - c_{12}}{c_{22} - c_{12}}, \quad k = \frac{2c_{12} - c_{11} - c_{22}}{c_{22} - c_{12}}$$

Free Vibrations

In solving the equations of motion (7) for a complete shell it is noted that there are no physical boundary conditions. The conditions to be imposed are that the displacements should be single-valued and bounded at every point of the sphere including the north and south poles.

Assume

$$p(\phi, t) = 0$$

$$v = V_n(\phi)R_n(t)$$

and

$$w = W_n(\phi)R_n(t) \tag{8}$$

we get

$$\ddot{R}_n + P_n^2 R_n = 0 \tag{9}$$

$$\frac{V_n'' + \cot\phi V_n' + (\alpha - \beta\cot^2\phi)V_n + \gamma W_n' + \delta\cot\phi W_n}{AV_n} = -P_n^2 \tag{10}$$

$$\frac{V_n' + \epsilon\cot\phi V_n + KW_n}{BW_n} = -P_n^2 \tag{11}$$

where $'$ means derivative with respect to ϕ.

We may eliminate W_n from equations (10) and (11) and obtain an ordinary differential equation on V_n as follows:

$$V_n'' + \cot\phi V_n' + \alpha_2 V_n \csc^2\phi + \alpha_3 V_n = 0 \tag{12}$$

where

$$\alpha_2 = -\frac{[\beta(K + P_n^2 B) + \epsilon(\delta - \gamma)]}{[K + P_n^2 B - \gamma]}$$

and

$$\alpha_3 = \frac{[(\alpha + P_n^2 A)(K + P_n^2 B) + \beta(K + P_n^2 B) + \delta\epsilon]}{[K + P_n^2 B - \gamma]}$$

if we put $x = \cos\phi$.

Then we obtain

$$(1 - x^2)\frac{d^2V_n}{dx^2} - 2x\frac{dV_n}{dx} + V_n\left(\alpha_3 + \frac{\alpha_2}{1 - x^2}\right) = 0 \tag{13}$$

The criterion to be applied here is that the solution should be bounded at all points of the sphere including the two poles. The only solutions which are bounded everywhere, including the points $x = \pm 1$, are:

$$V_n = (1 - x^2)^{\lambda/2}\zeta_n \tag{14}$$

where ζ_n are the Gegenbauer polynomials C_n^α given by Whittaker and Watson [6].

Transforming the differential equation (13) by equation (14) we get

$$(1 - x^2)\frac{d^2\zeta_n}{dx^2} - 2(1 + \lambda)x\frac{d\zeta_n}{dx} + \left[(\alpha_3 - \lambda) + \frac{\alpha_2 + \lambda^2 x^2}{1 - x^2}\right]\zeta_n = 0 \tag{15}$$

To remove the singularity at $x = \pm 1$ from the bracket term we put

$$\lambda^2 = -\alpha_2 \tag{16}$$

α_2 is essentially negative, so that we obtain:

$$(1 - x^2)\frac{d^2\zeta_n}{dx^2} - 2(1 + \lambda)x\frac{d\zeta_n}{dx} + [\alpha_3 - \lambda + \alpha_2]\zeta_n = 0 \tag{17}$$

The bounded solutions of this equation are the Gegenbauer polynomials [6]

$$\zeta_n = C_n^{\mu}(x) = \frac{(-2)^n\mu(\mu + 1)\ldots(\mu + n - 1)(1 - x^2)^{1/2-\mu}}{n!(2n + 2\mu - 1)(2n + 2\mu - 2)\ldots(n + 2\mu)} \frac{d^n[(1 - x^2)^{n+\mu-1/2}]}{dx^n} \tag{18}$$

The exact form of the D.E., of which (18) is the solution, is

$$(1 - x^2)\frac{d^2\zeta_n}{dx^2} - (2\mu + 1)x\frac{d\zeta_n}{dx} + n(n + 2\mu)\zeta_n = 0 \tag{19}$$

Comparing corresponding terms in equation (17) and equation (19) we have

$$2(1 + \lambda) = (2\mu + 1) \quad \text{or} \quad \mu = \lambda + \tfrac{1}{2}$$

and

$$\alpha_3 - \lambda + \alpha_2 = n(n + 2\mu)$$

From equation (16)

$$\lambda = \pm i\cdot(\alpha_2)^{1/2}$$

so

$$\alpha_3 \mp i(\alpha_2)^{1/2} + \alpha_2 = n^2 + 2n(\lambda + \tfrac{1}{2}) = n^2 + 2n(\pm i\cdot(\alpha_2)^{1/2} + \tfrac{1}{2}) \tag{19a}$$

Then a solution is

$$V_n = (1 - x^2)^{\lambda/2}C_n^{\lambda+1/2} \tag{20}$$

The corresponding W_n is determined by equation (11). It is

$$W_n = \frac{V_n' + \epsilon\cot\phi V_n}{-(P_n^2B + K)}$$

Consequently, for any integral value of n we have a pair of functions V_n, W_n satisfying the differential equations (10), (11).

Frequency Equation

The terms α_2, α_3 in equation (12) may be written

$$\alpha_2 = -\frac{\beta(1 - \alpha)(K + P_n^2B) + (\beta - \alpha)^2}{(1 - \alpha)(K + P_n^2B) + (1 - \alpha)^2} \tag{21}$$

and

$$\alpha_3 = \frac{(\alpha + \beta)(K + P_n^2B) + \dfrac{(\beta - 1)(\beta - \alpha)}{(1 - \alpha)} - (\alpha - 1)P_n^2B(K + P_n^2B)}{(K + P_n^2B) - (\alpha - 1)} \tag{22}$$

Now for integral values of n, equation (19a) gives the required relation between α_2 and α_3.

For any given orthotropic shell the constants α, β, K, and B are known and P_n^2 is the square of the circular frequency.

The frequency equation is immediately obtained by substituting the values of α_2, α_3 from equation (21) and equation (22) into equation (19a).

The equations may be written somewhat more conveniently for the actual calculation of frequencies.

We may write

$$\alpha_3 = \frac{C_1Q_n^2 + C_2Q_n + C_3}{Q_n + C_4} \tag{23}$$

where $Q_n = P_n^2B$ and C_i are constants in accord with equation (21) and

$$\alpha_2 = \frac{C_5Q_n + C_6}{C_7Q_n + C_8} \tag{24}$$

Solve equation (24) for Q and we have

$$Q_n = -\frac{C_8\alpha_2 - C_6}{C_7\alpha_2 - C_5} = Q_n' \text{ say} \tag{25}$$

Then from equation (23)

$$Q_n = \frac{(\alpha_3 - C_2) \pm [(C_2 - \alpha_3)^2 - 4C_1(C_3 - C_4\alpha_3)]^{1/2}}{2C_1} \tag{26}$$

Now obviously Q_n' must equal Q_n for the required simultaneous solution of equations (23) and (24).

The procedure just outlined obviously amounts to the determination of the roots of a biquadratic equation. We may express equation (19a) in terms of the parameter λ as follows:

$$\alpha_3 = \lambda^2 + n^2 + n + \lambda(2n + 1) \tag{27}$$

Inspection of (21) shows that α_2 is always negative for real frequencies, hence λ is always a positive real number.

Also, equation (25) is a fixed curve for Q as a function of α_3, since the C are constants. This equation in terms of λ may be written

$$Q_n = \frac{C_8\lambda^2 + C_6}{C_7\lambda^2 + C_5} \tag{28}$$

Now for a given integral value of n we must choose that value of λ which with the corresponding α_3 determines the intersection of curve (28) with the curves given by (26). In this manner the frequencies of vibration are readily determined. It may be noted that frequencies of vibration for the isotropic shell as a special case of the anisotropic shell may be determined readily with the aid of equations (25), (26), and (27), using the proper elastic constants. Calculated frequencies for the anisotropic shell using elastic constants previously determined [3] are shown in Table 1. The constants are

$C_{11} = 1.4 \times 10^{-6}h_s$, $C_{22} = 0.83 \times 10^{-6}h_s$, $C_{12} = -0.21 \times 10^{-6}h_s$.

The values of λ which determine the corresponding displacement functions are also shown. It may be noted that there are two main sets of frequencies but one set corresponds to negative values of λ, which give displacements unbounded at the positions $x = \pm 1$. These solutions are then discarded. Also, for positive values of λ there is an infinite set of frequencies which become indefinitely large with λ increasing. In addition, there are several values of frequencies in a second set which in the case of isotropic shells become an infinite bounded set. The frequencies for an isotropic shell of Poisson's ratio equal one third are shown in Table 4. The frequencies for several cases of anisotropy are shown in Tables 1, 2, and 3. The data on which the tables are based are as follows: The radius of each shell is 15 in. and the average thickness is 0.1 in. For purposes of calculation, the mass per unit area of the orthotropic shell is based on aluminum.

Table 1 Natural frequencies of vibration and other parameters for Case I

	Unbounded set				Bounded set			
n	Q'	$p_n' \times 10^{-4}$	$f_n' \times 10^{-3}$ cps	λ'	Q''	$p_n'' \times 10^{-4}$	$f_n'' \times 10^{-3}$ cps	λ''
0	3.77	2.52	4.01	1.43	0	0	0	1
1	6.86	3.39	5.39	1.36	0.58	0.987	1.57	0.66
2	11.83	4.46	7.10	1.32	0.7677	1.143	1.82	0
3	18.56	5.60	8.91	1.32				
4	26.80	6.73	10.71	1.312				
5	36.84	7.88	12.54	1.308				
6	48.50	9.04	14.38	1.305				
7	61.75	10.22	16.25	1.304				
8	76.61	11.37	18.09	1.304				
9	93.00	12.52	19.90	1.302				
10	111.04	13.70	21.80	1.301				

Table 2 Natural frequencies of vibration and other parameters for Case II

	Unbounded set				Bounded set			
n	Q'	$p_n' \times 10^{-4}$	$f_n' \times 10^{-3}$ cps	λ'	Q''	$p_n'' \times 10^{-4}$	$f_n'' \times 10^{-3}$ cps	λ''
0	3.4	2.56	4.07	1.217	0.00157	0	0	1.00
1	5.7	3.32	5.27	1.187	0.480	0.962	1.532	0.836
2	11.0	4.61	7.32	1.170	0.720	1.178	1.875	0.40
3	17.9	5.87	9.37	1.164				
4	26.2	7.04	11.20	1.161				
5	36.2	8.35	13.30	1.161				
6	47.8	9.61	15.27	1.159				
7	61.0	10.84	17.25	1.158				
8	75.8	12.09	19.23	1.158				
9	92.2	13.32	21.20	1.157				
10	110.5	14.60	23.22	1.157				

Table 3 Natural frequencies of vibration and other parameters for Case III

	Unbounded set				Bounded set			
n	Q'	$p_n' \times 10^{-4}$	$f_n' \times 10^{-3}$ cps	λ'	Q''	$p_n'' \times 10^{-4}$	$f_n'' \times 10^{-3}$ cps	λ''
0	3.10	2.78	4.43	1.070	0.00	0	0	1.00
1	5.82	3.81	6.06	1.060	0.382	0.979	1.558	0.92
2	10.10	5.03	8.00	1.057	0.540	1.164	1.854	0.79
3	16.40	6.41	10.18	1.054	0.620	1.247	1.985	0.61
4	24.00	7.75	12.32	1.054	0.660	1.287	2.050	0.40
5	31.25	8.84	14.05	1.053				
6	43.90	10.48	16.68	1.053				
7	56.10	11.83	18.85	1.052				
8	69.80	13.22	21.02	1.052				
9	85.00	14.57	23.20	1.052				
10	101.50	15.93	25.36	1.051				

Table 4 Natural frequencies of vibration and other parameters for Case IV (isotropic)

	Unbounded set				Bounded set			
n	Q'	$p_n' \times 10^{-4}$	$f_n' \times 10^{-3}$ cps	λ'	Q''	$p_n'' \times 10^{-4}$	$f_n'' \times 10^{-3}$ cps	λ''
0	3.00	2.86	4.55	1	0	0	0	1
1	5.65	3.92	6.24	1	0.354	0.982	1.560	1
2	10.00	5.23	8.33	1	0.498	1.165	1.852	1
3	15.90	6.58	10.48	1	0.577	1.253	2.000	1
4	23.40	8.21	13.06	1	0.600	1.278	2.030	1
5	32.35	9.39	14.94	1	0.619	1.300	2.067	1
6	42.80	10.80	17.20	1	0.632	1.312	2.085	1
7	54.80	12.23	19.47	1	0.637	1.318	2.097	1
8	68.30	13.64	21.70	1	0.645	1.325	2.106	1
9	83.30	15.07	23.95	1	0.648	1.330	2.115	1
10	99.90	16.49	26.22	1	0.652	1.333	2.120	1

The isotropic shell is considered to be steel of the same diameter and thickness. The density of aluminum is taken to be

$$\rho = 0.0945 \text{ lb per in.}^3$$

and

$$B = \rho \frac{h_m}{hs} a^2 \frac{C^*}{C_{22} - C_{12}}$$

Case I

$C_{11} = 1.4 \times 10^{-6} h_s$, $C_{22} = 0.83 \times 10^{-6} h_s$, $C_{12} = -0.21 \times 10^{-6} h_s$, reference [3]

$B = 5.93 \times 10^{-9}$ sec^2

Case II

$C_{11} = 1.2 \times 10^{-6} h_s$, $C_{22} = 0.90 \times 10^{-6} h_s$,

$C_{12} = -0.21 \times 10^{-6} h_s$, $B = 5.18 \times 10^{-9}$ sec^2

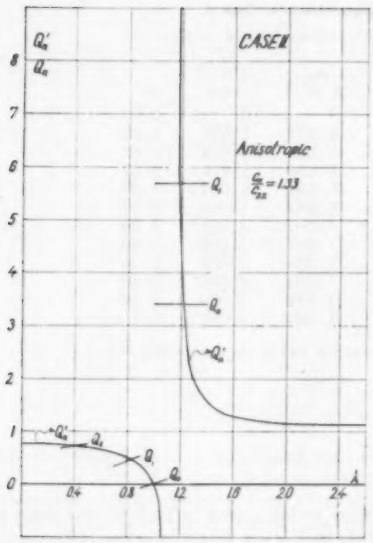

Fig 1

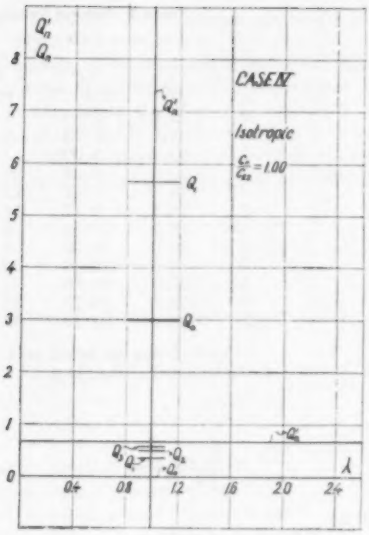

Fig. 2

Case III

$C_{11} = 1.05 \times 10^{-6}h_s$, $C_{22} = 0.95 \times 10^{-6}h_s$, $C_{12} = -0.3 \times 10^{-6}h_s$,

$B = 3.997 \times 10^{-9}$ sec^2

Case IV

$C_{11} = C_{22} = 0.33 \times 10^{-6}h$, $C_{12} = -0.11 \times 10^{-6}h$

ν = Poisson's ratio = 0.33

$B = 3.66 \times 10^{-9}$ sec^2

The density of the steel is taken as

$$\rho = 0.2836 \text{ lb per in.}^3$$

Case V

$C_{11} = 0.95 \times 10^{-6}h_s$, $C_{22} = 1.05 \times 10^{-6}h_s$, $C_{12} = -0.21 \times 10^{-6}h_s$

$B = 4.165 \times 10^{-9}$ sec^2

The second set of frequencies, which are shown in the tables with double primes and called the bounded set, may raise a question as to their physical interpretation. The question has already been answered by Lamb [1] where he points out that for a given increasing positive radial displacement in any one mode the tangential displacement may be increasing in either the positive or the negative direction. The finite number of frequencies occurring in this set for the orthotropic shell corresponds to inadmissible displacement functions as explained subsequently. One reason for calculating the frequencies for the four tables was to show definitely that as the anisotropy approached isotropy the number of frequencies in the bounded set increased in number.

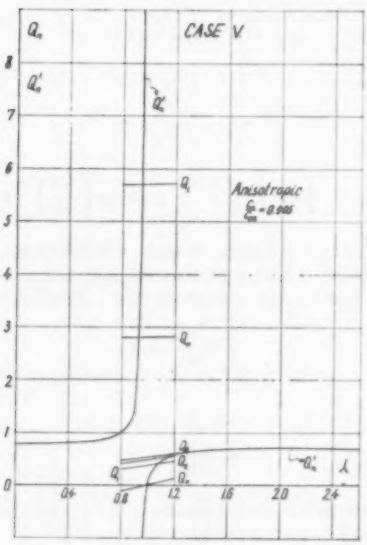

Fig. 3

Pure Radial Vibration

It is clear that for the isotropic shell a pure radial vibration is possible. In that case $v = 0$ and $w = Cf(t)$. Now consider vibrations for the anisotropic shell in which v is assumed to be zero; that is

$$v = 0$$

Using this assumption in equations (7) we find that

$$\gamma \frac{\partial w}{\partial \phi} + \delta \cot \phi w = 0$$

and

$$kw = B \frac{\partial^2 w}{\partial t^2} + Cp(\phi, t) \tag{29}$$

For free vibrations we may take $p = 0$. Now for the first of equations (29) we may write a solution in the form

$$w = w_1(\phi)T(t)$$

So

$$\gamma w_1' + \delta \cot \phi w_1 = 0$$

or

Table 5 Natural frequencies of vibration and other parameters for Case V

	Unbounded set				Bounded set			
n	Q'	$p_n' \times 10^{-4}$	$f_n' \times 10^{-3}$ cps	λ'[a]	Q''	$p_n'' \times 10^{-4}$	$f_n'' \times 10^{-3}$ cps	λ''
0	2.8	2.59	4.13	0.9335	0	0	0	1.0
1	5.7	3.70	5.89	0.9444	0.420	1.003	1.595	1.08
2	10.4	5.00	7.96	0.9470	0.567	1.166	1.854	1.14
3	17.0	6.38	10.15	0.9490	0.626	1.226	1.950	1.27
4	25.2	7.77	12.35	0.9497	0.668	1.226	2.014	1.50
5	35.1	9.17	14.60	0.9500	0.700	1.295	2.060	2.10
6	46.7	10.58	16.84	0.9501	0.700	1.295	2.060	2.20
7	60.0	11.99	19.08	0.9503	0.700	1.295	2.060	2.20
8	74.3	13.34	20.23	0.9506	0.700	1.295	2.060	2.20
9	91.4	14.80	23.54	0.9510	0.700	1.295	2.060	2.20
10	109.8	16.23	25.83	0.9512	0.700	1.295	2.060	2.20
20	460.0	33.16	52.70	0.9515	0.705	1.300	2.067	2.6

[a] The λ of this set being each less than unity, the corresponding radial displacements W_n are unbounded at the poles.

$$\frac{dw_1}{w_1} + \frac{\delta}{\gamma} \cot \phi d\phi = 0$$

The solution is:

$$w_1 = C_1(1 - x^2)^{-(\delta/2\gamma)}$$

and

$$w = C_1(1 - x^2)^{-(\delta/2\gamma)}T(t) \tag{30}$$

From

$$\ddot{T} - \frac{k}{B} T = 0$$

$$T = A \sin \left(\frac{-k}{B}\right)^{1/2} t + B \cos \left(\frac{-k}{B}\right)^{1/2} t \tag{31}$$

k is negative and B is positive so that $(-k/B)^{1/2}$ is real.

Now obviously if $\delta/2\gamma$ is positive the deflection at both poles is unbounded and a solution does not exist. Recalling that

$$\gamma = \frac{C_{12}}{C_{22}} - 1$$

and

$$\delta = \frac{C_{11}}{C_{22}} - 1$$

C_{12} is negative so γ is always negative; if $C_{11} > C_{22}$ the quantity δ is positive and we have a bounded solution and

$$w = 0 \text{ at } x = \pm 1$$

It appears then that for such a vibration the poles are fixed in space.

To obtain the forced vibrations we have

$$kw = B \frac{\partial^2 w}{\partial t^2} + CP(\phi)f(t) \tag{32}$$

Using separation of variables and assuming

$$P(\phi) = P_0(1 - x^2)^{-(\delta/2\gamma)} \tag{33}$$

where P_0 is a constant we get

$$kC_1(1 - x^2)^{-(\delta/2\gamma)}T = BC_1(1 - x^2)^{-(\delta/2\gamma)}\ddot{T} + CP_0(1 - x^2)^{-(\delta/2\gamma)}f(t)$$

or

$$\ddot{T} - \frac{k}{B} T = -\frac{C}{C_1} P_0 f(t)$$

This can readily be integrated by Laplace transform method for any $f(t)$. If the shell is not loaded as assumed it cannot vibrate in the shape

$$w_1 = C_1(1 - x^2)^{-(\delta/2\gamma)}$$

If the shell is isotropic $\delta = 0$ and

$$w_1 = C_1$$

$$w = C_1T(t)$$

If the orthotropic shell is not loaded as indicated by equation (33) then vibrations in other modal shapes will be excited. Also in that case

$$v \neq 0$$

It should be noted that this solution of the differential equations of motion is not contained among the solutions given by equations (20).

Initial Value Problems

Now that the differential equations of motion have been solved for free vibrations, we can in the usual manner solve any initial value problem in which the displacements and velocities are specified at time $t = 0$.

Any linear combinations of v_n and the corresponding linear combination of w_n are solutions of equations (10) and (11). Recalling that there are two sets of frequencies and related displacement functions we can write in general for v and w the following which are obviously solutions:

$$v = \sum v_{n1}[A_n \sin p_n't + B_n \cos p_n't] + v_{n2}[D_n \sin p_n''t + E_n \cos p_n''t]$$

and

$$w = (1 - x^2)^{-(\delta/2\gamma)} \left[F \sin \left(\frac{-k}{B}\right)^{1/2} t + G \cos \left(\frac{-k}{B}\right)^{1/2} t\right] + \sum w_{n1}[A_n \sin p_n't + B_n \cos p_n't] + w_{n2}[D_n \sin p_n''t + E_n \cos p_n''t] \tag{34}$$

where

$$v_n = (1 - x^2)^{\lambda/2}C_n^{\lambda+1/2}$$

and

$$w_n = \frac{v_n' + \epsilon \cot \phi v_n}{-(p_n^2 B + k)} = \frac{-(1 - x^2)^{1/2} \dfrac{dv_n}{dx} + \dfrac{\epsilon x}{(1 - x^2)^{1/2}} v_n}{-(p_n^2 B + k)}$$

So

$$v_{n1} = (1 - x^2)^{\lambda'/2} C_n^{\lambda' + 1/2}$$

$$w_{n1} = \frac{-(1 - x^2)^{1/2} \dfrac{dv_{n1}}{dx} + \dfrac{\epsilon x}{(1 - x^2)^{1/2}} v_{n1}}{-(p_n^2 B + k)}$$

and

$$V_{n2} = (1 - x^2)^{\lambda''/2} C_n^{\lambda'' + 1/2}$$

$$w_{n2} = \frac{-(1 - x^2) \dfrac{dv_{n2}}{dx} + \dfrac{\epsilon x}{(1 - x^2)^{1/2}} v_{n2}}{-(p_n^2 B + k)}$$

The λ and p_n' are calculated as shown under section in "Frequency Equations." Values of these parameters for an isotropic case and for four orthotropic cases are given in Tables 1 to 5, inclusive.

For each coefficient, say A_n in the function v, there is a corresponding one in the function w. Consequently, combinations like $A_n v_{n1} \sin p_n' t$ and $A_n w_{n1} \sin p_n' t$ will then satisfy the differential equations.

The C_n^μ functions which determine v_n are given for the first ten integers in Table 6. The coefficients used in these functions are given in Table 7. These tables therefore provide explicitly, the displacement functions for the first ten modes of vibration of the sphere.

The leading term in the function w outside of the summation sign is the portion of the solution for so-called pure radial vibration. Its corresponding function v is identically zero. This term is included only if $\delta > 0$; otherwise $F = G = 0$.

Now any initial conditions may be specified. At time $t = 0$ let the displacements and velocities be given as follows:

$$v = v^*, \quad w = w^*, \quad \dot{v} = \dot{v}^*, \quad \text{and} \quad \dot{w} = \dot{w}^*$$

so that at $t = 0$ we obtain

Table 6 Gegenbauer polynomials $C_n^\mu(x)$

n	$C_n^\mu(x)$	C_n^μ
0	C_0^μ	$= k_0(a_{00})$
1	$C_1^\mu(x)$	$= k_1(a_{11}x)$
2	C_2^μ	$= k_2(a_{02} + a_{22}x^2)$
3	C_3^μ	$= k_3(a_{13}x + a_{33}x^3)$
4	C_4^μ	$= k_4(a_{04} + a_{24}x^2 + a_{44}x^4)$
5	C_5^μ	$= k_5(a_{15}x + a_{35}x^3 + a_{55}x^5)$
6	C_6^μ	$= k_6(a_{06} + a_{26}x^2 + a_{46}x^4 + a_{66}x^6)$
7	C_7^μ	$= k_7(a_{17}x + a_{37}x^3 + a_{57}x^5 + a_{77}x^7)$
8	C_8^μ	$= k_8(a_{08} + a_{28}x^2 + a_{48}x^4 + a_{68}x^6 + a_{88}x^8)$
9	C_9^μ	$= k_9(a_{19}x + a_{39}x^3 + a_{59}x^5 + a_{79}x^7 + a_{99}x^9)$
10	C_{10}^μ	$= k_{10}(a_{0,10} + a_{2,10}x^2 + a_{4,10}x^4 + a_{6,10}x^6 + a_{8,10}x^8 + a_{10,10}x^{10})$

Constants k_i and a_{ij} are given in Table 7.

Table 7

n	k_i	a_{ij}
0	$k_0 = 1$	$a_{00} = 1$
1	$k_1 = 1$	$a_{11} = 2\mu$
2	$k_2 = 1$	$a_{02} = -\mu$, $a_{22} = 2\mu(\mu + 1)$
3	$k_3 = \dfrac{2\mu(\mu + 1)}{3}$	$a_{13} = -3$, $a_{33} = 2(\mu + 2)$
4	$k_4 = \dfrac{\mu(\mu + 1)}{6}$	$a_{04} = 3$, $a_{24} = -12(\mu + 2)$, $a_{44} = 4(\mu^2 + 5\mu + 6)$
5	$k_5 = \dfrac{\mu(\mu + 1)(\mu + 2)}{15}$	$a_{15} = 15$, $a_{35} = -20(\mu + 3)$, $a_{55} = 4(\mu^2 + 7\mu + 12)$
6	$k_6 = \dfrac{\mu(\mu + 1)(\mu + 2)}{90}$	$a_{06} = -15$, $a_{26} = 90(\mu + 3)$, $a_{46} = -60(\mu^2 + 7\mu + 12)$
		$a_{66} = 8(\mu^3 + 12\mu^2 + 47\mu + 60)$
7	$k_7 = \dfrac{\mu(\mu + 1)(\mu + 2)(\mu + 3)}{315}$	$a_{17} = -105$, $a_{37} = 210(\mu + 4)$, $a_{57} = -84(\mu^2 + 9\mu + 20)$
		$a_{77} = 8(\mu^3 + 15\mu^2 + 74\mu + 120)$
8	$k_8 = \dfrac{\mu(\mu + 1)(\mu + 2)(\mu + 3)}{2520}$	$a_{08} = 105$, $a_{28} = -840(\mu + 4)$, $a_{48} = 840(\mu^2 + 9\mu + 20)$
		$a_{68} = -224(\mu^3 + 15\mu^2 + 74\mu + 120)$, $a_{88} = 16(\mu^4 + 22\mu^3 + 179\mu^2 + 638\mu + 840)$
9	$k_9 = \dfrac{\mu(\mu + 1)(\mu + 2)(\mu + 3)(\mu + 4)}{11340}$	$a_{19} = 945$, $a_{39} = -2520(\mu + 5)$, $a_{59} = 1512(\mu^2 + 11\mu + 30)$
		$a_{79} = -288(\mu^3 + 18\mu^2 + 107\mu + 210)$
		$a_{99} = 16(\mu^4 + 26\mu^3 + 251\mu^2 + 1066\mu + 1680)$
10	$k_{10} = \dfrac{\mu(\mu + 1)(\mu + 2)(\mu + 3)(\mu + 4)}{113400}$	$a_{0,10} = -945$, $a_{2,10} = 9450(\mu + 5)$, $a_{4,10} = -12{,}600(\mu^2 + 11\mu + 30)$
		$a_{6,10} = 5040(\mu^3 + 18\mu^2 + 107\mu + 210)$
		$a_{8,10} = -720(\mu^4 + 26\mu^3 + 251\mu^2 + 1066\mu + 1680)$
		$a_{10,10} = 32(\mu^5 + 35\mu^4 + 485\mu^3 + 3325\mu^2 + 11{,}274\mu + 15{,}120)$

$$v^* = \sum v_{n1}B_n + v_{n2}E_n$$

$$w^* = G(1 - x^2)^{-k/2\gamma} + \sum w_{n1}B_n + w_{n2}E_n$$

$$\phi^* = \sum p_n' v_{n1}A_n + p_n'' v_{n2}D_n$$

and

$$\psi^* = \left(\frac{-k}{B}\right)^{1/2} F(1 - x^2)^{-k/2\gamma} + \sum p_n' w_{n1}A_n + p_n'' w_{n2}D_n$$

where

$$v_{n1} = (1 - x^2)^{\lambda'/2}C_n^{\lambda'+1/2}$$

$$v_{n2} = (1 - x^2)^{\lambda''/2}C_n^{\lambda''+1/2}$$

$$w_{n1} = -\frac{1}{k + Bp_n'^2}(v_{n1}' + \epsilon \cot \phi v_{n1})$$

and

$$w_{n2} = -\frac{1}{k + Bp_n''^2}(v_{n2}' + \epsilon \cot \phi\, v_{n2})$$

A case of especial interest is that in which the original displacements are specified and the velocities are zero. Then

$$\phi^* = 0 \quad \text{so} \quad A_n = D_n = 0$$

but then

$$w^* = \left(\frac{-k}{B}\right)^{1/2} F(1 - x^2)^{-(k/2\gamma)}$$

Consequently, for this case

$$F = 0$$

Functions describing the several cases of elastic compliances are as follows:

Isotropic case:

$$C_{11} = C_{22}$$

$$v_{n1} = v_{n2} = v_n = (1 - x^2)^{1/2}C_n^{1/2}$$

$$w_{n1} = \frac{-(1 - x^2)^{1/2}\dfrac{dv_n}{dx} + x(1 - x^2)^{-1/2}v_n}{-(p_n'^2B + k)}$$

and

$$w_{n2} = \frac{-(1 - x^2)^{1/2}\dfrac{dv_n}{dx} + x(1 - x^2)^{-1/2}v_n}{-(p_n''^2B + k)}$$

For this case then, in which the material of the shell is isotropic there are two distinct sets of frequencies p_n', p_n'' as shown for example in Table 4.

Finally

$$v^* = \sum v_n(B_n + E_n)$$

$$w^* = G + \sum w_{n1}B_n + w_{n2}E_n$$

Orthotropic case: $C_{11} > C_{22}\,\lambda'' \leq 1$ (Tables 1, 2, and 3) and causes corresponding functions to be unbounded at the poles so that there is only one set of allowable frequencies, namely, P_n'.

For this case we must then choose $E_n = 0$ and the constants for the solution are given by

$$v^* = \sum B_n v_{n1}$$

and

$$w^* = G(1 - x^2)^{-k/2\gamma} \sum B_n w_{n1}$$

The B_n are determined in the usual fashion as follows:

$$\int_{-1}^{1} v^* v_{m1}dx = \sum \int_{-1}^{1} B_n v_{n1}v_{m1}dx$$

It is quite clear that both v^* and w^* cannot be specified as purely arbitrary functions. This fact is obvious from the differential equations themselves which show that if v_n is specified the corresponding w_n is determined.

Orthotropic case: $C_{22} > C_{11}\,\lambda' < 0$ (Table 5) and causes corresponding functions to be unbounded at the poles so that there is only one set of allowable frequencies; namely, p_n''.

For this case we must choose $B_n = 0$ and the constants for the solutions are given by

$$v^* = \sum E_n v_{n2}$$

and

$$w^* = \sum E_n w_{n2}$$

The E_n are determined in the usual fashion as follows:

$$\int_{-1}^{1} v^* v_{m2}dx = \sum \int_{-1}^{1} E_n v_n v_{m2}dx$$

Forced Vibrations

There are various kinds of loading functions which may be considered. For the purpose of dealing with blast or explosive loadings we may represent the functions as follows:

$$p(\phi, t) = F(\phi)f(t)$$

The function $f(t)$ may be expressed in a trigonometric series to represent any reasonable function on some time interval of duration T_0.

In problems involving the type of loading now under consideration rest initial conditions are assumed; that is both displacement and velocity at each point are zero at time $t = 0$. The loading function now may be written

$$p(\phi, t) = F(\phi) \sum B_m \sin \frac{m\pi t}{T_0} \tag{35}$$

where m is an integer and the B_m can be calculated by the Fourier method for any time interval of duration T_0.

The solution of equations (7) must now consist of two parts for each displacement component v or w. To the solution of the homogeneous equation ($p \equiv 0$) must be added particular integrals. This can be accomplished readily if $F(\phi)$ in equation (35) is developed in a series of space functions of the type which correspond to the solutions w_n of the homogeneous differential equations.

The complete solution can then be written as follows:

$$v = \sum [v_{n1}[A_n \sin p_n't + B_n \cos p_n't] + v_{n2}[D_n \sin p_n''t + E_n \cos p_n''t]\} + v_{P1} \tag{36}$$

and

$$w = (1 - x^2)^{-k/2\gamma}\left[F \sin \left(\frac{-k}{B}\right)^{1/2} t + G \cos \left(\frac{-k}{B}\right)^{1/2} T\right]$$

$$+ \sum \{w_{n1}[A_n \sin p_n't + B_n \cos p_n't] + w_{n2}[D_n \sin p_n''t + E_n \cos p_n''t]\} + w_{PI} \quad (37)$$

where v_{PI} and w_{PI} are particular integrals satisfying the nonhomogeneous differential equations and for which v and w satisfy the initial conditions which for our problem are assumed to be rest conditions.

Acknowledgment

The authors wish to express appreciation for the sponsorship of the Office of Army Ordnance, under contract No. DA-30-115-509-ORD-912. Also, they wish to express their thanks to Mr. E. R. Krueger and Mr. Leslie E. Pénzes, graduate students of R. P. I., for their assistance with the solutions and calculations in this report.

References

1 Horace Lamb, "On the Vibrations of a Spherical Shell," *London Mathematical Society Proceedings*, vol. 14, 1883, p. 51, 56.

2 A. E. H. Love, "The Small Vibrations and Deformations of a Thin Elastic Shell," *Philosophical Transactions of The Royal Society*, vol. 179, 1888, p. 527.

3 W. H. Hoppmann, II, "Some Characteristics of the Flexural Vibrations of Orthogonally Stiffened Cylindrical Shells," *Journal of the Acoustical Society of America*, vol. 30, 1958, pp. 77–82.

4 G. Carrier, "The Bending of the Cylindrically Aeolotropic Plate," JOURNAL OF APPLIED MECHANICS, vol. 11, TRANS. ASME, vol. 66, 1944, p. A-129.

5 S. Timoshenko and S. Woinowsky-Krieger, "Theory of Plates and Shells," McGraw-Hill Book Company, Inc., New York, N. Y., second edition, 1959, p. 434, 446.

6 E. T. Whittaker and G. N. Watson, "Modern Analysis," Cambridge Press, Cambridge, England, third edition, 1920, p. 329.

NOBORU YAMAKI
Assistant Professor,
Institute of High Speed Mechanics,
Tôhoku University,
Sendai, Japan

Experiments on the Postbuckling Behavior of Square Plates Loaded in Edge Compression

In previous papers [1, 2],[1] the postbuckling behavior of rectangular plates under edge compression has been studied theoretically under eight different boundary conditions, and numerical solutions are presented for square plates with and without initial deflection. To compare with these results, experiments were carried out by using aluminum square plates, and the relations of the maximum deflection, stresses, and strains at typical points in the plate with applied loads were determined under four different boundary conditions. It is found that the experimental results are in reasonable agreement with those theoretically predicted.

It is well known that the failing strength of a rectangular plate under edge compression can exceed appreciably the buckling strength when the thickness is sufficiently small in comparison with its other dimensions. Thus it is of practical importance to clarify the postbuckling behavior of the plate, and numerous researches, both theoretical and experimental, have been carried out [3]. However, most of these studies seem to be confined to the case where the plate is simply supported along all the edges.

In previous papers [1, 2], the author investigated this problem theoretically under eight different boundary conditions and presented numerical solutions for square plates with and without initial deflection, assuming the Poisson's ratio as 1/3. To compare with these results, experiments were conducted under four different boundary conditions by using aluminum square plates with a side length of 11.8 in. and thickness of 0.04 and 0.05 in. In what follows, first the test equipment and procedures are described briefly and then experimental results are presented and discussed in some detail.

Test Equipment

The test fixture shown in Fig. 1 is designed for compression tests on 11.8 × 11.8 × 0.05-in. flat aluminum plate, the loading capacity of which is about 2200 lb. The jig consists essentially of a lower base, two equal side supports, and an upper frame, which are bolted to each other. A manual loading apparatus is fixed to the upper frame. The supporting and loading elements of this jig can be accommodated to test plates of different dimensions.

A schematic drawing of the loading apparatus is shown in Fig. 2. By turning the screw shaft, the loading head is moved vertically in the guide, and this motion is transmitted to the upper loading beam through a load-measuring beam or dynamometer, by which the plate is compressed between the loading beams.

The dynamometer is a centrally loaded rectangular beam with strain gages attached on both faces. The magnitude of the applied load can be determined by measuring the bending strains. Through preliminary calibration, it is found that the strain meter reading of 100μ in./in. corresponds to the load of 176 lb, and that this linear relation holds up to the load of 3500 lb. The loading beams are designed to be much stiffer than the test plate, so that the condition of constant displacement along the loaded edges, which is assumed in the previous papers, is satisfied.

Knife edges, as shown in Fig. 3, are used for supporting the plate along the edges. One and two pairs of these, respectively, are used for realizing the simply supported and clamped conditions. For fixing the knife edges, base plates are bolted to the side supports and further upper supporting beams and lower supporting bases are fixed to the side supports as seen in Fig. 1.

By using this method, four cases are treated, i.e., I—All edges simply supported, II—loaded edges simply supported, the other edges clamped, III—loaded edges clamped, the other edges simply supported, and IV—all edges clamped. Noting that the unloaded side edges are free from stresses, the loading condition here treated will be seen to correspond to the case (*b*) designated in the previous papers [1, 2].[2]

In Case II, the plate generally buckles into two half-waves in the direction of loading but these waves are not quite similar owing to the initial deflection. Considering the convenience for comparison with theory, the plate is further supported from each side by a pair of 0.04-in. steel plates along the horizontal center line, so that it may buckle into two perfect half-waves.

Test Plate

Square test plates with side length 11.8 in. are carefully manufactured from the aluminum sheets which are 16 in. wide, 48 in. long, 0.04 and 0.05 in. thick. The thinner one is used in Case II, while the thicker ones are used in other cases. The chemical composition of the aluminum sheets used is shown in Table 1.

In a previous paper [2], numerical solutions for both the membrane and bending stresses are obtained at the four typical points of the square plate in each case. To compare with these results, pairs of strain gages are mounted on opposite faces of the plate at each point as shown in Fig. 4. The positions where strains are to be measured are E, B, C, and F in Case II, while A, B, C, and D are used in other cases.

Since the plate is to be supported by knife edges along the sides as shown in Fig. 3, gages are mounted about 0.08 and 0.32 in.

[1] Numbers in brackets designate References at end of paper.

Contributed by the Applied Mechanics Division and presented at the Winter Annual Meeting, New York, N. Y., November 27–December 2, 1960, of The American Society of Mechanical Engineers.

Written discussion on this paper should be addressed to the Editorial Department, ASME, 29 West 39th Street, New York, N. Y., and will be accepted until July 10, 1961. Discussion received after the closing date will be returned. Manuscript received by ASME Applied Mechanics Division, March 24, 1960. Paper No. 60—WA-103.

[2] In the previous papers, another four cases corresponding to the loading condition (*a*), where side edges are kept straight by a distribution of normal stresses, the resultant of which is zero, are also treated. But these cases are not treated here as it seems to be difficult to realize this condition.

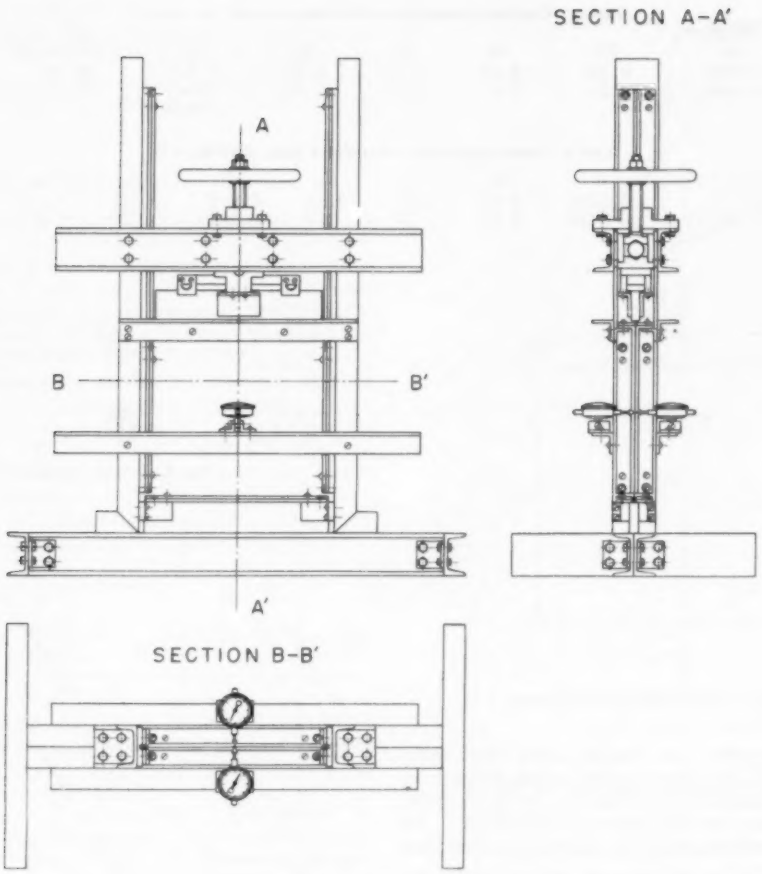

Fig. 1 Test equipment

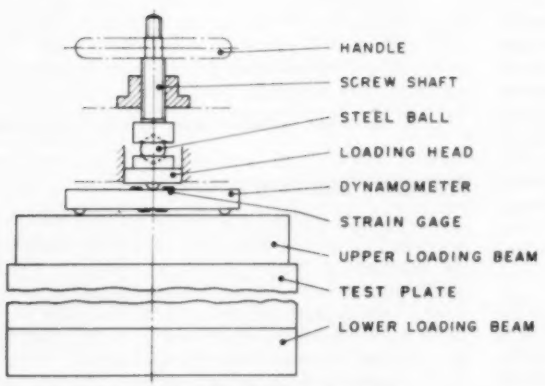

Fig. 2 Sketch of loading apparatus

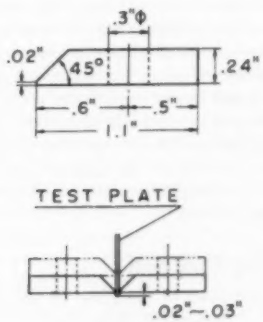

Fig. 3 Knife edge

Table 1 Chemical composition of aluminum sheets, per cent

Thickness, in.	Cu	Si	Fe	Mn	Zn	Al (by difference)
0.0388.....	0.086	0.15	0.46	0.041	0.015	99.25
0.0490.....	0.25	0.13	0.20	0.003	Not detected	99.42

Table 2 Elastic properties of test plates (h:in., E:10^6lb./in.^{2})

Case	h	E_r	E_t	E_m	ν_r	ν_t	ν_m
II.....	0.0388	9.89	9.83	9.86	0.318	0.311	0.315
I, III, IV...	0.0490	9.99	9.79	9.89	0.332	0.320	0.326

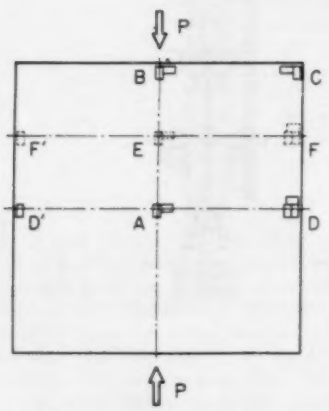

Fig. 4 Strain gage installation in test plate

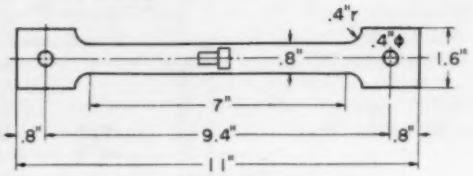

Fig. 5 Tension test specimen

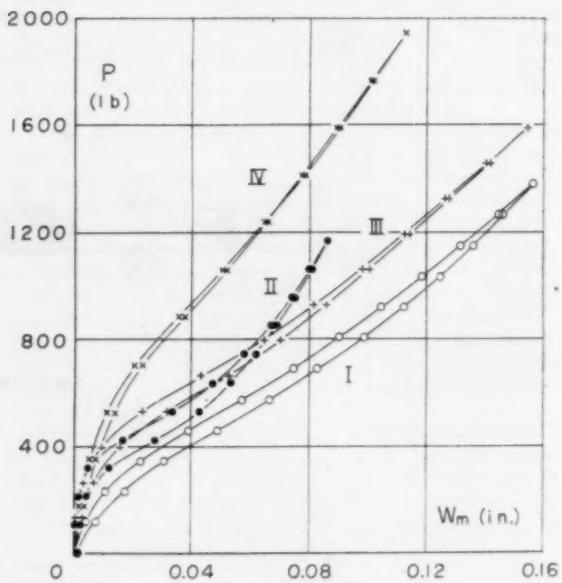

Fig. 6 Maximum deflection versus applied load in each case

inside the simply supported and clamped edges, respectively. At positions D and F, the strains in the loading direction are predicted to change so rapidly toward the edge that two adjacent gages are used to obtain the edge strain by extrapolation. The gages at D′ and F′ serve to check the uniformity of the compression.

Mounting the Test Plate

After removing the upper frame, the test plate is installed in the jig and the upper frame is added and bolted to the side supports. The knife edges are carefully fixed along the parallel lines 0.02 to 0.03 in. apart from the edges, Fig. 3, so that they are in smooth contact with the plate without exerting initial bending moments. The edges of the plate are coated with vaseline beforehand to diminish the friction. The upper loading beam and dynamometer placed on the upper edge of the plate are adjusted so that their center lines coincide with that of the test jig as shown in Fig. 2. The preparation for measurements is completed when the dial gages are mounted at the appropriate positions and the lead wires from the strain gages are connected to the strain indicator through switching boxes.

Measuring Equipment

The deflection of the plate at the point corresponding to the theoretical maximum deflection is measured by two dial gages with an accuracy of 0.0004 in. Thus in Cases I, III, and IV the gages are mounted at the center of the plate on each side, while in Case II they are mounted on one side of the plate at the points one fourth of the side length apart from the edges, respectively, along the vertical center line of the plate.

The applied load and strains in the plate are measured by a strain indicator through two sets of ten-point switching boxes. The wire strain gage of paper base with gage length 0.16 in. and resistance 60Ω is used throughout the experiments.

Preliminary Experiments

To determine the elastic properties together with the degree of anisotropy of the test plates, tension tests were conducted by using the specimens as shown in Fig. 5, which are cut from each aluminum sheet in both the rolling and transverse directions. Pairs of strain gages are mounted on both faces as shown. A mirror extensometer with gage length 4 in. and magnification factor 500 is used in parallel with the strain meter. Young's modulus is determined from the measurements using the extensometer, while Poisson's ratio is obtained as the ratio of the transverse and longitudinal strains read by the strain meter. The results are shown in Table 2. In this table, E, ν, and h denote Young's modulus, Poisson's ratio, and plate thickness, respectively, while subscripts r, t, and m stand for the values in the rolling and transverse directions and the average value. It will be seen that the plates may be regarded as almost isotropic.

From the stress-strain relations obtained in the tests, the limit of proportionality is found to be about 8500 psi; hence, care is taken not to exceed this limit in the following experiments. Further, the gage factor of the strain gage is determined as 1.74, from the comparison of the longitudinal strains obtained by both the methods.

Experimental Results and Discussions

Under four different boundary conditions mentioned in the foregoing, the plate deflection and strains under applied loads are measured and the results are compared with the previous theoretical solutions. In each case, measurements are repeated several times by inverting the top and bottom of the plate, and it is found that no appreciable change results except that the initial deflection slightly increases with the repetition of measurements.

Load-Deflection Relations. The maximum deflection of the plate is measured whenever the plate is loaded and unloaded at equal load increments. The readings of the two dial gages are found to be in good agreement. The experimental results in each case are shown in Fig. 6, where P and w_m denote the applied load and maximum deflection, respectively. It will be seen that the curves show small hysteresis loops owing to the friction along the edges. Here we will introduce the dimensionless load factor defined by

$$\lambda = Pa/\pi^2 Eh^3, \tag{1}$$

where a is the side length of the plate. Taking the average values of w_m for each load and rearranging the load-deflection diagrams in the dimensionless form using the values of h and E_m in Table 2, we obtain Figs. 7(a) and 7(b). In these figures, symbols ○ ● + and × show the experimental results, while solid and dotted curves, respectively, represent the theoretical results obtained in the previous paper [1] for the initially flat and deflected plates, the maximum deviation of which is $0.1h$.

From these figures, it will be seen that in Cases III and IV, both the results are in excellent agreement. In Cases I and II, the experimental results for deflection are smaller than those theoretically predicted, which is found to be attributable to the fact that the condition of free rotation along the loaded edges is not fully satisfied by using the knife edges.

Hoff, et al. [4] have carried out ingenious experiments for Case I, using square plates of fiberglass with $a = 20$ in., $h = 0.25$ in., $E = 2.20 \times 10^6$ psi, and $\nu = 0.14$, and employing needle bearings and knife edges, respectively, for the loaded and unloaded edges of the plate. Their results are shown in Fig. 7(a) by chain lines; designations 27a and 28a are the specification of the test plates. Hoff's results are seen to be in better agreement with theoretical ones, probably because the theoretical boundary conditions are realized satisfactorily.

Load-Strain Relations. In parallel with the deflection measurements, strains at the typical points in the plate, Fig. 4, are recorded at each applied load. Now we will take the x, y-axes along the center lines of the plate, so that the x-axis is perpendicular to the loading direction. Denoting by ϵ_x, ϵ_y; ϵ_x', ϵ_y' the strains at a point in the x and y-directions, on the convex and concave sides of the plate, respectively, the membrane strains, ϵ_x and ϵ_y, and the bending strains on the convex side of the plate, ϵ_x' and ϵ_y', are given as follows:

$$\begin{aligned} \epsilon_x &= {}^1/_2(\epsilon_x + \epsilon_x'), \qquad \epsilon_y = {}^1/_2(\epsilon_y + \epsilon_y'), \\ \epsilon_x' &= {}^1/_2(\epsilon_x - \epsilon_x'), \qquad \epsilon_y' = {}^1/_2(\epsilon_y - \epsilon_y') \end{aligned} \tag{2}$$

Here we will introduce the following dimensionless strain factors:

$$\begin{aligned} \bar{\epsilon}_x &= \epsilon_x a^2/\pi^2 h^2, \qquad \bar{\epsilon}_y = \epsilon_y a^2/\pi^2 h^2, \\ \bar{\epsilon}_x' &= \epsilon_x' a^2/\pi^2 h^2, \qquad \bar{\epsilon}_y' = \epsilon_y' a^2/\pi^2 h^2 \end{aligned} \tag{3}$$

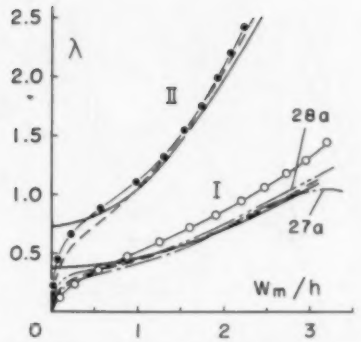

Fig. 7(a) Load-deflection relations for Cases I and II

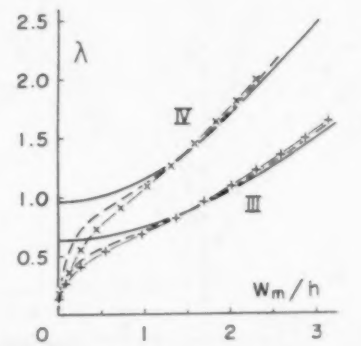

Fig. 7(b) Load-deflection relations for Cases III and IV

Taking the mean values of the strains for each load in the loading and unloading cases[3] and representing the load-strain relations in the dimensionless form, we obtain the results shown in Figs. 8(a) through 11(d) for each point under each boundary condition. The theoretical solutions[4] [2] are shown together for comparison. The meaning of the curves is the same as before.

From these figures, the following may be concluded:

1 A pair of knife edges is used for giving the simply supported conditions, but it is found that this method is not satisfactory for the loaded edges because it results in appreciable bending strains as seen from Figs. 8(b) and 9(b). However, the conditions of simple support along the unloaded edges are reasonably satisfied by this method as seen in Figs. 8(d) and 10(d).

2 Clamped edge conditions seem to be satisfied by using two pairs of knife edges.

3 In general, the agreement between the theory and experiment is fairly good. Some discrepancies noticeable in Cases I and II may be attributed to the afore-mentioned fact.

4 In Fig. 8(a), Hoff's results are shown together, which are seen to be in better agreement with the theory.

Load-Stress Relations. Here we will obtain the load-stress relations from the preceding load-strain relations and compare with the theoretical ones. Denoting by σ_x, σ_y the membrane stresses, and by σ_x', σ_y' the extreme bending stresses, we introduce the following nondimensional stress factors as in the previous paper:

[3] The load-strain relations showed some hysteresis characteristics as before.

[4] In the previous paper, numerical solutions are presented for the load-stress relations, from which the load-strain relations can be obtained without difficulty.

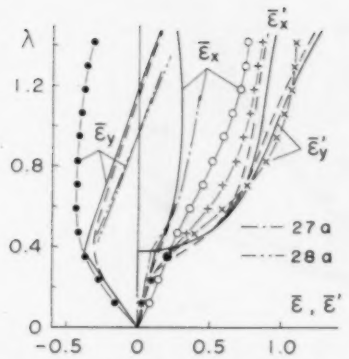

Fig. 8(a) Load-strain relations at position A in Case I

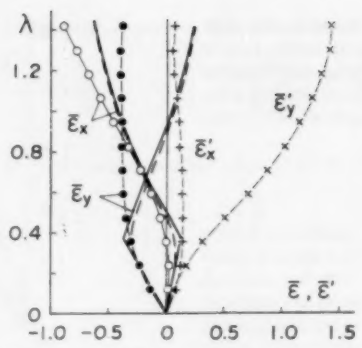

Fig. 8(b) Load-strain relations at position B in Case I

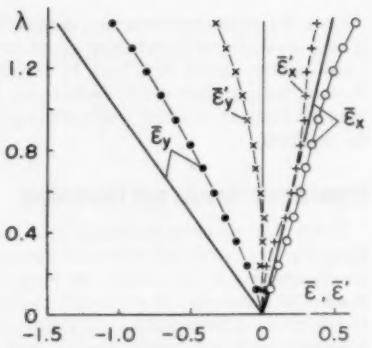

Fig. 8(c) Load-strain relations at position C in Case I

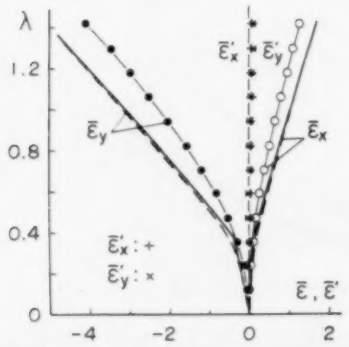

Fig. 8(d) Load-strain relations at position D in Case I

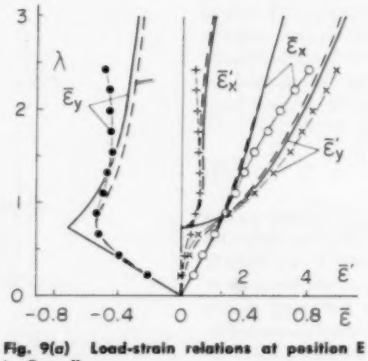

Fig. 9(a) Load-strain relations at position E in Case II

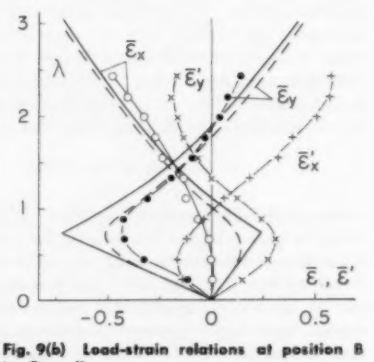

Fig. 9(b) Load-strain relations at position B in Case II

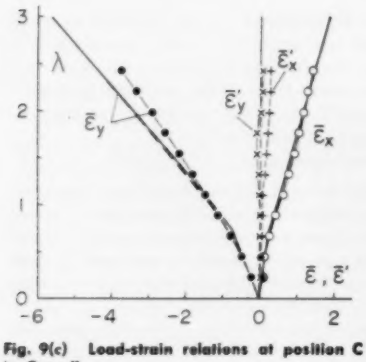

Fig. 9(c) Load-strain relations at position C in Case II

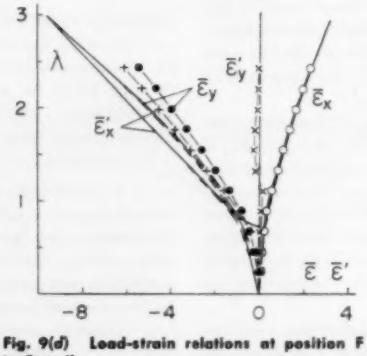

Fig. 9(d) Load-strain relations at position F in Case II

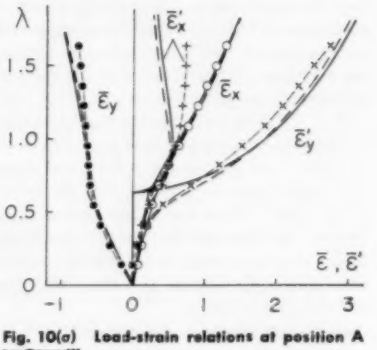

Fig. 10(a) Load-strain relations at position A in Case III

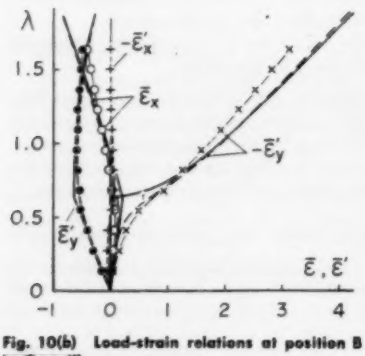

Fig. 10(b) Load-strain relations at position B in Case III

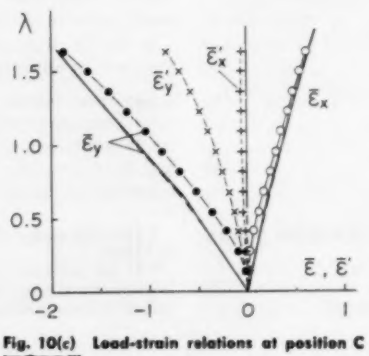

Fig. 10(c) Load-strain relations at position C in Case III

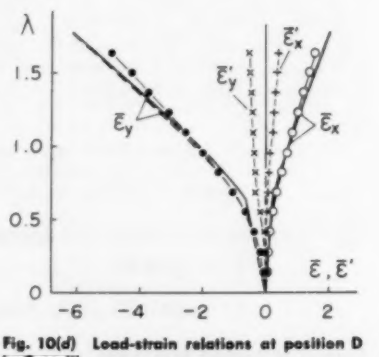

Fig. 10(d) Load-strain relations at position D in Case III

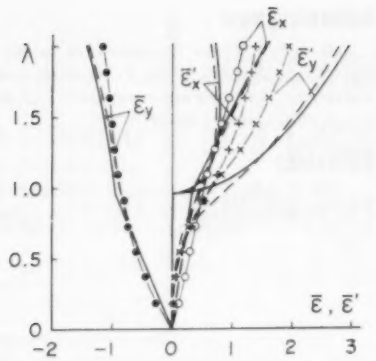

Fig. 11(a) Load-strain relations at position A in Case IV

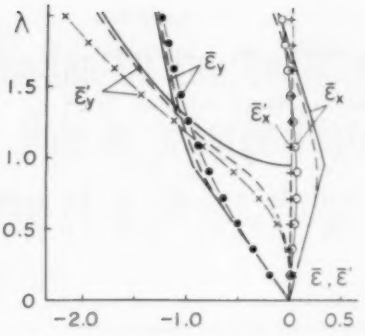

Fig. 11(b) Load-strain relations at position B in Case IV

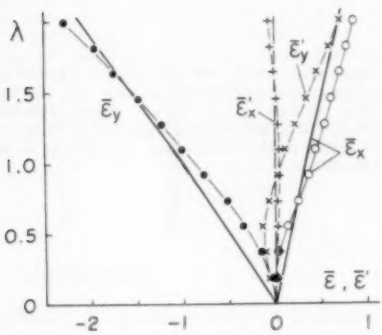

Fig. 11(c) Load-strain relations at position C in Case IV

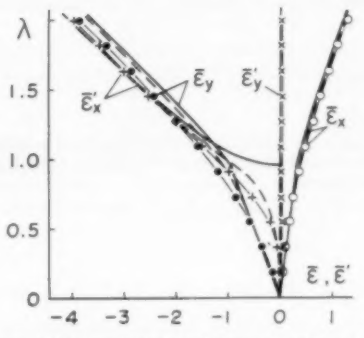

Fig. 11(d) Load-strain relations at position D in Case IV

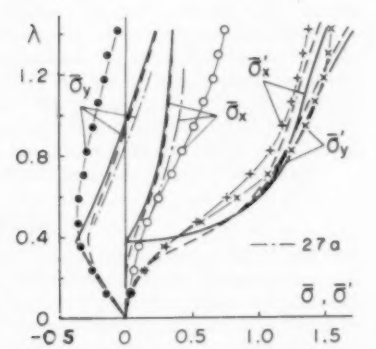

Fig. 12(a) Load-stress relations at position A in Case I

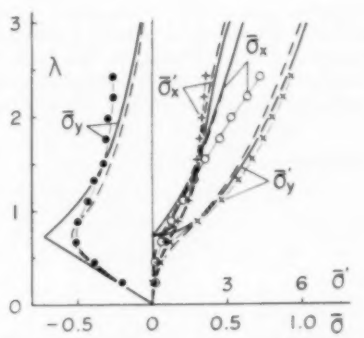

Fig. 12(b) Load-stress relations at position E in Case II

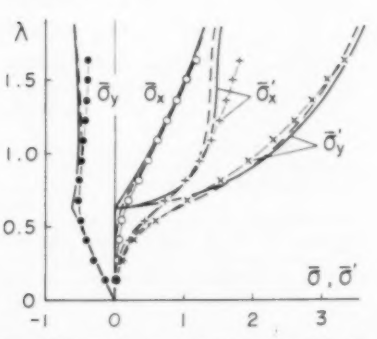

Fig. 12(c) Load-stress relations at position A in Case III

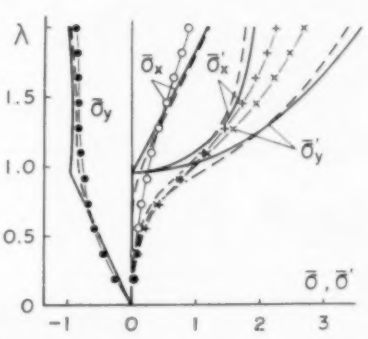

Fig. 12(d) Load-stress relations at position A in Case IV

$$\delta_x = \sigma_x a^2/\pi^2 E h^2, \qquad \delta_y = \sigma_y a^2/\pi^2 E h^2,$$
$$\delta_x' = \sigma_x' a^2/\pi^2 E h^2, \qquad \delta_y' = \sigma_y' a^2/\pi^2 E h^2 \tag{4}$$

These are related to the strain factors as follows:

$$\delta_x = \frac{1}{1-\nu^2}(\bar{\imath}_x + \nu\bar{\imath}_y), \qquad \delta_y = \frac{1}{1-\nu^2}(\bar{\imath}_y + \nu\bar{\imath}_x),$$
$$\delta_x' = \frac{1}{1-\nu^2}(\bar{\imath}_x' + \nu\bar{\imath}_y'), \qquad \delta'_y = \frac{1}{1-\nu^2}(\bar{\imath}_y' + \nu\bar{\imath}_x') \tag{5}$$

The stresses at the point of maximum deflection in each case are calculated from the preceding results by using the values of ν_m given in Table 2. The results are shown in Figs. 12(*a*) to 12(*d*), together with the theoretical ones.[5] In Fig. 12(*a*), Hoff's results are also shown. It will be seen that the experimental results, especially those by Hoff, compare favorably with the theoretical ones.

From the discussions in the foregoing, it will be concluded that the validity of the theoretical results is ascertained by experiments.

[5] The comparison at the other points in the plate is omitted to save space. The degree of coincidence is found to be similar as in the corresponding cases for strains.

Acknowledgment

The author wishes to express his hearty thanks to Professor Emeritus S. Higuchi, Profs. F. Numachi and O. Tamate, Tōhoku University, for their encouragement and discussions during the course of the present study.

References

1 N. Yamaki, "Postbuckling Behavior of Rectangular Plates With Small Initial Curvature Loaded in Edge Compression," JOURNAL OF APPLIED MECHANICS, vol. 26, TRANS. ASME, vol. 81, Series E, 1959, pp. 407–414.

2 N. Yamaki, "Postbuckling Behavior of Rectangular Plates With Small Initial Curvature Loaded in Edge Compression—(continued)," JOURNAL OF APPLIED MECHANICS, vol. 27, TRANS. ASME, vol. 82, Series E, 1960, pp. 335–342.

3 See, for example, F. Bleich, "Buckling Strength of Metal Structures," McGraw-Hill Book Company, Inc., New York, N. Y., 1952, and G. Gerard, "Handbook of Structural Stability, Part IV—Failure of Plates and Composite Elements," NACA TN 3784, 1957.

4 N. J. Hoff, B. A. Boley, and J. M. Coan, "The Development of a Technique for Testing Stiff Panels in Edgewise Compression," *Proceedings of The Society for Experimental Stress Analysis*, vol. 5, 1948, pp. 14–24. Further, see the following references concerning the experimental results: J. M. Coan, "Large Deflection Theory for Plates With Small Initial Curvature Loaded in Edge Compression," JOURNAL OF APPLIED MECHANICS, vol. 18, TRANS. ASME, vol. 73, 1951, pp. 143–151; S. Yusuff, "Large Deflection Theory for Orthotropic Rectangular Plates Subjected to Edge Compression," JOURNAL OF APPLIED MECHANICS, vol. 19, TRANS. ASME, vol. 74, 1952, pp. 446–450.

Stress Distribution on the Boundary of a Circular Hole in a Large Plate During Passage of a Stress Pulse of Long Duration

A. J. DURELLI
Professor in Civil Engineering, Illinois Institute of Technology, Chicago, Ill.
Assoc. Mem. ASME

W. F. RILEY
Research Engineer, Armour Research Foundation of Illinois Institute of Technology, Chicago, Ill.

A partial solution to the problem of the stress distribution on the boundary of a circular hole in a large plate during passage of a stress pulse of relatively long duration is presented. The solution was obtained experimentally by using a low-modulus model material in a combined photoelasticity and grid analysis. The long-duration stress pulse was applied by loading a small region on an edge of the plate with a falling weight. The hole was placed at a location in the plate where both dilatational and distortional waves would be felt. It was also located in such a way that a symmetric point was available for making free-field stress determinations. The results of the investigation indicate that a variable biaxial state of stress was produced in the free field. The study also indicates that the maximum compressive stress on the hole boundary can be computed with a fair degree of accuracy by applying the Kirsch solution for a hole in an infinite plate and considering the free-field biaxial stress conditions. The maximum tensile stresses on the hole boundary were always found to be smaller than the values predicted by the Kirsch formula.

Introduction

THE determination of the stress distribution in a large plate subjected to a time-dependent loading acting at one point along the boundary is difficult. A number of investigators have studied various phases of the problem. A mathematical treatment of some phases has been presented by Kolsky [1].[1] Others such as Christie [2] have employed photoelasticity methods.

The problem of determining the stress distribution on the boundary of a circular hole in a large plate during passage of a compressive stress wave was approached in this investigation through the use of experimental methods described in this and previous papers [3, 4, 5]. These methods utilize low-modulus materials in a combined photoelasticity and grid analysis.

Theoretical Considerations

When a time-dependent load is applied at a point on one edge of a semi-infinite plate, two basic waves are produced; namely, dilatational waves and distortional waves. These waves propagate radially from the point of load application with velocities C_1 and C_2, respectively. These velocities can be computed from the following equations:

$$C_1^2 = E/\rho(1 - \nu^2) \text{ (dilatational)}$$
$$C_2^2 = E/2\rho(1 + \nu) \text{ (distortional)}$$

where ρ = mass density (0.000103 lb sec^2/in.^{4})
E = modulus of elasticity (560 psi)
ν = Poisson's ratio (0.46)

Thus $C_1 = 2630$ in/sec, $C_2 = 1365$ in/sec

The dilatational wave is produced by radial displacements which occur at the point of load application. The maximum shearing stresses associated with this wave, at every point in the field, make an angle of 45 deg to the wave front. This maximum shear is independent of θ (angular position of the point, measured with respect to a line perpendicular to the edge of the plate at the point of load application) and, as a consequence, the photoelastic fringes associated with the dilatational wave form circular lines with the point of load application at the center.

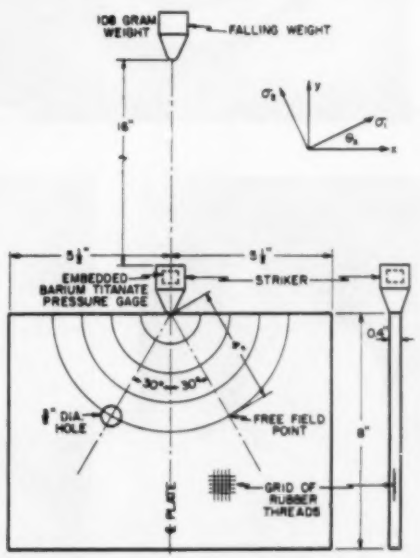

Fig. 1 Sketch of model illustrating loading, location of hole, and symmetric free-field point

[1] Numbers in brackets designate References at end of paper.

Presented at the Summer Conference of the Applied Mechanics Division, Chicago, Ill., June 14–16, 1961, of THE AMERICAN SOCIETY OF MECHANICAL ENGINEERS.

Discussion of this paper should be addressed to the Editorial Department, ASME, 29 West 39th Street, New York, N. Y., and will be accepted until July 10, 1961. Discussion received after the closing date will be returned. Manuscript received by ASME Applied Mechanics Division, June 17, 1960. Paper No. 61—APM-4.

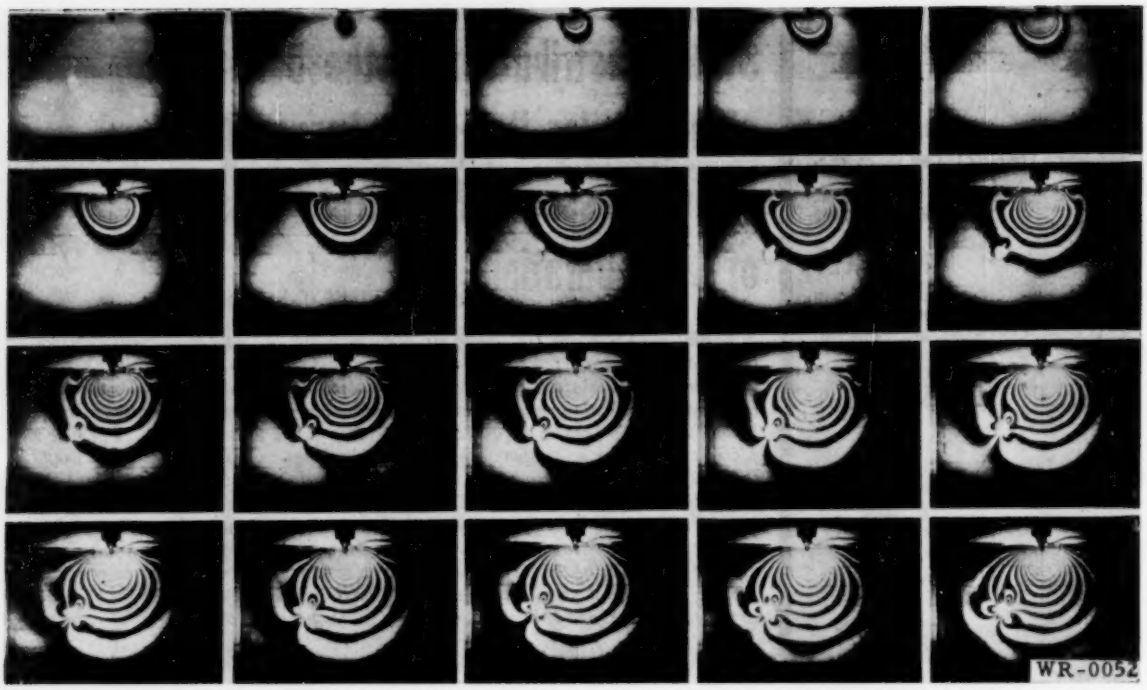

Fig. 2 Series of 20 consecutive photographs showing a compressive stress wave propagating past an open hole in a large plate of Hysol 8705; photographs were taken with a Fastax camera at 6960 frames per sec

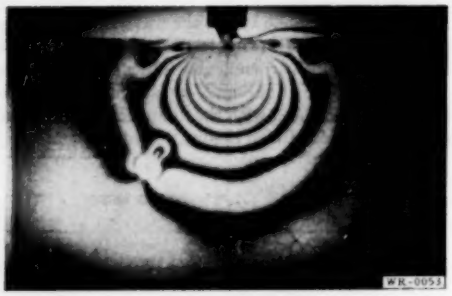

Fig. 3 Enlargement of frame 12 of Fastax record showing complete fringe pattern in plate, 1605 microsec after impact

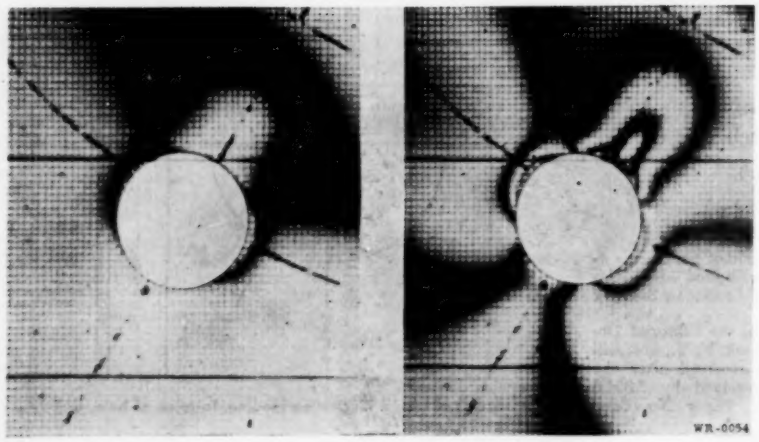

Fig. 4 Microflash photographs showing fringe-order distribution around boundary of hole 1100 microsec and 1710 microsec after impact

The distortional wave is produced by transverse or circumferential displacements; therefore the maximum shearing stresses at every point in the field are in the plane of the wave front. The photoelastic pattern associated with a distortional wave is quite complex since the magnitude of the maximum shear at a point is a function of the angular position θ of the point.

Experimental Procedure

A large plate with dimensions 0.4 in. × 8 in. × 11 in. was machined from a sheet of Hysol 8705. The sheet had an embedded rubber-thread grid with a $^1/_{32}$-in. grid spacing. A $^5/_8$-in. diam hole was located 4 in. from the point of load application along a radial line 30 deg from the center line of the plate. A sketch of the model is shown in Fig. 1. The location of the hole was chosen to give the maximum time for study before reflections return from the boundary. Also, the 30-deg orientation provides a symmetric point in the same model where free-field stresses can be simultaneously determined. The symmetric point is far enough removed from the hole so that any disturbances produced by the presence of the hole do not interfere with the free-field stress distribution. The 30-deg orientation also places the hole in a location where the influences of both the dilatational and distortional waves are felt. If the hole were located on the center line of the plate the distortional wave influence would be a minimum.

The loading of the model was accomplished by dropping a weight (108 grams) from a height of 16 in. on a hard plastic striker which was permanently positioned on the model, Fig. 1. A complete photographic record of the impact was obtained by using a 16-mm Fastax camera operating at 6960 frames per sec. The first 20 photographs of this record are shown in Fig. 2. These were the frames used in the analysis and they cover a time period of approximately 3000 microsec. The total time duration of the pulse, applied by the falling weight, was approximately 12,000 microsec.

rehe Fastax records were suitable for making fringe-order de-Ttminations at the symmetric free-field point and for studying the over-all wave-propagation phenomena. The records were not suitable, however, for precise fringe-order determinations at the hole boundary or for grid measurements. It can be seen readily in Fig. 3, which is an enlargement of frame 12 from the Fastax record, that while the over-all detail is good the grid and fringe detail near the hole are washed out.

In order to obtain photographs suitable for grid measurements at the symmetric point and photographs suitable for precise fringe-order determination at the hole boundary, a series of 20-microflash photographs were obtained at approximately 200-microsec intervals after impact. The microflash photographs were sequenced by using a specially built timer unit which was triggered with a barium-titanate pressure gage embedded in the striker. Two representative photographs of the fringe distribution around the hole are shown in Fig. 4. It can be seen readily from these photographs that the fringe order at the boundary of the hole can be determined accurately. The grid was also sufficiently clear to permit strain measurements to be made with a fair degree of accuracy at the symmetric free-field point.

Analysis of Data

Ten microflash photographs were selected for analysis. These records covered the interval of time from 1320 microsec after impact until 3075 microsec after impact. The beginning of the time interval was chosen when the 0.5-order fringe reached the symmetric point in the field. This was the first instant at which the response around the hole boundary was sufficient to make fringe-order determinations. The end of the interval was chosen to insure that reflections were not influencing the distribution around the hole.

The Fastax and microflash records were used to obtain the fringe-order distribution around the hole, the fringe order at the symmetric point in the free field, and the two strains ϵ_x and ϵ_y at the symmetric point in the free field. The experimentally determined values for the fringe order as a function of time at the symmetric free-field point are shown in Fig. 5. (Similar curves for the two strains ϵ_x and ϵ_y are shown in Fig. 6.) It was possible to make very accurate fringe-order determinations. The two

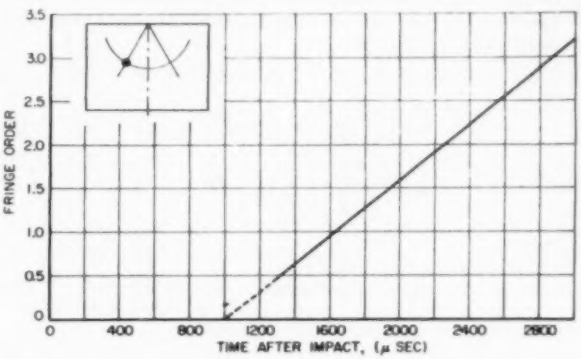

Fig. 5 Fringe order at symmetric free-field point as a function of time after impact

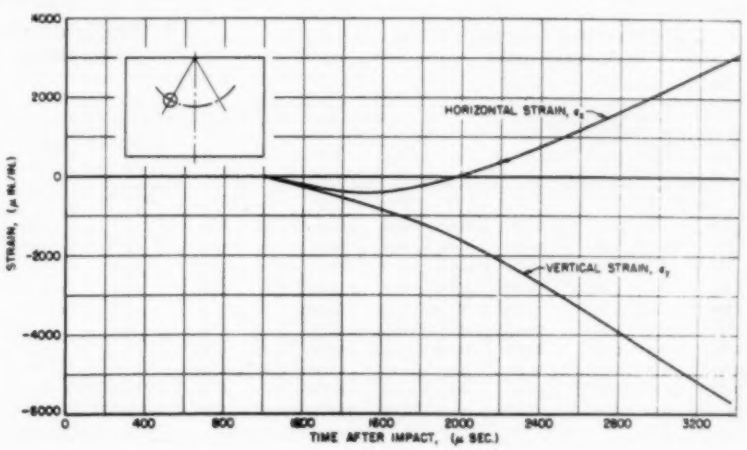

Fig. 6 Horizontal strain ϵ_x and vertical strain ϵ_y at symmetric free-field point as a function of time after impact

strain curves, however, represent smooth curves through experimental data exhibiting considerable scatter. A large number of measurements were made on each film and the average was used to improve the accuracy. It is estimated that the strain curves may be in error by as much as 15 per cent. The data shown in Figs. 5 and 6 were then used to obtain the two principal stresses and their directions. This was accomplished through the use of the following equations.

The relationship between stress and strain for the case of plane stress is as follows:

$$\sigma_x = \frac{E}{1-\nu^2}(\epsilon_x + \nu\epsilon_y)$$
$$\sigma_y = \frac{E}{1-\nu^2}(\epsilon_y + \nu\epsilon_x) \tag{1}$$

where

σ_x = normal component of stress on a plane whose normal lies in x-direction
σ_y = normal component of stress on a plane whose normal lies in y-direction
E = modulus of elasticity (Young's modulus)
ν = Poisson's ratio
ϵ_x = normal component of strain in x-direction
ϵ_y = normal component of strain in y-direction

Both σ_x and σ_y can be determined from the grid data if the material properties are known. In general, the two stresses σ_x and σ_y are not principal stresses, therefore other relations must be developed for obtaining the principal stresses from the experimental data. Use can be made of the first invariant of stresses as follows:

$$\sigma_x + \sigma_y = \sigma_1 + \sigma_2 \text{ (first invariant)}$$
$$\sigma_1 = \frac{\sigma_x + \sigma_y}{2} + \frac{\sigma_1 - \sigma_2}{2} \tag{2}$$
$$\sigma_2 = \frac{\sigma_x + \sigma_y}{2} - \frac{\sigma_1 - \sigma_2}{2}$$

where

σ_1 = maximum principal stress
σ_2 = minimum principal stress

The photoelastic-stress optic law states that

$$\frac{\sigma_1 - \sigma_2}{2} = \frac{nf_\sigma}{t} \tag{3}$$

where n = fringe order
f_σ = material fringe value in shear
t = thickness of model

By substituting equations (1) and (3) into (2), equations relating the experimentally determined quantities ϵ_x, ϵ_y, and n to the principal stresses σ_1 and σ_2 are obtained:

$$\sigma_1 = \frac{E}{2(1-\nu)}(\epsilon_x + \epsilon_y) + \frac{nf_\sigma}{t}$$
$$\sigma_2 = \frac{E}{2(1-\nu)}(\epsilon_x + \epsilon_y) - \frac{nf_\sigma}{t} \tag{4}$$

The directions of the principal stresses can also be determined from the experimental data using the well-known relationship

$$\text{Cos } 2\theta_x = \frac{\epsilon_x - \epsilon_y}{\epsilon_1 - \epsilon_2} \tag{5}$$

where

$$\epsilon_1 - \epsilon_2 = \frac{1+\nu}{E}(\sigma_1 - \sigma_2) = \frac{2(1+\nu)}{E}\left[\frac{nf_\sigma}{t}\right] \tag{6}$$

The angle θ_x indicates the direction of the principal stress with respect to the x-axis, Fig. 1. Individual values for ϵ_1 and ϵ_2 can be computed by using the results of equation (6) together with the grid data (ϵ_x and ϵ_y) and the first invariant of strain.

Complete stress and strain information was computed from the experimental data and the properties of the model material. Curves which show the modulus of elasticity and the stress fringe value of the material (Hysol 8705) as a function of strain rate are shown in previous publications by the authors [3, 4]. The remaining material properties which are independent of the rate of loading are as follows:

ν = 0.46 (Poisson's ratio)
ρ = 0.000103 lb sec^2/in^4 (mass density)

In using equations (4) the only unknown quantity is the modulus of elasticity E. Since the modulus is strain-rate dependent, a value for the strain rate had to be established for each instant of time studied. For this purpose the rate of change of ϵ_y (the measured strain having the largest magnitude) with time was used to estimate the rate of change of ϵ_2 (principal strain having the greatest magnitude) with time. Since it was found that the rate of change of ϵ_y with time varied from 2 in/in/sec to about 4 in/in/sec, a value of 6 in/in/sec was estimated as the strain rate of ϵ_2. From the material-property curves this established the following values for E and f_σ.

E = 560 psi
f_σ = 0.52 psi in/fringe

With these values established it was possible to compute all the desired quantities. These are shown tabulated in Table 1. A

Experimental Data					Quantities Computed from Experimental Data					
Frame No.	Time After Impact	Fringe Order	ϵ_x	ϵ_y	ϵ_1	ϵ_2	σ_1	σ_2	θ_x	σ_1/σ_2
	μ Sec	-	in/in	in/in	in/in	in/in	psi	psi	Degrees	-
6D	1320	0.50	-.00030	-.00045	.00132	-.00207	0.26	-1.04	43.7	-0.25
7D	1560	0.88	-.00045	-.00080	.00236	-.00361	0.50	-1.79	43.3	-0.28
8D	1710	1.12	-.00035	-.00102	.00311	-.00448	0.75	-2.17	42.5	-0.34
9D	1910	1.45	-.00010	-.00140	.00416	-.00566	1.11	-2.66	41.2	-0.42
10D	2110	1.78	.00020	-.00190	.00518	-.00688	1.43	-3.20	40.1	-0.45
11D	2300	2.08	.00055	-.00240	.00612	-.00797	1.75	-3.66	38.5	-0.48
12D	2475	2.37	.00090	-.00290	.00703	-.00903	2.04	-4.12	38.1	-0.50
13D	2675	2.70	.00135	-.00355	.00805	-.01025	2.37	-4.65	37.2	-0.51
14D	2875	3.02	.00185	-.00415	.00908	-.01138	2.73	-5.12	36.4	-0.53
15D	3075	3.30	.00230	-.00480	.00993	-.01243	2.99	-5.59	35.7	-0.54

Table 1 Stresses and strains at a point in free field symmetric with respect to the center of the hole

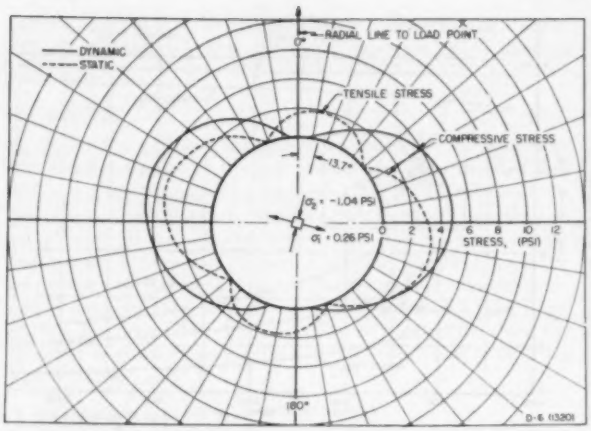

Fig. 7 Static and dynamic-stress distributions on hole boundary 1320 microsec after impact. Static distribution was computed from biaxial state of stress at symmetric point at same instant of time; this holds through series, Figs. 7–13, inclusive.

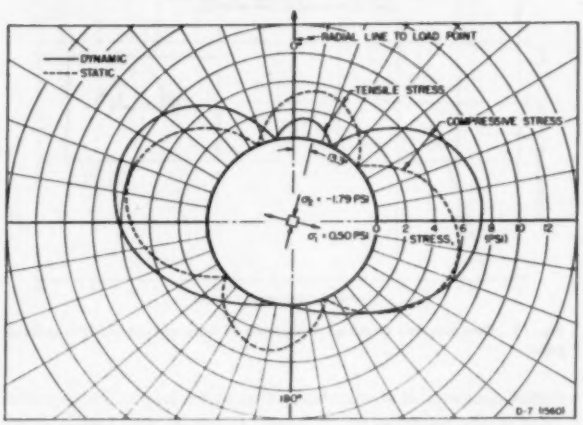

Fig. 8 Static and dynamic-stress distributions on hole boundary 1560 microsec after impact

check on the rate of change of ϵ_2 with time shows that the estimated value of 6 in/in/sec was a good one. If the estimated value did not agree with the actual value the table of values would have to be recomputed until the two were brought into agreement.

At this point it should be mentioned that the material-property curves were determined for a uniaxial state of stress where the ratio between ϵ_1 and ϵ_2 was -0.46. In the current study these results were used in a biaxial stress field where the ratio of ϵ_1 to ϵ_2 varied. Under these conditions it must be assumed that the strain rate of ϵ_3 (the principal strain greatest in magnitude) has the predominant influence and the different strain rates for ϵ_1 in the uniaxial and biaxial states produce only secondary influences. Otherwise, the strain-rate dependence of the material properties must be determined for every condition of biaxiality encountered.

Dynamic Stress Distribution

The dynamic stresses around the hole were computed directly from the photoelastic data using equation (3) since the radial component of the boundary stress vanishes. An equivalent static stress distribution around the hole was then computed using the well-known Kirsch solution for a hole in an infinite plate under

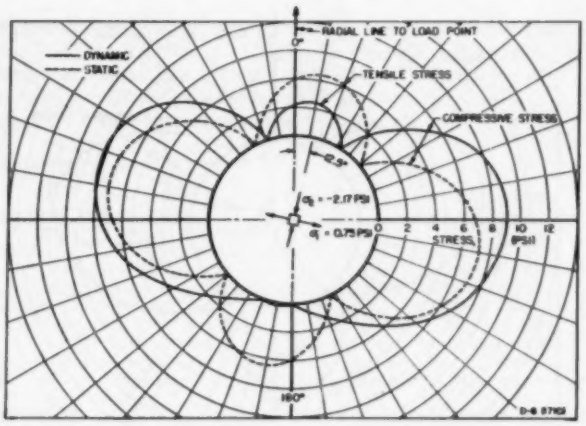

Fig. 9 Static and dynamic-stress distributions on hole boundary 1710 microsec after impact

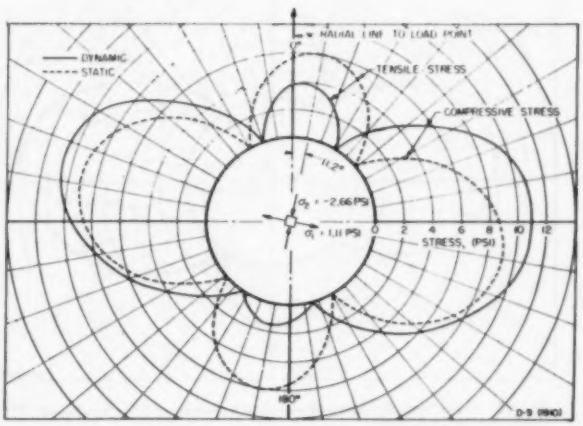

Fig. 10 Static and dynamic-stress distributions on hole boundary 1910 microsec after impact

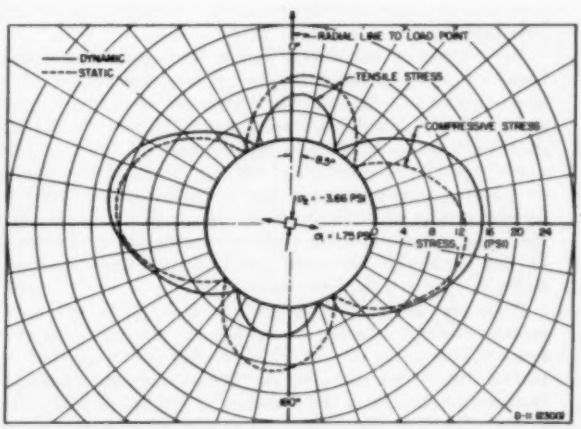

Fig. 11 Static and dynamic-stress distributions on hole boundary 2300 microsec after impact

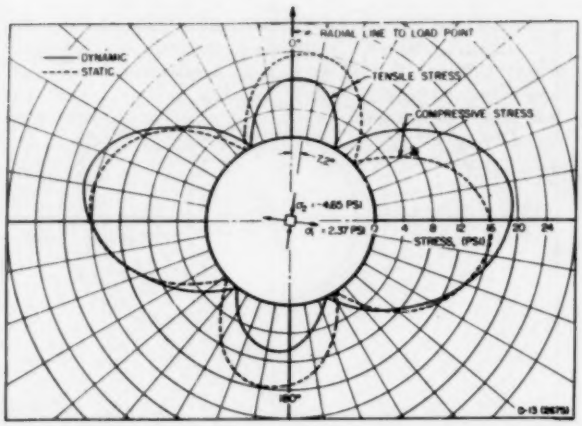

Fig. 12 Static and dynamic-stress distributions on hole boundary 2675 microsec after impact

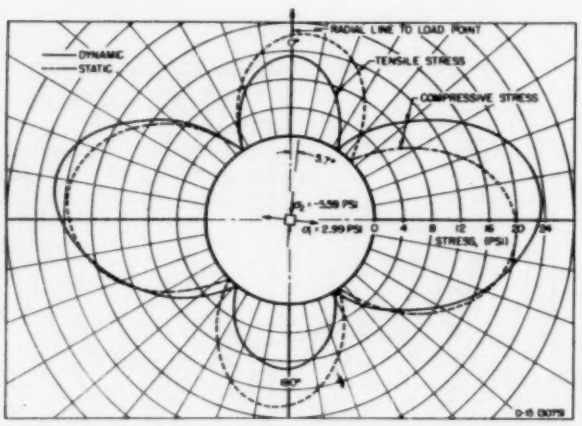

Fig. 13 Static and dynamic-stress distributions on hole boundary 3075 microsec after impact

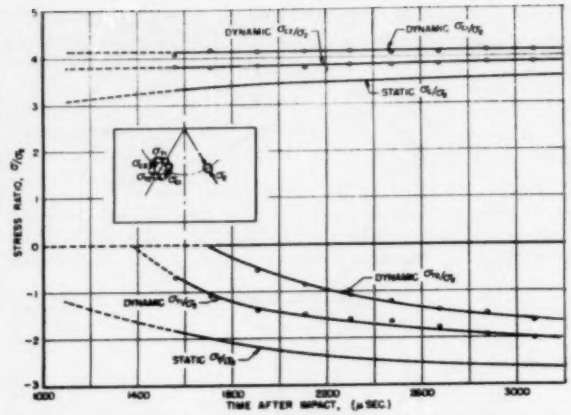

Fig. 14 Ratios of maximum tensile and compressive stresses on hole boundary to free-field compressible stress at various times after impact

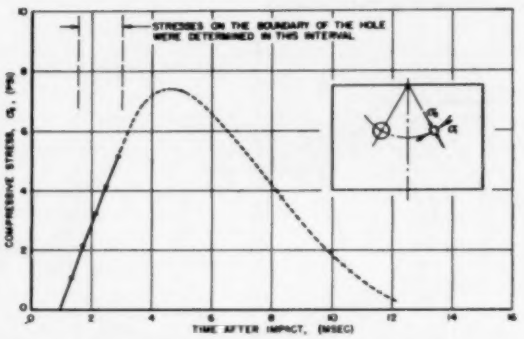

Fig. 15 Compressive stress as a function of time at symmetric free-field point

uniaxial tension or compression. Static loads capable of producing a stress field equivalent to the biaxial stress field at the symmetric point were used in these calculations. The results of the static and dynamic-stress determinations for a number of times after impact are shown in Figs. 7–13.

At the center of each of these figures the magnitudes and directions of the corresponding free-field stresses are plotted. It is interesting to note that the compressive stresses at positions 90 and 270 deg from the radial line through the point of load application build up much more rapidly than the tensile stresses which appear at positions 0 and 180 deg. In Fig. 7 the dynamic compressive stresses are larger than the corresponding static compressive stresses while the tensile stresses are still zero. In Fig. 8 the tensile stresses at 0 deg begin to develop ahead of those at 180 deg. From this time on the nonsymmetric distribution slowly begins to approach the static distribution.

While the individual values of stress at all points on the boundary are of considerable significance, the maximum compressive and tensile stresses which develop are of greatest importance to the designer. In Fig. 14 the maximum tensile and compressive stresses on the boundary of the hole are compared to the maximum compressive stress (σ_2) which occurs at the symmetric point in the free field at the same instant of time. The static values of stress in this figure have been computed for the biaxial condition of stress which exists at the free-field symmetric point at the same instant of time. It can be seen readily from this figure that the compressive stresses on the hole boundary are larger than they would be in an equivalent static field. The differences are probably not significant, however, since they decrease as the peak of the wave front passes. The tensile stresses developed on the hole boundary are always smaller under dynamic loading than predicted. In Fig. 14 it is possible that the differences between the static and dynamic values late in the impact are due to the fact that the model was not of infinite size. For a finite-size model the maximum stresses must be larger.

Since the biaxiality of the stress field at the free-field point was known for a portion of the impact and could be estimated with some degree of accuracy for the other portion, it was possible to compute the value of σ_2 for the entire period of the impact from the photoelastic data. The magnitude of σ_2 as a function of time is shown plotted in Fig. 15. The dashed portion of the curve was determined by using a stress ratio of -0.60. This figure indicates that the falling weight produces a loading equivalent to a stress pulse of about 12,000 microsec duration. Using the velocity of propagation of the zero-order fringe this pulse would have a length equal to approximately 75 hole diameters. The front of the pulse (rise from zero to peak) was approximately 20 hole diameters in length. The portion of the pulse studied in this program was 15 per cent of the total pulse or 75 per cent of the front of the pulse. A study of a greater portion of the pulse would be possible only if larger plates or pulses of shorter duration were used. This was accomplished in a later program where explosives

were used to give pulse durations at the symmetric point in the free field of 2500 microsec duration. This work will be reported separately.

Conclusions

The results of this investigation indicate that the maximum compressive stresses on the hole boundary can be computed with a fair degree of accuracy by employing the Kirsch solution for a hole in an infinite plate and considering the free-field, biaxial-stress conditions. It was also established that the maximum tensile stresses are always smaller than predicted. In drawing conclusions based on this work it should be remembered that the stress pulse employed had a length of approximately 75 hole diameters. The front of the pulse was not very steep, therefore the gradient of stress along a portion of the pulse equal to one hole diameter was small.

Acknowledgment

The research reported in this paper was part of a project conducted at Armour Research Foundation under the sponsorship of Air Force Special Weapons Center, Air Research and Development Command. The authors wish to express their appreciation to Mr. E. H. Wang, Chief, Structures Division, and Capt. J. T. Pantall for their encouragement and support.

References

1 H. Kolsky, "Stress Waves in Solids," Oxford University Press, London, England, 1952.

2 D. G. Christie, "Reflection of Elastic Waves From a Free Boundary," *Philosophical Magazine*, vol. 46, 1955, pp. 527–541.

3 J. W. Dally, W. F. Riley, and A. J. Durelli, "A Photoelastic Approach to Transient Stress Problems Employing Low-Modulus Materials," JOURNAL OF APPLIED MECHANICS, vol. 26, TRANS. ASME, vol. 81, Series E, 1959, pp. 613–620.

4 A. J. Durelli, J. W. Dally, and W. F. Riley, "Developments in the Application of the Grid Method to Dynamic Problems," JOURNAL OF APPLIED MECHANICS, vol. 26, TRANS. ASME, vol. 81, Series E, 1959, pp. 629–634.

5 J. W. Dally, A. J. Durelli, and W. F. Riley, "Photoelastic Study of Stress Wave Propagation in Large Plates," *Proceedings of SESA*, vol. 17, 1960, pp. 33–50.

G. V. PARKINSON
Associate Professor of Mechanical Engineering, University of British Columbia, Vancouver, B. C., Canada. Mem. ASME

N. P. H. BROOKS
Graduate Student, Department of Mechanical Engineering, University of British Columbia, Vancouver, B. C., Canada

On the Aeroelastic Instability of Bluff Cylinders

The validity of quasi-steady theory, using experimental aerodynamic coefficients, to explain the observed aeroelastic instability of bluff cylinders in a uniform stream is examined for several cylinder sections. Only plunging oscillation is considered, and the analytical model is an oscillator with nonlinear damping dependent on the aerodynamic coefficients. Static and dynamic wind-tunnel tests were made of cylinder models of square, rectangular, and D-section. The D-section and the short rectangular sections behaved dynamically like the circular cylinder, showing plunge instability only near resonance with the von Karman vortex street. In complete contrast, the square and long rectangular sections showed plunge instability with amplitude increasing with wind speed for all speeds above a critical value. These dynamic results were in quite good agreement with the theoretical predictions, using the static test data.

This paper examines the applicability of quasi-steady theory, using experimental aerodynamic coefficients, to the observed aeroelastic instability of certain bluff cylinders in uniform transverse air streams. The phenomenon was known as early as 1907, when Lanchester [1][1] described his "aerial tourbillion," a semicircular or D-section cylinder, with flat face perpendicular to a uniform stream, which developed a steady rotation about an axis parallel to the stream when given an initial spin. In engineering practice, the phenomenon has been observed in the galloping of ice-laden transmission lines, the vibration of tall smokestacks, and catastrophically in the oscillation of the first Tacoma Narrows suspension bridge. No complete theory of the instability is available, mainly because there is no complete aerodynamic theory for any separated flow, particularly a nonstationary one.

[1] Numbers in brackets designate References at end of paper.

Presented at the Summer Conference of the Applied Mechanics Division, Chicago, Ill., June 14–16, 1961, of The American Society of Mechanical Engineers.

Discussion of this paper should be addressed to the Editorial Department, ASME, 29 West 39th Street, New York, N. Y., and will be accepted until July 10, 1961. Discussion received after the closing date will be returned. Manuscript received by ASME Applied Mechanics Division, July 7, 1960. Paper No. 61—APM-g.

Several semiempirical theories have been proposed, however, and some have gained fairly general acceptance. For circular cylinders, the source of the observed instability must be the fluctuating nature of the wake, whether organized as a Karman vortex street [2] or random [3]. For sections capable of combined plunging and twisting oscillation, linear flutter theories have been proposed by various authors [4, 5, 6].

For noncircular sections constrained to plunging oscillation, the instability criterion proposed by Den Hartog [7] has been used. He states: "a section is dynamically unstable if the negative slope of the lift curve is greater than the ordinate of the drag curve," the aerodynamic data being obtained from static wind-tunnel tests. Steinman [8] has taken a similar approach in his theory of suspension-bridge oscillations. A theory using stationary aerodynamic coefficients to determine the aerodynamic forces acting on a vibrating body is usually called quasi-steady, and in the present paper this approach leads to a motion governed by a nonlinear differential equation with a small damping term, which can be solved readily.

Theory

Fig. 1 shows the geometry of a vibrating cylinder section in a uniform flow, assumed two dimensional. The elastic mounting is assumed to be linear, and the nonaerodynamic damping

Nomenclature

y = lateral displacement of vibrating cylinder
h = lateral dimension of cylinder section
s = length of cylinder
m = mass of vibrating system
r = coefficient of viscous damping of vibrating system
k = spring constant of vibrating system
t = time
$(\dot{})$ = time derivative
q = $(k/m)^{1/2}$ = circular frequency of free undamped oscillation of system
V = air velocity
α = angle of attack of relative wind to cylinder section = $\tan^{-1}(\dot{y}/V)$
V_{rel} = air velocity relative to vibrating cylinder
ρ = air density
p = aerodynamic pressure on cylinder relative to free-stream value as datum
L = aerodynamic lift on cylinder
D = aerodynamic drag on cylinder
F_y = lateral component of aerodynamic force on cylinder
$C_p = \dfrac{p}{(\rho/2)V_{rel}^2}$ = pressure coefficient
$C_L = \dfrac{L}{(\rho/2)V_{rel}^2hs}$ = lift coefficient
$C_D = \dfrac{D}{(\rho/2)V_{rel}^2hs}$ = drag coefficient
$C_{F_y} = \dfrac{F_y}{(\rho/2)V^2hs}$ = lateral force coefficient
a_1, a_3 = coefficients of polynomial approximation to C_L versus α-curve

(Continued on next page)

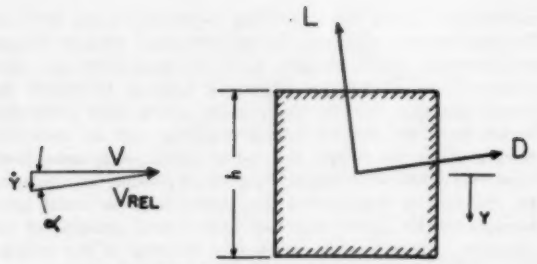

Fig. 1 Cylinder section and flow geometry

viscous. Accordingly, the equation of motion of the cylinder is

$$m\ddot{y} + r\dot{y} - F_y + ky = 0 \tag{1}$$

where m, r, and k are constant, and

$$F_y = C_{F_y} \frac{\rho}{2} hs V^2$$

is the lateral component of the instantaneous aerodynamic force on the cylinder. This force is assumed to be given by lift and drag components L and D corresponding to a relative wind of velocity V_{rel} at angle of attack $\alpha = \tan^{-1}(\dot{y}/V)$, as shown in Fig. 1, and with values as determined by static wind-tunnel tests at the same α. It follows that

$$C_{F_y} = -(C_L + C_D \tan \alpha) \sec \alpha \tag{2}$$

where

$$L = C_L \frac{\rho}{2} hs V_{rel}^2, \quad D = C_D \frac{\rho}{2} hs V_{rel}^2$$

The experimental curves of C_L and C_D versus α can be approximated by polynomials. All of the sections considered here are symmetrical about an axis in the stream direction, and accordingly C_L is an odd function of α, and C_D an even function. The later calculations are simplified if the C_L polynomial is of the fifth power or less, and the C_D polynomial of the fourth power or less. In fact, the polynomials used are

$$C_L = -a_1\alpha + a_3\alpha^3 \tag{3}$$

$$C_D = b_0 - b_2\alpha^2 + b_4\alpha^4 \tag{4}$$

Equations (3) and (4) are substituted in equation (2), α is replaced by $\tan^{-1}(\dot{y}/V)$, and the resulting expression is expanded in powers of $(\dot{y}/V)$. Terms beyond $(\dot{y}/V)^5$ are neglected, and the result is

$$C_{F_y} = A\left(\frac{y}{V}\right) - B\left(\frac{y}{V}\right)^3 - C\left(\frac{\dot{y}}{V}\right)^5 \tag{5}$$

where

$$A = a_1 - b_0 \tag{6}$$

$$B = a_3 - b_2 - \frac{a_1}{6} + \frac{b_0}{2} \tag{7}$$

$$C = b_4 - \frac{a_3}{2} + \frac{b_2}{6} + \frac{11a_1}{120} - \frac{b_0}{8} \tag{8}$$

Equation (5) is substituted into equation (1), dimensionless variables and parameters are introduced as defined under Nomenclature, and the equation of motion becomes

$$\ddot{Y} - \epsilon(1 - P\dot{Y}^2 - Q\dot{Y}^4)\dot{Y} + Y = 0 \tag{9}$$

With $Q = 0$, equation (9) reduces to Rayleigh's equation [9]. If ϵ, P, and Q are all positive, equation (9) gives a build-up of oscillation from rest to a steady-state amplitude, and if they are all negative, any oscillatory disturbance is damped out. Examination of the definitions of ϵ, P, and Q reveals the significance of this. U and n are positive, and B and C are either positive or zero for the sections considered later. Therefore, if $U > U_0$, corresponding to the aerodynamic forces being large enough to overcome the structural damping, the stability is determined by the sign of A, which is seen to be simply Den Hartog's criterion.

In the present problem ϵ is a very small number, and as a result, equation (9) is readily solved by the method of Krylov and Bogoliubov [10]. If a solution is assumed in the form

$$Y = \bar{Y} \sin (T + \vartheta) \tag{10}$$

the fact that ϵ is small leads to the result that $\bar{Y}$ is a slowly varying function of T, and ϑ is constant to the first order in ϵ. The solution for $\bar{Y}(T)$ is obtained without difficulty (Appendix), and appears in the form:

$$\epsilon T = \ln \left[\frac{\bar{Y}^2}{\bar{Y}_0^2} \left(\frac{\bar{Y}_s^2 - \bar{Y}^2}{\bar{Y}_s^2 - \bar{Y}_0^2} \right)^{\frac{\bar{Y}_s^2}{\bar{Y}_s^2 - \bar{Y}_i^2}} \left(\frac{\bar{Y}^2 - \bar{Y}_i^2}{\bar{Y}_0^2 - \bar{Y}_i^2} \right)^{\frac{-\bar{Y}_i^2}{\bar{Y}_s^2 - \bar{Y}_i^2}} \right] \tag{11}$$

where

$$\bar{Y}_s^2, \bar{Y}_i^2 = U^2 \left\{ -\frac{3B}{5C} \pm \left[\left(\frac{3B}{5C} \right)^2 + \frac{8A}{5C} \left(1 - \frac{U_0}{U} \right) \right]^{1/2} \right\} \tag{12}$$

Once the polynomial approximations to $C_L(\alpha)$ and $C_D(\alpha)$

Nomenclature

b_0, b_2, b_4 = coefficients of polynomial approximation to C_D versus α-curve
A, B, C = coefficients of polynomial approximation to C_{F_y}
$T = qt$ = dimensionless time variable
$(')$ = derivative with respect to T
$Y = y/h$ = dimensionless vibration displacement
$\bar{Y}$ = dimensionless vibration amplitude
$(\ )_0$ = initial value
$(\ )_s$ = steady-state value
$\bar{Y}_i$ = imaginary root of amplitude equation
$U = \dfrac{V}{qh}$ = dimensionless air velocity
$\beta = \dfrac{r}{2mq}$ = dimensionless viscous damping coefficient
$n = \dfrac{\rho h^2 s}{2m}$ = dimensionless mass parameter
$U_0 = \dfrac{2\beta}{nA}$ = critical air velocity
$\epsilon = nA(U - U_0)$, $P = \dfrac{B}{AU(U - U_0)}$, $Q = \dfrac{C}{AU^4(U - U_0)}$ = parameters of nonlinear damping term in vibration equation
d = longitudinal dimension of rectangular cylinder section
f = vortex shedding frequency, cps
$S = fh/V$ = Strouhal number

have been determined, A, B, and C are given by equations (6–8). $U_0 = (2\beta/nA)$ can then be determined from the known constants of the system, and from measurement of the nonaerodynamic damping coefficient β, which is proportional to the logarithmic decrement of the system in the absence of aerodynamic forces. The dimensionless stationary vibration amplitude $\bar{Y}_s$ can then be found as a function of dimensionless air velocity U from equation (12). The amplitude-time relation, equation (11), requires an additional parameter, the initial amplitude $\bar{Y}_0$. This is estimated from the decay record used to determine β, by considering the damping to be partially coulomb, to account for the finite decay period. The amount is too small to influence the viscous coefficient appreciably, but it indicates initial amplitudes needed for build-up to occur. $\bar{Y}(T)$ can then be found from equation (11), as can T_s, defined as T for $\bar{Y} = 0.99\bar{Y}_s$.

For one of the test conditions examined later, b_4 can be taken as zero in equation (4), because of the limited range of α. Accordingly, C can be taken as zero in equation (5), and Q in equation (9). This simplifies the solution for $\bar{Y}(T)$, which becomes (Appendix):

$$\epsilon T = 2 \ln \left[\frac{\bar{Y}_s}{\bar{Y}_0} \tan \sin^{-1} \left(\frac{\bar{Y}}{\bar{Y}_s} \right) \right] \tag{13}$$

where

$$\bar{Y}_s = U \left[\frac{4A}{3B} \left(1 - \frac{U_0}{U} \right) \right]^{1/2} \tag{14}$$

Experimental Method

The experimental data of this paper were obtained in the low-speed wind tunnel of the Mechanical Engineering Department of the University of British Columbia. The test section of this tunnel is 104 in. long, 36 in. wide, and 27 in. high, and the cylinders were mounted vertically at the center of the principal cross section.

The aerodynamic coefficients were determined from pressure distributions measured on fixed cylinders. (Shear stresses are too small to require consideration in these bluff-cylinder flows.) Cylinder sections tested were a 2-in. D-section, a 2-in. by 2-in. square, and a 2-in. by 1-in. rectangle. The D-section cylinder was of hardwood with a brass center section containing the pressure taps. The other cylinders were of aluminum and brass. They passed through sealed holes in the floor and ceiling of the tunnel, and were long enough that the spanwise variation of pressure could be measured by shifting the relative position of the brass section. No appreciable variation was noted in the tests, and the results are therefore considered to represent two-dimensional flow conditions. Pressures were measured individually on an alcohol micromanometer, using a switching board, and C_p values were determined in the usual way. C_p-distributions over each section were obtained in this manner for a range of α, with increments of 1, 2, or 5 deg. C_L and C_D were determined for each α by graphical integration. Each cylinder was tested at a constant Reynolds number, either 33,000 or 66,000, considerably higher than the Reynolds-number range for the dynamic tests. This is felt to be unimportant, however, in view of the negligible Reynolds-number effects generally observed for bluff cylinders with well-defined separation points at sharp edges. The data were not corrected for tunnel-wall effects, except for comparison with other published data.

Dynamic tests were made on vertical balsa cylinders suspended by four light horizontal coil springs in the plane of the tunnel cross section. Sections tested included rectangles with $h = 1$ in. and various values of d from $^1/_2$ in. to 2 in., a 2-in. D-section, and a 1.9-in. circular cylinder. Clearances between the cylinder ends and the tunnel floor and ceiling varied from $^1/_8$ in. to $^1/_4$ in. The same springs were used for all tests, and cylinder natural frequencies for lateral plunging lay in the range 8–10 cps. The cylinders were allowed six degrees of freedom to reduce the system damping, but the only modes which were detectably excited were the desired lateral plunging and an undesired twisting about the stream axis, which appeared in some tests. These two modes were separated as far as possible by weighting the cylinders at their mid-section, and, except as noted later, the data in the figures represent pure lateral plunging of the cylinders. There was no evidence of twisting of the cylinder section (the motion in all tests was observed with a stroboscopic tachometer), so that flutter was not a mechanism in these tests.

The dynamic test conditions were not exactly two-dimensional, because of the end clearances and the presence of the mounting springs in the air stream. However, preliminary trials had indicated this arrangement was better than mounting the elastic system externally, because of the considerable effects of the holes through which the vibrating cylinders had to extend.

All dynamic models were tested through a wide range of air velocities, and the mode, amplitude, and frequency of oscillation from rest at each velocity were recorded. In a few tests, the models were given an initial amplitude. Transient amplitude-time records of the vibration build-up were obtained by mounting on the cylinder a light metal strip which extended through a narrow slot in the tunnel ceiling. This strip blocked the light of a lamp from a long photocell which had been masked so that lateral displacement of the strip produced a linear response in a pen recorder in the photocell circuit.

For all of the cylinders tested, both at rest and in oscillation, hot-wire measurements were made in the wake to determine vortex-shedding frequencies as functions of air velocity. Measurements were made by comparing the hot-wire output with that of an audio oscillator in the form of Lissajous figures on an oscilloscope.

One series of tests was made on the 1-in. square cylinder with increased damping in the form of a transverse oil trough mounted flush in the tunnel floor with a thin metal plate fixed to the cylinder immersed in the oil.

Results

The first series of tests was made on the D-section, because of its wide use as an example of Den Hartog's criterion of bluff-cylinder instability. Preliminary wind-tunnel tests on dynamic models, however, revealed instability only for certain limited ranges of air velocity, and the two-dimensional pressure tests were accordingly carried out to see if the criterion actually was satisfied for the D-section. Fig. 2 shows a representative selection of the pressure-distribution curves. It is seen that

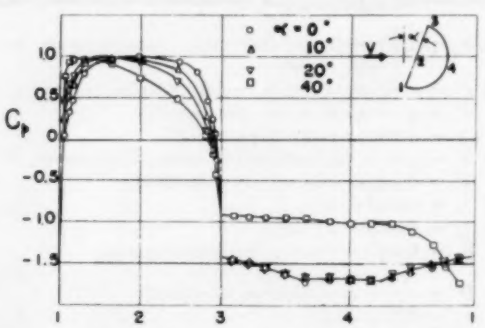

Fig. 2 Pressure distributions for D-section cylinder. Reynolds number 66,000.

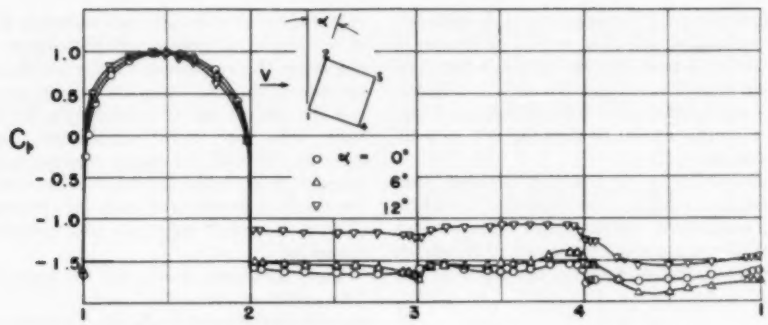

Fig. 3 Pressure distributions for square cylinder. Reynolds number 66,000.

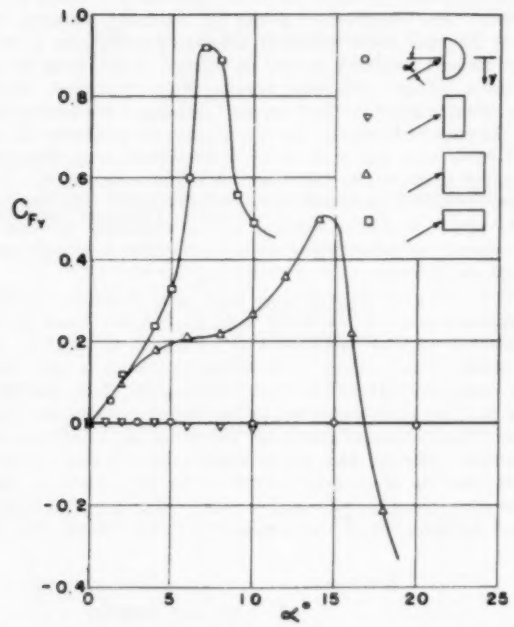

Fig. 4 Lateral aerodynamic force coefficients. Reynolds numbers 66,000 (○, ▽, △) and 33,000 (□).

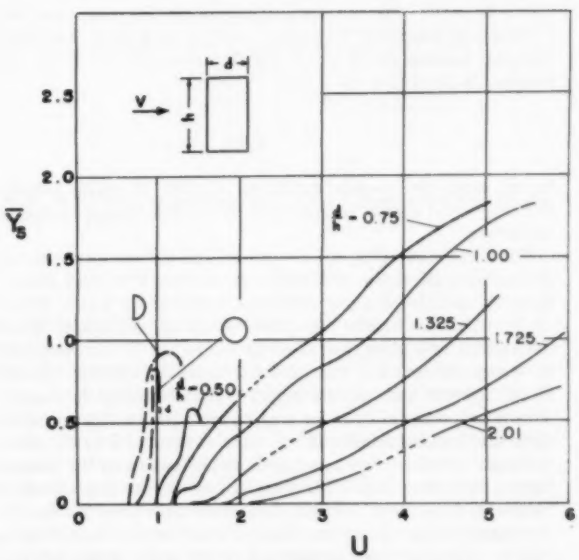

Fig. 5 Experimental curves of dimensionless steady-state plunge amplitude versus dimensionless air velocity for several cylinders

the wake underpressure on the cylindrical afterbody is almost exactly symmetrical up to $\alpha = 20$ deg. A pronounced suction peak, corresponding to the streamline pattern suggested by Den Hartog,[2] does not occur until about $\alpha = 40$ deg. Now, so long as the pressure on the afterbody is symmetrical with respect to the symmetry axis of the cylinder section, there is no lateral force on the cylinder, and it is neutrally stable with respect to the quasi-steady aerodynamic forces. In the present notation,

$$(dC_{F_y}/d\alpha) = 0$$

for small α, and $A = 0$. These results for the D-section are in good agreement with those of Cheers,[3] from direct force measurements, which indicate a very small negative (i.e., stable) value of A. Cheers' data were taken only at intervals of 10 deg in α.

Shortly after these results were obtained, Mr. C. Scruton of The National Physical Laboratory in England informed the senior author of tests he had performed on cylinders of square section, which were found to satisfy Den Hartog's criterion for instability. Of the results of these tests, the static measurements of $C_L(\alpha)$ and $C_D(\alpha)$ are reported in [11], and a stability diagram from dynamic tests is reported in [12]. It was therefore decided to test a series of rectangular sections with sharp edges, including the square, for which a selection of the measured pressure distributions is presented in Fig. 3. It is seen that an increasing asymmetry in the underpressure on the afterbody develops with increasing α, and in the direction for instability. These results are best summarized by a plot of C_{F_y} versus α, which is given in Fig. 4 for the D-section, the square, and the 2 by 1 rectangle (tested both with the long dimension across the stream and along it). Both the D-section and the rectangle with $d/h = 1/2$ show completely neutral stability up to $\alpha = 20$ deg, because of the previously mentioned symmetry of the wake underpressure. On the other hand, the square shows strong instability up to $\alpha = 14$ deg, and the rectangle with $d/h = 2$ shows even stronger instability up to $\alpha = 7$ deg.

The next objective was to correlate these results with dynamic tests, and results for some of the models mentioned previously are shown in Fig. 5, which gives curves of dimensionless plunging

[2] Reference [7], p. 301.
[3] Reference [4], fig. 13.

amplitude versus dimensionless air velocity for each cylinder. The behavior of the rectangles with $d/h = 0.75$ or greater is seen to be strikingly different from that of the short rectangle or the D-section, which behave much like the circular cylinder. (Three other short rectangles, with $d/h = 0.375$, 0.656, and 0.583, were tested, and gave results similar to that for $d/h = 0.50$. These results are omitted for clarity.)

Several features of the results in Fig. 5 should be noted. For all of the cylinders but the D-section, the value of U at which plunging oscillation commenced corresponded closely with resonance between the plunging natural frequency of the elastic system and the stationary vortex-shedding frequency of the cylinder; i.e.,

$$U = U_0 \triangleq \frac{1}{2\pi \mathbf{S}}$$

where $\mathbf{S} = fh/V$ is the stationary-cylinder Strouhal number, f being the shedding frequency in cps. For the D-section, plunging commenced at about half the above value of U, and reached its maximum at

$$U \triangleq \frac{1}{2\pi \mathbf{S}}$$

In all cases the models oscillated at their plunging natural frequency, and vortex shedding occurred at this frequency during oscillation.

The short rectangles, the D-section, and the circular cylinder all reached peak plunge amplitudes at values of U slightly greater than U_0, and the plunging oscillation subsided for higher values of U. The previously mentioned torsional oscillation about the stream axis then developed at values of U corresponding to resonance between the torsional natural frequency of the elastic system and the stationary vortex-shedding frequency. This is proportional to U for a given cylinder with sharp edges, since the Strouhal number is constant. Values of $\mathbf{S}$ for the short rectangle and D-section agree with values measured by Roshko for the flat plate [13]. The torsional mode died out at higher values of U, and no further oscillations developed within the test range of air velocities. The torsional data are omitted in Fig. 5. Clearly, these oscillations of the short rectangles and the D-section can be considered vortex-excited, just as for the circular cylinder.

The plunge amplitude of the rectangles with $d/h = 0.75$ or greater in each case increased with U up to the test limits (caused by limitations on the elastic system). For three of the cylinders there were short ranges of U in which the undesired torsional mode would develop from rest, although plunging (shown by dotted lines in Fig. 5) could be obtained by adjusting U into this range while the model was already plunging at another value of U.

The fact that the start of oscillation corresponded to resonance with vortex shedding of course suggests that this is also the mechanism of excitation for these longer rectangles. However, Scruton's previously mentioned stability diagram for the square cylinder showed that this behavior occurred only if the non-aerodynamic damping was very low, as was the case here. For somewhat higher damping, a small vortex-excited plunge would occur for a short range of U, followed by a range with no oscillation. Then, the type of plunge shown for the square cylinder in Fig. 5 would begin at some larger value of U, unrelated to vortex shedding. This was investigated by introducing the viscous oil damper mentioned earlier into a further series of tests on the square cylinder, and general agreement with Scruton's result was obtained.

The results for the square cylinder were used to investigate the validity of the quasi-steady theory. The experimental values of $C_L(\alpha)$ and $C_D(\alpha)$ are plotted in Fig. 6 as are the curves of two sets of polynomial approximations. The solid curves approximate the conditions for the oscillation in the absence of the viscous damper, when the amplitudes were relatively large, and the dashed curves approximate the highly damped conditions, with their lower amplitudes. The experimental data agree closely with the values reported in [11]. The method of calculation of stationary amplitudes was outlined earlier, and the results are compared with the experimental data in Fig. 7. (Values of system constants and coefficients are given in the Appendix.)

Good agreement is seen for the example with low damping. The agreement on initial values of U is fortuitous, since the experimental start of oscillation is determined by vortex shedding (note the arrow in Fig. 7) and not by damping, as in the theory. However, the good agreement over the whole range of U is interesting, since no use is made of the dynamic test data in the theory. The experimental points for the highly damped test show the small vortex excitation mentioned earlier near $U = 1$, and then no oscillation is evident until $U = 4.3$, when an increasing plunge oscillation begins. Two theoretical curves are shown in Fig. 7 for this example. The upper one corresponds to the measured value of the viscous damping coefficient β, and the lower to a higher value of β determined from Scruton's stability diagram for the observed initial value of U. The experimental points lie between these two curves. It is probable that actual structural damping during oscillation was higher because of extraneous vibrations than the value measured under quiet conditions.

Calculation of the amplitude-time curve requires an initial amplitude, and this was taken to be $\hat{Y}_0 = 0.003$, based on the estimated coulomb component of structural damping in the measured decay curves. Theoretical curves using this value are compared with results from experimental chart records in Fig. 8. Fair agreement is seen for the example with low damping. Again two theoretical curves are shown for the highly damped example. The one using the measured value of β does not agree well with the chart data, except in the total build-up time. The other, using the same higher value of β used in Fig. 7, gives good agreement if $\hat{Y}_0$ is increased to 0.064. Again, the un-

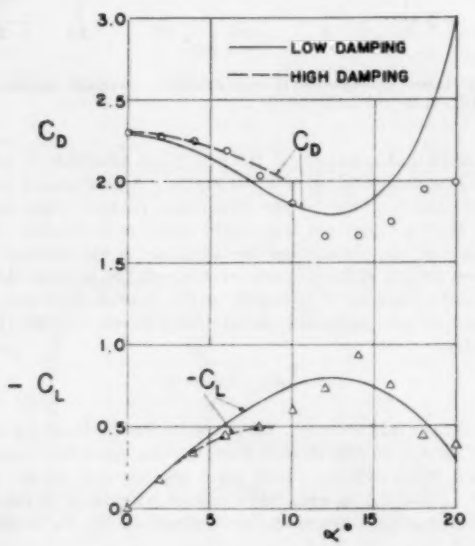

Fig. 6 Polynomial approximating curves to $C_L(\alpha)$ and $C_D(\alpha)$ for square section. Test data at Reynolds number = 66,000.

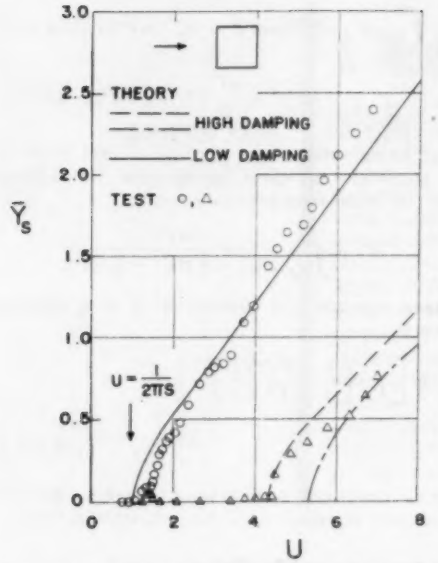

Fig. 7 Dimensionless steady-state plunge amplitude versus dimensionless air velocity for square cylinder

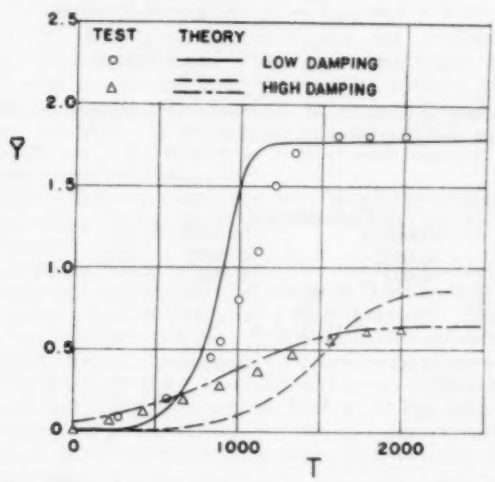

Fig. 8 Dimensionless plunge amplitude versus dimensionless time for square cylinder. (○, ———), $U = 5.64$; (△, – – –, – · – · –) $U = 6.74$

certainty of the actual amount of structural damping during oscillation is pointed out.

Finally, in Fig. 9 theoretical and experimental build-up times are compared, using only the measured values of β and $\bar{Y}_0 = 0.003$. Good agreement is seen in both examples, except for the points at the lowest values of U in the low-damping example. These presumably represent the times for the initial vortex-excited build-up.

Discussion

It is recognized that a quasi-steady theory for the oscillation of a bluff cylinder cannot represent conditions accurately, because the instantaneous geometry and immediate past history of the wake are different for the oscillating cylinder and its static counterpart, and the important forces are largely determined

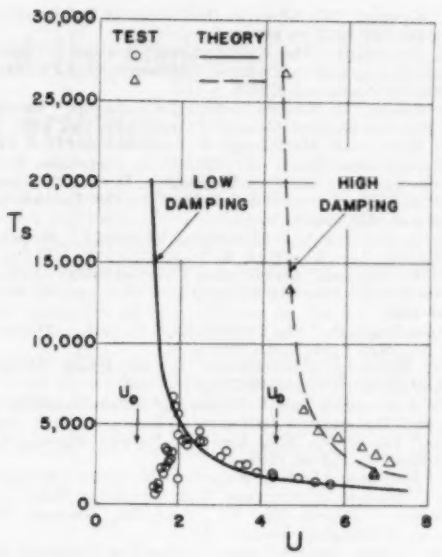

Fig. 9 Dimensionless build-up time versus dimensionless air velocity for square cylinder

by the wake characteristics. However, the foregoing results suggest that the theory can be of some use, since Den Hartog's criterion appears to discriminate between different forms of excitation. Cylinders with neutral or positive stability ($A \leq 0$) oscillate under vortex excitation, while unstable cylinders ($A > 0$) exhibit plunging oscillation similar to that predicted by the theory.

The D-section and the short rectangles are neutrally stable because of the symmetry of the pressure distribution on their afterbodies. It is probable that this effect is closely related to the length of the afterbodies. Roshko[4] infers from measurements in the wake of a two-dimensional flat plate that the actual formation of vortexes from the separation shear layers takes place about two plate widths downstream. Short cylinder afterbodies would not interfere appreciably with this process, but long ones would inhibit the vortex formation and would produce asymmetries in the time-average wake pressures when the cylinder sections were at small angles of attack.

Finally, it should be pointed out that the foregoing theory applies only to plunging oscillation from rest. It does not rule out the possibility of flutter instability of the D-section, if suitably mounted elastically, or of autorotation, as in Lanchester's aerial tourbillion, in which the initial spin puts the section into the α-range for instability. Also, on cylinders of short axial length, three-dimensional flow effects seem to be important, and no attempt has been made to account for these.

Acknowledgments

The investigation reported here forms part of a continuing program supported by grants from the Canadian National Research Council. The experimental phase was carried out by the junior author as part of his master's thesis program.

References

1 F. W. Lanchester, "Aerodynamics," Constable, London, England, 1907, p. 44.

[4] Reference [13], p. 6.

2 C. Scruton, "Wind-Excited Oscillations of Tall Stacks," *The Engineer*, vol. 199, 1955, pp. 806–808.
3 A. Davenport, "The Wind-Induced Vibration of Guyed and Self-Supporting Cylindrical Columns," *Transactions of The Engineering Institute of Canada*, vol. 3, 1959, p. 119.
4 F. Cheers, "A Note on Galloping Conductors," Report No. MT-14, National Research Council of Canada, Ottawa, 1950.
5 F. Bleich, C. B. McCullough, R. Rosecrans, and G. S. Vincent, "The Mathematical Theory of Vibration in Suspension Bridges," U. S. Department of Commerce, Washington, D. C., 1950, chapter 7.
6 F. Rocard, "Dynamic Instability," Crosby Lockwood, London, England, 1957, chapter 6.
7 J. P. Den Hartog, "Mechanical Vibrations," McGraw-Hill Book Company, Inc., New York, N. Y., fourth edition, 1956, p. 299.
8 D. B. Steinman, "Aerodynamic Theory of Bridge Oscillations," *Transactions of The American Society of Civil Engineers*, vol. 115, 1950, pp. 1180–1260.
9 Lord Rayleigh, "The Theory of Sound," vol. 1, Dover Publications, Inc., New York, N. Y., 1945, p. 79.
10 N. Minorsky, "Introduction to Non-Linear Mechanics," Edwards, Ann Arbor, Mich., 1947, pp. 186–188.
11 C. F. Cowdrey and J. A. Lawes, "Force Measurements on Square and Dodecagonal Sectional Cylinders at High Reynolds Numbers," Report No. NPL/Aero/351, National Physical Laboratory, Teddington, August, 1959.
12 C. Scruton and D. E. J. Walshe, "A Means for Avoiding Wind-Excited Oscillations of Structures With Circular or Nearly Circular Cross-Section," Report No. NPL/Aero/335, National Physical Laboratory, Teddington, October, 1957.
13 A. Roshko, "On the Drag and Shedding Frequency of Two-Dimensional Bluff Bodies," NACA TN 3169, July, 1954.

APPENDIX

Solution for $\bar{Y}(T)$

It is shown in [10],[5] that substitution of equation (10) into equation (9) leads to the equation for $\hat{Y}$:

$$\dot{\hat{Y}} = \frac{\epsilon}{2\pi}\int_0^{2\pi}(1 - P\hat{Y}^2\cos^2\vartheta - Q\hat{Y}^4\cos^4\vartheta)\hat{Y}\cos^2\vartheta\,d\vartheta$$

$$= \frac{\epsilon\hat{Y}}{2}\left\{1 - \tfrac{3}{4}P\hat{Y}^2 - \tfrac{5}{8}Q\hat{Y}^4\right\} \quad (15)$$

Equating the right side of equation (15) to zero yields the stationary amplitudes, as given by equation (12). Integrating equation (15) in the form

$$\epsilon T = \int_{\hat{Y}_0^2}^{\hat{Y}^2}\frac{d\hat{Y}^2}{\hat{Y}^2(1 - \frac{3}{4}P\hat{Y}^2 - \frac{5}{8}Q\hat{Y}^4)} \quad (16)$$

one obtains equation (11) directly. If $Q = 0$, equation (16) integrates to

$$\epsilon T = 2\ln\left[\frac{\hat{Y}}{\hat{Y}_0}\left(\frac{1 - \hat{Y}_0^2/\hat{Y}_s^2}{1 - \hat{Y}^2/\hat{Y}_s^2}\right)^{1/2}\right]$$

$$\doteq 2\ln\left[\frac{\hat{Y}/\hat{Y}_0}{(1 - \hat{Y}^2/\hat{Y}_s^2)^{1/2}}\right] \quad (17)$$

because $\hat{Y}_0^2$ is negligibly small in usual examples. Equation (17) is conveniently expressed in the form of equation (13).

System Constants and Coefficients

Air density $\rho = 0.00230$ slug/cu ft. For the square cylinder:

$$h = 1.00 \text{ in.}, \; s = 26.5 \text{ in.}, \; q = 55.6 \text{ rad/sec}$$

$$m = 0.0192 \text{ slug}, \; n = \frac{\rho h^2 s}{2m} = 0.000922$$

Measured and calculated constants and coefficients for Figs. 6, 7, 8, and 9 are given in Table 1.

Table 1

Item	Low damping	High damping	
		Measured	Inferred
β	0.00152	0.0062	0.0077
$\hat{Y}_0$	0.003	0.003	0.064
a_1, a_2	5.40, 37.8	5.40, 101	
b_0, b_2, b_4	2.29, 21.2, 223	2.29, 10.2, 0	
A, B, C	3.11, 16.8, 208	3.11, 91.0, 0	
$U_0 = \frac{2\beta}{nA}$	1.06	4.33	5.36
U for Fig. 8	5.64	6.74	

[5] Reference [10], pp. 186–188.

A Modification of the Coulomb-Mohr Theory of Fracture[1]

BURTON PAUL
Technik, Inc.,
Garden City, N. Y.
Assoc. Mem. ASME

The inability of the Coulomb-Mohr theory of fracture to explain the main features of compression, tension, and torsion tests on brittle materials is pointed out. It is shown that the introduction of suitably chosen tension cut-offs and "friction angles" removes this deficiency and leads to a satisfactory explanation of the fracture stresses and angles of fracture for these three simple tests. The modified Coulomb-Mohr theory is a three-parameter theory, but all three parameters in principle can be obtained from only two simple tests. It is shown that in the case of cast iron there is an extremely close relationship between cohesive resistance in shear and nominal ultimate strength in single or double shear. The modified theory fits the data of Coffin, Cornet, and Grassi on biaxial fracture of cast iron very well. The three-dimensional fracture surface is described and used to explain some apparently anomalous points in the experimental data. Finally, a hypothesis is advanced which explains the appearance of concavities in the yield locus for certain classes of materials.

1 Introduction

It is generally accepted today that virgin ductile metals will begin yielding when either the maximum shear stress or maximum octahedral shear stress reaches a critical value. These two theories of yielding alone (out of many theories proposed throughout the years) have been well verified experimentally within the rather broad limits of error considered acceptable for such theories.

Unfortunately, the controversy over the correct phenomenological criterion of fracture for intrinsically brittle materials still continues.

The phrase "intrinsically brittle" will be used in this paper to describe materials which fail by cleavage in both tension tests and torsion tests, with very little plastic flow prior to failure. We exclude from discussion such phenomena as the notch embrittlement of otherwise ductile metals, fatigue fractures, and fracture after considerable plastic flow. We shall further restrict our considerations to that wide class of materials such as cast iron, concrete, limestone, and so on, which in addition to being intrinsically brittle are known to fracture along oblique planes in simple compression tests.

It is recognized of course that the criterion of fracture is superseded by a criterion of yielding for states of stress where the mean normal stress is highly compressive. This fact has been amply demonstrated by the high-pressure experiments of Bridgman [1],[2] Karman, Böker, and others [2, 3].[3] This paper shall be concerned only with criteria of *fracture*, not of *yielding* under high pressures. Among the numerous theories which have been advanced to explain the nature of fracture for those states of stress well removed from pure hydrostatic compression are those based upon limiting values of strain, energy consumption, and minute imperfections. Also proposed have been theories based upon one or more of the following stress variables: Maximum normal stress, maximum shear stress, octahedral shear stress, combinations of shear and normal stress, and others.

Unfortunately, most of the foregoing theories can only predict the occurrence of fracture over a very limited range of possible stress states. Furthermore, they all suffer from the deficiency that they cannot adequately explain the angles of obliquity observed in many fractured specimens. Finally, the theories advanced to date cannot satisfactorily correlate the observed stresses and angles of fracture for the three most common tests in the strength-of-materials laboratory; viz., the simple tension, torsion, and compression tests.

In order to explain the presence of oblique fractures observed in compression tests on masonry cylinders, Coulomb [4, 5] proposed that failure occurs when the shearing stress reaches the cohesive resistance in shear S_s of the material. In order to describe the observed angle which the fractured plane made with the axis of the specimen Coulomb introduced another parameter, the so-called coefficient of friction μ.

Although Coulomb made the dubious assumption that the cohesive resistance in shear S_s is equal to the ultimate strength in tension S_t, the predicted angle of the fractured plane depends only on the parameter μ and is unaffected by this assumption. In any case, Coulomb's theory for compression involves two material constants, S_s and μ, both of which can be obtained in a uniaxial compression test.

If Coulomb's theory is generalized to arbitrary states of stress, where σ and τ represent normal stress and shear stress, respectively, on a generic plane, it takes the form

$$(|\tau| + \mu\sigma)_{\max} = (T)_{\max} = S_s \tag{1}$$

In equation (1) the quantity $|\tau| + \mu\sigma$, which we shall henceforth speak of as a virtual shear stress, is given the symbol T. T is uniquely defined for each plane passing through a given point where the state of stress is specified.

Equation (1) is a specialization of the more general relationship:

$$\text{Function of } (|\tau|, \sigma) = \text{const} \tag{2}$$

[1] This paper was prepared at Brown University under the sponsorship of the U. S. Army Ordnance Corps, Office of Ordnance Research.

[2] Numbers in brackets designate References at end of paper.

[3] References [2] and [3] summarize a great deal of the available data on brittle fracture and contain numerous other References.

Contributed by the Applied Mechanics Division and presented at the Winter Annual Meeting, New York, N. Y., November 27–December 2, 1960, of The American Society of Mechanical Engineers.

Discussion of this paper should be addressed to the Editorial Department, ASME, 29 West 39th Street, New York, N. Y., and will be accepted until July 10, 1961. Discussion received after the closing date will be returned. Manuscript received by ASME Applied Mechanics Division, April 19, 1960. Paper No. 60—WA-31.

Equation (2) has been interpreted physically to represent the envelope of all sets of three-dimensional Mohr's circles which can be drawn for a given material at the state of incipient failure. Equation (2) therefore defines a general criterion of failure known as Mohr's theory of failure [20, 2, p. 215]. Equation (1) and its underlying concepts will therefore be referred to in this paper as the Coulomb-Mohr theory of fracture.

Among all the phenomenological theories of fracture which have been proposed, it appears to the author that the Coulomb-Mohr theory has been gaining the widest circle of adherents among engineers and perhaps geologists, in recent years. At least it would appear so if one examines the latest edition of Timoshenko [6], Nadai [2], and the works of Soderberg [7] and Jaeger [8]. Therefore it would be well to determine just how closely this theory fits the available experimental evidence.

In the following section a geometric derivation is given for the quantitative expression of the Coulomb-Mohr theory of fracture. In Section 3 the basic shortcomings of the theory are pointed out with specific reference to the simple tension, torsion, and compression tests. It is also shown how a direct shear test may, in certain cases, be used to obtain one of the required material constants. In Section 4 a simple modification of the theory is proposed which removes the shortcomings previously noted. In Section 5 it is shown how well the modified theory fits the extensive experimental data on cast iron of Grassi and Cornet [9, 10] and Coffin [11], for biaxial states of stress. In Section 6 the nature of the proposed theory is explored for general three-dimensional states of stress, and it is shown how some of the apparently inconsistent experimental data can be explained by the three-dimensional theory. Conclusions are stated in Section 7, and a tentative hypothesis which would explain the appearance of concavities in the fracture locus, under certain circumstances, is discussed in the Appendix. The appearance of such concavities affords a striking contrast with the necessarily convex yield loci of ductile metals [22].

2 A Geometric Interpretation of Coulomb-Mohr Theory

The normal stress σ, and shear stress τ acting on a given plane through a generic point in a stressed body can be expressed in terms of the three principal stresses σ_{I}, σ_{II}, σ_{III}, and the direction cosines of the normal to the given plane. Mohr's well-known graphical construction [2, p. 96] enables one to represent $|\tau|$ and σ as ordinate and abscissa, respectively, in a plane diagram, as indicated in Fig. 1. If the convention is adopted that $\sigma_{\mathrm{III}} \leqslant \sigma_{\mathrm{II}} \leqslant \sigma_{\mathrm{I}}$, the point $(\sigma, |\tau|)$ must fall within the cross-hatched region shown in Fig. 1. The directed distances OA, OB, OC represent to a suitable scale the principal stresses σ_{I}, σ_{II}, σ_{III}.

The virtual shear stress $T = |\tau| + \mu\sigma$ can be represented for any point in the $(\sigma, |\tau|)$-plane by a line segment, running parallel to the $|\tau|$-axis, from the point $(\sigma, |\tau|)$ to the line $O'O$. The line $O'O$ is to be drawn such that it makes an angle

$$\Phi = \arctan \mu \tag{3}$$

with the abscissa.

Obviously, for a given value of σ, such as at point P, the greatest value of T occurs for the point Q which lies on the largest principal circle; that is, the distance RQ represents the greatest virtual shear stress for all planes where the normal stress has magnitude $\sigma = OP$. Since the line segment RQ represents the largest value of T for a given value of σ, the maximum possible value of RQ must represent the largest virtual shear acting on any physical plane. The largest possible value of RQ is denoted by $R'Q'$ in Fig. 1. The point Q' is located where a line parallel to $O'O$ is tangent to the circle $AQ'C$, centered at D. Therefore the line $Q'D$ must be perpendicular to $O'O$ and intersect it at a point E. The Coulomb-Mohr theory of fracture requires that

$$T_{\max} = Q'R' = S_s$$

that is

$$\frac{ED + DQ'}{\cos \Phi} = \frac{OD \sin \Phi + DQ'}{\cos \Phi} = S_s$$

Since

$$OD = (\sigma_{\mathrm{I}} + \sigma_{\mathrm{III}})/2 \quad \text{and} \quad DQ' = (\sigma_{\mathrm{I}} - \sigma_{\mathrm{III}})/2$$

it follows that

$$\frac{\sigma_{\mathrm{I}}(1 + \sin \Phi)}{2 S_s \cos \Phi} - \frac{\sigma_{\mathrm{III}}(1 - \sin \Phi)}{2 S_s \cos \Phi} = 1 \tag{4}$$

Equation (4) is the basic analytical expression which describes the Coulomb-Mohr criterion of failure in terms of the two extreme principal stresses and the two material constants S_s and Φ.

If it is assumed that fracture occurs on that plane where T is maximum, Fig. 1 can be used to find the plane of fracture. The point Q' represents the image of that plane whose normal lies in the plane of the major and minor principal axes and makes an angle $\theta_1 = 1/2 \angle ADQ'$ with the major principal axis. The trace of the plane of fracture is indicated by a jagged line in Fig. 2(*a*). From the geometry of Fig. 1 it is evident that

$$\theta_1 = 45^\circ - \Phi/2 \tag{5}$$

It should be noted that the main features of the foregoing derivation are concerned only with the state of plane stress defined by σ_{I} and σ_{III}, and the corresponding largest circle in Fig. 1. In dealing with this circle it is meaningful to consider the lower half plane (not shown in Fig. 1) to be the domain of negative shear stress τ. Since the Coulomb-Mohr theory is only concerned with the absolute value of τ, the reflection of point Q' in the abscissa of Fig. 1 locates another point which satisfies the criterion of failure. This point corresponds to a plane whose normal makes an angle

$$\theta_2 = {}^1/_2(360^\circ - 2\theta_1)$$

with the major principal axis; that is,

$$\theta_2 = 180^\circ - \theta_1 = 135^\circ + \Phi/2 \tag{6}$$

The trace of this second fracture plane is indicated by the jagged line in Fig. 2(*b*) where it may be observed that the fracture plane is the reflection in the minor principal axis of the fracture plane shown in Fig. 2(*a*).

In summary, equations (5) and (6) state that the plane of fracture is always parallel to the intermediate principal axis, and

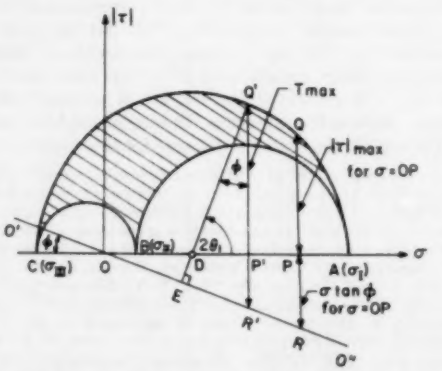

Fig. 1 Construction for Coulomb-Mohr theory

makes an angle of either $\pm(45° - \Phi/2)$ with the minor principal axis.

3 Inadequacy of Coulomb-Mohr Theory for Simple Tension and Simple Shear

Simple Compression. Since the Coulomb theory was originally proposed to describe the simple compression test it is possible, in principle, to obtain the two material constants S_c and Φ in such a test. If the ultimate compressive stress is denoted by S_c it follows that fracture occurs when

$$\sigma_I = \sigma_{II} = 0, \quad \sigma_{III} = -S_c$$

Substituting these values into equation (4) leads to

$$S_c = \frac{S_t(1 - \sin \Phi)}{2 \cos \Phi} = \frac{S_t}{2}\left(\frac{1 - \sin \Phi}{1 + \sin \Phi}\right)^{1/2} \tag{7}$$

If one denotes the angle of fracture in the compression test as β_c, to be measured positively as shown in Fig. 3, it is apparent that

$$|\beta_c| = 45° - \Phi/2 \quad \text{or} \quad \Phi = 90° - 2|\beta_c| \tag{8}$$

for either of the two equally probable modes of fracture shown in Fig. 3. Thus the material constants Φ and S_c are fully defined by the simple compression test. Although there is little published experimental data on observed values of β_c for different materials, Bouton, in an unpublished Master's thesis [12, 13] has described an extremely large number of compression tests on cast iron. Despite a significant difference in the quality of two different grades of cast iron tested, the mean angles of fracture (these angles are $90° - \beta_c$) for the two materials were 54.8 and 55.0 deg, respectively. Hodgkinson [14] on the basis of numerous tests on cast-iron cylinders of all grades stated: "In cast iron the angle is such that the height of the wedge is somewhat less than 3/2 of the diameter." This would correspond to an angle of fracture of just under 56 deg. Assuming a value of $90° - \beta_c = 55°$ for cast iron leads to the conclusion that $\Phi \doteq 20°$ or $\mu \doteq 0.36$ for cast iron. Of course there is no *a priori* reason why all grades of cast iron should have the same value of Φ, but the evidence of Bouton and Hodgkinson indicates this may be approximately so.

Simple Tension. If fracture occurs at an ultimate stress S_t in a simple tension test, the state of stress at fracture is given by

$$\sigma_I = S_t, \quad \sigma_{II} = \sigma_{III} = 0$$

If the Coulomb-Mohr theory of fracture governs, equation (4) predicts

$$S_t = \frac{2S_c \cos \Phi}{1 + \sin \Phi} = S_c \frac{(1 - \sin \Phi)}{(1 + \sin \Phi)} \tag{9}$$

where the last step follows from equation (7).

Furthermore, the angle of fraction β_t measured as shown in Fig. 4 is given by

$$|\beta_t| = 45° - \Phi/2 \tag{10}$$

Equations (9) and (10) are both inconsistent with observed facts. It is well known [13, p. 110] that brittle materials fracture on planes normal to the direction of a pure tensile stress. Assuming that a value of $\Phi = 20°$ is reasonably accurate for cast iron, the Coulomb-Mohr theory predicts that β_t will be approximately 35 deg, which is most definitely contrary to experience. It also should be observed that if Φ is constant for all grades of cast iron the ratio of compressive strength to tensile strength, as predicted by equation (9), must also be constant. For the case of cast iron with $\Phi = 20°$, the Coulomb-Mohr theory requires that $S_c/S_t = 2.04$. Experimental results suggest, however, that cast iron does not have a constant ratio of compressive to tensile strength. For example, Fig. 5 shows a plot of tensile strength versus compressive strength. The experimental points are taken from the data of [15]. Despite the wide scatter it seems evident that the tensile strength does tend to decrease as the compressive

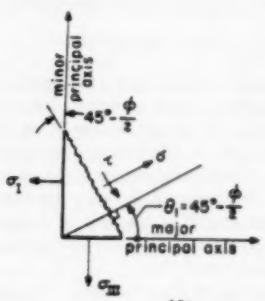

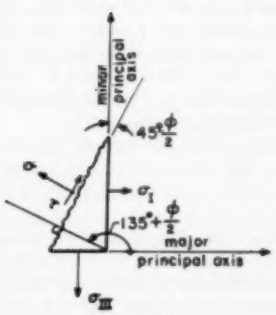

Fig. 2 Equally probable planes of fracture according to Coulomb-Mohr theory

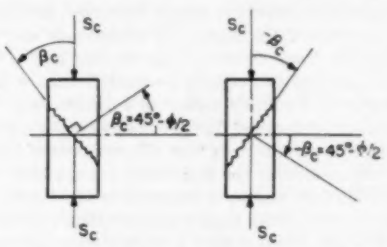

Fig. 3 Modes of fracture in simple compression according to Coulomb-Mohr theory

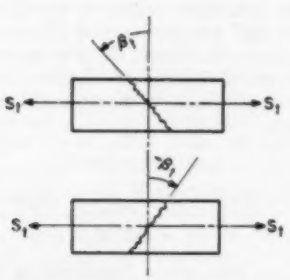

Fig. 4 Modes of fracture in simple tension according to Coulomb-Mohr theory

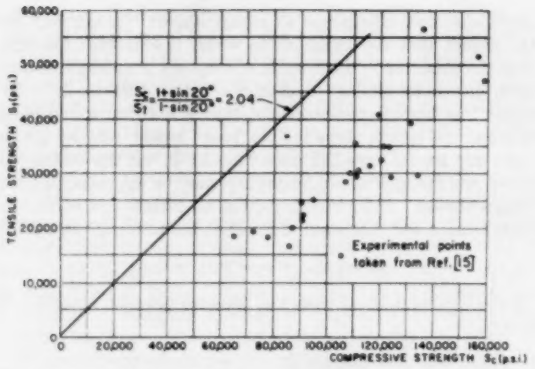

Fig. 5 Tensile strength versus compressive strength for gray cast iron

strength decreases. It appears highly dubious, however, that these parameters decrease in simple proportion as required by equation (9). Most certainly the curve $S_c/S_t = 2.04$ required by Coulomb-Mohr theory (for $\Phi = 20°$), is not in accord with the experimental data, as shown in Fig. 5. It should be noted that values of S_c/S_t higher than 6 have been reported by Hodgkinson [14], corresponding to $\Phi \doteq 20°$.

Thus the Coulomb-Mohr theory is defective in two respects, for the simple tension test; viz., it predicts incorrect angles of fracture, and incorrect ratios of tensile to compressive strength (at least for cast iron).

Simple Shear, Torsion Tests. The most common method of simulating a state of simple shear is by means of the torsion test on circular cylinders. If τ_u represents the shear stress at the outermost radius of a twisted rod, when fracture occurs, it may easily be shown that the state of stress at fracture is given by

$$\sigma_I = \tau_u, \quad \sigma_{II} = 0, \quad \sigma_{III} = -\tau_u$$

Hence equation (4) requires that

$$\tau_u = S_c \cos \Phi, \tag{11}$$

if the Coulomb-Mohr theory is valid. Moreover, as shown by the discussion of Section 2, the trace of the fracture surfaces may take either of the two forms shown in Fig. 6; that is, the Coulomb-Mohr theory predicts two equally probable values of helix angle for the trace of the fractured surface in a torsion test. Although the experimentally observed fracture traces are seldom very uniform helices, it is quite certain that all specimens of a given material fail with essentially the same helix angle, rather than with either of two distinct angles, as required by the theory. For example, the Coulomb-Mohr theory requires that a cast-iron specimen with $\Phi = 20°$ would exhibit a crack inclined at 10 or 80 deg to the axis of the torsion specimen. It is well known that cast iron, and most other brittle materials, fail by cleavage along a plane whose trace is actually inclined to the axis by an angle of approximately 45 deg. This fact is easily demonstrated by twisting a piece of ordinary blackboard chalk to failure.

Equations (11) and (9) lead to the conclusion that the ultimate strength in torsion τ_u is related to the ultimate strength in tension S_t by the equation

$$\tau_u = (1/2)(1 + \sin \Phi)S_t \tag{12}$$

For an angle of friction $\Phi = 20°$, equation (12) would require that

$$\tau_u = 0.671 S_t$$

However, it has been noted frequently in experiments on materials such as cast iron and concrete [16, p. 133], [17] that the ultimate shear strength in torsion τ_u is practically the same

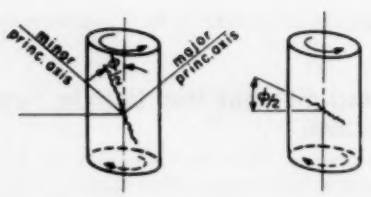

Fig. 6 Modes of fracture in simple torsion according to Coulomb-Mohr theory

as the ultimate tensile strength S_t. The fact that τ_u is practically identical with S_t for cast iron is clearly indicated by the data of Cornet and Grassi [9, 10] and Coffin [11], which will be discussed in greater detail in the next section. Thus the Coulomb-Mohr theory does not explain the results of the simple torsion test satisfactorily.

Composite Data. It is now evident that the Coulomb-Mohr theory cannot reconcile the results of the three most common laboratory tests on brittle materials. However, it has been advocated in recent years [6, 7] that the two independent parameters of the theory be taken as S_t and S_c, the ultimate strengths in tension and compression, respectively. If this procedure is followed, equation (4) can be written as

$$\frac{\sigma_I}{S_t} - \frac{\sigma_{III}}{S_c} = 1 \tag{13}$$

Writing the fracture criterion in this form does not invalidate equations (9) which lead to the result

$$S_c/S_t = (1 + \sin \Phi)/(1 - \sin \Phi) \tag{14}$$

Furthermore, if fracture due to simple shear occurs when $\sigma_I = \sigma_{III} = \tau_u$, equation (13) leads to the conclusion

$$(S_t/\tau_u) = 1 + (S_t/S_c) \tag{15}$$

It may be noted that equation (14) predicts a fixed ratio of compressive strength to tensile strength for a material with constant friction angle. If, as in the case of cast iron, $\Phi \doteq 20°$ it must follow that $S_c/S_t \doteq 2.04$ which is, as we have seen in Fig. 5, hardly the case. Alternately, equation (14) *defines* the angle Φ in terms of S_c/S_t. However, it is easily verified that the experimentally observed angles of fracture in compression, and even more so in tension or torsion are not consistent with the angle Φ defined by equation (14).

It should also be noted that equation (15) is not in accord with the observed fact that the tensile strength is essentially equal to the torsional strength for most brittle materials.

Possibility of Measuring S_s by Direct Shear Test. As pointed out by Bouton [12] there are several practical difficulties in the direct measurement of the angle Φ. However, according to the Coulomb-Mohr theory Φ is related to both S_c and S_s by means of equation (7). Therefore if one could measure both S_s and S_c it would be a simple matter to compute Φ.

Equation (7) implies that the ratio S_s/S_c is a material constant which (for constant Φ) is independent of variation in S_c or S_t, for a given material. For example, if $\Phi = 20°$ it follows that $S_s/S_c = 0.351$.

Although a rather complicated state of stress must exist in the vicinity of a die producing single or double shear in a test fixture, it seems reasonable that there might be a fairly close relationship between the nominal direct shear stress S_d at fracture and the cohesive shear resistance S_s. Fig. 7 shows the relationship between S_d and S_s determined by the "Impact Committee" [15] for cast iron. The line $S_d/S_c = 0.351$ has been superposed on the

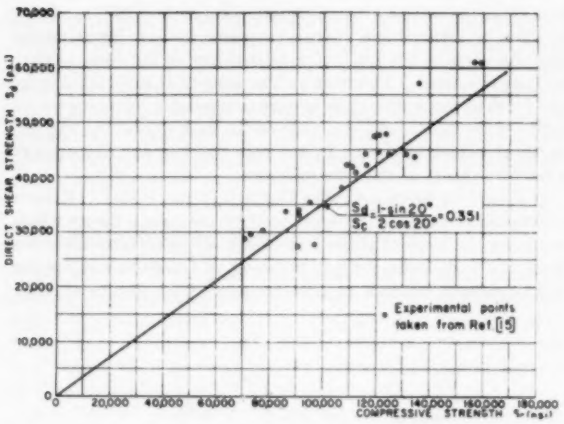
DIRECT SHEAR STRENGTH S_d (psi)
COMPRESSIVE STRENGTH S_c (psi)
$\frac{S_d}{S_c} = \frac{1-\sin 20°}{2\cos 20°} = 0.351$
Experimental points taken from Ref [19]

Fig. 7 Strength in direct shear versus compressive strength for gray cast iron

data. Had we made the assertion that S_d is identical with S_s, Fig. 7 would represent a fair verification of equation (7) for $\Phi = 20°$.

It seems reasonable in view of the scatter associated with all types of tests on brittle materials to assume, at least for approximate calculations, that S_d, the nominal fracture stress in direct shear, is essentially proportional to, and very nearly equal to S_s, the theoretical cohesive shear strength.

Additional experimentation on a wider class of materials may determine whether or not the similarity of S_t and S_d is strictly fortuitous in the case of cast iron. A detailed study of this question is beyond the scope of this paper.

4 Modification of Coulomb-Mohr Theory of Fracture

The discussion up to this point seems to indicate that although the Coulomb-Mohr theory of fracture (with properly chosen parameters) can describe the compression test adequately, it cannot under any circumstance provide a realistic description of tension tests or torsion tests. On the other hand, the data available imply that the maximum normal stress theory of fracture can explain fully the results of both tension and torsion tests, but cannot explain the results of compression tests. Therefore it would seem reasonable to assume that a brittle material will fracture on either that plane where the virtual shear stress T reaches a critical value S_s, or on that plane where the maximum tensile stress σ_I reaches a critical value S_t, *whichever occurs first.*[4]

If a material fails by cleavage in simple torsion, as does cast iron, concrete, and other structural materials, it is impossible to find the two parameters S_t and Φ from the tension or torsion test; consequently, these data must be obtained from a compression test (or some other test where fracture is not along a principal plane).

The proposed modification of Coulomb-Mohr theory will explain fully the results of all three simple tests (tension, torsion, compression). Although it is true that the modified theory is a three-parameter theory rather than a two-parameter theory, such as the unmodified Coulomb-Mohr theory, it is possible, at least in principle, to obtain all requisite data in only two tests; viz., a compression and a tension (or torsion) test. However, these two tests are required even for the unmodified theory characterized by equation (13). Thus, in principle, no additional physical test is required to use the modified theory. However, it may prove desirable in practice to actually make a direct shear test, as discussed in the last section.

Before considering the quantitative details of the theory and its agreement with experimental data, it might be well to point out that somewhat similar ideas have been proposed before in the very extensive literature on this subject. For example, Dorn [3] has suggested that a maximum-shear-stress law be used with tension cutoffs. Cowan [18] has actually suggested the use of the Coulomb-Mohr theory with tension cutoffs for concrete. However, as shown in Section 6 of this paper, Cowan's choice of tension cutoffs reduces his theory to precisely the unmodified form of the theory for all biaxial states of stress and most triaxial states of stress. Thus all of the defects of the unmodified theory discussed in Section 3 are still present in Cowan's theory.

What are believed to be the principal contributions of the present paper are (*a*) the clarification of the method used to choose the parameters of the theory, and (*b*) to show, on the basis of available data, that the proposed theory adequately describes a typical brittle material; viz., cast iron.

5 General Biaxial States of Stress: Application to Cast Iron

Let us now consider a state of stress where one of the three principal stresses vanishes. Arabic numerals rather than Roman numerals will now be used for the subscripts of the principal stresses. It will be assumed that $\sigma_3 = 0$ and σ_1 and σ_2 may take on any values, positive or negative. Any such state of stress may be represented by a point in a plane having Cartesian axes with σ_1, for abscissa and σ_2 for ordinate. The locus of all points in this plane for which fracture impends will be referred to as the fracture curve or fracture locus for the material. For an isotropic material, symmetry requires that the fracture curve be symmetrical about the line $\sigma_1 = \sigma_2$.

In the first quadrant where $\sigma_1 > 0$, $\sigma_2 > 0$, it follows that the algebraically least principal stress $\sigma_{III} = \sigma_3$ vanishes; therefore the Coulomb-Mohr theory, equation (4), predicts that $\sigma_I = \text{const}$; that is, fracture occurs whenever σ_1 or σ_2 reaches a certain constant critical value which may be chosen to be the ultimate tensile strength S_t. Similarly, in the third quadrant where $\sigma_1 < 0$, $\sigma_2 < 0$, the maximum principal stress is $\sigma_{III} = \sigma_3 = 0$, so that failure occurs whenever $-\sigma_1 = S_c$ or $-\sigma_2 = S_c$. Thus there is no essential difference between the Coulomb-Mohr theory and the maximum-normal-stress theory in the first and third quadrants, in so far as stresses are concerned. There is, however, a great difference in regard to the nature of the fractured surfaces. However, we shall concentrate in this section only on the stresses.

In the fourth quadrant $\sigma_1 = \sigma_I$ is positive and $\sigma_2 = \sigma_{III}$ is negative, and the Coulomb-Mohr theory takes the form of equation (13). We have already seen that the use of equation (13) predicts incorrect results for both the angle of fracture and the ultimate shear stress in a simple torsion test. Fig. 8 shows a sketch of the unmodified Coulomb-Mohr theory for the two-dimensional states of stress.

The modified Columb-Mohr theory proposed in Section 4 requires that fracture occurs when $\sigma_1 = S_t$ or when $T = S_s$, whichever occurs first. The former condition is represented by the tension cutoffs shown in Fig. 8, and the latter condition is expressed by equation (4). In using equation (4) one should note that $\sigma_1 = \sigma_I$ and $\sigma_{III} = \sigma_2$ in the fourth quadrant; and $\sigma_I = 0$, $\sigma_{III} = \sigma_2$ in the third quadrant. Equation (4) is represented by the solid inclined lines indicated in Fig. 8. It should be noted that in the fourth quadrant the slope m of the inclined branch of the modified fracture curve is found, from equation (4), to be

$$m = d\sigma_2/d\sigma_1 = (1 + \sin \Phi)/(1 - \sin \Phi) \qquad (16)$$

[4] On the basis of the discussion presented up to this point there is no evidence to either support or contradict the additional hypothesis that fracture will occur if the minimum normal stress σ_{III} reaches some critical value before T reaches S_s or σ_I reaches S_t. Reasons for rejecting this additional hypothesis, for the case of cast iron, will be discussed in section 6.

In the case of cast iron it has been seen that the results of simple compression tests on cast iron imply that $\Phi \doteq 20°$. Therefore, according to the modified theory, $m \doteq 2.04$ for cast iron. Fig. 9 shows experimental data obtained by Grassi and Cornet [9] in tests on gray cast iron. It should be observed that the experimental points seem to lie on a fracture curve characteristic of the proposed modified Coulomb-Mohr theory. Furthermore, the use of $\Phi = 20°$ correlates the data quite well. On the other hand, one could perhaps fit a better inclined straight line to the data and thereby determine an average value of Φ from these data and equation (16), rather than merely use the value $\Phi = 20°$, estimated from other tests.

Fig. 10 shows similar data obtained by Coffin [11] for gray cast iron. The slope of the inclined branch of the modified fracture curve shown corresponds to $\Phi = 20°$. The experimental points in the third quadrant do not lie on the horizontal line predicted by the Coulomb-Mohr (modified or unmodified) theory. At first this might indicate that a different mechanism of fracture governs in the third quadrant of the principal stress plane as suggested by Coffin [11], and Fisher [19]. However, as will be seen in the next section, these apparently anomalous points may be quite simply explained and do, in fact, support the theory proposed.

Fig. 11 shows later data obtained by Cornet and Grassi [10] for inoculated iron. Although the slope of the inclined branch of the fracture curve may be chosen to correspond to $\Phi = 20°$, as shown by the solid inclined line, there is no *a priori* reason for assuming that the angle of friction for inoculated iron is the same as that for gray cast iron. Therefore in the absence of further information (such as angle of fracture in pure compression) one may prefer to fit a different straight line, such as the dash-dot line in Fig. 11, to the experimental data. In any case the data seem to support a fracture theory of the type proposed.

It should be mentioned that Coffin [11] and Fisher [19] have attempted to correlate the data shown by means of a theory which combines the ideas of stress concentrations at carbon-iron interfaces and a distortion-energy criterion of failure except for the third quadrant where it became necessary for Coffin to consider

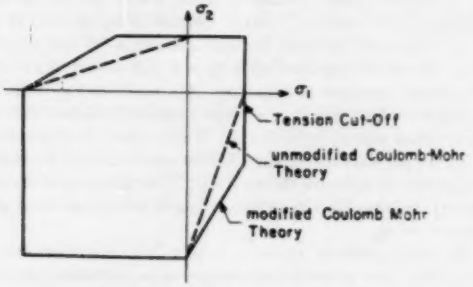

Fig. 8 Fracture curves for biaxial states of stress according to modified and unmodified Coulomb-Mohr theory

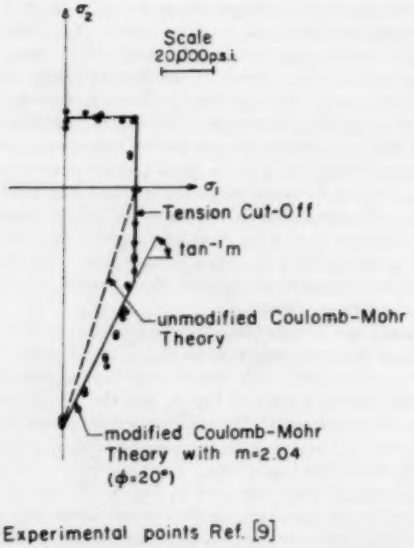

Fig. 9 Data of Grassi and Cornet on gray cast iron

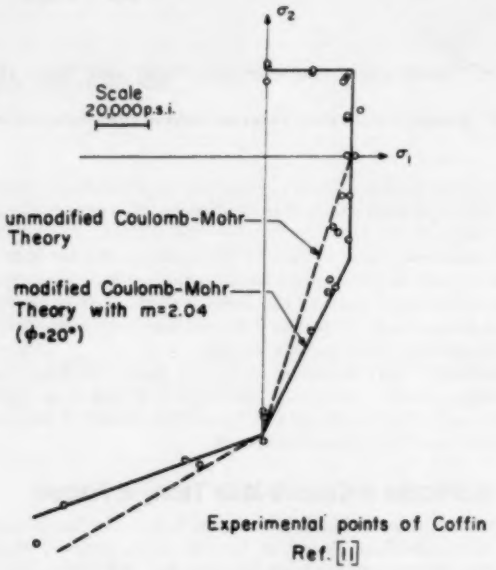

Fig. 10 Data of Coffin on gray cast iron

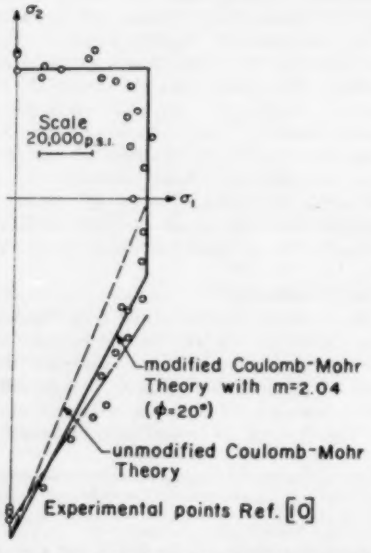

Fig. 11 Data of Cornet and Grassi on inoculated iron

the effect of mean normal stress as well as octahedral shear stress. The resulting nonlinear fracture curves do not seem to fit the experimental data any better than the much simpler theory presented here, and may indeed be based on a false interpretation of Coffin's data for the four points, shown in Fig. 10, in the third quadrant of the σ_1, σ_2-plane. This point may perhaps be clarified somewhat by a discussion of the fracture surface for general triaxial states of stress.

6 Three-Dimensional States of Stress

The locus of all possible combinations of the three principal stresses which result in fracture is a surface in a Cartesian three-space with co-ordinates σ_1, σ_2, σ_3. This surface will be referred to as the "fracture surface" (to be distinguished from "fractured surface" which will designate a physical surface produced by rupture of the material).

The fracture surface corresponding to the Coulomb-Mohr theory may be derived from equation (4) which can be written in the form

$$\sigma_{III} - m'\sigma_I = -S_c \tag{17}$$

Upon consideration of the various principal stresses, which may be either maximal or minimal, one is led to the conclusion that the three-dimensional fracture surface is the convex shell formed by the six planes:

$$\begin{aligned} \sigma_1 &= -S_c + m'\sigma_2 \qquad \sigma_2 = -S_c + m'\sigma_1 \\ \sigma_2 &= -S_c + m'\sigma_3 \qquad \sigma_3 = -S_c + m'\sigma_2 \\ \sigma_3 &= -S_c + m'\sigma_1 \qquad \sigma_1 = -S_c + m'\sigma_3 \end{aligned} \tag{18}$$

The six planes represented by equations (18) enclose an irregular hexagonal pyramid [21] whose axis makes equal angles with all three co-ordinate axes. If one adopts the unmodified form of the Coulomb-Mohr theory which predicts the correct ultimate strength in tension, consistency with equation (13) requires that $m' = S_c/S_t$. Fig. 12 shows a sketch of the corresponding fracture surface for the case $S_c/S_t = 3$.

On the other hand, if one adopts the modified form of the theory, which will predict the correct type of fractured surfaces, m' is defined [cf. equation (16)] by

$$m' = m = (1 + \sin \Phi)/(1 - \sin \Phi)$$

Furthermore, the modified theory requires that the equations of the fracture surface (18) be supplemented by the tension cutoffs

$$\sigma_1 = S_t, \qquad \sigma_2 = S_t, \qquad \sigma_3 = S_t \tag{19}$$

Fig. 13 shows a sketch of the modified fracture surface with $S_c/S_t = 3$ and $m = 2.04(\Phi = 20°)$.

Fig. 14 shows the fracture surface proposed by Cowan [18]. Since the proposed tension cutoffs are so close to the vertex of the pyramid it is clear that any state of biaxial stress is completely uninfluenced by the tension cutoffs so that the biaxial fracture locus is similar to that of the unmodified Coulomb-Mohr theory depicted in Fig. 8. Thus Cowan's theory is subject to all of the faults previously described (cf. Section 3) of the unmodified theory.

It is well known that many materials which are otherwise brittle become ductile in the presence of large hydrostatic pressures [1, 2]. Therefore one might expect the fracture surface to be intersected and superseded by a yield surface somewhere in the octant of large negative mean normal stress. The determination of the shape of the yield surface and the region where it intersects the fracture surface will require a great deal of experimental research and will not be considered further in this paper. It will be

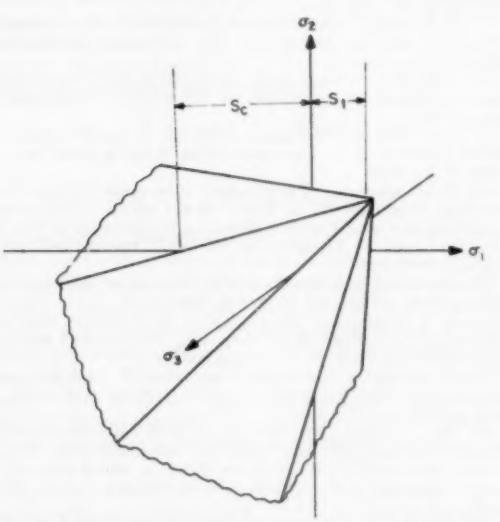

Fig. 12 Fracture surface for unmodified Coulomb-Mohr theory

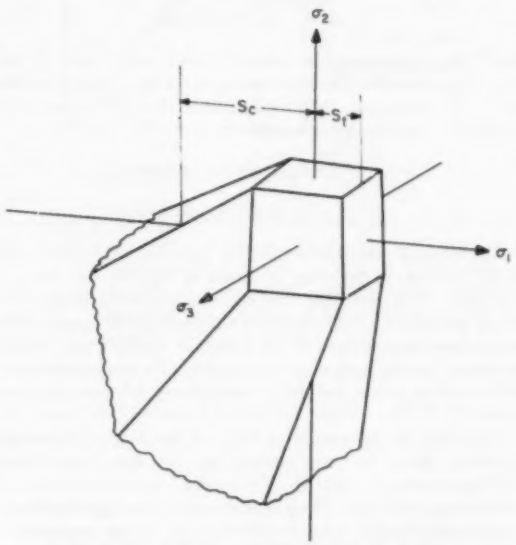

Fig. 13 Fracture surface for modified Coulomb-Mohr theory

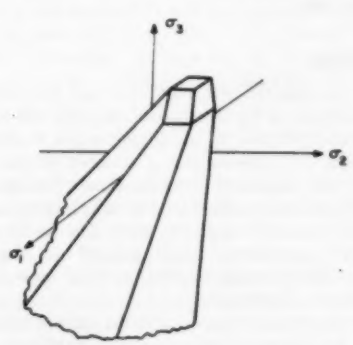

Fig. 14 Fracture surface proposed by Cowan, reference [18]

seen, however, that although Coffin [11] made a few tests in that octant of stress space where the yield surface can possibly govern, the mean normal pressure for these experiments was low enough so that the fracture surface might still govern rather than the yield surface.

To see this we note that there are four points among Coffin's data where $\sigma_2 < \sigma_1 < 0$. In this region the fracture surface has the equation

$$\sigma_3 = -S_c + m'\sigma_3 \tag{20}$$

Furthermore, these tests were not strictly two-dimensional since there was an external pressure p creating a normal stress

$$\sigma_3 = -p \tag{21}$$

at the outer surface of the tubular specimens. In order to estimate the influence of this third principal stress let us assume as a first approximation that the circumferential stress σ_1 (called σ_t by Coffin) is related to the pressure by the "hoop-stress" formula,

$$p = -\sigma_1 t/a \tag{22}$$

where t is wall thickness and a is the mean radius of the tube. Upon combining equations (20), (21), and (22) it is seen that the Cololumb-Mohr theory requires that fracture occur when

$$\sigma_2 = -S_c + (m't/a)\sigma_1 \tag{23}$$

For Coffin's specimens $t = 0.100$ in., $a = 0.550$ in., and $(S_c/S_t) = 3.3$. Equation (23) therefore becomes, for the unmodified theory ($m' = S_c/S_t$) and for the modified (with $\Phi = 20°$, or $m = 2.04$) Coulomb-Mohr theory, respectively,

$$\sigma_2 = -S_c + 0.60\sigma_1 \quad \text{(unmodified)} \tag{24}$$

$$\sigma_2 = -S_c + 0.37\sigma_1 \quad \text{(modified)} \tag{25}$$

The straight line represented by equation (25) gives a somewhat better fit to the data, as shown in Fig. 10, then does equation (24). It appears then that the influence of the third principal stress predicted by the modified Coulomb-Mohr theory offers a satisfactory explanation of the points in Coffin's data which he explained on the basis of a combination of a stress-concentration effect and an octahedral shear-stress theory influenced by normal stress.

Although the agreement of three of the four points with the modified theory is quite satisfactory, one should not conclude without reservation that the yield surface has not yet intersected the fracture surface in these experiments. The significance of the experimental points is somewhat obscured by the tendency of the specimens to fail by buckling. It is not clear from Coffin's paper whether or not actual fractures either preceded or followed the onset of buckling.

7 Conclusions

It has been pointed out that although the Coulomb-Mohr theory of fracture, in the form most commonly advocated, fails to explain several features of the simple torsion, tension, and compression tests, the introduction of suitably chosen tension cutoffs and friction angle will bring the theory into good agreement with these three types of tests. Although the proposed theory involves three material constants, they can all be obtained, in principle, from two tests. In the case of cast iron it has been shown that one of the three required material constants can be determined from a direct shear test.

If the proposed theory is used with the angle of friction observed in a simple compression test (by measuring obliquity of fractured plane), it has been shown that the theory will quite accurately predict fracture under biaxial states of stress such as those produced in the experiments of Cornet and Grassi, and Coffin, on cast iron.

A comparison has been made of the three-dimensional fracture surfaces associated with both the unmodified and modified forms of the theory. It has also been shown that the three-dimensional form of the modified theory offers a simple explanation of some experimental data which have previously been explained on the basis of a more complex theory involving the ideas of notch effective stress and a pressure-sensitive octahedral shear theory. It appears plausible, but by no means definite, that the points obtained by Coffin in the third quadrant of the (σ_1, σ_3)-plane lie on the fracture surface rather than on the yield surface which supersedes the fracture surface for high levels of hydrostatic pressure.

Finally, a few remarks are made in the Appendix concerning a tentative hypothesis which would explain the appearance of concavities in the fracture locus for certain types of materials.

References

1 P. W. Bridgman, "Fracture and Hydrostatic Pressure," in Fracturing of Metals, American Society for Metals, Cleveland, Ohio, 1948.

2 A. Nadai, "Theory of Flow and Fracture of Solids," McGraw-Hill Book Company, Inc., New York, N. Y., second edition, 1950.

3 J. E. Dorn, "The Effect of Stress State on the Fracture Strength of Metals," in Fracturing of Metals, American Society for Metals, Cleveland, Ohio, 1948.

4 C. A. Coulomb, "Sur une Application des Regles de Maximis et Minimis a quelques Problemes de Statique, relatifs a l'Architecture," *Memoires de Mathematique et de Physique*, Academie Royal des Sciences, par divers Savans, Année 1773, Paris, France, 1776.

5 S. Timoshenko, "History of Strength of Materials," McGraw-Hill Book Company, Inc., New York, N. Y., 1953.

6 S. Timoshenko, "Strength of Materials, Part II," D. Van Nostrand Company, Inc., Princeton, N. J., third edition, 1956, pp. 457–462.

7 C. R. Soderberg, "Working Stresses," article in Handbook of Experimental Stress Analysis, edited by M. Hetényi, John Wiley & Sons, Inc., New York, N. Y., 1950.

8 J. C. Jaeger, "Elasticity Fracture and Flows," Methuen and Company, Limited, London, England, 1956.

9 R. C. Grassi and I. Cornet, "Fracture of Gray-Cast-Iron Tubes Under Biaxial Stresses," JOURNAL OF APPLIED MECHANICS, vol. 16, TRANS. ASME, vol. 71, 1949, pp. 178–182.

10 I. Cornet and R. C. Grassi, "Fracture of Inoculated Iron Under Biaxial Stress," JOURNAL OF APPLIED MECHANICS, vol. 22, TRANS. ASME, vol. 77, 1955, pp. 172–174.

11 L. F. Coffin, "The Flow and Fracture of a Brittle Material," JOURNAL OF APPLIED MECHANICS, vol. 17, TRANS. ASME, vol. 72, 1950, pp. 233–248.

12 C. Bouton, "Theory and Experiments on the Laws of Crushing Strength of Short Prisms," thesis for MS degree at Washington University, 1891.

13 J. B. Johnson, "Johnson's Materials of Construction," sixth edition, edited by F. E. Turneaure, John Wiley & Sons, Inc., New York, N. Y., 1926.

14 E. Hodgkinson, "Experimental Researches on the Strength and Other Properties of Cast Iron," second edition. This volume is bound together with Practical Essays on the Strength of Cast Iron, fifth edition by T. Tredgold, edited by E. Hodgkinson, London, England, 1860–1861.

15 Report of Subcommittee XV, Committee A-3, on Impact Testing, *Proc. ASTM*, vol. 33, part I, 1933, p. 87.

16 H. E. Davis, G. E. Troxell, and C. T. Wiskocil, "The Testing and Inspection of Engineering Materials," McGraw-Hill Book Company, Inc., New York, N. Y., second edition, 1955.

17 H. J. Gikley, discussion of paper by P. Anderson entitled "Experiments With Concrete in Torsion," *Trans. ASCE*, vol. 100, 1935, p. 943.

18 H. J. Cowan, "The Strength of Plain, Reinforced and Prestressed Concrete Under the Action of Combined Stresses, With Particular Reference to the Combined Bending and Torsion of Rectangular Sections," *Magazine of Concrete Research*, vol. 5, 1953, pp. 75–86.

19 J. C. Fisher, "A Criterion for the Failure of Cast Iron," ASTM Bulletin, No. 181, 1952, pp. 74–75.

20 O. Mohr, "Welche Umstande bedingen die Elastizitatsgrenze und den Bruch eines Materiales?" *Zeitschrift des Vereines Deutscher Ingenieure*, Band 44, 1900, p. 1524 and 1572.
21 R. T. Shield, "On Coulomb's Law of Failure in Soils," *Journal of Mechanics and Physics of Solids*, vol. 4, 1955, pp. 10–16.
22 D. C. Drucker, "A More Fundamental Approach to Plastic Stress-Strain Relations," *Proceedings*, First U. S. National Congress of Applied Mechanics, published by ASME, 1952, pp. 487–491.

APPENDIX

Possibility of Concavities in Fracture Curve

The term $\mu\sigma$ which appears in the Coulomb-Mohr theory [cf. equation (1)] may be thought of merely as the dominant term of a power series in σ representing the more general theory of Mohr [cf. equation (2)]. However, the parameter $\mu = \text{arc tan } \Phi$ is usually interpreted as a coefficient of friction. In fact, Bouton [12] made actual measurements of the coefficient of friction for cast iron and found surprisingly close correlation with the Coulomb theory of fracture. If one thinks of μ as a frictional coefficient, it is easy to see why compressive normal stresses have a tendency to strengthen a material. On the other hand, it is not intuitively evident how a frictional mechanism can act to weaken a material, as required by the Coulomb-Mohr theory, when the normal stress on the plane of fracture is tensile.

It therefore seems reasonable to examine the implications of the hypothesis that the modified Coulomb-Mohr theory is valid when the normal stress on the plane of fracture is compressive, but the "frictional" force vanishes when the normal stress is tensile; that is,

$$\mu = \text{const} \geq 0 \text{ (for } \sigma < 0) \tag{26}$$

$$\mu = 0 \text{ (for } \sigma > 0) \tag{27}$$

It should be noted that when equation (27) is valid the unmodified Coulomb-Mohr criterion reduces precisely to the maximum-shear-stress criterion of failure. It is desirable to be able to formulate the present hypothesis in terms of the principal stresses, and in particular to determine in which parts of the principal stress space equations (26) or (27) are applicable. For simplicity, the following discussion will be restricted to cases of plane stress, although the extension of the results to triaxial states of stress parallels completely the work of Section 6.

In the first quadrant of the (σ_1, σ_2)-plane both the maximum-shear-stress theory and the modified Coulomb-Mohr theory lead to the same result; namely, fracture occurs when $\sigma_1 = S_t$.

A distinction between the two theories exists in the fourth quadrant, which for convenience will be divided into two parts, designated as regimes I and II, where

$$-\sigma_1 < \sigma_2 < 0 < \sigma_1 \text{ in regime I}$$

and

$$\sigma_2 < -\sigma_1 < 0 < \sigma_1 \text{ in regime II.}$$

These regimes are illustrated in Fig. 16.

Fig. 15 shows a typical set of Mohr's circles for a state of stress corresponding to regime II. It should be observed that the geometry is essentially that of Fig. 1, with $\sigma_1 = \sigma_{\text{I}}$, $\sigma_2 = \sigma_{\text{III}}$, $\sigma_3 = \sigma_{\text{II}} = 0$, and with point M representing the intersection of the major principal circle with the ordinate. The angle DMO is designated as α. It should be observed that in the region where σ is positive $\Phi = 0$, so that the straight line $O'OO''$ in Fig. 1 is replaced by the two segments $O'O$ and OO'' in Fig. 15, where the angles of inclination, to the abscissa, of the two segments are Φ and 0, respectively.

It may be observed that if $\Phi < \alpha$ the maximum value of T is given by $Q'R'$ as in Figs. 1 and 15, so that failure occurs on a plane where $\sigma < 0$ and equation (4) is valid. On the other hand,

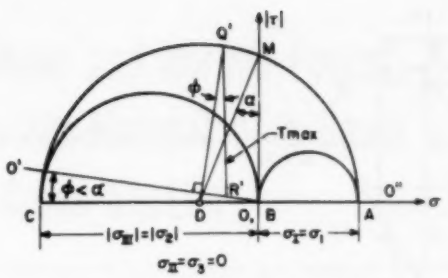

Fig. 15 Typical Mohr's circles for regime II

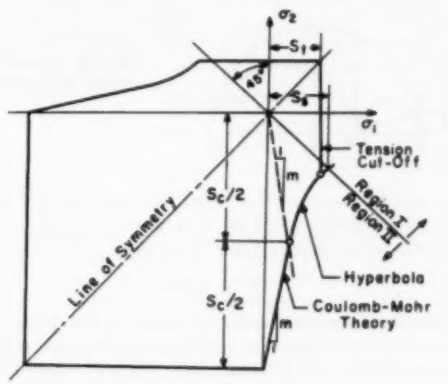

Fig. 16 Fracture curve for $S_c/2m < S_t$ and $S_c > S_t$

if the angle Φ in Fig. 15 is gradually increased, it will become apparent that when $\Phi = \alpha$ the maximum value of T is given by OM. As Φ is increased still further, so that $\Phi > \alpha$, it may be seen that the maximum value of T remains equal to $OM = (-\sigma_1\sigma_2)^{1/2}$. Therefore the criterion of fracture for regime II is given by equation (4) for $\Phi < \alpha$ and by

$$(-\sigma_1\sigma_2)^{1/2} = S_a, \quad \text{for} \quad \Phi > \alpha \tag{28}$$

Equation (28) defines a hyperbola whose range of validity is given by

$$\sin \Phi < \sin \alpha \tag{29}$$

From Fig. 15 it may be observed that

$$\sin \alpha = OD/DM = -(\sigma_1 + \sigma_2)/(\sigma_1 - \sigma_2) \tag{30}$$

It is interesting to note that the right-hand side of equation (30) is equal to the so-called "Lode parameter" frequently used in the theory of plasticity [2, p. 106]. Upon substitution of equation (30) into inequality (29) and the use of equation (16) one obtains for the range of validity, in regime II, of equation (28)

$$\frac{\sigma_2}{\sigma_1} > -\frac{1 + \sin \Phi}{1 - \sin \Phi} = -m \tag{31}$$

That is, the hyperbola described by equation (28) supersedes the straight line of slope m in that part of regime II above the broken line shown in Fig. 16.

It is evident that the hyperbolic fracture curve intersects the straight line where $\sigma_2 = -S_c/2$. It is a straightforward matter to show that the slope of the hyperbola is continuous with that of the straight line at the point

$$(\sigma_1, \sigma_2) = (S_c/2m, -S_c/2)$$

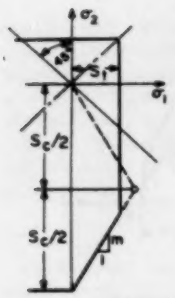

Fig. 17 Fracture curve for $S_c/2m > S_t$ and $S_c > S_t$

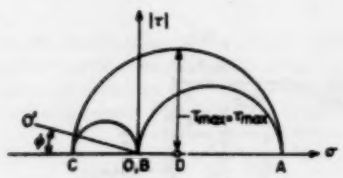

Fig. 18 Typical Mohr's circles for regime I

It also may be seen that the inclined straight line will be intercepted by the tension cutoff $\sigma_1 = S_t$ before it is intercepted by the hyperbola (as shown in Fig. 17), unless

$$S_c/S_t < 2m \tag{32}$$

In short, a hyperbolic branch will appear in that part of regime I defined by inequality (31), provided inequality (32) is satisfied.

It is significant that although there are good reasons [22] for believing that the yield curve for a ductile material could not have concavities such as that produced by the hyperbola in Fig. 16, no such restriction has been established for fracture curves.

It will now be shown that the hyperbolic branch of the fracture curve can never extend into regime I. Fig. 18 shows a typical set of Mohr's circles for regime I. It is obvious that regardless of the value of Φ, $T_{max} = \tau_{max}$ so that the criterion of failure in regime I is the maximum-shear-stress criterion, augmented by the tension cutoff $\sigma_1 = S_t$.

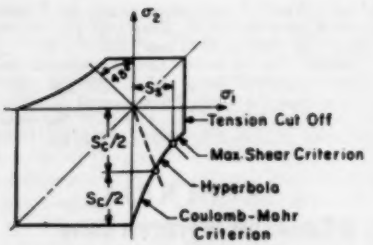

Fig. 19 Fracture curve for $S_c/2m < S_t$ and $S_c < S_t$

If the tension cutoff governs throughout regime I, as, for example, shown in Fig. 16, it follows that $S_t < S_c$. On the other hand, when $S_c < S_t$ the maximum-shear-stress criterion governs in part of regime I as shown in Fig. 19. Finally, in order to show that Figs. 16, 17, 19 cover all possibilities it should be noted that when $S_c/S_t > 2m$, as indicated in Fig. 17, the only possibility is to have $S_c > S_t$. This follows from the fact [cf. equation (7)] that

$$\frac{S_c}{S_t} = \frac{1}{2\sqrt{m}}\frac{S_c}{S_t} \geq \frac{2m}{2\sqrt{m}} = \sqrt{m} \geq 1$$

Whether or not the hypothesis advanced in this Appendix is meaningful for any real materials can only be determined experimentally.

For the experiments of Cornet and Grassi and Coffin described in Section 5, the difference between the modified Coulomb-Mohr theory and the theory of this Appendix is so slight that experimental scatter prevents a comparative evaluation of the two theories.

The Effect of Shear and Normal Forces on the Fully Plastic Moment of a Beam of Rectangular Cross Section[1]

B. G. NEAL[2]

Professor of Civil Engineering, University College of Swansea, Swansea, Wales, G. B. Now Professor of Applied Science, Imperial College of Science and Technology, London, England

The value of the fully plastic moment of a beam is known to be reduced by both normal and shear forces, and their separate effects have been studied in some detail, but little attention has been paid to the reduction caused by normal and shear forces acting simultaneously. This problem is discussed with reference to a cantilever beam of rectangular cross section subjected to both shear and normal forces at the free end. Upper and lower bounds to the collapse load are determined, and the results are presented in the form of interaction relations between the shear and normal forces and the bending moment at the clamped end of the cantilever at collapse.

Introduction

THE PLASTIC methods of structural analysis for framed structures depend essentially on the plastic hinge concept. A plastic hinge cannot undergo any rotation until the bending moment reaches a value termed the fully plastic moment, but can undergo an indefinite amount of rotation while the bending moment remains constant at the fully plastic value. In many applications of the plastic methods, the fully plastic moment is treated as a constant for a member of a given cross section and material, but it is known that its value is affected by both axial force and shear force at the hinge section. In structural frames subjected to statical loading, the effect of shear force is usually small, and axial force only becomes important in heavily loaded columns. However, under conditions of dynamical loading, the applied loads may be considerably greater than those which would cause failure by plastic collapse under statical loading, so that shear and axial forces may become large enough to have a substantial effect on the value of the fully plastic moment. At present, very little knowledge is available concerning the effect on the value of the fully plastic moment of both shear and axial forces acting simultaneously, although Horne [1][3] has suggested an approach for I beams based on the empirical relationship put forward by Heyman and Dutton [2] for the effect of shear. The object of the present paper is to study this problem for members of rectangular cross section.

The effect of axial force on the fully plastic moment in the absence of shear is well understood [3]. Several investigations into the effect of shear force on the fully plastic moment of beams of both rectangular cross section and of I-section have also been carried out [4–9], but here the position is less satisfactory. As pointed out by Drucker [8], this is primarily because the problem is not a local one; it is not permissible simply to discuss the values of shear force and bending moment producing a condition of full plasticity at one particular cross section without also discussing conditions in the adjoining structure. Consider for example the three problems illustrated in Fig. 1, it being required to find the value W_c of W at which collapse would occur in each case. The beams are supposed to be of rectangular cross section, breadth b and depth h, so that the fully plastic moment M_p in pure bending is given by

$$M_p = \frac{1}{4} bh^2\sigma_0, \tag{1}$$

σ_0 being the yield stress in pure tension or compression. Furthermore, the greatest shear force V_p which could be sustained in the absence of any normal force or bending moment is given by

$$V_p = bh\tau_0, \tag{2}$$

where τ_0 is the yield stress in pure shear, and has the value $0.5\sigma_0$

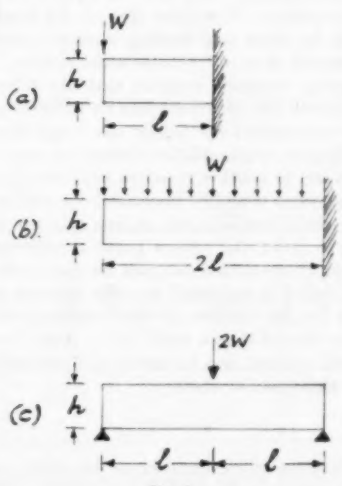

Fig. 1

---

[1] These results were obtained in the course of research which was partially supported by Norfolk Naval Shipyard under contract N189(40621A) X with Brown University.

[2] Visiting Professor, Brown University, August 1959–February 1960.

[3] Numbers in brackets designate References at end of paper.

Contributed by the Applied Mechanics Division and presented at the Winter Annual Meeting, New York, N. Y., November 27–December 2, 1960, of THE AMERICAN SOCIETY OF MECHANICAL ENGINEERS.

Written discussion on this paper should be addressed to the Editorial Department, ASME, 29 West 39th Street, New York, N. Y., and will be accepted until July 10, 1961. Discussion received after the closing date will be returned. Manuscript received by ASME Applied Mechanics Division, May 31, 1960. Paper No. 60—WA-102.

or $0.577\sigma_0$ depending on whether the Tresca or von Mises yield criterion is assumed.

At collapse, plastic hinges would form at the built-in ends of the two cantilevers and at the center of the simply supported beam beneath the load. In each case the shear force V_0 at the plastic hinge position has the value W_c while the bending moment M_0 is $W_c l$, so that

$$W_c = V_0 = M_0/l \tag{3}$$

Thus if the formation of the plastic hinges depended solely on the values of V_0 and M_0, the value of W_c would be precisely the same for each of the three problems. However, in Fig. 1(*a*), the influence of the free end of the cantilever on conditions at the clamped end is clearly more pronounced than for the cantilever of Fig. 1(*b*), particularly if l is comparable with h. Moreover, the uniformly distributed pressure on the upper surface in Fig. 1(*b*) will have a different effect than the heavily localized loading at the free end in Fig. 1(*a*). In Fig. 1(*c*) the precise manner of application of the central concentrated load will influence the formation of the plastic hinge in a different way than the built-in conditions of Figs. 1(*a*) and 1(*b*), which in turn could be specified in several ways. Thus for each of the three problems in Fig. 1 the value of W_c would be different, and in each case would also depend on the precise details of the supporting and loading arrangements.

It is therefore apparent that the three problems indicated in Fig. 1 are basically different and, in addition, a more precise specification of the manner of loading and of the support arrangements is required before each problem is properly defined. The solution for any one problem could be represented by plotting W_c as a function of l/h, and a different curve would be obtained in each case.

The bending moment M_0 and shear force V_0 at the plastic hinge are conveniently specified by the nondimensional quantities m and v, where

$$m = M_0/M_p \qquad v = V_0/V_p \tag{4}$$

Since $W_c = M_0/l$, an alternative representation is obtained by plotting m as a function of l/h. Also, it can be shown from equations (1), (2), (3), and (4) that

$$m = v\,\frac{4l\tau_0}{h\sigma_0} \tag{5}$$

so that another representation would be a plot of m as a function of v for each problem. This latter type of plot would give interaction curves for shear and bending moment, which of course would be expected to be different for each problem.

The foregoing discussion suggests that the differences which may exist between the (m, v) relations for different problems will become less pronounced the higher the length/depth ratio l/h becomes. Thus an (m, v) relation derived for any one situation might be applied to another situation with the expectation that the results obtained would be reasonably accurate so long as l/h was not too small, that is to say, so long as v was not too large. Bearing this in mind, the present paper is concerned only with the derivation of interaction relations for the cantilever problem of Fig. 1(*a*), but it is suggested that the relations obtained can also be used for the solution of other problems with a suitable restriction on the maximum value of v. Axial force N is considered as well as shear, and its intensity is specified by the nondimensional parameter n, where

$$n = N/N_p \tag{6}$$

N_p is the axial force which would cause the entire cross section to become fully plastic, and is given by

$$N_p = bh\sigma_0 \tag{7}$$

Thus the objective of the paper is to determine interaction relations between m, v, and n for the cantilever situation depicted in Fig. 2. No attempt is made to obtain precise solutions; instead, the theorems of limit analysis are used to bound the relations from above and below. As will be seen, it is difficult to obtain good upper bounds, but lower bounds are found which are believed to be close to the true interaction relations, and which in any case will furnish conservative results when used for the solution of problems.

Lower Bound

Fig. 2 shows a cantilever of rectangular cross section, breadth b, and depth h, which is of length l and is subjected to a transverse shear force V and a normal force N at the free end. First, a lower bound solution will be derived; this involves the determination of a system of stresses which satisfies the conditions of equilibrium throughout the cantilever, and which is such that the yield condition is not violated at any point. Assuming conditions either of plane stress or of plane strain, the equations of equilibrium are, in the notation of Fig. 2,

$$\frac{\partial\sigma_x}{\partial x} + \frac{\partial\tau_{xy}}{\partial y} = 0 \tag{8}$$

$$\frac{\partial\sigma_y}{\partial y} + \frac{\partial\tau_{xy}}{\partial x} = 0 \tag{9}$$

Following Drucker's approach [8] for the case of zero axial force, a stress distribution is sought in which σ_y is everywhere zero. In such a distribution, it is seen from equation (9) that τ_{xy} is independent of x. Thus in equation (8)

$$\frac{\partial\sigma_x}{\partial x} = -\frac{d\tau_{xy}}{dy} \tag{10}$$

At the free end of the cantilever, it is supposed that the normal force N is uniformly distributed over the cross-sectional area, so that

$$\sigma_x = \frac{N}{bh} = n\sigma_0, \text{ for } x = 0$$

using equations (6) and (7). Then by integrating equation (10) it follows that

$$\sigma_x = n\sigma_0 - x\,\frac{d\tau_{xy}}{dy} \tag{11}$$

It is now supposed that at the clamped end the yield criterion of either Tresca or von Mises is just satisfied over the entire cross section. This criterion is taken to be

$$\sigma_x^2 + 4v^2\tau_{xy}^2 = \sigma_0^2 \tag{12}$$

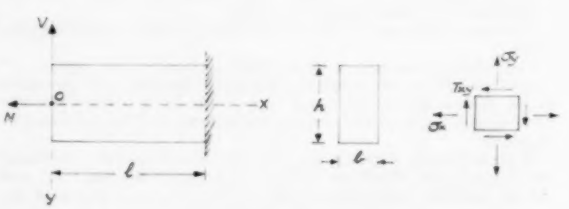

Fig. 2 Cantilever

If $\nu = 1$, this equation represents the Tresca yield criterion for conditions of either plane stress or plane strain, whereas with $\nu = 0.866$ the von Mises yield criterion for plane stress is obtained. The results which follow could also be adapted, if required, to plane strain conditions with the von Mises yield criterion by taking $\nu = 1$ and replacing σ_0 by $1.155\sigma_0$.

From equations (11) and (12), it follows that when $x = l$,

$$\sigma_x = n\sigma_0 - l\frac{d\tau_{xy}}{dy} = \pm(\sigma_0^2 - 4\nu^2\tau_{xy}^2)^{1/2} \tag{13}$$

From Fig. 2 it is seen that if n is zero, σ_x will be negative when $y = -h/2$, whereas when $y = h/2$, σ_x will be positive. This suggests that the negative value of the radical in equation (13) will determine the distribution of τ_{xy} in the region $-h/2 < y < y_0$, while the positive value will correspond to the region $y_0 < y < h/2$, where the value of y_0 is yet to be determined. This will be verified later.

Equation (13) may be put in a convenient form by the substitutions

$$\tau_{xy} = \frac{\sigma_0}{2\nu}\sin\phi, \qquad n = \cos\alpha \tag{14}$$

giving

$$\frac{l}{2\nu}\cos\phi\frac{d\phi}{dy} = \cos\alpha \pm \cos\phi \tag{15}$$

The value of α may be restricted to the range $0 - \pi/2$ while covering all possible values of n from 0 to 1.

Integration of equation (15) leads to

$$\frac{2\nu}{l}\left(\frac{h}{2} + y\right) = \phi - 2\cot\alpha\tanh^{-1}\left(\tan\frac{\alpha}{2}\tan\frac{\phi}{2}\right), \qquad -\frac{h}{2} < y < y_0$$

$$\frac{2\nu}{l}\left(\frac{h}{2} - y\right) = \phi + 2\cot\alpha\tanh^{-1}\left(\cot\frac{\alpha}{2}\tan\frac{\phi}{2}\right), \qquad y_0 < y < \frac{h}{2} \tag{16}$$

the constants of integration being evaluated by noting that τ_{xy} must be zero at the upper and lower boundaries of the beam. If the value of ϕ when $y = y_0$ is denoted by ψ, it follows from equations (16) that

$$\frac{\nu h}{l} = \psi + \cot\alpha\tanh^{-1}(\cot\alpha\tan\psi) \tag{17}$$

$$\frac{2y_0}{h} = \frac{\tanh^{-1}(\operatorname{cosec}\alpha\sin\psi)}{\psi\tan\alpha + \tanh^{-1}(\cot\alpha\tan\psi)} \tag{18}$$

It will be seen from equation (17) that $(\cot\alpha\tan\psi)$ cannot exceed unity. Since α lies in the range $0 - \pi/2$, this implies that $\alpha \geq \psi$. The significance of this restriction is readily understood by considering the extreme cases $\alpha = \psi$ and $\alpha = \pi/2$. In the first case $\tanh^{-1}(\cot\alpha\tan\psi) = \infty$, so that $l/\nu h = 0$. When $\alpha = \pi/2$, $n = 0$, and since $\cot\alpha = 0$ it follows that $l/\nu h = 1/\psi$, which is the result obtained by Drucker [8] for zero normal force. Thus all possible values of $l/\nu h$ are covered by a variation of α between the limits ψ and $\pi/2$.

In this solution the distributions of stress can be obtained from equations (18), (17), (16), and (11). These distributions must satisfy the equilibrium equations (8) and (9) and are therefore statically admissible. The yield criterion (12) is just satisfied over the entire cross section when $x = l$, and it is easily verified that $(\sigma_x^2 + 4\nu^2\tau_{xy}^2)$ is less than σ_0^2 for smaller values of x. The stress distributions therefore satisfy all the requirements for a lower bound solution.

Before V and M are evaluated, it is of interest to examine the distributions of shear and normal stress across the section at the clamped end. These are readily determined from equations (18), (17), (16), and (12). For instance, taking $n = 0.6$, so that $\alpha = \cos^{-1} 0.6$, and choosing $\psi = \pi/4$, the value of y_0 is found from equation (18) to be $-0.345h$, and from equation (17), $\nu h/l = 1.515$. Equations (16) then determine ϕ and thus τ_{xy}, as a function of y, and corresponding values of σ_x are found from equation (12). Fig. 3 shows the distributions of stress obtained in this way.

In Drucker's solution for the case of zero axial force [8] it was found that for short beams such that $l/\nu h < 2/\pi$, the shear stress was constant at the value τ_0 in a central core of the beam, within which the normal stress was zero. Similar distributions of stress should be obtained from the present solution for $n = 0$, or $\alpha = \pi/2$. To obtain these distributions it is necessary to approach this limiting case by taking $\alpha = \pi/2 - \beta$, where β is small, and $\psi = \alpha - \gamma$, where γ is also small. It is then found from equation (17) that

$$\frac{\nu h}{l} = \frac{\pi}{2} + \frac{1}{2}\beta\log\left(1 + \frac{2\beta}{\gamma}\right)$$

From this equation it is seen that $\nu h/l$ will not differ appreciably from $\pi/2$ unless γ is of smaller order than β, in fact of the order of $\beta\exp(-1/\beta)$. Bearing this in mind, calculations were made for the case $\beta = 0.5° = 0.00873^c$, with $\nu h/l = 3$, so that $\gamma = 2\beta e^{-3\pi}$. With these values y_0 is found from equation (18) to be $-0.246h$, and the distributions of τ_{xy} and σ_x obtained from equations (17), (16), and (12) are illustrated in Fig. 4. It will be seen that τ_{xy} is

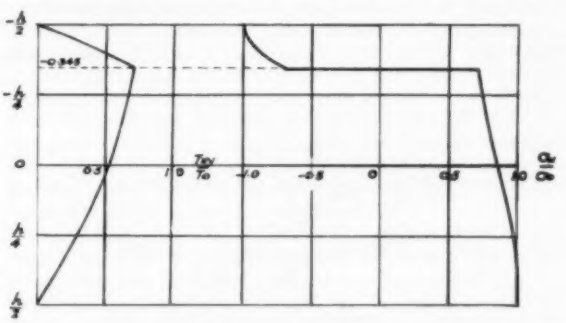

Fig. 3 Stress distribution at clamped end for moderate shear, $n = 0.6$

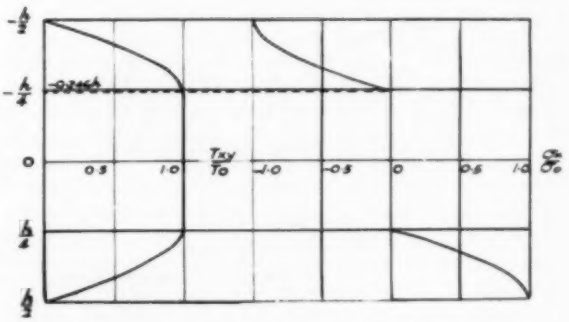

Fig. 4 Stress distribution at clamped end for high shear, $n = 0$

practically constant at the value τ_0 in a central core of depth approximately $0.49h$, and Drucker's solution [8] for $n = 0$ gives the depth of this zone as $0.48h$.

The shear force V at the free end may be evaluated as

$$V = b\int_{-h/2}^{h/2} \tau_{xy}\,dy$$

Using equations (14) and (15), this integral can be put in the form

$$v\left(\frac{\nu h}{l}\right) = \frac{1}{2}\int_0^{\psi} \frac{\sin\phi\cos\phi}{\cos\alpha + \cos\phi}\,d\phi + \frac{1}{2}\int_{\psi}^{0} \frac{\sin\phi\cos\phi}{\cos\alpha - \cos\phi}\,d\phi = \int_0^{\psi} \frac{\sin\phi\cos^3\phi}{\cos^2\alpha - \cos^2\phi}\,d\phi$$

whence

$$v\left(\frac{\nu h}{l}\right) = 1 - \cos\psi + 2\cos\alpha[\tanh^{-1}(\cos\alpha\sec\psi) - \tanh^{-1}(\cos\alpha)] \quad (19)$$

The bending moment M at the built-in end can be evaluated directly by integrating the distribution of normal stress σ_x for $x = l$. However, it is simpler to make use of the relation $M = Vl$, or from equation (5),

$$m = 2v\left(\frac{l}{\nu h}\right) \quad (20)$$

It is now possible to determine the relationship between m, v, and n in this lower bound solution. In fact, if $n = \cos\alpha$ is specified, equation (17) determines $l/\nu h$ as a function of ψ. Hence from equations (19) and (20), both v and m are known as functions of ψ, thus defining a parametric relationship between these two quantities. In Fig. 5, m is shown plotted against v for values of n at intervals of 0.2. This figure would be incomplete unless it included reference to the connection between m and v, equation (20). This is done by plotting lines of constant length/depth ratio. For this purpose ν was assumed to have the value 1 corresponding to the Tresca yield criterion.

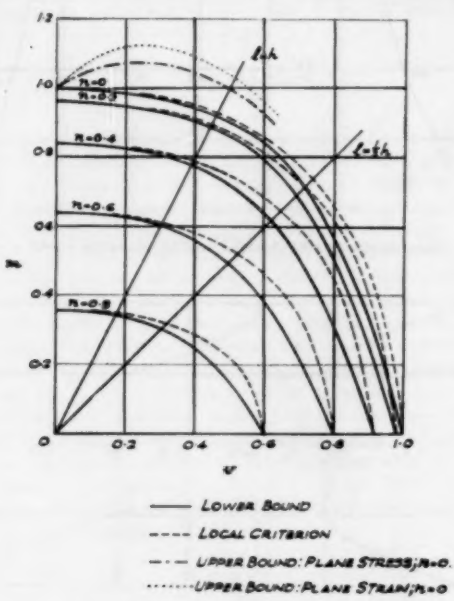

Fig. 5 Interaction curves

One further remark must be made concerning this lower bound solution. It was assumed at the beginning of the analysis that the normal force N was distributed uniformly over the free end of the cantilever. However, the distribution of the shear force V was left unspecified, and in fact it was tacitly assumed that the distributions which eventually emerged from the analysis, of the form indicated in Fig. 3 and 4, were acceptable simply because they were statically equipollent with the end load V. In any physical situation represented by Fig. 2, it would be difficult to specify the actual distribution of shear stress at the free end of the cantilever. Although the approach adopted might be thought to be justified by Saint Venant's principle, it will be seen from Fig. 5 that the effect of shear only becomes marked when l is less than h, which is precisely the region in which Saint Venant's principle would not be expected to apply. This is a further fundamental obstacle in the way of determining a unique interaction relation.

The lower bound solution could presumably be improved, in the sense of obtaining higher values of m for given values of v and n, if the distribution of normal force N over the free end was also left unspecified. However, in view of the foregoing remarks it would be difficult to attach any more significance to a solution obtained in this way than to the aforementioned solution, and the analysis has therefore not been attempted.

Upper Bound

The development of an upper bound solution for the cantilever problem of Fig. 2 presents considerable difficulty. The first approach will be made through the concept of a "local" criterion, in which strain changes at failure are assumed to occur only at the clamped end of the beam, although it will be seen that it is not at all clear what significance can be attached to results obtained in this way.

Local Criterion. A local criterion was developed by Drucker [8] for the cantilever problem of Fig. 2 with $N = 0$, and his analysis is readily extended to include the effect of normal force.

At the limit load, the deformation is wholly plastic while the stresses remain constant. The plastic deformation considered at any point at the clamped end consists of a longitudinal strain ϵ_x and a shear strain γ_{xy}. As in the lower bound analysis, it is assumed that $\sigma_y = 0$, so that the only stresses to be considered are σ_x and τ_{xy}. Assuming the Tresca criterion of yielding, it follows that all deformation takes place in the xy-plane, so that $\epsilon_z = 0$. To insure incompressibility, it is thus necessary that

$$\epsilon_y = -\epsilon_x \quad (21)$$

The deformations are therefore specified in terms of the two strain components ϵ_x and γ_{xy}. In order that the principal directions of stress and of strain increment should coincide, it can be shown that

$$\frac{\gamma_{xy}}{2\epsilon_x} = \frac{2\tau_{xy}}{\sigma_x} \quad (22)$$

Combining this relation with the yield condition, equation (12) ($\nu = 1$), it is found that

$$\sigma_x = \sigma_0\left[1 + \left(\frac{\gamma_{xy}}{2\epsilon_x}\right)^2\right]^{-1/2}$$

$$\tau_{xy} = \frac{1}{2}\sigma_0\left[1 + \left(\frac{2\epsilon_x}{\gamma_{xy}}\right)^2\right]^{-1/2} \quad (23)$$

It is now assumed that

$$\epsilon_x = \left(\frac{2y}{h}\right)\epsilon + \epsilon'$$

$$\gamma_{xy} = \gamma \tag{24}$$

where ϵ, ϵ', and γ are constants, so that the longitudinal strain consists of a constant strain ϵ' together with a linear variation of strain from $-\epsilon$ to ϵ from top to bottom of the section, and the shear strain is constant across the section. ϵ, ϵ', and γ specify the magnitudes of the local deformations at the clamped end corresponding to hinge rotation, axial extension and shear, respectively.

Combining equations (23) and (24), values for the bending moment, normal force, and shear force at the clamped end are found by integrating across the section to be

$$M = \frac{1}{2}bh^2\sigma_0\int_{-1}^{1}\eta(\eta\epsilon + \epsilon')[\gamma^2 + 4(\eta\epsilon + \epsilon')^2]^{-1/2}\,d\eta$$

$$N = bh\sigma_0\int_{-1}^{1}(\eta\epsilon + \epsilon')[\gamma^2 + 4(\eta\epsilon + \epsilon')^2]^{-1/2}\,d\eta$$

$$V = \frac{1}{4}bh\sigma_0\int_{-1}^{1}\gamma[\gamma^2 + 4(\eta\epsilon + \epsilon')]^{-1/2}\,d\eta$$

where

$$\eta = 2y/h$$

Integrating these expressions, it is found that

$$\begin{aligned} m &= (\coth\alpha - \alpha\,\mathrm{cosech}^2\alpha)\,\mathrm{sech}^2\beta \\ n &= \tanh\beta \\ v &= (\alpha\,\mathrm{cosech}\,\alpha)\,\mathrm{sech}\,\beta \end{aligned} \tag{25}$$

where

$$\sinh\theta = 2(\epsilon + \epsilon')/\gamma$$

$$\sinh\phi = 2(\epsilon - \epsilon')/\gamma$$

$$\alpha = {}^1/_2(\theta + \phi), \qquad \beta = {}^1/_2(\theta - \phi)$$

β is readily eliminated from equations (25), giving

$$\begin{aligned} m &= (1 - n^2)(\coth\alpha - \alpha\,\mathrm{cosech}^2\alpha) \\ v^2 &= (1 - n^2)\alpha^2\,\mathrm{cosech}^2\alpha \end{aligned} \tag{26}$$

It will be seen from these equations that the relationship between $m/1 - n^2$ and $v/(1 - n^2)^{1/2}$ according to the local criterion is precisely the same as the relationship between m and v for the case of zero axial thrust. This latter relationship was, of course, obtained by Drucker [8]. It was also obtained by Hodge [9], who suggested that it represented a true upper bound on the interaction relation. However, as pointed out by Drucker, this solution does not meet all the requirements of upper bound analysis. In the localized region of deformation, transverse strains $\epsilon_y = -\epsilon_x$ have been shown to occur, and there would therefore be a "mismatch" at the junction between this region and the remaining, rigid part of the cantilever; further, there would be some mismatch at the built-in end. The energy absorption in the regions of mismatch would not be negligible, and if it was included in the analysis a true upper bound would be obtained in which the estimates of the limit loads would be higher than those corresponding to equations (26).

Hodge [9] also showed that the (m, v) relationship for $n = 0$ which is contained in equations (26) could be derived by what appeared to be a lower bound approach. This involved maximizing the moment

$$M = b\int_{-h/2}^{h/2}\sigma_x y\,dy$$

at the clamped end, while keeping constant the shear force

$$V = b\int_{-h/2}^{h/2}\tau_{xy}dy,$$

σ_x and τ_{xy} being made to satisfy the Tresca criterion of yielding across the section. However, conditions of equilibrium along the length of the cantilever were not considered, and in addition τ_{xy} was not made zero at $y = \pm h/2$. Since the conditions used by Hodge were less stringent than those required for a true lower bound solution, it would appear that the estimates of limit load derived would be higher than for the lower bound.

It therefore appears that equations (26) give an interaction relation which is lower than a particular upper bound and higher than a particular lower bound. Thus it is not possible to decide whether these equations provide an upper or a lower bound, and they can therefore only be regarded as furnishing an estimate of the actual solution.

In Figs. 5, (m, v) relations according to equations (26) are plotted for values of n at intervals of 0.2. It will be seen that the agreement between these relations and the lower bound solution already obtained is quite striking for $l > h$, and is reasonable for $l > 0.5h$.

Green's Upper Bound Solutions. Upper bound solutions for the cantilever problem of Fig. 2 were examined in some detail by Green [6], who pointed out the effect of varying the support conditions at the built-in end. Most of Green's solutions were obtained for conditions of "strong" support, in which the cantilever is supposed to be built in to fully rigid material, so that no plastic deformation can occur beyond $x = l$ in Fig. 2. Green also examined the effect of assuming a weaker support condition in which some plastic deformation could occur beyond $x = l$ in the lower half of the beam only, and showed that for this condition the limit load was lower than for the strongly supported case. However, the precise physical significance of the weaker support condition assumed by Green is difficult to determine, and accordingly attention will be confined to the solution for the strongly supported cantilever.

For conditions of plane stress, and using the von Mises yield criterion, an upper bound solution for the strongly supported cantilever was obtained by Green for the case of zero axial thrust. The corresponding (m, v) relation is shown in Fig. 5. This relation is directly comparable with the lower bound relation for $n = 0$, which is valid for either the von Mises or the Tresca yield criterion, whereas the local criterion solution was obtained using the Tresca criterion. It will be seen that this upper bound solution gives values of m greater than unity for values of v less than about 0.5. This is a consequence of the strong support condition assumed, which causes the beam to rotate about a point some distance from the built-in end at the limit load.

Over the range of values of m and v for which it is valid, this solution furnishes values of m exceeding the lower bound values by not more than 11 per cent, and in view of the restrictive nature of the strong support conditions this may be regarded as providing satisfactory evidence in favor of the lower bound results for $n = 0$.

Although Green's upper bound solution for plane stress only applied to the case of zero axial thrust, an upper bound solution for plane-strain conditions was found for the case in which both shear and normal forces were present, strong support conditions being assumed. This solution can be used to derive interaction relations using either the von Mises or the Tresca yield criterion, but since the lower bound interaction relations plotted in Fig. 5 are applicable to conditions of plane strain only if the Tresca criterion is assumed, this criterion has been used in interpreting Green's plane-strain solution. To avoid confusing the diagram, only the solution for $n = 0$ is plotted in Fig. 5, from which it will be seen that this solution has the same basic characteristics as the plane-stress solution, although the values of m are somewhat higher. For values of n, greater than zero, the solution exhibits the same characteristic as for $n = 0$; namely, that $dm/dv > 0$

for small values of v, and this effect is more pronounced the higher the value of n.

Apart from the special case $n = 0$, the plane-strain solutions referred specifically to four values of l/h; namely, 8, 4, 2, and 1. For each value of l/h, v was evaluated as a function of n; corresponding values of m can of course be found at once from equation (5). Examination of these results shows that the discrepancy between this solution and the lower bound solution for a given value of l/h depends on n, and is greatest for values of n of about 0.5. The maximum discrepancy also increases with decrease of l/h as follows:

l/h	8	4	2	1
Discrepancy, per cent	6	11	21	28

This effect is a natural consequence of the assumption of the strongly supported condition, which becomes more dominant for smaller values of l/h.

Suggested Interaction Relation

Bearing in mind that the use of a lower bound interaction relation will lead to conservative results, it is suggested that the lower bound which has been derived for the cantilever problem of Fig. 2 could be used as an interaction relation for other physical situations to provide useful solutions. As pointed out by Drucker [8], quite a good approximation to the curves for $n = 0$ is the relation

$$m = 1 - v^4$$

It will be recalled that for the local criterion solution, the relationship between $m/1 - n^2$ and $v/(1 - n^2)^{1/2}$ is precisely the same as the relationship between m and v for the case of zero axial thrust. This suggests that the interaction relation

$$\frac{m}{1 - n^2} = 1 - \frac{v^4}{(1 - n^2)^2}$$

or

$$m + n^2 + \frac{v^4}{1 - n^2} = 1 \tag{27}$$

would represent a good approximation to the lower bound interaction relation for all values of m, v, and n. This is in fact so; equation (27) furnishes values of the limit load which are generally slightly higher than the lower bound values. The relation is exact for $v = 0$, and the discrepancy never exceeds 5 per cent over the full range of values of m, n, and v. It is therefore suggested that equation (27) could be used as an empirical interaction relation between m, n, and v for rectangular cross sections.

References

1 M. R. Horne, "The Full Plastic Moments of Sections Subjected to Shear Force and Axial Load," *British Welding Journal*, vol. 5, 1958, p. 170.

2 J. Heyman and V. L. Dutton, "Plastic Design of Plate Girders With Unstiffened Webs," *Welding and Metal Fabrication*, vol. 22, 1954. p. 265.

3 K. Girkmann, "Bemessung von Rahmentragwerken unter Zugrundelegung eines ideal-plastischen Stahles," *Sitzungsberichte der Akademie der Wissenschaften in Wien*, Abt. IIa, vol. 140, 1931, p. 679.

4 M. R. Horne, "The Plastic Theory of Mild Steel Beams With Particular Reference to the Effect of Shear Forces," *Proceedings of the Royal Society*, series A, vol. 207, 1951, p. 216.

5 C.-F. A. Leth, "The Effect of Shear Stresses on the Carrying Capacity of I-Beams," Technical Report No. A-11-107, Brown University, 1954.

6 A. P. Green, "A Theory of the Plastic Yielding Due to Bending of Cantilevers and Fixed-Ended Beams," *Journal of Mechanics and Physics of Solids*, vol. 3, 1954, p. 143.

7 E. T. Onat and R. T. Shield, "The Influence of Shearing Forces on the Plastic Bending of Wide Beams," *Proceedings of the Second U. S. National Congress of Applied Mechanics*, Ann Arbor, Mich., 1954, p. 535.

8 D. C. Drucker, "The Effect of Shear on the Plastic Bending of Beams," JOURNAL OF APPLIED MECHANICS, vol. 23, TRANS. ASME, vol. 78, 1956, p. 509.

9 P. G. Hodge, Jr., "Interaction Curves for Shear and Bending of Plastic Beams," JOURNAL OF APPLIED MECHANICS, vol. 24, TRANS. ASME, vol. 79, 1957, p. 453.

On Normal Vibrations of a General Class of Nonlinear Dual-Mode Systems

R. M. ROSENBERG
Professor,
Department of Mechanical Engineering,
University of California,
Berkeley, Calif.

Free vibrations in normal modes are examined for a system consisting of two unequal (or equal) masses, interconnected by a nonlinear coupling spring, and each mass connected by nonlinear unequal (or equal) anchor springs to fixed points. All spring forces are odd functions, and proportional to the k'th power, of the spring deflections, where k is a real, positive number. The frequency-amplitude relations for the in and out-of-phase modes are derived without approximation, the stability of these modes is analyzed, and several numerical examples are worked out. A surprising feature of these systems is that they may have a greater number of normal modes than they have degrees of freedom.

In two earlier papers [1, 2][1] the free normal vibrations of a system like that illustrated in Fig. 1 were discussed. It consists of two masses m_1 and m_2 which may be equal or unequal, connected to fixed points by the anchor springs S_1 and S_3 which, again, may be equal or unequal, and interconnected by a coupling spring S_2. All springs may be nonlinear, but the spring forces in all springs are odd functions of the spring deflections; in other words, each spring resists being compressed in the same amount as it resists being extended. The concept of normal modes has been defined precisely for this system [2], and it was shown that two classes of systems (of the type under discussion here) exist for which the ratios of the displacements of the two masses are identically equal to constants for all time when the system vibrates in normal modes. One class is the so-called "symmetric system" in which the two masses are equal to each other, as are the anchor springs. The other class is a system which may be entirely unsymmetric with respect to the masses as well as the anchor springs. It is characterized by the property that all springs resist being deflected with a force which is directly proportional to the same positive power k of the spring deflections, where k is an odd integer. In systems of this class, the forces derivable from the potential energy are functions which are homogeneous of degree k in the displacements of the masses. Therefore these systems have been called the "homogeneous systems of degree k" [2]. In this paper we discuss the normal modes and their stability for a class of systems which is a generalization of the homogeneous systems of odd-integer degree. The generalization consists in removing the restriction that k be an odd integer, and replacing it by the wider restriction that k be a positive finite number. However, we retain the property that the spring forces are odd functions of the spring deflections.

Homogeneous systems are of great interest for a variety of reasons. In the first place, their frequency-amplitude response, called by Klotter [3] the backbones, can be obtained in terms of tabulated functions. Therefore, the approximations usually encountered in the analysis of nonlinear systems are not necessary even when the systems are strongly nonlinear; i.e., when they are not in the neighborhood of linear systems. In the second place, the linear system belongs to this class, because it is the homogeneous system of degree 1. Thus the theory presented here is a generalization of that of the linear system. Since the linear system has furnished generating solutions for systems of the Duffing type lying in the neighborhood of the linear case, it is clear that an exact discussion of the homogeneous systems provides points of departure for the treatment of cases neighboring on any of them. In the third place, since we shall remove the restriction that k be a positive, odd integer and replace it by the much more general one $0 < k < \infty$, we are now in a position to discuss with precision a continuous spectrum of systems ranging from the highly nonlinear one with soft springs through the linear to the highly nonlinear with hard springs.[2] Finally, the homogeneous systems represent cases of practical interest whenever the springs are actually of the character prescribed by the theory.

Among the unsymmetric cases which fall within the scope of this investigation is that of the nonlinear dynamic vibration absorber since it has the configuration of Fig. 1 with one anchor spring absent.

The Equations of Motion

When the spring forces of the general system are odd polynomials of the spring deflections, the equations of motion are [2]

$$\left.\begin{aligned} m_1\ddot{x} &= -\sum_n^r a_n x^n - \sum_n^s A_n(x-y)^n \\ m_2\ddot{y} &= -\sum_n^t b_n y^n + \sum_n^s A_n(x-y)^n \end{aligned}\right\} \quad n = 1, 3, \ldots \quad (1)$$

[2] In hard springs the stiffness increases with increasing deflection; in soft springs it decreases with increasing deflection.

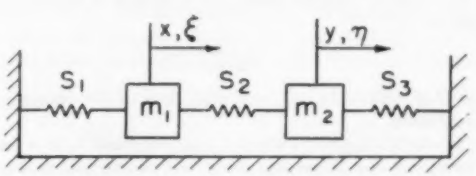

Fig. 1

[1] Numbers in brackets designate References at end of paper.

Contributed by the Applied Mechanics Division of The American Society of Mechanical Engineers and presented at the 10th International Congress of Applied Mechanics, Stresa, Italy, August 31-September 7, 1960.

Written discussion on this paper should be addressed to the Editorial Department, ASME, 29 West 39th Street, New York, N. Y. and will be accepted until July 10, 1961. Discussion received after the closing date will be returned. Manuscript received by ASME Applied Mechanics Division, May 31 1960.

In these equations, the right-hand sides are derivable from a potential energy which is evidently a function of the displacements x, y and of the constants a_n, b_n, A_n. By means of the transformations

$$\xi = m_1^{1/2}x, \quad \eta = m_2^{1/2}y \tag{2}$$

the equations of motion go over into

$$\begin{aligned} \ddot{\xi} &= -\sum_n^r \frac{a_n}{m_1^{1/2}}\left(\frac{\xi}{m_1^{1/2}}\right)^n - \sum_n^s \frac{A_n}{m_1^{1/2}}\left(\frac{\xi}{m_1^{1/2}} - \frac{\eta}{m_2^{1/2}}\right)^n \\ \ddot{\eta} &= -\sum_n^t \frac{b_n}{m_2^{1/2}}\left(\frac{\eta}{m_2^{1/2}}\right)^n + \sum_n^s \frac{A_n}{m_2^{1/2}}\left(\frac{\xi}{m_1^{1/2}} - \frac{\eta}{m_2^{1/2}}\right)^n \end{aligned} \tag{3}$$

where the right-hand sides are again derivable from a potential function; however, this potential depends now not only on the quantities listed in the foregoing, but on the masses as well. Equations (3) are mathematically completely equivalent to (1); however, their physical meaning is quite different. While (1) are the equations of motion of the system pictured in Fig. 1, (3) are the equations of motion of a unit which moves in the $\xi\eta$-plane under forces derivable from a potential function which involves all parameters of the problem.

The homogeneous system of odd-integer degree k emerges from (3) as

$$\begin{aligned} \ddot{\xi} &= -\frac{a_k}{m_1^{1/2}}\left(\frac{\xi}{m_1^{1/2}}\right)^k - \frac{A_k}{m_1^{1/2}}\left(\frac{\xi}{m_1^{1/2}} - \frac{\eta}{m_2^{1/2}}\right)^k \\ \ddot{\eta} &= -\frac{b_k}{m_2^{1/2}}\left(\frac{\eta}{m_2^{1/2}}\right)^k + \frac{A_k}{m_2^{1/2}}\left(\frac{\xi}{m_1^{1/2}} - \frac{\eta}{m_2^{1/2}}\right)^k \end{aligned} \tag{4}$$

This system may be generalized in such a way that any real k in the interval $0 < k < \infty$ is admitted by replacing (4) with the equations

$$\begin{aligned} \ddot{\xi} &= -\frac{a_k}{m_1^{1/2}}\left(\frac{\xi}{m_1^{1/2}}\right)\left|\frac{\xi}{m_1^{1/2}}\right|^{k-1} \\ &\quad - \frac{A_k}{m_1^{1/2}}\left(\frac{\xi}{m_1^{1/2}} - \frac{\eta}{m_2^{1/2}}\right)\left|\frac{\xi}{m_1^{1/2}} - \frac{\eta}{m_2^{1/2}}\right|^{k-1} \\ \ddot{\eta} &= -\frac{b_k}{m_2^{1/2}}\left(\frac{\eta}{m_2^{1/2}}\right)\left|\frac{\eta}{m_2^{1/2}}\right|^{k-1} \\ &\quad + \frac{A_k}{m_2^{1/2}}\left(\frac{\xi}{m_1^{1/2}} - \frac{\eta}{m_2^{1/2}}\right)\left|\frac{\xi}{m_1^{1/2}} - \frac{\eta}{m_2^{1/2}}\right|^{k-1} \end{aligned} \tag{5}$$

It is this system of equations on which all future development is based. The right-hand sides are seen to be still homogeneous functions of degree k. They may be derived from a potential function given by

$$\begin{aligned} U = &-\frac{a_k}{k+1}\left|\frac{\xi}{m_1^{1/2}}\right|^{k+1} - \frac{b_k}{k+1}\left|\frac{\eta}{m_2^{1/2}}\right|^{k+1} \\ &- \frac{A_k}{k+1}\left|\frac{\xi}{m_1^{1/2}} - \frac{\eta}{m_2^{1/2}}\right|^{k+1} \end{aligned} \tag{6}$$

if use is made of the fact that $x|x|^{k-1} = |x|^k \operatorname{sgn} x$, and that $d|x|/dx = \operatorname{sgn} x$. Consequently, the equations of motion may be written as

$$\ddot{\xi} = U_\xi, \ddot{\eta} = U_\eta \tag{7}$$

where U is defined by (6), and subscripts in (7) denote partial differentiation.

In the earlier paper [2] where k was restricted to be a positive odd integer it was shown that there exist two normal modes: the i-mode where the two masses move in phase, and the o-mode where the two masses move out of phase. These modes are defined by two straight lines in the $\xi\eta$-plane, both passing through the origin. Therefore these modes can be identified with two constants $c_{i,o}$ which satisfy

$$\eta(t)/\xi(t) \equiv c_{i,o} = \tan\theta_{i,o} \tag{8}$$

and the inclinations of these lines to the ξ-axis are the angles $\theta_{i,o}$. These angles are the roots of the transcendental equation

$$\tan 2\theta = \frac{2(1-\sin 2\theta)^{\frac{k-1}{2}}}{\beta_k[\frac{1}{2}(1-\cos 2\theta)]^{\frac{k-1}{2}} - \alpha_k[\frac{1}{2}(1+\cos 2\theta)]^{\frac{k-1}{2}}} \tag{9}$$

if the two masses are equal [2]. In (9), $\alpha_k = a_k/A_k$, $\beta_k = b_k/A_k$, and we require $A_k \neq 0$. This latter restriction is consistent with the problem in hand because $A_k = 0$ would imply the absence of a coupling spring between the two masses. If the two masses are not equal, a relation similar to (9) can also be derived by the methods described in the earlier paper [2]. This new relation must contain the mass ratio $\mu = m_1/m_2$ as an additional parameter, and it reduces to (9) when $\mu = 1$. The new formula is

$$\begin{aligned} \tan 2\theta = &\left\{2\mu^{1/2}[\tfrac{1}{2}(1+\mu) + \tfrac{1}{2}(1-\mu)\cos 2\theta \right. \\ &\left. - \mu^{1/2}\sin 2\theta]^{\frac{k-1}{2}}\right\} \Big/ \left\{\mu^{\frac{k-1}{2}}\beta_k[\tfrac{1}{2}(1-\cos 2\theta)]^{\frac{k-1}{2}} \right. \\ &- \alpha_k[\tfrac{1}{2}(1+\cos 2\theta)]^{\frac{k-1}{2}} + (\mu-1)[\tfrac{1}{2}(1+\mu) \\ &\left. - \tfrac{1}{2}(1-\mu)\cos 2\theta - \mu^{1/2}\sin 2\theta]^{\frac{k-1}{2}}\right\} \end{aligned} \tag{10}$$

One need investigate the roots of (10) only for mass ratios in the interval $0 < \mu \leq 1$ because, when the masses are unequal, one may always designate the smaller of the two by m_1 and the larger by m_2. The anchor spring attached to the smaller mass is then characterized by the constant a_k and its deflection by $x = \xi/m_1^{1/2}$, while the anchor spring attached to the larger mass is identified with b_k and its deflection by $y = \eta/m_2^{1/2}$.

In homogeneous systems of odd-integer degree, the two straight lines of slopes c_i and c_o have been shown [2] to intersect all lines of constant potential orthogonally. In the linear case $k = 1$, the equipotential lines are concentric ellipses and the modal relations intersect each other orthogonally. Moreover, in the linear system the modal relations are axes of symmetry for the equipotential lines. These properties are easily deduced from equations (9) and (10) when one puts $k = 1$ in them, and they are illustrated in Fig. 2(*a*).

It is a remarkable property of the homogeneous nonlinear system, easily deduced from (9) or (10), that the straight modal relations do *not* intersect each other orthogonally. This follows from the fact that (9) or (10) does not remain unchanged when θ is replaced by $\theta + (\pi/2)$. One can further demonstrate the unexpected fact that, in consequence of their nonorthogonal mutual intersection, the modal relations can *not*, in general, be axes of symmetry for the equipotential lines. The proof follows immediately from the following theorem: A curve C which is symmetric with respect to a straight line (A) and has point symmetry with respect to a point P on (A) is also symmetric with respect to (B), where (B) is a straight line intersecting (A) orthogonally at P. The proof of this theorem becomes evident when a point P' on C is reflected first in P and then in (A).

Clearly, if a modal line is an axis of symmetry for the equipotential lines, it follows from the foregoing theorem that another modal line must exist which intersects the first orthogonally at the origin. But if this were true, (9) and (10) would have to remain unchanged when θ is replaced by $\theta + (\pi/2)$; as pointed out before, this is not the case. Therefore these straight lines are not in

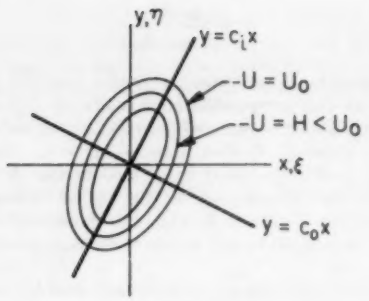

Fig. 2(a)

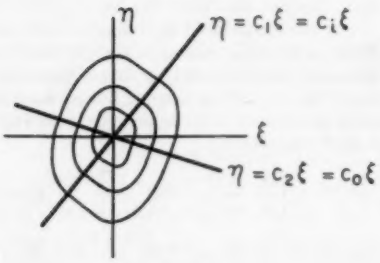

Fig. 2(b)

general axes of symmetry for the equipotential lines even though they intersect each of these lines orthogonally. The manner in which the equipotential lines and the modal relations behave with respect to each other is shown in Fig. 2(*b*).

While (9) and (10) were derived only for homogeneous systems of *odd-integer* degree they are also applicable to noninteger values of k. The reason for the general validity of these formulas is that modal relations $\eta(\xi)$ are always odd provided the equipotential lines are symmetric with respect to the origin [2]. But (6) may be regarded as an equation of the form $f(U, \xi, \eta) = \text{const}$, and it is seen to be symmetric with respect to the U-axis in the $U\xi\eta$-space. Consequently, (9) and (10) carry over unchanged into the general homogeneous system.

By means of (9) (when $m_1 = m_2$) or (10) (when $m_1 \pm m_2$), one can always find constants $c_{i,o}$ which define the modes. In all that follows it is assumed that this has been done. As was shown for (9) [2] and can easily also be demonstrated for (10), the angles $\theta_{i,o}$ satisfy the inequalities $\pi/4 \leq \theta_i < \pi/2$ and $3\pi/4 \leq \theta_o < \pi$, so that c_i is a positive constant defining an in-phase mode, and c_o is negative defining an out-of-phase mode. The former will be referred to as the "i-mode" and will be identified by the subscript i, and a similar convention will identify the out-of-phase mode by the term o-mode and the subscript o.

Because of the symmetry properties of the equipotential lines, the motion may be analyzed by considering the equations of motion (4) either in the half-plane $\xi \geq 0$ or $\eta \geq 0$.

The Backbone Curves

Once the constants $c_{i,o}$ have been found from (9) or (10) the equations of motion can be decoupled because the normal modes *are* the generalized co-ordinates in which the equations separate. If one replaces η by $c_i\xi$ in the first of (4) and attaches the subscript i to the dependent variable, one has

$$\ddot{\xi}_i = -m_i^{-\frac{k+1}{2}} [a_k + A_k(1 - \mu^{1/2}c_i)^k]\xi_i^k \qquad (11)$$

In a similar way, the equation of motion of mass m_1 in the o-mode is obtained as

$$\ddot{\xi}_o = -m_1^{-\frac{k+1}{2}} [a_k + A_k(1 - \mu^{1/2}c_o)^k]\xi_o^k \qquad (12)$$

These equations are called the "modal equations" [1]. Clearly, similar equations for the motion of the mass m_2 can be obtained by substituting $\xi = c_{i,o}^{-1}\eta$ in the second of (4).

From the modal equations one can obtain the frequency-amplitude relations in both modes, and for both masses. These relations have been called by Klotter [3] the "backbones" because of the role they play in the problem of forced vibrations. We shall adopt this convenient and descriptive term and show how the backbones are found for the motions of m_1 in the i-mode.

In accordance with the definition of normal modes [2], (11) and (12) must be integrated so as to satisfy the initial conditions

$$\xi_{i,o}(0) = \chi_{i,o}, \quad \dot{\xi}_{i,o}(0) = 0 \qquad (13)$$

A first integral of these equations is elementary, and the second in terms of gamma functions is tabulated as a definite integral [4], if one integrates over a quarter period when $\xi_{i,o}$ goes from $\chi_{i,o}$ to zero. The fact that equations like (11) and (12) can be integrated in terms of beta functions and subsequently reduced to gamma functions was observed and utilized earlier by McDuff and Curreri [5].

The backbone for the i-mode of mass m_1 is found as

$$\omega_{i1}^2(k, \chi_i) = \left[\frac{\Gamma\left(\frac{1}{k+1} + \frac{1}{2}\right)}{\Gamma\left(\frac{1}{k+1}\right)}\right]^2 \pi \frac{k+1}{2} m_1^{-\frac{k+1}{2}} [a_k + A_k(1 - \mu^{1/2}c_i)^k]\chi_i^{k-1}$$

If one defines $\nu_{i1}^2 = \omega_{i1}^2/A_k$, the backbone equation becomes

$$\nu_{i1}^2(k, \chi_i) = \left[\frac{\Gamma\left(\frac{1}{k+1} + \frac{1}{2}\right)}{\Gamma\left(\frac{1}{k+1}\right)}\right]^2 \pi \frac{k+1}{2} m_1^{-\frac{k+1}{2}} [\alpha_k + (1 - \mu^{1/2}c_i)^k]\chi_i^{k-1} \qquad (14)$$

A similar relation for the o-mode of mass m_1 is found if one replaces the subscript i by o in (14). While equivalent relations for the i and o-modes of mass m_2 could be found by dealing with the second of the equations of motion (4), it will be shown in the following that this step is unnecessary because the backbones of the two masses in either mode satisfy a simple algebraic relation. In fact, one need compute only one of the backbones for one of the masses because the backbones for the same mass in the two modes satisfy an equation which is much simpler than (14).

Some general observations of interest may be drawn from (14); for one, that equation must remain valid in the linear case. When $k = 1$, (14) becomes

$$\nu_{i1}^2(1, \chi_i) = \frac{\alpha_1 + (1 - \mu^{1/2}c_i)}{m_1} = \nu_{N}^2(1) \qquad (15)$$

As expected, this relation does not contain the amplitude χ_i; thus we obtain the well-known result that, in the linear case, the frequency of free vibrations is the same for all amplitudes. The constant c_i is (in the linear case) found from the smaller principal root of

$$\tan 2\theta = \frac{2\mu^{1/2}}{\mu(1 + \beta_k) - (1 + \alpha_k)} \qquad (16)$$

This equation is obtained if one puts $k = 1$ in (10). When the

subscript i is replaced by o in (15) and c_o is determined from the larger principal root of (16), the backbone for the o-mode of the linear system is found. Therefore both backbones are distinct parallel lines in the frequency-amplitude plane, both parallel to the amplitude axis. These are the only backbones having this property. When $0 < k < 1$, the backbones are curves such that

$$\lim_{\chi_{i,o} \to 0} \nu_{i,o}^2 = \infty, \quad \lim_{\chi_{i,o} \to 0} \frac{d\chi_{i,o}}{d\nu_{i,o}} = 0 \tag{17}$$

and when $1 < k < \infty$,

$$\lim_{\chi_{i,o} \to 0} \nu_{i,o}^2 = 0 \tag{18}$$

A second special case is $k = 3$. For this value, the backbones are straight lines intersecting the origin of the frequency-amplitude plane. For $1 < k < 3$,

$$\lim_{\chi_{i,o} \to 0} \frac{d\chi_{i,o}}{d\nu_{i,o}} = 0 \tag{19}$$

while for $3 < k < \infty$,

$$\lim_{\chi_{i,o} \to 0} \frac{d\chi_{i,o}}{d\nu_{i,o}} = \infty \tag{20}$$

The general character of the backbones for these cases is shown in Fig. 3. Since $0 < k < 1$ defines a soft spring, and $1 < k < \infty$ a hard one, it is seen that the familiar character of the backbones is preserved. When the springs are soft the frequency decreases with increasing amplitude; when they are linear the frequency is independent of the amplitude; and when they are hard the frequency increases with increasing amplitude.

An unexpected feature of the system is that the frequencies of the i-mode are not always real while those of the o-mode always are. It will be recalled that the modal constants $c_{i,o}$ depend on the parameters α_k, β_k, μ, k, and that c_i is always positive while c_o is negative. Since $c_i > 0$, inspection of (14) shows that the frequency ν_{ii} is imaginary whenever

$$\mu > \left[\frac{\alpha_k^{1/k} + 1}{c_i(\alpha_k, \beta_k, \mu)}\right]^2 \tag{21}$$

Thus any system whose parameters satisfy the inequality (21) cannot vibrate in the in-phase normal mode. One can easily show that this case may actually arise. For instance, consider a system which is symmetric with respect to the masses but not to the anchor springs, so that $\mu = 1$ and $\alpha_k \neq \beta_k$. Thus the inequality to be satisfied is

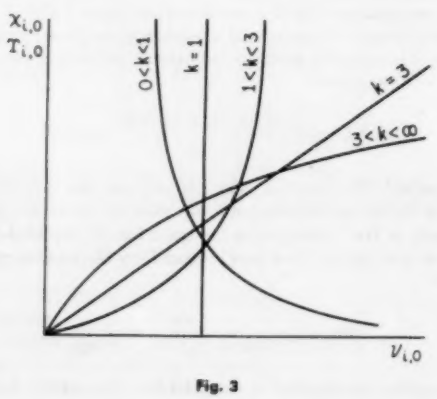

Fig. 3

$$1 > \frac{\alpha_k^{1/k} + 1}{c_i(\alpha_k, \beta_k, 1)} \tag{22}$$

But from the bounds established earlier for θ_i as $\pi/4 \leq \theta_i < \pi/2$ it is seen that the corresponding bounds on c_i are $1 \leq c_i < \infty$. If the system is also symmetric with respect to the anchor springs, it has been shown [1, 2] that $c_i(\alpha_k, \alpha_k, 1) = 1$. Therefore for $\beta_k \neq \alpha_k$, c_i must exceed unity by an amount that depends on β_k only. Since the denominator of (22) can be increased at will through suitable choices of β_k while the numerator remains unchanged, it is possible to find values of the parameters such that (22) is satisfied.

A comparable phenomenon in the o-mode does not exist because it is always true that

$$1 - \mu^{1/2} c_o > 0 \tag{23}$$

It was stated earlier that only the backbone for one of the masses in one of the modes need be computed, and that that for the other mode of the same mass, and that for the two modes of the other mass can then be found by simple formulas. Suppose the backbone of the i-mode for mass m_1 has been computed from (14). That for the o-mode of the same mass is then given for any value ν^* of the frequencies by

$$\chi_o(\nu^*, k) = \left[\frac{\alpha_k + (1 - \mu^{1/2} c_i)^k}{\alpha_k + (1 - \mu^{1/2} c_o)^k}\right]^{1/(k-1)} \chi_i(\nu^*, k) \tag{24}$$

provided that the frequency ν_i is real; i.e., that (21) is not satisfied. The backbones for the other mass are obtained for any value of the frequency from

$$T_{i,o}(\nu^*, k) = c_{i,o} \chi_{i,o}(\nu^*, k) \tag{25}$$

where $T_{i,o}$ are the amplitudes of mass m_2 in the i and o-modes, respectively. Equation (24) is found by deriving an expression similar to (14) for the o-mode of mass m_1 and then computing the ratio ν_{oi}^2/ν_{ii}^2 for equal values of the frequency. Equation (24) is a direct consequence of the existence of the straight modal relations.

Superabundant Modes

One of the unexpected features of nonlinear systems having two degrees of freedom is that they may have more than two normal modes.[3] This is a feature not shared by linear systems and, therefore, of special interest.

Consider, for example, a homogeneous system which is also symmetric. For simplicity, we shall assume that the degree of homogeneity is an odd integer; however, the demonstration which we are about to give can be immediately generalized to other homogeneous systems.

The potential function of a symmetric system is

$$U = -\frac{a_k}{k+1}(x^{k+1} + y^{k+1}) - \frac{A_k}{k+1}(x - y)^{k+1}$$

or, in polar co-ordinates,

$$U = \frac{r^{k+1}}{k+1}[-a_k(\cos^{k+1}\theta + \sin^{k+1}\theta) - A_k(\cos\theta - \sin\theta)^{k+1}] \tag{26}$$

A necessary condition for the existence of straight modal relations in the sense of (8) is that [2]

$$\frac{\partial U}{\partial \theta} = \Theta_1(\theta)\Theta_2(r, \theta)$$

[3] The author is indebted to Prof. C. P. Atkinson and Mr. W. M. Keese who constructed a special example having four modes.

and, when $-U$ is positive, definite, this condition is also sufficient. The modal relations are, then, the roots of $\Theta_1(\theta) = 0$; if that equation has more than two roots, there exist more than two normal modes. In the case of (26), $\Theta_1 = 0$ becomes

$$\tfrac{1}{2}\alpha_k(\cos^{k-1}\theta - \sin^{k-1}\theta)\sin 2\theta + (\cos\theta - \sin\theta)^{k-1}\cos 2\theta = 0 \tag{27}$$

After some algebraic and trigonometric manipulations, the last equation can be written as

$$\cos 2\theta\left\{\left(\frac{1}{2}\right)^{\frac{k-1}{2}}\alpha_k \sin 2\theta \sum_{i=0,1,2,\ldots}^{\frac{k-1}{2}} C_i \cos^i 2\theta + (1-\sin 2\theta)^{\frac{k-1}{2}}\right\} = 0 \tag{28}$$

where the C_i are binomial coefficients if k is an odd integer, and they are combinations of Gamma functions whose arguments depend on k, when k is not an odd integer.

It is seen that

$$\Theta_1(\theta) = R_1(\theta)R_2(\theta)$$

where $R_1 = \cos 2\theta$, and R_2 is the quantity in the braces in (28). Putting $R_1(\theta) = 0$ furnishes the roots $\theta_1 = \pi/4$, $\theta_2 = 3\pi/4$ which all symmetric systems satisfy [1]. Thus these roots are the i and o-modes in which the absolute values of the displacements of the two masses are equal at all times. However, the real roots of $R_2 = 0$ (if they exist) depend on α_k and on k.

In the following we show for the case $k = 3$, that these roots can be easily obtained in physical systems. When $k = 3$, (27) becomes

$$[(\tfrac{1}{2}\alpha_3 - 1)\sin 2\theta + 1]\cos 2\theta = 0$$

From $\cos 2\theta = 0$ we find $\theta_1 = \pi/4$, $\theta_2 = 3\pi/4$. Real roots of

$$(\tfrac{1}{2}\alpha_3 - 1)\sin 2\theta + 1 = 0$$

exist when $\alpha_3 \geq 4$, or when $\alpha_3 \leq -4$. When $\alpha_3 > 0$, the quantity $-U$ is positive, definite, and the necessary and sufficient conditions for the existence of straight modal relations are satisfied. The additional roots are

$$\theta_{3,4} = -\frac{1}{2}\sin^{-1}\frac{2}{\alpha_k - 2}$$

It is readily verified that $\theta_{1,2}$ define modal relations which are axes of symmetry for the equipotential lines since

$$R_1(2\theta) = R_1(2\theta + \pi)$$

while $\theta_{3,4}$ define modal relations which are *not* lines of symmetry for the equipotential lines since

$$R_2(2\theta) \pm R_2(2\theta + \pi)$$

Finally, it is of interest to observe that the superabundant modes, defined by $\theta_{3,4}$, are necessarily o-modes since

$$\frac{\pi}{2} < \theta_{3,4} < \pi$$

Therefore this system has one i-mode and three o-modes.

Stability of the Normal Modes

It is clear that a conservative system cannot become unstable in the sense that the amplitudes become unbounded. Thus the stability analysis consists in examining the stability of the *solutions*, not of the system. The stability of the normal oscillations cannot be deduced from the uncoupled equations of motion (11) and (12) which were used to find the response in normal modes; it must be deduced from the coupled equations (4) and (5). This fact was reported and utilized earlier [1]; however, it appears to have been exploited originally by Tobias [6].

Let $\xi = \xi^*(t)$ and $\eta = \eta^*(t)$ be motions whose stability is to be examined. Then the substitution in the first of (4), for instance, of

$$\xi = \xi^*(t) + \rho(t), \quad \eta = \eta^*(t) \tag{29}$$

with $|\rho(t)|$ sufficiently small for all t, and subsequent expansion in powers of small quantities with only linear terms retained, yields the equation of the first variation

$$\ddot{\rho}_1 + m_1^{-\frac{k+1}{2}} k[a_k\xi^{*k-1} + A_k(\xi^* + \mu^{1/2}\eta^*)^{k-1}]\rho_1 = 0 \tag{30}$$

where the subscript 1 on ρ indicates that (30) is the variational equation of the equation of motion of mass m_1. One can specialize (30) to be the stability equation of the i-mode by putting

$$\xi^* = \xi_i^*(t), \quad \eta^* = \eta_i^*(t) = c_i\xi_i^*(t), \quad \rho_1 = \rho_{i1}(t) \tag{31}$$

If the motion to be examined is the o-mode, all subscripts i in (31) are replaced by o.

We shall show the derivation of the stability conditions for the i-mode of mass m_1 only. Those for the o-mode of m_1 and for the i and o-modes of m_2 are derived in the same way and yield similar, but not identical, results.

The substitution of (31) in (30) leads to an equation with time-dependent coefficients because $\xi^* = \xi_i^*(t)$. When the motion whose stability is to be examined is periodic, as is the case here, the time-dependent coefficient is also periodic, and the variational equation is of the Hill type. The usual procedure in stability analyses is then to expand the periodic coefficient in a Fourier series and to retain only the leading terms of that series [7]. This procedure is equivalent to regarding the motion as simple harmonic by writing

$$\xi_i^*(t) = \chi_i \cos\omega_i t \tag{32}$$

In systems where the spring forces contain terms that are linear in the spring deflections the substitution of (31) and (32) in (30) would lead to a Mathieu equation, and the stability properties of that equation are well known. However, in homogeneous systems, the indicated substitutions lead instead to a Hill equation in which the periodic coefficient contains the terms $\cos^{k-1}\omega_i t$. Unfortunately, the details of the stability property of this Hill equation are not known. In order to circumvent this difficulty, we make use of the relation [8]

$$\cos^{k-1}\omega_i t = 2^{-(k-2)}\left\{\frac{1}{2}\binom{k-1}{\frac{k-1}{2}} + \sum_{j=0,1,2,\ldots}^{(k-3)/2}\binom{k-1}{j}\cos(k-1-2j)\omega_i t\right\}, \quad k = 3, 5, \ldots \tag{33}$$

where the $\binom{n}{r}$ are binomial coefficients. Equation (33) is a Fourier sum whose coefficients decrease rapidly in absolute magnitude when the sum is written in ascending order of the frequencies. Retaining only the fundamental terms, (33) becomes

$$\cos^{k-1}\omega_i t \cong 2^{-(k-2)}\left\{\frac{1}{2}\binom{k-1}{\frac{k-1}{2}} + \binom{k-1}{\frac{k-3}{2}}\cos 2\omega_i t\right\} \tag{34}$$

Equation (34) holds within the limits of the stated approximations when k is an odd, positive integer. It may be generalized to apply to all real, positive values of k by expressing the binomial coefficients in terms of their equivalents in Gamma functions. This transforms (34) into

$$\cos^{k-1}\omega_i t = 2^{-(k-2)}\left\{\frac{1}{2}\frac{\Gamma(k)}{\left[\Gamma\left(\frac{k+1}{2}\right)\right]^2} + \frac{\Gamma(k)}{\Gamma\left(\frac{k+3}{2}\right)\Gamma\left(\frac{k-1}{2}\right)}\cos 2\omega_i t\right\} \quad (35)$$

The substitution of (31), (32), and (35) in (30) leads now to the Mathieu equation

$$\frac{d^2\rho_{i1}}{dz^2} + (\delta_{i1} + \epsilon_{i1}\cos z)\rho_{i1} = 0$$

where $z = 2\omega_i t$, and

$$\delta_{i1} = 2^{-k}\nu_{i1}^{-2}m_1^{-\frac{k+1}{2}}k[\alpha_k + (1-\mu^{1/2}c_i)^{k-1}]\chi_i^{k-1}\frac{\Gamma(k)}{\left[\Gamma\left(\frac{k+1}{2}\right)\right]^2}$$

$$\epsilon_{i1} = 2^{-k}\nu_{i1}^{-2}m_1^{-\frac{k+1}{2}}k[\alpha_k + (1-\mu^{1/2}c_i)^{k-1}]\chi_i^{k-1}\frac{\Gamma(k)}{\Gamma\left(\frac{k+3}{2}\right)\Gamma\left(\frac{k-1}{2}\right)}$$

The parameters δ_{i1} and ϵ_{i1} can be further simplified if the quantity $\nu_{i1}^{-2}\chi_i^{k-1}$ is replaced by its equivalent found from the frequency-amplitude relation (14). After some algebraic manipulations, the Mathieu parameters become

$$\begin{aligned}\delta_{i1} &= M(k)f_{i1}(\alpha_k, \beta_k, \mu, c_i, k)\\ \epsilon_{i2} &= 2\frac{k-1}{k+1}\delta_{i1}\end{aligned} \quad (36)$$

where

$$M(k) = \frac{k\Gamma(k)\left\{\Gamma\left(\frac{1}{k+1}\right)\right\}^2}{2^k\pi(k+1)\left\{\Gamma\left(\frac{k+1}{2}\right)\Gamma\left(\frac{1}{k+1}+\frac{1}{2}\right)\right\}^2}$$

$$f_{i1} = \frac{\alpha_k + (1-\mu^{1/2}c_i)^{k-1}}{\alpha_k + (1-\mu^{1/2}c_i)^k}$$

The Mathieu parameters for the o-mode of mass m_1 are found by replacing the subscript i in (36) by o. Those for the i-mode of mass m_2 are similar, but not identical to (36). They are

$$\begin{aligned}\delta_{i2} &= M(k)f_{i2}(\alpha_k, \beta_k, \mu, c_i, k)\\ \epsilon_{i2} &= 2\frac{k-1}{k+1}\delta_{i2}\end{aligned} \quad (37)$$

where $M(k)$ has been defined in the foregoing, and

$$f_{i2} = \frac{\beta_k + \left(\frac{1-\mu^{1/2}c_i}{\mu^{1/2}c_i}\right)^{k-1}}{\beta_k + \left(\frac{1-\mu^{1/2}c_i}{\mu^{1/2}c_i}\right)^k}$$

As before, the parameters for the o-mode of mass m_2 are found by replacing the subscript i in (34) by o.

The quantities $M(k)$ and ϵ/δ depend on the constant k only and thus may be computed once for all k. This has been done for the interval $0 < k \leq 4$ and the results are plotted in Fig. 4(a) and (b).

The simple relation

$$\epsilon = 2\frac{k-1}{k+1}\delta \quad (38)$$

which holds for either mode and either mass shows that for a given k the relation between the Mathieu parameters is linear. If one writes $\epsilon = \epsilon(k, \delta)$ one has

$$\epsilon(0, \delta) = -2\delta;\quad \epsilon(1, \delta) = 0;\quad \epsilon(3, \delta) = \delta;\quad \epsilon(\infty, \delta) = 2\delta$$

Thus, for any given value of k in $0 \leq k \leq \infty$, (38) defines a family of straight lines of slope $-2 \leq d\epsilon/d\delta \leq 2$ in the $\epsilon\delta$-plane, all passing through the origin. These lines are the loci of points (ϵ, δ) which define the stability of the motion.

The $\xi\delta$-plane is divided into stable and unstable domains as shown in Fig. 5, where the stable regions are indicated by shading. Clearly, the loci of the points (ϵ, δ) discussed in the foregoing

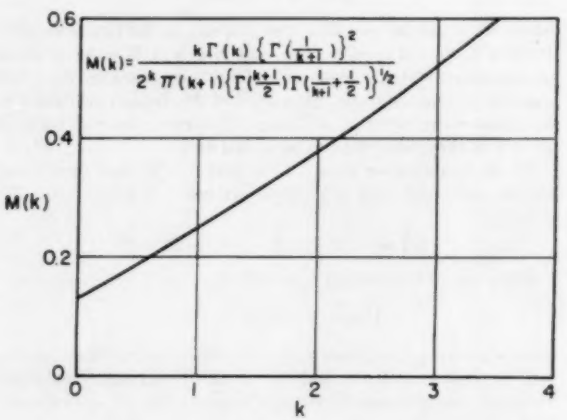

Fig. 4(a)

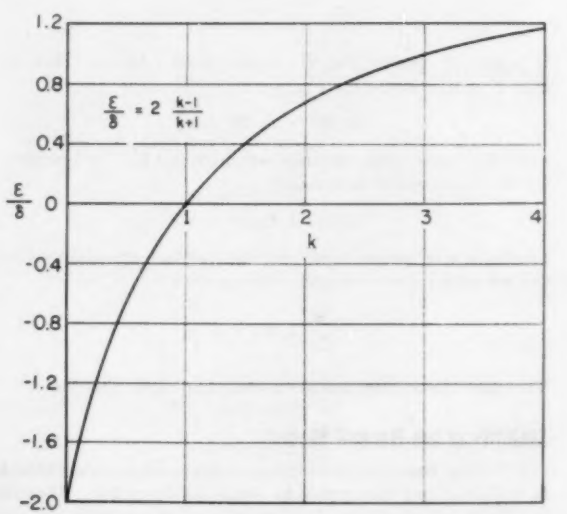

Fig. 4(b)

pass through both, stable and unstable domains. If the points characteristic for the stability of the oscillation of a given system lie in a (open) stable domain, the oscillation is stable. If they lie on the boundary of, or are imbedded in an unstable domain, the oscillation is in general unstable. The only boundary points between stable and unstable regions which belong to the stable domain are those lying on the δ-axis. Therefore the δ-axis is composed entirely of stable points. Inasmuch as $\epsilon(1, \delta) = 0$, the δ-axis is the locus of the "stability points" when $k = 1$. Therefore normal oscillations of the linear system are always stable.

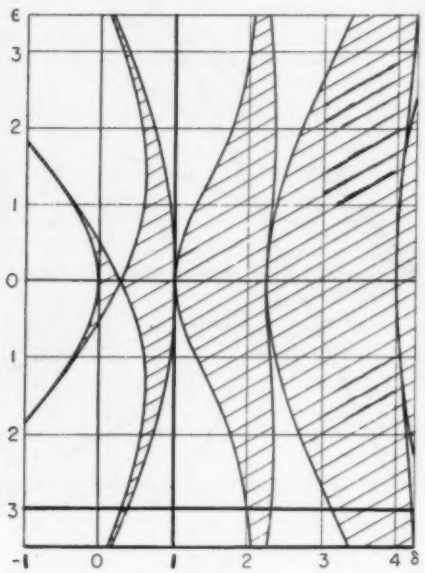

Fig. 5

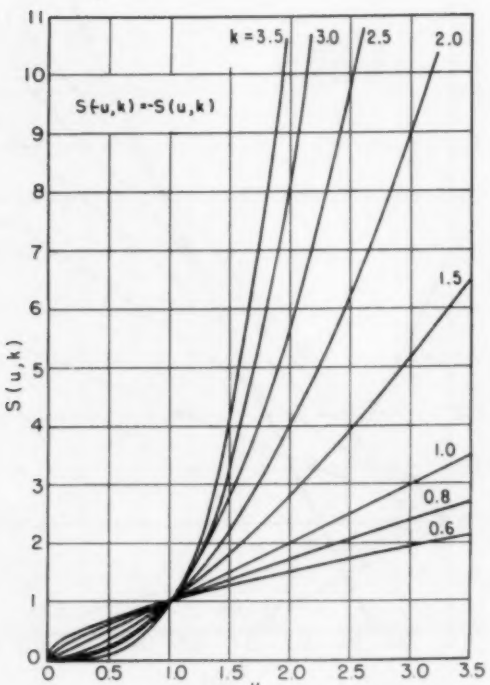

Fig. 6

A casual glance at the results of the stability investigation may create the impression that the instabilities of the solutions are merely beats. This thought is quite natural when it is realized that the variational equations are obtained by perturbing the initial amplitude of only one of the masses. Nevertheless, this impression is not correct as will be seen from the following arguments.

Linear systems are quite as capable of executing beats as nonlinear ones. Therefore it would have to be expected that the types of instabilities demonstrated here could also be shown to exist in the linear system. However, the linear system arises when $k = 1$ and it follows from (38) that $\epsilon = 0$ when $k = 1$. The same result applies for the inhomogeneous, symmetric system [1]. But when $\epsilon = 0$, the stability points of the homogeneous system, and the stability characteristics of the inhomogeneous one, lie on the positive δ-axis which is composed entirely of stable points. In other words, linear systems are always stable. It is evident, therefore, that *the instabilities exhibited here are not beats.*

The results of the stability investigation of homogeneous systems differ in two important respects from those of the symmetric, inhomogeneous system [1]. One is that the Mathieu parameters are independent of the amplitudes $\chi_{i,o}$ and $T_{i,o}$ of the motion of masses. Consequently, the oscillation is stable (unstable) at all amplitudes if it is stable (unstable) at any nonvanishing amplitude. In the nonlinear inhomogeneous system on the other hand, the stability of the oscillation does depend on the amplitude, and the stability points are replaced by lines called the "stability characteristics" [1].

The other new feature of the results reported here is that, in either mode, the Mathieu parameters are different for the motion of the two masses. Thus it is quite possible that, in a given mode, the motion of one of the masses is stable while the other is not. This feature is a direct consequence of the disymmetry of the system. Since it is physically clear that the mode cannot be stable if the motion of one of the masses is unstable, it is necessary to modify the stability criterion by the statement that a normal solution is stable only if the motion of both masses is stable. Instability of the motion of either mass indicates instability of the mode.

Numerical Examples

The foregoing theory has been applied to systems of the following characteristics:

$$m_1 = m_2, \quad a_k = 2, \quad A_k = 1, \quad b_k = \tfrac{1}{2} \text{ (all } k\text{)}$$

$$k = 0.6, 0.8, 1.0 \text{ (linear)}, 1.5, 2.0, 2.5, 3.0, 3.5$$

With this choice of values of k, the types of springs examined include soft, linear, and hard ones. The spring forces as functions of the spring deflections have essentially the appearance shown in Fig. 6, except that in this illustration the constants a_k, A_k, and b_k do not have the actual values used in the computations. The constants c_i and c_o which define the amplitude ratios of the two masses have been computed from (9) and are shown as functions of k in Fig. 7. The backbones for the i-mode of mass m_1 are shown in Fig. 8 and those for the o-mode of the same mass in Fig. 9. Figs. 8 and 9 were computed from (14) and (24).

The results of the stability investigation of the i-mode of masses m_1 and m_2 are shown in Fig. 10. Those for the o-mode of both masses are shown in Fig. 11. The solid dots give the stability results for mass m_1, the open ones for mass m_2.

Conclusion

Homogeneous systems, as defined in (5) or (6) and (7), con-

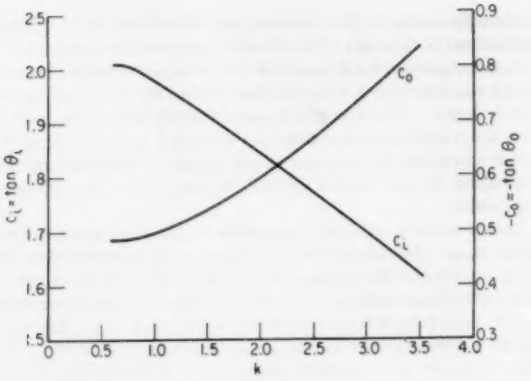

Fig. 7

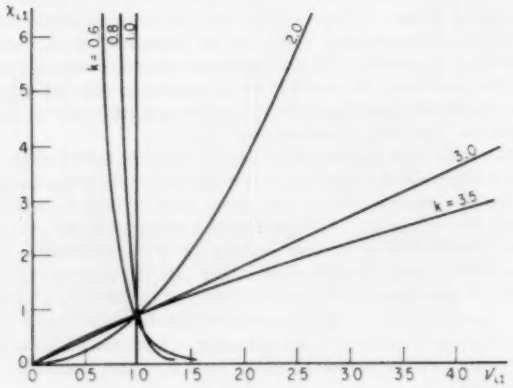

Fig. 8

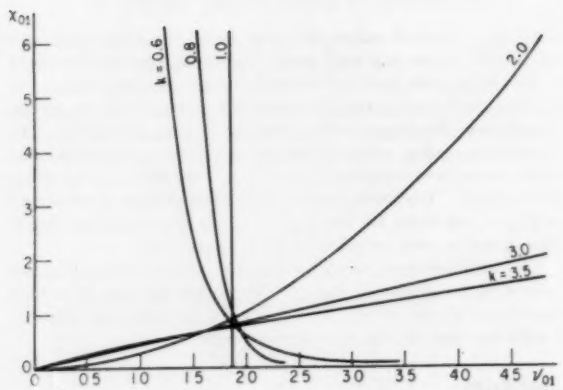

Fig. 9

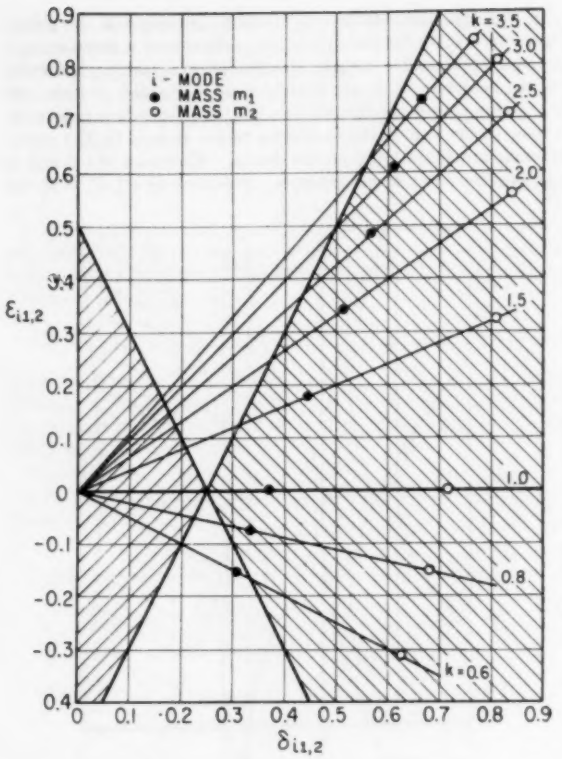

Fig. 10

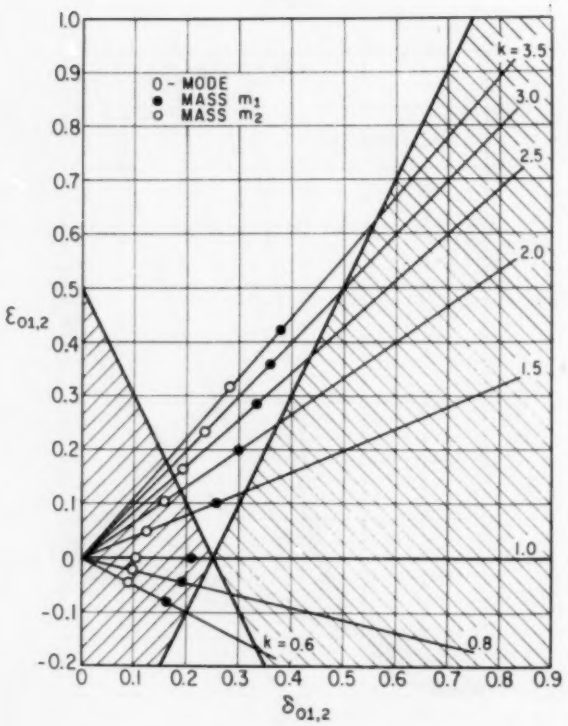

Fig. 11

stitute a class of dual-mode systems whose free vibrations in normal modes can be discussed without the approximations usually necessary in the treatment of vibrations of nonlinear systems. Inasmuch as the linear system is a member of this class, the homogeneous system of degree k represents a broad generalization on the linear system.

A study of the behavior of dual-mode homogeneous systems of noninteger degree provides a great deal of information regarding the normal response of conservative dual-mode systems in general because the theory covers a continuous spectrum of cases ranging from the strongly nonlinear with soft springs through the linear to the strongly nonlinear with hard springs.

A surprising feature of the nonlinear systems and one which has no counterpart in the linear case is that systems which have only two degrees of freedom may have more than two normal modes. An investigation on a special symmetric, homogeneous system of degree 3 has shown that one i-mode and three o-modes exist, and all are stable.

In the past, the investigation of systems neighboring on the linear one (by means of perturbation or iteration methods) has done much to improve our understanding of the behavior of nonlinear systems. The theory presented here is a point of departure for the discussion of systems neighboring on any homogeneous system. These neighboring systems include not only those in which the spring forces are more complex than in homogeneous systems, but also those in which damping forces of small amplitude are present, or the problem of forced vibrations in which a periodic forcing function of small amplitude acts on one of the masses. The discussion of systems neighboring on the homogeneous ones will be reported in the near future.

Acknowledgment

Financial aid from the National Science Foundation which has supported this investigation is gratefully acknowledged.

References

1 R. M. Rosenberg and C. P. Atkinson, "On the Natural Modes and Their Stability in Nonlinear Two-Degree-of-Freedom Systems," JOURNAL OF APPLIED MECHANICS, vol. 26, TRANS. ASME, vol. 81, Series E, 1959, pp. 377–385.

2 R. M. Rosenberg, "Normal Modes of Nonlinear Dual-Mode Systems," JOURNAL OF APPLIED MECHANICS, vol. 27, TRANS. ASME, vol. 81, Series E, 1960, p. 263.

3 K. Klotter, "Steady State Vibrations in Systems Having Arbitrary Restoring and Arbitrary Damping Forces," *Proceedings of the Symposium on Nonlinear Circuit Analysis*, Polytechnic Institute of Brooklyn, April, 1953, pp. 234–257.

4 H. B. Dwight, "Tables of Integrals and Other Mathematical Data," The Macmillan Company, New York, N. Y., third edition, 1957, p. 197.

5 J. N. McDuff and J. R. Curreri, "Vibration Control," McGraw-Hill Book Company, Inc., New York, N. Y., 1958, p. 73.

6 S. A. Tobias, "Free Undamped Vibrations of Imperfect Circular Disks," *Proceedings of The Institution of Mechanical Engineers*, vol. 171, 1957, p. 691.

7 J. J. Stoker, "Nonlinear Vibrations," Interscience Publishers, Inc., New York, N. Y., 1950.

8 R. M. Rosenberg, "On the Periodic Solutions of the Forced Oscillator Equation," *Quarterly of Applied Mathematics*, vol. 15, 1958, pp. 341–354.

T. C. HU
Research Assistant,
Division of Applied Mathematics,
Brown University, Providence, R. I.

R. T. SHIELD
Professor,
Division of Applied Mathematics,
Brown University, Providence, R. I.

Uniqueness in the Optimum Design of Structures[1]

A procedure was developed previously [1][2] for the determination of the optimum design of a sandwich shell or structure. The uniqueness of the optimum design obtained by this procedure is investigated and it is shown that all optimum designs admit a common collapse mode. This result is used to prove the uniqueness of minimum-weight designs obtained in previous work.

Introduction

THE problem of optimum design is to find a structure which will carry given loads and which will be optimum for a given criterion. The criterion may be minimum volume or minimum moment of inertia, for example. For homogeneous materials, minimum weight coincides with minimum volume.

In the minimum-weight design of a frame with constant cross section between joints, only a finite number of variables is involved, and the determination of the design reduces to a problem of linear programming if the unit weight of a member is assumed to be linearly proportional to the full plastic moment of that member. Foulkes [2] has developed necessary and sufficient conditions for such designs. The optimum design is usually defined by a vertex of the solution space and is therefore unique. The minimum-weight design is not unique when the surface of minimum weight defined by the weighting function of the structure coincides with one face of the solution space. The case in which the unit weight of a member is proportional to the nth power of the full plastic moment has been treated by Prager [3].

For the minimum-weight design of a structure when continuously varying strength is allowed, Drucker and Shield [1, 4, 5] have found sufficient conditions for the determination of the design. The sufficient conditions can be used to obtain an absolute minimum-weight design of a sandwich shell or structure, and a relative minimum-weight design of a solid shell. Shield [1] has extended the sufficient conditions to obtain optimum designs which have minimum values of the functional

$$\int h f(P) dA,$$

where h is the thickness of the face sheets of a sandwich shell or the thickness of a solid shell, $f(P)$ is a prescribed function of position, and dA is an element of area of the middle surface. For $f(P) \equiv 1$, the optimum criterion corresponds to minimum weight of a homogeneous material. If $f(P)$ is taken to be the density of the material to be used at the point P, the criterion gives the minimum-weight design in the nonhomogeneous case. In most cases, $f(P)$ is positive and is so assumed in the following.

The following work is concerned with the uniqueness of the optimum design of a sandwich shell. The sufficient condition of reference [1] states that a design is optimum if it is about to collapse in a special deformation mode (defined later in the text). It is shown that if an optimum design satisfying this condition exists, then any other optimum design must also admit the special deformation mode as a collapse mode. This result specifies the position of the stress point on the yield surface at every section of a shell of optimum design. In particular cases, the equilibrium equations may then be sufficient to insure uniqueness of the optimum design, but no general result has been obtained. However, an examination of the optimum designs obtained in previous work [1, 4, 5, 6, 7, 8, 9] shows that they are unique. That nonunique optimum designs may exist when the yield surface contains a flat is shown by an example.

Criterion for Optimum Design

The fundamental theorems used in obtaining optimum designs are the theorems of limit analysis formulated by Drucker, Greenberg, and Prager [10]. Prager [11] extended the theorems of limit analysis to structures characterized by generalized stresses Q_n ($n = 1, 2, \ldots, N$) and generalized strain rates q_n ($n = 1, 2 \ldots, N$). The results of limit analysis apply to elastic, perfectly plastic materials, changes in geometry being neglected. In the following, a rigid, perfectly plastic material is assumed although the results carry over to the elastic, perfectly plastic case. The behavior of the rigid, perfectly plastic material is characterized by a positive yield function F which is a function of the generalized stress Q_n. The material remains rigid under states of stress for which $F(Q_n) < K^2$, where K is a constant. Plastic flow can occur under states of stresses for which $F(Q_n) = K^2$. States of stress for which $F(Q_n) > K^2$ are not permissible. The yield condition $F(Q_n) = K^2$ can be considered to define a hypersurface in the N-dimensional stress space. Plastic flow can occur under a state of stress represented by a point Q_n on the yield surface. In the same space, the strain rate can be represented by a vector with components proportional to q_n. The vector is normal to the yield surface at a regular point and at singular points lies in the fan bounded by the normals at adjacent points. The restriction on the strain-rate vector will be referred to as the normality condition.

The rate D_A at which energy is dissipated due to plastic action is given by

$$D_A = Q_n q_n = Q_1 q_1 + Q_2 q_2 + \ldots + Q_N q_N \qquad (1)$$

per unit area of the middle surface. A repeated suffix n implies summation over the values $n = 1, 2, \ldots, N$. For a convex yield surface, the normality condition insures that the dissipation rate D_A is uniquely determined by the strain rates q_n. It should be noted that shear forces, which enter into the equations of equi-

---

[1] The results presented in this paper were obtained in the course of research sponsored by the Office of Ordnance Research, Department of the Army, under Contract No. DA-19-020-ORD-4795.

[2] Numbers in brackets designate References at end of paper.

Presented at the Summer Conference of the Applied Mechanics Division, Chicago, Ill., June 14–16, 1961, of THE AMERICAN SOCIETY OF MECHANICAL ENGINEERS.

Discussion of this paper should be addressed to the Editorial Department, ASME, 29 West 39th Street, New York, N. Y., and will be accepted until July 10, 1961. Discussion received after the closing date will be returned. Manuscript received by ASME Applied Mechanics Division, October 5, 1959. Paper No. 61—APM-1.

librium, are not included in the generalized stresses Q_n as they do no work during deformation of the structure.

The sandwich shell has a core of prescribed thickness H (usually constant) between two identical face sheets of variable thickness h, where $h \ll H$. The core carries shear force only while the face sheets carry direct stresses and so provide moment and force resultants across a section of the shell. In this case the dissipation rate D_A is linearly proportional to h, and the dimensions of the yield surface are also linearly proportional to h. Thus if the thickness h is different for two designs at a section of the shell, the two designs will have geometrically similar yield surfaces for that section.

If a shell of thickness h is at collapse, then the rate at which the applied forces do work during deformation is equal to the rate of dissipation of energy,

$$\int D_A dA = \int T_i u_i dA + 2 \int F_i u_i h \, dA. \tag{2}$$

Here $u_i (i = 1, 2, 3)$ are the velocity components of the middle surface of the shell, and T_i, F_i are the components of the applied force and body force, respectively. The body force F_i is assumed to act only if material is present, and any body force acting on the core is included in the forces T_i. A repeated suffix i implies summation over the values $i = 1, 2, 3$. Equation (2) can be written

$$\int \Delta_A dA = \int T_i u_i dA, \tag{3}$$

where the modified dissipation rate Δ_A is given by

$$\Delta_A = Q_n q_n - 2F_i u_i h. \tag{4}$$

It has been shown [1] that if a design can be found which is just at the point of collapse under the loads and which has a collapse mode such that

$$\frac{1}{f(P)} \frac{\Delta_A}{h} = \frac{1}{f(P)} \left\{ \frac{Q_n q_n}{h} - 2F_i u_i \right\} = \text{const} \tag{5}$$

over the shell, then the functional $\int hf(P)dA$ will have an absolute minimum value for shells designed to be at or below collapse under the given loads T_i, F_i. (The strain rate q_n is associated with the stresses Q_n by the normality condition, and the stresses Q_n are at yield and satisfy the equilibrium equations with the given loads T_i, F_i.) The condition (5) is independent of the design thickness h because of the linear dependence of the dissipation rate $Q_n q_n$ on h. However, the form of the condition does depend in general upon the position of the stress point Q_n on the yield surface which in turn is influenced by the particular type of loading of the shell. In some cases, for example the minimum-weight design of circular plates under arbitrary transverse loading [8], the same collapse mode satisfying (5) can be used to determine optimum designs for a variety of prescribed loads. An example of a strong dependence of the collapse mode satisfying (5) on the prescribed loading has been furnished by Heyman [12] in work on the minimum-weight design of framed structures.

Uniqueness of the Optimum Design

Greek subscripts will be used to refer to different designs for the same applied loads, and, as before, the subscript n will be used for the components of the generalized stress vector and strain-rate vector and i will be used for the components of velocity and applied force. We assume that a design α has been found which is at collapse under a mode $u_{\alpha i}$ satisfying condition (5) and which is therefore an optimum design. If another design β is also an optimum design, then by definition

$$\int h_\alpha f(P)dA = \int h_\beta f(P)dA. \tag{6}$$

It will now be shown that the design β admits the mode $u_{\alpha i}$ as a collapse mode. By assumption, we have

$$\frac{1}{f(P)} \left\{ \frac{Q_{\alpha n} q_{\alpha n}}{h_\alpha} - 2F_i u_{\alpha i} \right\} = \text{const} \tag{7}$$

over the shell. The stresses $Q_{\alpha n}$ and $Q_{\beta n}$ are in equilibrium under the given loads, and equating the rate at which work is done by the applied loads to that done by the internal stresses in the deformation mode $u_{\alpha i}$, it follows that

$$\int T_i u_{\alpha i} dA = \int [Q_{\alpha n} q_{\alpha n} - 2F_i u_{\alpha i} h_\alpha] dA = \int [Q_{\beta n} q_{\alpha n} - 2F_i u_{\alpha i} h_\beta] dA. \tag{8}$$

In deriving equations (8), $u_{\alpha i}$ is an actual collapse mode for the design α but is considered as a virtual mode for the design β. With (6) and (7),

$$\int [Q_{\alpha n} q_{\alpha n} - 2F_i u_{\alpha i} h_\alpha] dA = \int \frac{1}{f(P)} \left\{ \frac{Q_{\alpha n} q_{\alpha n}}{h_\alpha} - 2F_i u_{\alpha i} \right\} h_\alpha f(P) dA = \int \left\{ \frac{Q_{\alpha n} q_{\alpha n}}{h_\alpha} - 2F_i u_{\alpha i} \right\} h_\beta dA.$$

If this result is substituted in (8), it follows that

$$\int \left[\frac{Q_{\alpha n}}{h_\alpha} - \frac{Q_{\beta n}}{h_\beta} \right] q_{\alpha n} h_\beta dA = 0. \tag{9}$$

In the N-dimensional stress space, the stress point $Q_{\alpha n}/h_\alpha$ lies on the (convex) yield surface corresponding to unit thickness of the face sheets, and the strain rate $q_{\alpha n}$ is associated with the point $Q_{\alpha n}/h_\alpha$ by the normality condition. Thus $Q_{\alpha n}/h_\alpha$ is defined also in the regions, if any, where h_α is zero. The stress point $Q_{\beta n}/h_\beta$ ($h_\beta \neq 0$) lies inside or on the unit yield surface as the design β is at or below collapse. The convexity of the unit yield surface then gives

$$\left(\frac{Q_{\alpha n}}{h_\alpha} - \frac{Q_{\beta n}}{h_\beta} \right) q_{\alpha n} \geq 0. \tag{10}$$

As inequality (10) holds where $h_\beta \neq 0$, it follows that in order to satisfy (9) we must have equality in (10), that is,

$$\frac{Q_{\alpha n} q_{\alpha n}}{h_\alpha} = \frac{Q_{\beta n} q_{\alpha n}}{h_\beta}. \tag{11}$$

For a strictly convex yield surface, equation (11) implies that the stress points $Q_{\alpha n}/h_\alpha$ and $Q_{\beta n}/h_\beta$ coincide at each section of the shell where $h_\beta \neq 0$. If the yield surface contains a flat, then where $q_{\alpha n}$ is associated with the flat, $Q_{\alpha n}/h_\alpha$ and $Q_{\beta n}/h_\beta$ must lie on the flat of the unit yield surface, Fig. 1. The strain-rate $q_{\alpha n}$ is therefore associated with the stress distribution $Q_{\beta n}$ so that the design β admits the mode $u_{\alpha i}$ as a collapse mode, and condition (5) is satisfied by the design β in the collapse mode $u_{\alpha i}$.

Thus, if an optimum design exists which admits a collapse mode satisfying condition (5), then any other design which is also op-

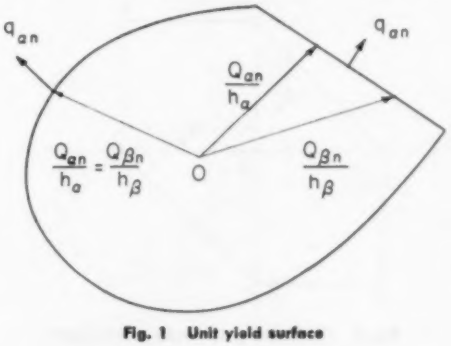

Fig. 1 Unit yield surface

timum admits the same collapse mode. For a strictly convex yield surface, the stress vector Q_α/h with end point on the unit yield surface is then known as a function of position over the shell for all optimum designs. For a yield surface which is not strictly convex, there may be regions of the shell where the stress vector Q_α/h of an optimum design is not completely specified but is restricted to represent points on a flat of the unit yield surface. The thickness h and the stresses Q_α for an optimum design are determined by the equations of equilibrium of the shell together with these restrictions on the vector Q_α/h. In addition, edge conditions or other support conditions on the stresses Q_α must be satisfied. Whether this procedure leads to a unique design thickness h or not depends upon the form of the equilibrium equations and the boundary conditions imposed. Examples of unique designs for minimum volume are discussed in the next section.

Examples

Previous work on structures of sandwich construction has determined minimum-volume designs for circular plates under symmetric transverse loading [5, 6, 7] and arbitrary transverse loading [8], elliptical plates under arbitrary loading [9], and circular cylindrical shells under symmetric loading [1]. By using the results of the previous section it can be shown that the designs obtained are unique. As an illustration of the method, the minimum-volume design obtained in [8] for a built-in circular plate under given nonsymmetric transverse loading is shown in the following to be unique.

Minimum-volume designs have also been determined for circular disks under conditions of plane stress and loaded symmetrically in the plane of the disk [4, 5]. A similar argument to that used here for sandwich shells can be employed to show that the designs are unique. As for the sandwich shell, the rate of dissipation per unit area is linearly proportional to the thickness for a disk under conditions of plane stress.

Consider a horizontal sandwich circular plate with a built-in edge and loaded by a distribution of pressure p on the upper face. Using Tresca's yield condition, Fig. 2, and neglecting body forces, Onat, Schumann, and Shield [7] showed that a velocity field satisfying condition (5) is, for $f(P) = 1$,

$$w = \begin{cases} \frac{1}{2}c(2R^2 - 3r^2) & 0 \leq r \leq \frac{2}{3}R, \\ \frac{1}{2}c(r - R)^2 & \frac{2}{3}R \leq r \leq R, \end{cases} \qquad (12)$$

where w is the downward deflection rate, R is the radius of the circular plate, r measures distance from the center, and c is a positive constant. The velocity field is obtained from condition (5) by assuming that the central region $r < \frac{2}{3}R$ of the plate is at regime A of the Tresca hexagon, Fig. 2, and the annular region $\frac{2}{3}R < r \leq R$ is at regime C of the Tresca hexagon. A minimum-volume design for an arbitrary distribution of pressure was obtained in [8] using the velocity field (12). As all minimum volume designs must admit the collapse mode (12), they must involve regime A for $r < \frac{2}{3}R$ and regime C for $\frac{2}{3}R < r \leq R$. The curvature rate $\kappa_{r\theta}$ is zero because the velocity field (12) is rotationally symmetric, so that the bending moment $M_{r\theta}$ is zero and the bending moments M_r, M_θ can be identified with the principal moments M_1, M_2 of Fig. 2. Thus in the central region $M_r = M_\theta = M_0$, where M_0 is the maximum bending moment $\sigma_0 H h$, and for equilibrium

$$\frac{\partial^2 M_0}{\partial r^2} + \frac{1}{r}\frac{\partial M_0}{\partial r} + \frac{1}{r^2}\frac{\partial^2 M_0}{\partial \theta^2} = -p(r, \theta) \quad (r < \tfrac{2}{3}R). \qquad (13)$$

In the annular region, $M_r = -M_0$, $M_\theta = 0$, and the equilibrium equation reduces to

$$\frac{\partial}{\partial r}(rM_0) = rp(r, \theta) \quad (\tfrac{2}{3}R < r \leq R). \qquad (14)$$

At the junction $r = \frac{2}{3}R$ of the two regions, M_r and the shear force Q_r are continuous for equilibrium. These conditions require M_0 to be zero at $r = \frac{2}{3}R$ and $|\partial M_0/\partial r|$ must be continuous. For $p(r, \theta)$ piecewise continuous, the Poisson equation (13) has a unique continuously differentiable solution in the central region satisfying the condition $M_0 = 0$ on the boundary $r = \frac{2}{3}R$. The magnitude of $\partial M_0/\partial r$ at the junction can then be determined. The general solution of (14) is given by

$$rM_0 = \int_{\frac{2}{3}R}^{r}\int_{\frac{2}{3}R}^{\xi} \rho p(\rho, \theta)\, d\rho\, d\xi + rB(\theta) + E(\theta), \qquad (15)$$

where $B(\theta)$ and $E(\theta)$ are functions of θ only. These functions are uniquely determined by the known values of M_0 and $\partial M_0/\partial r$ at $r = \frac{2}{3}R$, and M_0 (and hence h) is then uniquely defined by (15) in the annular region. The uniqueness of the minimum volume design has therefore been demonstrated. Note that, in order to obtain this result, it is not necessary to show that the velocity field (12) is the only collapse mode which satisfies condition (5) and which is associated with the minimum-volume design. However, it is a straightforward matter to show that (12) is in fact the only velocity field with these properties.

The following example of a nonunique situation is somewhat artificial as it involves an infinite region. It also depends upon the yield surface containing a flat. Taking x,y-axes in the plane of the plate, it is required to design a sandwich plate of minimum volume in the infinite strip $|y| \leq b$ loaded by uniform pressure p over the rectangular area $|x| \leq a$, $|y| \leq b$. Conditions of simple support apply at the edges $y = \pm b$ of the plate. (Built-in support at the edges also leads to nonunique designs.) Neglecting body force and with the yield condition of Fig. 2, condition (5) with $f(P) \equiv 1$ is satisfied by the velocity field

$$w = \tfrac{1}{2}c(b^2 - y^2), \qquad (16)$$

and w is zero at the edges; c is a positive constant. The curvature rates κ_{xx} and κ_{yx} are zero and κ_{yy} is constant. The x and y directions are principal curvature-rate directions so that we may identify M_x and M_y with M_1 and M_2, the bending moment M_{xy} being zero. The curvature rate is associated with all moment points on the flat AB in Fig. 2. Assuming first that moment point A applies throughout the plate, $M_x = M_y = M_0$ and equilibrium requires

$$\frac{\partial^2 M_0}{\partial x^2} + \frac{\partial^2 M_0}{\partial y^2} = -p(x, y), \qquad (17)$$

where $p(x, y)$ has the constant value p in the loaded rectangle and is zero elsewhere. Equation (17) has to be solved for M_0 subject to the boundary condition $M_0 = 0$ on $y = \pm b$. A unique solu-

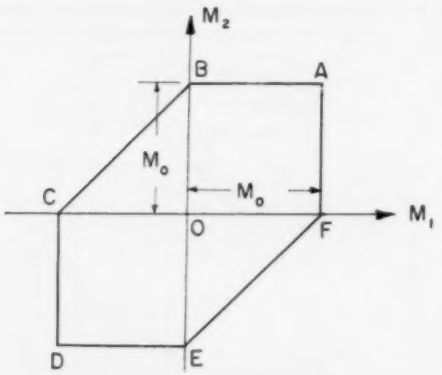

Fig. 2 The Tresca yield condition for plates

tion with continuous first derivatives exists and M_0 is nonnegative in the strip. A second optimum design is obtained by assuming that regime B applies, $M_x = 0$, $M_y = M_0$. For equilibrium,

$$\frac{\partial^2 M_0}{\partial y^2} = -p(x, y) \tag{18}$$

and the solution satisfying $M_0 = 0$ on $y = \pm b$ is

$$M_0 = \begin{cases} \frac{1}{2}p(b^2 - y^2) & |x| \leq a, \\ 0 & |x| > a. \end{cases} \tag{19}$$

That is, the load is carried by a finite rectangular plate.

References

1 R. T. Shield, "On the Optimum Design of Shells," JOURNAL OF APPLIED MECHANICS, vol. 27, TRANS. ASME, vol. 82, Series E, 1960, pp. 316–322.

2 J. Foulkes, "Minimum Weight Design of Structural Frames," *Proceedings of the Royal Society*, London, England, vol. 223, Series A, 1954, pp. 432–494.

3 W. Prager, "Minimum-Weight Design of a Portal Frame," *Proceedings of the ASCE*, vol. 82, October 1956, paper 1073.

4 D. C. Drucker and R. T. Shield, "Design for Minimum Weight," *Proceedings of the 9th International Congress of Applied Mechanics*, Brussels, Belgium, 1956.

5 D. C. Drucker and R. T. Shield, "Bounds on Minimum Weight Design," *Quarterly of Applied Mathematics*, vol. 15, 1957, 269–281.

6 W. Freiberger and B. Tekinalp, "Minimum Weight Design of Circular Plates," *Journal of the Mechanics and Physics of Solids*, vol. 4, 1956, pp. 294–299.

7 E. T. Onat, W. Schumann and R. T. Shield, "Design of Circular Plates for Minimum Weight," *Journal of Applied Mathematics and Physics (ZAMP)*, vol. 8, 1957, pp. 485–499.

8 W. Prager and R. T. Shield, "Minimum Weight Design of Circular Plates Under Arbitrary Loading," *Journal of Applied Mathematics and Physics (ZAMP)*, vol. 10, 1959, pp. 421–426.

9 R. T. Shield, "Plate Design for Minimum Weight," *Quarterly of Applied Mathematics*, vol. 18, 1960, pp. 131–144.

10 D. C. Drucker, W. Prager, and H. J. Greenberg, "Extended Limit Design Theorems for Continuous Media," *Quarterly of Applied Mathematics*, vol. 9, 1952, pp. 381–389.

11 W. Prager, "General Theory of Limit Design," Sectional Lecture, *Proceedings of the 8th International Congress of Applied Mechanics*, Istanbul, Turkey, 1952.

12 J. Heyman, "On the Absolute Minimum-Weight Design of Framed Structures," *Quarterly Journal of Mechanics and Applied Mathematics*, vol. 12, 1959, pp. 314–324.

The Bending, Buckling, and Flexural Vibration of Simply Supported Polygonal Plates by Point-Matching

H. D. CONWAY
Professor of Mechanics,
Cornell University,
Ithaca, N. Y.

The bending by uniform lateral loading, buckling by two-dimensional hydrostatic pressure, and the flexural vibrations of simply supported polygonal plates are investigated. The method of meeting the boundary conditions at discrete points, together with the Marcus membrane analog [1],[1] is found to be very advantageous. Numerical examples include the calculation of the deflections and moments, and buckling loads of triangular square, and hexagonal plates. A special technique is then given, whereby the boundary conditions are exactly satisfied along one edge, and an example of the buckling of an isosceles, right-angled triangle plate is analyzed. Finally, the frequency equation for the flexural vibrations of simply supported polygonal plates is shown to be the same as that for buckling under hydrostatic pressure, and numerical results can be written by analogy. All numerical results agree well with the exact solutions, where the latter are known.

In a former series of investigations, the method of solving certain boundary-value problems by meeting the boundary conditions at discrete points (hereinafter called "point-matching") has been applied to such problems as the torsion of prismatical bars and bending of clamped plates [2, 3, 4], eigenvalue problems of buckling and flexural vibrations of clamped plates [5], and systems of equations encountered in plane-stress and strain and axisymmetrically loaded cylinders [6]. The method is not confined to these, but is applicable to a much wider range of boundary-value problems.

When coupled with the Marcus membrane analog [1], which has the effect of reducing the order of the differential equations involved to two, so that only one boundary condition is necessary, the method is particularly valuable for certain investigations on the bending, buckling, and flexural vibrations of simply supported polygonal plates. These are now presented.

Analysis

(a) Bending of Plates. As is well known, the solution of the Lagrange equation for the small-deflection bending of thin plates

$$D\nabla^4\omega = D\nabla^2\nabla^2 w = q \tag{1}$$

requires two conditions to be satisfied at all points on the boundary or boundaries. However, following the Marcus method [1] and adding the moment equations

$$M_x = -D\left(\frac{\partial^2 w}{\partial x^2} + \nu\frac{\partial^2 w}{\partial y^2}\right);\quad M_y = -D\left(\frac{\partial^2 w}{\partial y^2} + \nu\frac{\partial^2 w}{\partial x^2}\right) \tag{2}$$

we obtain

$$\frac{M_x + M_y}{1+\nu} = M = -D\nabla^2 w \tag{3}$$

Hence equation (1) becomes

$$\nabla^2 M = -q \tag{4}$$

the well-known, second-order equation for a laterally loaded membrane.

For a simply supported polygonal plate, it is easily shown that M is zero on the boundary. Thus there is an analogy with the torsion of a prismatical rod of polygonal cross section, for which

$$\nabla^2\phi = -2G\alpha,\ \phi = 0 \text{ on boundary}$$

with the usual notation. It follows that, if the solution to the corresponding torsion problem is known, $M = (M_x + M_y)/(1+\nu)$ is also known everywhere in the simply supported plate. Knowing M, equation (3) then gives the deflections w whence M_x and M_y may be found from equation (2). However, in the case of a *regular* polygon, they may be found directly at the center. Here the values of M_x and M_y are equal since the deflection surface there is spherical, and hence

$$M_x = M_y = M(1+\nu)/2 \tag{5}$$

These moments are either the largest or close to the largest in the plate.

To solve the problem of the torsion of a rod of regular prismatical section and hence, by analogy, to find the central moments in the corresponding simply supported plate, the method of point-matching [2, 3, 4] is convenient and accurate. Consider, for example, the case of a square of side $2a$ and writing the approximate stress function in the form

$$\phi = -G\alpha r^2/2 + A + Br^4\cos 4\theta + Cr^8\cos 8\theta \tag{6}$$

the values of A, B, and C are found by solving the three simultaneous equations obtained by writing $\phi = 0$ at the centers, ends, and quarter points of the sides. It is found that [3]

$$A = 0.589825G\alpha a^2;\ B = -0.092369G\alpha/a^2;$$
$$C = 0.0025437G\alpha/a^6$$

[1] Numbers in brackets designate References at end of paper.

Contributed by the Applied Mechanics Division and presented at the Winter Annual Meeting, New York, N. Y., November 27–December 2, 1960, of The American Society of Mechanical Engineers.

Discussion of this paper should be addressed to the Editorial Department, ASME, 29 West 39th Street, New York, N. Y., and will be accepted until July 10, 1961. Discussion received after the closing date will be returned. Manuscript received by ASME Applied Mechanics Division, March 16, 1960. Paper No. 60—WA-38.

By analogy with the uniformly loaded square plate we write $2G\alpha = q$ and obtain

$$M_{r=a} = 0.294913\ qa^2 = 0.073728\ q(2a)^2$$

Thus at the center

$$M_x = M_y = M(1 + \nu)/2 = 0.04792\ q(2a)^2 \quad (7)$$

for $\nu = 0.3$. These are also the maximum moments. The agreement with the factor of 0.0479 found in the conventional manner [7] is more than satisfactory.

To find the deflections, the value of M obtained by analogy from equation (6) is substituted in equation (3) which, when integrated, gives

$$-Dw = Ar^2/4 + Br^4/20 \cos 4\theta + Cr^{10}/36 \cos 8\theta - qr^4/64 + A' + B'r^4 \cos 4\theta + C'r^8 \cos 8\theta \quad (8)$$

The new constants A', B', and C' are also found by writing $w = 0$ at the centers, ends, and quarter points of the sides, and solving the three resulting simultaneous equations. Thus

$$A' = -0.065076\ qa^4;\ B' = 0.009371\ q;\ C' = -0.000125\ q/a^4$$

The maximum deflection is then

$$w_{max} = -A'/D = 0.004067\ q(2a)^4/D \quad (9)$$

the factor agreeing excellently with that of 0.00406 found conventionally [7].

The exact solution for the torsion of an equilateral-triangle rod is well known, and the moments at the center of a simply supported and uniformly loaded equilateral-triangle plate are then exactly determined. These have been found by Woinowsky-Krieger [8], their value being

$$M_x = M_y = (1 + \nu)\ qa^2/54 = 0.0241\ qa^2 \quad (10)$$

where a is the height of the triangle. This differs but little from the maximum moment of $0.0259\ qa^2$ (8). The maximum deflection is $qa^4/972D$.

The torsion of the regular hexagonal bar has also been investigated by point-matching [3], and the moments at the center of the corresponding simply supported plate are immediately found by analogy. Omitting the details since they are the same as before, we find, for the center

$$M_x = M_y = 0.17578\ qa^2 \quad (11)$$

where $2a$ is here the perpendicular distance apart of any two parallel edges. This result is apparently new and while it may not be quite the maximum moment, it is evidently very close to it.

The deflections may again be found from equation (3) as in the case of the square. This procedure gives

$$A' = -0.054788\ qa^4;\ B' = 0.003803\ q;\ C' = -0.000238\ q/a^4$$

and hence

$$w_{max} = -A'/D = 0.054788\ qa^4/D \quad (12)$$

Summarizing, the moments at the centers of the equilateral triangle, square, and hexagonal plates circumscribed by a circle of radius R are given in Table 1(a), where they are compared with the result for a simply supported plate of that radius found in the conventional way. The maximum deflections for these plates are also tabulated in Table 1(b).

Table 1(a) Values of factor k in $M_x = M_y = kqR^2$ at center of uniformly loaded, and simply supported plates

Equilateral triangle	Square	Hexagon	Circle
0.0542	0.0958	0.1318	0.20625

Poisson's ratio = 0.3

Table 1(b) Values of factor k' in $w_{max} = k'\ qR^4/D$ for uniformly loaded, and simply supported plates

Equilateral triangle	Square	Hexagon	Circle
0.00521	0.01627	0.03082	0.06370

Poisson's ratio = 0.3

(b) Buckling of Plates. We now consider the buckling of a simply supported polygonal plate under hydrostatic loading in its plane, for which the differential equation is

$$D\nabla^4 w + P\nabla^2 w = 0 \quad (13)$$

From equation (3), this becomes

$$\nabla^2 M + k^2 M = 0;\ k^2 = P/D \quad (14)$$

the value of M on the boundary again being zero.[2]

To utilize the point-matching method, we first write

$$M = \sum_{n=0}^{\infty} F_n(r) \cos n\theta, \sin n\theta \quad (15)$$

Substituting in equation (14) then gives Bessel's differential equation, the solution being

$$F_n(r) = A_n J_n(kr) + B_n Y_n(kr) \quad (16)$$

Omitting the Bessel functions of the second kind for a solid plate since these are singular at $r = 0$,

$$M = \sum_{n=0}^{\infty} A_n J_n(kr) \cos n\theta, \sin n\theta \quad (17)$$

The series for M is then truncated, the number of undetermined constants being equal to the number of boundary points at which M is equated to zero. The resulting determinant when equated to zero then gives the values of the buckling loads. Of course, when due advantage can be taken of symmetry, such as in the case of a regular polygonal plate, the number of terms retained may be quite small and the labor is considerably lightened. In other cases, the digital computer is invaluable.

As a first example, we consider the case of a square plate since the exact solution is well known, and a test of the accuracy of the method is thus provided. The plate and the co-ordinate system adopted are shown in Fig. 1. Taking due advantage of symmetry and retaining only three terms, we write

$$M = AJ_0(kr) + BJ_4(kr) \cos 4\theta + CJ_8(kr) \cos 8\theta \quad (18)$$

[2] The same equation holds for w.

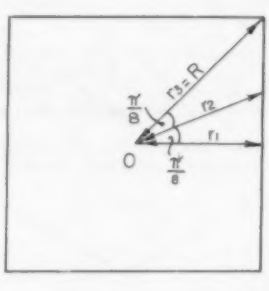

Fig. 1 Co-ordinate system for square plate

The boundary points selected for convenience are at $\theta = 0$, 22.5, and 45 deg, the radii being denoted r_1, r_2, and r_3, respectively. Substituting $M = 0$ in equation (18) for these points, the equation for the buckling loads is then

$$\frac{J_0(kr_1)J_8(kr_2) + J_0(kr_2)J_8(kr_1)}{J_0(kr_3)J_8(kr_2) + J_0(kr_2)J_8(kr_3)} + \frac{J_4(kr_1)}{J_4(kr_3)} = 0 \qquad (19)$$

where $r_3 = R$, $r_2 = 0.7654\,R$, and $r_1 = 0.7071\,R$.

A convenient compilation of Bessel functions of high order for the evaluation of the first root of equation (19) is that of Cambi [9]. Using these tables, it is found that the first root is given by

$$kR = 3.1416 \qquad (20)$$

in excellent agreement with the exact value of $kR = \pi$.

As a second example, we consider the simply supported hexagonal plate shown in Fig. 2 and write

$$M = AJ_0(kr) + BJ_6(kr)\cos 6\theta + CJ_{12}(kr)\cos 12\theta \qquad (21)$$

The boundary points selected for convenience are here at $\theta = 0$, 15, and 30 deg, the respective radii being denoted r_1, r_2, and r_3. The buckling equation then obtained is

$$\frac{J_0(kr_1)J_{12}(kr_3) + J_0(kr_3)J_{12}(kr_1)}{J_0(kr_3)J_{12}(kr_2) + J_0(kr_2)J_{12}(kr_3)} + \frac{J_6(kr_1)}{J_6(kr_3)} = 0 \qquad (22)$$

where $r_3 = R$, $r_2 = 0.8966\,R$, $r_1 = 0.8660\,R$.

The first root of this equation is easily obtained, being

$$kR = 2.672 \qquad (23)$$

Generalizing the foregoing, it follows that the buckling loads of regular polygons of n-sides can be approximately found from the roots of the equation

$$\frac{J_0(kr_1)J_{2n}(kr_2) + J_0(kr_2)J_{2n}(kr_1)}{J_0(kr_3)J_{2n}(kr_2) + J_0(kr_2)J_{2n}(kr_3)} + \frac{J_n(kr_1)}{J_n(kr_3)} = 0 \qquad (24)$$

where $r_3 = R$, $r_2 = R(\cos \pi/n)/(\cos \pi/2n)$, $r_1 = R \cos \pi/n$, R = radius of circumscribing circle.

In summary, the buckling loads kR for the equilateral triangle, square, and hexagonal plates circumscribed by a circle of radius R are given in Table 2, where they are compared with the result for a simply supported circular plate of that radius found in the conventional way.

Table 2 Values of kR, $k^2 = P/D$, for the buckling of simply supported plates

Equilateral triangle	Square	Hexagon	Circle
4.19	3.14	2.67	2.05

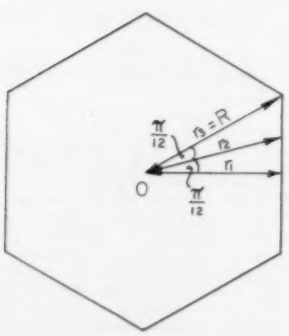

Fig. 2 Co-ordinate system for hexagonal plate

For the case of a plate loaded laterally and in its plane, we may write

$$M = q/k^2 + \sum_{n=0}^{\infty} A_n J_n(kr)\cos n\theta,\ \sin n\theta,\ P \text{ compressive}$$

$$M = -q/k^2 + \sum_{n=0}^{\infty} A_n I_n(kr)\cos n\theta,\ \sin n\theta,\ P \text{ tensile} \qquad (25)$$

and the moments at the center of a regular polygon may be obtained as before by point-matching.

A method for meeting the boundary conditions *exactly* on one edge will now be considered, the isosceles triangle shown in Fig. 3 being given as an example. The buckling of this plate might have been treated in the foregoing manner, but the following technique has the advantage of reducing the number of equations and hence the labor in solving them. We write here

$$M = AJ_1(kr)\cos\theta + BJ_3(kr)\cos 3\theta + CJ_5(kr)\cos 5\theta \qquad (26)$$

it being noted that all trigonometrical terms have a common factor $\cos\theta$. Extracting this

$$M = \cos\theta[AJ_1(kr) + BJ_3(kr)(4\cos^2\theta - 3) + CJ_5(kr)(16\cos^4\theta - 20\cos^2\theta + 5)] \qquad (27)$$

Because of the factor $\cos\theta$, $M = 0$ is satisfied automatically along the vertical side. The required three equations are then obtained by writing $M = 0$ in the square-bracketed term for the corners and one intermediate point.

As a numerical example, the isosceles right-angled triangle plate is treated, since the exact solution is well known and thus provides a check. For convenience, the points taken are for $\theta = 0$, 30 and 90 deg, the radii being a, $b = 0.73205\,a$ and a, respectively. Substituting in the square-bracketed term of equation (7), the resulting equation obtained is

$$2\,J_1(kb)J_3(ka) + J_1(ka)J_3(kb) = 0,\ b = 0.73205\,a \qquad (28)$$

The first root of this equation is

$$ka = 5.03 \qquad (29)$$

which differs from the exact value of $ka = 4.97$ by a little more than 1 per cent. It would therefore appear that the corresponding buckling loads obtained for the general isosceles triangle would be satisfactory. More points would increase the accuracy, but also the labor. Incidentally, an approach similar to the fore-

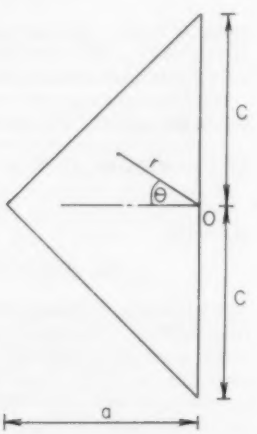

Fig. 3 Co-ordinate system for isosceles-triangle plate

going was found to be very satisfactory in calculating the maximum shearing stresses in rods of isosceles triangle and other cross sections [4].

(c) Flexural Vibrations of Plates. The flexural vibrations of a simply supported polygonal plate will now be discussed. The differential equation is here

$$D\nabla^4 w + \rho h \frac{\partial^2 w}{\partial t^2} = 0 \tag{30}$$

where ρ is the density of the material, and h is the thickness. Writing $w = w_0 e^{ipt}$, this becomes

$$D\nabla^4 w_0 - \rho h p^2 w_0 = 0 \tag{31}$$

Now

$$(M_x + M_y)/D(1 + \nu) = M/D = -\nabla^2 w = -\nabla^2 w_0 e^{ipt} \tag{32}$$

whence

$$\nabla^4 M - k^4 M = (\nabla^2 + k^2)(\nabla^2 - k^2)M = 0, \; k^4 = \rho h p^2/D \tag{33}$$

The general solution of equation (33) is then

$$M = \sum_{n=0}^{\infty} [A_n J_n(kr) + B_n I_n(kr)] \cos n\theta, \sin n\theta, \tag{34}$$

the Bessel functions of the second kind and of real and imaginary argument being omitted for a solid plate.

The boundary conditions are $M = 0$ and $\nabla^2 M = 0$. Substituting the second boundary condition in equation (34) and noting that

$$\nabla^2(J_n[kr] \cos n\theta, \sin n\theta) = -k^2 J_n(kr) \cos n\theta, \sin n\theta$$

$$\nabla^2(I_n[kr] \cos n\theta, \sin n\theta) = k^2 I_n(kr) \cos n\theta, \sin n\theta \tag{35}$$

we find that, on the boundary

$$\sum_{n=0}^{\infty} [A_n J_n(kr) + B_n I_n(kr)] \cos n\theta, \sin n\theta = 0$$

$$\sum_{n=0}^{\infty} [A_n J_n(kr) - B_n I_n(kr)] \cos n\theta, \sin n\theta = 0 \tag{36}$$

Thus for obtaining the frequency equation for any simply supported polygonal plate, we need only satisfy

$$\sum_{n=0}^{\infty} A_n J_n(kr) \cos n\theta = 0 \tag{37}$$

on the boundary. This is the same boundary-value problem as is encountered in the buckling of a polygonal plate under two-dimensional hydrostatic pressure, and hence the problems are analogous.[3] The method of point-matching is again advantageous and accurate.

By the foregoing analogy and transposing from Table 2, the fundamental frequencies of flexural vibration of equilateral triangle, square, and hexagonal plates circumscribed by a circle of radius R are given in Table 3. They are there compared with the result for a simply supported circular plate of that radius found in the conventional way. It should be noted that the kR-values for the circular plates in Tables 2 and 3 are not the same. This is as might be expected, since M is not zero on the edge of a circular plate, and an analogy between buckling and vibration does not exist.

[3] They are also analogous to the problem of the vibrating membrane. These analogies are discussed by the author in [11].

Table 3 Values of kR, $k^4 = \rho h p^2/D$, for fundamental frequencies of simply supported plates

Equilateral triangle	Square	Hexagon	Circle
4.19	3.14	2.67	2.22

Finally, it may be remembered that the technique for meeting the boundary conditions exactly on one edge also may be utilized here.

Remarks

It will be seen from the problems treated in this paper and from those dealt with in the References, that the method has certain definite advantages. It is simple and direct, and the computation of the coefficients requires only the solution of linear equations, for which the modern, high-speed computer is eminently suited. The specified points at which boundary conditions are satisfied may be clustered in regions of greatest interest, and indeed it is sometimes possible to meet the boundary conditions exactly there. It is particularly suited to problems with irregular boundaries, and has this advantage over, for example, the Rayleigh-Ritz method.

On the other hand, the method has certain disadvantages. It does not give bounds to the solutions, nor have questions of convergence been settled. It is better suited to sections which are compact; elongated sections may lead to inaccuracies [10]. Some boundary conditions are obviously easier to handle than others.

The foregoing are a few of the advantages and disadvantages. Others will doubtless appear with further investigation. It is true that the method is not a panacea. However, it would seem that point-matching, when used with care, can be a very valuable tool for the approximate solution of certain boundary-value problems.

References

1 H. Marcus, "Die Theorie elastischer Gewebe," Julius Springer Verlag, Berlin, Germany, 1932.

2 J. Barta, "Über die näherungsweise Lösung einiger zweidimensionaler Elastizitätsaufgaben," *Zeitschrift für angewandte Mathematik und Mechanik*, vol. 17, 1937, p. 184.

3 H. D. Conway, "The Approximate Analysis of Certain Boundary Value Problems," JOURNAL OF APPLIED MECHANICS, vol. 27, TRANS. ASME, vol. 82, Series E, June, 1960, pp. 275–277.

4 H. D. Conway, "Torsion of Prismatical Rods With Isosceles Triangle and Other Cross Sections," JOURNAL OF APPLIED MECHANICS, vol. 27, TRANS. ASME, vol. 82, Series E, March, 1960, p. 209.

5 H. D. Conway and A. W. Leissa, "A Method for Investigating Buckling Loads of Plates and Certain Other Eigenvalue Problems," JOURNAL OF APPLIED MECHANICS, vol. 27, TRANS. ASME, vol. 82, Series E, 1960, p. 557.

6 H. D. Conway, "On Some Systems of Equations Encountered in Thin Plate and Elasticity Theory," submitted to JOURNAL OF APPLIED MECHANICS.

7 S. Timoshenko and S. Woinowsky-Krieger, "Theory of Plates and Shells," McGraw-Hill Book Company, Inc., New York, N. Y., second edition, 1959, p. 120.

8 S. Woinowsky-Krieger, "Berechnung der ringsum frei aufliegenden gleichseitigen Dreiecksplatte," *Ingenieur-Archiv*, vol. 4, 1933, p. 254.

9 E. Cambi, "Eleven and Fifteen-Place Tables of Bessel Functions," Dover Publications, Inc., New York, N. Y., 1948.

10 H. Poritsky and C. E. Danforth, "On the Torsion Problem," *Proceedings*, Third U. S. National Congress of Applied Mechanics, 1958, p. 431.

11 H. D. Conway, "Analogies Between the Buckling and Vibration of Polygonal Plates and Membranes," *Canadian Aeronautical Journal*, September, 1960.

Journal of APPLIED MECHANICS

Design Data and Methods

It is important that the data contained in technical papers be made readily available to design engineers. In order to satisfy these needs of industry, this section of the Journal includes a concise presentation of data and information drawn chiefly from papers previously published by the Applied Mechanics Division of The American Society of Mechanical Engineers.

Design of Thin-Walled Torispherical and Toriconical Pressure-Vessel Heads[1]

R. T. SHIELD[2] and D. C. DRUCKER[3]

Summary

The failure under hydrostatic test of a large storage vessel designed in accordance with current practice stimulated earlier analytical studies. This paper gives curves and a table useful for the design and analysis of the knuckle region of a thin torispherical or toriconical head of an unfired cylindrical vessel. A simple but surprisingly adequate approximate formula is presented for the limit pressure, np^D, at which appreciable plastic deformations occur:

$$\frac{np^D}{\sigma_0} = \left(0.33 + 5.5\,\frac{r}{D}\right)\frac{t}{L} + 28\left(1 - 2.2\,\frac{r}{D}\right)\left(\frac{t}{L}\right)^2 - 0.0006,$$

where p^D is the design pressure, σ_0 is the yield stress of the material, and n is the factor of safety. The thickness t of the knuckle region is assumed uniform. Upper and lower bound calculations were made for ratios of knuckle radius r to cylinder diameter D of 0.06, 0.08, 0.10, 0.12, 0.14, and 0.16, and ratios of spherical cap radius L to D of 1.0, 0.9, 0.8, 0.7, and 0.6. Toriconical heads may be designed or analyzed closely enough by interpreting φ_0 in Table 1 as the complement of the half angle of the cone.

Introduction

The design of pressure vessels requires the long experience distilled into the ASME Code to avoid overlooking many important factors. In principle, the most straightforward of the difficult problems is the design of an unreinforced knuckle region of uniform thickness in an unfired pressure vessel subjected to interior pressure. This topic is discussed at length in the Code and it might well be expected that little remained to be resolved. Surprisingly, analytical studies[4-6] stimulated by reports of a failure under hydrostatic test demonstrated conclusively that the thickness required by the Code is inadequate for a range of designs. This range is one of small pressures and consequently of vessels whose wall thickness is small compared with the knuckle radius as well as the radius of the vessel itself. It did not, in all likelihood, engage the serious attention of the framers of the Code who were concerned primarily with pressures exceeding several hundred pounds per square inch. At these higher pressures, a sharply curved knuckle would have a radius which is not very large compared with the wall thickness, and so the knuckle would not be flexible and weak.

A design of adequate strength must provide a reasonable factor of safety against reaching the limit pressure, the pressure at which significantly large plastic deformation will take place. Many additional practical matters as well must be taken into account in the design. Among these are corrosion allowance, thinning allowance, and joint efficiency. They will not be considered here except by implication in the designation of the limit pressure as np^D, where n is a factor of safety and p^D is the design or working pressure.

The limit pressure is especially significant in a cold environment for those steels which are prone to brittle fracture. Appreciable plastic deformation below the transition temperature is almost certain to initiate a brittle fracture. Above this rather ill-defined transition temperature, the shape of a vessel of ductile material will be able to change sufficiently to carry the pressure without catastrophic failure. The pressure simply cold forms the head to a quite different but much better shape for containing pressure.

A Qualitative Discussion of the Behavior of Pressure Vessels

A thin-walled vessel under interior pressure is most efficient when it can carry the pressure as a membrane in biaxial tension. However, the shape required for this desirable membrane behavior[6] has a height of head $H = 0.26D$ which often appears too large from the fabrication or space utilization point of view. Torispherical heads are employed to reduce H appreciably, but they cannot act in biaxial tension; they must carry circumferential compression on the knuckle and also resist bending. Their load-

[1] The results presented in this paper were obtained in the course of research sponsored by the Office of Naval Research under Contract Nonr 562(10) with Brown University, Providence, R. I.

[2] Professor of Applied Mathematics, Brown University, Providence, R. I.

[3] Professor of Engineering, Brown University. Mem. ASME.

[4] G. D. Galletly has studied elastic behavior in "Torispherical Shells—A Caution to Designers," *Journal of Engineering for Industry*—TRANS. ASME, vol. 81, Series B, 1959, pp. 51–62, and "On Particular Integrals for Toroidal Shells Subjected to Uniform Internal Pressure," JOURNAL OF APPLIED MECHANICS, vol. 25, TRANS. ASME, vol. 80, 1958, pp. 412–413.

[5] D. C. Drucker and R. T. Shield have studied plastic behavior in "Limit Strength of Thin-Walled Pressure Vessels With an ASME Standard Torispherical Head," Proceedings, Third U. S. National Congress of Applied Mechanics, ASME, 1958, pp. 665–672, and "Limit Analysis of Symmetrically Loaded Thin Shells of Revolution," JOURNAL OF APPLIED MECHANICS, vol. 26, TRANS. ASME, vol. 81, Series E, 1959, pp. 61–68.

[6] R. A. Struble, "Biezeno Pressure Vessel Heads," JOURNAL OF APPLIED MECHANICS, vol. 23, TRANS. ASME, vol. 78, 1956, pp. 642–645.

Discussion of this paper should be addressed to the Secretary, ASME, 29 West 39th Street, New York 18, N. Y., and will be accepted until July 10, 1961, for publication at a later date. Discussion recived after the closing date will be returned.

Manuscript received by ASME Applied Mechanics Division, September 20, 1960.

Table 1

$\frac{L}{D}$	$\frac{r}{D}$	φ_0 (deg)	$\frac{H}{D}$	$\frac{p^M D}{2\sigma_0 t}$	$\frac{L}{D}$	$\frac{r}{D}$	φ_0 (deg)	$\frac{H}{D}$	$\frac{p^M D}{2\sigma_0 t}$
1.0	0.06	27.91	0.1694	0.064	0.9	0.06	31.59	0.1844	0.079
	0.08	27.16	0.1815	0.087		0.08	30.81	0.1957	0.108
	0.10	26.39	0.1937	0.111		0.10	30.00	0.2072	0.139
	0.12	25.58	0.2063	0.136		0.12	29.16	0.2188	0.171
	0.14	24.75	0.2190	0.163		0.14	28.27	0.2306	0.205
	0.16	23.88	0.2319	0.190		0.16	27.35	0.2427	0.240
0.8	0.06	36.48	0.2050	0.101	0.7	0.06	43.43	0.2353	0.134
	0.08	35.69	0.2152	0.139		0.08	42.64	0.2440	0.184
	0.10	34.85	0.2256	0.179		0.10	41.81	0.2528	0.238
	0.12	33.97	0.2360	0.221		0.12	40.93	0.2619	0.296
	0.14	33.06	0.2468	0.265		0.14	40.01	0.2710	0.357
	0.16	32.09	0.2577	0.312		0.16	39.02	0.2804	0.423
0.6	0.06	54.57	0.2869	0.185					
	0.08	53.87	0.2934	0.256					
	0.10	53.13	0.3000	0.333					
	0.12	52.34	0.3068	0.417					
	0.14	51.50	0.3136	0.507					
	0.16	50.60	0.3207	0.606					

$$H = L - (L - r)\cos\varphi_0$$

$$\sin\varphi_0 = \left(\frac{1}{2} - \frac{r}{D}\right)\Big/\left(\frac{L}{D} - \frac{r}{D}\right)$$

$$\frac{p^M D}{2\sigma_0 t} = \frac{rD}{L(L - r)}$$

carrying capacity as pure membranes (no moment resistance), shown in Table 1 as $p^M D/2\sigma_0 t$ and plotted on some of the graphs at $t/D = 0$, is extremely low. Actually, a very thin shell acting as a membrane would buckle in circumferential compression.

As the pressure builds up, it tends to force the spherical cap outward along the axis and the meridional membrane tensions pull the toroidal knuckle inward toward the axis. If the torus wall is thick enough to avoid buckling but thin compared with the radius of the knuckle, and the material does not work-harden, a plastic hinge circle will form at B, Fig. 1, to permit the central region of the knuckle to compress in the circumferential direction and bend inward. A hinge circle will form at C in the spherical cap and the third hinge circle A usually forms in the cylinder. The entire knuckle region between A and C is plastic because inward motion of appreciable extent means plastic contraction of the circumference. A thin-walled sharply curved knuckle region is far weaker than the main part of the spherical cap or the cylindrical portion of the vessel. On the other hand, if the torus wall is not so thin compared with the knuckle radius, the knuckle region is stiff and strong and acts somewhat like a stiffening ring at the junction of a spherical cap and a cylinder. The ASME Code which requires very little variation of $np^D D/\sigma_0 t$ with t/D apparently contains the implicit assumption that ordinarily the resistance to inward motion of the knuckle region is adequately high. Although true for vessels designed to carry large pressure, the assumption is not valid for many storage vessels and other low-pressure containers. For these thin-walled vessels there is a large variation of the value of $np^D D/2\sigma_0 t$ with t/D as shown in Figs. 2–5. On the other hand, the dotted lines for values of $np^D D/2\sigma_0 t$ greater than unity show that, for less sharply curved knuckles and for relatively thick knuckles, the knuckle region is stronger than the main cylindrical part of the vessel.

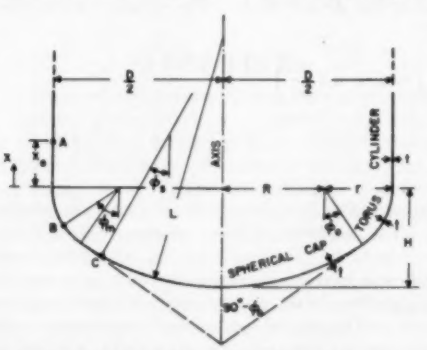

Fig. 1 Torispherical head, showing dimensions and locations of hinge circles A, B, C. (The equivalent toriconical head is shown by the dashed line which is tangent to the torus at its lower end.)

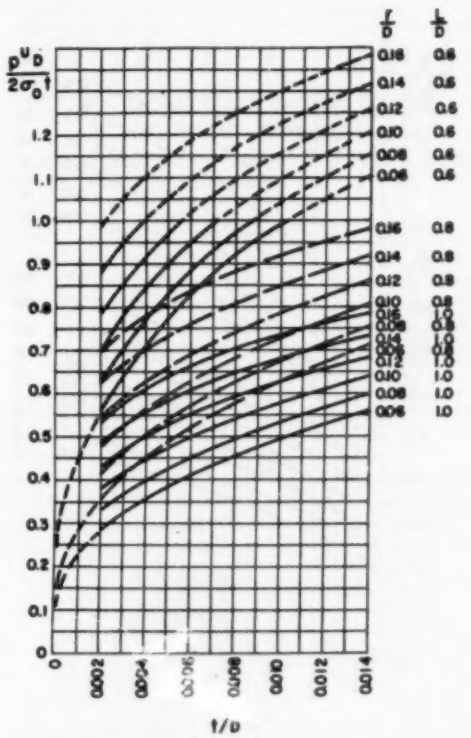

Fig. 2 Upper (unsafe) bound on limit pressure. $L/D = 0.6, 0.8, 1.0$.

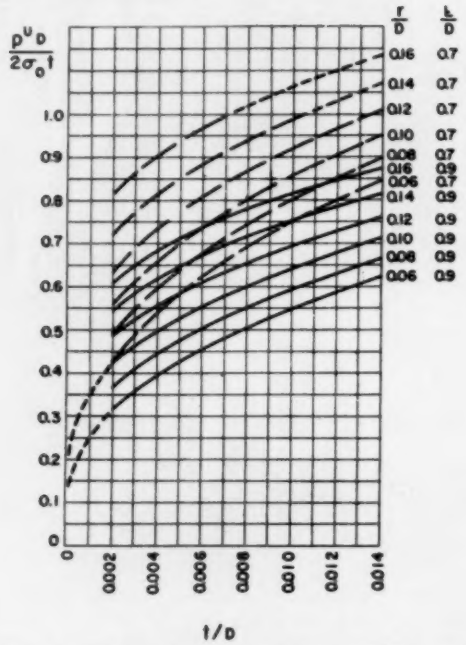

Fig. 3 Upper (unsafe) bound on limit pressure. $L/D = 0.7, 0.9$.

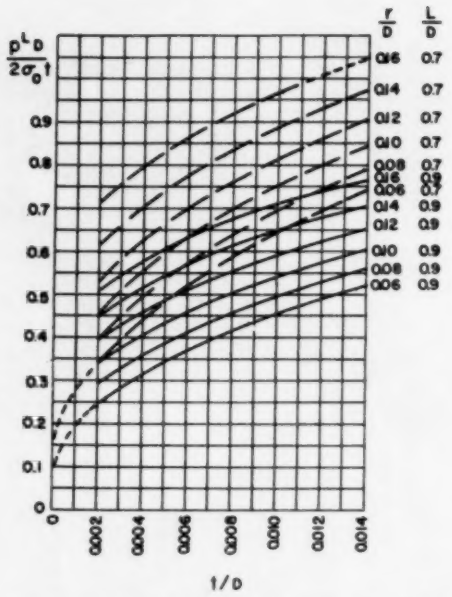

Fig. 5 Lower (safe) bound on limit pressure. $L/D = 0.7, 0.9$.

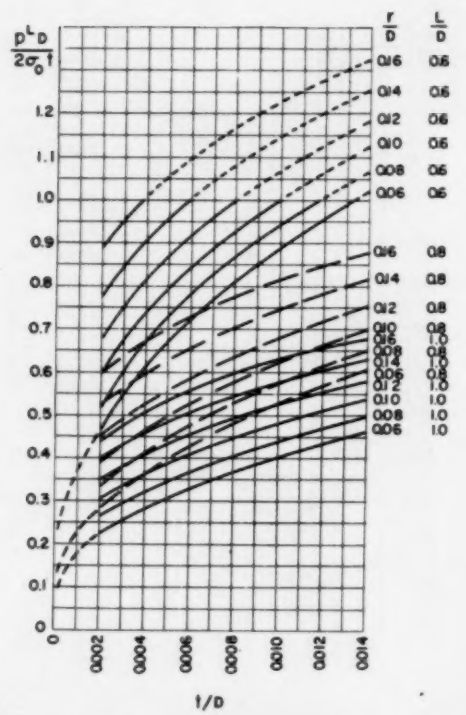

Fig. 4 Lower (safe) bound on limit pressure. $L/D = 0.6, 0.8, 1.0$.

Design Curves and Formula

The upper and lower bound theorems of limit analysis and design[7] were used to calculate the limit pressure. Therefore, even within the usual idealizations of the theory of plasticity, the exact answer is bounded rather than determined directly. Curves are plotted in Figs. 2 and 3 for $p^U D/2\sigma_0 t$, the upper (unsafe) values computed for $np^D D/2\sigma_0 t$, and in Figs. 4 and 5 for $p^L D/2\sigma_0 t$, the lower (oversafe) values. The designer then can make an independent judgment of the appropriate values to use.

However, if moderate accuracy is good enough or if a preliminary design is sought, Fig. 6 should prove a very helpful alternative. An approximate plot of t/D versus H/D for discrete values of np^D/σ_0, it gives a clear picture of the penalty to be paid for the advantage of decreasing the axial length of the vessel. The agreement with the mean of the upper and lower bound calculations, also shown in Fig. 6, varies with r/D and L/D but to a much smaller extent than might be expected.

Remarkably good agreement with the limit calculations can be achieved through use of the variable t/L which is of prime importance in the ASME Code. The excellent fit of the simple formula

$$\frac{np^D}{\sigma_0} = \left(0.33 + 5.5\,\frac{r}{D}\right)\frac{t}{L} + 28\left(1 - 2.2\,\frac{r}{D}\right)\left(\frac{t}{L}\right)^2 - 0.0006$$

is illustrated in Fig. 7, a plot of t/L versus np^D/σ_0 for two values of r/D. The relatively minor variation with L/D is also a feature of the Code. However, the Code calls for a linear variation of t/L with increasing pressure, and there is no way of adjusting a straight line to the proper curves without being unsafe or far too safe. The lack of safety is all too evident in Fig. 8, a

[7] D. C. Drucker, W. Prager, and H. J. Greenberg, "Extended Limit Design Theorems for Continuous Media," *Quarterly of Applied Mathematics*, vol. 9, 1952, pp. 381–389.

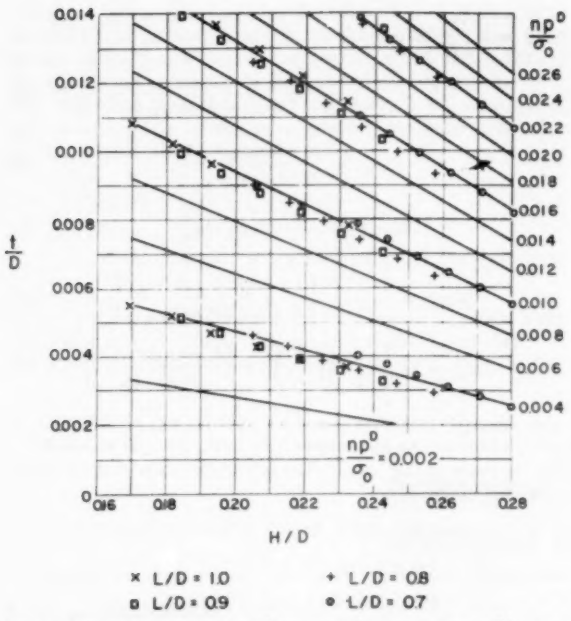

Fig. 6 Approximate curves for t/D versus H/D for constant np^D/σ_0 (for $L/D = 0.6$, H/D varies from 0.29 to 0.32)

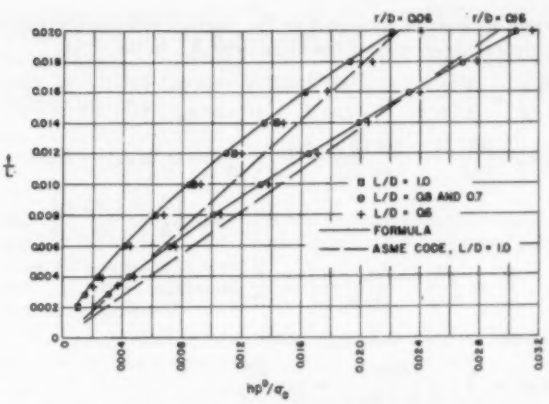

Fig. 7 Comparison of formula with average of upper and lower bounds and with ASME Code for $r/D = 0.06$ and 0.16

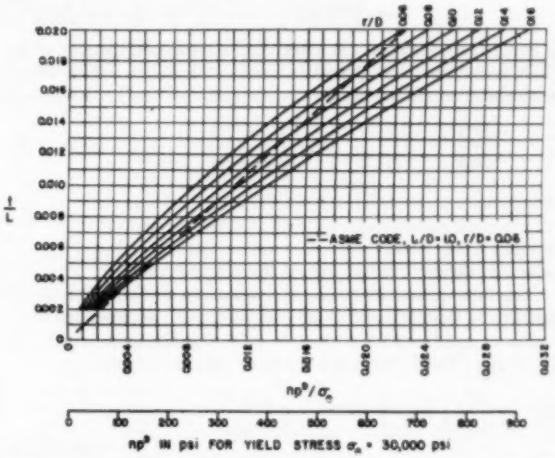

Fig. 8 Plot of $np^D/\sigma_0 = (0.33 + 5.5\ r/D)t/L + 28\ (1 - 2.2r/D)(t/L)^2 - 0.0006$; np^D/σ_0 must not exceed $2t/D$

plot of the formula for discrete values of r/D, which permits the designer to select t/L for a given pressure or to check the pressure-carrying capacity of an existing design. Again the designer is urged to return to Figs. 2–5 to obtain upper and lower bounds on his factor of safety if he is forced to design with a very small margin.

The Appendix contains detailed information on the basis and the methods of calculation of Figs. 2–5. It supplements the discussion contained in the earlier papers[5] and is not complete in itself. In essence, the Tresca or maximum shearing stress criterion of yield is employed and the yield surface for the shell is a cut-off parabolic approximation to the exact shape for a symmetrically loaded cylindrical shell.

Toriconical Heads

The values of t/L and np^D/σ_0 plotted for a given torus apply equally well to torispherical and to toriconical heads. Table 1 can be used to obtain the appropriate interpolated value of L/D for Figs. 2–5 if desired. The angle φ_0 is the complement of the torus angle and therefore the complement of the half angle of the cone.

APPENDIX

The equations of equilibrium for the various portions of the vessel, cylinder, torus and sphere are given in the references of footnote 5. The term involving the circumferential bending moment M_θ is omitted from the equations of equilibrium for the torus and the sphere as M_θ has little influence in carrying load for thin shells at sections not too near the axis of symmetry. The meridional bending moment M_φ is similarly omitted but its derivative is retained.

As M_θ is considered as a passive moment in the curved portions of the shell as well as in the cylinder, full use of M_φ and the meridional and circumferential force resultants N_φ and N_θ in carrying the internal pressure p is obtained by using the yield condition on N_φ, N_θ, M_φ for the cylinder. In order to approximate to this yield condition or surface, the circumscribing surface consisting of a parabolic cylinder with four cut-off planes is used.[6] In the region of interest between the hinge circles A, B, C of Fig. 1, N_φ is tensile and N_θ is compressive. For this region to be at yield, the parabolic prism yield surface requires

$$N_\varphi - N_\theta = \sigma_0 t, \quad |M_\varphi| \leq \frac{1}{4}\sigma_0 t^2\{1 - (N_\varphi/\sigma_0 t)^2\}. \qquad (1)$$

It is assumed that at the hinge circles A and C in the cylinder and the sphere, M_φ attains its largest negative value, and at hinge circle B in the torus, M_φ attains its largest positive value. The shear force Q is zero at the hinge circles. Under these conditions the equations of equilibrium can be integrated to provide the distribution of N_θ, N_φ, M_φ, and Q in the plastic region.

It is found that in the cylinder,

$$M_\varphi = -\frac{1}{4}\sigma_0 t^2\left\{1 - \left(\frac{pD}{4\sigma_0 t}\right)^2\right\} + \frac{1}{2}\sigma_0 \frac{t}{D}\left(2 + \frac{pD}{2\sigma_0 t}\right)(x_0 - x)^2, \qquad (2)$$

$$Q = -\sigma_0 \frac{t}{D}\left(2 + \frac{pD}{2\sigma_0 t}\right)(x_0 - x), \qquad (3)$$

where x measures distance from the junction with the torus and x_0 defines the location of the hinge circle A. In the torus,

$$\frac{M_\varphi}{r\sigma_y t} = \frac{1}{4}\frac{t}{r}\left\{1 - \left(\frac{pD}{2\sigma_y t}\right)^2 \frac{(R + r\sin\varphi_m)^2}{D^2\sin^2\varphi_m}\right\} - \frac{pR}{2\sigma_y t}\frac{[1 - \cos(\varphi - \varphi_m)]}{\sin\varphi_m} + \frac{r}{R}\cos\varphi\,[k(\varphi_m) - k(\varphi)] + \log\left\{\frac{R + r\sin\varphi}{R + r\sin\varphi_m}\right\}, \quad (4)$$

$$\frac{Q}{\sigma_y t} = \frac{pR}{2\sigma_y t}\frac{\sin(\varphi_m - \varphi)}{\sin\varphi_m} + \frac{r}{R}\sin\varphi\,[k(\varphi) - k(\varphi_m)], \quad (5)$$

where

$$k(\varphi) = \int_{\varphi_0}^{\varphi} \frac{R\,d\varphi}{R + r\sin\varphi} = \frac{2R}{(R^2 - r^2)^{1/2}}\left[\tan^{-1}\left\{\frac{r + R\tan\frac{1}{2}\varphi}{(R^2 - r^2)^{1/2}}\right\}\right]_{\varphi_0}^{\varphi}, \quad (6)$$

φ is the angle between the meridional normal and the axis of the shell, and φ_m is the location of the hinge circle B. In the sphere, with the assumption that $\varphi - \varphi_0$ is small,

$$\frac{M_\varphi}{L\sigma_y t} = -\frac{1}{4}\frac{t}{L}\left\{1 - \left(\frac{pL}{2\sigma_y t}\right)^2\right\} + \frac{1}{2}(\varphi - \varphi_s)^2, \quad (7)$$

$$\frac{Q}{\sigma_y t} = \varphi - \varphi_s, \quad (8)$$

where φ_s defines the location of the hinge circle C.

The four quantities p, φ_m, φ_s, and x_0 are determined from the conditions that M_φ and Q are continuous at the junctions of the cylinder and torus ($x = 0$, $\varphi = \pi/2$) and the torus and sphere ($\varphi = \varphi_0$). These conditions can be written

$$\left(2 + \frac{pD}{2\sigma_y t}\right)\left(\frac{x_0}{D}\right)^2 = j(\varphi_m)\left(\frac{pD}{2\sigma_y t}\right)^2 + a(\varphi_m)\frac{pD}{2\sigma_y t} + b(\varphi_m), \quad (9)$$

$$\left(2 + \frac{pD}{2\sigma_y t}\right)\frac{x_0}{D} = c(\varphi_m)\frac{pD}{2\sigma_y t} + d(\varphi_m), \quad (10)$$

$$(\varphi_0 - \varphi_s)^2 = l(\varphi_m)\left(\frac{pD}{2\sigma_y t}\right)^2 + e(\varphi_m)\frac{pD}{2\sigma_y t} + f(\varphi_m), \quad (11)$$

$$\varphi_0 - \varphi_s = g(\varphi_m)\frac{pD}{2\sigma_y t} + h(\varphi_m), \quad (12)$$

where the functions not previously defined are given by

$$a(\varphi_m) = -2\frac{rR}{D^2}\frac{(1 - \sin\varphi_m)}{\sin\varphi_m}, \quad (13)$$

$$b(\varphi_m) = 2\frac{r}{D}\log\left\{\frac{R + r}{R + r\sin\varphi_m}\right\} + \frac{t}{D}, \quad (14)$$

$$c(\varphi_m) = \frac{R}{D}\cot\varphi_m, \quad (15)$$

$$d(\varphi_m) = -\frac{r}{R}[k(\pi/2) - k(\varphi_m)], \quad (16)$$

$$e(\varphi_m) = -2\frac{rR}{LD}\frac{[1 - \cos(\varphi_m - \varphi_0)]}{\sin\varphi_m}, \quad (17)$$

$$f(\varphi_m) = 2\frac{r^2}{LR}\cos\varphi_0 k(\varphi_m) + 2\frac{r}{L}\log\left\{\frac{R + r\sin\varphi_0}{R + r\sin\varphi_m}\right\} + \frac{t}{L}, \quad (18)$$

$$g(\varphi_m) = \frac{R}{D}\frac{\sin(\varphi_m - \varphi_0)}{\sin\varphi_m}, \quad (19)$$

$$h(\varphi_m) = -\frac{r}{R}\sin\varphi_0\,k(\varphi_m), \quad (20)$$

$$j(\varphi_m) = -\frac{1}{2}\frac{t}{D}\left\{\frac{1}{4} + \frac{(R + r\sin\varphi_m)^2}{D^2\sin^2\varphi_m}\right\}, \quad (21)$$

$$l(\varphi_m) = -\frac{1}{2}\frac{t}{L}\left\{\left(\frac{L}{D}\right)^2 + \frac{(R + r\sin\varphi_m)^2}{D^2\sin^2\varphi_m}\right\}. \quad (22)$$

Equations (9)–(12) were solved for $pD/2\sigma_y t$, φ_m, φ_s, and x_0/D for given values of the parameters t/D, L/D, and r/D which define the geometry of the vessel. The following values of the parameters were used:

$$t/D = 0.002, 0.004, 0.006, 0.008, 0.010, 0.012, 0.014$$

$$L/D = 1.0, 0.9, 0.8, 0.7, 0.6$$

$$r/D = 0.06, 0.08, 0.10, 0.12, 0.14, 0.16$$

In the numerical method used, a trial value $\varphi_m{}^a$ was chosen for φ_m and the functions of φ_m occurring on the right-hand sides of equations (9)–(12) were evaluated. By elimination of $\varphi_0 - \varphi_s$ between (11) and (12), a quadratic equation was obtained for $pD/2\sigma_y t$. The positive root of this equation was then substituted in (9) and (10) to give two values of $(x_0/D)^2$. The difference between these two values was evaluated and the procedure was repeated with another trial value $\varphi_m{}^b$ for φ_m, and again the difference between the two values of $(x_0/D)^2$ was found. Linear interpolation between $\varphi_m{}^a$ and $\varphi_m{}^b$ was then used to give a better approximation to the true value of φ_m. The process was repeated until the magnitude of the difference between the two values of $(x_0/D)^2$ as provided by (9) and (10) was less than 10^{-7}.

For a few of the thinner vessels (12 out of the 210 considered), the upper hinge circle A does not lie in the cylinder but is located in the torus, and the analysis requires a straightforward modification. The details of this modification will not be given here.

The value of the pressure p obtained from equations (9)–(12) (or from the modified analysis) is the limit pressure p^U for the head with the parabolic yield surface. As this surface circumscribes the exact yield surface for the cylinder, p^U is an upper bound to the true limit pressure. The values of p^U are shown in Figs. 2 and 3. A lower bound $p^L = \lambda p^U$ is obtained by choosing the factor λ so that the stress points λN_φ, λN_θ, λM_φ lie within the yield surface for the cylinder for all sections of the plastic region. The factor is given by

$$\lambda = (P^2 - 4P + 12)/2(P^2 - 4P + 8), \quad (23)$$

where $P = p^U D/2\sigma_y t$, the critical section being the hinge circle A in the cylinder. The factor varies from 0.82 to 0.90 as P varies from 0.5 to 1.0, and the values of $p^L D/2\sigma_y t$ are given in Figs. 4 and 5. The average of the upper and lower bounds will be sufficiently close to the true limit pressure for practical purposes. Thus we put $np^D = (p^U + p^L)/2$, where p^D is the design pressure and n the factor of the safety against collapse.

For a given thickness ratio t/D, the limit pressure np^D increases as r/D increases, and decreases as L/D increases. The ratio H/D of the height of the head to the diameter depends similarly on the ratios r/D, L/D, as can be seen from Table 1. In Fig. 6, approximate curves for t/D versus H/D for constant

values of np^D/σ_0 are shown for the range $0.17 < H/D < 0.28$ covered by the ranges 0.06 to 0.16 for r/D and 0.7 to 1.0 for L/D. Actual points for $np^D/\sigma_0 = 0.004$, 0.010, 0.016, and 0.022 are also shown for comparison with the approximate curves.

It was found that, for a fixed value of r/D, the variation of np^D/σ_0 with t/L is almost independent of the ratio L/D. For $L/D = 0.7$ and 0.8, the formula

$$\frac{np^D}{\sigma_0} = \left(0.33 + 5.5\,\frac{r}{D}\right)\frac{t}{L} + 28\left(1 - 2.2\,\frac{r}{D}\right)\left(\frac{t}{L}\right)^3 - 0.0006 \quad (24)$$

provides values of np^D/σ_0 which are very close (e.g., within 3 per cent for $t/L = 0.010$) to the values calculated from $np^D = (p^U + p^L)/2$. Formula (24) is also adequate for $L/D = 1.0$, 0.9, and 0.6 as can be seen from Fig. 7, in which the formula (24) is compared with the values calculated from $np^D = (p^U + p^L)/2$ for the cases $r/D = 0.06$ and 0.16. Comparison with the ASME Code for Unfired Pressure Vessels is also made in Fig. 7. The ASME Code gives

$$\frac{p^D}{SE} = 2\,\frac{t}{L}\Big/\left(M + 0.2\,\frac{t}{L}\right), \quad (25)$$

where $M = \frac{1}{4}[3 + (L/r)^{1/2}]$, S is the maximum allowable stress, and E is the efficiency of the welded joints. For the present purposes, SE was taken to be σ_0/n.

Acknowledgment

The authors would like to thank Mrs. Lois Paul for her assistance with the computations.

Hydrodynamic Lubrication of a Roller Bearing—Introduction of Parameters to Obtain Charts for Calculation

F. W. v. HACKEWITZ[1]

Nomenclature

E = modulus of elasticity (21,000 kg/sq mm for steel), kg/sq mm
P = radial load on cylindrical roller per unit effective roller length, kg/mm
P^* = relative load on cylindrical roller P/R_i, kg/sq mm
R = radius of cylindrical roller, mm
R_i = radius of inner ring raceway, mm
R^* = relative radius of cylindrical roller $\dfrac{R/R_i}{1 + R/R_i}$
h = smallest oil-film thickness to be found at contact between rolling body and inner ring, mm
h^* = relative oil-film thickness h/R_i
k_1, k_2, k_3 = constant coefficients
n = resultant rotating speed of the bearing, i.e., rotating speed of inner ring relative to outer ring, rpm
p_m = peak pressure in contact area between roller and inner ring, kg/sq mm
u = parameter, angle deg
α = reduction parameter $R^*p_m^2/k_1^2k_2$
β = reduction parameter h^*/k_3
γ = pressure coefficient of viscosity of lubricating oil at operating temperature [2],[2] sq mm/kg. The coefficient γ supposes an oil where $\log [\eta(p)/\eta_0]$ is proportional to the pressure p as to justify $\eta(p) = \eta_0 e^{\gamma p}$. Some lubricating oils obey this law, but there are other oils in use, which show deviation. Thus a verification of the proper pressure dependence of viscosity is advisable for each particular case.
η_0 = viscosity of lubricating oil at atmospheric pressure and operating temperature, kg sec/sq mm
η_r = resultant viscosity of lubricating oil at the rolling contact [3], kg sec/sq mm
μ = deformation parameter which is defined in Dörr's work [1]. The parameter's definition fixes two limiting end points: One for $\mu = 0$, where no elastic deformation occurs at the rolling contact, and the other for $\mu = 2$, with maximum elastic deformation, i.e., no oil film separating the contacting rolling bodies (Hertzian case). Dörr derives simplified formulas valid for $0 \leqslant \mu \leqslant 1.7$, thus covering the greatest part of the parameter range. Our calculation is based on these simplified formulas.
ν = Poisson's ratio (0.303 for steel)
π = 3.14159...
e = 2.71828...

[1] SKF Central Laboratoriet, Göteborg, Sweden.
[2] Numbers in brackets indicate References at end of paper.
Manuscript received by ASME Applied Mechanics Division, June 9, 1960; final draft, January 17, 1961.

Introduction

In a recent note [3] hydrodynamic formulas have been proposed to calculate contact pressure and oil-film thickness in a lubricated cylindrical roller bearing. These formulas use Dörr's derivations for elastic deformation at the rolling contact [1], and a pressure-dependent viscosity [2]. Their numerical evaluation is cumbersome, demanding extensive calculation.

Relative and dimensionless magnitudes are introduced in the following. They help to establish charts which represent isothermal results for different bearing design and various running conditions, thus aiding in the engineer's rapid investigation.

The charts show a minimum oil-film thickness at certain combinations of roller load and running speed.

General Calculation

Conditions are more severe at the inner contact than at the outer contact. We calculate, therefore, relationships for the inner contact only. Introducing the following reduction parameters

$$R^* \equiv \frac{R/R_i}{1 + R/R_i} \quad (1)$$

$$P^* \equiv P/R_i, \text{ kg/sq mm} \quad (2)$$

$$h^* \equiv h/R_i \quad (3)$$

$$k_1 \equiv \frac{\pi E}{12(1 - \nu^2)}, \text{ kg/sq mm} \quad (4)$$

$$k_2 \equiv \frac{0.457^2 30}{\pi}$$

$$= 1.994 \tag{5}$$

$$k_2 \equiv \frac{6.5\pi}{30}$$

$$= 0.6807 \tag{6}$$

into the three corresponding formulas of Ref. [3], and substituting for the deformation parameter μ, we obtain two basic formulas:

$$O = +2k_1k_2P^{*3} - 7.3R^*p_m{}^3P^{*2} - 5.3k_1R^{*2}p_m{}^3n\eta_c \tag{7}$$

$$O = +2.7k_1R^*h^*P^*n\eta_c + 0.7h^*P^{*3} - k_1k_2R^{*2}(n\eta_c)^2 - k_2R^*P^{*2}n\eta_c \tag{8}$$

and eliminating $n\eta_c$ these two equations are thrown into one relationship

$$+P^{*3} - 4.65\frac{R^*p_m{}^2}{k_1{}^2k_2}k_1P^{*2} - \left[7.155\frac{R^*p_m{}^2}{k_1{}^2k_2}\cdot\frac{h^*}{k_2} - 3.65\left(\frac{R^*p_m{}^2}{k_1{}^2k_2}\right)^2\right]k_1{}^2P^* + 21.2\left(\frac{R^*p_m{}^2}{k_1{}^2k_2}\right)^2\frac{h^*}{k_2}k_1{}^3 = 0 \tag{9}$$

Reducing further with

$$\alpha \equiv \frac{R^*p_m{}^2}{k_1{}^2k_2} \tag{10}$$

and

$$\beta \equiv \frac{h^*}{k_2}, \tag{11}$$

we write

$$+P^{*3} - 4.65\alpha k_1P^{*2} - [7.155\alpha\beta - 3.65\alpha^2]k_1{}^2P^* + 21.2\alpha^2\beta k_1{}^3 = 0 \tag{9a}$$

One principal root $P^* = f(\alpha, \beta)$ of the cubic equation (9a) gives the explicit solution for all practical cases, because normally

$$\alpha < +0.6624 + 2.824\beta + [+19.10\beta^2 + 15.34\beta + 1.051]^{1/2} \tag{12}$$

This particular root is obtained with

$$P^* = k_1\alpha\left\{(9.54\,\beta/\alpha + 4.743)^{1/2}\cos\left(\frac{u}{3}\right) + 1.55\right\} \tag{13}$$

where

$$u = 180° - \text{arc cos}\left\{\sqrt{\alpha}\,\frac{5.055\beta - 0.8951\alpha}{(2.385\beta + 1.186\alpha)^{3/2}}\right\} \tag{14}$$

R^* indicates geometric proportions of the bearing.

We consider now R^* to be constant and establish a chart for the four principal variables P^*, p_m, h^*, and $n = f(P^*, p_m)$, since from (7) and (8), with $\alpha(p_m)$ introduced,

$$n^* = \left(\frac{P^*}{k_1}\right)^2\frac{2P^* - 7.3k_1\alpha}{5.3R^*\eta_c\alpha} \tag{15}$$

where

$$\eta_c = \gamma\eta_0\,\frac{p_m}{1 - e^{-\gamma p_m}} \tag{16}$$

as shown in Ref. [3].

Taking n as abscissa and P^* as ordinate, the curves P^* (p_m = const) = $f(n)$ and P^* (h^* = const) = $f(n)$ can be plotted when assuming various values for p_m and h^*, and calculating P^* from equations (13) and (14), and n from (15) and (16) subsequently.

Slope equations may be helpful to trace the curves, thus

$$\frac{\partial P^*(p_m = \text{const})}{\partial n} = \frac{5.3k_1{}^3R^*\eta_c\alpha}{P^*(6P^* - 14.6k_1\alpha)} \tag{17}$$

and

$$\lim_{P^*\to 0}\frac{\partial P^*(h^* = \text{const})}{\partial n} = \frac{k_1}{2.7}\cdot\frac{R^*\eta_0}{h^*} \tag{18}$$

The curves of P^* (h^* = const) = $f(n)$ show a minimum oil-film thickness for certain corresponding values P^* and n. The point of minimum can be determined by forming $\partial n(h^* = \text{const})/\partial P^* = 0$ which gives a condition for $h^* \to h^*_{\min}$.

$$p_m\frac{\partial P^*}{\partial p_m} = \frac{k_1{}^2\alpha^2(14.6P^* + 84.8k_1\beta) - k_1\alpha P^*(9.3P^* + 14.31k_1\beta)}{k_1\alpha(9.3P^* + 7.155k_1\beta) - 3.65k_1{}^2\alpha^2 - 3P^{*2}} = \frac{2P^{*3}(3\eta_0 - \eta_c e^{-\gamma p_m}) - 7.3k_1\alpha P^*(\eta_0 - \eta_c e^{-\gamma p_m})}{\eta_0(6P^* - 14.6k_1\alpha)} \tag{19}$$

Dörr [1] specifies a limit of application for his deformation parameter, which reads

$$\mu = \frac{2}{1 + \dfrac{k_1R^*n\eta_c}{P^{*2}}} \leqslant 1.7$$

or

$$P^{*2} \leqslant \frac{17}{3}k_1R^*n\eta_c \tag{20}$$

A hydrodynamic solution can be obtained, though with extended calculation, for heavier loads, where the deformation parameter approaches the maximum value $\mu = 2$ [5]. The relatively high roller load, however, gives then increasing importance to several disturbing factors. These are hysteresis of elastic deformation, hysteresis of oil viscosity due to dynamic pressure, and local temperature rise in the rolling contact. It would seem that these complex phenomena are not sufficiently explored to be included in technical calculations. Condition (20) may so be justified, which excludes extremely heavy loads to be treated with the foregoing relationships.

Example

Let us assume a steel bearing and a lubricating oil [4] of $\eta_0 = 11$ centipoise $= 1.122 \times 10^{-9}$ kg/sq mm and $\gamma = 0.195$ sq mm/kg, which operates at 130 F.

We calculate $P^* = f(n)$ with various h^* and p_m by using equations (13), (14), (15), and (16) accordingly with $R/R_i = 0.1$, 0.2, and 0.3, since normally $0.1 \leqslant R/R_i \leqslant 0.3$. Three charts are then established, one for each ratio R/R_i (see Figs. 1, 2, and 3).

An interpolation between the values on the charts gives results for each particular ratio R/R_i.

At a given revolving speed the oil-film thickness at the contact decreases at first with the load imposed on the roller (roller entering the loaded zone of bearing). The decreasing rate of oil-film becomes rapidly smaller with heavier roller loads until a point of minimum oil-film is attained beyond which the film thickness starts to increase slowly. To determine this minimum oil-film thickness $h_{\min}{}^*$ we use relationship (19) together with the corresponding calculated values of P^*, h^*, p_m, and n, and obtain thus

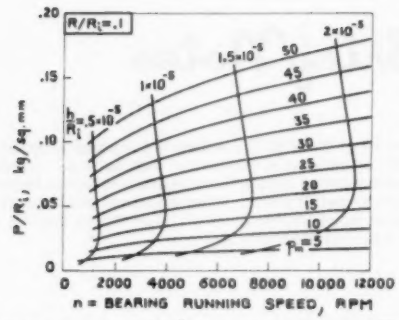

Fig. 1 Contact pressure p_m, kg/sq mm, and relative oil-film thickness h/R_i for $R/R_i = 0.1$

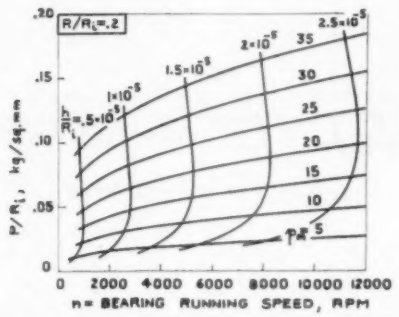

Fig. 2 Contact pressure p_m, kg/sq mm, and relative oil-film thickness h/R_i for $R/R_i = 0.2$

$$P^*(h^* = h_{\min}^*) = f(n)$$

for each ratio R/R_i (see Fig. 4).

A temperature rise can be achieved in the rolling contact, when high running speed and heavy load are simultaneously imposed on the bearing. The flow of lubricant becomes then more viscous and the pressure coefficient changes. Taking the example's lubricating oil [4], with $\eta_0 = 4$ centipoise and $\gamma = 0.125$ sq mm/kg for the higher oil temperature of 210 F, we have

$$\eta_c|_{210\,F} \approx 0.24\eta_c|_{120\,F}$$

supposing contact pressures $p_m > 10$ kg/sq mm, i.e., $1 \gg e^{-\gamma p_m}$. Heavier contact pressure and smaller oil-film thickness are then calculated; e.g., for $P/R_i = 0.1$ kg/sq mm and $n = 6000$ rpm we obtain

$$p_m|_{210\,F} \approx 1.4p_m|_{120\,F} \quad \text{and} \quad h^*|_{210\,F} \approx 0.4h^*|_{120\,F}$$

in the example's range $0.1 \leqslant R/R_i \leqslant 0.3$. Thus, determine

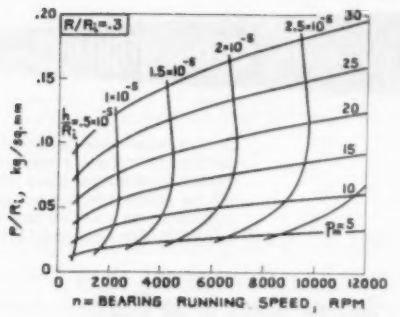

Fig. 3 Contact pressure p_m, kg/sq mm, and relative oil-film thickness h/R_i for $R/R_i = 0.3$

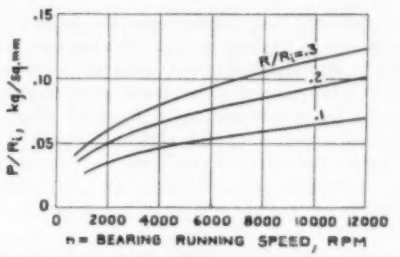

Fig. 4 Relative roller load P/R_i, kg/sq mm, versus bearing running speed n, rpm, for $h^* = h^*_{\min}$

values for various running temperatures by taking the isothermal results on the chart and multiplying them with the particular temperature coefficient.

References

1 J. Dörr, "Schmiermitteldruck und Randverformungen des Rollenlagers," *Ingenieur-Archiv*, vol. 22, 1954, section 3, pp. 171–193.

2 P. L. Kapitsa, "Hydrodynamic Theory of Lubrication During Rolling," *Journal of Technical Physics* (Russian), vol. 25, 1954, section 4, pp. 747–762.

3 F. W. v. Hackewitz, "The Influence of Kapitsa's Viscosity on the Hydrodynamic Lubrication of a Cylindrical Roller Bearing as Affecting Contact Pressure and Oil-Film Thickness," JOURNAL OF APPLIED MECHANICS, vol. 25, TRANS. ASME, vol. 80, 1958, p. 621, equations (5*a*, 5*b*, 5*c*).

4 M. D. Hersey and R. F. Hopkins, "Viscosity of Lubricants Under Pressure," ASME publication, 1954, p. 32, oil number A4f-3(P-82).

5 D. Dowson and G. R. Higginson, "A Numerical Solution to the Elasto-Hydrodynamic Problem," *Journal of Mechanical Engineering Science* (London), vol. 1, 1959, pp. 6–15.

Journal of APPLIED MECHANICS

Brief Notes

On the recommendation of the Executive Committee of the ASME Applied Mechanics Division, it was decided to initiate a section devoted to brief notes on technical matters in mechanics. These notes must not be longer than 750 words (about 2½ double-spaced typewritten pages, including figures) and will be subject to the usual review procedure prior to publication. After approval such notes will be published as soon as possible, normally in the next issue of the Journal. The notes should be submitted to the Technical Editors of the Journal of Applied Mechanics.

Surface Waves in an Elastic Half Space[1]

C. C. CHAO,[2] H. H. BLEICH,[3] and J. SACKMAN[4]

AT LARGE distances from a disturbance, the major effects near the surface are due to Rayleigh waves. This has been discovered theoretically by Rayleigh and is well confirmed by seismological experience. It is the purpose of the present paper to give suitable expressions for the determination of Rayleigh effects due to transient normal pressures on the surface. Specifically, closed form solutions are presented for the effect of a concentrated load, suddenly applied and maintained thereafter. Any general pressure distribution may then be treated by integration in space and time.

The complete effect of a suddenly applied concentrated load has been treated by Pekeris [1, 2],[5] who also obtained response curves for certain displacements requiring lengthy numerical integrations. As noted by Pekeris [2], and long ago found by Sommerfeld [3], the surface effects can be obtained by the transform approach as contributions of certain poles, ignoring branch integrals which occur in a complete solution. This approach is used hereafter. Introducing the clearly appropriate simplification of considering the depth small versus the radial distance from the force, relatively simple closed form expressions will be obtained for stresses and displacements.

By superposition this concentrated force solution can be used to obtain approximate solutions for various types of distributed pressure loadings on the surface of the half space.

Analysis

The geometry of the problem is depicted in Fig. 1 where a concentrated force (P positive downward, and varying with time as the step function) acts on the surface of an elastic half space. Reference [1] (Equations (3, 9, 16–19)) gives the Hankel-Laplace transforms of the potentials from which the transforms of the vertical and radial displacements, u_z and u_r, respectively, may be derived:

$$u_z(r,t) = \frac{P}{4\pi^2\mu i}\int_0^\infty d\xi \int_{a-i\infty}^{a+i\infty} J_0(\xi r)\xi\,[(2\xi^2+k^2)e^{-k\alpha z+pt} - 2\xi^2 e^{-k\beta z+pt}]\left[\frac{\alpha k}{M(\xi)}\right]\frac{dp}{p} \quad (1)$$

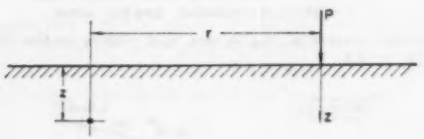

Fig. 1

$$u_r(r,t) = \frac{P}{4\pi^2\mu i}\int_0^\infty d\xi \int_{a-i\infty}^{a+i\infty} J_1(\xi r)\,[(2\xi^2+k^2)e^{-k\alpha z+pt} - (2\xi^2+k^2)^{1/2}(\xi^2+k^2)^{1/2}e^{-k\beta z+pt}]\left[\frac{\xi^2}{M(\xi)}\right]\frac{dp}{p}$$

where

$$h^2 = \left(\frac{p}{c_p}\right)^2 \quad k^2 = \left(\frac{p}{c}\right)^2 \quad c^2 = \frac{\mu}{\rho}, \quad c_p^2 = \frac{\lambda+2\mu}{\rho} = 3c^2$$

$$k\alpha = (\xi^2+h^2)^{1/2} \qquad k\beta = (\xi^2+k^2)^{1/2} \qquad i = \sqrt{-1} \quad (1a)$$

$$M(\xi) = (2\xi^2+k^2)^2 - 4k^2\xi^2\alpha\beta$$

For simplicity, similar to [1], the two Lamé constants have been set equal, $\lambda = \mu$. In order to insure decay of the displacements at infinity, the branch of the square root must be chosen to yield a positive real part.

The approximate solution for the Rayleigh phase is obtained from Equations (1) by utilizing only the residues of the integrals at the (Rayleigh) poles, $p = \pm\dfrac{ik\xi}{\gamma}$, with $\gamma = \left(\dfrac{1}{2}\right)(3+\sqrt{3})^{1/2}$ (reference [2]). The contribution from the poles is:

$$u_z = -\frac{P}{\pi\mu r}\left[\frac{\left(\gamma^2-\frac{1}{3}\right)^{1/2}}{\dot{F}(\gamma)}\right]\mathrm{Im}\left\{\frac{1-2\gamma^2}{(\nu^2-1)^{1/2}}+\frac{2\gamma^2}{(\omega^2-1)^{1/2}}\right\}$$

$$u_r = \frac{P}{\pi\mu r}\left[\frac{\gamma}{\dot{F}(\gamma)}\right]\mathrm{Re}\left\{(1-2\gamma^2)\left[1-\frac{\nu}{(\nu^2-1)^{1/2}}\right] + 2(\gamma^2-1)^{1/2}\left(\gamma^2-\frac{1}{3}\right)^{1/2}\left[1-\frac{\omega}{(\omega^2-1)^{1/2}}\right]\right\} \quad (2)$$

where, again, that branch of the square root must be taken which yields a positive real part, and where

$$\omega = [\tau + il(\gamma^2-1)^{1/2}]/\gamma$$

$$\nu = \left[\tau + il\left(\gamma^2-\frac{1}{3}\right)^{1/2}\right]\Big/\gamma \quad (2a)$$

$$\tau = \frac{ct}{r}, \quad l = \frac{z}{r}, \quad \dot{F}(\gamma) = -\frac{8\sqrt{3}}{3}\gamma$$

Since only the Rayleigh phase is being considered, these expressions are only applied to shallow depths ($l \ll 1$) and to values of the time near the arrival time of the Rayleigh wave ($\tau \doteq \gamma$). Using these restrictions, Equations (2) may be approximately simplified to the final form:

[1] This paper is a result of investigations sponsored by The RAND Corporation with Paul Weidlinger, Consulting Engineer, New York, N. Y.

[2] Assistant Professor, Aeronautical Engineering, Stanford University, Palo Alto, Calif.

[3] Director, Institute of Flight Structures, Columbia University, New York, N. Y. Mem. ASME.

[4] Assistant Professor, Institute of Flight Structures, Columbia University, New York, N. Y.

[5] Numbers in brackets indicate References at end of Note.

Manuscript received by ASME Applied Mechanics Division, May 31, 1960.

$$u_z = K_1 \left(\gamma^2 - \frac{1}{3}\right)^{1/2} \operatorname{Im}\left[(1 - 2\gamma^2)Z_1^{-1/2} + 2\gamma^2 Z_2^{-1/2}\right]$$

$$u_r = K_1\gamma \operatorname{Re}\left[(1 - 2\gamma^2)Z_1^{-1/2} + 2(\gamma^2 - 1)^{1/2}\left(\gamma^2 - \frac{1}{3}\right)^{1/2} Z_2^{-1/2}\right] \quad (3)$$

where

$$K_1 = \frac{3P}{8\sqrt{6\gamma}\,\pi\mu r^{1/2}z^{1/2}}$$

$$Z_1 = \frac{\tau - \gamma}{l} + i\left(\gamma^2 - \frac{1}{3}\right)^{1/2} \quad (3a)$$

$$Z_2 = \frac{\tau - }{l} + i(\gamma^2 - 1)^{1/2}$$

From these expressions for the displacements, expressions for the stress components may be derived by routine differentiation where $l \ll 1$, $\tau \doteq \gamma$ is used again:

$$\sigma_{zz} = K_2(2\gamma^2 - 1)^2 \operatorname{Re}[Z_1^{-3/2} - Z_2^{-3/2}]$$

$$\sigma_{rz} = K_2(-2\gamma)\left(\gamma^2 - \frac{1}{3}\right)^{1/2} \operatorname{Im}\left[Z_1^{-3/2} - Z_2^{-3/2}\right] \quad (4)$$

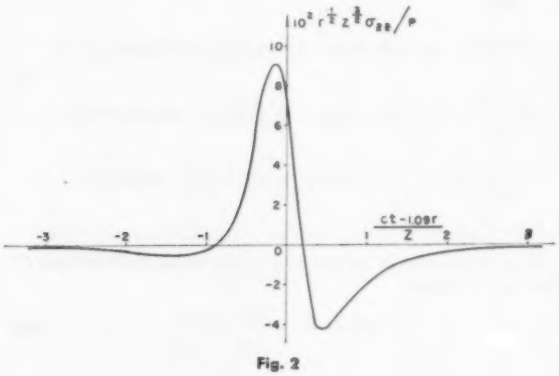

Fig. 2

$$\sigma_{\theta\theta} = K_2\left(\frac{1 - 2\gamma^2}{3}\right) \operatorname{Re}\left[Z_1^{-3/2}\right]$$

$$\sigma_{rr} = K_2(1 - 2\gamma^2) \operatorname{Re}\left[\left(2\gamma^2 + \frac{1}{3}\right) Z_1^{-3/2} + (1 - 2\gamma^2)Z_2^{-3/2}\right]$$

where

$$K_2 = \frac{3P}{16\sqrt{6\gamma}\,\pi r^{1/2}z^{3/2}} \quad (4a)$$

The numerical evaluation of Equations (3) and (4) is simple. Not only are the expressions in closed form, but each of the responses, for a given medium, is solely a function of a single parameter, the nondimensional time τ. Fig. 2 shows as example the vertical stress σ_{zz} $\left(\text{note } \frac{\tau - \gamma}{l} = \frac{ct - \gamma r}{z}\right)$.

References

1 C. L. Pekeris, "The Seismic Surface Pulse," Proceedings of National Academy of Science, vol. 41.7, 1955, pp. 469–480.

2 C. L. Pekeris and Hanna Lifson, "Motion of the Surface of a Uniform Elastic Half-Space Produced by a Buried Pulse," *Journal of the Acoustical Society of America*, vol. 29, November, 1957, pp. 1233–1238.

3 A. Sommerfeld, "Uber die Ausbreitung der Wellen in der drahtlosen Telegraphie," *Annalen der Physik*, 4 Folge, vol. 28, 1909, pp. 667–736.

Extension of Nadai's Sand Hill Analogy to Multiply Connected Cross Sections

M. E. GURTIN[1]

THE SAND HILL analogy due to Nadai [1][2] for the fully plastic torsion of cylindrical or prismatic bodies was extended to the case of multiply connected cross sections by Sadowsky [2]. It is the purpose of this note to present an alternative extension of the foregoing analogy to multiply connected regions which from an experimental point of view may offer certain advantages over the procedure given in [2].[3]

To discuss the fully plastic torsion of a cylindrical or prismatic bar, let the z-axis of the rectangular Cartesian co-ordinates (x, y, z) be parallel to the generators of the cylindrical or prismatic surface of the bar, and let the cross section Γ of the bar in the plane $z = 0$ be bounded by the simple closed curves C_i $(i = 0, 1, 2, \ldots n)$. The equation of equilibrium can then be fulfilled by relating the components τ_{zx} and τ_{zy} of the shearing stress in the x,y-plane to the components of the gradient of a *stress function* $\psi(x, y)$ as follows:

$$\tau_{zx} = \partial\psi/\partial y, \quad \tau_{zy} = -\partial\psi/\partial x.$$

According to the yield condition $\tau_{zx}^2 + \tau_{zy}^2 = k^2 = \text{const}$, the stress surface $z = \psi(x, y)$ is a surface of the constant maximum slope k. For a simply connected cross section, Nadai [1] remarked that this stress surface can be modeled by heaping sand on a horizontal tray that has the shape of the considered cross section.

Sadowsky [2] suggested the following extension of this analogy to multiply connected cross sections. Again a horizontal tray is used that has the shape of the cross section. Through each hole in this tray passes a closely fitting thin-walled cylindrical tube with a vertical axis. Initially, the horizontal brims of these tubes are sufficiently far above the tray so that a sand heap formed on the tray does nowhere reach the elevation of a rim. The tubes are then pushed downward through the hole of the tray and sand is allowed to pour through them until the brim of each tube is completely surrounded by sand. At this stage, the sand hill models the stress surface for the fully plastic torsion of the considered cross section.

Another modification of Nadai's sand hill analogy will now be described. For brevity, only a doubly connected cross section will be considered, but the method is readily extended to cross sections of higher connectivity.

Let the exterior and interior boundaries of the doubly connected cross section be denoted by C_0 and C_1, respectively, Fig. 1. Using Nadai's sand hill analogy, determine first the stress surface for the simply connected cross section bounded by C_0. Then level this sand hill to the height of the contour line C^* that encloses C_1

[1] National Defense Fellow, Division of Applied Mathematics, Brown University, Providence, R. I.

[2] Numbers in brackets indicate References at end of Note.

[3] For an extensive discussion of this procedure together with several interesting photographs of stress surfaces modeled by means of this sand hill analogy, see Nadai [3].

Manuscript received by ASME Applied Mechanics Division, June 6, 1960.

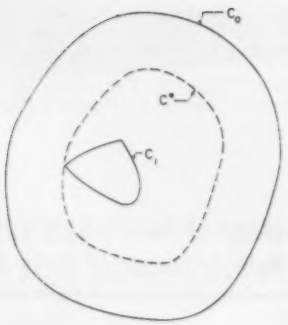

Fig. 1

and has at least one point in common with C_1. Finally, heap sand on a second horizontal tray that has the boundaries C^* and C_1. A model of the stress surface for the fully plastic torsion of the doubly connected cross section is obtained by putting this second sand hill on top of the leveled first sand hill. In particular, the limiting value of the torque equals product of the combined volume of the two sand hills with twice the ratio of the yield stress k to the slope of the sand hills.

Acknowledgment

The author wishes to thank Professor W. Prager for his criticisms and suggestions.

References

1 A. Nadai, "Der Beginn des Fliessvorgangs in einem tordierten Stab," *Z. angew. Math. Mech.*, vol. 3, 1923, pp. 442–454.

2 M. A. Sadowsky, "An Extension of the Sand Heap Analogy in Plastic Torsion Applicable to Cross Sections Having One or More Holes," JOURNAL OF APPLIED MECHANICS, vol. 8, TRANS. ASME, vol. 63, 1941, p. A-166.

3 A. Nadai, "Theory of Flow and Fracture of Solids," McGraw-Hill Book Company, Inc., New York, N. Y., 1950, p. 505.

Three-Dimensional Flow About Yawed Cylinders

D. BENENSON[1]

In reference [1],[2] Sears treats the case of incompressible, laminar flow about a yawed infinite (symmetrical) cylinder wherein the external spanwise velocity is considered to be a constant. Consider now the case in which the external spanwise flow is represented by a power series in x (compare reference [2]); then (refer to Fig. 1 for notation)

$$U_0 = u_1 x + u_3 x^3 + u_5 x^5 \ldots \tag{1a}$$

$$V_0 = v_0 + v_1 x + v_2 x^2 \ldots \tag{1b}$$

As is well known ([1], for example), for the case considered, chordwise and normal velocities within the boundary layer are not dependent upon the spanwise velocity. Therefore the solutions for the chordwise and normal velocities can be obtained from the corresponding problem in two-dimensional flow; in the manner shown in [3], these velocities are expressed as

$$u = u_1 x f_1' + 4u_3 x^3 f_3' + 6x^5 \left[u_5 g_5' + \frac{u_3^2}{u_1} h_5' \right] + \ldots \tag{2a}$$

$$w = -\sqrt{\frac{\nu}{u_1}} \left[u_1 f_1 + 12 u_3 x^2 f_3 + 30 x^4 \left(u_5 g_5 + \frac{u_3^2}{u_1} h_5 \right) \ldots \right] \tag{2b}$$

where $f_1, f_3, \ldots$ are functions of η only, and $\eta = z\sqrt{\frac{u_1}{\nu}}$. Use of the parameter η indicates the analysis to be applicable to the case in which the leading edge shape is round-nosed rather than wedge-shaped. The differential equations and their solutions are shown in [3].

To determine the spanwise velocity, consider the boundary-layer equation in the spanwise direction

$$uw_x + ww_z = U_0 V_{0x} + \nu w_{zz} \tag{3}$$

Let the spanwise velocity be represented as

$$v_0 = v_0 P_0 + v_1 x P_1 + v_2 x^2 P_2 + \ldots \tag{4}$$

where $P_0, P_1 \ldots$ are functions of η only.

Substitution of equations (2) and (4) into equation (3) and arrangement of the resulting equations in terms of powers of x yield the differential equations for the P_n:

$$\begin{aligned} &P_n'' + f_1 P_n' - n f_1' P_n = -n \\ &+ \frac{u_3 v_{n-2}}{u_1 v_n} [-(n-2) + 4(n-2) f_3' P_{n-2} - 12 f_3 P_{n-2}'] \\ &+ \frac{u_5 v_{n-4}}{u_1 v_n} [-(n-4) + 6(n-4) f_5' P_{n-4} - 30 f_5 P_{n-4}'] \\ &+ \frac{u_7 v_{n-6}}{u_1 v_n} [-(n-6) + 8(n-6) f_7' P_{n-6} - 56 f_7 P_{n-6}'] \\ &+ \frac{u_9 v_{n-8}}{u_1 v_n} [-(n-8) + 10(n-8) f_7' P_{n-8} - 90 f_9 P_{n-8}'] \\ &+ \ldots \end{aligned} \tag{5}$$

As in the manner of [3], in order to determine the functions P_n once and for all, let

$$P_2 = H_2 + \frac{u_3 v_0}{u_1 v_2} K_2 \tag{6a}$$

$$P_3 = H_3 + \frac{u_3 v_1}{u_1 v_3} K_3 \tag{6b}$$

$$P_4 = H_4 + \frac{u_3 v_2}{u_1 v_4} K_4 + \frac{u_5 v_0}{u_1 v_4} L_4 + \frac{u_3^2 v_0}{u_1^2 v_4} M_4 \tag{6c}$$

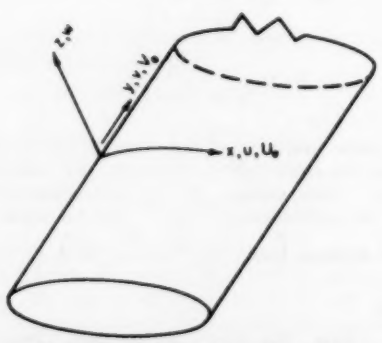

Fig. 1 Co-ordinate system and notation

[1] Research Engineer, Westinghouse Research Laboratories, Pittsburgh, Pa.

[2] Numbers in brackets indicate References at end of Note.

Manuscript received by ASME Applied Mechanics Division, October 6, 1960.

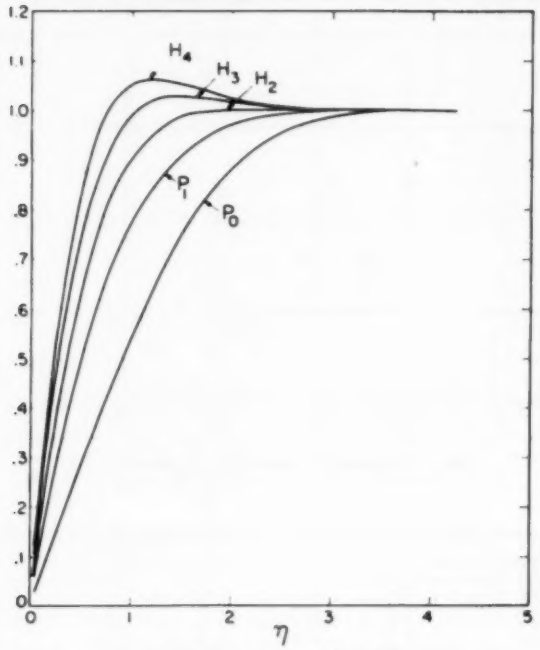

Fig. 2 Spanwise velocity functions

The expression for the spanwise flow, equation (4), becomes then

$$v = v_0P_0 + v_1P_1x + \left[v_2H_2 + \frac{u_3}{u_1}v_0K_2\right]x^2 + \left[v_2H_3 + \frac{u_3}{u_1}v_1K_3\right]x^3 + \left[v_4H_4 + \frac{u_3}{u_1}v_3K_4 + \left(\frac{u_3}{u_1}\right)^2 v_0M_4 + \frac{u_5}{u_1}v_0L_4\right]x^4 \ldots \quad (7)$$

Substitution of equations (6) into equations (5) yields the set of equations

$$P_0'' + f_1P_0' = 0 \quad (8a)$$

$$P_1'' + f_1P_1' - f_1'P_1' = -1 \quad (8b)$$

$$H_2'' + f_1H_2' - 2f_1'H_2 = -2 \quad (8c)$$

$$K_2'' + f_1K_2' + 2f_1'K_2 = -12f_2P_0' \quad (8d)$$

$$H_3'' + f_1H_3' - 3f_1'H_3 = -3 \quad (8e)$$

$$K_3'' + f_1K_3' - 3f_1'K_3 = -1 + 4f_2'P_1 - 12f_2P_1' \quad (8f)$$

$$H_4'' + f_1H_4' - 4f_1'H_4 = -4 \quad (8g)$$

$$K_4'' + f_1K_4' - 4f_1'K_4 = -2 + 8f_2'H_2 - 12f_2H_2' \quad (8h)$$

$$L_4'' + f_1L_4' - 4f_1'L_4 = -30g_3P_0' \quad (8i)$$

$$M_4'' + f_1M_4' - 4f_1'M_4 = 8f_2'K_2 - 12f_2K_2' - 30h_3P_0' \quad (8j)$$

etc.

with boundary conditions

$$f_1(0) = f_1'(0) = f_2(0) = f_2'(0) = g_3(0) = g_3'(0) = h_3(0) = h_3'(0) = 0$$

$$f_1'(\infty) = 1;\ f_2'(\infty) = \frac{1}{4};\ g_3'(\infty) = \frac{1}{6};\ h_3'(\infty) = 0$$

$$P_n(0) = H_n(0) = K_n(0) = L_n(0) = M_n(0) = 0$$

$$P_n(\infty) = H_n(\infty) = 1;\ K_n(\infty) = L_n(\infty) = M_n(\infty) \quad 0$$

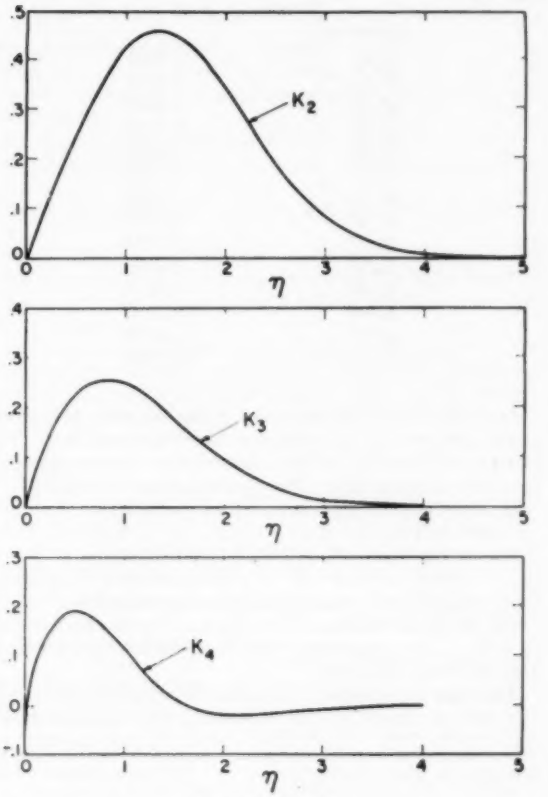

Fig. 2 (continued)

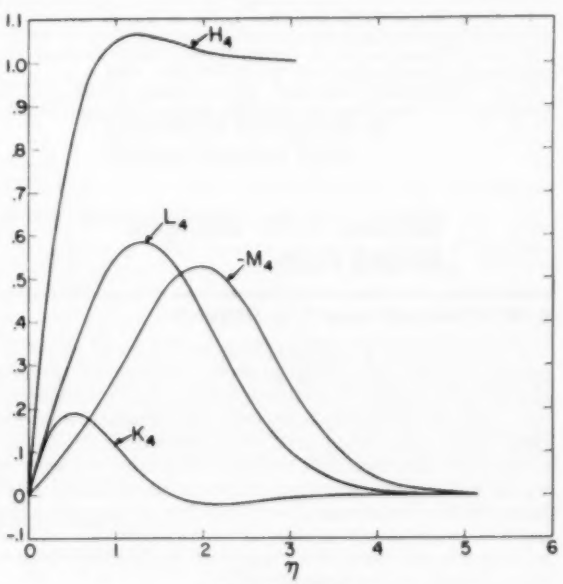

Fig. 2 (concluded)

Solutions of equations (8), obtained by numerical methods, are shown in Fig. 2.

When $v_0 \neq 0$, $v_1 = v_2 \ldots = 0$, equation (7) becomes essentially that treated in [1].

Table 1

Function	
$f_1''(0)$	1.2326
$f_3''(0)$	0.7244
$g_0''(0)$	0.6348
$h_0''(0)$	0.1192
$P_0'(0)$	0.5653
$P_1'(0)$	1.2042
$H_2'(0)$	1.6952
$K_2'(0)$	0.5100
$H_3'(0)$	2.1138
$K_3'(0)$	0.6696
$H_4'(0)$	2.4875
$K_4'(0)$	0.7799
$L_4'(0)$	0.6730
$M_4'(0)$	−0.2278

As is well known, the separation of the chordwise flow occurs at the same location as is found in two-dimensional flow. The location for separation of the spanwise flow depends upon the form of the external flow. The required values of the derivatives of the chordwise and spanwise velocities, evaluated at the surface, are shown in Table I.

For the case treated in [1], wherein, essentially, $u_3/u_1 = -1$, $u_5 \ldots = 0$ and $v_0 \neq 0$, $v_1 = v_2 \ldots = 0$, separation of the spanwise flow would not occur prior to that of the chordwise flow.

For the case in which $u_3/u_1 = -1$, $u_4 \ldots = 0$ and $v_1/v_0 = -1$, $v_2 = v_3 \ldots = 0$, separation of the spanwise flow occurs prior to that of the chordwise flow.

The shape of the limiting streamline, determined from the relation $dy/dx = \lim_{z \to 0} v/u = \lim_{y \to 0} v'(0)/u'(0)$ (for example, reference [1]), can be obtained for particular external flows from the information presented in Table 1.

References

1 W. R. Sears, "The Boundary Layer of Yawed Cylinders," *Journal of the Aeronautical Sciences*, vol. 15, January, 1948, pp. 49–52.

2 A. G. Hansen and H. Z. Herzig, "Cross Flows in Laminar, Incompressible Boundary Layers," NACA TN 3651, 1956.

3 H. Schlichting, "Boundary Layer Theory," McGraw-Hill Book Co., Inc., New York, N. Y., fourth edition, 1960, pp. 146–155.

Vibrations of Thin Rectangular Isotropic Plates

R. W. CLAASSEN[1] and C. J. THORNE[2]

WE PRESENT here four graphs giving the first ten vibration frequencies of a clamped rectangular plate as a function of the ratio of sides and one graph of nodal lines to illustrate the "transition" from one mode of vibration to another. This transition is characteristic of the behavior at certain points, where the individual frequency curve has an abrupt change in slope, and two separate curves, with the same symmetry properties, almost touch. Similar results for a rectangular plate clamped on two opposite edges and free on the other two edges as well as tables, discussion of convergence, and complete mathematical details in both boundary-value problems are available [1].[3]

[1] Mathematician, Pacific Missile Range, Point Mugu, Calif.

[2] Supervisory Mathematician, Pacific Missile Range, Point Mugu, Calif.

[3] Numbers in brackets indicate References at end of Note.

Manuscript received by ASME Applied Mechanics Division, May 12, 1960.

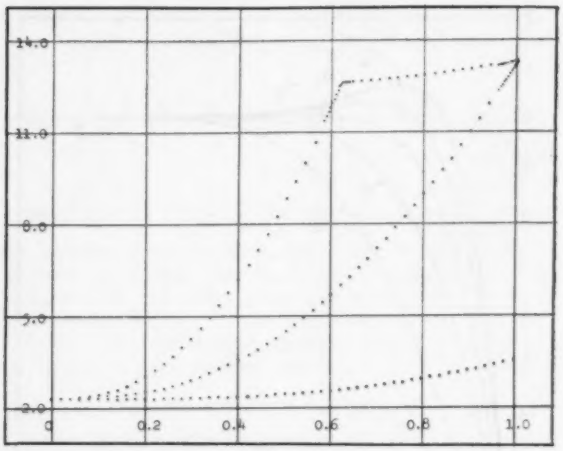

Fig. 1 Frequency K, symmetric in x, symmetric in y

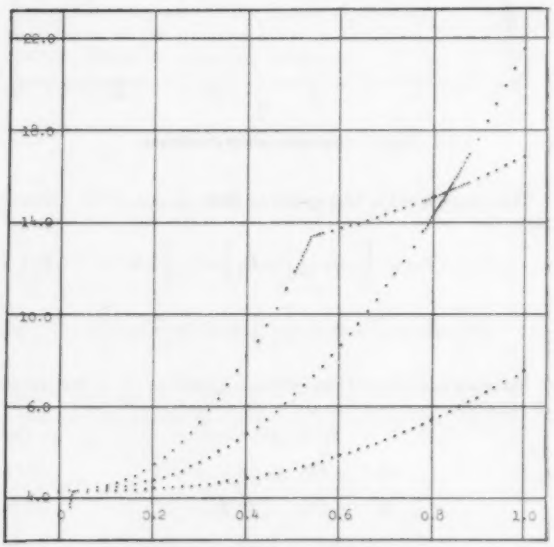

Fig. 2 Frequency K, symmetric in x, antisymmetric in y

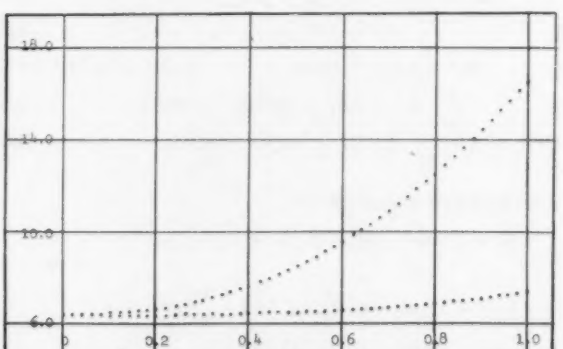

Fig. 3 Frequency K, antisymmetric in x, symmetric in y

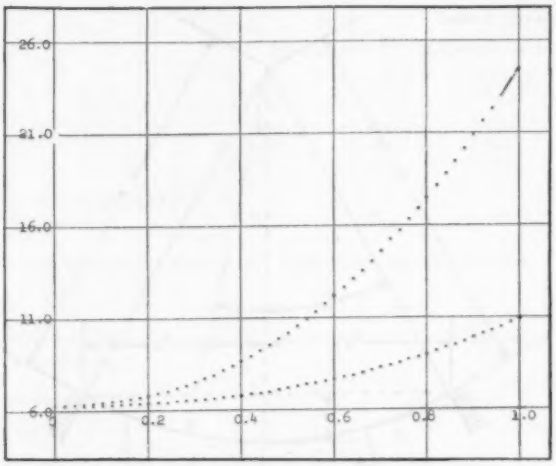

Fig. 4 Frequency K, antisymmetric in x, antisymmetric in y

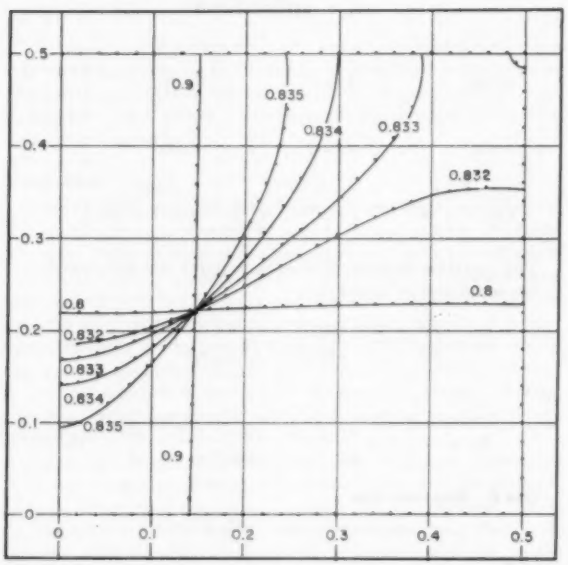

Fig. 5 Nodal patterns for various b/a ratios, symmetric in x, antisymmetric in y

The theory used is the Fourier series method suggested by Green [2] and illustrated in several problems among which was the vibration frequencies for a square plate. Fletcher and Thorne [3] used the same method in several static deflection problems in thin plates.

The differential equation to be solved is [4]

$$Eh^3[w_{XXXX} + 2w_{XXYY} + w_{YYYY}] = -3\rho(1 - \nu^2)w_{tt}; \quad 0 < X < a, 0 < Y < b, \quad t > 0, \quad (1)$$

and appropriate boundary conditions.

Here $$w_{XXXX} = \frac{\partial^4 w}{\partial X^4}$$

Assuming $w(X, Y) = W(x, y) \sin(2\pi ft + \phi)$, where $x = \pi X/a$, $y = \pi Y/b$,

$$W_{xxxx} + 2k^2W_{xxyy} + k^4W_{yyyy} = K^4W,$$

where $k = a/b$ and $Eh^3\pi^4K^4 = 12a^4\rho(1 - \nu^2)f^2$.

Figs. 1 to 4 show the first three and two K's as a function of k for mode shapes symmetric and antisymmetric about $x = \pi/2$ and $y = \pi/2$ as follows:

Fig. 1—symmetric about $x = \pi/2$ and $y = \pi/2$.

Fig. 2—symmetric about $x = \pi/2$, antisymmetric about $y = \pi/2$.

Fig. 3—antisymmetric about $x = \pi/2$, symmetric about $y = \pi/2$.

Fig. 4—antisymmetric about $x = \pi/2$ and $y = \pi/2$.

Fig. 5 is a graph of the nodal pattern for $\pi/2 < x < \pi$ and $\pi/2 < y < \pi$, the second frequency of Fig. 2 and values of k near the "transition" point.

The results obtained here and in [1] agree to the accuracy that could be expected with all previous results we have checked [5, 6, 7]. Warburton's equation (16) does not allow for the "transition" points observed here.

References

1 R. W. Claassen and C. J. Thorne, "Transverse Vibrations of Thin Rectangular Isotropic Plates," NOTS 16, August, 1960, China Lake, Calif. NAVWEPS Report 7016, NOTS TP 2379, Unclassified.

2 A. E. Green, "Double Fourier Series and Boundary Value Problems," Proceedings of the Cambridge Philosophical Society, 1944.

3 H. J. Fletcher and C. J. Thorne, "Bending of Thin Rectangular Plates," Proceedings of the Second U. S. National Congress of Applied Mechanics, ASME, 1954, pp. 389–406.

4 A. E. H. Love, "The Mathematical Theory of Elasticity," Cambridge University Press, 1934, pp. 455–496.

5 G. B. Warburton, "The Vibration of Rectangular Plates," Proceedings of The Institution of Mechanical Engineers, 1954.

6 Dana Young, "Vibration of Rectangular Plates, by the Ritz Method," JOURNAL OF APPLIED MECHANICS, vol. 17, TRANS. ASME, vol. 72, 1950, pp. 448–453.

7 Susume Tomotika, "On the Transverse Vibration of a Square Plate With Four Clamped Edges," Guggenheim Aeronautical Laboratory, CalTech, Report 129, 1935.

Frequencies of Vibration of Shallow Spherical Shells

W. H. HOPPMANN II[1]

IN A paper in 1946,[2] Reissner presented a study of the symmetric vibrations of a shallow elastic spherical shell. Using a variational method, he determined a formula for approximating the lowest characteristic frequency. As happens for such approximations, however, the estimations of frequency can be in error as much as 18 per cent as shown in the present Note.

Because of the importance of Reissner's work for the design of shells to withstand dynamic loads, the purpose of the present Note is to provide direct solutions of the determinantal frequency equation for two boundary conditions, clamped and simply supported edge.

Nomenclature

a = radius of sphere

r_0 = half the base chord

[1] Professor of Mechanics, The Rensselaer Polytechnic Institute, Troy, N. Y. Mem. ASME.

[2] Eric Reissner, "On Vibrations of Shallow Spherical Shells," *Journal of Applied Physics*, vol. 17, 1946, pp. 1038–1042.

Manuscript received by ASME Applied Mechanics Division, September 30, 1960.

h = thickness of sphere
s = rise of arc (sagitta)
ϕ_0 = half angle subtended by arc
E = Young's modulus
ν = Poisson's ratio

$$N' = \frac{Eh}{1-\nu^2}$$

M_ϕ = bending moment = M_r in the limit
p_n = circular frequency
w = radial displacement (positive inward toward center)
v = tangential displacement (tangent to meridian of sphere)
r = radial distance from point on sphere to axis of symmetry

$$\alpha^2 = \frac{\rho h p_n^2}{N'}$$

$$K^4 = \frac{\rho h p_n^2}{D}$$

$$m_1^2 = \frac{1+\nu}{a} = \frac{2(1+\nu)s}{a}$$

$$m_2^2 = \frac{(1+\nu)N'}{Da}$$

$$\beta^4 = K^4 - \frac{2(1+\nu)N'}{a^2 D} = K^4 - \frac{2}{a}m_2^2$$

$J_0(x)$ = Bessel function of order zero
$J_1(x)$ = Bessel function of order one

A sketch of the shell is shown in Fig. 1.

Analysis

The equations of motion used for the analysis in this Note were based on the theory of shells given by S. Timoshenko.[3] The equations were reduced in complexity to apply to the case under consideration by assuming that the angle $\phi_0 \to 0$ so that $\sin\phi_0 \to 0$ and $\cos\phi_0 \to 1$. Angle ϕ_0 defines the boundary of the shell. The resulting equations agree exactly with those developed by Reissner.[2]

Solutions of these equations turn out to be as follows:

$$v = -m_1^2\left\{\frac{B_1 J_1(\mu_1 r)}{\alpha^2-\mu_1^2} + \frac{B_2 J_1(\mu_2 r)}{\alpha^2-\mu_2^2} + \frac{B_3 J_1(\mu_3 r)}{\alpha^2-\mu_3^2}\right\}$$

and

$$w = -\left\{\frac{B_1}{\mu_1}J_0(\mu_1 r) + \frac{B_2}{\mu_2}J_0(\mu_2 r) + \frac{B_3}{\mu_3}J_0(\mu_3 r)\right\}$$

$$x_i = (\mu_i r_0)^2$$

are, for a given frequency p_n, the roots of the following cubic equation:

$$\left[\frac{(1-\nu^2)\rho r_0^2}{E}p_n^2 - x\right]\left[x^2 - 12(1-\nu^2)\rho\frac{p_n^2 r_0^4}{Eh^2} + 96\frac{s^2}{h^2}(1+\nu)\right] + 48(1+\nu)^2\frac{s^2}{h^2}x = 0$$

Also the x_i must be such as to satisfy the determinantal equation given by the assumed boundary conditions.

Boundary Conditions

Case A. Clamped Edge

$$w_n(r_0) = w_n'(r_0) = v_n(r_0) = 0$$

and so

$$\begin{vmatrix} \frac{J_0(x_1)}{x_1} & , & \frac{J_0(x_2)}{x_2} & , & \frac{J_0(x_3)}{x_3} \\ J_1(x_1) & , & J_1(x_2) & , & J_1(x_3) \\ \frac{J_1(x_1)}{(\alpha r_0)^2 - x_1^2}, & & \frac{J_1(x_2)}{(\alpha r_0)^2 - x_2^2}, & & \frac{J_1(x_3)}{(\alpha r_0)^2 - x_3^2} \end{vmatrix} = 0$$

This equation is given in Reissner's paper but not solved. It should also be noted that

$$B_2 = \frac{x_3^2 - x_1^2}{x_2^2 - x_3^2}\cdot\frac{(\alpha r_0)^2 - x_2^2}{(\alpha r_0)^2 - x_1^2}\frac{J_1(x_1)}{J_1(x_3)}B_1$$

and

$$B_3 = -\left[1 + \frac{x_3^2 - x_1^2}{x_2^2 - x_3^2}\cdot\frac{(\alpha r_0)^2 - x_2^2}{(\alpha r_0)^2 - x_1^2}\right]\frac{J_1(x_1)}{J_1(x_3)}B_1$$

Case B. Momentless Edge

$$w_n(r_0) = v_n(r_0) = M_\phi(r_0) = 0$$

and so

$$\begin{vmatrix} \frac{J_0(x_1)}{x_1} & , & \frac{J_0(x_2)}{x_2} & , & \frac{J_0(x_3)}{x_3} \\ J_1(x_1)(1-\nu) - x_1 J_0(x_1), & & J_1(x_2)(1-\nu) - x_2 J_0(x_2), & & J_1(x_3)(1-\nu) - x_3 J_0(x_3) \\ \frac{J_1(x_1)}{(\alpha r_0)^2 - x_1^2} & , & \frac{J_1(x_2)}{(\alpha r_0)^2 - x_2^2} & , & \frac{J_1(x_3)}{(\alpha r_0)^2 - x_3^2} \end{vmatrix} = 0$$

also

$$B_3 = -\frac{\frac{(\alpha r_0)^2 - x_1^2}{(\alpha r_0)^2 - x_2^2}\cdot\frac{J_1(x_2)}{J_1(x_1)} - \frac{x_1 J_0(x_2)}{x_2 J_0(x_1)}}{\frac{(\alpha r_0)^2 - x_1^2}{(\alpha r_0)^2 - x_3^2}\cdot\frac{J_1(x_3)}{J_1(x_1)} - \frac{x_1 J_0(x_3)}{x_3 J_0(x_1)}}B_2 = \lambda B_2$$

and

$$B_1 = \left[\frac{-x_3 J_0(x_2)}{x_2 J_0(x_1)} + \lambda\frac{x_1 J_0(x_3)}{x_3 J_0(x_1)}\right]B_2$$

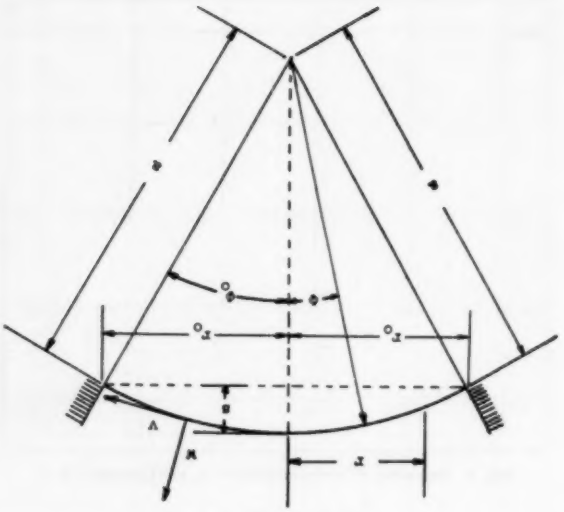

Fig. 1 Section of shell

[3] S. Timoshenko and S. Woinowsky-Krieger, "Theory of Plates and Shells," McGraw-Hill Book Co., Inc., New York, N. Y., 2nd edition, 1959, pp. 434–446.

Table 1 Frequencies of vibration

	Frequencies for clamped edge in rps				Frequencies for momentless edge in rps			
n^a	$\frac{s}{r_0} = 0$	$\frac{s}{r_0} = \frac{0.5}{6}$	$\frac{s}{r_0} = \frac{1.0}{6}$	$\frac{s}{r_0} = \frac{1.6}{6}$	$\frac{s}{r_0} = 0$	$\frac{s}{r_0} = \frac{0.5}{6}$	$\frac{s}{r_0} = \frac{1.0}{6}$	$\frac{s}{r_0} = \frac{1.6}{6}$
1	4,400	9,000	16,000	22,000	2,100	9,000	16,000	21,000
2	17,160	19,000	22,000	29,000	12,760	15,000	20,000	29,000
3	38,390	39,000	40,000	43,000	31,850	32,000	34,000	38,000
...	...	...	...	...	...	...	...	...
Reissner fundamental frequency	4,400	9,340	16,900	26,000				

[a] n is the number of mode of symmetrical bending vibration. The fundamental mode is given by $n = 1$.

The functions $J_0(x)$ and $J_1(x)$ were evaluated with the aid of standard tables.[4]

Parameters

$$\nu = \frac{1}{3}, \frac{h}{a} = \frac{0.25}{15} = \frac{1}{60}$$

$$\frac{E}{\rho} = \frac{30 \times 10^6}{0.2836} \text{(in lb units)}$$

The case $s = 0$ is for the flat plate and the frequencies were calculated from the usual plate theory which results from taking the differential equation of motion as $s = 0$ and the boundary conditions are $w = 0$ and $w' = 0$ for clamped edge; $w = 0$, $M_r = 0$ for momentless edge.

Discussion

It may be seen that the frequencies of vibration were computed for a particular value of ν and ratio E/ρ. Consequently, the table of values (Table 1) is approximately applicable only for materials such as steel and aluminum. While the table may therefore have some practical value, its main purpose is to show how the frequencies vary with s/r_0 and how the correctly computed fundamental frequency compares with that given by Reissner's formula based on the approximations he used with the variational method. It was also desirable to get an idea of the actual amount of computational labor involved in completely working out a problem of this type.

The results of the calculations given in the paper show that Reissner's fundamental frequency formula can be in error as much as 18 per cent, with the error increasing as s/r_0 increases. Also, the results are not limited to the fundamental frequency. In addition, the normal shapes for the various modes were calculated as means of identifying the various frequencies. See Table 2. The procedure was particularly pertinent for the fundamental mode because the first calculation seemed to indicate an eigen frequency much lower than that shown in Table 1. This apparent fundamental frequency was finally ruled out upon computing its corresponding shape which showed clearly that the boundary conditions were then not satisfied.

Finally, it may be emphasized that the modal shapes and frequencies can be readily computed with aid of the tables of $J_0(z)$ and $J_1(z)$ referred to previously[4] and with electric desk calculating machines.

It is finally concluded that the solutions for the flexural vibrations of shallow spherical shells derived by Reissner are satisfactory and can be used practically in the case of any given structural problem of the assumed type. On the other hand, his approximate formula for fundamental frequency does not appear to be at all satisfactory.

[4] "Table of Bessel Functions $J_0(z)$ and $J_1(z)$ for Complex Argument," Columbia University Press, 1947.

Table 2 Number of nodes between center and edge

	Clamped			Simply supported		
n	$s = 0.5$	$s = 1.0$	$s = 1.6$	$s = 0.5$	$s = 1.0$	$s = 1.6$
1	0	0	0	0	0	0
2	1	1	1	1	1	1
3	2	2	2	2	2	2

Acknowledgments

The author wishes to thank Mr. David E. Broadhead and Miss Dolores B. Peck, participants in the National Science Foundation Program for High School Teachers at Rensselaer Polytechnic Institute, for their extensive calculations in connection with the problem of this note.

A Formula for the Torsional Stiffness of Rectangular Sandwich Plates

SHUN CHENG[1]

THIS paper contains a derivation of a formula for the torsional stiffness of rectangular sandwich plates under the following assumptions. The plate consists of two thin facings and a thick core of such construction that the stresses in the core parallel to facings and the variation of the face stresses over the thickness of the facings are negligible. The facings are isotropic and of equal thickness while the core may be orthotropic. The torsional stiffness of rectangular sandwich plates has been derived by various authors [1, 2].[2] In spite of these solutions, the development of the present formula is justified in the sense that it is simple enough to permit its use in design. At the same time the results of computations based on the present formula agree closely with results based on the infinite series solution given in [1]. This formula is obtained through the use of a variational principle and the Saint Venant semi-inverse method.

Introduction

The present paper is concerned with the torsion of rectangular sandwich plate as considered previously by P. Seide [2], H. G. McComb [3], the present author [1], and others. The type of sandwich plate investigated consists of two thin external members called facings, bonded to a relatively thick internal member called the core. The core material is assumed to be much more flexible than the face material. Whereas previous solutions [1, 2] were in the form of infinite series for which computations are tedious, the solution obtained here is a rather simple expression. The methods employed in [1] and [2] for obtaining the infinite

[1] Department of Mechanics, University of Wisconsin, Madison, Wis.

[2] Numbers in brackets indicate References at end of Note.

Manuscript received by ASME Applied Mechanics Division, October 20, 1960.

series solutions are essentially the same except that the simplifying assumption of negligible core shear stress in the plane of the plate is used in [1] but not in [2]. The method used in the present paper is based on the variational theorem of complementary energy in conjunction with Lagrangian multipliers. This method of approach has been developed by E. Reissner [4, 5], C. T. Wang [6, 7], I. S. Sokolnikoff [8], and others. In some elasticity problems this approach has been found to be convenient. For example, Reissner used this method for the derivation of the stress displacement relationshiips of plates [9, 5] and shells [10].

Nomenclature

G, E = shear modulus and Young's modulus of facings
t = thickness of facings
h = half thickness of core
b = width of sandwich
G_{xz}, G_{yz} = shear modulii of core
x, y, z = rectangular co-ordinates, Fig. 1
τ = shear stress in facings, Fig. 2
τ_x = shear stress in core, Fig. 2
λ, v_1, v_2, v_3 = Lagrangian multipliers

$$r^2 = \frac{4G_{xz}\left(\frac{b}{h}\right)^2}{G\left(\frac{t}{h}\right)\left(2+\frac{t}{h}\right)^2}$$

A, B, C = constants
T = torque
θ = angle of twist
l = length of sandwich

Analysis

We consider a rectangular sandwich plate consisting of a core of thickness $2h$ and two facings of thickness t each as shown in Fig. 1. The external torque T is applied in the yz-plane. The assumptions made are as follows:

1 The external torque T is applied by shear stresses applied at the ends of the plate. These stresses are distributed in the proper way to avoid variations in stresses with the longitudinal co-ordinate. This assumption characterizes the Saint Venant theory of torsion.

2 The facings are treated as isotropic solid membranes. On the basis of this assumption, the shearing stresses in facings normal to their planes may be neglected and the stresses in facings parallel to their planes may be assumed to be distributed uniformly over the thickness of the facings.

3 The shear modulus G_{xy} of the core has been assumed to be small in comparison to the shear modulus G_{xz} and hence is set equal to zero.

The second and third assumptions somewhat limit the general applicability of the present formula. However, it should give an adequate result for combinations such as honeycomb core and metal facings.

The transverse shears are predominantly taken by the core. Hence these shearing stresses should be taken into account in the analysis of sandwich plates. Guided by the Saint Venant semi-inverse method, we assume all stresses equal to zero except τ and τ_x which are assumed to be functions of y only (Fig. 2). All equations of equilibrium are satisfied identically except

$$\frac{d\tau}{dy} = \frac{2h\tau_x}{t(2h+t)} \tag{1}$$

Since we are using the Saint Venant semi-inverse method, we do not attempt to satisfy boundary conditions at $x = 0$ and $x = l$, but, instead, specify that the stresses satisfy the following conditions:

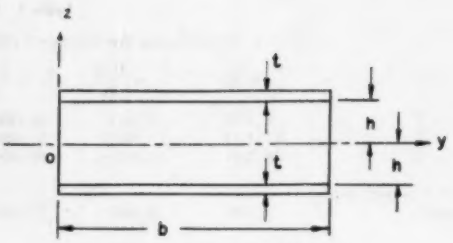

Fig. 1 Cross section of plate

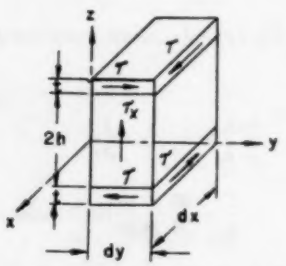

Fig. 2 Differential element $dydx$

1 The summation of forces in the vertical direction is equal to zero

$$\int_0^b 2h\tau_x dy = 0 \tag{2}$$

2 The resultant torque due to stresses is equal to the applied torque T

$$T = \int_0^b t(2h+t)\tau dy - \int_0^b 2h\tau_x y dy \tag{3}$$

Other boundary conditions are

$$\tau = 0, \quad y = 0, \quad \text{and } y = b. \tag{4}$$

To obtain further equations, use is made of the stress strain relation. This is done here through the use of a variational principle. We obtain additional equations as Euler equations which play the role of suitable stress strain relations and natural boundary conditions by requiring that strain energy of the system be a minimum with Equations (1, 2, 3, and 4) as admissibility conditions on the variation of τ and τ_x. Thus the expression to be varied with Lagrange multipliers λ, v_1, v_2, θ, and v_3 is of the form

$$I = \int_0^b \left\{ \frac{tl}{G}\tau^2 + \frac{lh}{G_{xz}}\tau_x^2 + \lambda\left[\frac{d\tau}{dy} - \frac{2h\tau_x}{t(2h+t)}\right]\right\} dy + v_1\tau(0) + v_2\tau(b) + \theta\left[T - t(2h+t)\int_0^b \tau dy + 2h\int_0^b \tau_x y dy\right] + 2hv_3\int_0^b \tau_x dy \tag{5}$$

where λ is a function of y, and v_1, v_2, θ, and v_3 are constants. It is seen that these four constants represent the generalized boundary displacements.

When the variation of I is equated to zero and integration by parts is carried out, the following equation is obtained:

$$\delta I = \int_0^b \left\{\left[\frac{2tl}{G}\tau - \frac{d\lambda}{dy} - t(2h+t)\theta\right]\delta\tau\right.$$

$$+ 2h\left[\frac{l}{G_{xz}}\tau_x - \frac{\lambda}{t(2h+t)} + \theta y + v_3\right]\delta\tau_x\Big\}\,dy$$
$$+ [v_1 - \lambda(0)]\delta\tau(0) + [v_2 + \lambda(b)]\delta\tau(b) = 0 \quad (6)$$

Since equation (6) must be satisfied identically for any arbitrary variation of the stress functions τ and τ_x, the variation equations which must be satisfied by τ, τ_x, λ, θ, v_1, v_2, and v_3 and which render the integral I a minimum take the following forms:

$$\frac{d\lambda}{dy} - \frac{2tl}{G}\tau + t(2h+t)\theta = 0 \quad (7)$$

$$\frac{l}{G_{xz}}\tau_x - \frac{\lambda}{t(2h+t)} + \theta y + v_3 = 0 \quad (8)$$

$$v_1 - \lambda(0) = 0,\ v_2 + \lambda(b) = 0 \quad (9)$$

Substituting τ_x from Equation (1) into Equation (8), then differentiating Equation (8) with respect to y and substituting $d\lambda/dy$ from (7) into (8), we obtain

$$\frac{d^2\tau}{dy^2} - \left(\frac{\tau}{b}\right)^2\tau = \frac{-4hG_{xz}\theta}{t(2h+t)l} \quad (10)$$

where

$$\tau^2 = \frac{4G_{xz}\left(\frac{b}{h}\right)^2}{G\left(\frac{t}{h}\right)\left(2+\frac{t}{h}\right)^2} \quad (11)$$

It can be verified by direct substitution that the general solution of Equation (10) is given by

$$\tau = A\sinh\frac{\tau}{b}y + B\cosh\frac{\tau}{b}y + C \quad (12)$$

where

$$C = G(2h+t)\frac{\theta}{l} \quad (13)$$

Substitution of boundary condtions (4) leads to the following equations for A and B in terms of C

$$A = \frac{(\cosh\tau - 1)}{\sinh\tau}C, \quad B = -C \quad (14)$$

thus

$$\tau = C\left[\frac{(\cosh\tau - 1)}{\sinh\tau}\sinh\frac{\tau}{b}y - \cosh\frac{\tau}{b}y + 1\right] \quad (15)$$

The shear stress τ_x is obtained by substituting (15) into (1)

$$\tau_x = \sqrt{\frac{tG_{xz}}{hG}}\left[\frac{(\cosh\tau - 1)}{\sinh\tau}\cosh\frac{\tau}{b}y - \sinh\frac{\tau}{b}y\right]C \quad (16)$$

Introducing Equations (15) and (16) into (3), then integrating, we obtain

$$C = \frac{T}{2t(2h+t)b\left[1 - \frac{2(\cosh\tau - 1)}{\tau\sinh\tau}\right]} \quad (17)$$

The torsional stiffness is obtained from Equations (17) and (13)

$$\frac{T}{\frac{\theta}{l}} = 2t(2h+t)^2Gb\left[1 - \frac{2(\cosh\tau - 1)}{\tau\sinh\tau}\right] \quad (18)$$

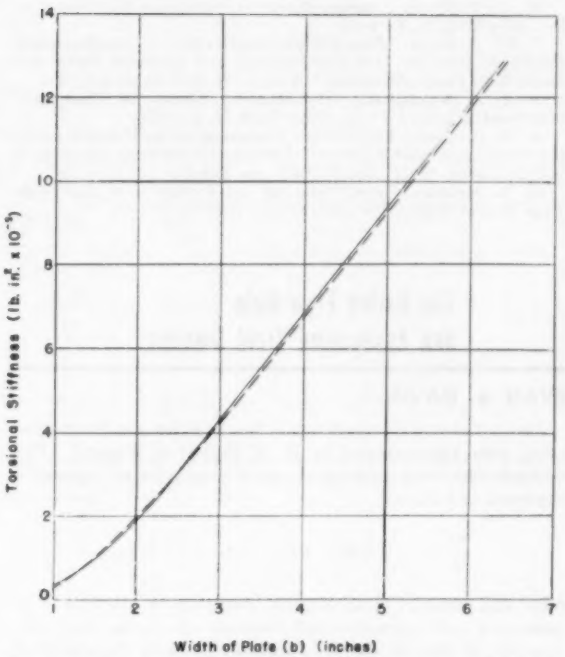

Fig. 3 Results of the two methods. Solid line represents solution of the present method. Dotted line represents the infinite series solution [1].

Numerical Computations and Conclusions

The results of computations based on Equation (18) and results based on the infinite series solution given in reference [1] are shown in Fig. 3. The computations were for sandwich plates of various widths and the following properties:

$$G_{xz} = 25{,}000 \text{ psi}$$
$$G = 4 \times 10^6 \text{ psi}$$
$$h = 0.25 \text{ in.}$$
$$t = 0.0125 \text{ in.}$$

The results show a maximum difference of 3 per cent in the torsional stiffness between the two methods. Their differences can be attributed to small errors or lack of using sufficient terms in the infinite series It may be concluded that the present result, which is in a form similar to R. Bredt's formula for thin tubular sections [1], is in excellent agreement with the infinite series solution [1].

Calculations made with the more accurate solution of reference [2] for this same sandwich plate, but with G_{xy} taken as 0, 2000 psi, and 20,000 psi, indicate that the effect of G_{xy} on the torsional rigidity is very small.

References

1 S. Cheng, "Torsion of Rectangular Sandwich Plates," Forest Products Laboratory, No. 1871, 1959.

2 P. Seide, "On the Torsion of Rectangular Sandwich Plates," Journal of Applied Mechanics, vol. 23, Trans. ASME, vol. 78, 1956, pp. 191–194.

3 H. G. McComb, Jr., "Torsional Stiffness of Thin Walled Shells Having Reinforcing Cores and Rectangular, Triangular, or Diamond Cross Sections," NACA TN 3749, 1956.

4 E. Reissner, "On a Variational Theorem in Elasticity," *Journal of Mathematics and Physics*, vol. 29, 1950, pp. 90–95.

5 E. Reissner, "On Bending of Elastic Plates," *Quarterly of Applied Mathematics*, vol. V, April, 1947, pp. 55–68.

6 C. T. Wang, "Applied Elasticity," McGraw-Hill Book Co., Inc., New York, N. Y., 1953.
7 C. T. Wang, "Principle and Application of Complementary Energy Method for Thin Homogeneous and Sandwich Plates and Shells With Finite Deflections," NACA TN 2620, February, 1952.
8 I. S. Sokolnikoff, "Mathematical Theory of Elasticity," McGraw-Hill Book Co., Inc., New York, N. Y., 1956.
9 E. Reissner, "The Effect of Transverse Shear Deformation on the Bending of Elastic Plates," JOURNAL OF APPLIED MECHANICS, vol. 12, TRANS ASME, vol. 67, 1945, pp. A69–77.
10 E. Reissner, "Small Bending and Stretching of Sandwich-Type Shells," NACA TN 1832, March, 1949.

The Bailey Flow Rule and Associated Yield Surface

EVAN A. DAVIS[1]

ABOUT twenty-five years ago a flow rule for combined stress creep tests was suggested by R. W. Bailey[2] of England. This flow rule which was a part of a general creep behavior rule can be expressed as follows:

$$\frac{d\epsilon_1^{\,p}}{dt} = \frac{1}{\phi}\left[(\sigma_1 - \sigma_2)^n - (\sigma_3 - \sigma_1)^n\right], \text{ etc.} \qquad (1)$$

Since this was part of an analysis of creep data, the topic of an associated yield surface was not discussed. It may be of interest, however, to look at the yield surface for which Equations (1) represent the associated flow rule. The mathematical expression for such a surface is

$$[(\sigma_1 - \sigma_2)^{n+1} + (\sigma_2 - \sigma_3)^{n+1} + (\sigma_3 - \sigma_1)^{n+1}] = 2\sigma_0^{n+1} \qquad (2)$$

where σ_0 is the yield point in pure tension.

For $n = 1$ or $n = 3$, Equation (2) represents a cylinder in principal stress space identical with the Mises yield surface. For values of n greater than 3 the Bailey yield surface lies inside the Mises cylinder as indicated in the customary two-dimensional plot shown in Fig. 1. For values of n between 1 and 3 the corresponding surface lies outside the cylinder. As n approaches infinity the Bailey yield surface approaches the Tresca hexagonal surface. Thus the Bailey yield criterion includes both the Mises and the Tresca surfaces.

If n is an odd integer it is not difficult to show that the left side of Equation (2) is a function of the second and third invariants of the stress deviator tensor. For such values the Bailey surface falls in one of the classes described by Edelman and Drucker[3] in their general discussion of yield surfaces. For other values of n it may be more difficult to show a relationship between Equation (2) and the invariants, but the surface still meets the requirements of a reasonable yield surface.

[1] Advisory Engineer, Westinghouse Research Laboratories, Westinghouse Electric Corporation, Pittsburgh, Pa.
[2] R. W. Bailey, "The Utilization of Creep Test Data in Engineering Design," *Journal of The Institution of Mechanical Engineers*, vol. 131, 1935, pp. 131–269.
Manuscript received by ASME Applied Mechanics Division, December 9, 1960.

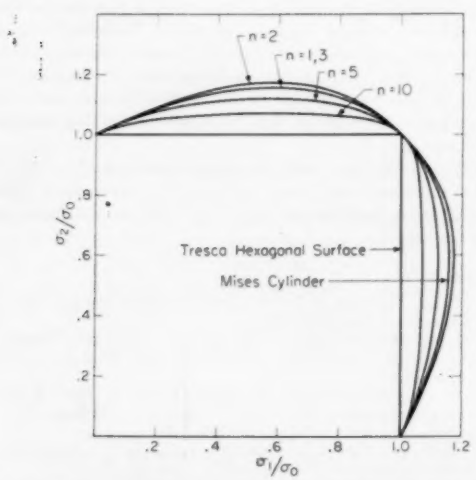

Fig. 1 Partial section along plane $\sigma_3 = 0$ of Bailey yield surface

Application of the Heat Balance Integral to Problems of Cylindrical Geometry[1]

T. J. LARDNER[2] **and F. V. POHLE**[3]

Nomenclature

- a = radius of cylindrical hole
- c = specific heat per unit mass
- H = constant flux
- k = thermal conductivity
- r = radial distance measured from axis of cylinder
- T = temperature
- t = time
- α = diffusivity, $k/\rho c$
- δ = penetration depth $\delta(t)$, measured from $r = a$
- η = $1 + (\delta/a)$
- θ = defined by Equation (2)
- ρ = mass density

E. M. SPARROW, in a recent discussion, has indicated that some inaccuracy is present in the application of Goodman's heat balance integral approach to problems involving nonplanar geometry [1].[4] The problem investigated by Sparrow was the determination of the temperature distribution in the region exterior to a cylindrical hole in the infinite space. The region is initially at zero temperature and the surface temperature of the cylindrical boundary is suddenly raised to a constant value. No details of the solution are presented, but the conclusion is that ". . . this inaccuracy was connected with the choice of a polynomial approximation for the temperature profile."

It is the purpose of this Note to present the analysis for the problem in which the cylindrical hole is exposed to a constant heat flux and to show the dependence of the surface temperature on the assumed temperature profile. Although this problem differs from that of Ref. [1] in the specification of the boundary condition, the dependence of the results upon the assumed profile will be the same. Two spatial temperature profiles will be investigated:

[3] F. Edelman and D. C. Drucker, "Some Extensions of Elementary Plasticity Theory," *Journal of The Franklin Institute*, vol. 251, June, 1951, pp. 581–605.

[1] The results presented in this Note were obtained in the course of research sponsored by the AFOSR under Contract AF 49(638)-302.
[2] Research Assistant, Polytechnic Institute of Brooklyn, Brooklyn, N. Y.
[3] Professor of Applied Mechanics, Polytechnic Institute of Brooklyn; currently, Professor of Mathematics, Adelphi College, Garden City, N. Y.
[4] Numbers in brackets indicate References at end of Note.
Manuscript received by ASME Applied Mechanics Division, October 20, 1960.

one, the usual parabolic shape employed in planar problems carried over to the radial co-ordinate; two, a modified parabolic profile to be discussed subsequently. It will be found that the usual parabolic approximation leads to poor agreement with the exact solution while the latter profile, the modified parabolic distribution, leads to results as accurate as the integral solution in planar problems. Furthermore, reference is given to other work employing the heat balance approach.

Analysis

The problem to be treated by the integral method has been outlined above. Since an exact solution is known [2], this will be used to check the accuracy of the integral approximations. Thus the heat balance integral method will be applied to the heat-conduction equation in cylindrical co-ordinates under the assumption of a radial temperature distribution between the surface of the cylinder and the penetration depth.

Integration of the heat-conduction equation

$$\alpha \frac{1}{r}\frac{\partial}{\partial r}\left(r\frac{\partial T}{\partial r}\right) = \frac{\partial T}{\partial t},$$

over the heated portion of the region yields

$$-ak\left.\frac{\partial T}{\partial r}\right)_{r=a} = \rho c \frac{\partial \theta}{\partial t}, \tag{1}$$

where

$$\theta = \int_a^{a+\delta} rT(r)dr, \tag{2}$$

a is the radius of the hole, and $\delta(t)$ is the penetration depth measured from the boundary. The boundary conditions to be satisfied are:

$$\begin{aligned} &\text{at } r = a, \qquad -k(\partial T/\partial r) = H, \\ &\text{at } \quad r = a + \delta, \quad -k(\partial T/\partial t) = 0, \end{aligned} \tag{3}$$

where H is the constant heat flux. If the spatial temperature distribution is assumed to be parabolic, it can be verified that

$$T = (H/2k\delta)[(\delta + a) - r]^2 \tag{4}$$

satisfies Equations (3). The heat balance integral, Equation (1), leads to the following expression for the penetration depth as a function of time:

$$(24\alpha t/a^2) = (\delta/a)^3 + 4(\delta/a)^2. \tag{5}$$

As a becomes indefinitely large, the penetration depth depends on the square root of time which is the known result [3]. It is also seen that Equation (5) together with Equation (4) yields the time history of the surface temperature

$$(T_s k/Ha) = (\delta/2a). \tag{6}$$

This result is presented in Fig. 1 together with the exact solution; agreement between the two solutions is poor. Fig. 1 shows in addition the surface temperature history for the profile

$$T = \frac{-(Ha/k)[(\delta + a - r)/a]^2}{(\delta/a)[2\ln[(\delta + a)/a] + (\delta/a)]} \ln\frac{r}{\delta + a}, \tag{7}$$

which combines the quadratic dependence on r with that of a logarithmic term; it can be verified that this equation satisfies the boundary conditions, Equations (3). The motivation behind the selection of this profile will be discussed in the next section.

The penetration depth relation for Equation (7) is

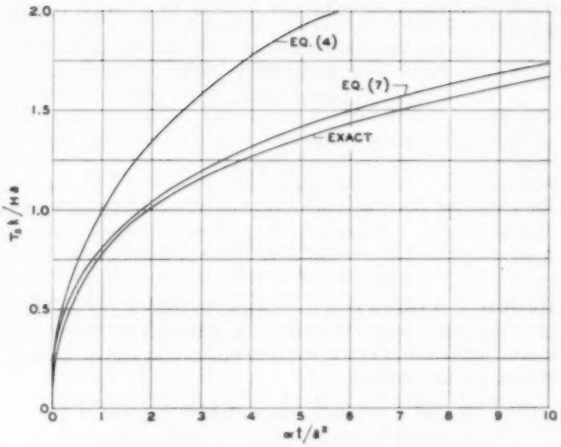

Fig. 1 Surface temperature of the region bounded internally by a circular cylinder of radius a, with zero initial temperature and constant flux H at the surface

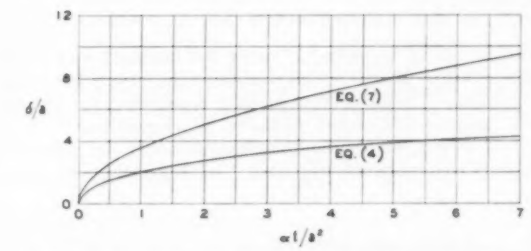

Fig. 2 Penetration depth versus time for different profiles

$$\alpha t/a^2 = \frac{-[(72\eta^2 - 96\eta + 36)\ln\eta - 13\eta^4 + 36\eta^2 - 32\eta + 9]}{144(\eta - 1)(2\ln\eta + \eta - 1)}, \tag{8}$$

where $\eta = 1 + (\delta/a)$. For large values of time,

$$\alpha t/a^2 = 13\eta^2/144, \tag{9}$$

from which the surface temperature is found,

$$(T_s k/Ha) = (1/2)\ln(3.32\alpha t/a^2); \tag{10}$$

the exact solution gives

$$(T_s k/Ha) = (1/2)\ln(2.24\alpha t/a^2). \tag{11}$$

Finally, the penetration depth history for the two profiles is shown in Fig. 2.

Discussion

It can be seen from Fig. 1 that the parabolic assumption is inaccurate as an approximation to the exact solution. This is to be expected since the volume into which the heat diffuses does not remain the same for equal increments of r (as in the planar case), and as a consequence a modification in the assumed profile is necessary. This modification given by Equation (7) involves a logarithmic multiplier of the usual parabolic profile. The logarithmic term corresponds to the steady-state solution for a hollow cylinder of radii r and $a + \delta$ which permits the asymptotic form of the surface temperature history to agree in form with the exact solution; this is shown in Equations (10) and (11). A further indication of the form of the modified profile can be de-

duced from the heat-conduction equation in spherical co-ordinates

$$\alpha \frac{1}{r^2} \frac{\partial}{\partial r} \left(r^2 \frac{\partial T}{\partial r} \right) = \frac{\partial T}{\partial t}.$$

If

$$u = Tr,$$

the heat-conduction equation in spherical co-ordinates becomes

$$\alpha \frac{\partial^2 u}{\partial r^2} = \frac{\partial u}{\partial t}.$$

However, it is known that the integral method works well for a parabolic profile when the equation is of this planar form. Since a parabolic profile in r for u would be expected to lead to favorable results, the modification

$$T = u(1/r),$$

where u is parabolic in r, becomes apparent for the spherical case. Finally, since $(1/r)$ is the steady-state solution, the corresponding modified profile in cylindrical co-ordinates would be expected to have the form

$$T = u(\ln r),$$

which is that of Equation (7) under the boundary conditions, Equations (3). Therefore, this establishes the form of the profile to be employed in problems of cylindrical geometry, namely, the usual parabolic distribution multiplied by a logarithmic function of r; of course, the resulting profile must satisfy the prescribed boundary conditions of the problem. In the present case, the result for the surface temperature history obtained with the modified profile agrees favorably with the exact solution, Fig. 1.

The foregoing analysis and discussion have shown that the behavior of the surface temperature with time is strongly dependent upon the form of the assumed profile and that polynomial approximations for the profile will lead to poor results. The introduction of logarithmic terms as multipliers of powers of r for cylindrical geometry leads to better agreement with the exact solution in the present example. Similar conclusions apply to the spherical case for which the steady-state solution is $(1/r)$, Ref. [4].

As a final comment, a recent book by Veinik will be noted [5] which contains extensive applications of the integral method to problems of both planar and nonplanar geometries under the assumption of polynomial spatial temperature distributions. In addition, Equation (5) is also derived in this book; however, no comparison with the exact solution is given and hence no statement of accuracy is made.

References

1 E. M. Sparrow, discussion of "The Melting of Finite Slabs," by T. R. Goodman and J. J. Shea, JOURNAL OF APPLIED MECHANICS, vol. 27, TRANS. ASME, vol. 82, 1960, Series E, p. 598.

2 H. S. Carlsaw and J. C. Jaeger, "Conduction of Heat in Solids," Oxford University Press, London, 1959, second edition, p. 338.

3 T. R. Goodman, "The Heat Balance Integral and Its Application to Problems Involving a Change of Phase," TRANS. ASME, vol. 80, 1958, pp. 335–342.

4 T. J. Lardner and F. V. Pohle, "A Note on the Application of the Heat Balance Integral to Problems of Non-Planar Geometry," PIBAL Report No. 585, Polytechnic Institute of Brooklyn, January, 1961.

5 A. I. Veinik, "Approximate Calculation of Heat Conduction Processes," Gosud. Energetich. Izdat., Moscow, 1959, para. 24.

Journal of APPLIED MECHANICS

Discussion

Forced Lateral Vibration of a Uniform Cantilever Beam With Internal and External Damping[1]

J. L. KRAHULA.[2] The stress-analysis theory in solid bodies subjected to small strains has been most thoroughly investigated and developed for linearly elastic bodies. The increasing use of polymers and plastics calls for extension of this work to bodies which exibit stress-strain relations involving one or more time derivatives of both the stress and strain components. This paper is a significant contribution toward this goal. The author capably brings out the complexities involved in this type of stress analysis as evidenced by his equation (9). He also uses an appropriate numerical method to minimize the complexity and thus is able to solve a theoretical problem with remarkable accuracy. While the standard linear solid used has certain general features common to actual solids, it does not reproduce precisely the behavior of any actual metal. To represent the behavior of a real metal in detail even over a limited frequency range would probably require a model consisting of Maxwell units in parallel or Voigt units in series and hence higher-order time derivatives in the stress-strain relations.

In addition to elastic response to stress, viscoelastic materials exhibit a delayed elastic response and viscous flow which remain after the stress has been removed. The four-element model introduced and investigated by Prof. E. H. Lee[3] exhibits all three types of response. There are some polymers[4] which have been found to obey this law for limited strain and hence it would have been better to derive, instead of equation (9), that corresponding to Prof. E. H. Lee's four-element model.

J. D. SWANNACK.[5] The paper is a useful addition to beam-vibration theory. The cantilever beam is probably the best one to consider because of its great economic significance. In the Jet Age, it may be supposed that turbine blades are the only important cantilever beams. Heavy industry, however, abounds with cantilever structures. In many of these cases, the only tangible damping exists in the supporting system at the base of the cantilever.

[1] By Ho Chong Lee, published in the September, 1960, issue of the JOURNAL OF APPLIED MECHANICS, vol. 27, TRANS. ASME, vol. 82, Series E, pp. 551–556.

[2] Associate Professor of Mechanics, Rensselaer Polytechnic Institute, Hartford Gradute Center, East Windsor Hill, Conn. Mem. ASME.

[3] E. H. Lee, "Stress Analysis for Visco-Elastic Materials," *Proceedings of the Conference on The Properties of Materials at High Rates of Strain*, London, England, April, 1957.

[4] H. Leaderman, "Elastic and Creep Properties of Filamentous Materials," *Proceedings of the Seventh International Congress on Rheology*, 1954.

[5] Chief Design Analyst, Fairbanks-Morse and Company, Beloit, Wis. Mem. ASME.

As material is removed from the structure, one eventually must consider whatever distributed damping can be found.

Considering the first mode, what per cent of critical damping does the example represent? It would be the writer's thought that almost any variety of damping would leave the space phase shapes unchanged as long as the work per inch were essentially the same. Has work been done with another damping theory?

Author's Closure

The author wishes to thank Dr. Krahula and Mr. Swannack for their interesting comments and questions. In relation to Mr. Swannack's first question, if one defines critical damping in a continuous system as that value which gives an aperiodic solution in free vibration, it is seen that the model adopted here would not have such a solution because of the element k. Perhaps, instead of a percentage of critical damping, a computation of the dissipation energy might be more valuable for practical purposes, but the derivation is quite complex and the author did not find a simple expression for this quantity.

As for the second question, some work has been done only for Kelvin (or Voigt) solids, which are listed in the References of the paper. In this respect, Dr. Krahula's suggestion of a four-element model or other types of models seems interesting, even though one can be assured of the added complexities involved as the number of elements is increased.

Thermal Transfer in Turbulent Gas Streams. Effect of Turbulence on Local Transport From Spheres[1]

R. A. SEBAN.[2] This paper essentially presents local heat-transfer coefficients, at a Reynolds number of 3640, to correspond to the previously published results (author's reference [22]) for the effect of free-stream turbulence on the total heat transfer from spheres. A discussion on that paper considered certain questionable features of the kind of turbulence produced by the perforated plate that was used as a generator, and those queries are also important in the consideration of the present results. In short, they indicated that doubt existed, for sphere positions of 7 in. and closer to the generator, about the relative isotropy of the turbulence and even about the relative uniformity of the mean speed distribution. These items are important in relation to the present paper because it gives the first experimental indication that an increase in the free-stream turbulence level decreases the heat transfer to the laminar boundary-layer flow over the front part of the body. Other experimental results, obtained with circular cylinders, have shown an increase, maximum at the stagnation point and diminishing as the free-stream velocity gradient is reduced. One advantage to those measurements was a more direct method of evaluating the local heat flux, and it may be that the fluxes, found in the present experiments by a corrected determination of the temperature gradient in the stream, were themselves subject to an error that depended on the turbulence level. Also, it is notable that most of the decrease in the local coefficient at the stagnation point, as shown in Fig. 8 of the paper, occurred between the condition of operation without the plate and the lowest turbulence level achieved with it. If the former operation was in a different position, and perhaps without the additional duct downstream of the nozzle, there is a chance that the velocity distribution around the sphere was altered. Such a change would, of course, change the heat-transfer coefficient in the region of laminar flow.

It is the absence of information on the velocity distribution over the sphere surface that makes impossible a final critical comparison of the measured coefficients and the predicted ones in the region of laminar flow. However, there is reasonable expectation that at the front of the sphere the deviation of the velocity distribution from that corresponding from potential motion was not too great. The theories are based on such a distribution and, contrasted to other experimental results, those of the present authors are shown by Fig. 9 to be distinguished by the expected correspondence with prediction.

[1] By W. W. Short, R. A. S. Brown, and B. H. Sage, published in the September, 1960, issue, of the JOURNAL OF APPLIED MECHANICS, vol. 27, TRANS. ASME, vol. 82, Series E, pp. 393–402.

[2] Professor, Mechanical Engineering, Heat Power Systems, University of California, College of Engineering, Berkeley, Calif. Mem. ASME.

Transient Heat Conduction in a Rod of Finite Length With Variable Thermal Properties[1]

G. M. DUSINBERRE.[2] The writer wishes to question the utility of diffusivity as a fundamental property in this sort of analysis. For example, consider a piece of iron or steel passing through the transition between α and γ. The specific heat is infinite. Thus the diffusivity is zero, and this is not very helpful in analysis.

Most heat-transfer systems operate at constant pressure. Then equation (1) of the paper is better written in the form:

$$\frac{\partial}{\partial x}\left(k\frac{\partial T}{\partial x}\right) = \frac{\partial^2 K}{\partial x^2} = \rho\frac{\partial i}{\partial t}$$

where i is the specific enthalpy.

When this is written in finite-difference form, one is led to the following computation procedure:

1 Given the set of T, find the set of K.
2 From these, find the set of Δi.
3 From these, find the new set of i.
4 From these, find the new set of T.

Thus greater generality is attained than by the use of κ as a function of K. It is possible to write K as a unique function of i, but T is generally needed, not only as a matter of interest but also in order to write the equations for convective boundary nodes. It is not difficult to write the stability criteria for the choice of Δt.

T. GOODMAN.[3] The authors are to be commended for their workmanlike consideration of the error introduced by the finite-difference procedure. The writer would merely like to point out to the authors the convergence proof for the nonlinear heat-conduction equation contained in a paper by Douglas.[4]

Authors' Closure

The authors assume that there is no change of phase within the temperature range considered. When there is phase change, the heat of transformation must be included as one does for latent heat. The problem of using diffusivity or specific heat is then a matter of choice, neither of which is infinite or zero at the tem-

[1] By W. H. Chu and H. N. Abramson, published in the December, 1960, issue of the JOURNAL OF APPLIED MECHANICS, vol. 27, TRANS. ASME, vol. 82, Series E, pp. 617–622.

[2] Department of Mechanical Engineering, The Pennsylvania State University, University Park, Pa. Fellow ASME. (Deceased.)

[3] Manager, Applied Mathematics Department, Allied Research Associates, Inc., Boston, Mass.

[4] J. Douglas, Jr., "On the Numerical Integration of Quasi-Linear Parabolic Differential Equations," *Pacific Journal of Mathematics*, vol. 6, 1956, pp. 35–42.

perature of transformation. On the other hand, the authors agree with Professor Dusinberre's generalization of introducing enthalpy for cases in which there is phase change, since temperature is a single-valued or well-defined function of enthalpy which includes the term representing heat absorbed for transformation.

The authors would like to thank Dr. Goodman for bringing out an interesting reference.[4] A mere convergence proof, however, may not be sufficient to assess the actual error contained after many steps of integration. The authors would like to point out that, in the problem considered, the bound for space derivatives are very large at early steps but decrease rapidly as time increases. If bounds of derivatives independent of time are employed, the estimated error growing "exponentially" with these bounds would be much too large to be of practical value.

Hydrodynamic Entrance Lengths for Incompressible Laminar Flow in Rectangular Ducts[1]

E. M. SPARROW.[2] The paper represents an interesting contribution to the growing literature on flow in noncircular ducts. In evaluating the results and establishing their relation to other geometries, it might have been useful to have made further comparisons with the circular tube. In particular, a plot of $C_{ap}/(C_{ap})_{est}$ which includes the data in Fig. 7 along with a curve for the circular tube would have been helpful in visualizing the role of duct shape in modifying the entrance length.

In Fig. 6, there is shown a rather close agreement between the center-line velocity results of the present analysis and those of Schlichting. It would be of interest to know whether the same sort of agreement would be achieved if the comparison were to be made at some other location in the cross section.

Author's Closure

The author appreciates Professor Sparrow's kind remarks. Accordingly, the ratio of apparent friction factor to the asymptotic friction factor $C_{ap}/(C_{ap})_{est}$ is plotted against the nondimensional distance $(z/DeRe)$ for the aspect ratios shown in Fig. 1 along with the data for a circular pipe.

The suggested comparison of the velocity profiles of the present analysis for $\gamma = 0$ (parallel plates system) with those from Schlichting's analysis is not made in view of the difficulty in extracting information from such a comparison, especially when both methods are approximations to the true situation.

[1] By L. S. Han, published in the September, 1960, issue of the JOURNAL OF APPLIED MECHANICS, vol. 27, TRANS. ASME, vol. 82, Series E, pp. 403–409.

[2] Professor of Mechanical Engineering, University of Minnesota, Minneapolis, Minn. Assoc. Mem. ASME.

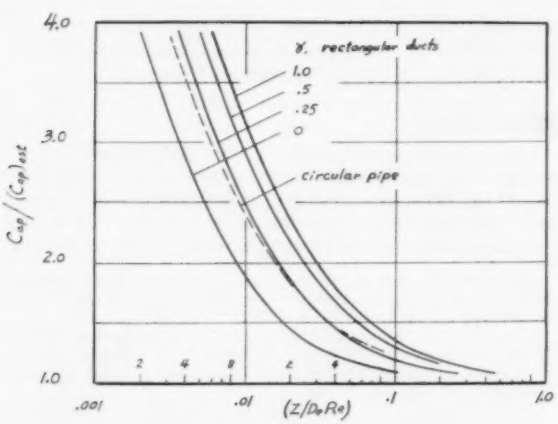

Fig. 1

Elastic-Plastic Bending of Curved Bars of Constant and Variable Thickness[1]

S. A. MURCH.[2] Besides supplying interesting results concerning thickness variation in the state of plane stress, this paper also provides a convenient summary of some of the existing literature on the elastic-plastic bending of curved bars, including the state of plane stress with uniform thickness, as well as the state of plane strain. In connection with the latter, a few words are in order concerning equations (4) and (5) of the paper, the validity of which has been insured for a rigid, perfectly plastic material by both Hill and Lubahn and Sachs, as pointed out in reference [2] of the paper.

For the limiting case of a bar of elastic, perfectly plastic material, as the inner ρ_i and outer ρ_o elastic-plastic boundaries meet (i.e., as the elastic zone vanishes), however, the validity of equations (4) and (5) of the paper has been established only recently[3] and even then only partially. This does not, however, affect the results given in Table 1 of the paper, since the values of b/a selected are well within the range for which the validity of equations (4) and (5) of the paper is completely established.[3]

The limitation imposed on the range of b/a stems from the piecewise linear nature of the Tresca yield surface. The stress distribution presented in reference [2] of the paper and employed more recently by Eason[4] to obtain the displacements for a compressible material, assumes that σ_z remains the intermediate principal stress throughout the entire range of plastic deformation. That this is the case (in the state of plane strain) for only a restricted range of b/a and Poisson's ratio ν has been thoroughly discussed elsewhere.[3] It suffices to say here that for certain ranges of these parameters the state of stress in either of the plastic regions of the bar may reach a singular regime of the Tresca yield surface. When this occurs, the state of stress ceases to be statically determinate and four possibilities present themselves: No singular regimes are encountered (case A); a singular regime is encountered in the plastic zone I $a \leq r \leq \rho_i$ (cases B and C, depending on the order of appearance with the plastic zone II $\rho_o \leq r \leq b$); and a singular regime is encountered in both zones I and II (case D).

Equations (4) and (5) of the paper under discussion have been shown in reference [2] of the paper to hold in the fully plastic state for case A and only recently[3] for the cases B and C. The validity of equations (4) and (5) for case D, as the limiting case of an elastic, perfectly plastic solution when the elastic domain vanishes, remains to be shown. This case is of little practical importance as far as curved bar analysis is concerned, since b/a

[1] By H. D. Conway, published in the December, 1960, issue of the JOURNAL OF APPLIED MECHANICS, vol. 27, TRANS. ASME, vol. 82, Series E, pp. 733–734.

[2] Assistant Research Engineer, Institute of Engineering Research, University of California, Berkeley, Calif. Assoc. Mem. ASME.

[3] S. A. Murch, "On the Pure Bending of an Elastic, Perfectly Plastic Curved Bar in the State of Plane Strain," *Journal of The Franklin Institute*, vol. 270, 1960, pp. 301–316.

[4] G. Eason, "The Elastic-Plastic Bending of a Compressible Curved Bar," *Applied Scientific Research*, Series A, vol. 9, 1960, pp. 53–63.

is such that the barlike character is lost. Other applications may exist, however.

In the state of plane stress for uniform thickness, σ_z remains the intermediate principal stress (except at the boundaries $r = a, b$ of the bar, where $\sigma_r = \sigma_z = 0$; $\sigma_\theta = \pm\sigma$ which present no difficulties). Indeed, the point is not even mentioned by Swida nor in another recent paper by Eason.[5]

It is easily checked through equations (9) and (10) of the paper that, for the particular form of h selected, again no difficulties of this type are encountered; however, for general h this need not be the case.

It should be added that, in view of Eason's recent paper,[5] comparisons between plane stress (for uniform h) and plane strain (when $\nu = 1/2$) are now possible, employing the von Mises yield criterion. The case of variable thickness, however, remains a point for further investigation.

Author's Closure

The author appreciates the interesting and pertinent remarks by Mr. Murch, and thanks him for the additional references.

Buckling of Circular Cones Under Axial Compression[1]

PAUL SEIDE.[2] In this paper an attempt is made to prove the formula

$$P_{cr} = P_{cyl\,\infty} \cos^2\alpha = \frac{2\pi\, Et^2 \cos^2\alpha}{[3(1 - \nu^2)]^{1/2}} \qquad (1)$$

is the lowest value of P_{cr} that satisfies the stability determinant of Seide[3] for values of Poisson's ratio ν other than zero. The reasoning used is that, if "the value of P_{cr} is smaller than $P_{cyl\,\infty}$ $\cos^2\alpha$, the stability determinant will contain Bessel functions of complex numbers" and "such a determinant is *not likely* to yield a real value for the critical load." When equation (1) is substituted into the stability determinant, it is found that pairs of columns are identical, which means that the determinant is identically equal to zero, without regard to the locations of the radius-thickness ratios of the ends of the cone.

Unfortunately, such a procedure is invalid since the stability determinant is not correct for P_{cr} equal to $P_{cyl\,\infty}\cos^2\alpha$. For this case the solution of the differential equation of Seide[3] is different from that given for P_{cr} greater than $P_{cyl\,\infty}\cos^2\alpha$ and the correct stability determinant may vanish only for certain combinations of values of the radius-thickness ratio at both ends of the cone. The stability determinant for P_{cr} less than $P_{cyl\,\infty}\cos^2\alpha$ can be put into real form, and at this point it does not appear to be possible to state *a priori* that this determinant will not vanish for some combination of values of load coefficient, semivertex angle, and radius-thickness ratio of both ends. Only for ν equal to zero was it possible to obtain the result of equation (1) without resorting to large-scale numerical investigation of the equations. It is the writer's belief, however, that the correct minimum for Poisson's ratios other than zero differs by only a very few per cent from this result, as indicated by some calculations being made at the present time for the case of combined axial compression and external pressure.

The test results are also open to question, as is usually the case when more than one investigator has worked on the buckling of shells under axial compression. Tests have been made at Space Technology Laboratories by Victor Weingarten and recorded recently.[4] These tests indicate that the correction coefficient applicable to conical shells under axial compression may be considerably greater than that given by the Kanemitsu-Nojima equation using the average radius of convective-thickness ratio, and thus even greater than the results using the greatest radius of curvature. In a private discussion with the author it appeared that this discrepancy might be due to the somewhat unusual end conditions of his tests which consisted of the cone resting on a spherical surface. It is debatable whether this restraint would be equivalent to the bulkheads rigid in their own plane that is assumed by the theory of Seide[3] and approximated in Morgan, et al.,[4] since inward motion of the shell walls would not necessarily be prevented.

Authors' Closure

The authors wish to thank Dr. Seide for his discussion.

He is entirely correct that the stability determinant as given by Seide[3] is not correct for P_{cr} equal to $P_{cyl\,\infty}\cos^2\alpha$, and therefore the author's reasoning to show that the formula

$$P_{cr} = P_{cyl\,\infty}\cos^2\alpha = \frac{2\pi Et^2\cos^2\alpha}{[3(1 - \nu^2)]^{1/2}}$$

is the lowest value of P_{cr} that satisfies the stability determinant of Seide[3] is invalid for values of Poisson's ratio ν other than zero. The reason the afore-mentioned stability determinant is invalid in this case is due to the fact the required four independent solutions (Eq. 17, Seide[3]) of the second-order equations (Eqs. 15, Seide[3]) degenerate into only two independent solutions and thus no longer represent a complete solution.

It should be pointed out, however, that the afore-mentioned erroneous reasoning by the authors does not invalidate their test results and conclusions as presented in the paper.[1]

The authors believe that the boundary conditions for their cones approximated pinned supports. During testing of these cones, no apparent displacements normal to the generator at the boundaries were observed. Only after very large displacements in postbuckling range was the friction insufficient to prevent these normal displacements.

Tests of the buckling of cylinders and cones reported recently by Space Technology Laboratories, Inc. (STL)[4] resulted in higher buckling correction coefficients for cylindrical shells under axial compression than those reported previously in numerous papers.[5,6,7] As noted by Mr. Seide, the test results for cones obtained at STL show higher buckling coefficients than those reported by the authors. These observations would seem to indicate a general discrepancy between the STL results and those of others, not just a discrepancy between the STL results and those results of the authors.

[5] G. Eason, "The Elastic-Plastic Bending of a Curved Bar by End Couples in Plane Stress," *The Quarterly Journal of Mechanics and Applied Mathematics*, vol. 13, 1960, pp. 334–358.

[1] By Leslie Lackman and Joseph Penzien, published in the September, 1960, issue of the JOURNAL OF APPLIED MECHANICS, vol. 27, TRANS. ASME, vol. 82, Series E, pp. 458–460.

[2] Member of the Technical Staff, Space Technology Laboratories, Inc., Los Angeles, Calif. Assoc. Mem. ASME.

[3] Paul Seide, "Axisymmetric Buckling of Circular Cones Under Axial Compression," JOURNAL OF APPLIED MECHANICS, vol. 23, TRANS. ASME, vol. 78, 1956, pp. 625–628.

[4] E. J. Morgan, Paul Seide, and V. I. Weingarten, "Semiannual Report on Development of Design Criteria for Elastic Stability of Thin Shell Structures," Space Technology Laboratories Report STL/TR-59-0000-09959, July 1-December 31, 1959.

[5] S. B. Batdorf, M. Schildcrout, and M. Stein, "Critical Stress of Thin-Walled Cylinders in Axial Compression," NACA TN 1343, 1947.

[6] S. Kanemitsu and N. Nojima, "Axial Compression Tests of Thin Circular Cylinders," a Master of Science thesis, California Institute of Technology, 1939.

[7] L. A. Harris, H. S. Suer, W. T. Skene, and R. J. Benjamin, "The Stability of Thin-Walled Unstiffened Circular Cylinders Under Axial Compression Including the Effects of Internal Pressure," Preprint No. 660, Institute of the Aeronautical Sciences.

Communication

Statistical Theory of Communication. By Y. W. Lee. John Wiley & Sons, Inc., New York, N. Y., 1960. Cloth, 6 × 9 in., xvii and 509 pp. $16.75.

REVIEWED BY V. E. BENEŠ[1]

PROFESSOR LEE'S book is an introductory account intended for an engineering audience. Except for very few passages, the presentation is detailed, at an elementary level, and slow enough so that the book could be used by undergraduates who know some Fourier analysis and electrical engineering. The principal emphasis is on harmonic analysis rather than on stochastic processes and probability. The part of probability theory that is covered in the text consists of elementary probability and simple random wave-forms, e.g., shot noise. The bulk of the book is devoted to the properties and uses of spectra and correlation functions in linear systems, e.g., the Wiener-Hopf equation.

Since mechanical and electrical systems differ mostly in point of the bandwidths and frequencies of the signals, the emphasis on harmonic analysis in the book makes it more interesting to mechanical engineers than would have been a treatise (equally well described by the title) on abstract information after the style of Feinstein or Khinchin. The book is valuable in two chief respects: (*a*) It contains a careful explanation of generalized harmonic analysis; (*b*) it gives a usable exposition and a collection of examples from the classical theory of linear optimum least-squares filtering and prediction. Further than this it does not go, because the statistical and probabilistic aspects of the theory occupy such an elementary and ancillary place in the exposition.

No attempt is made to present the material in the context of the general theory of stochastic processes. The sophisticated detection methods suggested by mathematical statistics (e.g., maximum likelihood, likelihood ratios) are not mentioned, and neither are the linear representations and Hilbert space methods of Karhunen, Loéve, Grenander, and Parzen. Perhaps these topics do not belong in even a graduate text. Still, there are other, simpler topics (covered by the title) that could have been included; e.g., the special properties of Gaussian processes, particularly in regard to nonlinear prediction with a concave even error criterion (instead of the squared error), the role of conditional expectations, the use of Fokker-Planck equations to describe the passage of white noise through a dynamical system (linear or not), and so forth.

The attenuated nature of the probabilistic material may leave unsophisticated readers with erroneous impressions of simplicity or complexity. For example, the distinction between the autocorrelation of a function and the covariance of an ensemble (stochastic process) is blurred, and the senses in which harmonic analysis can be applied to a process are not adequately explained. On the other hand, during the lip service to statistical mechanics in the chapter on ensemble averages it is not explained that ergodic hypotheses are not necessary for the existence of a covariance function, and so for harmonic analysis of the process.

The work is a gracious, well-deserved tribute to N. Wiener from his former student. Nevertheless, some references to other contributors to the field were in order. The reviewer was surprised to find no mention of Khinchin and Kolmogorov, nor of Bochner. The methods of Shannon and Bode for optimal filtering and prediction, with their useful physical interpretations in terms of white noise, deserved mention in connection with the Wiener-Hopf equation. The author's debt to his mentor sometimes beclouds the exposition: the phrase "the Wiener theorem" occurs too frequently to be informative for someone who is not already familiar with the signal contributions of Wiener to harmonic analysis and cannot tell from the context which theorem of Wiener is meant.

[1] Bell Telephone Laboratories, Inc., Murray Hill, N. J.

Combustion

The Internal Combustion Engine in Theory and Practice. By C. F. Taylor. John Wiley & Sons, Inc., New York, N. Y., 1960. Cloth, x and 574 pp., illus. $16.

REVIEWED BY E. GLAISTER[2]

A SPECIFICATION for the production of a definitive book on the theory and practice of internal-combustion engines might require the author to have spent at least 20 years in personal research and in directing the work of others, to possess a sound knowledge of thermodynamics, preferably some teaching experience, a critical and balanced judgment which takes account of the contributions of other workers in the field, an awareness of the needs both of the advanced student and the designer, and the ability for lucid exposition. Such a specification might well have been written around the qualifications of the author of the present book, who is Director of the Sloan Laboratories for Aircraft and Automotive Engines and Professor of Automotive Engineering at M.I.T., and it can be said at once, almost without reserve, that his book comes well up to our expectations.

The present volume, the first of two, deals with thermodynamics, fluid flow, and performance. Vol. II is to cover fuels, combustion, materials, dynamics, and design procedure. On the whole, the treatment is well-balanced, and although it is only natural that topics in which the author and his team have been personally involved should be given more detailed consideration than others, the author's outlook is comprehensive.

Chap. I is introductory; Chap. II contains a succinct and lucid treatment of the air cycle and emphasizes the essential interrelation of the constant-volume, constant-pressure, and "mixed" variants. The use of dimensionless ratios both here and in Chap. IV for the idealized fuel-air cycle is valuable in affording a concise statement of the effect of compression ratio on cycle quantities. Chap. III contains a rather brief discussion of the thermodynamics of the working fluid, leading to the use of the charts provided at the end of the book, and Chap. IV extends the discussion to the evaluation of the indicator diagram and the efficiency of fuel-air cycles. Chap. V discusses the actual cycle and the effect of operating variables on the indicator diagram. The M.I.T. balanced-pressure indicator is described—the Bibliography contains a reference to the "Farnboro' " prototype (but not to the first description of this indicator by Wood in *Rep. and Memo.* 807 of April, 1922, or Proc. I. Mech. E., 1923).

Chap. VI contains a useful discussion of the factors which control volumetric efficiency, a topic whose importance is often insufficiently stressed, and Chap. VII presents a very complete treatment of the 2-stroke engine and the scavenging process, much of it based on original work at M.I.T. The discussion on heat loss and engine cooling in Chap. VIII is valuable, although in view of the supremacy (until the advent of the gas turbine) of the air-

[2] City and Guilds College, Department of Mechanical Engineering, London, England.

cooled aero engine, it is perhaps surprising that the discussion should be virtually confined to liquid-cooled engines. Chaps. IX and X deal respectively with engine friction and pumping losses and with types of compressor and exhaust turbines. In Chap. XI, which discusses the effect of cylinder size on performance, some striking comparisons justify the simple analysis which indicates that bhp/in.^{2} of piston area should be nearly independent of cylinder size. The effect of decreasing cylinder size for a given total engine displacement is mentioned, but one would have welcomed some discussion of the related topic of bore/stroke ratio, particularly in view of the marked trend toward "oversquare" cylinders shown in the author's Fig. 12.3(d) in the following chapter.

Chap. XIII, on the performance of supercharged engines, gives an impression of undue condensation, although the illustrative examples are valuable. To your reviewer it seems a pity to omit any mention of methods of predicting the performance of a supercharged aero engine at altitude (obsolescent though the type may be), especially when this might logically follow the excellent treatment of volumetric efficiency given in Chap. VI. The Bibliography is an excellent one.

These minor and personal criticisms apart, the book can be confidently recommended as a major and significant contribution to the literature of the internal-combustion engine.

Analog and Digital Computers

Handbook of Automation, Computation, and Control, vol. II. By Eugene M. Grabbe, Simon Ramo, and D. E. Wooldridge. John Wiley & Sons, Inc., New York, N. Y., 1959. Cloth 6 × 10 in., xxiii and 1070 pp. $17.50.

REVIEWED BY JOHN R. WARD[3]

This second volume of a three-volume handbook maintains the level of excellence achieved in the first volume, which was reviewed in the September, 1959, issue of the JOURNAL OF APPLIED MECHANICS.

A wide coverage of the principles of design, application, and programming of analog and digital machines is presented with, naturally, a heavy emphasis on the digital instrument. Applications are restricted to computation and data processing, since the control aspect is to be covered in the third volume. Somewhat more applied than the first volume, reference is frequently made to systems and circuits currently in use.

Once again the treatment is extremely concise, permitting a rapid review of any particular area, a review which may be deepened by way of the useful and extensive references provided.

This volume belongs beside its forerunner.

Transport Phenomena

Transport Phenomena. By R. B. Bird, W. E. Stewart, and E. N. Lightfoot. John Wiley & Sons, Inc., New York, 1960. Cloth, 6 × 10 in., xxi and 780 pp. $13.75.

REVIEWED BY D. B. SPALDING[4]

THE activities of the Wisconsin group of chemical engineers in strengthening the foundations and developing the structure of the theory of transport phenomena have attracted considerable attention in teaching circles. The publication of the present handsome volume is therefore an important occasion and an opportunity for appraising the work which has been accomplished. This work is, however, too massive for the present review to contain more than provisional comments and reflections; time, and experience of using the book as an aid to teaching, are needed before a full appraisal will be possible.

The authors take the view that the transport of momentum, energy, and material ought to be considered as a single subject which should rank with thermodynamics, mechanics, and other basic engineering sciences. Despite the facts that the law of conservation of momentum is incompletely similar to those of energy and matter, and that radiative transfer is a tiresome anomaly, there is much to be said for this view. The authors exploit its possibilities to the full, emphasizing and re-emphasizing the similarities between the three types of transport phenomena by parallel treatment and by cross-referencing.

Since they are writing what would normally be three books within one pair of covers, and since they have clearly resolved to discuss thoroughly every topic that they treat at all, it is inevitable that the book fails to cover all the ground which it has been customary to require undergraduate and postgraduate students of fluid mechanics, heat transfer, and mass transfer to know about; additional texts will be needed in every case. Since there are numerous suitable texts available for fluid mechanics and heat transfer, gaps in these subjects (or rather branches of *the* subject) can easily be filled. It is more questionable, however, whether the student can pass easily from Bird, Stewart, and Lightfoot's section on mass transfer to the relatively few alternative works on the subject; for the authors have not here provided many bridges leading to the traditional procedures of chemical engineers. Nor, which is perhaps more surprising in view of their interests in mathematical techniques and in "similarities," have they made connection with the studies of fuel combustion and of ablation made in the past decade; they do not mention the important class of problems involving simultaneous heat transfer, mass transfer, and chemical reaction which are rendered soluble by the assumption of a Lewis number of unity.

Because of the relative newness of mass transfer as a scientific discipline, the reviewer has concentrated on this portion of the book; he opened the book with two questions in mind: Have the authors succeeded in the important task of effecting a smooth juncture between the subjects of mass transfer and fluid mechanics, so that the resources of aerodynamic theory (particularly boundary-layer theory) can be freely used by chemical engineers? And have they made accessible to undergraduates (and their teachers) the relevant advances in the theory of multicomponent gases as represented by the book of Hirschfelder, Curtiss, and Bird?

The answer cannot, in the reviewer's opinion, be an unqualified affirmative in either case. To take the second question first, the authors give their greatest attention to binary mixtures where they do an excellent job; they also explain clearly the influence of the choice of reference plane (mass-centered or mole-centered) on the magnitude of the diffusion flux. Yet most practical diffusion problems take place in multicomponent mixtures, and something of more relevance to these might have been expected than a brief citation of some of the results of Hirschfelder, et al., followed by a single application to a one-dimensional three-component problem.

To tackle now the second question, the authors do make an approach to boundary-layer theory; they treat the flat plate in laminar flow with a binary mixture in which all fluid properties are uniform. However, the reader may be left in doubt as to how to proceed when these properties are not uniform, if only because in one attack on the problem the authors' concentration variable is the molal density, while in the second it is the mole fraction. Which should be used when a density gradient is present? In the reviewer's opinion the answer is: neither; for, since the solution of the momentum equation only gives the *mass*-flux den-

[3] Assistant Professor, Division of Engineering, Brown University, Providence, R. I.

[4] Department of Mechanical Engineering, City and Guilds College, London, England.

sity, the *mass*-centered diffusion flux must be considered, which implies that the appropriate concentration variable is the *mass fraction*. It is often necessary to use the mass-centered system for another reason also: When chemical reaction occurs, moles are not conserved, whereas mass is; the mass fraction also recommends itself when the molecular weight of the diffusing substance is uncertain, as in the case of a hydrocarbon fuel diffusing toward a flame. The reviewer did not find in the book any statement of the above views (which may be wrong) or of any alternative recommendations for dealing with problems of this kind, which arise in almost every practical application of mass-transfer theory.

It would, however, be entirely unfitting to close this review on a critical note. The reviewer has therefore saved until the end an expression of his profound admiration for a work which is scholarly, lucid, and elegant. The authors have taken almost unprecedented pains to aid the student's labors; careful definitions, helpful notation, lively examples, and handsome printing make this work one of which the authors, and the publishing house, can take a well-justified pride. Students, teachers, and industrial scientists will be grateful to them for a long time to come.

Fluid Mechanics

Lectures on Fluid Mechanics. Lectures in Applied Mathematics, Vol. II. By Sydney Goldstein with J. M. Burgers. Interscience Publishers, Inc., New York, 1960. Cloth, xvi and 309 pp. $5.

REVIEWED BY JOSEPH H. CLARKE[5]

THIS volume contains the written version of a series of lectures which were given by Sidney Goldstein at Boulder, Colo., in 1957, and were designed to acquaint mature mathematicians with fluid mechanics. An arresting aspect is that Goldstein was to deal with the entire subject in only twelve lectures. Thus he has had to pass over all but what he regards as the essential ideas, achievements, and problems. Since he clearly accepted his assignment with some gravity, it is interesting to peruse what one of the elder statesmen of fluid mechanics saw fit to present in his account. The result is not a survey because the coverage is incomplete and the choice of material is, to a considerable extent, arbitrary and personal; and, while very succinct, it is no mere cataloguing of topics. The result *is* a satisfying and thoughtful series of lectures set forth with a definite point of view not to be found in more formal treatises. At times the mellow, reflective, and trenchant remarks conjure a setting in which the reader shares Goldstein's hearthside over sherry. The volume will certainly reward readers with many different points of view.

The classification of the subject and hence the chapter headings are conventional, except for the early point at which electromagnetic effects are introduced. The volume contains two tours de force. One is a new careful formulation of the field equations of magnetohydrodynamics, regarded as the electrodynamics of a moving medium. Subjoined to this are two detailed problems of magnetohydrodynamics provided by J. M. Burgers. The second is on an asymptotic solution to the Navier-Stokes equation for flow past a flat plate. The book contains an interesting discussion of the Newtonian stress-strain rate relations from the point of view of molecular relaxation or lag phenomena, as well as other comments on the relationship between the field and molecular formulations. There is a short chapter on the related matters of mixtures and chemical kinetics. Some absorbing remarks are offered on the theoretical question of whether the classical Helmholtz-Kirchhoff free-streamline theory can be regarded as the correct, if unstable, limit of the steady viscous flow as the viscosity tends to zero. Other interesting observations, not entirely looked for in such a development, are salted throughout the volume.

[5] Associate Professor, Division of Engineering, Brown University, Providence, R. I.

Thermal Stresses

Theory of Thermal Stresses. By Bruno A. Boley and Jerome H. Weiner. John Wiley & Sons, Inc., New York, London, 1960. xv and 586 pp. $15.50.

REVIEWED BY W. PRAGER[6]

THE PUBLICATION of this comprehensive text on the theory of thermal stresses is particularly welcome at a time when the design requirements in rocket propulsion and nuclear power have greatly enhanced the importance and extended the scope of this field. By devoting about two fifths of the book to a careful treatment of the fundamentals of thermoelasticity (Part I) and heat conduction (Part II), the authors have achieved a nearly self-contained presentation of their subject. The rest of the book consists of two parts dealing with the analysis of thermal stresses in elastic (Part III) and inelastic (Part IV) systems. The unequal development of these subjects is strikingly illustrated by the fact that Part II, which is almost twice as long as Part IV, discusses a large number of applications regarding thermal stresses in elastic beams, rings, trusses, frames, disks, and plates, and thermoelastic stability. Part IV, on the other hand, is primarily concerned with the basic formulation of viscoelastic and elastic-plastic behavior in the presence of temperature changes, and only a few specific applications are treated.

In the writing of a work of this ambitious scope, decisions on emphasis cannot be avoided that are readily explained in terms of the authors' interests but may otherwise appear arbitrary. For example, throughout the book the elastic coefficients are treated as temperature-independent quantities, but no effort is made to justify this, whereas the effect of the mechanical coupling term in the equation of heat conduction is discussed at great length. On the whole, however, the authors have achieved a remarkable balance in the treatment of the fundamental aspects of the theory and its applications, and the book is bound to become a standard reference in the literature on this field.

Wave Propagation

Wave Propagation in a Random Medium. By L. A. Chernov. Translated by R. A. Silverman. McGraw-Hill Book Company, Inc., New York, N. Y., 1960. Cloth, 7½ × 10 in., viii and 168 pp.

REVIEWED BY J. LYELL SANDERS, Jr.[7]

THE BOOK is divided into three parts, the ray theory, the wave theory, and applications to focusing systems. The author's treatment of his subject is lucid and concise. Not too much specialized mathematical equipment is required of the reader, but some familiarity with the technological problems in the field is helpful. The book serves both as an introduction to the subject and a summary of recent results of Russian work in the field. The translation is good.

The book begins with a discussion of the relevant statistical characteristics of the medium, in particular the correlation function of the refractive index. Following this is a treatment of the problems of scatter and fluctuations in transit time and intensity in so far as the ray approximation is adequate. The subject of scattering is developed further by use of the wave theory and the method of small perturbations in a following chapter. Fluctuations in amplitude are then treated by the wave theory using both the ordinary method of small perturbations and Rytov's method.

[6] L. Herbert Ballou University Professor, Brown University, Providence, R. I.

[7] Associate Professor of Structural Mechanics, Division of Engineering and Applied Physics, Harvard University, Cambridge, Mass.

For most practical values of the parameters involved, Rytov's method is subject to fewer limitations and is therefore preferred.

A chapter is devoted to the subject of correlation and autocorrelation of amplitude and phase in space and time based on the wave theory. The third section of the book on focusing systems is an application of the wave theory to the study of the mean distribution and the fluctuations in intensity of an image due to inhomogeneities in the medium. A familiar example of the subject material is the twinkling of stars which the author proves to be more readily observable to the naked eye than with a large telescope.

Plastic Deformation

Ermittlung eingeschrankt plastischer Verformungen im Sand unter Flachfundamenten (Determination of limited plastic deformations of sand under shallow foundations). By Dr. Ing. Hans U. Smoltczyk. Ernst und Sohn, Berlin, 1960. Paper, 7 × 10 in.

REVIEWED BY J. BRINCH HANSEN[8]

THE first part of the book deals with the bearing capacity of foundations subjected to vertical or inclined (but centric) loads. After having given the well-known solutions for weightless soil, the author proceeds to the more complicated case of "heavy" soil. He uses here a variant of the method indicated by Lundgren and Mortensen (Proc. Third. Int. Conf. Soil Mechanics, Zürich, 1953, vol. I, p. 409) and extends it in an approximative way to inclined loads.

Like the majority of writers on plasticity theory, the author pays small or no attention to the compatibility of the deformations in the state of failure. Nor does he seem to be fully aware of the behavior of composite ruptures involving elastic as well as plastic zones. Consequently, his calculations can be severely criticized from a theoretical point of view, although his numerical results may possibly be approximately correct.

In the opinion of the reviewer, the main value of the book lies in its second part, dealing with the "elastic" (reversible) and "plastic" (irreversible) deformations of sand before actual failure. As typical examples, the author analyzes a direct shear test and a consolidation test and indicates simple empirical relationships between stresses and strains for the elastic and plastic components in both tests. It is interesting to notice that elastic shear deformations follow a similar law as indicated by Ritter for concrete, and that the logarithms of plastic shear deformations have approximately a linear relationship to the shear stresses.

By combining the obtained relationships with Fröhlich's pressure distribution below a foundation, the author finally develops a method for calculating the settlements and soil movements for any loading not producing failure in the soil. It is, however, questionable whether Fröhlich's pressure distribution is compatible with the nonlinear stress-strain relationships used by the author.

Random Variables

Introduction to Probability and Random Variables. By G. P. Wadsworth and J. G. Bryan. McGraw-Hill Book Company, Inc., New York, N. Y., 1960. Cloth, 6 × 8 in., vii and 292 pp. $8.75.

REVIEWED BY A. CEMAL ERINGEN[9]

THIS BOOK consists of eight chapters. In the first chapter some preliminary mathematics such as the differentiation of a definite integral, the characteristics of gamma and beta functions, and the idea of permutations is introduced. The probability concept and laws of probability, from the standpoint of frequency rather than from the notion of measure, are given in Chap. 2 without loss in rigor. Chap. 3 deals with discrete random variables. Some elementary distributions (binomial, Poisson, etc.) are introduced and illustrated with good clarity. Chap. 4 treats continuous random variables. Gamma, beta, and normal distributions are discussed and illustrated with interesting engineering examples. The inclusion of more than a few sentences on the more sophisticated concept of the central limit theorem would have been desirable even at this level because of its broad implications. Joint distributions and some derived distributions from the normal, e.g., the chi-square distribution, occupy Chap. 5 and 6. Mathematical expectations and the concept of moments are given in Chap. 7. The last chapter is devoted to some statistical applications. The inclusion of a chapter on stochastic processes, even briefly, would have been most valuable to the beginning reader by providing an introduction to another important area.

The book is well illustrated and has a wealth of problems. The style is excellent. In its spirit and content the book is on a level with the excellent book by H. Cramer, "The Elements of Probability Theory and Some of Its Applications" (Wiley, 1955), but it contains more illustrative examples and problems. It is highly recommended for a first course in the field.

Fluid Mechanics

The Science of Fluid Mechanics. Physical Foundations From the Engineer's Viewpoint. Vol. 1, Hydro- and Aerostatics Motion of Perfect Fluids. By O. Tietjens. Springer Verlag, Berlin, 1960. Cloth, xvi and 536 pp. DM 66.

REVIEWED BY J. KESTIN[10]

IT IS trite, but nevertheless true, to say that every generation must anew relearn the old, basic truths. Professor O. Tietjen's Volume I of the Science of Fluid Mechanics does teach with a purpose, and admirably restates the fundamentals. The purpose is simple, and yet, owing to its simplicity, so seldom achieved by others, and probably by no one yet, to the same extent. The purpose is to provide a clear, easily understandable, well-grounded body of theoretical knowledge which does not contradict observational facts. To quote Professor Tietjen's quotation from Daniel Bernoulli's letter on d'Alembert to Leonard Euler: "His *pièce sur les vents* contrives to say nothing, and though I have read all, I still know as much about the *ventis*, as I did before." The reader, and particularly the young student, will advance no such complaint about Professor Tietjen's admirable exposition. He will learn much about winds, the navigation of clouds, balloons, as well as about flow fields, ideal and real fluids, the distinction between potential and rotational flows, the part played by viscosity, about capillarity, the distinction between fluids and solids, and many topics of similar importance. Even established specialists will know more about Fluid Mechanics, after studying the present book, than they did before. Every step has been thought out carefully and with purpose; at every step observation serves as the basis for theory and care is taken to discover just how far, and to what limits, any particular theory or approximation can be used to advantage, i. e., to represent the facts of nature.

Professor O. Tietjens is a mathematician by education, which guarantees the soundness of his mathematical apparatus. In addition, he matured under L. Prandtl's personal guidance and so acquired Prandtl's intense reverence and feeling for physical facts. In this he is a true inheritor of the best tradition of the natural philosophers of the eighteenth and nineteenth centuries.

The present Vol. 1 is devoted to the study of the physical

[8] Professor, Technical University, Copenhagen, Denmark.

[9] Professor, Division of Engineering Sciences, Purdue University, Lafayette, Ind.

[10] Professor, Division of Engineering, Brown University, Providence, R. I.

foundations of the mechanics of the flow of *perfect fluids*. It carefully describes the properties of liquids and gases (Chap. 1), equilibrium and stability (Chap. 2), surface tension (Chap. 3), potentional flows (Chapts. 4 and 5), flows with free surfaces (Chap. 6), and rotational and vortex flows (Chap. 7). The book has been printed and turned out with the usual excellence associated with Messrs. Julius Springer, but the pictures surpass anything encountered before, even in Springer books. They are imaginative in their conception, undoubtedly Professor Tietjen's, and little masterpieces of execution. The large number of flow diagrams showing streamlines (in white) and potential lines (in black) on a light-gray background cannot fail to imprint itself on the student's visual imagination and so to aid him materially in his ponderings on this elusive and fascinating subject. One cannot help but impatiently look forward to the Vol. 2 which will include viscous and compressible flows.

Your reviewer hopes that this impressive work will be speedily and urgently made accessible in translation to all whose command of the German language is inadequate to allow them to get acquainted with it at once.

Thermal Turbomachines

Thermische Turbomaschinen, vol. 2. By W. Traupel. Springer Verlag, Berlin, Goettingen, Heidelberg, 1960. Cloth, 10$^{9}/_{8}$ × 7$^{1}/_{8}$ in., viii and 420 pp. DM 61.50.

REVIEWED BY M. J. SCHILHANSL[11]

THE following sentences may be quoted from the preface to the second volume of Traupel's book on thermal turbomachines.

"The concept that all essential features of a thermal turbomachine are determined by aerodynamical and thermodynamical aspects and that the remainder is simply routine, unfortunately, is very widespread. It is, however, far from being true, so much so that design work is grossly underestimated as an intellectual achievement."

This quotation illustrates the spirit in which the second volume is written; in general, it is on the same level as the first volume. It can be highly recommended for the use of engineering staffs and in graduate schools.

The first three chapters of the second volume are devoted to the problems of regulation of steam turbines, compressors, and gas turbines. The succeeding three deal with stress problems of blades, rotors, and casings. Temperature effects and cooling problems are discussed in the seventh chapter while the next two chapters treat blade vibrations and critical rotor speeds. An appendix gives some information on materials best suited for application at elevated temperatures.

There are a few points where the reviewer disagrees with the author. They are:

Section 15.3: Equation 1 on page 147 should read

$$M = M_0 - \rho\omega^2 \int_0^l y(r_N + x[1 - \cos\beta])f\,dx$$

The replacement of sin β by $1 - \cos\beta$ must consequently also be made in equations 7, 8, and 9.

Section 15.7: Equation 1 on page 177—expressing the clamping moment of a beam with fixed ends holds only if the external load is perpendicular to one of the principal axes of inertia.

Section 16.14: (*a*) To simplify the stress analysis of a radical flow rotor by making it symmetrical in any respect is a highly questionable procedure. (*b*) The suggestion concerning a radial flow rotor with a shroud (page 220), namely, to neglect the mutual interference of disk and shroud and the tangential moments due to the asymmetry, is still more questionable. First, a shroud with a conical mean surface does not behave like a plane disk. Second, the mutual interference depends upon the shape of the blades to be expressed in terms of magnitude and orientation of the principal radii of curvature of blade surface—both finite or one finite and the other infinitely large or both infinitely large. The interference is strongest if the blades are plane and in meridional planes.

Section 19.10: The statement at the bottom of page 324 about centrifugating effects on torsional vibrations of blades disregards the effect of the product of mass inertia. The torsional frequency corrected for this effect can be lower than the frequency of the blade at rest.

[11] Professor Emeritus, Cranston, R. I.

175th ANNIVERSARY

Verlag Friedr. Vieweg und Sohn, Braunschweig, Germany

and PRIZE

On the occasion of its 175th Anniversary, the above publishing house has instituted a series of prizes for important papers in the fields of mathematics, physics, and chemistry which are suitable for publication in book form.

The publishers will be glad to send details concerning the conditions for the award of prizes to interested readers.

TRANSACTIONS OF THE ASME
Series E

Journal of
APPLIED MECHANICS
VOLUME 28 . SERIES E . NUMBER 2
June 1961

CONTENTS

CONTINUED

DESIGN DATA AND METHODS

292 **Design of Thin-Walled Torispherical and Toriconical Pressure-Vessel Heads**
R. T. Shield and D. C. Drucker

297 **Hydrodynamic Lubrication of a Roller Bearing—Introduction of Parameters to Obtain Charts for Calculation**
F. W. v. Hackewitz

BRIEF NOTES

Surface Waves in an Elastic Half Space 300
C. C. Chao, H. H. Bleich, and J. Sackman

Extension of Nadai's Sand Hill Analogy to Multiply Connected Cross Sections 301
M. E. Gurtin

Three-Dimensional Flow About Yawed Cylinders 302
D. Benenson

Vibrations of Thin Rectangular Isotropic Plates 304
R. W. Claassen and C. J. Thorne

305 Frequencies of Vibration of Shallow Spherical Shells
W. H. Hoppmann II

307 A Formula for the Torsional Stiffness of Rectangular Sandwich Plates
Shun Cheng

310 The Bailey Flow Rule and Associated Yield Surface
E. A. Davis

310 Application of the Heat Balance Integral to Problems of Cylindrical Geometry
T. J. Lardner and F. V. Pohle

DISCUSSION

312 Discussion of previously published papers by *Ho Chong Lee; W. W. Short, R. A. S. Brown, and B. H. Sage; W. H. Chu and H. N. Abramson; L. S. Han; H. D. Conway; Leslie Lackman and Joseph Penzien*

BOOK REVIEWS

Statistical Theory of Communication 316

The Internal Combustion Engine 316

Handbook of Automation, Computation, and Control 317

Transport Phenomena 317

Lectures on Fluid Mechanics 318

318 Theory of Thermal Stresses

318 Wave Propagation in a Random Medium

319 Determination of Limited Plastic Deformations

319 Probability and Random Variables

319 The Science of Fluid Mechanics

320 Thermische Turbomaschinen

NOW AVAILABLE—

SECTION 3 of the 1960 ASME TRANSACTIONS
containing contents of the
1960 Issues of the Journal of Applied Mechanics

This Section is for you because—it provides the laboratory and field data, experience records, opinions of authorities in the fields involved, and the reports of significant research projects—knowledge that you need to forge ahead in your field of specialization.

The data and information that this book places at your constant and immediate service are contained in the 135 papers and notes on technical matters in mechanics listed at the right. They were presented at ASME Meetings and Conferences under the sponsorship of the Applied Mechanics Division.

Cloth Binding **8½" x 11½"**

760 Pages **Indexed**

$16.00* ($8.00* to ASME members)

A Theory of Lubrication With Turbulent Flow and Its Application to Slider Bearing
Effect of the Wall on Two-Phase Turbulent Motion
Melting of Finite Slabs
Heat Exchanger Tube-Sheet Design—3. U-Tube and Bayonet-Tube Sheets
Mechanics of the Sheet-Bending Process
Relaxation of a Cylinder on a Rigid Shaft
Strain-Hardening Solutions to Axisymmetric Disks and Tubes
Effect of Shear Deformations on Bending of Rectangular Plates
Plastic Stress Concentration at a Circular Hole in an Infinite Sheet Subjected to Equal Biaxial Tension
Stresses in the Plastic Range Around a Normally Loaded Circular Hole in an Infinite Sheet
Dynamical Saint Venant Principle
Correlation of Theoretical and Photothermoelastic Results on Thermal Stresses in Idealized Wing Structures
Stresses in a Circular Cylinder Having an Infinite Row of Spherical Cavities Under Tension
Transient Thermal Stresses in a Semi-Infinite Slab
Stress-Strain Relations and Strain-Energy Expressions in the Theory of Thin Elastic Shells
Effect of Shear on Plastic Deformation of Beams Under Transverse Impact Loading
The Half Space Under Pressure Distributed Over an Elliptical Portion of Its Plane Boundary
Earth Motion Beneath a Prescribed Boundary Displacement
Elastic Bending of Columns Due to Dynamic Axial Forces Including Effects of Axial Inertia
Dominance of Shear Stresses in Early Stages of Impulsive Motion of Beams
Elastic-Plastic Response of Thin Spherical Shells to Internal Blast Loading
Assessment of Flow Disturbances and Blunt Body Traveling at Supersonic Speeds Owing to Flow Disturbances in Free Stream
Possible Similarity Solutions for Laminar Free Convection on Vertical Plates and Cylinders
Annual Damper for a Freely Precessing Gyroscope
Heat Transfer for Laminar Flow in Ducts With Arbitrary Time Variations in Wall Temperature
Study of the Stability of Externally Pressurized Gas Bearings
Theoretical Analysis of a Dynamic Thermocouple: 2—The Continuous Area Interface
Normal Modes of Nonlinear Dual-Mode Systems
Classical Normal Modes in Damped Linear Dynamic Systems
Vibration Response of a Linear Undamped System Resting on a Nonlinear Spring
Approximate Analysis of Certain Boundary Value Problems
Stresses in a Slab Having a Spherical Cavity Under Circular Bending
Elastic Equilibrium of a Plate With a Reinforced Elliptical Hole
Method of Solution for the Elastic Quarter-Plane
Thermal Stress in a Viscoelastic-Plastic Plate With Temperature-Dependent Yield Stress
Prediction of Creep Failure Time for Pressure Vessels
Plastic Behavior of Rotating Cylinders
Optimum Design of Shells
Yield Conditions for Rotationally Symmetric Shells Under Axisymmetric Loading
Approximate Analysis of the Influence of Aerodynamic Heating and Initial Twist on the Torsional Stiffness of Thin Wings
Postbuckling Behavior of Rectangular Plates With Small Initial Curvature Loaded in Edge Compression
Junction Problem of Solid-Slotted Cylindrical Shells
Three and Two-Dimensional Disturbances of Pipe Flow
Indeterminateness of the Boundary Conditions of the Mixing of Two Parallel Streams
Thermal Transfer in Turbulent Gas Streams. Effect of Turbulence on Local Transport From Spheres
Hydrodynamic Entrance Lengths for Incompressible Laminar Flow in Rectangular Ducts
Stability of a Turbine-Generator Rotor Including the Effects of Certain Types of Steam and Bearing Excitations
Saint Venant's Principle: Elastic Shells and Plates
Airy Stress Functions of Plane Dislocation Problems
Effect of Pressure on Bending Characteristics of Actuator System
Contact Problem for Viscoelastic Bodies
Stresses in Curved Beams of Noncircular Center Line
Shear Buckling of Bars
Buckling of Circular Cones Under Axial Compression
Additional Deflection of a Cantilever Due to Elasticity of Support
Thermoelastic Stresses in Beams
Elastic Instability of Rectangular Sandwich Panel of Orthotropic Core With Different Face Thicknesses and Materials
Transient and Residual Thermal Stresses in an Elastic-Plastic Cylinder
Strain-Hardened Circular Cylindrical Shells
Elastoplastic Thick-Walled Sphere Subjected to a Radial Temperature Gradient
Rupture Instability of Plane Membranes and Solids
Expansion of Thick-Walled Cylinders Fabricated From Cold Bent Plates
Dispersion of Flexural Waves in an Elastic, Circular Cylinder
Modeling of Large Transient Elastic and Plastic Deformations of Structures Subjected to Blast Loading
Shock Spectra of a Nonlinear System
Forced Flexural Vibrations of Sandwich Plates in Plane Strain
Extensional Vibrations and Waves in a Circular Disk and a Semi-Infinite Plate
Effect of Small Hub-Radius Change on Bending Frequencies of a Rotating Beam
Forced Lateral Vibration of a Uniform Cantilever Beam With Internal and External Damping
A Method for Investigating Certain Eigenvalue Problems of the Buckling and Vibration of Plates
Dynamical Response of an Elastic Half-Space to Tangential Surface Loadings
Special Class of Self-Sustained Oscillations
Random Excitation of a Loaded Nonlinear String
Use of Nonsinusoidal Approximating Functions for Nonlinear Oscillation Problems
Two-Dimensional Gas Jets
Compressibility Effects of the Lubricant for Two-Dimensional Slider Bearings
Heat Transfer and Sublimation at a Stagnation Point in Potential Flow
Transient Heat Conduction in a Rod of Finite Length With Variable Thermal Properties
Transient Conduction in Coaxial Cylinders With Relative Motion and Heat Generation
Thermal Stresses in an Elastic, Work-Hardening Sphere
Axially Symmetric Waves in Elastic Rods
Vibrations and Waves in Elastic Bars of Rectangular Cross Section
Subharmonic Oscillations of a Pendulum
Plane-Stress Unloading Waves Emanating From a Suddenly Punched Hole in a Stretched Elastic Plate
Plastic-Wave Propagation Effects in Transverse Impact of Membranes
Motion and Loading of a Hinged Ramp Which Supports a Sliding Mass
An Analytical Method for Locating the Burmester Points for Five Infinitesimally Separated Positions of the Coupler Plane of a Four-Bar Mechanism
Steady-State Undamped Vibrations of a Class of Non-linear Discrete Systems
A Unified Criterion for the Degree of Constraint of Plain Kinematic Chains
Approximate Synthesis of Spatial Linkages
Thermal Stresses Due to Disturbance of Uniform Heat Flow by an Insulated Ovaloid Hole
Sinusoidal Excitation of a System With Bilinear Hysteresis
Forced Oscillations of a Semi-Infinite Rod Exhibiting Weak Bilinear Hysteresis
Random Excitation of a System With Bilinear Hysteresis
Vibrations of Elastic Sandwich Cylindrical Shells
Free, Transverse Vibrations of a Solid Elastic Mass in an Infinitely Long, Rigid, Circular-Cylindrical Tank
Free Vibration of Continuous Skin-Stringer Panels
A Class of Nonlinear Axisymmetric Plate Problems
Flexural Stress Waves in an Infinite Elastic Plate Due to a Suddenly Applied Concentrated Transverse Load
Propagation of Axisymmetric Waves in an Unlimited Elastic Shell
Plastic Analysis of Circular Conical Shells
Elastic Half Plane Subjected to Surface Tractions With Random Magnitude or Separation
Response of an Elastic Half-Space to a Moving Blast Wave
The Penetration of Hard-Steel Spheres Into Plane Metal Surfaces
Stress Distributions Analyzed in Bispherical Co-Ordinates
Elastic Plastic Bending of Curved Bars of Constant and Variable Thickness

BRIEF NOTES

Buckling and Deflection of Isosceles-Triangular Plates
The Creep Deflection of a Rivet in Double Shear
Torsion of Prismatical Rods With Isosceles-Triangle Cross Sections
Buckling of a Beam on a Number of Elastic Restraints
Second Approximation for Buckling Loads
Method of Numerical Evaluation of a Large Determinant
On the Griffith-Irwin Fracture Theory
On the Flexure of Plastic Plates
Induced Velocities in Two-Dimensional Cascade Theory
Relation Between Stress Concentration and Boundary Displacement
Bending of an Isotropic Triangular Plate
Simplified Analysis of a Thrust-Augmentation System
Stress Concentration in a Rotating Disk
Stress-Displacement Relations for Shell Membranes in Oblique Co-Ordinates
Stability Problem of Shallow Translational Shells
Transient Response of Linear Viscoelastic Plates
Hydrodynamic Pocket Bearing
Graphical Investigation of Geometric Aspects of the Hertz Problem
Effect of Axial Constraint on Instability of Thin Circular Shells
Coupled Bending and Torsional Vibrations of Restrained Thin-Walled Beams
Energy Absorption of Aluminum Tubing
Vibrations of Thin Paraboloidal Shells of Revolution
The Lowest Natural Frequency of Elastic Arcs
An Accurate Expression for Gas-Pressure Drop
Flow of Liquid Metal Past a Porous Flat Plate

DISCUSSION **BOOK REVIEWS**

Also available in bound form:

Sections 1 and 2 of the 1960 ASME TRANSACTIONS

Section 1 contains the papers and discussions published in the 1960 issues of the JOURNALS OF ENGINEERING FOR POWER AND INDUSTRY.

SECTION 2 contains the 159 papers and discussions published in the 1960 issues of the JOURNALS OF HEAT TRANSFER AND BASIC ENGINEERING.

PRICES: **$16.00* for each section ($8.00* to ASME members)**
$38.00* for all three sections (19.00* to ASME members)

***Plus mailing charges if remittance does not accompany the order.**

THE AMERICAN SOCIETY OF MECHANICAL ENGINEERS

29 W. 39th Street **New York 18, N. Y.**